Editors

Deog Ki Hong

Chang-Hwan Lee

Hyun Kyu Lee

Dong-Pil Min

Tae-Sun Park

Mannque Rho

COMPACT STARS

The Quest for New States of Dense Matter

COMPACT STARS

This page is intentionally left blank

Proceedings of the KIAS-APCTP International Symposium
on Astro-Hadron Physics

COMPACT STARS

The Quest for New States of Dense Matter

Seoul, Korea 10–14 November 2003

Editors

Deog Ki Hong & Chang-Hwan Lee

Pusan National University, Korea

Hyun Kyu Lee

Hanyang University, Seoul, Korea

Dong-Pil Min

Seoul National University, Seoul, Korea

Tae-Sun Park

Korea Institute for Advanced Study, Seoul, Korea

Mannque Rho

CNRS, France

Korea Institute for Advanced Study, Seoul, Korea

Sponsors

Korea Institute for Advanced Study (KIAS)
Asia Pacific Center for Theoretical Physics (APCTP)
The DaeWoo Foundation

VOD and copies of talks are available at the workshop homepage http://conf.kias.re.kr/astro.htm
or directly from http://icprmr.snu.ac.kr/PHP/KIAS/200311/index.php.
This service is provided by the Information Center for Physics Research (ICPR).

World Scientific

NEW JERSEY • LONDON • SINGAPORE • BEIJING • SHANGHAI • HONG KONG • TAIPEI • CHENNAI

Published by

World Scientific Publishing Co. Pte. Ltd.

5 Toh Tuck Link, Singapore 596224

USA office: Suite 202, 1060 Main Street, River Edge, NJ 07661

UK office: 57 Shelton Street, Covent Garden, London WC2H 9HE

British Library Cataloguing-in-Publication Data
A catalogue record for this book is available from the British Library.

COMPACT STARS: THE QUEST FOR NEW STATES OF DENSE MATTER
Proceedings of the KIAS–APCTP International Symposium on Astro-Hadron Physics

ISBN 981-238-954-7

Printed in Singapore by World Scientific Printers (S) Pte Ltd

PREFACE

This is the third in the series of meetings in the field of "astro-hadron physics" held in Korea funded jointly by Asian Pacific Center for Theoretical Physics (APCTP) and Korea Institute for Advanced Study (KIAS). The first was held in 1997 funded by APCTP and the second in 2000 funded by KIAS. That KIAS has figured prominently in promoting this area of research is highly appropriate. Astro-hadron physics is a newly developing field in its embryonic stage whose primary objective is to unravel the structure of extremely compact astrophysical objects in terms of hadron physics studied in controlled terrestrial experiments and described exactly by QCD (quantum chromodynamics). This pioneering field offers the kind of break-through opportunity that KIAS — whose primary mission is to enhance Korea's basic science — is tailored to.

The first meeting in the series was mostly focused on hadronic matter under extreme conditions and the second on explosive astrophysical processes. This meeting — which is probably the last in the series to be held in KIAS — brings the two disciplines equally balanced and closer. This feat is made possible partly because there has been an impressive experimental as well as theoretical progress in the former giving us a clearer picture of what could be going on in dense and/or hot matter. To give an example, the landscape of QCD phase diagram which was barren in the second meeting, with hardly any empirical data points on it, is now richly populated by both theoretical and experimental points. Some of what seem puzzling in astrophysical observations will soon be studied in the terrestrial laboratories: The machines under construction will be able to create super-dense matter presumed to be present in the deep interior of compact stars. Indeed, heavy-ion experiments at such big accelerators as RHIC are exposing a surprisingly rich excitation spectrum in what was once thought to be a uniform quark-gluon plasma, hinting at a novel structure of the early Universe.

It is important to recognize that this is a new field of physics in which the Asian Pacific region has a potential to play the leading role. Given the

powerful machines soon to operate, JPARC in Japan and SIS 300 in Germany, with both of which Korean experimenters are closely associated, and combined with the early start in theoretical efforts, the field offers definite discovery potentials to the Korean physicists, an opportunity absolutely not to be missed. This KIAS-APCTP meeting is a first step towards that goal.

Deog Ki Hong and Mannque Rho

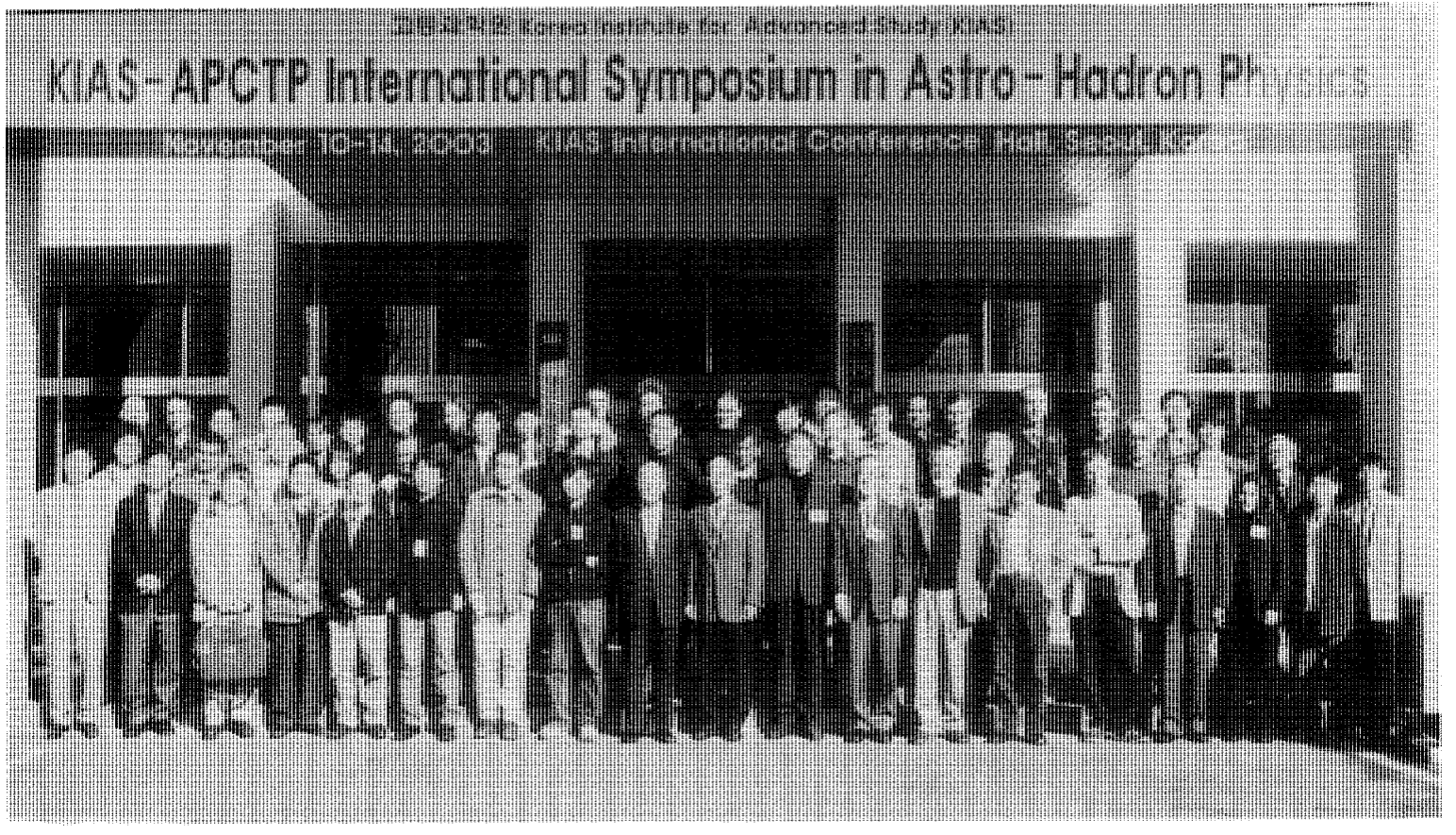
Copyright © Korea Institute for Advanced Study (KIAS)
KIAS-APCTP International Symposium in Astro-Hadron Ph
KIAS International Conference Hall

This page is intentionally left blank

CONTENTS

Neutrinos

LIST OF PARTICIPANTS

Hiroaki Abuki	*Yukawa Institute for Theoretical Physics, Japan* abuki@yukawa.kyoto-u.ac.jp
Deborah Aguilera	*University of Rostock, Germany* deborah@darss.mpg.uni-rostock.de
Batkhuu Battulga	*Research Center of Astronomy and Geophysics* batt@rcag.uri.mn
Gordon Baym	*University of Illinois, USA* gbaym@uiuc.edu
Wolfgang Bentz	*Tokai University, Japan* bentz@keyaki.cc.u-tokai.ac.jp
Jens Berdermann	*University of Rostock* jens.berdermann@stud.uni-rostock.de, Germany
David Blaschke	*University of Rostock, Germany* david.blaschke@physik.uni-rostock.de
Ignazio Bombaci	*University of Pisa, Italy* bombaci@df.unipi.it
Gerald Brown	*SUNY Stony Brook, USA* Ellen.Popenoe@sunysb.edu
Aurel Bulgac	*University of Washington, USA* bulgac@phys.washington.edu
Seung-Hyun Cha	*Seoul National University, Korea* oxtaca@hanmail.net
Eung Jin Chun	*Korea Institute for Advanced Study, Korea* ejchun@kias.re.kr
Jeremy Drake	*Smithsonian Astrophysical Observatory, USA* jdrake@dfa.harvard.edu
Hirotsugu Fujii	*University of Tokyo, Japan* hfujii@phys.c.u-tokyo.ac.jp

Norman Glendenning	*Lawrence Berkeley National Laboratory, USA* nkglendenning@lbl.gov
Masayasu Harada	*University of Nagoya, Japan* harada@eken.phys.nagoya-u.ac.jp
Michio Mashimoto	*Pusan National University, Korea* michioh@eken.phys.nagoya-u.ac.jp
Tetsuo Hatsuda	*University of Tokyo, Japan* hatsuda@phys.s.u-tokyo.ac.jp
Deog Ki Hong	*Pusan National University, Korea* dkhong@pusan.ac.kr
Seung-Woo Hong	*Sungkyunkwan University, Korea* swhong@skku.ac.kr
Soon-Tae Hong	*Ewha Womans University, Korea* soonhong@ewha.ac.kr
Tai Horikawa	*Tokai University, Japan* 3aspd004@keyaki.cc.u-tokai.ac.jp
Stephen Hsu	*University of Oregon, USA* hsu@duende.uoregon.edu
Chang Ho Hyun	*Institute of Basic Science, Sungkyunkwan Univertity, Korea* hch@color.skku.ac.kr
Batsaikhan Jamts	*Research Center of Astronomy and Geophysics* jamts_batsaikhan@yahoo.com
Takaaki Kajita	*ICRR, University of Tokyo, Japan* kajita@icrr.u-tokyo.ac.jp
David Kaplan	*Catech, USA* dlk@astro.caltech.edu
Joon-Il Kim	*Seoul National University, Korea* jikim@phya.snu.ac.kr
Sang Pyo Kim	*Kunsan National University, Korea* sangkim@kunsan.ac.kr
Soo-Bong Kim	*Seoul National University, Korea* sbkim@phya.snu.ac.kr
SunYoung Kim	*Sungkyunkwan University, Korea* ppurple98@hotmail.com

Masakiyo Kitazawa	*Kyoto University, Japan* masky@ruby.scphys.kyoto-u.ac.jp
Norimichi Kobayashi	*Tokai University, Japan* 3aspm010@keyaki.cc.u-tokai.ac.jp
Kuniharu Kubodera	*University of South Carolina, USA* kubodera@sc.edu
Shrinivas Kulkarni	*Caltech, USA* srk@anju.caltech.edu
Byung-Wuek Lee	*Seoul National University, Korea* lionkin7@phya.snu.ac.kr
Chang-Hwan Lee	*Pusan National University, Korea* clee@pusan.ac.kr
Eun Seon Lee	*SungKyunKwan University, Korea* silversool@hanmail.net
Hee-Jung Lee	*Pusan National University, Korea* hjlee@phya.snu.ac.kr
Hyun Kyu Lee	*Hanyang University, Korea* hklee@hepth.hanyang.ac.kr
Hyung Mok Lee	*Seoul National University, Korea* hmlee@astro.snu.ac.kr
Kang Seog Lee	*Chonnam National University, Korea* kslee@chonnam.chonnam.ac.kr
Sojin Lee	*SungKyunkwan University, Korea* woolralra@hanmail.net
Su Houng Lee	*Yonsei University, Korea* suhoung@phya.yonsei.ac.kr
Sungjun Lee	*Seoul National University, Korea* butucan@hotmail.com
Yeonwoo Lee	*Seoul National University, Korea* nuchy@hanmail.net
Dong-Pil Min	*Seoul National University, Korea* dpmin@phya.snu.ac.kr
Hirobumi Mineo	*National Taiwan University, Taiwan* mineo@phys.ntu.edu.tw

Jamil Muhammad	*Konkuk University, Korea* mjamil@konkuk.ac.kr
Dany Page	*I. Astronomia, UNAM, Mexico* page@astroscu.unam.mx
Byung-Yoon Park	*Chungnam University, Korea* bypark@chaosphys.cnu.ac.kr
Eun Seok Park	*Pusan National University, Korea* chaos5s@nate.com
Ha-Young Park	*Hanyang University, Korea* pinetaurus@hanmail.net
Jaehong Park	*Hanyang University, Korea* jaehong@ihanyang.ac.kr
Tae-Sun Park	*Korea Institute for Advanced Study, Korea* tspark@kias.re.kr
Madappa Prakash	*SUNY Stony Brook, USA* prakash@snare.physics.sunysb.edu
Krishna Rajagopal	*MIT, USA* krishna@ctp.mit.edu
Sanjay Reddy	*Los Alamos National Laboratory, USA* reddy@lanl.gov
Mannque Rho	*Saclay, France and KIAS, Korea* rho@spht.saclay.cea.fr
Chihiro Sasaki	*Nagoya University, Japan* sasaki@eken.phys.nagoya-u.ac.jp
Katsuhiko Sato	*Tokyo University, Japan* sato@phys.s.u-tokyo.ac.jp
Thomas Schaefer	*North Carolina State University, USA* thomas_schaefer@ncsu.edu
Ghy-Ryang Shin	*Andong University, Korea* gshin@andong.ac.kr
Byong-Uk Sohn	*Seoul National University, Korea* sohn@phya.snu.ac.kr
Young Jin Sohn	*Pusan National University, Korea* mega@top.phys.pusan.ac.kr

Chaejun Song	*Seoul National University, Korea* chaejun@phya.snu.ac.kr
Young-Ho Song	*Seoul National University, Korea* singer@phya.snu.ac.kr
Vikram Soni	*Nationl Physical Laboratory, India* v_soni@vsnl.com
Motoi Tachibana	*RIKEN, Japan* motoi@postman.riken.go.jp
Matsuura Taeko	*Tokyo University, Japan* matsuura@nt.phys.s.u-tokyo.ac.jp
Toshitaka Tatsumi	*Kyoto University, Japan* tatsumi@ruby@scphys.kyoto-u.ac.jp
Marten van Kerkwijk	*University of Toronto, Canada* mhvk@astro.utoronto.ca
Fridolin Weber	*San Diego State University, USA* fweber@sciences.sdsu.edu
Toshimitsu Yamazaki	*RIKEN, Japan* yamazaki@nucl.phys.s.u-tokyo.ac.jp
Shigehiro Yasui	*Osaka University, Japan* yasui@senri.rcnp.osaka-u.ac.jp
Kwang Yun Youm	*Hanyang University, Korea* jazzboys@hepth.hanyang.ac.kr

Compact Stars

This page is intentionally left blank

NEUTRON STARS AND THE PROPERTIES OF MATTER UNDER EXTREME CONDITIONS

GORDON BAYM

Department of Physics, University of Illinois at Urbana-Champaign
1110 W. Green Street, Urbana, IL, 61801 USA

This talk reviews our current understanding of the possible states of high-density matter found in the interiors of neutron stars – from the crust to the nuclear matter core, to exotic states including meson condensation, quark matter, and quark droplets – and discusses how observations of neutron stars, including masses and cooling, are beginning to confront theories of high density matter.

1. Introduction

Neutron stars are highly compact stellar objects with masses $\sim$ 1-2 $M_\odot$ (where $M_\odot$ is the mass of the sun), and radii of order 10 km. They are produced in the cores of stars that at the end of their evolution undergo gravitational collapse and subsequent supernova explosion. Neutron stars contain $\sim 10^{57}$ baryons, primarily in the form of the densest matter in the universe, with central densities approaching an order of magnitude beyond nuclear matter density, $\rho_0 \simeq 0.16$ baryons/fm$^3 \simeq 2.8 \times 10^{14}$ g/cm^3. Typical interior temperatures are relatively cold, $T \sim$ 1-100 KeV $\sim 10^7$-10^9 K, on a nuclear scale.[a]

Since the discovery of pulsars in the late 1960's, neutron stars have come to be recognized as the central engines in a variety of compact energetic astrophysical systems: isolated neutron stars (discussed here by Drake[9] and Kaplan[10]); compact accretion-powered binary x-ray sources (discussed here by van Kerkwijk,[11]) – including quasi-periodic oscillation sources (QPO's) – in which a neutron star orbits a more normal companion star; double neutron star binary pulsars; soft gamma-repeaters found in supernova remnants; and most likely gamma-ray burst sources (discussed here by Kulkarni[12]).

[a]Extensive reviews of the physics of neutron star interiors can be found in [1-8].

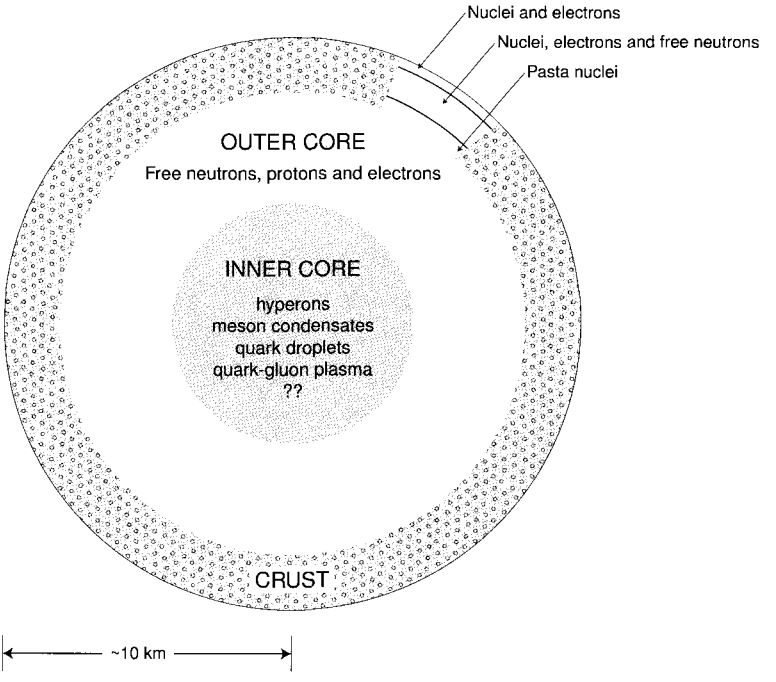

Figure 1. Schematic cross-section of a neutron star. Figure drawn by Michael Baym.

The ever-growing body of observational data on neutron stars, gathered with a wide variety of detectors from radio to gamma-ray, provides increasingly stringent constraints on theories of their constitution. Precision radio and optical timing measurements show that pulsars have remarkable long-term timing stability, and thus the neutron stars forming them must have reasonably thick rigid crusts anchoring stable magnetic fields. On the other hand, observed timing irregularities in pulsars – the occasional sudden speedups, or *glitches*, and smaller fluctuations in pulsar repetition frequencies – give clues to the internal structure of neutron stars, and support the idea that the interior is superfluid.[13] X-ray satellite observatories, from UHURU, first flown in 1970, which discovered x-ray binary sources, to the current Rossi XTE and Chandra satellites, have provided a wealth of information on the luminosity and thermal history of neutron stars – important probes of the states of matter in their interiors. [The first neutron star in fact discovered, that in Sco-X1, was detected in the x-ray by a balloon flight in 1962.]

Despite substantial work over the past half century, the nature of matter at the extreme densities in the cores of neutron stars remains uncertain. Many scenarios, from nuclear and hadronic matter, to exotic states involving Bose-Einstein condensation of pions or kaons, to bulk quark matter and quark matter in droplets, have been proposed. Ultrarelativistic heavy ion collision experiments at the Brookhaven Relativistic Heavy Ion Collider (RHIC), and in the coming years at the LHC in CERN, probe hot dense matter, from which one can gain hints of the properties of cold matter. However, the subject remains in a state of flux. These uncertainies in the properties of matter at densities much greater than ρ_0 are reflected in uncertainties in the maximum possible mass a neutron star, important in distinguishing a possible black hole from a neutron star by measurement of its mass. A better understanding of the possible states of matter in neutron star interiors can also enable us to infer whether an independent family of denser quark stars, composed essentially of quark matter, can exist. Astrophysical observations of neutron stars give valuable information about the possible states of dense matter and their properties. In this talk, I would like to review our present knowledge of neutron star interiors, and briefly discuss constraints on the matter they contain from observation.

2. Nuclei in the Crust

Neutron stars temperatures are low on the nuclear scale of MeV. In addition, nuclear processes in the early moments of a neutron star take place sufficiently rapidly compared with the cooling of the star that the matter essentially comes – via strong and electromagnetic, as well as weak, interactions – effectively into its ground state. The cross section of a neutron star interior is shown in Fig.1. The density, ρ, increases with increasing depth in the star. Beneath an atmosphere, compressed by gravity to less than 1 cm height, is a crust, typically $\sim$1 km thick, consisting, except in the molten outer tens of meters, of a lattice of bare nuclei immersed in a sea of degenerate electrons, as in a normal metal. The matter in the outer part of the crust is expected to be primarily ^{56}Fe, the ultimate end product of thermonuclear burning.

With increasing depth the electron Fermi energy rises, and at $\rho \gtrsim 8 \times 10^6 \mathrm{g/cm}^3$ electrons at the top of the Fermi sea begin to be captured by nuclei in the early moments of the star, converting protons into neutrons via $e^- + p \rightarrow n + \nu_e$. [The produced neutrino escapes the nascent neutron star.] The matter becomes more neutron rich and rearranges into a sequence, with

increasing density, of increasingly neutron rich nuclei, first ^{56}Fe, ^{62}Ni, and ^{64}Ni; then nuclei in the closed neutron shell, N=50: ^{84}Se, ^{82}Ge, ^{80}Zn, ^{78}Ni, and ^{76}Fe, followed by a sequence with N=82: ^{124}Mo, ^{122}Zr, ^{120}Sr, reaching ^{118}Kr at a density, $\rho_{drip} = 4.3 \times 10^{11}\mathrm{g/cm}^3 = 2 \times 10^{-4}\mathrm{fm}^{-3}$. Beyond this *neutron drip* point, the matter becomes so neutron rich that the continuum neutron states begin to be filled, and the still solid matter becomes permeated by a sea of free neutrons in addition to the sea of electrons. Pauli blocking of the final electron state prevents the nuclei that are deep in the crust, although unstable in the laboratory, from beta decaying via $n \rightarrow p + e^- + \bar{\nu}_e$. The particular nuclei present result from a competition between surface and Coulomb energies, plus shell structure. Near the drip line and above the results are, however, quite sensitive to uncertain spin-orbit effects and shell structure in highly neutron-rich nuclei (see discussion in [3]); future radioactive beam experiments will help to clarify this situation.

Above the neutron-drip point, the protons remain localized in nuclei in shells with $Z = 40$ or 50 as the matter continues to become more and more neutron rich. Then at about a density $\sim \rho_0/3$, Coulomb forces make spherical nuclei unstable, as in fission. The competition between surface and Coulomb energies leads to rather unusual structures, termed *pasta nuclei*, illustrated in Fig. 2. With increasing density the originally spherical nuclei (a) first become rod-like (b), and then laminar (c), with pure neutrons (the lighter regions in Fig. 2) filling the space between. At higher densities the system begins to turn "inside-out." The pure-neutron plates become thinner (d); eventually the neutrons form rods (e), and then spheres (f), with the regions between containing proton-rich matter.[14–16] Remarkably, over *half* the matter in the crust is in the form of these non-spherical configurations. Finally, at a density $\sim \rho_0/2$, the matter dissolves into a uniform liquid composed primarily of neutrons, plus some 5% protons and electrons, and a few muons. By charge neutrality the number density of electrons plus muons equals that of protons.

3. Nuclear Matter in the Interior

The high density matter in the liquid interior determines the gross structure of neutron stars, such as their mass density profiles, $\rho(r)$, radii, R, and moments of inertia, – as well as the maximum possible neutron star mass, M_{max}. The neutrino emissivity of the matter in the interior determines how rapidly neutron stars cool in their earlier years. Substantial progress has

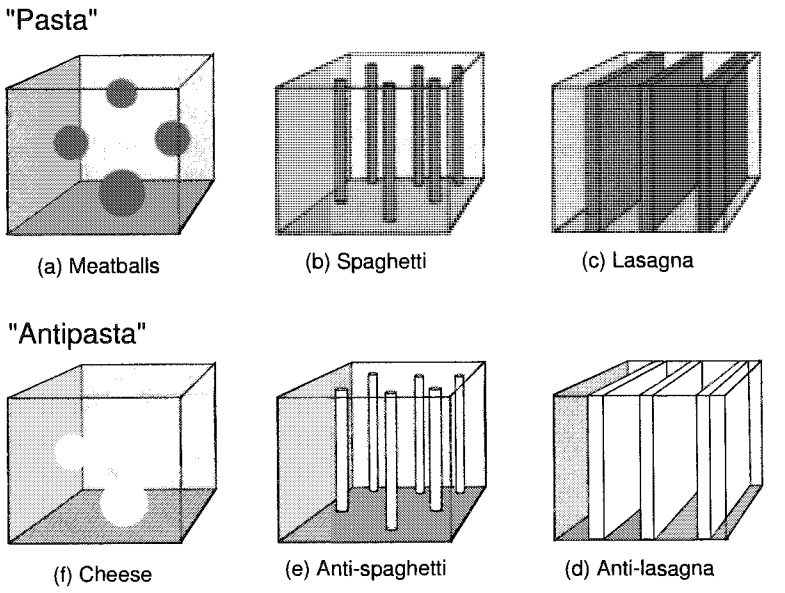

Figure 2. Sequence of nuclear shapes in the inner crust, from lowest densities (a) to highest (f). Figure kindly drawn and provided by F.K. Lamb.

been made in determining the properties the liquid near ρ_0 by extrapolation from laboratory nuclear physics. Considerable uncertainty remains however in pinning down the state of matter in the deep interiors. Various exotic scenarios, such as pion condensed and strangeness condensed matter, quark matter – including superconducting states, and strange quark matter (see [17,18]), have been proposed at higher densities.

Present calculations of the equation of state of the nuclear matter in neutron stars are based on nucleon-nucleon interactions extracted from pp and pn scattering experiments at energies below $\sim$ 300 MeV, constrained by fitting the properties of the deuteron. Examples of modern fits to the interactions are the Paris, Urbana-v_{14} (UV14), and Argonne-v_{18} (A18) two-body potentials, described, e.g., in [19,20]; the 18's refer to the number of different components, such as central, spin-orbit, etc., included in the interactions. With these potentials one proceeds to solve the many-body Schrödinger equation numerically via variational techniques to find the energy density as a function of baryon number.

While the two-body potentials give a reasonable binding energy of nuclear matter, the calculated equilibrium density turns out to be too high.

Similarly two-body potentials fail to produce sufficient binding of light nuclei ($A \leq 4$). The binding problems indicate that one must take into account intrinsic three-body forces acting between nucleons, such as the Brown-Green process in which two of the nucleons scatter becoming internally excited to an intermediate isobar state (Δ) while the third nucleon scatters from one of the isobars. The three-body forces must increase the binding in the neighborhood of ρ_0, but, to avoid overbinding nuclear matter, they must become repulsive at higher densities. This repulsion leads to a stiffening of the equation of state of neutron star matter at higher densities over that computed from two-body forces alone.

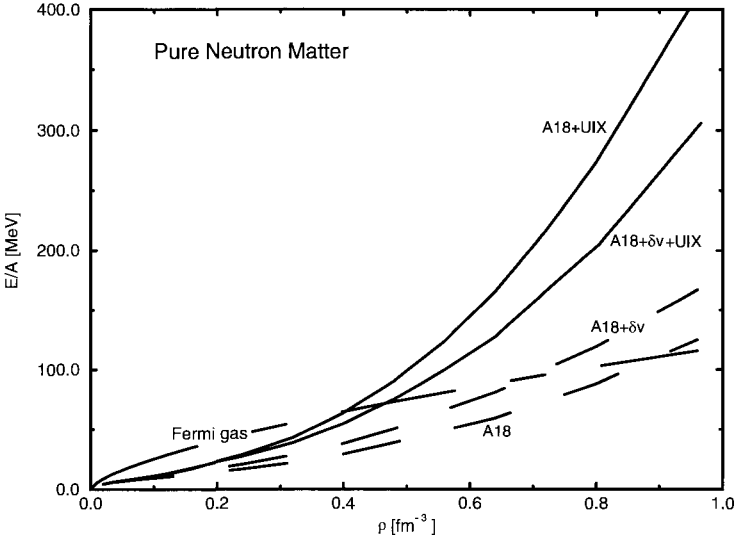

Figure 3. Energy per nucleon of pure neutron matter as a function of baryon density calculated with the Argonne A18 two body potential with and without the Urbana IX (UIX) three-body potential, and lowest order relativistic corrections, δv. From [20].

Figure 3 shows the energy per nucleon of neutron matter as a function of baryon density, calculated by Akmal et al.[20] with the Argonne A18 two-body potential, and Urbana UIX three-body potential, together with relativistic boost corrections (δv), accurate to order $(v/c)^2$. This equation of state is essentially the best available taking into account all two-nucleon data, and data from light nuclei. One sees here the stiffening of the equation of state from inclusion of three-body forces, slightly mitigated by relativistic effects.

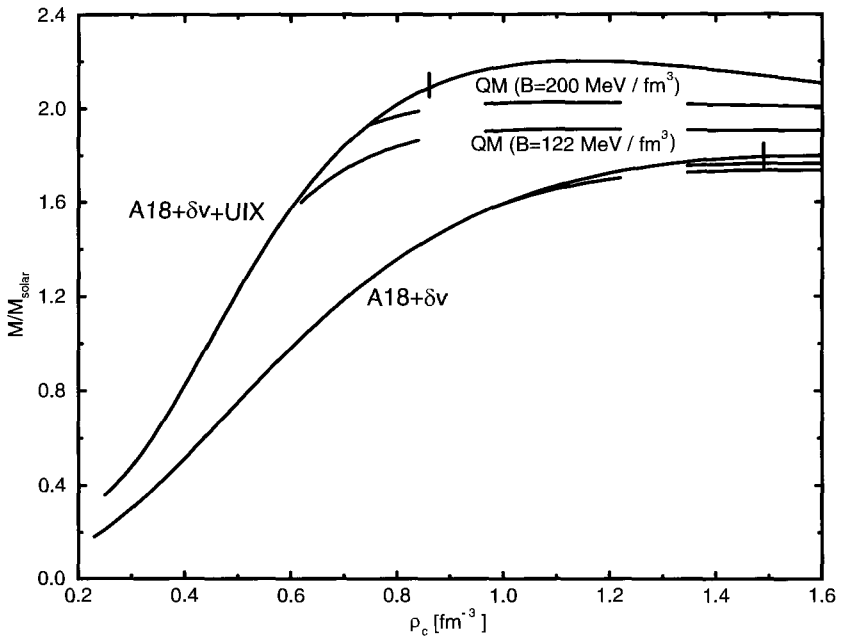

Figure 4. Neutron star mass vs. central density for the equations of state shown in Fig. 3, including beta equilibrium. The curves labelled QM show the effect of allowing for a transition to quark matter described in the simple MIT bag model, with bag constants $B = 122$ and 200 MeV/fm^3.

Figure 4 shows the gravitational mass vs. central density for families of stars calculated by integrating the TOV equation for the same equation of state as in Fig. 3, with beta equilibrium of the nucleons included. The maximum mass for the nucleonic equation of state, A18+δv+UIX, is $\sim 2.2 M_\odot$, consistent with observed neutron star masses. By constrast, without three-body forces, the maximum mass is $\sim 1.6 M_\odot$. The corresponding mass vs. radius of the families of models is shown in Fig. 5; the radii of these models vary little with mass, and are in the range 10-12 km, except at the extremes.

While an equation of state based on nucleon interactions alone gives an accurate description of neutron star matter in the neighborhood of ρ_0, it has several fundamental limitations. The first is that is does not take into account the rich variety of hadronic and quark degrees of freedom in the nuclear system that become important with increasing density. More generally, one should not expect beyond a few times ρ_0 that the forces between particles can be described in terms of static few-body potentials;

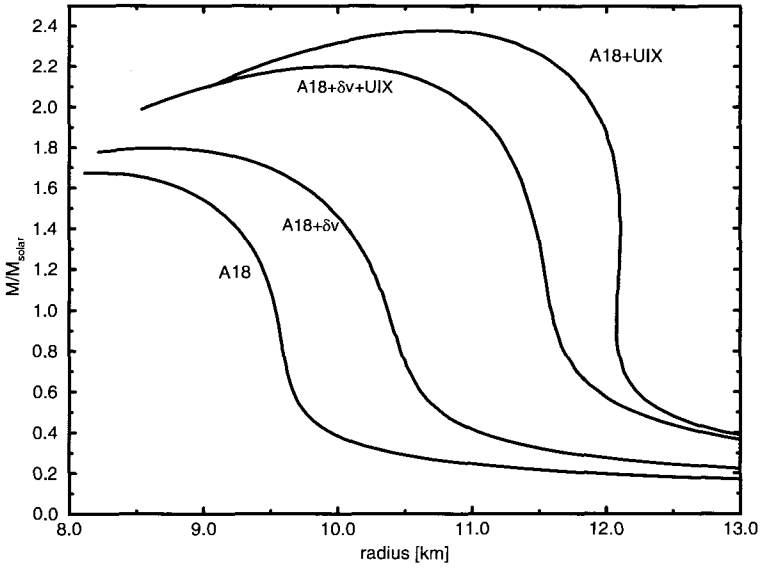

Figure 5. Mass vs. radius of neutron stars for the same models as in Fig. 4, .

nor can one continue to assume at higher densities that the system can even be described in terms of well-defined "asymptotic" laboratory particles. As one sees in Fig. 4, the density in the central cores rises well above ρ_0; equations of state and neutron star models based on consideration of nuclear matter alone should not be regarded as definitive.

Further hadronic degrees of freedom include Δ's, hyperons, and higher baryon resonances, as well as mesonic degrees of freedom. The Δ's can both be excited as real states in the matter at sufficiently high electron chemical potential, μ_e, e.g., via $n + e^- \rightarrow \Delta^-$, with the accompanying neutrino escaping from the star, and contribute indirectly through the three-body forces among nucleons. The major uncertainties in including them in the equation of state are their interactions with nucleons and with other Δ's, interactions that become increasingly important with increasing density.

Strange baryons, e.g., Λ and Σ, can similarly be excited via processes such as weak conversion of a neutron into a Λ, or electron capture, $e^- + n \rightarrow \Sigma^-$ Again lack of detailed knowledge of the interactions of hyperons prevents an accurate description of their effect on the equation of state.

4. Meson Condensates

The meson fields that mediate the low-energy interactions between baryons also become dynamical degrees of freedom with increasing density. In dense matter the meson fields can become macroscopically excited, leading to pion or kaon condensation. If mesons appear they macroscopically occupy the lowest available mode, i.e., form a condensate, as in ordinary Bose-Einstein condensation. The state of matter with condensed charged mesons would be superconducting. Such states in neutron stars would have enhanced neutrino emission and hence lead to more rapid cooling of the stars.

Charged pion condensation (reviewed in [21-24] would occur through a softening of a collective mode with the quantum numbers of the charged pion – an oscillation of the matter with spatially-varying nucleon spin (S=1) and isospin (I=1) – which at a critical density, ρ_π, goes to zero frequency at a critical wavevector, k_c, accompanied by the development of a macroscopic spatially-varying (p-wave) pion field, $\langle\pi\rangle \sim e^{i\mathbf{k}\cdot\mathbf{r}}$ – the condensate – of net negative charge. An analogous neutral pion condensed state can also be formed through softening of the neutron particle-hole collective mode; the neutral condensed state is characterized by a spatially-varying finite expectation value of the neutral pion field. Early estimates predicted the onset of charged pion condensation at $\rho_\pi \sim 2\rho_0$; however, these estimates are very sensitive to the strength of the effective neutron-hole proton repulsion in the I=1, S=1 channel (described by the Landau Fermi-liquid parameter g') which tends to suppress the condensation mechanism.

An alternative and perhaps more likely form of condensation involves spontaneous formation of kaons. The underlying chiral SU(3)⊗SU(3) symmetry of strong interactions implies that K mesons have an effective attractive interaction with nucleons, schematically of the form $H_{eff} \sim -\rho\bar{K}K$, where ρ is the baryon density and K is the K meson field, which acts as a density dependent term in the kaon effective mass, lowering its energy in the matter.[25] Extensive calculations by Brown and coworkers,[26,27] indicate that the energy of a K^- falls below μ_e at a critical density $\rho_K \sim$ 3-4 ρ_0; above this density the system should form a kaon or strangeness condensate with a macroscopic expectation value of the charged K field. Kaon condensation can lead to a substantial softening of the equation of state. Brown and Bethe[28] predict that in the presence of kaon condensation the maximum neutron star mass is only $\sim 1.5M_\odot$; stars that attempt to form with larger mass would collapse into black holes, a fate they predict for the core of SN1987A. Kaon condensation also enhances the neutrino

luminosity. The details of kaon condensation are, however, very sensitive to the interactions of K mesons in dense matter; see [29] for a critique.

5. Quark Matter and Quark Droplets

Nuclear matter is expected to undergo a transition to a quark-gluon plasma at sufficiently high baryon density. (Dynamics of the transition are discussed in [30].) A quark matter core in a neutron star would lead to enhanced neutrino luminosity and cooling. However, because of the well-known technical problems in implementing lattice gauge theory calculations at non-zero baryon density, we do not to date have a reliable estimate of the transition density at zero temperature or even compelling evidence that there is a sharp phase transition. Although estimates of the density range of the transition, $\sim 5 - 10\rho_0$, are possibly above the central density found in neutron stars models based on nuclear equations of state, the question of whether neutron stars can have quark matter cores remains open. Figure 4 shows effects of including quark matter cores, calculated in the simple MIT bag model, with bag parameter B =122 and 200 MeV/fm^3. In the absence of information about the equation of state at very high densities, the issue of whether a distinct family of quark stars with higher central densities than neutron stars can exist also remains open.

The transition from pure neutron matter to quark matter would occur at the density ρ_q, where the energy per baryon of quark matter crosses below that in neutron matter. However, the transition in matter in beta equilibrium, which contains the additional constraint of charge conservation, must proceed through a mixed phase, as Glendenning pointed out,[31] starting at density below the crossover density, ρ_q. The mixed phase should consist of large droplets of quark matter immersed in a sea of hadronic matter.[32,33] Formation of droplets is favored because the presence of s and d quarks allows a reduction in the electron density, and hence electron Fermi energy, and because it consequently permits an increase in the proton concentration in the hadronic phase. A typical droplet is estimated to have a radius of ~ 5 fm, and contain ~ 100 u, and ~ 300 d as well as s quarks, and thus having a net negative charge ~ 150. The onset of the droplet phase could, for favorable model parameters of the quark phase, be at a density as low as $\sim 2\rho_0$. At higher densities the quark droplets should go through a similar sequence of "pasta" phases as the nuclei in the inner crust. Such phases would be important since the quark dispersion relations in the phases (b)-(f), in the notation of Fig. 2, would not have a gap, and thus would also lead to enhanced neutrino cooling.

Quark matter at large density and low temperatures becomes a color superconductor.[17,34,35] Two pairing states with condensates antisymmetric in color and flavor and zero pair angular momentum are most energetically favorable: a two-flavor color-antitriplet 2SC or isoscalar state, in which only u and d quarks are paired; and for massless u, d, and s quarks, a color-flavor locked state[34] that breaks both color and flavor symmetry, containing, e.g., pairing of a red u quark with a blue s quark, a blue s quark with a green d quark, and a green d quark with a red u quark. The CFL state is the most stable for three flavors of massless quarks in the weak coupling limit, both at zero temperature, and near the critical temperature T_c.

The behaviors of the 2SC and CFL phases in rotating, magnetic neutron stars are quite different.[36] The isoscalar state, if a Type II superconductor, behaves analogously to that of superconducting protons in a neutron star, forming magnetic vortices in response to ordinary magnetic field with flux quantum $6\pi/\sqrt{3g^2+e^2}$, where g is the qcd coupling constant. In response to rotations, the state forms a very weak London magnetic field, $B \lesssim 1$ G, dominated by the gluonic component, as in a rotating superconductor.

On the other hand, the CFL phase forms U(1) vortices in response to rotation, as do superfluid neutrons, with a quantum of circulation, $3\pi/\mu$, where μ is the baryon chemical potential.[36] Such vortices could play a role[37] in the pinning and depinning of rotational vortices that give rise to pulsar glitches.[13] Vortices involving only a $U(1)_{em}$ phase of the gap are unstable[36]; however, the system does support stable magnetic vortices which involve the gradients of the full $SU(3)_c \times U(1)_{em}$ color structure.[38]

Even though the magnetic fields expected in neutron stars are below the estimated critical fields for flux expulsion, the flux diffusion times, of order $R_c^2/c^2\tau$, where R_c is the neutron star core radius, and τ is the microscopic scattering time, are of order millenia or longer.[36] Thus as with superconducting protons in neutron stars, magnetic fields in color superconducting matter would be frozen in an intermediate state composed of alternating regions of normal and superconducting material if the system is a Type I superconductor, or in a lattice of vortices in a Type II superconductor.

6. Neutron Star Masses

A general rule obeyed by families of neutron stars generated from a given equation of state is that the stiffer the equation of state, the higher is the maximum mass that a neutron star can have, but the lower is the central

density, ρ_c at the maximum mass. Lower central mass means that there is less room for exotic matter in the interior. The question then arises as to the extent that observations of neutron star masses place constraints on the equation of state.

Observations of millisecond binary radio pulsars, consisting of two orbiting neutron stars, have permitted accurate determinations of the masses of the neutron stars in them, as well as confirmed the existence of gravitational radiation; the masses lie in a relatively narrow interval, $\sim 1.35 \pm 0.04 M_\odot$,[39] a mass reminiscent of the Chandrasekhar core mass of the pre-supernova star. The newly discovered nearly in-plane binary neutron star system, J0737-3039, with masses of $1.34 M_\odot$ and $1.25 M_\odot$ is no exception.[40] If a mass of order $1.4 M_\odot$ were the maximum neutron star mass, then equations of state could allow for substantial exotica in the interior. For example, Brown and Bethe,[28] have substantial kaon condensation in their equation of state, with a corresponding maximum neutron star mass $\sim 1.5 M_\odot$.

The fact that the measured masses of neutron stars in binary neutron-star systems are tightly constrained does not mean that all neutron stars have such small masses; the constraint could arise from the narrow evolutionary track that allows the two neutron stars to remain bound after their predecessors underwent supernova explosions. Two measurements of late of neutron star masses in compact binary x-ray sources begin to call into question whether the maximum mass is indeed of order $1.4 M_\odot$. The first is that of the neutron star in the X-ray binary, Vela X-1, with mass deduced to lie in the range $1.86 \pm 0.16 M_\odot$.[41] As van Kirkwijk discusses,[11] the uncertainties in the measurement arise from understanding the dynamic behavior of the atmosphere of the B-supergiant companion star, HD 77581; while the reported mass, if confirmed, would rule out very soft equations of state, e.g., that of Bethe and Brown based on kaon condensation, the uncertainties in the determination do not allow one to make a definitive conclusion. The second measurement is that of the neutron star mass in the low mass x-ray binary, Cyg X-2, $1.78 \pm 0.23 M_\odot$.[42] [However, Titarchuk and Shaposhnikov[43] fit three x-ray bursts from this source with a lighter mass $\sim 1.4 M_\odot$.] Such higher masses in x-ray binaries would allow for some exotic matter to be present in neutron stars.

A very promising approach to measuring neutron star masses is through understanding the origins of QPO's, the KHz quasiperiodic oscillations observed in some by now 25 low mass x-ray binary neutron star systems.[44,45] The power spectra of these sources are characterized by pairs of peaks with a nearly constant frequency difference, $\Delta\nu$, e.g., in 4U1820-30 the upper

frequency is $\nu_2 \sim 1070$ Hz, with $\Delta\nu \simeq 280$ Hz[46]; as confirmed by burst oscillations,[47] e.g., in SAX J1808.4-3658,[48] $\Delta\nu$ is either the spin frequency of the neutron star, ν_{spin}, or $\nu_{spin}/2$.

In these objects, mass accreted from the companion star works its way through a disk down onto the neutron star. The high frequency QPO's arise from gas orbiting very close to the neutron star surface, where general relativistic effects are crucial. The key is that the innermost stable orbit that a particle circling a neutron star can have is at a radius $R_{\rm ISCO} = 6MG/c^2 = 3R_{\rm Schwarzschild}$. If, as is strongly suggested by detailed models,[47,49] ν_2 is an orbital frequency, at orbital radius r, so that $\nu_2 = (MG/r^3)^{1/2}$, then one finds powerful constraints on the neutron star mass and radius, R: from $r \geq 6MG/c^2$ and $r > R$, one readily finds that $M \leq c^3/12\sqrt{6}\,\pi\nu_2 G \simeq 2.19 M_\odot/\nu_2({\rm KHz})$ and $R \leq c/2\sqrt{6}\,\pi\nu_2 \sim 19.5\,{\rm km}/\nu_2({\rm KHz})$. Indeed, if plausibly $r = R_{\rm ISCO}$, then measurement of ν_2 yields a precise mass measurement; $M = c^3/12\sqrt{6}\,\pi G\nu_2$. For 4U1820-30 one would thus deduce a mass $\sim 2.0 M_\odot$. Such a mass can only come from a very stiff equation of state, which would not only exclude exotica such as quark matter in the cores of neutron stars, but would begin to confront even the best available nuclear equations of state, cf. Fig. 4, which give a maximum mass $\sim 2.2 M_\odot$.

7. Neutron Star Cooling

One of the potentially most powerful probes of the matter in neutron stars is x-ray measurement of neutron star surface luminosity and temperatures. When correlated with the age of the neutron stars, this information enables one to construct a cooling history of neutron stars.[50–52] In general, exotic states of matter tend to cool faster than nuclear matter cools via the modified URCA process. It is presently too early to tell whether the x-ray luminosity data indicate the presence of such exotic matter in neutron stars. Whether thermal radiation from the neutron star surface is being detected is uncertain; indeed effects of neutron star atmospheres and surface emissivity in the presence of strong magnetic fields need to be better understood. Also, significant uncertainties remain in the microscopics of the cooling processes. Observations also need to be compared with cooling scenarios for a range of neutrons star masses.[53] Future x-ray imaging and spectra should make it eventually possible to carry out a detailed comparison between cooling scenarios and observations, and thus to learn about the existence and properties of exotic matter in the cores of neutron stars.

Acknowledgments

I am very grateful to my colleagues K. Iida, F.K. Lamb, V.R. Pandharipande, and C.J. Pethick for many useful discussions. This work was supported in part by U.S. National Science Foundation Grant PHY00-98353.

References

1. G. Baym, and C. Pethick, *Ann. Rev. Nucl. Sci.* **25** (1975) 27.
2. G. Baym, and C. Pethick, *Ann. Rev. Astron. Astrophys.* **17** (1979) 415.
3. C. J. Pethick and D. G. Ravenhall, *Ann. Rev. Nucl. Part. Sci.* **45**, 429 (1995).
4. *The lives of neutron stars*, M. A. Alpar, Ü. Kiziloğlu, and J. van Paradijs, eds. (Kluwer, Dordrecht, 1995).
5. C. J. Pethick, A. Akmal, V. R. Pandharipande, and D. G. Ravenhall, in *Proc. 19^{th} Texas Symp. on Rel. Astrophys. and Cosmology*, Paris, Dec. 14-18, 1998.
6. H. Heiselberg and V.R. Pandharipande, *Ann. Rev. Nucl. Particle Sci.* **50**, 481 (2000).
7. N. Glendenning, *Compact Stars: Nuclear Physics, Particle Physics, and General Relativity*, 2^{nd} ed. (Springer Verlag, 2000).
8. F. Weber, *Pulsars as Astrophysical Laboratories for Nuclear and Particle Physics* (Institute of Physics, 1999).
9. J. Drake, these proceedings.
10. D. Kaplan, these proceedings.
11. M.H. van Kerkwijk, these proceedings.
12. S. Kulkarni, these proceedings.
13. G. Baym, R. Epstein and B. Link, *Physica* **B178** (1992) 1.
14. C. Lorenz, D. G. Ravenhall, and C. J. Pethick, *Phys. Rev. Lett.* **70** (1993) 379.
15. K. Oyamatsu, Nucl. Phys. **A561** (1993) 431.
16. G. Watanabe, K. Iida, and K. Sato, it Nucl. Phys. **A676**, 455 (2000), **A687**, 512 (2001). G. Watanabe, K. Sato, K. Yasuoka, and T. Ebisuzaki, nucl-th/0311083.
17. K. Rajagopal, these proceedings.
18. W. Bentz; I. Bombaci; M. Katazawa; V. Soni; M. Tachibana; and F. Weber, these proceedings.
19. R. B. Wiringa, V. Fiks, and A. Fabrocini, *Phys. Rev.* **C38** (1988) 1010.
20. A. Akmal, V.R. Pandharipande, and D.G. Ravenhall, *Phys. Rev.* **C58**, 1804 (1998).
21. G.E. Brown and W. Weise, *Phys. Rept.* **27** (1976) 1.
22. A.B. Migdal, *Rev. Mod. Phys* **50** (1978) 107.
23. G. Baym, in *Nuclear Physics with Heavy Ions and Mesons, Les Houches session XXX*, R. Balian, M. Rho, and G. Ripka, eds. (North-Holland Publ. Co., Amsterdam, 1978), p. 745.
24. G. Baym and D. K. Campbell, in *Mesons in Nuclei*, v. 3, M. Rho and D. Wilkinson, eds. (North-Holland Publ. Co., Amsterdam, 1979) p. 1031.
25. D. B. Kaplan and A. E. Nelson, *Phys. Lett.* **B175** (1986) 57.

26. G. E. Brown, K. Kubodera, M. Rho and, *Phys. Lett.* **B291** (1992) 355.
27. G. E. Brown, C.-H. Lee, M. Rho, and V. Thorsson, Nucl. Phys. **A567** (1994) 937; C.-H. Lee, G. E. Brown, and M. Rho, *Phys. Lett.* **B335** (1994) 266.
28. G. E. Brown and H. A. Bethe, *Astrophys. J.* **423** (1994) 659; H. Bethe, and G.E. Brown, *Astrophys. J.* **506**, 780 (1998).
29. V. R. Pandharipande, C. J. Pethick, and V. Thorsson, *Phys. Rev. Lett.* **75**, 4567 (1995).
30. N. Glendenning, these proceedings.
31. N. Glendenning, *Phys. Rev.* **D46** (1992) 1274.
32. H. Heiselberg, C. J. Pethick, and E. F. Staubo, *Phys. Rev. Lett.* **70** (1993) 1355.
33. V. R. Pandharipande and E. F. Staubo, in *Int. Conf. on Astrophys.*, B. Sinha, ed. (World Scientific, Singapore, 1993).
34. K. Rajagopal, *Nucl. Phys.* **A661** 150c, (1999); M. Alford, K. Rajagopal, and F. Wilczek, *Nucl. Phys.* **B537**, 443 (1999).
35. K. Iida and G. Baym, *Phys. Rev.* **D63**, 074018 (2001), Erratum: **D66** (2002) 059903(E); **D65**, 014022 (2001).
36. K. Iida and G. Baym, *Phys. Rev.* **D66**, 014015 (2002).
37. M. Alford, J.A. Bowers, and K. Rajagopal, Phys. Rev. D **63**, 074016 (2001).
38. I. Giannakis and H.-c. Ren, *Nucl. Phys.* **B669**, 462 (2003).
39. S.E. Thorsett and D. Chakrabarty, *Astrophys. J.* **512**, 288 (1999).
40. A.G. Lyne et al., *Science* **303**, 1153 (2004).
41. O. Barziv, L. Kaper, M. H. van Kerkwijk, J. H. Telting, and J. Van Paradijs, *Astron. Astrophys.* **377** 925 (2001).
42. J.A. Orosz, and E. Kuulkers, *MNRAS* **305**, 132 (1999).
43. L. Titarchuk and N. Shaposhnikov, *Astrophys. J.* **570**, L25 (2002).
44. M. van der Klis, *Ann. Rev. Astron. Astrophys.* **38**, 717 (2000).
45. F.K. Lamb, in *X-Ray Binaries and Gamma-Ray Bursts*, ed. E.P.J. van den Heuvel (Astron. Soc. Pacific, San Francisco, 2002).
46. W. Zhang, A.P. Smale,, T.E. Strohmayer, and J.H. Swank, *Astrophys. J.* **500**, L171 (1998).
47. F.K. Lamb and M.C. Miller, astro-ph/0308179.
48. D. Chakrabarty et al., *Nature* **424**, 42 (2003); R.A. Wijnands et al., *Nature* **424**, 44 (2003)
49. M.C. Miller, F.K. Lamb, and D. Psaltis, *Astrophys. J.* **508**, 791 (1998); *Nucl. Phys.* **B69**, 123 (1999).
50. C. J. Pethick, *Rev. Mod. Phys.* **64**, 1133 (1992).
51. D. Page E. and Baron, *Astrophys. J.* **354**, L17 (1990).
52. D. Page; D. Aguilera; J. Bendermann; M. Prakash; and S. Reddy, these proceedings.
53. D.G. Yakovlev and P. Haensel, *Astron. Astrophys.* **407**, 259 (2003).

QUARK DECONFINEMENT IN COMPACT STARS AND ASTROPHYSICAL IMPLICATIONS

IGNAZIO BOMBACI

Dipartimento di Fisica "E. Fermi", Università di Pisa
& INFN, Sezione di Pisa,
via Buonarroti, 2,
I-56127, Pisa, Italy
E-mail: bombaci@df.unipi.it

We explore some of the astrophysical consequences of the hadron-quark phase transition in compact stars. In particular, we describe a new model which is able to explain how a gamma-ray burst (GRB) can take place days or years after a supernova explosion. We show that above a threshold value of the gravitational mass a pure hadronic star ("neutron star") is metastable to the conversion into a quark star (hybrid star or strange star), *i.e.* a star made at least in part of deconfined quark matter. The stellar conversion process can be delayed if finite size effects at the interface between hadronic and deconfined quark matter phases are taken into account. A huge amount of energy, on the order of $10^{52} - 10^{53}$ ergs, is released during the conversion process and can produce a powerful gamma-ray burst. The delay between the supernova explosion generating the metastable neutron star and the new collapse can explain the delay inferred in GRB 990705 and in GRB 011211. Next, we explore the consequences of the metastability of "massive" neutron stars and of the existence of stable compact quark stars on the concept of limiting mass of compact stars.

1. The delayed Supernova–GRB connection

A mounting number of observational data [1,2,3,4,5,6,7] suggest a clear connection between supernova (SN) explosions and long-duration Gamma Ray Bursts (GRBs). In particular, the detection of X-ray spectral features in the X-ray afterglow of several GRBs, has given evidence for a possible time delay between the SN explosion and the associated GRB. In the case of GRB990705, GRB020813, and GRB011211, it has been possible to estimate the time delay between the two events. For GRB990705 the supernova explosion is evaluated to have occurred a few years before the GRB[2,8], a few months before the burst in the case of GRB020813 (ref.[7]), while for GRB011211 about four days before the burst[5].

These findings demand for a two-step explosion mechanism. The first event, in this scenario, is the supernova explosion which forms a compact stellar remnant, *i.e.* a neutron star (NS); the second catastrophic event is associated with the NS and it is the energy source for the observed GRB. These new observational data, and the two-step scenario outlined above, poses severe problems for most of the current theoretical models for the central energy source (the so-called *central engine*) of GRBs. The main difficulty of all these models is to understand the origin of the second "explosion", and to explain the long time delay between the two events.

In the so-called *supranova* model[9] for GRBs the second catastrophic event is the collapse to a black hole of a *supramassive* neutron star, *i.e.* a fast rotating NS with a baryonic mass M_B above the maximum baryonic mass $M_{B,max}$ for non-rotating configurations. In this model, the time delay between the SN explosion and the GRB is equal to the time needed by the fast rotating newly formed neutron star to get rid of angular momentum and to reach the limit for instability against quasi-radial modes where the collapse to a black hole occurs[10]. The supranova model needs a fine tuning in the initial spin period P_{in} and baryonic stellar mass $M_{B,in}$ to produce a supramassive neutron star that can be stabilized by rotation up to a few years. For example[10], if $P_{in} \geq 1.5$ ms, then the newborn supramassive neutron star must be formed within $\sim 0.03 M_\odot$ above $M_{B,max}$.

2. The nature of Neutron Stars: Hadronic or Quark Stars?

In a simplistic and conservative picture the core of a neutron star is modeled as a uniform fluid of neutron rich nuclear matter in equilibrium with respect to the weak interaction (β-stable nuclear matter). However, due to the large value of the stellar central density and to the rapid increase of the nucleon chemical potentials with density, hyperons (Λ, Σ^-, Σ^0, Σ^+, Ξ^- and Ξ^0 particles) are expected to appear in the inner core of the star. Other *exotic* phases of hadronic matter such as a Bose-Einstein condensate of negative pion (π^-) or negative kaon (K^-) could be present in the inner part of the star.

Quantum Chromodynamics (QCD) predicts a phase transition from hadronic matter to a deconfined quark phase to occur at a density of a few times nuclear matter saturation density. Consequently, the core of the more massive neutron stars is one of the best candidates in the Universe where such deconfined phase of quark matter (QM) could be found. Since β-stable hadronic matter posses two conserved "charges" (*i.e.*, electric

charge and baryon number) the quark-deconfinement phase transition proceeds through a mixed phase over a finite range of pressures and densities according to the Gibbs' criterion for phase equilibrium[11]. At the onset of the mixed phase, quark matter droplets form a Coulomb lattice embedded in a sea of hadrons and in a roughly uniform sea of electrons and muons. As the pressure increases various geometrical shapes (rods, plates) of the less abundant phase immersed in the dominant one are expected. Finally the system turns into uniform quark matter at the highest pressure of the mixed phase[12]. Compact stars which possess a "quark matter core" either as a mixed phase of deconfined quarks and hadrons or as a pure quark matter phase are called[13] *Hybrid Neutron Stars* or shortly *Hybrid Stars* (HyS). In the following of this paper, the more *conventional* neutron stars in which no fraction of quark matter is present, will be referred to as *pure Hadronic Stars* (HS).

A complementary manifestation of quark matter in compact stars is the possible existence of a new family of compact stars consisting completely of a deconfined mixture of *up* (u), *down* (d) and *strange* (s) quarks (together with an appropriate number of electrons to guarantee electrical neutrality) satisfying the so-called Bodmer–Witten hypothesis[14,15] (see also ref.[16]). Such compact stars have been called *strange quark stars* or shortly *strange stars*[17,18] (SS) and their constituent matter[19,20] as *strange quark matter* (SQM). Presently there is no unambiguous proof about the existence of strange stars, however, a sizable amount of observational data collected by the new generations of X-ray satellites, is providing a growing body of evidence for their possible existence[21,22,23,24,25,26].

Present accurate determinations of compact star masses in radio pulsar binaries[27] permit to rule out only *extremely soft* EOS, *i.e.* those giving M_{max} less than about 1.45 $M_{\odot}$. However, in at least two accreting X-ray binaries it has been found evidence for compact stars with higher masses. The first of these star is Vela X-1, with a reported mass[28] $1.88 \pm 0.13 M_{\odot}$, the second is Cygnus X-2, with a reported mass[29] of $1.78 \pm 0.23 M_{\odot}$. Unfortunately, mass determinations in X-ray binaries are affected by large uncertainties[30], therefore the previous quoted "high mass values" should always be handled with care.

In this paper (see ref.s[31,32] for more details), we study the effects of the hadron-quark deconfinement phase transition in stellar compact objects. We show that when finite size effects at the interface between the quark- and the hadron-phase are taken into account, pure Hadronic Stars, above a threshold value of the central pressure (gravitational mass), are metastable

to the *decay* (*conversion*) to hybrid neutron stars or to strange stars (depending on the properties of EOS for quark matter). The *mean-life time* of the metastable stellar configuration is related to the quantum nucleation time to form a drop of quark matter in the stellar center, and dramatically depends on the value of the stellar central pressure. The *delayed* stellar conversion liberates an enormous amount of energy, in the range of 0.5–1.7$\times 10^{53}$ erg, which could power a GRB. This model[31] explains the SN–GRB association and in particular the long time delay inferred for GRB990705, GRB020813, and GRB011211. Also, we explore the consequences of the metastability of "massive" pure Hadronic Stars and the existence of stable compact "quark" stars (hybrid neutron stars or strange stars) on the concept of limiting mass of compact stars[32].

3. Quantum nucleation of quark matter in hadronic stars

In the following, we assume that the compact star survives the early stages of its evolution as a pure hadronic star, and we study quark matter nucleation in cold (T = 0) neutrino-free hadronic matter.

In bulk matter the quark-hadron mixed phase begins at the *static transition point* defined according to the Gibbs' criterion for phase equilibrium

$$\mu_H = \mu_Q \equiv \mu_0\,, \qquad P_H(\mu_0) = P_Q(\mu_0) \equiv P_0 \tag{1}$$

where

$$\mu_H = \frac{\varepsilon_H + P_H}{n_{b,H}}\,, \qquad \mu_Q = \frac{\varepsilon_Q + P_Q}{n_{b,Q}} \tag{2}$$

are the chemical potentials for the hadron and quark phase respectively, ε_H (ε_Q), P_H (P_Q) and $n_{b,H}$ ($n_{b,Q}$) denote respectively the total (*i.e.*, including leptonic contributions) energy density, the total pressure and baryon number density for the hadron (quark) phase, in the case of cold matter.

Let us now consider the more realistic situation in which one takes into account the energy cost due to finite size effects in creating a drop of deconfined quark matter in the hadronic environment. As a consequence of these effects, the formation of a critical-size drop of QM is not immediate and it is necessary to have an overpressure $\Delta P = P - P_0$ with respect to the static transition point. Thus, above P_0, hadronic matter is in a metastable state, and the formation of a real drop of quark matter occurs via a quantum nucleation mechanism. A sub-critical (virtual) droplet of deconfined quark matter moves back and forth in the potential energy well separating the two matter phases (see discussion below) on a time scale

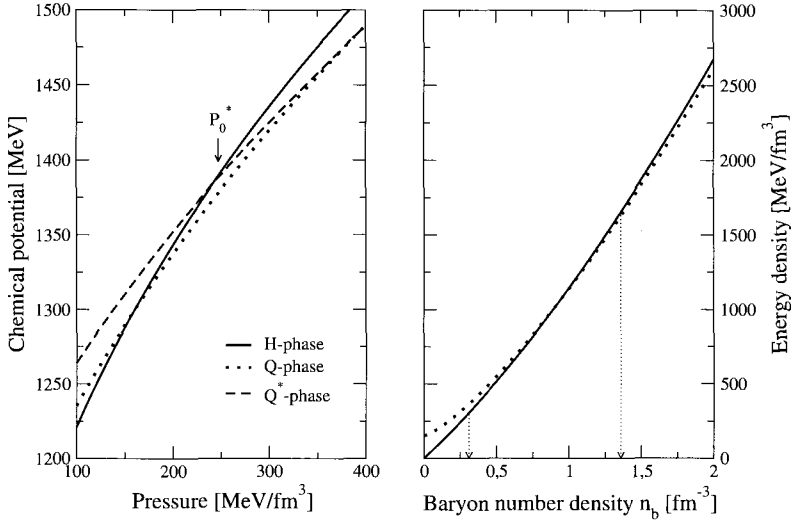

Figure 1. Chemical potentials of the three phases of matter (H, Q, and Q*), as defined by Eq. (2) as a function of the total pressure (left panel); and energy density of the H- and Q-phase as a function of the baryon number density (right panel). The hadronic phase is described with the GM3 model whereas for the Q and Q* phases is employed the MIT-like bag model with $m_s = 150$ MeV, $B = 152.45$ MeV/fm^3 and $\alpha_s = 0$. The vertical lines arrows on the right panel indicate the beginning and the end of the mixed hadron-quark phase defined according to the Gibbs criterion for phase equilibrium. On the left panel P_0^* denotes the static transition point.

$\nu_0^{-1} \sim 10^{-23}$ seconds, which is set by the strong interactions. This time scale is many orders of magnitude shorter than the typical time scale for the weak interactions, therefore quark flavor must be conserved during the deconfinement transition. We will refer to this form of deconfined matter, in which the flavor content is equal to that of the β-stable hadronic system at the same pressure, as the Q*-phase. Soon afterwards a critical size drop of quark matter is formed the weak interactions will have enough time to act, changing the quark flavor fraction of the deconfined droplet to lower its energy, and a droplet of β-stable SQM is formed (hereafter the Q-phase).

We have adopted rather common models for describing both the hadronic and the quark phase of dense matter. For the hadronic phase we used models which are based on a relativistic lagrangian of hadrons interacting via the exchange of sigma, rho and omega mesons. The parameters adopted are the standard ones[33]. Hereafter, we refer to this model as the GM equation of state (EOS). For the quark phase we have adopted

a phenomenological EOS (see *e.g.* ref.[19]) which is based on the MIT bag model for hadrons. The parameters here are: the mass m_s of the strange quark, the so-called pressure of the vacuum B (bag constant) and the QCD structure constant α_s. For all the quark matter model used in the present work, we take $m_u = m_d = 0$, $m_s = 150$ MeV and $\alpha_s = 0$.

In the left panel of Fig. 1, we show the chemical potentials, defined according to Eq. (2), as a function of the total pressure for the three phases of matter (H, Q*, and Q) discussed above. In the right panel of the same figure, we plot the energy densities for the H- and Q*-phase as a function of the corresponding baryon number densities. Both panels in Fig. 1 are relative to the GM3 model for the EOS for the H-phase and to the MIT bag model EOS for the Q and Q* phases with $B = 152.45$ MeV/fm^3.

To calculate the nucleation rate of quark matter in the hadronic medium we use the Lifshitz–Kagan quantum nucleation theory[34] in the relativistic form given by Iida & Sato[35]. The QM droplet is supposed to be a sphere of radius R and its quantum fluctuations are described by the lagrangian

$$L(R,\dot{R}) = -M(R)c^2\sqrt{1-(\dot{R}/c)^2} + M(R)c^2 - U(R)\,, \tag{3}$$

where $M(R)$ is the effective mass of the QM droplet, and $U(R)$ its potential energy. Within the Lifshitz–Kagan quantum nucleation theory, one assumes that the phase boundary (*i.e.* the droplet surface) moves slowly compared to the high sound velocity of the medium ($\dot{R} << v_s \sim c$). Thus the number density of each phase adjust adiabatically to the fluctuations of the droplet radius, and the system retains pressure equilibrium between the two phases. Thus, the droplet effective mass is given by[34,35]

$$M(R) = 4\pi\rho_H\Big(1-\frac{n_{b,Q*}}{n_{b,H}}\Big)^2 R^3\,, \tag{4}$$

ρ_H being the hadronic mass density, $n_{b,H}$ and $n_{b,Q*}$ are the baryonic number densities at a same pressure in the hadronic and Q*-phase, respectively. The potential energy is given by[34,35]

$$U(R) = \frac{4}{3}\pi R^3 n_{b,Q*}(\mu_{Q*} - \mu_H) + 4\pi\sigma R^2\,, \tag{5}$$

where μ_H and μ_{Q*} are the hadronic and quark chemical potentials at a fixed pressure P and σ is the surface tension for the surface separating the quark phase from the hadronic phase. The value of the surface tension σ is poorly known, and typical values used in the literature[12,35] range within 10–50 MeV/fm^2.

For sake of simplicity and to make our present discussion more trasparent, in the previous expression (5) for the droplet potential energy, we neglected the terms connected with the electrostatic energy and with the so-called curvature energy. The inclusion of these terms will not modifies the conclusions of the present study[35,32].

The process of formation of a bubble having a critical radius, can be computed using a semiclassical approximation. The procedure is rather straightforward. First one computes, using the well known Wentzel–Kramers–Brillouin (WKB) approximation, the ground state energy E_0 and the oscillation frequency ν_0 of the virtual QM drop in the potential well $U(R)$. Then it is possible to calculate in a relativistic framework the probability of tunneling as[35]

$$p_0 = \exp\left[-\frac{A(E_0)}{\hbar}\right] \tag{6}$$

where A is the action under the potential barrier

$$A(E) = \frac{2}{c}\int_{R_-}^{R_+} \left\{[2M(R)c^2 + E - U(R)] \times [U(R) - E]\right\}^{1/2} dR\,, \tag{7}$$

$R_\pm$ being the classical turning points.

The nucleation time is then equal to

$$\tau = (\nu_0 p_0 N_c)^{-1}\,, \tag{8}$$

where N_c is the number of virtual centers of droplet formation in the innermost region of the star. Following the simple estimate given in ref.[35], we take $N_c = 10^{48}$. The uncertainty in the value of N_c is expected to be within one or two orders of magnitude. In any case, all the qualitative features of our scenario will be not affected by the uncertainty in the value of N_c.

4. Results

In our scenario, we consider a purely hadronic star whose central pressure is increasing due to spin-down or due to mass accretion, *e.g.,* from the material left by the supernova explosion (fallback disc), from a companion star or from the interstellar medium. As the central pressure exceeds the threshold value P_0^* at static transition point, a virtual drop of quark matter in the Q*-phase can be formed in the central region of the star. As soon as a real drop of Q*-matter is formed, it will grow very rapidly and the original Hadronic Star will be converted to and Hybrid Star or to a Strange Star,

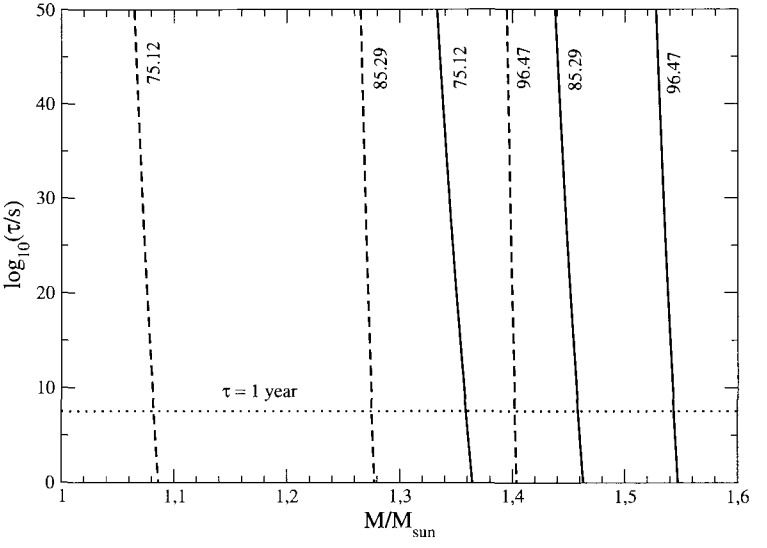

Figure 2. Nucleation time as a function of the maximum gravitational mass of the hadronic star. Solid lines correspond to a value of $\sigma = 30$ MeV/fm^2 whereas dashed ones are for $\sigma = 10$ MeV/fm^2. The nucleation time corresponding to one year is shown by the dotted horizontal line. The different values of the bag constant (in units of MeV/fm^3) are plotted next to each curve. The hadronic phase is described with the GM1 model.

depending on the detail of the EOS for quark matter employed to model the phase transition (particularly depending on the value of the parameter B within the model adopted in the present study).

The nucleation time τ, *i.e.*, the time needed to form a critical droplet of deconfined quark matter, can be calculated for different values of the stellar central pressure P_c which enters in the expression of the energy barrier in Eq. (5). The nucleation time can be plotted as a function of the gravitational mass M_{HS} of the HS corresponding to the given value of the central pressure, as implied by the solution of the Tolmann-Oppeneimer-Volkov equations for the pure Hadronic Star sequences. The results of our calculations are reported in Fig. 2 which is relative to the GM1 EOS for the hadronic phase. Each curve refers to a different value of the bag constant and the surface tension.

As we can see, from the results in Fig. 2, a metastable hadronic star can have a mean-life time many orders of magnitude larger than the age of the universe[36] $T_{univ} = (13.7 \pm 0.2) \times 10^9$ yr $= (4.32 \pm 0.06) \times 10^{17}$ s. As

the star accretes a small amount of mass (of the order of a few per cent of the mass of the sun), the consequential increase of the central pressure lead to a huge reduction of the nucleation time and, as a result, to a dramatic reduction of the HS *mean-life time*.

Table 1. The critical mass and energy released in the conversion process of an HS into a QS for several values of the Bag constant and the surface tension. Column labelled $M_{QS,max}$ denotes the maximum gravitational mass of the final QS sequence. The value of the critical gravitational mass of the initial HS is reported on column labelled M_{cr} whereas those of the mass of the final QS and the energy released in the stellar conversion process are shown on columns lallebed M_{fin} and E_{conv} respectively. BH denotes those cases in which the baryonic mass of the critical mass configuration is larger than the maximum baryonic mass of the QS sequence ($M^b_{cr} > M^b_{QS,max}$). In these cases the stellar conversion process leads to the formation of a black hole. Units of B and σ are MeV/fm^3 and MeV/fm^2 respectively. All masses are given in solar mass units and the energy released is given in units of 10^{51} erg. The hadronic phase is described with the GM1 model, m_s and α_s are always taken equal to 150 MeV and 0 respectively. The GM1 model preditcs a maximum mass for the pure HS of 1.807 $M_\odot$.

		$\sigma = 10$			$\sigma = 30$		
B	$M_{QS,max}$	M_{cr}	M_{fin}	E_{conv}	M_{cr}	M_{fin}	E_{conv}
208.24	1.769	1.798	BH		1.805	BH	
169.61	1.633	1.754	BH		1.778	BH	
136.63	1.415	1.668	BH		1.719	BH	
108.70	1.426	1.510	BH		1.615	BH	
106.17	1.433	1.490	BH		1.602	BH	
103.68	1.441	1.469	1.434	62.5	1.588	BH	
101.23	1.449	1.447	1.411	64.0	1.574	BH	
98.83	1.459	1.425	1.388	66.0	1.559	BH	
96.47	1.470	1.402	1.364	68.5	1.543	BH	
94.15	1.481	1.378	1.339	71.1	1.527	1.474	94.8
91.87	1.494	1.354	1.313	74.2	1.511	1.456	98.1
89.64	1.507	1.329	1.285	77.3	1.495	1.438	101.8
87.45	1.552	1.302	1.257	80.7	1.477	1.417	105.9
85.29	1.538	1.275	1.228	84.4	1.458	1.397	110.4
80.09	1.581	1.196	1.144	92.9	1.410	1.342	122.7
75.12	1.631	1.082	1.029	93.8	1.359	1.284	133.1
65.89	1.734	0.820	0.764	100.6	1.212	1.123	159.9
63.12	1.770	0.727	0.672	98.1	1.160	1.067	166.5
59.95	1.814	0.545	0.501	79.7	1.081	0.986	168.8

To summarize, in the present scenario pure hadronic stars having a central pressure larger than the static transition pressure for the formation of the Q*-phase are metastable to the "decay" (conversion) to a more compact

stellar configuration in which deconfined quark matter is present (*i.e.,* HyS or SS). These metastable HS have a *mean-life time* which is related to the nucleation time to form the first critical-size drop of deconfined matter in their interior (the actual *mean-life time* of the HS will depend on the mass accretion or on the spin-down rate which modifies the nucleation time via an explicit time dependence of the stellar central pressure). We define as *critical mass* M_{cr} of the metastable HS, the value of the gravitational mass for which the nucleation time is equal to one year: $M_{cr} \equiv M_{HS}(\tau = 1\mathrm{yr})$. Pure hadronic stars with $M_H > M_{cr}$ are very unlikely to be observed. M_{cr} plays the role of an *effective maximum mass* for the hadronic branch of compact stars. While the Oppenheimer–Volkov maximum mass[37] $M_{HS,max}$ is determined by the overall stiffness of the EOS for hadronic matter, the value of M_{cr} will depend in addition on the bulk properties of the EOS for quark matter and on the properties at the interface between the confined and deconfined phases of matter (*e.g.,* the surface tension σ).

To explore how the outcome of our scenario depends on the details of the stellar matter EOS, we have considered two different parameterizations (GM1 and GM3) for the EOS of the hadronic phase, and we have varied the value of the bag constant B. Moreover, we have considered two different values for the surface tension: $\sigma = 10$ MeV/fm^2 and $\sigma = 30$ MeV/fm^2. These results, in the case of the GM1 EOS, are summarized in Tab. 1.

In Fig. 3, we show the MR curve for pure HS within the GM1 model for the EOS of the hadronic phase, and that for hybrid stars or strange stars for different values of the bag constant B. The configuration marked with an asterisk on the hadronic MR curves represents the hadronic star for which the central pressure is equal to P_0^*. The full circle on the hadronic star sequence represents the critical mass configuration, in the case $\sigma = 30$ MeV/fm^2. The full circle on the HyS (SS) mass-radius curve represents the hybrid (strange) star which is formed from the conversion of the hadronic star with $M_{HS} = M_{cr}$. We assume[38] that during the stellar conversion process the total number of baryons in the star (or in other words the stellar baryonic mass) is conserved. Thus the total energy liberated in the stellar conversion is given by the difference between the gravitational mass of the initial hadronic star ($M_{in} \equiv M_{cr}$) and that of the final hybrid or strange stellar configuration with the same baryonic mass ($M_{fin} \equiv M_{QS}(M_{cr}^b)$):

$$E_{conv} = (M_{in} - M_{fin})c^2 \,. \tag{9}$$

The stellar conversion process, described so far, will start to populate the new branch of quark stars (the part of the QS sequence plotted as

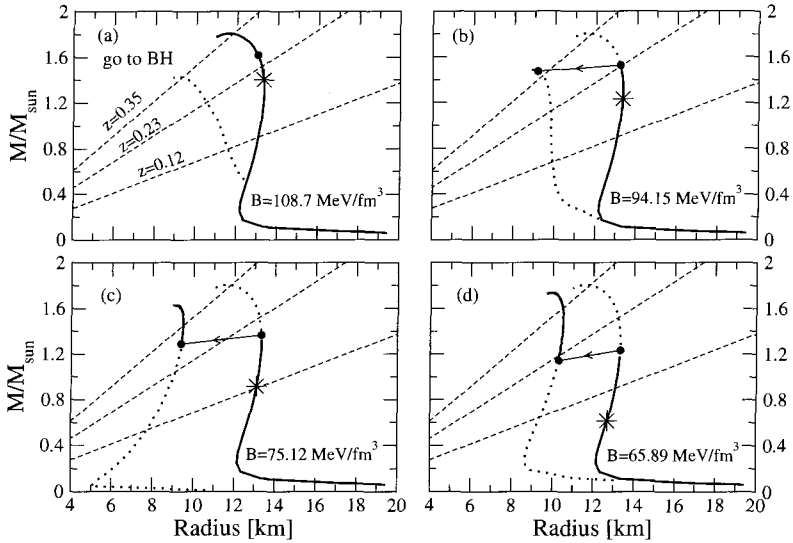

Figure 3. Mass-radius relation for a pure HS described within the GM1 model and that of the HyS or SS configurations for several values of the Bag constant and $m_s = 150$ MeV and $\alpha_s = 0$. The configuration marked with an asterisk represents in all cases the HS for which the central pressure is equal to P_0^*. The conversion process of the HS, with a gravitational mass equal to M_{cr}, into a final HyS or SS is denoted by the full circles connected by an arrow. In all the panels σ is taken equal to 30 MeV/fm^2. The dashed lines show the gravitational red shift deduced for the X-ray compact sources EXO 0748-676 ($z = 0.35$) and 1E 1207.4-5209 ($z = 0.12 - 0.23$).

a continuous curve in Fig. 3). Long term accretion on the QS can next produce stars with masses up to the limiting mass $M_{QS,max}$ for the quark star configurations.

As we can see from the results reported in Tab. 1, within the present model for the EOS, we can distinguish several ranges for the value of the bag constant, which gives a different astrophysical output for our scenario. To be more specific, in Fig. 4 we plot the maximum mass of the QS sequence, the critical mass and the corresponding final mass M_{fin} as a function of B, in the particular case of the GM3 model for the EOS of the hadronic phase and taking $\sigma = 30\text{MeV/fm}^2$. Let us start the following discussion from "high" values of B down to the minimum possible value B^V ($\sim 57.5\text{MeV/fm}^3$ for $\alpha_s = 0$) for which atomic nuclei will be unstable to the decay to a drop of deconfined u,d quark matter[19] (non-strange QM). **(1)** $B > B^I$. These "high" values of the bag constant do not allow the

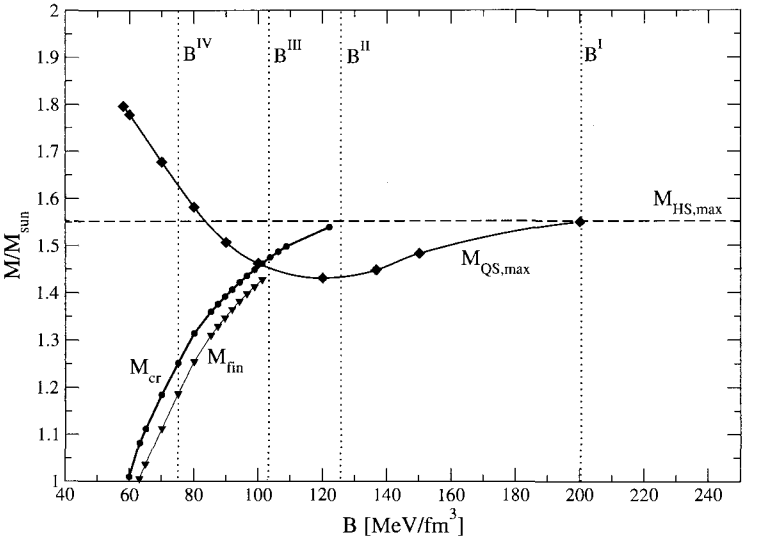

Figure 4. The maximum mass $M_{QS,max}$ for the quark star configuartions (HS or SS), the critical mass M_{cr} and the mass M_{fin} of the stable QS to which it evolves are plotted as a function of the bag constant B. The vertical doted lines labelled B^I – B^{IV} mark the boundary of different ranges of the bag constant which give a different astrophysical output for our scenario, as discussed in the text. The dashed horizontal line gives the value of the maximum mass for the pure hadronic star sequence. All the results are relative to the GM3 model for the EOS for the hadronic phase, the surface tension σ is taken equal to 30 MeV/fm^2.

quark deconfinement to occur in the maximum mass hadronic star either. Here B^I denotes the value of the bag constant for which the central density of the maximum mass hadronic star is equal to the critical density for the beginning of the mixed quark-hadron phase. For these values of B, all compact stars are pure hadronic stars.

(2) $B^{II} < B < B^I$. Now, in addition to pure HS, there is a new branch of compact stars, the hybrid stars; but the nucleation time $\tau(M_{HS,max})$ to form a droplet of Q*-matter in the maximum mass hadronic star, is of the same order or much larger than the age of the Universe. Therefore, it is extremely unlikely to populate the hybrid star branch. Once again, the compact star we can observe are, in this case, pure HS.

(3) $B^{III} < B < B^{II}$. In this case, the critical mass for the pure hadronic star sequence is less than the maximum mass for the same stellar sequence, *i.e.*, $M_{cr} < M_{HS,max}$. Nevertheless (for the present EOS model), the

baryonic mass $M^b(M_{cr})$ of the hadronic star with the critical mass is larger than the maximum baryonic mass $M^b_{QS,max}$ of the hybrid star sequence. In this case, the formation of a critical size droplet of deconfined matter in the core of the hadronic star with the critical mass, will trigger off a stellar conversion process which will produce, at the end, a black hole (see cases marked as "BH" in Tab. 1). As in the previous case, it is extremely unlikely to populate the hybrid star branch. The compact star predicted by these EOS models are pure HS. Hadronic stars with a gravitational mass in the range $M_{HS}(M^b_{QS,max}) < M_{HS} < M_{cr}$ (where $M^b_{QS,max}$ is the baryonic mass of the maximum mass configuration for the hybrid star sequence) are metastable with respect to a conversion to a black hole.
(4) $B^{IV} < B < B^{III}$. In this range for B one has $M_{cr} < M_{HS}(M^b_{QS,max})$. There are now two different branches of compact stars: pure hadronic stars with $M_{HS} < M_{cr}$, and hybrid stars with $M_{QS}(M^b_{cr}) < M_{QS} < M_{QS,max}$ (here $M_{QS}(M^b_{cr}) \equiv M_{fin}$ is the gravitational mass of the hybrid star with the same baryoinic mass of the critical mass hadronic star).
(5) $B^V < B < B^{IV}$. Finally, as B falls below the value B^{IV}, the Bodmer-Witten hypothesis starts to be fulfilled. Now the stable quark stars formed in the stellar conversion process are strange stars.

4.1. *The limiting mass of compact stars*

The possibility to have metastable hadronic stars, together with the feasible existence of two distinct families of compact stars, demands an extension of the concept of maximum mass of a "neutron star" with respect to the *classical* one introduced by Oppenheimer & Volkoff[37]. Since metastable HS with a "short" *mean-life time* are very unlikely to be observed, the extended concept of maximum mass must be introduced in view of the comparison with the values of the mass of compact stars deduced from direct astrophysical observation. Having in mind this operational definition, we call *limiting mass* of a compact star, and denote it as M_{lim}, the physical quantity defined in the following way:
(a) if the nucleation time $\tau(M_{HS,max})$ associated to the maximum mass configuration for the hadronic star sequence is of the same order or much larger than the age of the universe T_{univ}, then

$$M_{lim} = M_{HS,max}\,, \tag{10}$$

in other words, the limiting mass in this case coincides with the Oppenheimer–Volkoff maximum mass for the hadronic star sequence.

(*b*) If the critical mass M_{cr} is smaller than $M_{HS,max}$ (*i.e.* $\tau(M_{HS,max}) <$ 1 yr), thus the limiting mass for compact stars is equal to the largest value between the critical mass for the HS and the maximum mass for the quark star (HyS or SS) sequence

$$M_{lim} = max\left[M_{cr}\,, M_{QS,max}\right]. \tag{11}$$

(*c*) Finally, one must consider an "intermediate" situation for which 1yr $< \tau(M_{HS,max}) < T_{univ}$. As the reader can easely realize, now

$$M_{lim} = max\left[M_{HS,max}\,, M_{QS,max}\right], \tag{12}$$

depending on the details of the EOS which could give $M_{HS,max} > M_{QS,max}$ or vice versa.

In Fig. 5, we show the limiting mass M_{lim} calculated in the case of the GM1+Bag model (dashed line) and in the case of the GM3+Bag model (continuous line) as a function of the bag constant B. In the same figure, we compare our theoretical determination for M_{lim} with some of the "measured" masses of compact stars in radio pulsar binaries[27] and for the compact stars Vela X-1 (ref.[28]) and Cygnus X-2 (ref.[29]).

5. Quark Deconfinement Nova and GRBs

The delayed stellar conversion process, described so far, represents the second "explosion" – the *Quark Deconfinement Nova*[32] *(QDN)* – in the two-step scenario proposed by Berezhiani et al.[31] to explain the delayed SN-GRB connection.

As we can see from the results reported in Tab. 1, the total energy (E_{conv}) liberated during the stellar conversion process is in the range 0.5–1.7×10^{53} erg. This huge amount of energy will be mainly carried out by the neutrinos produced during the stellar conversion process. It has been shown[39] that near the surface of a compact stellar object, due to general relativity effects, the efficiency of the neutrino-antineutrino annihilation into e^+e^- pairs is strongly enhanced with respect to the Newtonian case, and it could be as high as 10%. The total energy deposited into the electron-photon plasma can therefore be of the order of 10^{51}–10^{52} erg.

The strong magnetic field of the compact star will affect the motion of the electrons and positrons, and in turn could generate an anisotropic γ-ray emission along the stellar magnetic axis. This picture is strongly supported by the analysis of the early optical afterglow for GRB990123 and GRB021211 (Ref.[40]), and by the recent discovery of an ultra-relativistic outflow from a "neutron star" in a binary stellar system[41]. Moreover, it

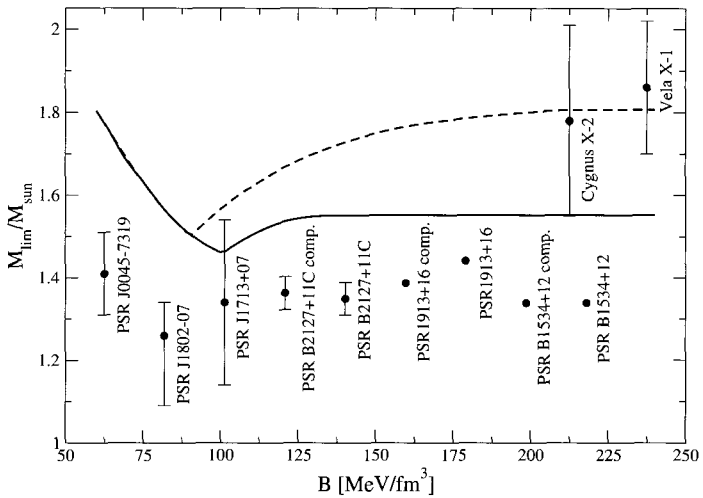

Figure 5. The limiting (gravitational) mass M_{lim}, according to generalized definition given in the present work, is plotted as a function of the Bag constant. Solid (dashed) lines show the results for the GM3+Bag (GM1+Bag) model. In both cases we take $\sigma = 30$ MeV/fm^2. The values of some "measured" masses of compact stars in radio pulsars and in Vela X-1 and Cygnus X-2 are also reported for comparison.

has been recently shown[42] that the stellar magnetic field could influence the velocity of the "burning front" of hadronic matter into quark matter. This results in a strong geometrical asymmetry of the forming quark matter core along the direction of the stellar magnetic axis, thus providing a suitable mechanism[42] to produce a collimated GRB. Other anisotropies in the GRB could be generated by the rotation of the star.

6. Summary

In this report, we have investigated the consequences of the hadron-quark deconfinement phase transition in stellar compact objects when finite size effects between the deconfined quark phase and the hadronic phase are taken into account. We have found that above a threshold value of the gravitational mass a pure hadronic star is metastable to the decay (conversion) to a hybrid neutron star or to a strange star. We have calculated the *mean-life time* of these metastable stellar configurations, the critical mass for the hadronic star sequence, and have explored how these quantities depend on the details of the EOS for dense matter. We have introduced an

extension of the concept of limiting mass of compact stars, with respect to the classical one given by Oppenheimer & Volkov. Within the astrophysical scenario proposed in the present work, the existence of compact stars with "small" radii (quark stars) does not exclude the existence of compact stars with "large" radii (pure hadronic stars), and *vice versa*. We have shown that the present scenario implies, as a natural consequence a two step-process which is able to explain the inferred "delayed" connection between supernova explosions and GRBs, giving also the correct energy to power GRBs.

There are various specific features and predictions of the present model, which we briefly mention in the following. The second explosion (QDN) take place in a "baryon-clean" enviroment due to the previous SN explosion. Is is possible to have different time delays between the two events since the *mean-life time* of the metastable hadronic star depends on the value of the stellar central pressure. Thus the model of Berezhiani et al.[31] is able to interpret a time delay of a few years (as observed[2,8] in GRB990705), of a few months (as in the case[7] of GRB020813), of a few days (as deduced[5] for GRB011211), or the nearly simultaneity of the two events (as in the case[6] of SN2003dh and GRB030329).

References

1. J.S. Bloom et al., Nature 401, 453 (1999).
2. L. Amati et al., Science 290, 953 (2000).
3. L.A. Antonelli et al., Astrophys. Jour.545, L39 (2000).
4. L. Piro et al., Science 290, 955 (2000).
5. J.N. Reeves et al., Nature 414, 512 (2002).
6. J. Hjorth et al, Nature 423, 847 (2003).
7. N.R. Butler et al., Astrophys. Jour.597, 1010 (2003).
8. D. Lazzati, G. Ghisellini, L. Amati, F. Frontera, M. Vietri and L. Stella, Astrophys. Jour., 556, 471 (2001).
9. M. Vietri and L. Stella, Astrophys. Jour.507, L45 (1998).
10. B. Datta, A.V. Thampan and I. Bombaci, Astron. and Astrophys. 334, 943 (1998).
11. N.K. Glendenning, Phys. Rev. D46, 1274 (1992).
12. H. Heiselberg, C.J. Pethick and E.F. Staubo, Phys. Rev. Lett. 70, 1355 (1993).
13. N.K. Glendenning, Compact Stars: Nuclear Physics, Particle Physics, and General Relativity, Springer Verlag (1996).
14. A.R. Bodmer, Phys. Rev. D4, 1601 (1971).
15. E. Witten, Phys. Rev. D30, 272 (1984).
16. H. Terazawa, INS-Report, 336 (INS, Univ. of Tokyo) (1979); J. Phys. Soc. Japan 58, 3555 (1989); J. Phys. Soc. Japan 58, 4388 (1989).

17. C. Alcock, E. Farhi and A. Olinto, Astrophys. Jour.310, 261 (1986).
18. P. Haensel, J.L. Zdunik and R. Schaefer, Astron. and Astrophys. 160, 121 (1986).
19. E. Farhi and R.L. Jaffe, Phys. Rev. D30, 2379 (1984).
20. J. Madsen, Lectures Notes in Physics Vol. 500, Springer Verlag, 162 (1999).
21. I. Bombaci, Phys. Rev. C55, 1587 (1997).
22. K.S. Cheng, Z.G. Dai, D.M. Wai and T. Lu, Science 280, 407 (1998).
23. X.-D. Li, I. Bombaci, M. Dey, J. Dey and E.P.J. van den Heuvel, Phys. Rev. Lett. 83, 3776 (1999).
24. X.-D. Li, S. Ray, J. Dey, M. Dey and I. Bombaci, Astrophys. Jour.527, L51 (1999).
25. R.X. Xu, Astrophys. Jour.570, L65 (2002).
26. J.J. Drake et al., Astrophys. Jour.572, 996 (2002).
27. S.E. Thorsett and D. Chakrabarty, Astrophys. Jour.512, 288 (1989).
28. H. Quaintrell et al., Astron. and Astrophys. 401, 313 (2003).
29. J.A. Orosz and E. Kuulkers, MNRAS 305, 132 (1999).
30. M.H. van Kerkwijk et al., Astron. and Astrophys. 303, 483 (1995).
31. Z. Berezhiani, I. Bombaci, A. Drago, F. Frontera and A. Lavagno, Astrophys. Jour.586, 1250 (2003).
32. I. Bombaci, I. Parenti and I. Vidaña, Astrophys. Jour.(submitted) (2003).
33. N.K. Glendenning and S.A. Moszkowski, Phys. Rev. Lett. 67, 2414 (1991).
34. I.M. Lifshitz and Y. Kagan, Sov. Phys. JETP 35, 206 (1972).
35. K. Iida and K. Sato, Prog. Theor. Phys. 1, 277 (1997); Phys. Rev. C58, 2538 (1998).
36. D.N. Spergel et al. Astrophys. Jour.Suppl., 148, 175 (2003).
37. J.R. Oppenheimer and G.M. Volkoff, Phys. Rev. 55, 374 (1939).
38. I. Bombaci and B. Datta, Astrophys. Jour.530, L69 (2000).
39. J.D. Salmonson and J.R. Wilson, Astrophys. Jour.517, 859 (1999).
40. B. Zhang, S. Kobayashi and P. Meszaros, Astrophys. Jour.595, 950 (2003).
41. R. Fender et al., Nature 427, 222 (2004).
42. G. Lugones, C.R. Ghezzi, E.M. de Gouveia Dal Pino and J.E. Horvath, Astrophys. Jour., 581, L101 (2002).

UNEXPECTED GOINGS-ON IN THE STRUCTURE OF A NEUTRON STAR CRUST

AUREL BULGAC
Department of Physics, University of Washington, Seattle WA 98195-1560, USA

PAUL-HENRI HEENEN
Service de Physique Nucléaire Théorique, Université Libre de Bruxelles,B 1050, Brussels, Belgium

PIOTR MAGIERSKI
Faculty of Physics, Warsaw University of Technology, ul. Koszykowa 75, 00-662, Warsaw, Poland

ANDREAS WIRZBA
Helmholtz-Institut für Strahlen- und Kernphysik, Universität Bonn,D-53115 Bonn, Germany

YONGLE YU
Department of Physics, University of Washington, Seattle WA 98195-1560, USA

We present a brief account of two phenomena taking place in a neutron star crust: the Fermionic Casimir effect and the major density depletion of the cores of the superfluid neutron vortices.

1. Fermionic Casimir effect and Neutron Star Crust

At a depth of about 500 m or so below the surface of a neutron star the nuclear matter (which consists mostly of neutrons plus a small percentage of protons and electrons in β-equilibrium) organize themselves in some exotic inhomogeneous solid phase [1]. As a matter of fact, neutron star crusts seem to be just about the only other places in the entire Universe, apart from planets, where one can find condensed matter, in particular a solid phase [2]. Moving from the neutron star surface inward, one finds at first a Coulomb crystal lattice of nuclei immersed in a very low density neutron

gas and even lower density electron gas. With increasing depth, the density and pressure increase, the nuclei get closer to each other and start evolving into some unusual elongated nuclei, which eventually become rods. These nuclear rods evolve gradually into plates, their place being taken later by tubes and bubbles (dubbed "inside out" nuclei) just before the average density becomes almost equal to the nuclear saturation density and the entire mixture of neutrons, protons and electrons become an homogeneous phase. The properties of this part of the neutron star have been the subject of a lot of studies, see Refs. [1,3,4,5,6,7,8,9,10,11,12,13,14,15,16,17] and other references therein. Most of these approaches however have missed a rather subtle and apparently important physical phenomenon, the fermionic counterpart of the Casimir interaction in such a medium [10,11,12,13,14].

In order to quickly explain the main physics ideas behind this new phenomenon, let us consider an over-simplified model of the neutron star crust. One can ask the rather innocuous question: "What is the ground state energy of an infinite homogeneous Fermi sea of noninteracting neutral particles with two hard spheres of radii a, separated by a distance r?" The naive and somewhat startling answer that perhaps one can place the two hard spheres almost anywhere with respect to each other and that the energy of the system will not be affected if one were to move the hard spheres around. The "theoretical argument" which can lead to such a conclusion is based on the same type of argumentation, which was used in Refs.[1,5,6,7] and allowed these authors to establish that by going deeper and deeper into the interior of the neutron star one finds a well defined sequence of "exotic" nuclear shapes. This traditional argumentation is based essentially on liquid drop model, which includes the volume, surface, Coulomb contributions to the ground state energy only. This is basically "classical thinking." For a person using "quantum reasoning" instead, the fact that the ground state of such a system in infinitely degenerate (corresponding to an arbitrary relative arrangement of the two hard spheres) will find such an answer most likely wrong. And indeed, a careful analysis of the problem reveals the fact that indeed a system of two hard spheres, immersed in an infinite Fermi sea of noninteracting particles at zero temperature has a well defined ground state. The correct answer, namely that the "interaction energy" of the two hard spheres of radius R, at distance r from each other, is somewaht even more surprising. One finds that

$$E_C \approx -\frac{\hbar^2 k_F^2}{m} \frac{R^2}{2\pi r(r-2R)} j_1[2k_F(r-2R)],$$

where $j_1(x)$ is the spherical Bessel function, k_F is the Fermi momentum and m is the fermion mass. "Why would this "interaction energy" be a non-monotonic function of the hard sphere separation r?" and, moreover, "How does interaction really emerges here, where one starts with such a simple system of non-interacting particles?" As one soon "discovers" the "culprit" is the wave character of the Quantum Mechanics really. Fermions even at zero temperature do not stop moving and the space is really "filled" with an infinite number of de Broglie's waves. These waves reflect from the two hard spheres and as in the case of any wind musical instrument, for some frequencies one would have a favorable wave interference while for other frequencies there will not such a favorable interference. In an infinite Fermi sea there is an infinite number of waves with all frequencies ranging from zero to the Fermi frequency. If one carefully adds up the effects of all these waves one readily arrives at the result above [10,11]. Things get a little bit more complicated when one adds more hard spheres, as then one naturally discovers that besides the "natural" two-body interactions there are genuine three- and four- and many-body interactions among these spheres. Moreover, there is absolutely no reason why not consider other type of objects, which could be immersed in this Fermi sea, like "logs" and "boards" and in principle almost anything else. Surprisingly all these combinations of various objects in various arrangements can be analyzed rather easily. What is surprising however is the fact that the characteristic interaction energy between such objects is of the same order as the energy differences between various phases in a neutron star crust [10,12,13,14] and when taken into account this fermionic Casimir energy can in "ruin perfect crystalline structures" found in all previous studies. These conclusions have been backed by more sophisticated fully microscopic calculations of the nuclear matter in a neutron star crust [8,9].

Instead of describing in more detail results which have been published already, we shall instead draw the attention of our readers here to another element which was overlooked in studies of the neutron star crust, and which is apparently going to influence a great deal of properties. In order to analyze the thermal and electric conductivities of the crust, which are important for understanding of the thermal evolution of neutron stars one has to go beyond the static approximation. The "nuclei" which are immersed in the neutron fluid, which indeed is a superfluid, can and do move. As with boats on a lake, when they start moving they make waves and one has to include the dynamics of the surrounding superfluid in any analysis. We shall limit ourselves here to quoting a single result, namely

the kinetic energy of two penetrable spheres,located at the distance r, immersed in a superfluid at velocities below the critical velocity for the loss of superfluidity. One then finds [18] that the kinetic energy of two such spheres becomes:

$$T = \frac{1}{2}(M_1^{ren}u_1^2 + M_2^{ren}u_2^2)$$

$$+4\pi m\rho_{out}\left(\frac{1-\gamma}{2\gamma+1}\right)^2\left(\frac{R_1R_2}{r}\right)^3\left[\vec{u}_1\cdot\vec{u}_2 - \frac{3}{r^2}(\vec{u}_1\cdot\vec{r})(\vec{u}_2\cdot\vec{r})\right]$$

where the renormalized masses of nuclei have the form:

$$M_i^{ren} = \frac{4}{3}m\rho_{in}\pi R_i^3\frac{(1-\gamma)^2}{2\gamma+1} = M_i\frac{(1-\gamma)^2}{2\gamma+1},$$

where $\vec{u}_i$ are the velocities of the two nuclei, $i = 1, 2$ and M_i and R_i denote the nuclear bare mass and radii of the $i-th$ nucleus, $\gamma = \rho_{out}/\rho_{in}$ and $\rho_{in,out}$ are the densities inside and outside the two nuclei. The somewhat unexpected cross term appearing above shows that the existence of mere motion of the two objects in a perfect fluid can lead to a velocity-dependent interaction, which decays with the separation as slows as the static Casimir Fermionic energy, namely as $1/r^3$. Further analysis shows that this velocity dependent-interaction is important as well when considering dynamical properties of neutron star crust [19].

2. The Spatial Structure of a Vortex in Low-Density Superfluid Neutron Matter

There is a long held belief that vortices in Fermi systems do not show any appreciable normal density variations and that only the anomalous density vanishes along the vortex axis, similarly to the behavior of the density (which is the order parameter) in Bose systems [20,21,22]. Thus it came as somewhat of a surprise the fact that in Fermi systems one can have a spatial structure of a vortex with a significant normal density depletion along the vortex axis [23,24,25]. What happens in low density superfluid neutron matter for example is the following. The magnitude of the pairing gap becomes comparable with the Fermi energy,

The possibility that the value of the superfluid gap can attain large values was raised more than two decades ago in connection with the BCS $\rightarrow$ BEC crossover [29,30]. One can imagine that one can increase the strength of the two–particle interaction in such a manner that at some point a real two–bound state forms, and in that case $a \rightarrow -\infty$. By continuing to

increase the strength of the two–particle interaction, the scattering length becomes positive and starts decreasing. A dilute system of fermions, when $\rho r_0^3 \ll 1$ (here r_0 is the interaction radius), will thus undergo a transition from a weakly coupled BCS system, when $a < 0$ and a is of order r_0, to a BEC system of tightly bound Fermion pairs, when $a > 0$ and a is of order r_0 again. In the weakly coupled BCS limit the size of the Cooper pair is given by the so called coherence length $\xi \propto \frac{\hbar^2 k_F}{m\Delta}$, which is much larger than the inter-particle separation $\approx \lambda_F = 2\pi/k_F$. In the opposite limit, when $k_F a \ll 1$ and $a > 0$, and when tightly bound pairs/dimers of size a are formed, the dimers are widely separated from one another. Surprisingly, these dimers also repel each other with a scattering length $0.6a$ [27,28] and thus the BEC phase is also (meta)stable. The bulk of the theoretical analysis in the intermediate region where $k_F|a| > 1$ was based on the BCS formalism [27,29,30,31] and thus is highly questionable. Even the simplest polarization corrections have not been included into this type of analysis so far. In particular, it is well known that in the low density region, where $a < 0$ and $k_F|a| \ll 1$ the polarization corrections to the BCS equations lead to a noticeable reduction of the gap [26]. Only a truly *ab initio* calculation could really describe the structure of a many Fermion system with $k_F|a| \gg 1$. In the limit $a = \pm\infty$, when the two–body bound state has exactly zero energy, and if $k_F r_0 \ll 1$, one can expect that the energy per particle of the system is proportional to $\varepsilon_F = \hbar^2 k_F^2/2m$, see Bertsch's 1999 MBX Many-Body Challenge [32]. This problem was recently solved essentially exactly by the variational calculations of Refs. [33,34]. The normal density at the vortex core is lowered, while the pairing field vanishes at the vortex axis as expected. In hindsight this result could have been expected. Large values of the pairing field correspond to the formation of atom pairs/dimers of relatively small sizes. When these dimers are relatively strongly bound and when they are also widely separated from one another, they undergo a Bose–Einstein condensation. For a vortex state in a 100% BEC system the density at the vortex axis vanishes identically. Therefore, by increasing the strength of the two–particle interaction, the Fermion system simply approaches more and more an ideal BEC system, for which a density depletion of the vortex core is expected.

Almost thirty years ago Anderson and Itoh [2] put forward the idea that vortices should appear in neutron stars and that they can also get pinned to the solid crust. They argued that the "star–quakes," observable on Earth as pulsar "glitches," apparently are caused by the vortex de–pinning in neutron star crust. This idea and its various implications have been examined

by numerous authors, see Refs. [21,24] and further references therein, but a general consensus does not seem to have emerged so far.

The profile of a vortex in neutron matter is typically determined using a Ginzburg–Landau equation, which is expected to give mostly a qualitative picture and its accuracy is difficult to estimate. Surprisingly, prior to Ref. [23] there exists only one microscopic calculation of a vortex in low density neutron matter [22]. The existence of a strong density depletion in the vortex core is going to affect appreciably the energetics of a neutron star crust. One can obtain a gross estimate of the pinning energy of a vortex on a nucleus as $E^V_{pin} = [\varepsilon(\rho_{out})\rho_{out} - \varepsilon(\rho_{in})\rho_{in}]V$, where $\varepsilon(\rho)$ is the energy per particle at density ρ, ρ_{in} and ρ_{out} are the densities inside and outside the vortex core and V is the volume of the nucleus. Naturally, this simple formula does not take into account a number of factors, in particular surface effects and the changes in the velocity profile and the pairing field. These last contributions were accounted for (with some variations) in the past [2,21]. However, if the density inside the vortex core and outside differ significantly one expects E^V_{pin} to be the dominant contribution. In the low density region, where $\varepsilon(\rho_{out})\rho_{out}/\varepsilon(\rho_{in})\rho_{in}$ is largest, one expects a particularly large anti–pinning effect ($E^V_{pin} > 0$). The energy per unit length of a simple vortex is expected to be significantly lowered when compared with previous estimates [2,21] by $\approx [\varepsilon(\rho_{out})\rho_{out} - \varepsilon(\rho_{in})\rho_{in}]\pi R^2$, where R is an approximate core radius.

References

1. G. Baym, H.A. Bethe, C.J. Pethick, Nucl. Phys. **A175** 225 (1971).
2. P.W. Anderson and N. Itoh, Nature, **256**, 25 (1975).
3. J.W. Negele and D. Vautherin, Nucl. Phys. **A207**, 298(1973).
4. P. Bonche and D. Vautherin, Nucl. Phys. **A372** 496.(1981); Astron. Astrophys. **112** 268 (1982).
5. C.J. Pethick and D.G. Ravenhall, Annu. Rev. Nucl. Part. Sci. **45** 429 (1995).
6. F. Douchin, P. Haensel, J. Meyer, Nucl. Phys. **A 665** 419 (2000).
7. F. Douchin, P. Haensel, Phys. Lett. **B485** 107 (2000).
8. P. Magierski, P.-H. Heenen, Phys. Rev. **C65** 045804 (2002).
9. P. Magierski, A. Bulgac, P.-H. Heenen, Int. J. Mod. Phys. **A17** 1059 (2002).
10. A. Bulgac, P. Magierski, Nucl. Phys. **A683** 695 (2001); Erratum: Nucl. Phys. **A703** 892 (2002).
11. A. Bulgac and A. Wirzba, Phys. Rev Lett. **87**, 120404 (2001).
12. A. Bulgac, P. Magierski, Phys. Scripta **T90** 150 (2001).
13. A. Bulgac, P. Magierski, Acta Phys. Pol. **B32** 1099 (2001).
14. P. Magierski, A. Bulgac, Acta Phys. Pol. **B32** 2713 (2001).

15. G. Watanabe, K. Sato, K. Yasuoka, T. Ebisuzaki, Phys. Rev. C 66, 012801 (2002); Phys. Rev. C 68, 035806 (2003).
16. C. J. Pethick and A. Y. Potekhin, Phys. Lett. **B 427**, 7 (1998).
17. P.B. Jones, Phys. Rev. Lett. **83**, 3589 (1999).
18. P. Magierski and A. Bulgac, preprint *Nuclear Hydrodynamics in the Inner Crust of Neutron Stars*, to appear in Acta Phys. Pol. **B**.
19. P. Magierski, preprint *In-medium ion mass renormalization and lattice vibrations in the neutron star crust*, to appear in Int. J. Mod. Phys. **E**.
20. P.G. de Gennes, *Superconductivity of Metals and Alloys*, Addison–Wesley, Reading MA, (1998); F. Gygi and M. Schlüter, Phys. Rev. B **43**, 7609 (1991); P.I. Soininen *et al.*, Phys. Rev. B **50**, 13883 (1994); N. Hayashi, *et al.*, Phys. Rev. Lett. **80**, 2921 (1998); M. Franz and Z. Tešanović, Phys. Rev. Lett. **80**, 4763 (1998); N. Nygaard, *et al.*, Phys. Rev. Lett. **90**, 210402 (2003).
21. P.W. Anderson, M.A. Alpar, D. Pines and J. Shaham, Phil. Mag. **45**, 227 (1982); M.A. Alpar, P.W. Anderson, D. Pines and J. Shaham, Ap. J. **278**, 791 (1984); M.A. Alpar, K.S. Cheng and D. Pines, Ap. J. **346**, 823 (1989); R.I. Epstein and G. Baym, Ap. J. **328**, 680 (1988); R.I. Epstein and G. Baym, Ap. J. **387**, 276 (1992); B. Link, R.I. Epstein and G. Baym, Ap. J. **403**, 285 (1993); P.B. Jones, Phys. Rev. Lett. **79**, 792 (1997). *ibid* **81**, 4560 (1998); *ibid* Mon. Not. R. Astron. Soc. **257**, 501 (1992); *ibid* Mon. Not. R. Astron. Soc. **296**, 217 (1998); P.M. Pizzochero, L. Viverit and R.A. Broglia, Phys. Rev. Lett. **79**, 3347 (1997).
22. F.V. De Blasio and Ø. Elgarøy, Phys. Rev. Lett. **82**, 1815 (1999); Ø. Elgarøy and F.V. De Blasio, A&A, **370**, 939 (2001).
23. Y. Yu and A. Bulgac. Phys. Rev. Lett. **90**, 161101 (2003).
24. P. Donati and P.M. Pizzochero, Phys. Rev. Lett. **90**, 211101 (2003).
25. A. Bulgac and Y. Yu, Phys. Rev. Lett. **91**, 90404 (2003)
26. L.P. Gorkov and T.K. Melik–Barkhudarov, Zh. Eksp. Teor. Fiz. **40**, 1452 (1961) [Sov. Phys. JETP **13**, 1018 (1961)]; H. Heiselberg, *et al.*, Phys. Rev. Lett. **85**, 2418 (2000).
27. M. Randeria, in *Bose–Einstein Condensation*, eds. A. Griffin, *et al.*, Cambridge Univ. Press (1995), pp 355–392.
28. P. Pieri and G.C. Strinati, Phys. Rev. B **61**, 15370 (2000) and cond-mat/0307421; D.S. Petrov, C. Salomon, G.V. Shlyapnikov, cond-mat/0309010; A. Bulgac, P.F. Bedaque and A.C. Fonseca, cond-mat/0306302.
29. A.J. Leggett, in *Modern Trends in the Theory of Condensed Matter*, eds. A. Pekalski and R. Przystawa, Springer–Verlag, Berlin, 1980; J. Phys. (Paris) Colloq. **41**, C7–19 (1980).
30. P. Nozières and S. Schmitt–Rink, J. Low Temp. Phys. **59**, 195 (1985).
31. C.A.R. Sá de Mello, *et al.*, Phys. Rev. Lett. **71**, 3202 (1993); J.R. Engelbrecht, *et al.*, Phys. Rev. B **55**, 15153 (1997).
32. G.A. Baker, Int. J. Mod. Phys. **B 15**, 1314 (2001).
33. J. Carlson, *et al.*, Phys. Rev. C **68**, 025802 (2003).
34. J. Carlson, *et al.*, Phys. Rev. Lett. **91**, 050401 (2003).

SLEUTHING THE ISOLATED COMPACT STARS

J. J. DRAKE

Smithsonian Astrophysical Observatory,
60 Garden Street, MS-3,
Cambridge, MA 02138, USA
E-mail: jdrake@cfa.harvard.edu

In the early 1990's, isolated thermally-emitting neutron stars accreting from the interstellar medium were predicted to show up in their thousands in the ROSAT soft X-ray all-sky survey. The glut of sources would provide unprecedented opportunities for probing the equation of state of ultra-dense matter. Only seven objects have been firmly identified to date. The reasons for this discrepency are discussed and recent high resolution X-ray spectroscopic observations of these objects are described. Spectra of the brightest of the isolated neutron star candidates, RX J1856.5−3754, continue to present interpretational difficulties for current neutron star model atmospheres and alternative models are briefly discussed. RX J1856.5−3754 remains a valid quark star candidate.

The observed population of stars as a function of mass, together with present day abundances of elements produced by nucleosynthesis in supernovae and observed extragalactic supernova rates, lead to the deduction that our Galaxy should be inhabited by 10^8-10^9 neutron stars—up to 1% of the stellar population. Following their birth at temperatures as high as 10^{11} K, neutron stars cool, cease pulsar activity and become essentially inactive and invisible in a fleeting 10^6-10^7 yr[51]. Consequently, although in the solar vicinity there are expected to be 2-3 $\times$ 10^{-4} pc^{-3} of these objects,[43] only about 1500 neutron stars are currently known. The majority of these were detected as radio pulsars, and the remainder became conspicuous through relative γ-ray or X-ray brightness. Most numerous among the latter minority are neutron stars in close binary systems, whose X-ray emission is driven by accretion of matter from a less evolved companion.

In the early 1990's, the launch of the ROSAT soft X-ray (0.1-2.5 keV) satellite rekindled earlier ideas[36] that isolated old radio-quiet neutron stars might be re-heated by accretion of interstellar material to sufficiently high

temperatures so as to be detectable in soft X-ray all-sky surveys[2,50]. Predictions of the number of objects that would be detected were made—the numbers ranged from the hundreds to thousands. Such a population of re-heated objects would be important for probing the old neutron star population and would provide a test of models of Galaxy evolution: in particular, supernova rates and the nucleosynthetic and energetic history of the interstellar medium (ISM).

More central to this meeting, the evolution and structure of neutron stars depends on the properties of matter at nuclear and supranuclear densities: observations of neutron stars—their masses, radii and cooling characteristics—might provide useful constraints for the equation of state (EOS) of ultra-dense matter[27,20], including tests of exotic particle and strange quark solutions (Fig. 1). Neutron stars provide extremes of phase space unattainable in terrestrial laboratories. In this context, re-heated isolated neutron stars would be important since their spectra would not be complicated by strong accretion or magnetospheric signatures and would provide a direct glimpse of the neutron star surface. This aspect of neutron star astrophysics comfortably promotes these objects to the very top of the *cosmic sexiness ladder* (Figure 1).

Prior to the first detailed high resolution spectroscopic observations obtained by the "next generation" *Chandra* and *XMM-Newton* X-ray observatories, it was hoped that identification of metallic atmospheric absorption lines would provide a measure of the gravitational redshift, from which the ratio of mass to radius, M/R, can be obtained. It has also been pointed out that simultaneous measurements of pressure-broadened line wavelengths and profiles can constrain both M and R[37]. For objects with fairly strong magnetic fields, X-ray spectra are also expected to host deep, broad proton cyclotron lines that can constrain the magnetic field strength, B. The apparent stellar radius (the "radiation radius", $R_\infty = R/\sqrt{1-2GM/Rc^2}$) can be derived from a measurement of the temperature and luminosity of the object, interpreted by means of models of the emergent spectra computed by solving simultaneously the radiative transfer and structure equations for the neutron star atmosphere.

Unfortunately, the numbers of neutron stars actually detected by ROSAT did not quite meet optimistic expectations, by a mere 3 orders of magnitude. Later high resolution spectra obtained by *Chandra* and *XMM-Newton* would also confound conventional interpretation.

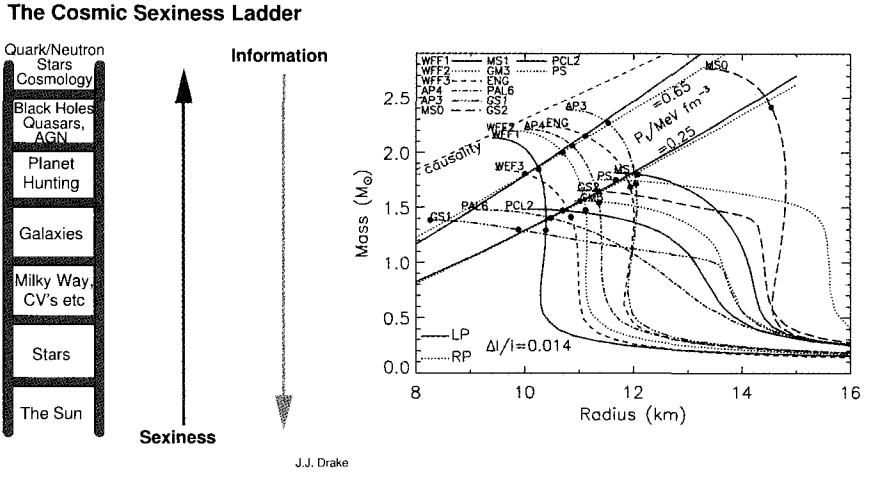

Figure 1. **Left:** The well-known fact that purported scientific "sexiness" of different fields of astrophysics is in general inversely proportional to the observational information available is illustrated by the *Cosmic Sexiness Ladder*. Owing to their possible use for probing fundamental physics and exotic states of matter, neutron stars and quark stars occupy the top rung. **Right:** Mass-radius curves for several different EOS for stars containing nucleons and, in some cases, hyperons[27].

Table 1. Known isolated, radio-quiet, thermally-emitting compact stars

Source	PSPC (count s^{-1})	T_{bb} (eV)	N_H (10^{20} cm^{-2})	$\log f_x/f_v$	Period (s)	Optical Excess?	Refs
RBS 1223	0.29	118	~1	~5	5.16	Yes	9,14,16
RBS 1556	0.88	100	< 1	~5	...	Yes	9,10,17
RBS 1774	0.11	92	4.6	$\gtrsim$3	...	...	13
RX J0720	1.69	79	1.3	5.3	8.37	Yes	6,7,8
RX J0806	0.38	78	2.5	> 3.4	11.37	...	11,15
RX J1856	3.64	57	2	4.9	...	Yes	2,3,4,5
RX J0420	0.11	57	1.7	> 3.3	22.7	...	12

References: (1) Stocke et al. 1995; (2) Walter et al. 1996; (3) Neuhauser et al. 1997; (4) Campana et al. 1997; (5) Walter & Matthews 1997; (6) Haberl et al. 1997; (7) Motch & Haberl 1998; (8) Kulkarni & van Kerkwijk 1998; (9) Schwope et al. 1999; (10) Motch et al. 1999; (11) Haberl et al. 1998; (12) Haberl et al. 1999; (13) Zampieri et al. 2001; (14) Hambaryan et al. 2002; (15) Haberl et al. 2002; (16) Kaplan et al. 2002; (17) Kaplan et al. 2003

1. IRaTE Neutron Stars: Cooling and Re-heating

Instead of the expected glut of thousands of isolated radio-quiet thermally-emitting neutron stars (IRaTE NS), only seven candidates have so far been identified. The identification process for these sources is not trivial, however, since firm identification requires exclusion of association with other

plausible counterparts, and since NS themselves are expected to be extremely faint in optical light ($V \gtrsim 25$ or so). The typical error in X-ray source positions in the ROSAT All-Sky Survey (RASS) is 10-15 arcsec, which is often sufficiently large to encompass possible culprits such as background active galactic nuclei or stars in our own galaxy. A 90% confidence upper limit to the total number in the ROSAT All-Sky Survey has been estimated as 67[46].

The seven current IRaTE NS candidates are characterized by remarkably similar properties: soft, thermal X-ray spectrum consistent with blackbody temperatures $kT \sim 100$ eV (at resolution $E/\Delta E \sim 2$); low X-ray luminosity, $L_X \approx 10^{30} - 10^{31} \mathrm{erg\,s^{-1}}$; lying behind a low column density of interstellar hydrogen, $N_H \sim 10^{20}$ cm^{-2}; extremely faint probable optical counterpart with $V \gtrsim 25$, corresponding to X-ray-to-optical flux ratios of $\log(f_x/f_v) \sim 4 - 6$; no association with a supernova remnant; and pulsation periods (detected in four of the seven so far) in the 5-20s range. These seven objects are summarised in Table1; more detailed reviews have been presented by other workers.[51,30]

The IRaTE NS are either young ($\lesssim 10^6$ yr), cooling objects, or else are much older and have been re-heated to, or sustained at, X-ray temperatures by accretion of ambient medium. The expected population of IRaTE NS still young enough to be X-ray bright can be estimated by combining a census of the present day population of intermediate-high mass stars with NS cooling models, though not without considerably uncertainty, as we discuss below. Re-heating an older population is even more complicated, since the accretion process itself depends critically on the neutron star magnetic field, rotation rate, and space velocity, as well as on the ISM density in which the star finds itself.

1.1. *Hot Young Ones*

The cooling of NS depends on the properties of matter at or near nuclear densities in the stellar core and crust. Cooling can be roughly divided into three stages: a very brief 10-100yr period of thermal relaxation of the interior; 10^5-10^6yr period of neutrino-dominated losses through Urca processes, neutrino bremsstrahlung, Cooper pairing of nucleons, electron-positron annihilation and plasmon decay[20]; and ending with photon-dominated cooling from the outer layers. The interior neutrino processes are dependent on the EOS and on the density, and consequently neutrino-dominated cooling rates are strongly mass-dependent, with more massive stars cooling much more

rapidly. While EOS and mass dependency of cooling rates leads to degeneracy in interpreting the observed temperatures of different objects of known age, the required masses for young to middle-aged NS ($\sim 10^3$-10^6yr) can be weakly constrained to the range 1.2-1.45$M_\odot$[20].

Applying NS cooling models, together with estimates of the local Galactic NS birthrate, the observed numbers of hot cooling objects detected through their thermal emission in soft X-rays appears to exceed the expected local disk population, but can be explained by the young stars that comprise the Gould Belt.[42]. If all the objects detected so far, including the seven IRaTE NS, are cooling objects, where are the thousands of re-heated objects and why are they not detected?

1.2. *Old Ones Trying to be Hot*

If the NS is hot, it will photoionize the surrounding medium whose accretion can then be arrested by the NS magnetic field. Both the magnetic field and spin of a NS act to inhibit accretion: the ram pressure of accreting material must overcome the radiation pressure generated by the spinning (assumed dipolar) magnetic field, and the gravitational pull must also overcome the magnetic field to within the corotation radius—the radius at which centrifugal force on particles contained by the spinning magnetosphere equal gravitational attraction. The different forces at play define four regimes of interaction with the ambient medium, depending on which dominates: *ejector* (outward radiation pressure); *georotator* (magnetic pressure, in analogy with the interaction of the Earth and solar wind); *propeller* (magnetic pressure prevents penetration of the centrifugal barrier); and accretor (gravity)[11,51,43]. These regimes are illustrated as a function of magnetic field strength, B, and space velocity, v, in Figure 2.

There are three large sources of uncertainty in placing the population of NS in Figure 2. The particular regime that a NS finds itself during its lifetime depends on a combination of its velocity, spin period and magnetic field strength. Both the initial strength and evolution of the magnetic field are not yet well-understood; in particular, whether or not the magnetic field decays significantly during the NS lifetime remains controversial (e.g. review by Verbunt[56]). It has been pointed out that for B field decay timescales of $\sim 10^9$yr, a NS might linger in the ejector or propeller state for a time comparable to or longer than the age of the Galaxy[28,8]. Importantly, the early estimates of the numbers of detectable accreting IRaTE NS assumed that all isolated NS would decay in magnetic field strength to a "low" value of $B \sim 10^9$ G, allowing accretion to proceed.

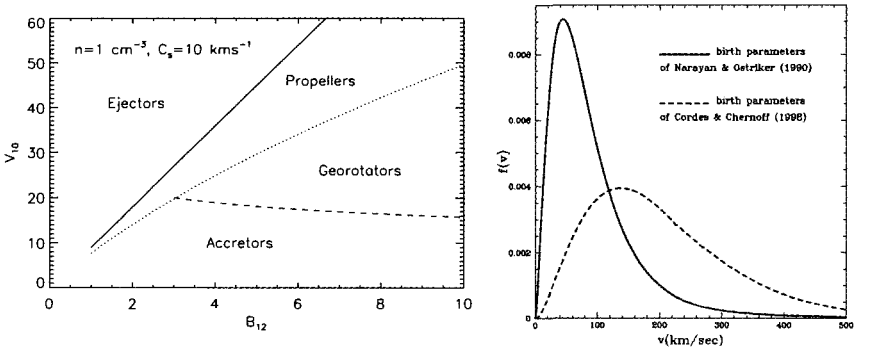

Figure 2. **Left:** The different interactions of a neutron star with the ISM as a function of the space velocity in units of 10 km s^{-1} and magnetic field strength in units of 10^{12} G[51]. **Right:** Comparison between neutron star initial velocity distributions[34,9] used in estimates of Bondi accretion rates[50,40].

Since they are powered by loss of gravitational potential energy of accreting matter, the X-ray luminosity of an accreting NS depends directly on the mass accretion rate, $\dot{M}$. The ROSAT predictions employed the Bondi-Hoyle formalism[3]

$$\dot{M}_{\rm Bondi} \approx \frac{4\pi G^2 M^2 \rho}{(v^2 + c_s^2)^{3/2}} \tag{1}$$

for hydrodynamic accretion, which applies only when the ambient medium is collisional on the scale size of the accretion radius, $r_{acc} = 2GM/v^2$. Here, ionization of the surrounding medium is essential because the Coulomb cross-section for protons, $\sigma_p \sim 2 \times 10^{14}$ cm^{-2} is two orders of magnitude larger than that for neutral particles, $\sigma_H \sim 3 \times 10^{16}$ cm^{-2}; neutrals can only accrete hydrodynamically for NS with space velocities no larger than $v \sim 1$ km s^{-1}—an impossibly small value. Ballistic accretion of non-interacting particles is much less efficient[1] and would be unable to drive X-ray emission. As long as the NS temperature is $T \gtrsim 10^5$ K it should be able ionize the ISM flow beyond the accretion radius, r_{acc}[1], but cooler objects producing too few ionizing photons to drive hydrodynamic accretion might never be reheated.

The applicability of the Bondi-Hoyle rate (Eqn. 1) has recently been criticised based on observed accretion rates around supermassive black holes[40] and on magnetohydrodynamic simulations of accretion onto magnetised

NS[49]. Perna et al.[40] suggest instead

$$\dot{M} \sim \left(\frac{R_{in}}{R_{acc}}\right)^{p} \dot{M}_{\rm Bondi} \qquad (2)$$

where R_{in} is a few tens of Schwarzchild radii and $p \sim 0.5$-1, giving $\dot{M} \sim 10^{-2}$-$10^{-4}\dot{M}_{Bondi}$, and predicted with this model a null detection rate of re-heated IRaTE NS in the RASS, in apparent agreement with observations.

Another important aspect of the Bondi accretion rate predictions is the dependency of $\dot{M}$ on v^{-3}: the predicted X-ray luminosity distribution of the accreting population then depends sensitively on the assumed NS velocity distribution. This velocity distribution depends on the NS birth rate through time, on the natal "kick" velocity resulting from anisotropic core collapse in the supernova explosion, and on the subsequent evolution of the velocity distribution in the Galactic gravitational potential over time—considerable uncertainties exist at each step. Recent work on pulsar velocities shows that the velocity distribution[34] used in RASS IRaTE NS predictions and that peaks sharply at ~ 45 km s^{-1} greatly overpredicts the fraction of low velocity stars[9] (Fig. 2). Adopting a more recent velocity distribution based on a sample of 49 young pulsars [9] leads to an order of magnitude reduction in the predicted number of detectable accreting NS[40]. With some confidence in estimated accretion rates, the observed limits to the detectable number of accreting IRaTE NS can also be used to constrain the NS velocity distribution. Using such arguments, the mean natal kick velocity appears to be $\gtrsim 200 - 300$ km s^{-1}[43].

In summary, the catastrophic overestimates of the detectable number of X-ray emitting IRaTE NS can be attributed to three main causes: (i) only a fraction of NS are likely to spend significant amounts of time as accreting objects owing to the longevity of the ejector and propeller phases[43]; (ii) the Bondi accretion rate likely substantially overestimates the true rate, possibly by orders of magnitude[49,40]; (iii) the assumed velocity distribution of accreting NS greatly overestimated the number of slow-moving objects.[9]

It is then very likely that the seven known IRaTE NS are young *cooling* objects[42]. This is potentially important for interpreting detailed spectroscopic observations: the surface composition of young objects might be expected to consist of heavy elements such as Mg, Si or Fe, depending on the degree of fall-back in the supernova event; accreting objects in contrast will have an atmosphere of pure H, since heavier metals gravitationally settle in a very short time.

2. High Resolution Spectroscopy of IRaTE NS

"The widespread astrophysical practice of declaring the nature of unresolved celestial objects is more entertainment than science"— Eugene Parker

Of the seven known IRaTE NS listed in Table 1, six have now been observed by *Chandra* or *XMM-Newton* and RBS 1774 should be observed by *XMM-Newton* in the coming year.

2.1. *RX J1856.5−3754*

"Simply a discovery that defies all known laws of physics"— National TV news, France 2

RX J1856.5−3754 was first identified as an isolated neutron star candidate from ROSAT observations of the Corona Australis star forming region[59]. It is the closest and X-ray brightest of the IRaTE NS and is therefore especially important for attempting to understand the structure and thermal evolution of neutron stars.

Optical and ultraviolet HST observations of RX J1856.5−3754 led to identification of an extremely faint blue counterpart to the X-ray source[58] and have provided estimates of the parallax and proper motion. A distance of 117 ± 12 pc was derived by Walter & Lattimer [57], superseding their earlier estimate of approximately half this value (61 pc) and supporting a larger distance of at least 100 pc implied by the measured ISM absorption[12]; at the same time, Kaplan and co-workers[22] had determined a range 110-200 pc, and based on more recent observations their preliminary value for the distance is now 175 pc (D. Kaplan, private communication).

Extrapolation of the ROSAT X-ray blackbody-like spectrum leads to significant underprediction of the optical flux, while pure hydrogen models overpredict it by factors of 30 or more[41]. Interpretation in terms of metal-dominated and two-blackbody models—ie models invoking surface temperature inhomogeneity such as a hot spot—alleviates this problem and initial analyses using the distance of 61 pc implied an upper limit to the radius of $R_\infty < 13$ km[41,57]—compatible only with the softest EOS.

Chandra observed RX J1856.5−3754 for 50 ks in 2000 March. These first 50 ks yielded a smooth, blackbody-liked spectrum[6] with none of the obvious line features predicted by heavy element atmosphere models. However, the spectra were noisy and RX J1856.5−3754 was observed under Director's time some 18 months later in 2001 October for a further 450 ks—about

ten times longer than a typical *Chandra* observation. All 500 ks of the combined data... yielded a smooth, blackbody-like spectrum with none of the obvious line features predicted by heavy element atmosphere models.[12] Timing analyses also failed to detect any sign of pulsations that might be expected from a hotspot or surface temperature inhomogeneities[12,44]; more recent *XMM-Newton* observations imply a pulse fraction upper limit of only 1.3% (2σ).[5]

> *"Astronomers have discovered two quarks with the Hubble Space Telescope"*—The Times (London)

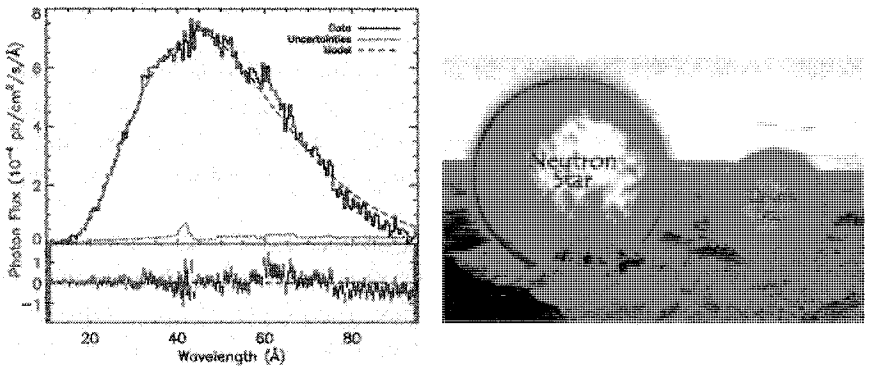

Figure 3. **Left:** *Chandra* LETGS spectrum of RX J1856.5−3754 with blackbody model and residuals (observations−model) [12]. Residuals are consistent with Poisson noise, allowing for detector gaps (∼60 Å) and calibration uncertainties. **Right:** Quark and neutron stars cunningly juxtaposed with the Grand Canyon to illustrate scale. The $5 \times 10^6 \sim 70$ kg visitors to the Grand Canyon each year that are inevitably accreted allow the stars to shine with a luminosity of $\sim 2 \times 10^{24}$ erg s^{-1}.

If it radiates like a blackbody, the radius of RX J1856.5−3754 can be derived from the distance and the observed luminosity obtained from the best-fit blackbody spectrum, as illustrated in Figure 3: $R_\infty = D\sqrt{L/\sigma T_\infty^4}$. This exercise yields a very small radius of $R_\infty = 3.2$-8.2 km[12] for an assumed distance in the range 111-200 pc.[22,12] Such a radius is incompatible with NS EOS and, combined with some expectations that they should have blackbody spectra,[60] lead to the speculation that RX J1856.5−3754 might indeed be a strange quark star[12] as had been suggested earlier based on ROSAT evidence alone[19]. This suggestion went down exceedingly well with the imaginative agents of publicity (Fig. 3, right panel).

2.1.1. *Arguments for a "Conventional" EOS*

"Quark stars signify unstable Universe"—Harvard University Gazette

It was subsequently argued that the revised distance[57] of 110-130 pc, combined with metal-dominated atmospheres or two-blackbody models, removes observational support for extremely soft EOS because such models yield radii compatible with canonical neutron stars[57]. However, even for these models the allowed range of radii also encompass quark star solutions[57] and these cannot be excluded. Moreover, the lines predicted by current metal-dominated model atmospheres are not supported by the observed smooth Planckian *Chandra* and *XMM-Newton* spectra, and two-component models rely on a special orientation of the spin and/or magnetic axes in order to meet the now stringent pulse fraction limit of current observations.

Another proposed explanation for a lack of metallic spectral features is that these are washed-out to leave a near blackbody spectrum in the case of a very rapidly spinning pulsar ($P \sim 1$ ms) [4]. However, such a short period does seem incompatible with other similar objects whose periods are in the 0.1-10s range, and based on the energetics of the Hα bow-shock nebula discovered in deep VLT imaging observations[55] would imply a very low magnetic field strength of 10^6-10^7 G.[53].

Qualitative arguments appealing to magnetic smearing of spectral lines have also been invoked to explain the lack of observed features.[52] In this work, $R_\infty > 16.5$ km was obtained from two-component surface T-varying blackbody analyses. While magnetic smearing arguments are plausible, the applicability of magnetized metal-dominated atmospheres to RX J1856.5−3754 has yet to be demonstrated, and the lack of observed pulsations for inhomogeneous T distributions again requires preferential spin/B orientation. Unencumbered by the burden of observational fact, it was nevertheless concluded that "Quark stars and neutron stars with quark matter cores can be ruled out with high confidence"...

We note that the latter two of the above cited studies[4,52] used a distance of 117 pc and canonical mass $M \sim 1.5 M_\odot$ to obtain true NS radii (as opposed to $_\infty$) of $\sim$ 14 km. Such a radius demands a hard EOS. If the preliminary distance of 175 pc (D. Kaplan, private communication) is confirmed, these radii will need to be upwardly revised to $\sim$ 20 km and would begin to look too large rather than too small, excluding all but the hardest equations of state unless the NS mass is extremely low ($\lesssim 0.3 M_\odot$).

2.2. *RX J0720.4 − 3125*

RX J0720.4 − 3125 is the second brightest IRaTE NS and was the first IRaTE NS to be observed by the new generation X-ray observatories on May 2000 in a 62.5 ks *XMM-Newton* pointing[38]. The EPIC-PN spectrum was well-represented by a blackbody and no spectral features were seen, apart from variations in the column density with pulse phase that may be explained in terms of energy-dependent beaming effects or cyclotron absorption[38,10]. Similar to RX J1856.5−3754, the optical spectrum is elevated above the extrapolated X-ray blackbody by a factor of 2.4 and shows signs of devation from a Rayleigh-Jeans tail[25].

The X-ray flux exhibits a modulation with a period of 8.31 s and a pulsed fraction of $\sim 15\%$[16,10]. The period derivative, $\dot{P} \sim 5 \times 10^{-14}\,\mathrm{ss}^{-1}$, was derived using the long timeline provided by both *ROSAT* and *XMM-Newton* data[61]. When interpreted in terms of magneto-dipolar braking, this deceleration implies a surface magnetic field of $\sim 2 \times 10^{13}$ G.[61] The currently favoured interpretation of RX J0720.4 − 3125 is in terms of a young off-beam radio pulsar[61,25].

Very recently, the X-ray spectrum of RX J0720.4 − 3125 in successive *XMM-Newton* observations has been seen to be slowly evolving away from a blackbody shape over a period of 3 years since the first observation and is becoming harder[13]. This surprising result has been tentatively interpreted[13] in terms of a model in which the observed quasi-blackbody is shaped by cyclotron-resonance scattering by electron-positron pairs in the magnetosphere[45] (see below). In this model, the changing spectral shape is caused by a gradual change in viewing angle as a result of precession of the NS.

2.3. *The Rest: RBS1223, RBS1556, RX J0806, RX J0420...*

With the exception of the "evolved" late RX J0720.4 − 3125 spectrum, the X-ray continuum spectra of all six IRaTE NS observed by *Chandra* or *XMM-Newton* to date appear to be consistent with blackbody energy distributions with temperatures in the range $kT \sim$ 40-100 eV. X-ray pulsations have been detected in four of the six with periods in the range 5-22s. Recent developments include the detection of a shallow broad absorption feature in RBS1223 at 270 eV and one at 450 eV in RX J1605.3+3249. These features have been interpreted in terms of proton cyclotron absorption[18,54]; B field strengths implied are 2-6 $\times 10^{13}$ and 10^{14} G, respectively. This

interpretation is favoured if these objects are young pulsars in which the radio beam does not cross the Earth as the derived B field is then similar to those determined for radio pulsars with similar long spin periods[18]. If the features are instead electron cyclotron lines, the implied B fields are weaker by the factor m_p/m_e, or ~ 2000.

There is a growing list of neutron stars observed by high resolution X-ray spectrometers on-board *Chandra* and *XMM-Newton* that appear to have featureless, thermal components. Two further examples are the middle-aged pulsar PSR B0656+14 and the anomalous X-ray pulsar 4U 0142+61[29] (see also the review of Pavlov et al.[39]). As with RX J1856.5−3754, they provide a challenge to current model atmospheres for neutron stars since both metal-dominated or pure H or He models are incapable of explaining their SEDs.

3. Are RX J1856.5−3754 and RX J0720.4 − 3125 "Naked"?

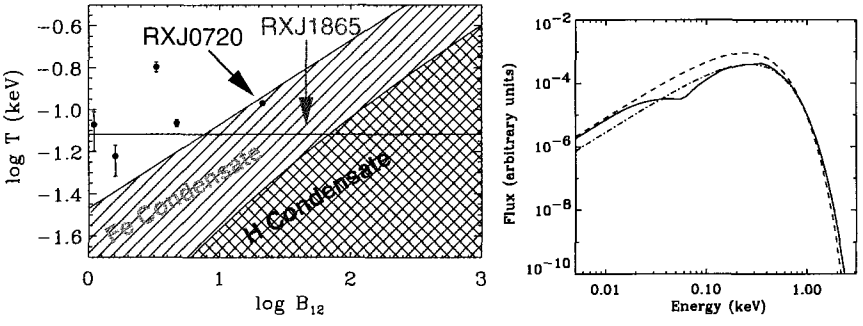

Figure 4. **Left:** Critical temperature for H and Fe as a function of the magnetic field.[53] Condensation is possible in the hatched region for Fe and in the cross-hatched region for H. The filled circles with error bars mark the position of five cool INSs; the horizontal line corresponds to RX J1856.5−3754. **Right:** Emergent spectrum (solid curve) from a neutron star with a condensed surface, and with effective temperature $T = 10^6$ K, $B = 2 \times 10^{13}$ G and a 0.002 g cm^{-2} overlying H layer. The dashed curve is a blackbody with the same temperature, while the dashed-dot curve corresponds to the best-fit blackbody to the model spectrum.

Based on theoretical arguments that cool neutron stars ($T \lesssim 10^6$ K) endowed with a rather high magnetic field ($B \gtrsim 10^{13}$ G) might undergo a phase transition to a solid state in the outermost layers,[26] it has been suggested that RX J1856.5−3754, and perhaps also RX J0720.4 − 3125, might be left "naked" with no gaseous atmosphere[53,6] (Fig. 4). Computed

spectra from naked neutron stars with a surface Fe composition are featureless and virtually indistinguishable from a blackbody in the 0.1-2 keV range for energies above the plasma frequency, though the solid surface has an emissivity $\sim 30-50\%$ lower than that of a blackbody. Below the plasma frequency, electron-phonon interactions devastate the emissivity and the spectrum plummets to zero.[53] The reduced X-ray emissivity leads to a larger radius than the blackbody radiation radius. This model is promising for explaining the X-ray SED of RX J1856.5−3754 and predicts an apparent star radius of $R_\infty \sim$ 10-12 km—compatible with quark star EOS, and in reach of soft NS EOS, especially if the distance of 175 pc is confirmed.

The optical excess above the X-ray blackbody can be explained in this model by a thin H layer that might have either been accreted, or has fallen back during the supernova explosion.[53,33] One example of the emergent spectrum from this model is illustrated in the right panel of Figure 4.

4. Cyclotron-resonance Scattering in an e^+-e^- pair plasma?

It has recently been proposed that the Planck-like spectrum of IRaTE NS might be explained by cyclotron-resonance scattering of the underlying stellar spectrum by an optically-thick $e+/-$ pair plasma that is maintained by the conversion of gamma-rays associated with the polar-cap and/or outer-gap accelerators.[45]. The scattering occurs within several radii of the neutron stars and prevents direct observations of thermal X-rays from the stellar surface. While quantitative modelling remains to be done, this intriguing suggestion would imply that we are looking at the magnetospheres rather than the photospheres if the IRaTE NS. An impenetrable magnetosphere would put serious dampers on attempts to use IRaTE NS to constrain the EOS, possibly precipitating a fall from the top of the *Cosmic Sexiness Ladder*.

5. Concluding Remarks and the Future

> *"One should always be suspicious of an experimental result until it is confirmed by theory"*—Sir Arthur Eddington

Arguments against there being a significant population of accretion-heated IRaTE NS, combined with population synthesis of young cooling objects, conspire to imply that the seven objects found to date belong to the latter class. The general similarity between objects such as RX J1856.5−3754 and RX J0720.4−3125 make it tempting to interpret the

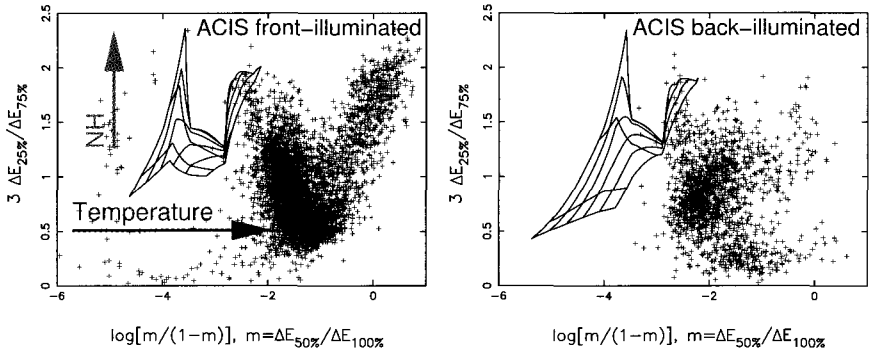

Figure 5. The ratio of 25% and 75% quantile photon energies for sources detected in Chandra fields observed using the ACIS detector plotted as a function of the normalised median photon energy. The vast majority of sources are active galactic nuclei and stellar coronae. The grid is comprised of analogous quantile ratio loci computed for blackbody spectra in the range 10^5-10^6 K as a function of temperature (increasing to the right) and intervening ISM absorption (increasing upward). Only a small handful of possible candidates lie within these regions.

IRaTE NS as young off-beam pulsars, or possibly as magnetar decendents[30]. However, there is as yet no satisfactory explanation for RX J1856.5−3754 that fits all available data without invoking ad hoc explanations for lack of pulsations, spectral features or optical excess. While the awkward observational data can with some effort be shoehorned into canonical theory, other quite different physical explanations are also possible. These include a strange quark star EOS and a solid phase naked star bereft of an optically thick atmosphere.

Only when we can understand the outer layers better will observations of these stars become potentially useful for constraining the EOS. Three areas for future progress lie in (i) including magnetic fields in metal-dominated models that, other than for their gaping X-ray holes, appear quite promising in explaining IRaTE NS SEDs; (ii) repeating observations of IRaTE NS already observed to search for secular variations that might betray aspects of the underlying nature of these stars; (ii) finding new IRaTE NS to enlarge the woefully small sample of known objects. In this regard, work is currently underway to search the entire database of *Chandra* observations for serendipitous sources that might be NS candidates (Fig. 5). While the sky coverage is small (a few 10's of square degrees), many pointings are deep and the 1 arcsec *Chandra* PSF should allow for rapid counterpart identification.

JJD was supported by NASA contract NAS8-39073 to the *Chandra X-ray Center* during the course of this work. I extend warm thanks to colleagues R. Torolla and S. Zane for stimulating collaborations on neutron stars and for illuminating discussions, to David Kaplan for permission to use his latest provisional parallax for RX J1856.5−3754, and to Pete Ratzlaff for help with *Chandra* analyses.

References

1. Alcock, C. and A. Illarionov, *ApJ* **235**, 541 (1980).
2. Blaes, O. and P. Madau, *ApJ* **403**, 690 (1993).
3. Bondi, H. and F. Hoyle, *MNRAS* **104**, 273 (1944).
4. Braje, T. M. and R. W. Romani, *ApJ* **580**, 1043 (2002).
5. Burwitz, V., F. Haberl, R. Neuhäuser, P. Predehl, J. Trümper, and V. E. Zavlin, *A&A* **399**, 1109 (2003).
6. Burwitz, V., V. E. Zavlin, R. Neuhäuser, P. Predehl, J. Trümper, and A. C. Brinkman, *A&A* **379**, L35 (2001).
7. Campana, S., S. Mereghetti, and L. Sidoli, *A&A* **320**, 783 (1997).
8. Colpi, M., R. Turolla, S. Zane, and A. Treves, *ApJ* **501**, 252 (1998).
9. Cordes, J. M. and D. F. Chernoff, *ApJ* **505**, 315 (1998).
10. Cropper, M., S. Zane, G. Ramsay, F. Haberl, and C. Motch, *A&A* **365**, L302 (2001).
11. Davidson, K. and J. P. Ostriker, *ApJ* **179**, 585 (1973)
12. Drake, J. J., and 10 colleagues, *ApJ* **572**, 996 (2002).
13. de Vries, C. P., J. Vink, M. Méndez, and F. Verbunt, *A&A* **415**, L31 (2004).
14. Haberl, F. and V. E. Zavlin, *A&A* **391**, 571 (2002).
15. Haberl, F., C. Motch, and W. Pietsch, *AN* **319**, 97 (1998).
16. Haberl, F., C. Motch, D. A. H. Buckley, F.-J. Zickgraf, and W. Pietsch, *A&A* **326**, 662 (1997).
17. Haberl, F., W. Pietsch, and C. Motch, *A&A* **351**, L53 (1999).
18. Haberl, F., A. D. Schwope, V. Hambaryan, G. Hasinger, and C. Motch, *A&A* **403**, L19 (2003).
19. Haensel, P., *A&A* **380**, 186 (2001).
20. Kaminker, A. D., D. G. Yakovlev, and O. Y. Gnedin, *A&A* **383**, 1076 (2002).
21. Kaplan, D. L., S. R. Kulkarni, M. H. van Kerkwijk, and H. L. Marshall, *ApJ* **570**, L79 (2002).
22. Kaplan, D. L., M. H. van Kerkwijk, and J. Anderson, *ApJ* **571**, 447 (2002).
23. Kaplan, D. L., S. R. Kulkarni, and M. H. van Kerkwijk, *ApJ* **579**, L29 (2002).
24. Kaplan, D. L., S. R. Kulkarni, and M. H. van Kerkwijk, *ApJ* **588**, L33 (2003).
25. Kaplan, D. L., M. H. van Kerkwijk, H. L. Marshall, B. A. Jacoby, S. R. Kulkarni, and D. A. Frail, *ApJ* **590**, 1008 (2003).
26. Lai, D., *RvMP* **73**, 629 (2001).
27. Lattimer, J. M. and M. Prakash, *ApJ* **550**, 426 (2001).
28. Livio, M., C. Xu, and J. Frank, *ApJ* **492**, 298 (1998).
29. H. L. Marshall and N. S. Schulz, *ApJL* **574**, 377 (2002)

30. Motch, C., *AIP Conf Proc* **599**, 244 (2001)
31. Motch, C. and F. Haberl, *A&A* **333**, L59 (1998).
32. Motch, C., F. Haberl, F.-J. Zickgraf, G. Hasinger, and A. D. Schwope, *A&A* **351**, 177 (1999).
33. Motch, C., V. E. Zavlin, and F. Haberl, *A&A* **408**, 323 (2003).
34. Narayan, R. and J. P. Ostriker, *ApJ* **352**, 222 (1990).
35. Neuhaeuser, R., H.-C. Thomas, R. Danner, S. Peschke, and F. M. Walter, *A&A* **318**, L43 (1997).
36. Ostriker, J. P., M. J. Rees, and J. Silk, *ApL* **6**, 179 (1970).
37. Paerels, F., *ApJ* **476**, L47 (1997).
38. Paerels, F., and 8 colleagues, *A&A* **365**, L298 (2001).
39. Pavlov, G. G., V. E. Zavlin, and D. Sanwal, *MPE Report* **278**, 273 (2002).
40. Perna, R., R. Narayan, G. Rybicki, L. Stella, and A. Treves, *ApJ* **594**, 936 (2003).
41. Pons, J. A., F. M. Walter, J. M. Lattimer, M. Prakash, R. Neuhäuser, and P. An, *ApJ* **564**, 981 (2002).
42. Popov, S. B., M. Colpi, M. E. Prokhorov, A. Treves, and R. Turolla, *A&A* **406**, 111 (2003).
43. Popov, S. B., M. Colpi, A. Treves, R. Turolla, V. M. Lipunov, and M. E. Prokhorov, *ApJ* **530**, 896 (2000).
44. Ransom, S. M., B. M. Gaensler, and P. O. Slane, *ApJ* **570**, L75 (2002).
45. Ruderman, M., **astro-ph/0310777** (2003).
46. Rutledge, R. E., D. W. Fox, M. Bogosavljevic, and A. Mahabal, *ApJ* **598**, 458 (2003).
47. Schwope, A. D., G. Hasinger, R. Schwarz, F. Haberl, and M. Schmidt, *A&A* **341**, L51 (1999).
48. Stocke, J. T., Q. D. Wang, E. S. Perlman, M. E. Donahue, and J. F. Schachter, *AJ* **109**, 1199 (1995).
49. Toropin, Y. M., O. D. Toropina, V. V. Savelyev, M. M. Romanova, V. M. Chechetkin, and R. V. E. Lovelace, *ApJ* **517**, 906 (1999).
50. Treves, A. and M. Colpi, *A&A* **241**, 107 (1991).
51. Treves, A., R. Turolla, S. Zane, and M. Colpi, *PASP* **112**, 297 (2000).
52. Truemper, J. E., V. Burwitz, F. Haberl, and V. E. Zavlin, **astro-ph/0312600** (2003).
53. Turolla, R., S. Zane, and J. J. Drake, *ApJ* **603**, 265 (2004).
54. van Kerkwijk, M. H., D. L. Kaplan, M. Durant, S. R. Kulkarni, and F. Paerels, **astro-ph/0402418** (2004).
55. van Kerkwijk, M. H. and S. R. Kulkarni, *A&A* **380**, 221 (2001).
56. Verbunt, F., *AIP Conf Proc* **308**, 351 (1994).
57. Walter, F. M. and J. M. Lattimer, *ApJ* **576**, L145 (2002).
58. Walter, F. M. and L. D. Matthews, *Nature* **389**, 358 (1997).
59. Walter, F. M., S. J. Wolk, and R. Neuhauser, *Nature* **379**, 233 (1996).
60. Xu, R. X., *ApJ* **570**, L65 (2002).
61. Zane, S., F. Haberl, M. Cropper, V. E. Zavlin, D. Lumb, S. Sembay, and C. Motch, *MNRAS* **334**, 345 (2002).

PHASE TRANSITIONS IN NEUTRON STARS

NORMAN K. GLENDENNING
Nuclear Science Division and
Institute for Nuclear & Particle Astrophysics
Lawrence Berkeley National Laboratory
Berkeley, California 94720
USA

Neutron stars are the densest objects in the universe today in which matter with several phases in adiabatic equilibrium can be found. Various high-density phases, both geometric and constitutional are spatially spread out by the pressure gradient in the star. Boundaries between phases slowly move, appear, or disappear as the density profile of the star is changed by the centrifugal force due to spindown caused by the magnetic torque of a pulsar, or the spinup of an x-ray neutron star because of the torque applied by mass accreted from a companion star. Phase transitions in turn produce their own imprint on the spin behavior through changes in the moment of inertia as one phase replaces another, in some cases on single stars, and in others on populations. These are the clues that we elucidate after first reviewing high-density phases.

1. A Brief History of Neutron Stars

- 1054 Chinese astronomer "observed the apparition of a guest star ...its color an iridescent yellow".
- 1933 Baade and Zwicky—binding energy of "closely packed neutrons" powers supernova.
- 1939 Oppenheimer, Volkoff and Tolman—neutron fermi gas.
- 1967 Pacini predicted magnetic dipole radiation.
- 1967 Hewish & Bell's serendipitous discovery of neutron stars producing a radio pulse once every revolution from beamed radiation along the magnetic axis which is fixed in the star. They are believed to be the *direct* product of core collapse a mature massive star and its the subsequent supernova.
- 1974 Hulse and Taylor binary neutron star pair in close orbit.

- 1984 Bacher's discovery of first Millisecond pulsar. They are believed to be very old supernova products that have been spun up by mass accretion from a low-mass companion star.
- 1992 Wolszczan & Frail, discovery of 3 planets around a neutron star.

2. Gross Features of Neutron Stars

- Surface gravity M/R of Black hole $=0.5$,
  Neutron star $=0.2$,
  Sun $=10^{-6}$
- Gravitational binding / Nuclear binding ~ 10
- Radius $= 10 - 12$km, Mass$\geq 1.44 M_{\odot}$
- Spin periods from seconds to milliseconds
- Neutron stars are degenerate objects ($\mu << T$).
- Stars are electrically neutral. $(Z_{\rm Net}/A \sim (m/e)^2 < 10^{-36})$
- Baryon number and charge are conserved.
- Strangeness not conserved (beyond 10^{-10} seconds).
- Millisecond pulsars have remarkably stable pulses:
  $P = 1.55780644887275 \pm 0.00000000000003$ ms
  (measured for PSR 1937+21 on 29 Nov 1982 at 1903 UT)

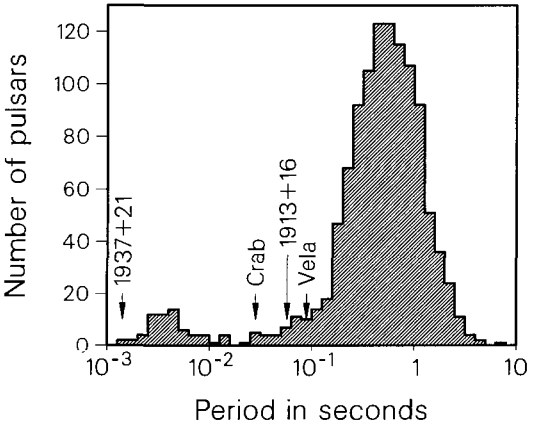

Figure 1. There are two classes of pulsars. The great bulk of known ones are the canonical pulsars with periods centered at about 0.7 seconds. The millisecond pulsars are believed to be an evolutionarily different class. They are harder to detect, and were first discovered in 1982.

3. Hyperonization

Free neutrons are unstable, but in a star the size and mass of a neutron star, *gravitational* binding energy is about ten times greater than *nuclear* binding so that neutrons are a stable component of dense stars. What about protons? The repulsive Coulomb force is so much stronger than the gravitational, that the net electric charge on a star must be very small ($Z_{\rm net}/(N+Z) < (m/e)^2 \sim 10^{-36}$). We can say that it is charge neutral. Since $m_p + m_e > m_n$, neutrons are the preferred baryon species. However, being Fermions, with increasing density of neutron matter, the Fermi level of neutrons will exceed the mass of proton and electron at some, not too high a density. Therefore, protons and electrons will also occupy neutron star matter. Because strangeness is conserved only on a weak interaction time-scale, this quantum number is not conserved in an equilibrium state. So with increasing density, the Pauli principle assures us that baryons of many species will be ingredients of dense neutral matter.[1,2]

Generally, it suffices to take the baryon octet into account together with electrons and muons. In Figure 2 we see that the Λ is most strongly populated in the center of a typical neutron star *if* quarks have not become deconfined at those densities. Notice that the lepton populations decrease as the populations of negatively charged hyperons increase. This is in accord with conservation of baryon number in the star. The number of electrons and muons are not by themselves conserved.

The equation of state is softened in comparison with a neutron matter equation of state. The softening means that the Fermi pressure is reduced so that hyperon matter cannot support as large a mass against gravitational collapse than would be the case otherwise. The hyperon transition is second order; particle populations vary continuously with density in a uniform medium. However, the densities reached in neutron star cores, 5 to 10 times nuclear matter density, are in all likelihood too high for baryons to exist as separate entities—quarks are likely to become deconfined at lower density than that. This is likely to be a first order phase transition.

4. First Order Transitions in Stars

Generally, physicists think of a phase transition such as from water to vapor as being *typical* of a first order transition. In the real world it is far from typical. Its characteristics are: if heated at constant pressure, the temperature of water and vapor will rise to 100 C and remain there until all the water has been evaporated before the temperature of the steam rises.

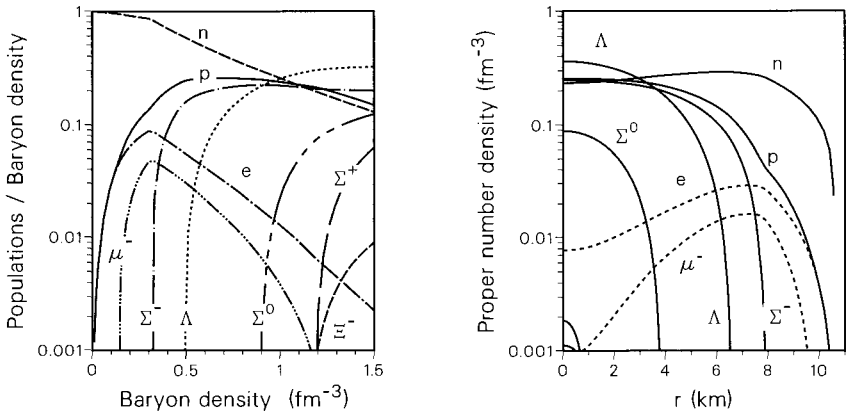

Figure 2. Particle populations as a function of baryon density in dense matter, and as a function of radial coordinate in a neutron star.

This is true of substances having *one* independent component (like H^2O). The situation can, and usually is much more interesting for substances with two or more independent components, as I recognized a few years ago.[3] Neutron stars are an example. The independent components are the conserved baryon and electric charge. Until about 1990, all authors forced stellar models into the mold of single-component substances by imposing a condition of *local* charge neutrality and ignoring the discontinuity in electron chemical potential at the interface of two phases in equilibrium. In 1992 I realized that all these models of phase transitions in nuclear matter—which has two independent conserved components, the total baryon charge and the electric charge—were intrinsically incorrect.[3] They cannot satisfy Gibbs criteria for phase equilibrium in complex systems. And I stressed that an altogether new set of phenomenon were introduced by solving the problem correctly. Indeed, a *Coulomb crystalline region* involving the two phases in equilibrium could form, an idea that had not previously come to light.[3]

4.1. *Degrees of freedom and driving forces*

Two features can come into play in phase transition of complex substances that are absent in simple substances. The degree(s) of freedom can be seen in the following way. Imagine assembling a star in a pure phase (say ordinary nuclear matter) with B baryons and Q electric charges, either positive, negative or zero. (Of course, more precisely, we consider a typical local inertial region.) The concentration is said to be $c = Q/B$. Now

consider another local region deeper in the star and at higher pressure with the same number of baryons and charges, but with conditions such that part of the volume is in the first phase and another part in the second phase. Suppose the baryons and charges in the two phases are distributed such that concentrations in the two phases are

$$Q_1/B_1 = c_1 \quad \text{and} \quad Q_2/B_2 = c_2\,.$$

The conservation laws are still satisfied if

$$Q_1 + Q_2 = Q, \qquad B_1 + B_2 = B\,.$$

Why might the concentrations in the two phases be different from each other and from the concentration in the other local volumes at different pressure? Because the *degree of freedom* of redistributing the concentration may be exploited by *internal forces* of the substance so as to achieve a lower free energy. In a single-component substance there was no such degree of freedom, and in an n-component substance there are $n-1$ degrees of freedom. In deeper regions of the star, still different concentrations may be favored in the two phases in equilibrium at these higher-pressure locations. So you see that the each phase in equilibrium with the other, may have continuously changing properties from one region of the star to another. (This is unlike the simple substance whose properties remain unchanged in each equilibrium phase, until only one phase remains.)

The key recognition is that conserved quantities (or independent components) of a substance are conserved *globally*, but need not be conserved *locally*.[3] Otherwise, Gibbs conditions for phase equilibrium cannot be satisfied. Let us see how this is done.

Gibbs condition for phase equilibrium in the case of two conserved quantities is

$$p_1(\mu_n, \mu_e, T) = p_2(\mu_n, \mu_e, T)$$

We have introduced the neutron and electron chemical potentials by which baryon and electric charge conservation are to be enforced. In contrast to the case of a simple substance, for which Gibbs condition—$p_1(\mu, T) = p_2(\mu, T)$—can be solved for μ, the phase equilibrium condition cannot be satisfied for substance of more than one independent component without additional conservation constraints. Clearly, *local* charge conservation ($q(r) \equiv 0$) must be abandoned in favor of global conservation

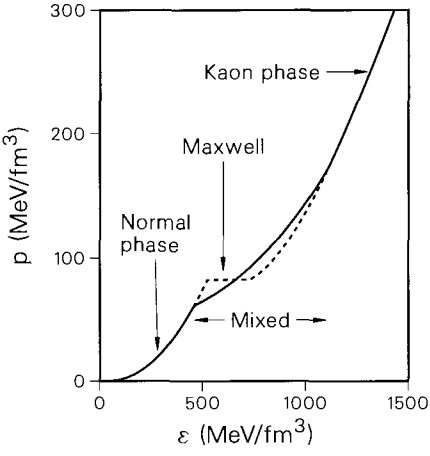

Figure 3. Solid line: equation of state for neutron star matter with a kaon condensed phase. Regions of the normal nuclear matter phase, the mixed phase, and the pure kaon condensed phase are marked. Notice that the pressure changes monotonically through the mixed phase. Dashed line: The Maxwell construction with the typical constant pressure region does not satisfy equality of the electron chemical potential in the two phases.

($\int q(r)q(r) \equiv 0$), which is after all what is required by physics. For a uniform distribution global neutrality reads,

$$(1-\chi)q_1(\mu_n, \mu_e, T) + \chi q_2(\mu_n, \mu_e, T) = 0\,,$$

where $\chi = V_2/V$, $V = V_1 + V_2$. Given T and χ we can solve for $\mu_n and \mu_e$. Thus the solutions are of the form

$$\mu_n = \mu_n(\chi, T), \qquad \mu_e = \mu_e(\chi, T)\,.$$

Because of the dependance on χ, we learn that all properties of the phases in equilibrium change with proportion, χ, of the phases. This contrasts with simple (one component) substances. These properties are illustrated for the pressure in Figure 3. Behavior of the pressure is illustrated for two cases: (1) a simple, and (2) a complex substance. In the latter case, the pressure is monotonic, as proven above. This is in marked contrast to the pressure plateau of the simple (one component) substance.

4.2. *Isospin symmetry energy as a driving force*

A well known feature of nuclear systematics is the valley of beta stability which, aside from the Coulomb repulsion, endows nuclei with $N = Z$ the greatest binding among isotones ($N + Z = \text{const}$). Empirically, the form of the symmetry energy is

$$E_{\text{N-sym}} = -\epsilon[(N - Z)/(N + Z)]^2 .$$

Physically, this arises in about equal parts from the difference in energies of neutron and proton Fermi energies and the coupling of the ρ meson to nucleon isospin current. Consider now a neutron star. While containing many nucleon species, neutron star matter is still very isospin asymmetric—it sits high up from the valley floor of beta stability—and must do so because of the asymmetry imposed by the strength of the Coulomb force compared to the gravitational.

Let us examine sample volumes of matter at ever-deeper depth in a star until we arrive at a local inertial volume where the pressure is high enough that some of the quarks have become deconfined; that both phases are present in the local volume. According to what has been said above,

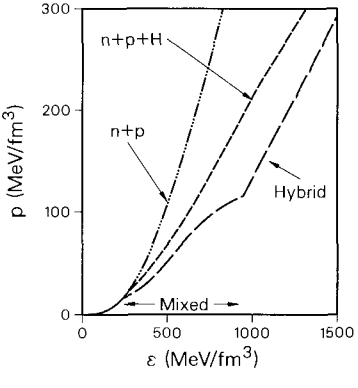

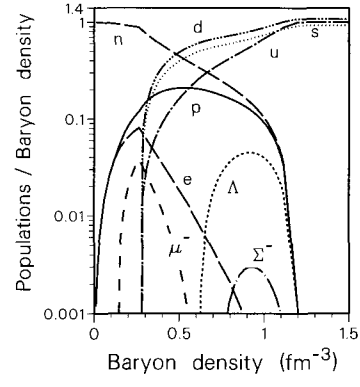

Figure 4. Equation of state for matter in *beta equilibrium* for three hypothetical models of dense nuclear matter; (1): only neutrons and protons are present (n + p), (2): in addition to neutrons and protons, hyperons (H) are also present (n + p + H), (3): *Hybrid* denotes the equation of state for which matter has a low density nuclear phase, an intermediate mixed phase, and a high-density quark phase. Discontinuities in slope signal the transition between these phases.

Figure 5. The particle populations are shown as a function of density as phases change. The low-density region, 0.3fm^{-3} ρ_B, is pure charge-neutral nuclear matter; the mixed nuclear and quark matter region lies in the density range $0.3 < \rho_B < 1.2$ fm^{-3}, and pure quark region lies above $\rho_{\text{B}} > 1.2$ fm^{-3} .

the highly unfavorable isospin of the nuclear phase can lower its repulsive asymmetry energy if some neutrons exchange one of their d quarks with a u quark in the quark phase in equilibrium with it. In this way the nuclear matter will become positively charged and the quark matter will carry a compensating negative charge, and the overall energy will be lowered. The *degree* to which the exchange will take place will vary according to the proportion of the phases—clearly a region with a small proportion of quark matter cannot as effectively relieve the isospin asymmetry of a large proportion of neutron star matter of its excess isospin as can a volume of the star where the two phases are in *more* equal proportion. We see this quantitatively in Figure 6 where the charge densities on hadronic and quark matter are shown as a function of proportion of the phases.

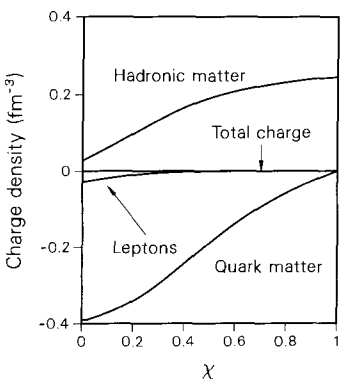

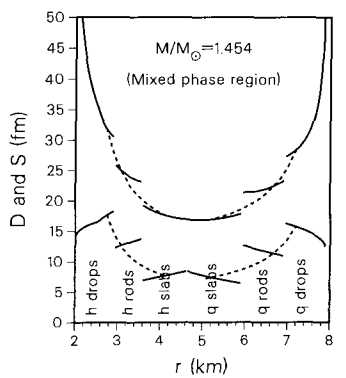

Figure 6. Charge densities on Hadronic and Quark matter as a function of proportion. Note that overall the mixture is neutral.

Figure 7. Diameter (bottom curve) and spacing (top curve) of the geometrical phases are shown as a function of position r in the star of $1.454M_\odot$. (see also Figure 8)

4.3. *Geometrical phases*

In equilibrium, the isospin driving force tends to concentrate positive charge on nuclear matter and compensating negative charge on quark matter. The Coulomb force will tend to break up regions of like charge while the surface interface energy will resist this tendency. The same competition is in play in the crust of the star where ionized atoms sit at lattice sites in an electron sea. For the idealized geometries of spheres, rods, or sheets of the rare phase immersed in the dominant one, and employing the Wigner-Seitz

approximation (in which each cell has zero total charge, and does not interact with other cells), closed form solutions exist for the diameter D, and spacing S of the Coulomb lattice. The Coulomb and surface energy for drops, rods or slabs ($d = 3, 2, 1$) have the form:

$$\epsilon_C = C_d(\chi)D^2\,, \quad \epsilon_S = S_d(\chi)/D\,,$$

where C_d abd S_d are simple algebraic functions of χ. The sum is minimized by $\epsilon_S = 2\epsilon_C$. Hence, the diameter of the objects at the lattice sites is

$$D = [S_d(\chi)/2C_d(\chi)]^{1/3}\,,$$

where their spacing is $S = D/\chi^{1/d}$ if the hadronic phase is the background or $S = D/(1-\chi)^{1/d}$ if the quark phase is background. Figure 7 shows the computed diameter and spacing of the various geometric phases of quark and hadronic matter as a function of radial coordinate in a hybrid neutron star.

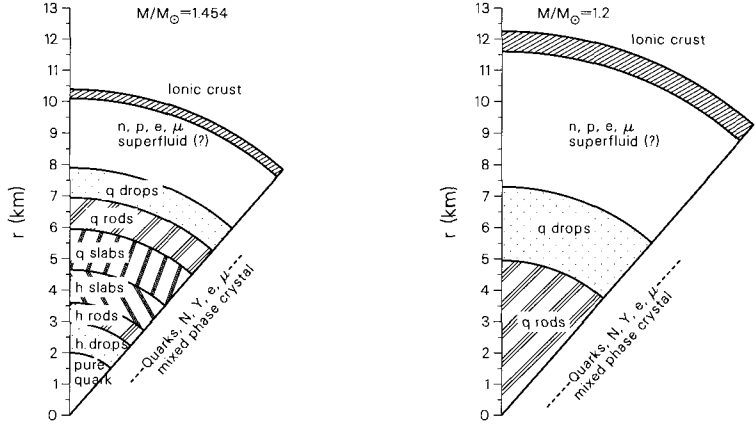

Figure 8. Pie sections showing geometric phases in two stars of different mass

4.4. *Color-flavor locked quark-matter phase (CFL)*

Rajagopal and Wilczek have argued that the Fermi surface of the quark deconfined phase is unstable to correlations of quarks of *opposite* momentum and *unlike* flavor and form BCS pairs[4]. They estimate a pairing gap of $\Delta \sim 100$ MeV. The greatest energy benefit is achieved if the Fermi surfaces of all flavors are equal in radius. This links color and flavor by an

invariance to simultaneous rotations of color and flavor. The approximate energy density corresponding to the gap is

$$\epsilon_{\Delta-\mathrm{CFL}} \sim -C(k_F\,\Delta)^2 \sim 50 \cdot C\ \mathrm{MeV/fm^3}\,,$$

where C is an unknown constant. This is another "driving force" as spoken of above *in addition* to the nuclear symmetry energy ϵ_{sym}. It acts, not to restore isospin symmetry in nuclear matter, but color-flavor symmetry in the quark phase. Alford, Rajagopal, Reddy, and Wilczek have argued that the CFL phase, which is *identically* charge neutral and has this large pairing gap *may* preempt the possibility of phase equilibrium between confined hadronic matter and the quark phase; that any amount of quark matter would go into the charge neutral CFL phase (with equal numbers of u, d and s quarks, irrespective of mass) and that the mixed phase spoken of above would be absent.[5] That the nuclear symmetry driving force would be overcome by the color-flavor locking of the quark phase leaving the degree of freedom possessed by the two-component system unexploited. The discontinuity of the electron chemical potential in the two phases, hadronic and quark matter would be patched by a spherical interface separating a core of CFL phase in the star from the surrounding hadronic phase. For that conclusion to be true, a rather large surface interface coefficient was chosen by dimensional arguments.

However, my opinion is that nature will make a choice of surface interface properties between hadronic and quark matter such that the degree of freedom of exchanging charge can be exploited by the driving forces (here two in number as discussed below). This is usually the case. Physical systems generally have their free energy lowered when a degree of freedom (as spoken of above) becomes available.

With two possible phases of quark matter, the uniform uncorrelated one discussed first, and the CFL phase as discussed by Rajagopal and Wilczek, there is now a competition between the CFL pairing and the nuclear symmetry-energy densities, and these energy densities are *weighted* by the volume proportion χ of quark matter in comparison with hadronic matter in locally inertial regions of the star. That is to say, ϵ_{CFL} and ϵ_{sym} are not directly in competition, but rather they are weighted by the relevant volume proportions. It is not a question of "either, or" but "one, then the other".

The magnitude of the nuclear symmetry energy density at a typical phase transition density of $\rho \sim 1/\mathrm{fm}^3$ is

$$\epsilon_{\mathrm{N-sym}} = -35[(N-Z)/(N+Z)]^2\ \mathrm{MeV/fm^3}\,.$$

To gain this energy a certain price is exacted from the disturbance of the symmetry of the uniform quark matter phase in equilibrium with it; $\epsilon_{\mathrm{Q-sym}}$. As can be inferred from Figure 6, the price is small compared to the gain. On the other side, the energy gained by the quark matter entering the CFL phase was written above and is offset by the energy not gained by the nuclear matter because the CFL preempts an improvement in its isospin asymmetry. So we need to compare

$$(1-\chi)\epsilon_{\mathrm{N-sym}} - \chi\,\epsilon_{\mathrm{Q-sym}} - [\epsilon_{\mathrm{surf}}(\chi) + \epsilon_{\mathrm{coul}}(\chi)]$$

with

$$\chi\,\epsilon_{\Delta\mathrm{-CFL}} - (1-\chi)\epsilon_{\mathrm{N-sym}}\,.$$

The behavior of these two lines as a function of proportion of quark phase χ in a local volume in the star is as follows:[a] The first expression for the net gain in energy due to the formation of a mixed phase of nuclear and uniform quark matter monotonically decreases from its maximum value at $\chi = 0$ while the second expression, the net energy gain in forming the CFL phase monotonically increases from *zero* at $\chi = 0$. Therefore as a function of χ or equivalently depth in the star measured from the depth at which the first quarks become deconfined, nuclear symmetry energy is the dominating driving force, while at some value of χ in the range $0 < \chi < 1$ the CFL pairing becomes the dominating driving force.

In terms of Figure 8, several of the outermost geometric phases in which quark matter occupies lattice sites in a background of nuclear matter are undisturbed. But the sequence of geometric phases is terminated before the series is complete, and the inner core is entirely in the CFL phase.

In summary, when the interior density of a neutron star is sufficiently high as to deconfine quarks, a charge neutral color-flavor locked phase with no electrons will form the inner core. This will be surrounded by one or more shells of mixed phase of quark matter in a uniform phase in phase equilibrium with confined hadronic matter, the two arranged in a Coulomb lattice which differs in dimensionality from one shell to another. As seen in Figure 6, the density of electrons is very low to essentially vanishing, because overall charge neutrality can be achieved more economically among the conserved baryon charge carrying particles. Finally, All this will be surrounded by uniform charge neutral nuclear matter with varying particle composition according to depth (pressure), (cf. Figure 5.)

[a]The behavior of the quantity in square brackets can be viewed in Figure 9.14 of reference [2, 2'nd ed.]

5. Rotation and Phase Transitions

Except for the first few seconds in the life of a neutron star, at which time they radiate the vast bulk of their binding energy in the form of neutrinos, we think of them as rather static objects. However the spin evolution at *millisecond* periods of rotation brings about centrifugally induced changes in the density profile of the star, and hence also in the thresholds and densities of various hyperons, dense phases such as kaon condensed phase and inevitably quark matter. We shall *assume* that the central density of the more massive millisecond pulsars—being centrifugally diluted—lies below the critical density for pure quark matter, while the central density of canonical pulsars, like the Crab, and more slowly rotating ones, lies above. We explore the consequences of such assumptions.

Because of the different compressibility of low and high-density phases, conversion from one phase to another as the phase boundary slowly moves with changing stellar spin (Fig. 9) results in a considerable redistribution of mass (Fig. 10) and hence change in moment of inertia over time. The time scale is of the order of 10^7 to 10^9 yr. The behavior of the moment of inertia while successive shells in the star are changing phase is analogous

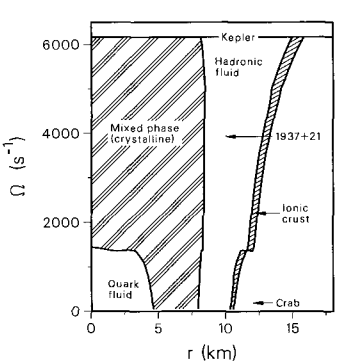

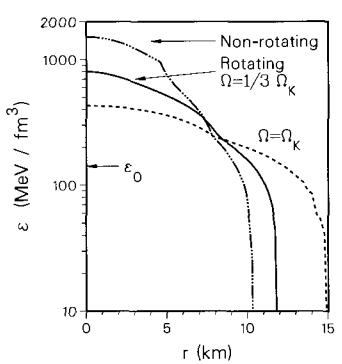

Figure 9. Radial boundaries at various rotational frequencies separating various phases. The frequencies of two pulsars, the Crab and PSR 1937+21 are marked for reference.

Figure 10. Mass profiles as a function of equatorial radius of a star rotating at three different frequencies. At low frequency the star is very dense in its core, having a 4 km central region of highly compressible pure quark matter. Inflections at $\epsilon \approx 220$ and 950 are the boundaries of the mixed phase.

to the so-called backbending behavior of the moment of inertia of deformed rotating nuclei brought about by a change of phase from one in which the coriolis force breaks nucleon spin pairing to one in which spins are paired. Compare Figs. 11 and 12.

Elsewhere we have discussed the possible effect of a phase transition on isolated millisecond radio pulsars.[6] Here we discuss x-ray neutron stars that have a low-mass non-degenerate companion. Beginning at a late stage in the evolution of the companion it evolves toward its red-giant stage and mass overflows the gravitational barrier between the donor and neutron star. The neutron star is spun up by angular momentum conservation of the accreted matter. The heated surface of the neutron star and its rotation may be detected by emitted x-rays.

In either case—neutron star accretors or millisecond pulsars—the radial thresholds of particle types and phase boundaries will move—either outward or inward—depending on whether the star is being spun up or down. The critical density separating phases moves slowly so that the conversion from one phase to another occurs little by little at the moving boundary. In a rapidly rotating pulsar that is spinning down, the matter density initially is centrifugally diluted, but the density rises above the critical phase transition density as the star spins down. Relatively stiff nuclear matter is converted to highly compressible quark matter. The overlaying layer of nuclear matter squeezes the quark matter causing the interior density to rise, while the greater concentration of mass at the center acts further to concentrate the mass of the star. Therefore, its moment of inertia decreases over and above what would occur in an immutable rotating gravitating fluid that is spinning down. If this occurs, the moment of inertia as a function of spin exhibits a backbend as in Figure 11. Such a phenomenon has been observed in nuclei, as illustreated in Figure 12.[18,19,20] The opposite evolution of the moment of inertia may occur in x-ray neutron stars that are spinning up when the spin change spans the critical region of phase transition.

As a result of the backbend in moment of inertia, an isolated ms pulsar may cease its spindown and actually spin up for a time, even though loosing angular momentum to radiation as was discussed in a previous work.[6] An x-ray neutron star with a companion may pause in its accretion driven spinup until quark matter is driven out of the star, after which it will resume spinup. Spinup or spin down occurs very slowly, being controlled by the mass accretion rate or the magnitude of the magnetic dipole field, respectively. So, the spin anomaly that might be produced by a conversion of matter from one phase to another will endure for many millions of years.

If it were fleeting it would be unobservable. But enduring for a long epoch—if the phenomenon occurs at all—it has a good chance of being observed.

A very interesting work by Spyrou and Stergioulas has recently appeared in the above connection.[7] They perform a more accurate numerical calculation for a rotating relativistic star, as compared to our perturbative solution. They find that the backbend in our particular example occurs very close to, or at the maximum (non-rotating) star, but that it is generic for stars that are conditionally stabilized by their spin. This is possibly the situation for some or eventually all accretors.

In fact, we expect a phase transition to leave a *permanent* imprint on the distribution in spins of x-ray accretors. Because of the increase of moment of inertia during the epoch in which the quark core is driven out of a neutron star as it is spun up by mass accretion, spinup is—during this epoch—hindered. Therefore we expect the population of accretors to be clustered in the spin-range corresponding to the expulsion of the quark phase from the stellar core. Spin clustering was reported in the population of x-ray neutron stars in binaries that were reported in data from the Rossi X-ray Timing Explorer.[8] However, later observations failed to confirm this.

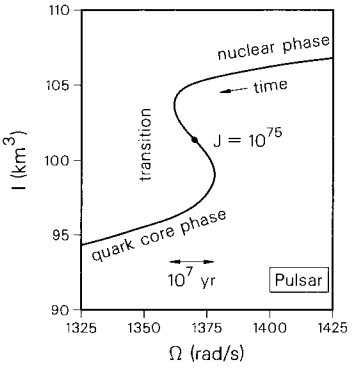

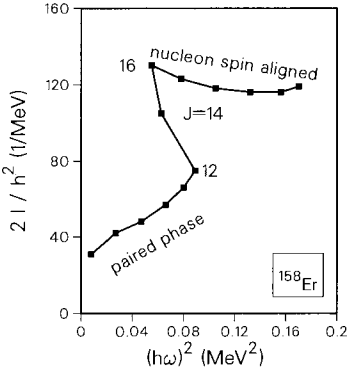

Figure 11. Development of moment of inertia of a model neutron star as a function of angular velocity. The backbend in this case is similar to what is observed in some rotating nuclei. (Adapted from Ref. [6].)

Figure 12. Backbending in the rotating Er nucleus and an number of others was discovered in the 1970s.

6. Calculation

The theory and parameters used to describe our model neutron star are precisely those used in previous publications. Its initial mass is $M = 1.42 M_\odot$, close to the mass limit. The confined hadronic phase is described by a generalization of a relativistic nuclear field theory solved at the mean field level in which members of the baryon octet are coupled to scalar, vector and vector-isovector mesons.[9,2] The parameters [6,10] of the nuclear Lagrangian were chosen so that symmetric nuclear matter has the following properties: binding energy $B/A = -16.3$ MeV, saturation density $\rho = 0.153\ \mathrm{fm}^{-3}$, compression modulus $K = 300$ MeV, symmetry energy coefficient $a_{\mathrm{sym}} = 32.5$ MeV, nucleon effective mass at saturation $m^\star_{\mathrm{sat}} = 0.7m$. These together with the ratio of hyperon to nucleon couplings of the three mesons, $x_\sigma = 0.6$, $x_\omega = 0.653 = x_\rho$ yield the correct Λ binding in nuclear matter.[10]

Quark matter is treated in a version of the MIT bag model with the three light flavor quarks ($m_u = m_d = 0$, $m_s = 150$ MeV) as described. [11] A value of the bag constant $B^{1/4} = 180$ MeV is employed.[6] The transition between these two phases of a medium with two independent conserved charges (baryon and electric) has been described elsewhere.[3] We use a simple schematic model of accretion. [12,13,14] All details of our calculation can be found elsewhere.[15,16,17]

7. Results

The spin evolution of accreting neutron stars as determined by the changing moment of inertia and the evolution equation[15] is shown in Fig. 13. We assume that up to $0.4 M_\odot$ is accreted. Otherwise the maximum frequency attained is less than shown. Three *average* accretion rates are assumed, $\dot{M}_{-10} = 1$, 10 and 100 (where $\dot{M}_{-10}$ is in units of $10^{-10} M_\odot$/y).

We compute a frequency distribution of x-ray stars in low-mass binaries (LMXBs) from Fig. 13, for *one* accretion rate, by assuming that neutron stars begin their accretion evolution at the average rate of one per million years. A different rate will only shift some neutron stars from one bin to an adjacent one. The donor masses in the binaries are believed to range between 0.1 and $0.4 M_\odot$ and we assume a uniform distribution in this range and repeat the calculation shown in Fig. 13 at intervals of $0.1 M_\odot$. The resulting frequency distribution of x-ray neutron stars is shown in Fig. 14; it is striking. A spike in the distribution signals spinout of the quark matter core as the neutron star spins up. This feature would

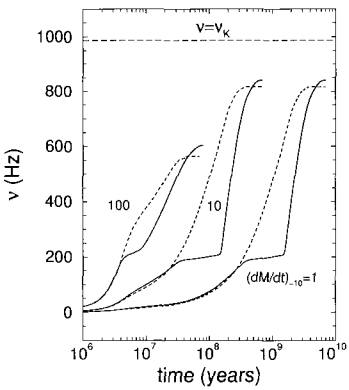

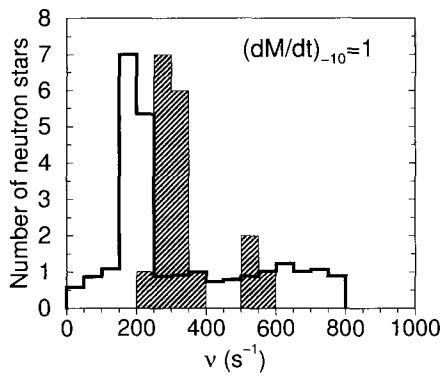

Figure 13. Evolution of spin frequencies of accreting neutron stars with (solid curves) and without (dashed curves) quark deconfinement if $0.4M_{\odot}$ is accreted. The spin plateau around 200 Hz signals the ongoing process of quark confinement in the stellar centers. Spin equilibrium is eventually reached. (From Ref. [15].)

Figure 14. Calculated spin distribution of the underlying population of x-ray neutron stars for one accretion rate (open histogram) is normalized to the number of observed objects (18) at the peak. Data on neutron stars in low-mass X-ray binaries (shaded histogram) is from Ref. [8]. These results have not been observed in later observations, however. The spike in the calculated distribution corresponds to the spinout of the quark matter phase. Otherwise the spike would be absent. (From Ref. [15].)

be absent if there were no phase transition in our model of the neutron star.

The data in Fig. 14 is gathered from Tables 2–4 of the review article of van der Klis concerning discoveries made with the Rossi X-ray Timing Explorer.[8] However, later observations have failed to confirm the original report.

8. Conclusion

We find that if a clustering in rotation frequency of accreting x-ray neutron stars in low-mass binaries were discovered, it could be caused by the progressive conversion of quark matter in the core to confined hadronic matter, paced by the slow spinup due to mass accretion. When conversion is completed, normal accretion driven spinup resumes. To distinguish this conjecture from others, one would have to discover the inverse phenomenon—a spin anomaly near the same frequency in an isolated ms pulsar.[6] If such a discovery were made, and the apparent clustering of x-ray accretors is

confirmed, we would have some degree of confidence in the hypothesis that a dense matter phase, most plausibly quark matter, exists from birth in the cores of canonical neutron stars, is spun out if the star has a companion from which it accretes matter, and later, having consumed its companion, resumes life as a millisecond radio pulsar and spins down.

Acknowledgments

This work was supported by the Director, Office of Energy Research, Office of High Energy and Nuclear Physics, Division of Nuclear Physics, of the U.S. Department of Energy under Contract DE-AC03-76SF00098.

References

1. N. K. Glendenning, Phys. Lett. **114B** (1982) 392; Astrophys. J. **293** (1985) 470.
2. N. K. Glendenning, *Compact Stars* (Springer–Verlag New York, 1'st ed. 1996, 2'nd ed. 2000).
3. N. K. Glendenning, Phys. Rev. D **46** (1992) 1274.
4. K. Rajagopal and F. Wilczek, Phys.Rev.Lett. **86** (2001) 3492.
5. M. Alford, K. Rajagopal, S. Reddy, and F. Wilczek, Phys.Rev. D **64** (2001) 074017.
6. N. K. Glendenning, S. Pei and F. Weber, Phys. Rev. Lett. **79** (1997) 1603.
7. N.K. Spyrou and N. Sterigoulas, Astron. & Astrophys., **395** (2002) 151.
8. M. van der Klis, Ann. Rev. Astron. Astrophys, **38** 717 (2000).
9. N. K. Glendenning, Astrophys. J. **293** (1985) 470.
10. N. K. Glendenning and S. A. Moszkowski, Phys. Rev. Lett. **67** (1991) 2414.
11. E. Farhi and R. L. Jaffe, Phys. Rev. D **30** (1984) 2379.
12. R. F. Elsner and F. K. Lamb, Astrophys. J. **215** (1977) 897.
13. P. Ghosh, F. K. Lamb and C. J. Pethick, Astrophys. J. **217** (1977) 578.
14. V. M. Lupinov, *Astrophysics of Neutron Stars*, (Springer-Verlag, New York, 1992.
15. N. K. Glendenning and F. Weber, Astrophys. J. Lett **559** (2001) L119.
16. N. K. Glendenning and F. Weber, astro-ph/0010336 (2000).
17. N. K. Glendenning and F. Weber, *Signal of quark deconfinement in millisecond pulsars and reconfinement in accreting x-ray neutron stars*, in Physics of Neutron Star Interiors, Ed. by Blaschke, Glendenning and Sedrakian (Springer-Verlag, Lecture Notes Series, 2001).
18. B. R. Mottelson and J. G. Valatin, Phys. Rev. Lett. **5** (1960) 511.
19. A. Johnson, H. Ryde and S. A. Hjorth, Nucl. Phys. **A179** (1972) 753.
20. F. S. Stephens and R. S. Simon, Nucl. Phys. **A183** (1972) 257.

SEARCHING FOR COMPACT OBJECTS IN SUPERNOVA REMNANTS: INITIAL RESULTS

D. L. KAPLAN, S. R. KULKARNI
Department of Astronomy
105-24 California Institute of Technology
Pasadena, CA 91125, USA
E-mail: dlk@astro.caltech.edu, srk@astro.caltech.edu

D. A. FRAIL
National Radio Astronomy Observatory
P.O. Box O
Socorro, NM 87801, USA
E-mail: dfrail@nrao.edu

B. M. GAENSLER, P. O. SLANE
Harvard-Smithsonian Center for Astrophysics
60 Garden Street, MS-6
Cambridge, MA 02138, USA
E-mail: bgaensler@cfa.harvard.edu, slane@cfa.harvard.edu

E. V. GOTTHELF
Columbia Astrophysics Laboratory
Columbia University
550 West 120th Street
New York, NY 10027, USA
E-mail: evg@astro.columbia.edu

Most astronomers now accept that stars more massive than about $9\,M_\odot$ explode as supernovae and leave stellar remnants, either neutron stars or black holes. However, less than half of the SNRs within 5 kpc have identified central sources. Here, we discuss a systematic effort to search for compact central sources in the remaining 23 SNRs of this distance limited sample. As the first part of this survey, we are able to state with some confidence that there are no associated central sources down to a level of one tenth of that of the Cas A central source, $L_X \lesssim 10^{31}$ ergs s^{-1}, in four SNRs (G093.3+6.9, G315.4−2.3, G084.2+0.8, and G127.1+0.5). We compare our limits with cooling curves for neutron stars and find that any putative neutron stars in these SNRs must be cooling faster than that expected for traditional $1.35\,M_\odot$ neutron stars.

1. Introduction

Understanding the deaths of massive stars is one of the frontiers of modern astrophysics. The detection of neutrinos from SN 1987A dramatically illustrated that more massive stars undergo core collapse[1]. The outcome of core collapse can either be a neutron star or a black hole[2]. However, there are great uncertainties in the mapping between initial mass of the star and the end product, and even more uncertainties in the natal properties of the stellar remnant. It is these uncertainties that give observers opportunities to make new discoveries and theorists to predict or "postdict" these discoveries.

The natal properties of the stellar remnant involves delicate physics but has strong observations ramifications. The gravitational binding energy of a neutron star is 10^{53} erg, of which only 1% appears to be coupled to the ejecta (which ultimately powers the SNR). Even more minuscule fractions go into rotational energy, kinetic energy (bulk motion) and magnetic fields. It is now generally agreed that three dimensional effects in the explosion determine the natal properties[3,4].

The discovery of pulsars in the Vela SNR[5] and the Crab Nebula[6] made concrete the suggestion that core collapse results in neutron stars[7], some of which manifest themselves as radio pulsars. Young pulsars, in addition to pulsing in the radio, can and usually do power synchrotron nebulae[8] that are indirect markers of pulsars. These synchrotron nebulae are commonly called pulsar wind nebulae, or PWNe. Over the following two decades, the notion that neutron stars resemble the Crab pulsar guided the search for central objects as well as intensive radio mapping of SNRs. As a result of these efforts, the term "composite" SNR (PWN + shell) was added to the SNR lexicon (see Milne *et al.*[9]).

However, recent developments have severely revised our picture of young neutron stars. Most importantly, astronomers have come to accept of tremendous diversity in the natal properties of young neutron stars. Anomalous X-ray pulsars[10] (AXPs), soft γ-ray repeaters[11] (SGRs), nearby thermal and radio quiet neutron stars[12], long period radio pulsars with high inferred magnetic fields[13,14] (HBPSR) are now routinely found in astronomical literature. These new classes of neutron stars have primarily come from high energy (X-ray and γ-ray) observations.

While this diversity is clearly demonstrated observationally, theory and simulation cannot yet constrain the fundamental birth properties of neutron stars[15]. Models still have difficulties achieving explosions, much less following the activity in the post-collapse object in any detail.

2. Survey Design

Three years ago we began a program of observationally investigating the stellar remnants in a volume-limited census of Galactic supernova remnants. The approach we took was inspired by the first light picture of *Chandra*, the discovery of a central X-ray source in the well-studied and youngest known supernova remnant in our Galaxy, Cassiopeia A[16]. The nature of the object (Fig. 1) continues to be debated[17–19]. However, one conclusion is crystal clear: the X-ray source is not a standard radio pulsar (unbeamed or otherwise).

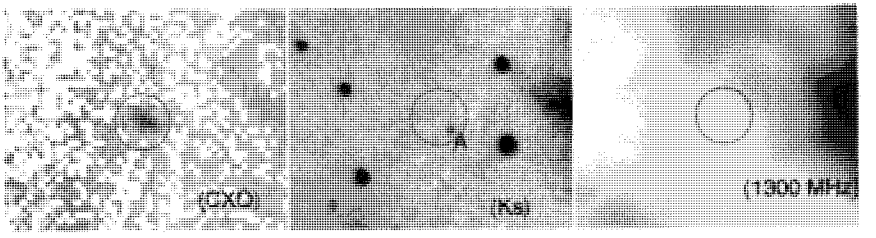

Figure 1. Images of the X-ray point source in Cas A — *Chandra* ACIS first-light image[16] (left); Keck NIRC K_s-band (2.2 μm, right)[20]; VLA 1300 MHz (right). Error circle is 2.3″ in radius; images are $\sim$ 20″ on a side, with north up and east to the left. Our optical/IR work leads us to conclude that star A is a foreground M dwarf — not an unexpected coincidence given the low latitude of Cas A.

The basis of our effort is that observationally, all central sources in SNRs known to date, regardless of the band of their initial identification (γ-ray, X-ray, or radio) appear to possess detectable X-ray emission. Theoretically, we expect thermal X-ray emission from young neutron stars. Thus, on both counts the search for central sources in young remnants is very well motivated. However, a follow-up program is essential since many other foreground sources such as flare stars, young stars, and accreting sources and background sources such as AGN dominate the source counts[21,22]. Fortunately, the sub-arcsecond spatial resolution of *Chandra* allow efficient filtering of such contaminating objects.

To this end, we have identified a sample of SNRs within 5 kpc of the Sun (Fig. 2). Most of these SNRs are expected to contain central neutron stars: $\lesssim$ 20% are expected to result from Type Ia SNe and thus not contain a central compact source, while $\sim$ 20% (dependent on the stellar initial

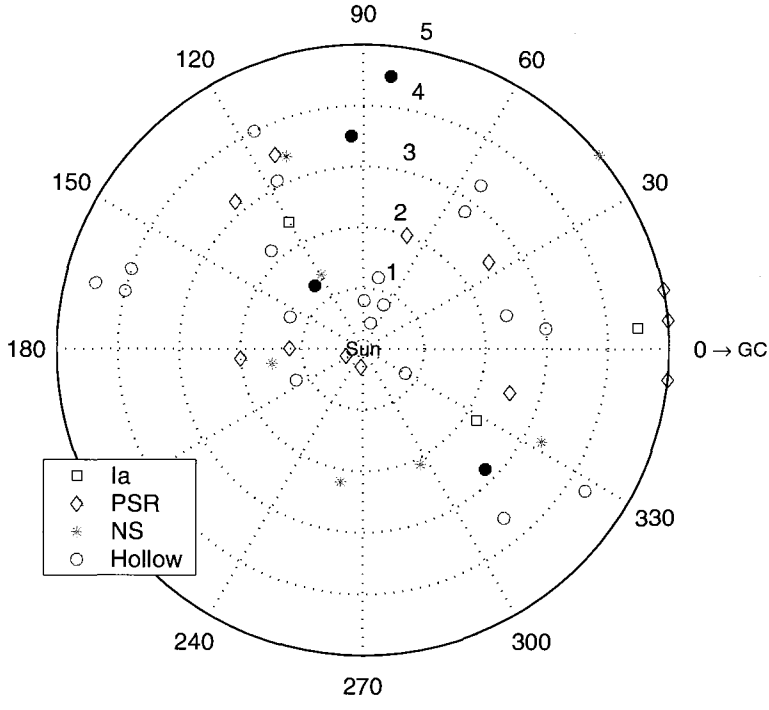

Figure 2. Galactic distribution of SNRs from *et al.*[23]. Galactic longitude l (degrees) is plotted against distance (kpc), with the Sun at the origin and the Galactic center to the right. Black squares are the Ia SNRs, blue diamonds are associated with radio pulsars, green asterisks are associated with other types of neutron stars (RQNS, *etc.*), and the red circles are the hollow SNRs. The four filled circles are the SNRs from this paper with detailed analyses.

mass function, the limiting mass for black holes, and binary evolution[24]) are expected to host a central black hole that may not be easily identified as such. Thanks to the persistent efforts by astronomers over the past four decades, central sources have been detected in the X-ray and/or radio bands in 18 of these SNRs, and three have been identified as probable Type Ia SNe. In some cases, only a centrally located PWN is detected, but in those cases (i.e. IC 443) it is reasonably assumed that the PWN is powered by a central compact source. We are then left with the SNRs that have no obvious indication of central sources: the hollow SNRs.

Dividing the hollow remnants by size, we successfully proposed for a "large" *Chandra* effort in AO-3 to image the nine smallest SNRs. This

initial allocation has been supplemented with additional time in AO-4 of *Chandra* and AO-2 of *XMM*. Followup of the X-ray sources has been undertaken with a plethora of ground based telescopes in the optical and near-IR bands. Here, we report the first analysis of four SNRs (Fig. 3) for which the followup is now complete. For more details, see Kaplan *et al.*[23].

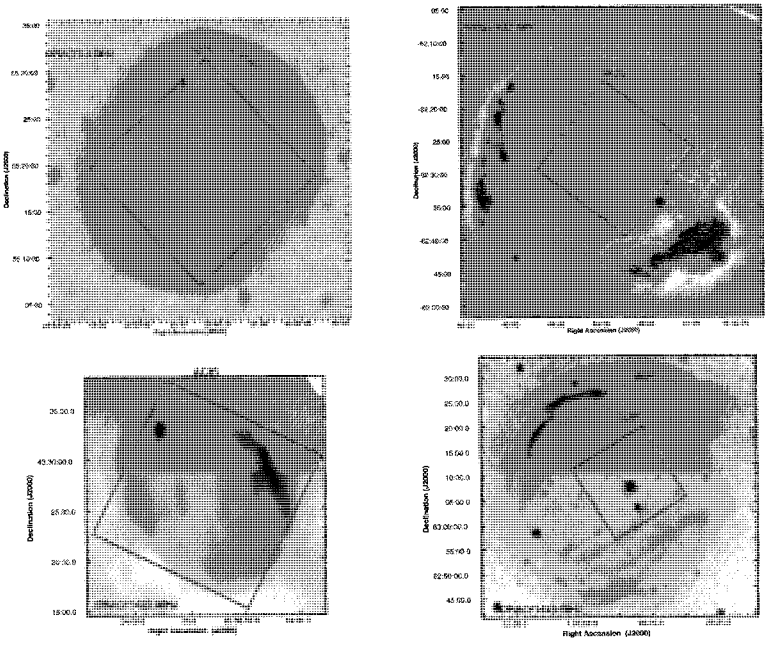

Figure 3. Radio images of the SNRs whose analyses are presented in Kaplan *et al.*[23], with the field covered by the *Chandra* ACIS detector shown by the boxes. Upper left: SNR G093.3+6.9; upper right: SNR G315.4−2.3; lower left: SNR G084.2+0.8; lower right: SNR G127.1+0.5. The image of SNR G315.4−2.3 also has contours that show the diffuse X-ray emission (measured by the *ROSAT* PSPC) of the RCW 86 complex.

3. X-ray Observations

The X-ray observations of the SNRs were designed to detect cooling neutron stars down to a luminosity of 1/10 that of the Cas A-type source, which are among the least luminous of the central sources[17,23]. For the primary sample of sources observed with *Chandra*, we used the 16′ field of the ACIS-I array. This array covered much if not all of the SNRs (Fig. 3), and should encompass neutron stars with velocities < 700 km s^{-1} in the worst cases.

The *Chandra* observations had durations of 15–50 ksec, and detected 10–50 sources in each field with ≥ 10 counts.

4. Followup Observations

After identifying X-ray sources with *Chandra* the question is then to determine which, if any, are the compact remnants of the SNRs. We have used source-count statistics[22,25,26] to estimate the number of foreground/background sources given the $N_{\rm H}$ and diffuse SNR background toward each target, and these numbers roughly agree with the detected counts. Because of their small X-ray count-rates, weeding out interlopers requires multi-wavelength observations.

Isolated neutron stars have high X-ray to optical flux ratios[27] (Fig. 4). Interloper sources, on the other hand, typically have much brighter optical/IR counterparts[21,28]. In the Galactic plane, the majority of sources are either nearby bright stars or active late-type stars. The extragalactic sources are usually AGN or star-forming galaxies, although some nearby spiral galaxies are also detectable[29]. Deep optical/IR imaging is therefore an efficient way to identify background sources, and we follow our X-ray observations with successively deeper optical and IR observations, identifying progressively fainter counterparts as we go.

With deep optical and infrared imaging we were able to identify probable counterparts to all of the X-ray sources in the four SNRs discussed here. Figure 4 contains examples of these counterparts, showing that they are consistent with the known Galactic and extragalactic X-ray source populations. Additionally, we used X-ray hardness to determine likely source classifications and found that this was consistent with the results of Figure 4.

5. Initial Results

All of the X-ray sources in SNRs G093.3+6.9, G315.4−2.3, G084.2+0.8, and G127.1+0.5 can be reasonably identified either with foreground or background sources. Therefore, there does not appear to be any detected neutron star in these SNRs. There are a small number of cases where either the association or the type of source (star versus galaxy) is uncertain, either due to an optical/IR detection in only one band and/or a detection at a somewhat large distance from the X-ray source, but there are certainly no sources that scream out "I am a neutron star." If we accept this, we can then draw two limits to the flux of any compact central source: a

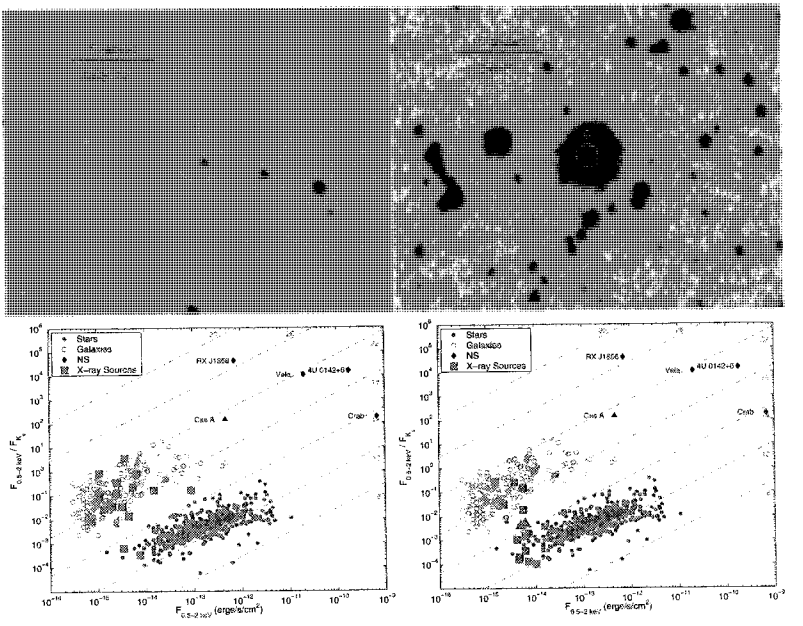

Figure 4. **Top**: examples of counterparts to X-ray sources. At left is a galaxy with $R - K_s > 6$ mag, while at right is a G5V star. **Bottom**: X-ray-to-K_s flux ratio vs. X-ray flux for sources in SNR G093.3+6.9 (left) and SNR G315.4−2.3 (right). Sources from the CDF/Orion studies[25,26] and selected neutron stars are also plotted. Stars from CDF/Orion are blue asterisks, galaxies are green circles. Selected neutron stars are black diamonds/limits, and are labeled. The unidentified X-ray sources are the red squares/limits. The diagonal lines represent constant magnitude, and are labeled by that magnitude.

conservative limit (Limit I), and a loose limit (Limit II). The conservative limit will be the flux of the brightest source for which the optical/IR counterpart is at all in doubt. We gives these limits, converted to luminosities for various possible source models (thermal emitter, radio pulsar, AXP) in Table 1.

We then plot these limits (incorporating uncertainties in both distance and age) in Figure 5 along with the luminosities of other neutron stars found in SNRs. The limits for SNR G127.1+0.5 are significantly below those of the other SNRs as it had never been observed in the X-rays before, so we did not know what the level of the diffuse background would be and therefore selected an exposure time that would guarantee sufficient counts from a source above even the most pessimistic background.

Table 1. Limits on Central Sources in SNRs G093.3+6.9, G315.4−2.3, G084.2+0.8, and G127.1+0.5

Model	$L_X \times 10^{31}$ ergs s^{-1}	
	Limit I	Limit II
SNR G093.3+6.9:		
BB ($kT_\infty = 0.25$ keV)	2.6	1.1
PL ($\Gamma = 1.5$)	3.7	1.6
PL ($\Gamma = 3.5$)	7.3	3.2
PWN ($\Gamma = 1.5$, $\theta = 1'$)	30	
SNR G315.4−2.3:		
BB ($kT_\infty = 0.25$ keV)	4.5	1.1
PL ($\Gamma = 1.5$)	6.4	1.6
PL ($\Gamma = 3.5$)	12.4	3.0
PWN ($\Gamma = 1.5$, $\theta = 1'$)	40	
SNR G084.2−0.8:		
BB ($kT_\infty = 0.25$ keV)	2.0	1.2
PL ($\Gamma = 1.5$)	2.9	1.7
PL ($\Gamma = 3.5$)	5.7	3.4
PWN ($\Gamma = 1.5$, $\theta = 1'$)	40	
SNR G127.1+0.5:		
BB ($kT_\infty = 0.25$ keV)	0.1	0.1
PL ($\Gamma = 1.5$)	0.3	0.1
PL ($\Gamma = 3.5$)	0.2	0.1
PWN ($\Gamma = 1.5$, $\theta = 1'$)	3	

Note: Luminosities were computed using W3PIMMS. The luminosities are corrected for absorption and the known distances of the SNRs, and are in the 0.3–8.0 keV band. The models are 0.25 keV blackbody (typical of sources like Cas A), $\Gamma = 1.5$ powerlaw (typical of radio pulsars[30]), $\Gamma = 3.5$ powerlaw (typical of AXPs), and $\Gamma = 1.5$ powerlaw for a $1'$ extended source (typical of PWNe). PWN limits are neither type I or type II but are instead simple $3\,\sigma$ limits.

6. PWN Limits

Pulsar wind nebulae (PWNe), are bright, centrally condensed nebulae with non-thermal (power-law) X-ray and radio spectra often associated with young, energetic pulsars and SNRs (here we refer only to "bubble" PWNe, as differentiated by the bow-shock PWNe produced by the motion of the pulsars through the ambient medium; for reviews, see Chevalier[33] or Gaensler[34]). The photon indices range[30] from 1.3–2.3, similar to those of pulsars, but they are roughly ~ 10 times as luminous[35] for a given $\dot{E}$ and the sizes range from a few arcseconds to several arcminutes. PWNe,

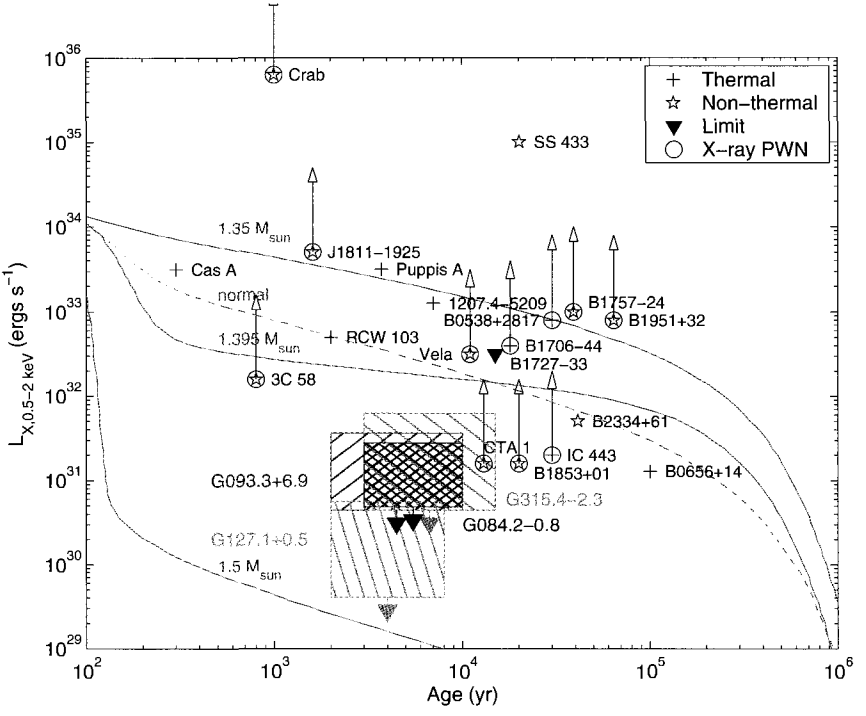

Figure 5. X-ray luminosities (0.5–2 keV) as a function of age for neutron stars in SNRs from Kaplan *et al.*[23] and Table 1. Sources whose emission is primarily thermal are indicated with plus symbols, those whose emission is primarily non-thermal are indicated with stars, and those with only limits are indicated with triangles. The sources that have X-ray PWNe, which are typically > 10 times the X-ray luminosity of the neutron stars themselves, are circled and the PWN luminosities are indicated by arrows. We also plot the limits to blackbody emission from sources in SNRs G093.3+6.9 (red hatched region), G315.4−2.3 (green hatched region), G084.2+0.8 (blue cross-hatched region), and G127.1+0.5 (gold hatched region). The cooling curves are the 1p proton superfluid models from Yakovlev *et al.*[31] (solid lines, with mass as labeled) and the normal (i.e., non-superfluid) $M = 1.35\,M_\odot$ model (dot-dashed line), assuming blackbody spectra and $R_\infty = 10$ km. These curves are meant to be illustrative of general cooling trends, and should not be interpreted as detailed predictions. Faster cooling than the curves is possible, due either to the presence of exotic particles in the NS core or to the full onset of direct Urca cooling for a heavier NS[32].

both X-ray and radio, offer a great advantage over bare radio pulsars for inferring the existence of neutron stars: they are unbeamed. This fact has historically been used in a number of cases to infer the existence of energetic pulsars where the pulsar had not been seen itself, such as 3C 58[36,37], N157B[38], and Kes 75[39].

Any PWNe in the SNRs discussed here are $\gtrsim 3000$ yrs old and may have already interacted with the reverse shocks[40], so their sizes and brightnesses would be hard to predict. We therefore estimate limits on PWNe for a fiducial size of 1 pc $\approx 1'$ — we did not detect any sources with those sizes in our images except for the known thermal emission from RCW 86. We set limits on the emission by assuming a typical $\Gamma = 1.5$ powerlaw, as seen in Table 1. These limits are below the luminosities of virtually all young PWNe detected in X-rays [41], but are consistent with some older sources such as the Vela PWN, CTB 80, and W44 [42]. However, these PWNe all have significant non-thermal radio emission, emission that is not present in SNRs G093.3+6.9, G315.4−2.3, G084.2+0.8, or G127.1+0.5 since they are all shell-type SNRs.

7. Conclusions

Above we discussed observations of four shell remnants (G093.3+6.9, G315.4−2.3, G084.2+0.8, G127.1+0.5) — the first segment of a larger survey — that failed to find any convincing neutron stars. There are reasons why standard neutron stars were not found in these SNRs: they could have fallen in the gap between the chips, they could have escaped our field of view due to a very high velocities[a], they could be undetectable black holes, or they could not exist owing to the SNRs being the results of Type Ia explosions. All of these scenarios are unlikely for a single source, and even more so for all four, but are technically possible. If, on the other hand, these scenarios do not apply, then four remnants contain neutron stars that are fainter than our X-ray detection limit (typically, $L_X \lesssim 10^{31}$ erg s^{-1} in the 0.5–10 keV band).

We now consider this last (and most interesting) possibility. In the absence of other forms of energy generation (accretion, rotation power, magnetic field decay) the minimum X-ray flux one expects is set by the cooling of the neutron star. From Figure 5 we immediately see that the central neutron stars in these four remnants must be cooler than those present for example in the similarly-aged Puppis A, PKS 1205−51/52 and RCW 103.

Our knowledge of the physics of cooling is by no means firm. There is

[a]To not be visible in SNRs G093.3+6.9, G315.4−2.3, or G084.2+0.8, the neutron star would have to be moving faster than 1500 km s^{-1}: true for $\lesssim 1\%$ of known pulsars[43]. For SNR G127.1+0.5, the neutron star would have to be moving faster than 700 km s^{-1}: true for $\lesssim 10\%$ of known pulsars[43].

considerable debate among theorists as to which of the multitude of physical processes can significantly affect the cooling output and as to which of the physical parameters (mass, rotation rate, magnetic field) controls these processes[44]. Nonetheless, there is agreement that more massive neutron stars (with their larger mean densities) cool more rapidly than those with smaller mass; this expectation is illustrated in Figure 5. Thus our upper limits can be made consistent with the cooling possibility provided the central neutron stars in these four SNRs are more massive than known cooling neutron stars. Indeed, the known examples of radio-quiet objects could well result from a strong selection effect, namely the earlier X-ray observations by *Einstein* and *ROSAT* detected the warmer cooling neutron stars (ignoring the neutron stars detected because of non-thermal emission). The existing data may already hint at a parameter affecting cooling, as exemplified by PSR J0205+6449[45] and the Vela pulsar[46], but also possibly by PSR B1853+01[47] and RX J0007.0+7302[48].

Of course, we also do not see rotation-powered pulsars such as the majority of the objects in SNRs within 5 kpc. Recent observations are finding pulsars with lower radio luminosities and values of $\dot{E}$ than ever before, and our limits would only be consistent with these newer sources. One might then ask why we see neither a standard cooling neutron star nor a standard active pulsar, assuming that there is no intrinsic correlation between these properties. It is possible that there truly are no neutron stars in these SNRs, allowing one to speculate wildly about what actually is there.

Acknowledgments

D. L. K. is supported by a fellowship from the Fannie and John Hertz Foundation.

References

1. Hirata, K., Kajita, T., Koshiba, M., Nakahata, M. & Oyama, Y. *Physical Review Letters* **58**, 1490 (1987).
2. Woosley, S. E., Heger, A. & Weaver, T. A. *Reviews of Modern Physics* **74**, 1015 (2002).
3. Burrows, A. *Nature* **403**, 727 (2000).
4. Kifonidis, K., Plewa, T., Janka, H.-T. & Müller, E. *A&A* **408**, 621 (2003).
5. Large, M. I., Vaughan, A. E. & Mills, B. Y. *Nature* **220**, 340 (1968).
6. Staelin, D. H. & Reifenstein, E. C. *Science* **162**, 1481 (1968).
7. Baade, W. & Zwicky, F. *Proceedings of the National Academy of Science* **20**, 254 (1934).

8. Weiler, K. W. & Panagia, N. *A&A* **70**, 419 (1978).
9. Milne, D. K. *et al. MNRAS* **188**, 437 (1979).
10. Mereghetti, S., Chiarlone, L., Israel, G. L. & Stella, L. in *Neutron Stars, Pulsars, and Supernova Remnants,* (Becker, W., Lesch, H. & Trümper, J., eds), 29, (2002). (astro-ph/0205122).
11. Hurley, K. in *5th Compton Symposium,* (McConnell, M., ed). AIP Press, (2000). (astro-ph/9912061).
12. Pavlov, G. G., Sanwal, D., Garmire, G. P. & Zavlin, V. E. in *ASP Conf. Ser. 271: Neutron Stars in Supernova Remnants,* (Slane, P. O. & Gaensler, B. M., eds), 247, (2002).
13. Camilo, F. *et al. ApJ* **541**, 367 (2000).
14. Gotthelf, E. V., Vasisht, G., Boylan-Kolchin, M. & Torii, K. *ApJ* **542**, L37 (2000).
15. Burrows, A., Ott, C. D. & Meakin, C. in *3-D Signatures in Stellar Explosions*, (2003). (astro-ph/0309684).
16. Tananbaum, H. *IAUC* **7246**, 1 (1999).
17. Chakrabarty, D., Pivovaroff, M. J., Hernquist, L. E., Heyl, J. S. & Narayan, R. *ApJ* **548**, 800 (2001).
18. Murray, S. S., Ransom, S. M., Juda, M., Hwang, U. & Holt, S. S. *ApJ* **566**, 1039 (2002).
19. Pavlov, G. G., Zavlin, V. E., Aschenbach, B., Trümper, J. & Sanwal, D. *ApJ* **531**, L53 (2000).
20. Kaplan, D. L., Kulkarni, S. R. & Murray, S. S. *ApJ* **558**, 270 (2001).
21. Hertz, P. & Grindlay, J. E. *AJ* **96**, 233 (1988).
22. Mushotzky, R. F., Cowie, L. L., Barger, A. J. & Arnaud, K. A. *Nature* **404**, 459 (2000).
23. Kaplan, D. L. *et al. ApJS* submitted (2004).
24. Heger, A., Fryer, C. L., Woosley, S. E., Langer, N. & Hartmann, D. H. *ApJ* **591**, 288 (2003).
25. Brandt, W. N. *et al. AJ* **122**, 2810 (2001).
26. Feigelson, E. D. *et al. ApJ* **574**, 258 (2002).
27. Hulleman, F., van Kerkwijk, M. H. & Kulkarni, S. R. *Nature* **408**, 689 (2000).
28. Grindlay, J. *et al. Astronomische Nachrichten* **324**, 57 (2003). (astro-ph/0211527).
29. Barger, A. J. *et al. AJ* **126**, 632 (2003).
30. Gotthelf, E. V. *ApJ* **591**, 361 (2003).
31. Yakovlev, D. G., Gnedin, O. Y., Kaminker, A. D., Levenfish, K. P. & Potekhin, A. Y. in *High Energy Studies of Supernova Remnants and Neutron Stars: 34th COSPAR Scientific Assembly,* (Becker, W. & Hermsen, W., eds), (2003). (astro-ph/0306143).
32. Yakovlev, D. G., Kaminker, A. D., Haensel, P. & Gnedin, O. Y. *A&A* **389**, L24 (2002).
33. Chevalier, R. A. *Memorie della Societa Astronomica Italiana* **69**, 977 (1998).
34. Gaensler, B. M. in *Texas in Tuscany: XXI Symposium on Relativistic Astrophysics,* (Bandiera, R., Maiolino, R. & Mannucci, F., eds), 297 (World Scientific, Singapore, 2003). (astro-ph/0303427).

35. Gotthelf, E. V. in *ASP Conf. Ser.: IAU Symposium 218: Young Neutron Stars and Their Environments,* (Camilo, F. & Gaensler, B. M., eds), (2004).
36. Becker, R. H., Helfand, D. J. & Szymkowiak, A. E. *ApJ* **255**, 557 (1982).
37. Frail, D. A. & Moffett, D. A. *ApJ* **408**, 637 (1993).
38. Wang, Q. D. & Gotthelf, E. V. *ApJ* **509**, L109 (1998).
39. Becker, R. H. & Helfand, D. J. *ApJ* **283**, 154 (1984).
40. van der Swaluw, E., Downes, T. P. & Keegan, R. *A&A* submitted (2003). (astro-ph/0311388).
41. Possenti, A., Cerutti, R., Colpi, M. & Mereghetti, S. *A&A* **387**, 993 (2002).
42. Pavlov, G. G., Kargaltsev, O. Y., Sanwal, D. & Garmire, G. P. *ApJ* **554**, L189 (2001).
43. Arzoumanian, Z., Chernoff, D. F. & Cordes, J. M. *ApJ* **568**, 289 (2002).
44. Yakovlev, D. G., Gnedin, O. Y., Kaminker, A. D. & Potekhin, A. Y. in *Neutron Stars, Pulsars, and Supernova Remnants*, 287, (2002).
45. Slane, P. O., Helfand, D. J. & Murray, S. S. *ApJ* **571**, L45 (2002).
46. Pavlov, G. G., Zavlin, V. E., Sanwal, D., Burwitz, V. & Garmire, G. P. *ApJ* **552**, L129 (2001).
47. Petre, R., Kuntz, K. D. & Shelton, R. L. *ApJ* **579**, 404 (2002).
48. Slane, P. O. *et al. ApJ* in press (2003). (astro-ph/0310250).

FORMATION AND EVOLUTION OF BLACK HOLES IN THE GALAXY

CHANG-HWAN LEE

Department of Physics, and Nuclear Physics & Radiation Technology Institute
Pusan National University, Busan 609-735, Korea
E-mail: clee@pusan.ac.kr

We have shown that if the Fe core in a presupernova star is to be sufficiently massive to collapse into a black hole, earlier in the evolution of the star the He core must be covered (clothed) by a hydrogen envelope during He core burning and removed only following this, in, e.g. common envelope evolution. This is classified as Case C mass transfer. These previous arguments were based chiefly on stellar evolution, especially depending on the way in which ^{12}C burned. In this work we argue for Case C mass transfer on the basis of binary evolution. This has the consequence that the final separation a_f following common envelope evolution will depend nearly linearly on the mass of the companion m_d which becomes the donor after the He core of the giant has collapsed into the black hole. We show that the reconstructed preexplosion separations of the black hole binaries are consistent with our evolution scenario.

1. Introduction

In Table 1 of Lee et al.[1] (denoted as LBW) the seven SXTs with shortest periods had K- or M-star companions and the unclassified companion in XTE 1859+226 may also well be K or M because of its short period $P = 0.380$ days. The progenitor binaries of these would have involved $\sim 25M_\odot$ giants and $\sim 1-2M_\odot$ companions, the latter having had some mass stripped off by the black hole. In other words, all of the shortest period SXTs are successfully evolved with the *same* Case C mass transfer[2].

We[3] emphasized that in Case C mass transfer the orbital separations for the above progenitor binaries in Roche Lobe contact are at $\sim 1700R_\odot(\pm \sim 10\%)$, ~ 8 AU, for ZAMS $20M_\odot$ black hole progenitor and $1M_\odot$ companion star. Progenitors with more massive companions and the larger initial separation necessary for Case C mass transfer could have removed the H-envelope of the giant with spiral-in to larger final separations a_f, since their drop in gravitational energy of the more massive companion is then

sufficient to remove the envelope, and we shall see that this is indeed what happens.

In LBW we listed Nova Scorpii and IL Lupi as undergoing mass transfer while in main sequence. Beer & Podsiadlowski[4] have carried out a detailed, convincing numerical evolution of Nova Scorpii, showing that the orbit has widened substantially under nearly conservative mass transfer. Podsiadlowski et al.[5] (denoted as PRH) have recently extended such calculations to the other binaries with evolved companions, showing that they all began mass transfer in main sequence, although V404 Cyg, J1550−564 and probably GRS 1915+105 will have progressed beyond main sequence. The PRH calculations generally support the schematic LBW calculations of mass transfer, but have the added advantage that by beginning the transfer in main sequence, sufficient mass can be transferred in the traditional sub Eddington limit. Whereas we do not believe this to be necessary in the case of black holes, seeing no reason why the accretion across the event horizon could not be substantially hyper Eddington (and PRH also covers this case, as a possibility) the standard PRH scenario allays the fear of the greatly hyper Eddington scenario which may go against "accepted wisdom".

In Case C mass transfer there is a great regularity expressed in the roughly linear dependence of companion mass on orbital separation of the giant black hole progenitor and companion on the companion mass

$$a_f \propto \frac{M_d}{M_\odot}\left(\frac{M_{\rm giant}}{M_\odot}\right)^{-0.55} R \qquad (1)$$

following the spiral-in stage which removes the envelope of the giant[1]. Except for the roughly square root dependence on giant mass, this relation is linear. Here the companion (donor) mass is labelled M_d, a_f is the separation of the He-star, companion binary following spiral-in in common envelope evolution, and R is the initial radius of the giant at the start of common envelope evolution. The dependence on $M_{\rm giant}$ is weak, the interval

$$20M_\odot < M_{\rm giant} < 30M_\odot \qquad (2)$$

being used by LBW[1]. The term depending on giant mass originates from the term $M_{\rm He}/M^2_{\rm giant}$ in common envelope evolution. The relation Eq. (1) is particularly useful because, as we shall argue, R is nearly constant, $\sim 1000R_\odot$, to within $\sim 10\%$. Because the giant evolutionary time is so short, a_f is essentially the preexplosion separation of black hole and donor.

We thus have three classes:

(i) The 8 AML (angular momentum loss) SXTs with K or M-star main sequence companions come from binaries which overfill their Roche Lobe during spiral in, as discussed in LBW. Their periods are decreased as they transfer mass to the companion black hole, as they lose angular momentum by magnetic braking and gravitational waves.

(ii) The next six SXTs which established Roche contact while in main sequence, some of them having evolved beyond.

(iii) The special case of the continuously shining Cyg X-1 which we place just before its Roche Lobe, the companion now undergoing unstable mass transfer to its lower mass companion black hole.

Interestingly, we find that the division between the unevolved main sequence class (i) and evolved companion (ii) is given accurately by Fig. 2 of de Kool et al.[6], who plot the mass of the companion which undergoes angular momentum loss by gravitational waves and magnetic braking, both as functions of time. They obtain the companion mass of $2M_{\odot}$ as giving the division. We find this to be true for $M_{\rm giant} = 20M_{\odot}$ in Eq. (1).

Note that the binaries with late main sequence companions Nova Scorpii and IL Lupi are special in that these binaries have experienced large mass loss, which can be explained as in LBW by magnetohydrodynamic effects, not included in the evolution discussed here. One may wonder why just there two binaries, with ZAMS companion masses, have lost a sizable fraction of their progenitor He star masses, whereas there is no sign of a kick outwards in separation from copious mass loss in the Class (i) SXTs.

The above regularity shows immediately that at least the first class with K and M companions must have a very large a_i (LBW find $a_i \sim 1700R_{\odot}$ for a $20M_{\odot}$ black hole progenitor with $1M_{\odot}$ companion) corresponding to a giant radius of $\sim 1000R_{\odot}$, so that the binding energy of the giant envelope, which decreases inversely with its radius, is small enough to be furnished by the drop in gravitational binding energy of the low-mass companion as it spirals in to its Roche Lobe.

As developed in many papers[1,3] and backed by evolutionary calculations[5,7,8,9], the above delineation into three classes, depending upon companion mass, can be understood if the giant is required to finish (or nearly finish) He core burning before common envelope evolution takes place; i.e., if the mass transfer is essentially Case C.

In Sec. 2, we discuss the stellar evolution necessary to produce models which allow Case C mass transfer for ZAMS $20-30M_{\odot}$ stars. In Sec. 3, we

review the role of carbon burning. In Sec. 4, we discuss that Case B mass transfer would not only allow too much of the He envelope to blow away and leave too much ^{12}C after He core burns, but also is disfavored by the population of SXTs. We summarize our conclusion in Sec. 5.

2. The Case for Case C Mass Transfer

In LBW we found that the Schaller et al.[10] $20M_\odot$ star had the characteristics we desire for Case C mass transfer, but that the latter was not possible for their $25M_\odot$ star. We therefore constructed "by hand" models in which the stellar radius as function of burning stage had a similar shape to the $20M_\odot$ star, all the way up to $30M_\odot$.

We show in Fig. 1 the results of the Schaller et al.[10] stellar evolution for a ZAMS $20M_\odot$ star. It is seen that the main increase in radius comes after the start of He core burning (which begins while H shell burning is still going on). With further He core burning there is a flattening off of the radius versus burning stage and then a further increase in radius towards the end of and following He core burning. Our model requires that mass transfer take place during this last period of increase in radius, so that the orbital separation ($\sim 3/2$ of the giant radius) is well localized $a_{i,\mathrm{RLOF}} \sim 1700R_\odot$ at the time of Roche Lobe contact, or $a_{i,t=0} \sim 1500R_\odot$ initially, the difference due to mass loss by wind, with accompanying widening of the orbit.

It is made clear[1,3] that for Case C (or very late Case B) the radii of the relevant stars must have the following behavior, as shown in Fig. 1.

(i) They must increase rapidly in radius with hydrogen shell burning and with the early He core burning, which begins while the hydrogen shell burning is still going on.

(ii) The radii must flatten off, or actually decrease with further He core burning. This is so that if the companion reaches the Roche Lobe it will reach it before or early in He core burning. Then the He core made naked by common envelope will mostly blow away by the strong Wolf-Rayet type winds, and the final Fe core will be too low in mass to collapse into a high mass black hole[7].

(iii) The third (obvious) characteristic is that the stellar radius must grow following He core burning, because the massive star must be able to reach its Roche Lobe during this time. The massive star has only $\lesssim 10^4$ years of its life left, so wind losses no longer can carry much of it away.

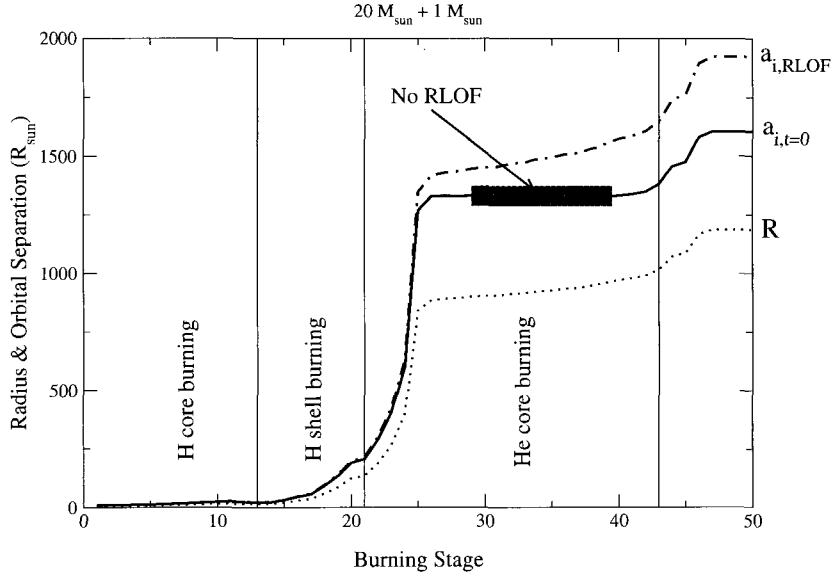

Figure 1. Radius of black hole progenitors (R) and the initial orbital separations (a_i) of the progenitors of X-ray transient binaries with a $1M_\odot$ companion. The burning stage in the x-axis corresponds to that of Schaller et al.[10] **A)** The lower dotted curves (R) corresponds to the radius of the black hole progenitors taken from Schaller et al.[10] That for the $25M_\odot$ star is similar but for the $30M_\odot$ the radius does not increase following the end of He core burning. **B)** From the mass of the primary at the tabulated point one can calculate the semimajor axis of a binary with a $1M_\odot$ secondary in which the primary fills its Roche Lobe, and this semimajor axis is shown in the upper dot-dashed curve ($a_{i,\mathrm{RLOF}}$). **C)** The solid curves ($a_{i,t=0}$) correspond to the required initial separations after corrections of the orbit widening due to the wind mass loss, $a_{i,t=0} = a_{i,\mathrm{RLOF}} \times (M_p + M_d)/(M_{p,0} + M_d)$ where M_p is the mass of the black hole progenitor at a given stage and $M_{p,0} = 20M_\odot$ is the ZAMS mass of the black hole progenitor. Primaries at the evolutionary stages marked by the shaded area cannot fill their Roche Lobe for the first time at that stage, but have reached their Roche Lobe at an earlier point in their evolution.

Portegies Zwart et al.[11] have pointed out that wind loss from the giant preceding common envelope evolution is important and we follow their development in identifying the "No RLOF" part of the curve in Fig. 1. Because of the wind loss the binary widens. The Roche Lobe overflow will take place during the very rapid increase in radius of the giant in the beginning of He core burning, or in very late Case B or in Case C mass transfer.

The binary has widened too much by the time the giant has reached the flat part of the R vs stage curve. In fact, it cannot transfer mass during this stage, because it will have already come to Roche contact during early Case B. This is made clear by the shaded area in the solid line in Fig. 1. Brown et al.[9] have shown that the SXTs with main sequence companions can be evolved with a $1 - 1.25 M_{\odot}$ companion mass, so the above results may be directly applicable. For higher mass companions, this shaded area becomes smaller because the effect of the winds is smaller. This makes the intermediate Case B mass transfer possible. However, in this case, high-mass black holes may not form because the Fe core is not massive enough to form high-mass compact objects as we discussed above[7]. Furthermore, as in Fig. 2, the probability of the intermediate Case B mass transfer is small compared to that of Case C mass transfer.

Now, in fact, the curve of radius vs burning stage for the next massive star, of ZAMS $25 M_{\odot}$, by Schaller et al.[10] does not permit Roche Lobe contact during Case C at all, the winds having widened the binary too much by the time the giant radius begins its last increase in late He core burning. In the ZAMS $30 M_{\odot}$ star, there is no increase in R at this stage, so Case C mass transfer is not possible.

The lack of increase in R for the more massive stars is due to the cooling effect by strong wind losses. As shown by LBW[1] giant progenitors as massive as $30 M_{\odot}$ are necessary as progenitors of some of the black holes in the SXTs, especially for the binaries with evolved companions, in order to furnish the high mass black hole masses. These authors reduce wind losses by hand, forcing the resulting curve of R vs burning stage to look like that for a ZAMS $20 M_{\odot}$ shown in Fig. 1 during the He core burning where the effect of wind loss is important. In other words, in order to get the observed regularities in the evolution of SXTs, especially Eq. (1) which gives the linear dependence on M_d of the preexplosion separation of the binary, we must manufacture R vs burning stage curves for which mass transfer can be possible both early in Case B and in Case C. With early Case B mass transfer, or intermediate Case B mass transfer if it occurs, the winds during He core burning are so strong that not enough of an Fe core is left to result in a high-mass black hole, rather, a low-mass compact object results[7].

This story is somewhat complicated, but there have been many years of failures in trying to evolve black holes in binaries without taking into account the effects of binarity (mass transfer in our model) on the evolution. On the other hand, de Kool et al.[6] had no difficulty in evolving A0620−00

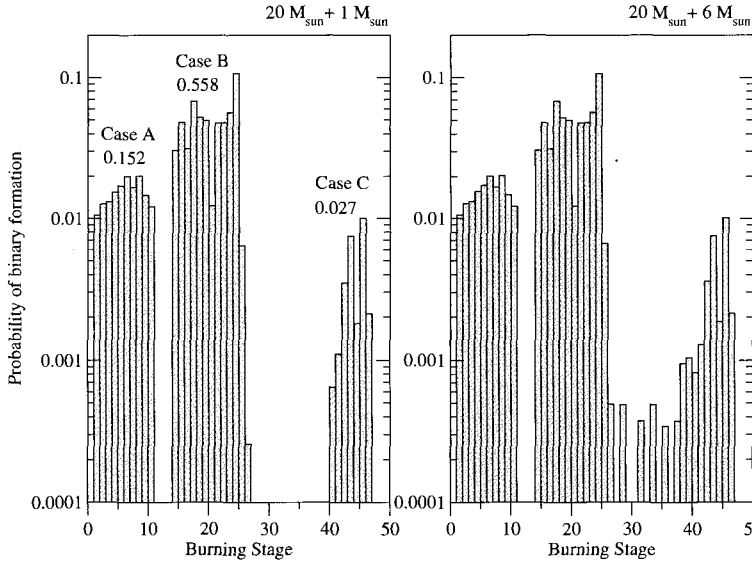

Figure 2. Probability of initial binary formation, in which the Roche Lobe overflow starts between the two adjacent burning stages of the $20M_\odot$ ZAMS star. The burning stages are the same as in Fig. 1. The probability (logarithmic distribution of initial binary separation) is given by $P = \log(a_{n+1}/a_n)/7$ where the initial binary separation $a_{i,t=0}$ is between a_n and a_{n+1}, and the logarithmic distribution is normalized by the total logarithmic interval "7" of Bethe & Brown[12]. Three different cases of mass transfer are marked by Case A, B, and C. The numbers for each case in the left panel are the total of the probabilities in each case. In the left hand panel, the radii for the Case B mass transfer between stage 14 and stage 27 are $R = 22 - 892R_\odot$ with the corresponding initial binary separation $a_{i,t=0} = 33 - 1330R_\odot$. For Case C mass transfer between stages 40-47, $R = 971 - 1185R_\odot$ and $a_{i,t=0} = 1331 - 1605R_\odot$. With a $6M_\odot$ companion, the intermediate Case B mass transfer is possible as in the right panel. However, the total probability for the intermediate Case B mass transfer is $\sim 10\%$ of that for the late Case B and Case C mass transfer.

in Case C mass transfer. The necessity in a similar evolution for the other black hole binaries was, however, not realized at that time.

3. Dependence on the $^{12}C(\alpha,\gamma)^{16}O$ Rate

Brown et al.[7] showed that the mass at which single stars went into high-mass black holes was determined by the $^{12}C(\alpha,\gamma)^{16}O$ rate. For the

Woosley[13] rate of 170 keV barns, stars from $8 - 18M_{\odot}$ would go into neutron stars, the narrow range from $18 - 20M_{\odot}$ into low-mass black holes (We believe 1987A to be an example.) and the stars from $20M_{\odot}$ on up to a maximum mass determined by wind losses, possibly $\sim 30M_{\odot}$ into high-mass black holes.

The main conclusion of Brown et al.[7] was that the massive star must be clothed by its H envelope during most, if not all, of its He core burning, if the core is to be massive enough so as to collapse into a high-mass black hole.

Schaller et al.[10] used ~ 100 keV barns for the $^{12}C(\alpha,\gamma)^{16}O$ rate, and we can check that their central ^{12}C abundance following He core burning goes down to $\sim 15\%$ for their $25M_{\odot}$ star. In fact their $25M_{\odot}$ star does expand quite rapidly just at their stage 43, the end of He core burn. However, large wind losses cause the binary to widen too much for Case C mass transfer, and these must be cut down somewhat as done by LBW if Case C is to be made possible.

One consequence of the skipping of convective carbon burning is that the remaining lifetime of the core should be substantially foreshortened. Whereas convective carbon burning takes hundreds of years, neon and oxygen burning take only $\sim$ one year. The interpolation from ^{12}C to ^{16}O burning via radiative and shell ^{12}C burning and neon burning, which remains even when the central ^{12}C is less than 15%, will smooth out any abrupt change, but the foreshortening should none the less be appreciable. It lessens the time available for tidal interactions in the He-star, donor binary lifetime.

Our considerations apply to Galactic metallicity. With low metallicity, the opacity is less and winds would not be expected to blow off naked He envelopes. Thus, Case A, AB or B mass transfer might not be expected to lead to only low-mass compact objects. The LMC with metallicity about 1/4 Galactic, has two continuously shinning X-ray binaries, LMC X-1 and LMC X-3, even though the total LMC mass is only $\sim 1/20$ of Galactic.

There is an important caveat to the large expected effect from lower metallicity and stronger winds. As discussed in Brown et al.[7] (see their Table 2) the mass loss rate has to be lowered by a factor of 3 from the preferred rate (which fits the fractional period change $\dot{P}/P$ in V444 Cyg) before the convective ^{12}C burning is skipped (with a central 12% ^{12}C abundance). In fact, even then [14] the compact core is only 1.497, only large enough to collapse into a low-mass compact object. But, in the Fryer et al.[14] calculations, the compact core is brought back up to $10.7M_{\odot}$ by fallback, sufficient

for collapse into a high-mass black hole (as in the $5.2M_{\odot}$ remnant obtained when the mass loss rate is cut down by a factor of 2, rather than 3). However, in a binary magnetohydrodynamic effects should help expel the outer matter in the explosion, cutting down the fallback.

From the above one can see that even cutting winds down will not necessarily make Case B mass transfer possible. Perhaps more important is the lack of ^{4}He needed to burn the last ^{12}C left. As the triple alpha reaction depends on the third power of the helium mass fraction it loses against the $^{12}C(\alpha,\gamma)^{16}O$ reaction toward the end of central helium burning; i.e., carbon is mostly burned rather than produced toward the end of central helium burning. That switch typically appears at a central helium mass fraction of $\sim 10-20\%$. Most importantly, as can be seen from the central carbon abundances at the end of He burning, which decreases from 35% to 22% with the lowering of wind losses by a factor of 6 the He fraction is too low to burn the final carbon[14]. Only with the 6-fold reduction in wind from the Woosley et al.[13] rate (which is 3-fold from our preferred value) is convective carbon burning skipped. (With a 4-fold lowering from WLW, the convective carbon burning goes on for 500 years.)

In the clothed stars, on the other hands, the growth of the He core and accompanied injection of helium after this time leads to a further decrease of carbon as compared to the bare helium cores that do not have this additional supply of helium. We believe the above may be the most important difference between naked and clothed He cores.

4. Evolutionary Consequences If Case B Were Possible

We see from Eq. (1) that the preexplosion separation a_f scales linearly with M_D, a relation that was used in LBW to evolve all binaries with evolved companions. Note that the range of a_i also depend on the donor masses through the changes in Roche Lobe radii as in Fig. 3. In LBW we used this scaling, which also followed from the Webbink[15] common envelope evolution, and showed that the evolution of all of the SXTs could be understood in terms of it.

During H shell burning and He core burning the radius R of the giant increases rapidly up to $\sim 892R_{\odot}$. During the increase from $\sim 892R_{\odot}$ to $971R_{\odot}$ the wind losses widen the orbit at such a rate that there is no RLOF as shown in Fig. 1. This may change with decreased wind losses, but we expect any increase in the $a_{i,t=0}$ to be small, and neglect it here. Consequently, Case B mass transfer could be early, taking place with H shell burning or early He core burning.

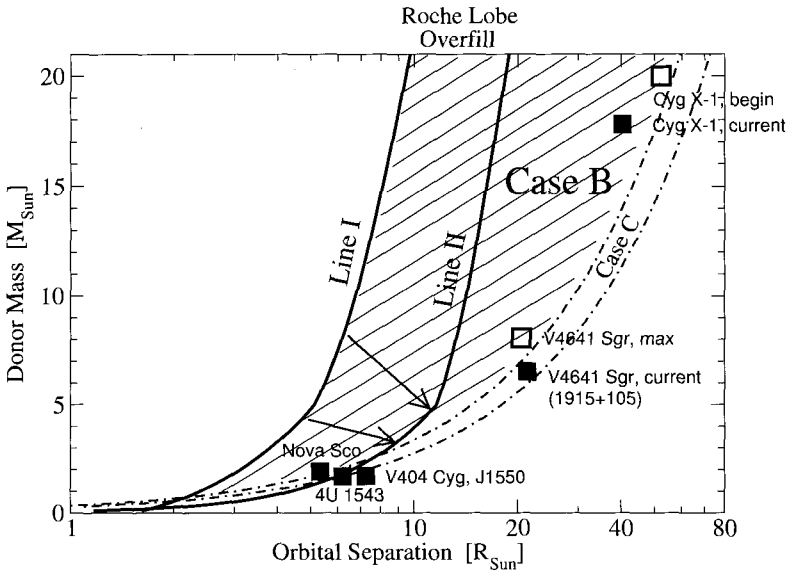

Figure 3. Orbital separations after common envelope evolution for Case B and Case C mass transfer. Dot-dashed lines are the limits for the Case C mass transfer with $M_p = 30M_\odot$, $M_{\rm He} = 11M_\odot$, and $\lambda\alpha_{ce} = 0.2$ (see LBW). All the area to the left of the left dot-dashed line is Case B mass transfer (shaded area). Line I is the sum of the radius of the companion and that of the He core which is assumed to be $1.5R_\odot$. Line II is the orbital separation corresponding to the Roche Lobe overfill right after the spiral-in during the common envelope evolution. The companion stars in binaries between Line I and II will be inside their Roche Lobe (Roche Lobe overfill) when they finish common envelope evolution, and they will be pushed out with mass transfer as indicated by arrows or they will lose in the common envelope evolution. Those binaries ($M_{\rm donor} > 2.5M_\odot$) between Line II and the left boundary of Case C will be outside of the common envelope even with Case B mass transfer. Reconstructed preexplosion orbital separation and black holes masses of SXTs with evolved companions are marked by black squares (refer to Fig. 11 of LBW.) If the high mass black hole formation in Case B mass transfer were possible, the probability of observing them in Case B is ~ 7 times larger than in Case C. However, for the donor masses $\gtrsim 2M_\odot$, we see no SXTs in Case B, while we have two observations, V4641 Sgr and GRS 1915+105 in which the reconstructed data is consistent with Case C. We have put in both the reconstructed data with maximum initial black hole mass (open square), and the present position of V4641 Sgr (filled square) in order to show the uncertainty in reconstruction. The small change in orbital separation shows this binary to give an excellent fiducial preexplosion separation. Because of the long period, mass loss in the explosion will be low (LBW). Cyg X-1 may have had the preexplosion separation shown by the open box; its current separation is shown by the filled box. Although the a_f is linear with companion mass M_d, the curves delineating Case C mass transfer curve up when the orbital separation is plotted logarithmically.

Suppose Case B mass transfer takes place during the stages between 15 and 27 as in Fig. 2. Certainly it can, although we say the results will be a binary with a low-mass compact object. It would most likely do so for radii from $\sim$ 22 to $892R_\odot$, and the corresponding initial binary separation from $\sim 33R_\odot$ to $1330R_\odot$. We set the lower limit to be the radii at the stage 15 following the gap between Case A and Case B mass transfer in Fig. 2. For the total binary logarithmic interval we take the 7 of Bethe & Brown[12]. With the above $33 - 1330R_\odot$ the fractional logarithmic interval is $\ln(1330/33)/7 \sim 0.53$ whereas for Case C mass transfer it is $\ln(1604/1331)/7 = 0.026$. Thus, for a logarithmic distribution of binaries, Case B mass transfer is favored by a factor $\sim$ 20. What would the consequences of this be, assuming it to be possible ?

First of all let us consider SXTs like V4641 Sgr which is just beginning to cross the Herzsprung gap; this consideration also includes GRS 1915+105 which was shown by LBW to be a late V4641 Sgr on the other side of the Herzsprung gap. Both had the large, ZAMS $\sim 6.5 - 8M_\odot$ companions. V4641 Sgr has at present radius $R = 21.3R_\odot$. and from the closeness of black hole and companion masses, could not have been narrower than $\sim 20.5R_\odot$ $(= 21.3 \times (\frac{9.61 \times 6.53}{8.07^2})^2 R_\odot)$ at which separation the companion and black hole mass would have been of nearly equal mass, which could have been as massive as $8M_\odot$ originally.

By way of example of how Case B mass transfer might function, we consider binaries with $M_{\rm He} = 11M_\odot$ and $M_{\rm D} = 8M_\odot$; i.e., binaries similar to our reconstructed V4641 Sgr at the time of black hole formation, as an example. The orbital separation for Roche Lobe overflow is $\sim 13.2R_\odot$, taking the donor radius to be $4.5R_\odot$. The radius of an $11M_\odot$ He star is $1.5R_\odot$, so the sum of donor radius plus He-star radius is $6R_\odot$. If the binary separation is smaller than this, it will merge during the evolution. So the range of orbital separations for Roche Lobe overfill after common envelope evolution is $\sim 6 - 13R_\odot$. This means that if the companion star spirals in from anywhere between an initial 823 and $1770R_\odot$ it will overfill its Roche Lobe. It will then transfer mass to the He star until it fits into its new Roche Lobe with reduced mass. Because of the substantial logarithmic interval $\ln(1770/823)/7 = 0.11$, nearly 1/5 of the entire Case B logarithmic interval, or nearly 4 times the entire Case C logarithmic interval. Conditions of Roche Lobe overfill for various donor masses are summarized in Fig. 3.

Now consider the case that the binary ended up with the orbital separation of $6R_\odot$ after common envelope evolution. Since the separation for

the Roche Lobe filling is $4.5R_\odot/0.35 \sim 12.9R_\odot$, the donor will lose mass until the radius of the donor fits its Roche Lobe. If we assume conservative mass transfer[2], the mass transfer will stop before the donor reaches $\sim 4M_\odot$. Furthermore, if the explosion occurs before the donor radius fits its Roche Lobe, the orbit will be widened during the explosion. This will reduce the mass loss from the donor star, so the final reduced main sequence mass will be larger than $4M_\odot$ as indicated by arrow in Fig. 3.

The chance of seeing the SXTs with massive companions before they evolve is small, even if the high mass black hole formation is possible in Case B mass transfer, either because the binary will end up beyond its Roche Lobe on Line II or because the mass transfer during the early main sequence stage will be small if it ended up along the Line II and will increase the binary radius beyond the Roche Lobe. Note that the life time of main sequence with ZAMS mass $\gtrsim 2M_\odot$ is shorter than the time scale of the orbital separation (e.g., Fig. 2 of De Kool et al. 1987, without magnetic braking). Instead, they will become SXTs when they evolve. In the case of V4641 Sgr with initial companion mass $M_d = 8M_\odot$, $M_{\rm BH} = 8M_\odot$ we estimate that after common envelope evolution $a_f \sim 1.5R_L$. Since the radius more than doubles in late main sequence evolution[10] it will reach its Roche Lobe before then. We thus find that all companions with masses $> 2M_\odot$, aside from that in Cyg X-1, establish Roche contact in main sequence. In Fig. 3, therefore, all binaries between Line I and the boundary of Case B and Case C will become SXTs with evolved companions, if high mass black hole formation in Case B mass transfer were possible. In that case, from Fig. 3, one can see that there should be ~ 8 times more SXTs with evolved companions (with initial donor mass $> 2.5M_\odot$). On the other hand, from Fig. 3, we expect ~ 4 times more SXTs with companions in main sequence if Case B mass transfer were possible.

Chiefly we see from our discussion of possible Case B mass transfer in the SXT evolution that there would be no correlation between companion mass and preexplosion separation, since the possible initial separations a_i would be very widely spread. In many cases, the orbit following spiral-in would overfill its Roche Lobe and mass exchange or loss would spread out the companion masses, each binary filling its Roche Lobe. The validity of Eq. (1) depends on the possible post supergiant radii R being within a narrow range, consequently a narrow range in the preexplosion orbital separation a_i. We show in Fig. 3 that empirically the relation Eq. (1) is satisfied with our preferred common envelope efficiency $\lambda\alpha_{ce} = 0.2$ of LBW. Of course this depends on the reconstruction of preexplosion orbits

by LBW, which generally is supported by PRH although they give a wide range of possibilities.

LBW noted that the evolution of Cyg X-1 also fits into our Case C mass transfer scenario as in Fig. 3. Assume the progenitor of the black hole to be a ZAMS $25M_{\odot}$ giant (with $8.5M_{\odot}$ He star which we assume to go into a black hole of the same mass because very little mass is lost in the case of such a long period). Following the supergiant stage of the massive giant a ZAMS $20M_{\odot}$ companion removes the envelope, coming to an a_f of $\sim 50R_{\odot}$ $(= (20M_{\odot}/8M_{\odot}) \times 20R_{\odot})$, where $8M_{\odot}$ and $20R_{\odot}$ are the reconstructed black hole mass and a_f at the time of explosion in V4641 Sgr. We followed the linear scaling of a_f with M_d here. The companion now transfers $2.2M_{\odot}$ to the black hole in unstable, but conservative mass transfer. This brings the separation a down to the present $40R_{\odot}$.

5. Discussion

The work of LBW[1] has been amalgamated with that of PRH (Podsiadlowski et al. 2002). Both papers agree that common envelope evolution must come following helium core burning; i.e., be Case C. Our work is based on the nearly linear relationship Eq. (1) between separation following common envelope evolution and companion (donor) mass. By choosing the common envelope parameter $\lambda\alpha_{ce} = 0.2$, we are able to evolve those binaries with K and M-star companions, which we believe to be the success of LBW and our earlier works.

The PRH evolutions clarify that all of the binaries with the possible exception of Cyg X-1 could have made Roche contact in main sequence evolution of the companion, as in the earlier work by Beer & Podsiadlowski[4]. This makes it possible to evolve all of the binaries with sub-Eddington rate of mass transfer (although we do not believe this to be necessary in the case of black holes).

LBW and PRH agree that the present evolutionary tracks of supergiants from ZAMS masses $\sim 20 - 30M_{\odot}$ and possibly greater, must be changed so as to allow Case C mass transfer. An example of how to do this was constructed (by hand) in LBW.

We would like to point out that there are uncertainties due to the radius evolution of massive stars and the parameterization of mixing, etc. In particular, stars that use the LeDoux criterion or a small amount of semiconvection burn helium as red supergiants, while those with Schwarzschild or a lot of semiconvection stay blue much of the time. Rotationally induced mixing also plays a role as in Langer and Maeder[16].

Acknowledgments

This work was supported by Research Institute for Basic Sciences, Pusan National University (2003).

References

1. C.-H. Lee, G.E. Brown, and R.A.M.J. Wijers, *Astrophysical Journal* **575**, 996 (2002) (LBW).
2. G.E. Brown and C.-H. Lee, *New Astronomy* **9**, 225 (2004).
3. C.-H. Lee and G.E. Brown, *Int. J. of Mod. Phys.* **A 18**, 527 (2003).
4. M. Beer and Ph. Podsiadlowski, *Mon. Not. of Royal. Astron. Soc.* **331**, 351 (2002).
5. Ph. Podsiadlowski, S. Rappaport, and Z. Han, MNRAS **341**, 385 (2003) (PRH).
6. M. de Kool, E.P.J. van den Heuvel, and E. Pylyser, *Astron. and Astrophys.* **183**, 47 (1987).
7. G.E. Brown, A. Heger, N. Langer, C.-H. Lee, S. Wellstein, and H.A. Bethe, *New Astronomy* **6**, 457 (2001).
8. G.E. Brown, C.-H. Lee, S.F. Portegies Zwart, and H.A. Bethe, *Astrophysical Journal* **547**, 345 (2001).
9. G.E. Brown, C.-H. Lee, and T. Tauris, *New Astronomy* **6**, 331 (2001).
10. G. Schaller, D. Schaerer, G. Meynet, and A. Maeder, *Astron. and Astrophys. Suppl.* **96**, 269 (1992).
11. S.F. Portegies Zwart, F. Verbunt, and E. Ergma, *Astron. and Astrophys.* **321** 207 (1997).
12. H.A. Bethe and G.E. Brown, *Astrophysical Journal* **506**, 780 (1998).
13. S.E. Woosley, N. Langer, and T.A. Weaver, *Astrophysical Journal* **448** 315 (1995); S.E. Woosley and T.A. Weaver, ApJS **101**, 181 (1995).
14. C.L. Fryer, A. Heger, N. Langer, and S. Wellstein, *Astrophysical Journal* **578**, 335 (2002).
15. R.F. Webbink, *Astrophysical Journal* **277**, 355 (1984).
16. N. Langer and A. Maeder, *Astron. and Astrophys.* , **295**, 685 (1995).

A NEW WINDOW TO THE GROUND STATE OF QUARK MATTER: STRANGE QUARK MATTER, STRANGE STARS AND STRANGELETS

VIKRAM SONI

National Physical Laboratory, K.S. Krishnan Marg,New Delhi 110012, India
E-mail: vsoni@del3.vsnl.net.in

DIPANKAR BHATTACHARYA

Raman Research Institute, Bangalore 560080,India
E-mail: dipankar@rri.res.in

If strange quark matter is the true ground state of matter, it must have lower energy than nuclear matter. Simultaneously, 2 flavour quark matter must have higher energy than nuclear matter, for otherwise the latter would convert to the former. We show, using an effective chiral lagrangian, that the existence of a new lower energy ground state for 2 flavour quark matter, the pion condensate, shrinks the window for SQM to be the ground state of matter and sets constraints on the current strange quark mass and the sigma particle mass which may be precluded by the data and thus point to the implausibility of SQM being the true ground state of matter. In consequence, this points to the implausibility of strange stars and also almost eliminates the doomsday risk of the world being eaten up by strangelets produced at a heavy ion accelerator. Further, this analysis provides the unexpected bonus, that the phase diagram of QCD at finite density is such that chiral symmetry remains spontaeously broken at all density!

1. Introduction

The hypothesis that the true ground state of baryonic matter may have a roughly equal fraction of u,d and s quarks, termed strange quark matter (SQM) is of recent origin [1]. This is based on the fact that at some density, when the down quark chemical potential is larger than the strange quark mass, conversion to strange quarks can occur. This reduces the energy density by having 3 (u,d and s) fermi seas instead of just 2 (u, d), and can yield a state of energy lower than nuclear matter. It is also possible to explain why such a state has escaped detection.

This involves at least two puzzles.

i) Why does ordinary 2 flavour nuclear matter, the observed ground state of baryonic matter, not decay into strange quark matter.

The answer is that this decay is not like the radioactive decay of unstable nuclei, as the nucleons cannot decay one by one as it is not energetically favourable for the nucleon to change into a Λ. The entire nuclear matter has to transmute into strange quark matter and this requires a high order of the flavour changing weak interaction which renders the cross section to be exponentially and unobservably small.

ii) Why was this matter not created in the evolution of the universe?

This is due to the fact that as the universe cooled past a temperature equivalent to the strange quark mass , strange quark matter was not the chosen state of high entropy. Since the u and d quarks have almost neglible masses at this scale, as the temperature dropped further, the strange quarks were Boltzmann suppressed leaving just the u and d quarks, which as we know coverted largely into nucleons. For details we refer the reader to Refs. [1,2,3].

It is really quite remarkable that the ground state cannot be realised easily! Only if we can produce high baryon density by compression can SQM be realised - for example, in the interior of neutron stars,

We now turn to the theoretical underpinning of the case for SQM being the potential ground state of matter.

We already know, empirically as well as theoretically, the ground state energy per baryon, E_B, of saturation nuclear matter - 930 MeV for the Fe 56 nuclei. However, for calculating quark matter we take recourse to phenomenological models, which are pointers but foundationally inadequate and here lies the uncertainty.

The usual ground state calculation for SQM treats the quarks as a free fermi gas of current quarks. This quark matter is in a chirally restored state (CRQM). The volume in which these quarks live comes at a cost of a constant energy density that provides 'confinement.' It is equivalently the same constant value of negative pressure and hence is often called the bag pressure term. This is a simple extension of the MIT bag philosophy, where the origin of the constant energy density is the fact that quarks must be confined. The bag pressure sets the equilibrium or ground state energy density and the baryon density. It can be fixed from the nucleon sector. Further structure can be introduced by adding interaction between the quarks, eg, one gluon exchange. Such a phenomenological model has been used by Witten [1] and later by Jaffe and Farhi[2] and others for SQM (see ref.[3] for a review).

2. Chiral Symmetry

It is clear that such a model is phenomenological and does not, for example, address the issue of the spontaneous breaking of chiral symmetry - an essential feature of the strong interactions. We know that for the strong interactions the vacuum is a state with spontaneously broken chiral symmetry (SBCS). On the other hand, the quark matter in the bag, in the state above, is in a chirally restored (CRQM) state. This means that as in the case of Superconductivity it costs energy to expel the chiral condensate which characterises the true vacuum state. Clearly, this will act just like the bag energy density/pressure. However, its value will be determined by the energy density of the chiral condensate. Such a term binds but does not confine. Confinement, thus requires further input than just a bag pressure

All results for the SQM state will depend on the model that is used to describe it and the ground state thereof. We work with an effective chiral model, which is more versatile and which allows the system to dynamically choose, without prejudice, the lowest energy ground state - with or without spontaneous chiral symmetry breaking. We find that there is a plurality of ground states. Of these, we find that one particular ground state has the property of chiral restoration at high density and parallels the MIT bag state used in most previous estimates, where the ground state is a fermi sea of current quarks (CRQM) with the bag pressure provided by absence of the chiral condensate. This regime sets the connection between the paramaters of the chiral model and the MIT bag model used in refs.[1,2,3].

Unlike for the MIT bag case where the bag pressure is a parameter,in our formulation, it is the the chiral condensate energy with a negative sign and is given in terms of the parameters of low energy phenomenology - the pion decay constant, f_π, which is precisely known and the scalar coupling or the σ mass, which is rather poorly 'known'.

There are, however, other ground states for this model, in which the pattern of symmetry beaking is different at high density, for example, the pion condensed (PC) ground state in which the chiral symmetry is still spontaneously broken (but with expectation values that are space dependent, see later) at high density. Such a state has lower ground state energy than the former and thus needs to be considered in the description quark matter. As we show it is found to influence the regime of existence of SQM importantly.

2.1. *Effective chiral lagrangian*

We consider this issue in the framework of an intermediate chiral symmetric Lagrangian that has chiral spontaneous symmetry breaking. Such an effective Lagrangian has quarks, gluons and a chiral multiplet of $[\vec{\pi}, \sigma]$ that flavor couples only to the quarks. For $SU(2)_L x SU(2)_R$ chiral symmetry, we have

$$L = -\frac{1}{4} G^a_{\mu\nu} G^a \mu\nu - \sum \overline{\psi} \left(D + g_y(\sigma + i\gamma_5 \vec{\tau}\vec{\pi}) \right) \psi$$
$$-\frac{1}{2}(\partial\mu\sigma)^2 - \frac{1}{2}(\partial\mu\vec{\pi})^2 - \frac{\lambda^2}{4}(\sigma^2 + \vec{\pi}^2 - (f_\pi)^2)^2 \qquad (1)$$

The masses of the scalar (PS) and fermions follow on the minimization of the potentials above. This minimization yields

$$< \sigma >^2 = f_\pi^2 \qquad (2)$$

where f_π is the pion decay constant It follows that

$$m^2\sigma = 2\lambda^2 (f_\pi)^2 \qquad m_q = m = g < \sigma >= g f_\pi \qquad (3)$$

This theory is an extension of QCD by additionally coupling the quarks to a chiral multiplet , ($\vec{\pi}$ and σ) [4,5,6].

This Lagrangian has produced some interesting physics at the mean field level [6,7]

It provides a quark soliton model for the nucleon in which the nucleon is realized as a soliton with quarks being bound in a skyrmion configuration for the chiral field expectation values [5,6].

Such a model gives a natural explanation for the 'proton spin puzzle'[8], satisfies the Gottfried sum rule [9] and can also yield from first principles (but with some drastic QCD evolution), structure functions for the nucleon which are close to the experimental ones [10].

In a finite temperature field theory such an effective Lagrangian also yields screening masses that match with those of a finite temperature QCD simulation with dynamical quarks [11] and also gives a consistent equation of state for strongly interacting matter at all density [12,6].

We shall first briefly establish the parameters of the above effective Lagrangian and the specific connection with the MIT bag model of confinement used in previous treatments of SQM.

I) As already pointed out above, the nucleon in this model is realised as a soliton in a chiral symmetry broken background with quark bound states [5,6,7]. This sets the value of the yukawa coupling, g, required to fit the nucleon mass in a Mean Field Theory (MFT) treatment to be , g = 5.4.

II) For the description of the nucleon the dependence on the scalar coupling, λ , is marginal as long as it is not too small. Further, in MFT , the QCD coupling does not play a role; only if 1 gluon exchange is included does the QCD coupling enter.

However, λ, determines the scalar mass and also determines the chiral condensate energy density/pressure which is an important parameter for the quark matter phase.

III) There are no other parameters except f_π, the pion decay constant which is set to 93 Mev.

This model has been extended to the SU(3) flavour group for treating the case of strange quark matter [13].

3. Preliminaries for SQM

1) The connection to MIT bag description of quark matter is set as follows. The last term in the above lagrangian, the potential functional,

$\frac{\lambda^2}{4}(\sigma^2 + \vec{\pi}^2 - (f_\pi)^2)^2$

is minimized by the VEV's (space uniform expectation values)

$(< \sigma >= f_\pi, < \vec{\pi} >= 0)$

and is equal to zero at the minimum.

In MFT at high density (as we shall see), when chiral symmetry is restored, $(< \sigma >= 0, < \vec{\pi} >= 0)$, this term reduces to a constant energy density term equal to

$\frac{\lambda^2}{4}(f_\pi)^4$

Besides, due to chiral symmetry restoration the constituent mass of the quarks also vanishes , leaving free massless quarks. This reduced lagrangian, for high density is no different from MIT bag quark matter with

$B = \frac{\lambda^2}{4}(f_\pi)^4$

This completes the identification of the bag pressure term in this model. It shows that bag pressure is automatically generated by chiral restoration and is controlled simply by the scalar coupling or equivalently the sigma mass.

2) We first briefly describe the logical basis for the investigation of the QM ground states vis a vis the usual nuclear matter ground state at saturation density. Here, we follow Jaffe and Farhi [2].

1. We fix coordinates by noting that SQM can be the true ground state only if its, E_B, is lower than the lowest energy per baryon found in nucleii, 930 Mev for iron, as done by Jaffe and Farhi [2].

2. We calculate the 2 flavour quark matter ground states and fix a lower bound for the only free parameter in our lagrangian, the scalar coupling; or equivalently, we get a lower bound on the chiral condensate pressure (or bag pressure) from the condition that the 2 flavour quark matter state must have higher E_B than nuclear matter - otherwise nuclear matter would be unstable to conversion to the 2 flavour QM. As pointed out in ref.[2] this condition is that bulk 2 flavour quark matter must have, $E_B > 934$ Mev.

3. We calculate the SQM with the parameters established in 2 above and see if for SQM, E_B, is smaller than that given in 1, above. If this is the case,and as, E_B, increases monotonically with the scalar coupling (or the chiral condensate pressure), we get an upper bound on the chiral condensate pressure (or bag pressure), when E_B crosses beyond 930 MeV. SQM can then exist, as the true ground state, in this interval between the two bounds.

4. The patterns of symmetry breaking - the SU(2) case

1) For the space uniform phase the pattern of symmetry breaking is such that the expectation values of the meson fields are uniform, given below.

At zero density they are just the VEVs.

$$< \sigma > = f_\pi \tag{4}$$

$$< \vec{\pi} > = 0 \tag{5}$$

For arbitrary density we allow the expectation value to change in magnitude, as it becomes a variational parameter that is determined by energy minimization at each density.

$$< \sigma > = F \tag{6}$$

$$< \vec{\pi} > = 0 \tag{7}$$

This phase has two features, a chiral restoration at some baryon density (above nuclear density), ρ_X, followed, with increasing density, by an absolute minimum in E_B, at $\rho_C > \rho_X$

Since E_B decreases monotonically with density till the chiral restoration density, ρ_X, and then continues to decrease till the minimum is reached at

ρ_C, this implies that the density regime till ρ_C is unstable and has negative pressure. This has been recently conjectured as the density at which self-bound droplets of quarks form, which may be related to nucleons. Further, since at this density chiral symmetry is restored, these 'nucleons' will be like those in the MIT bag model in which chiral symmetry is unbroken inside the nucleons.

We would like to clarify this issue.

From the comparison of this phase with the nucleon and nucleonic 'phase' arising from the same model (see [6,12]), it is clear that the nucleonic phase is always of lower energy than the uniform phase above, upto a density of roughly 3 times the nuclear density, which is above the chiral restoration density in the uniform phase. Further, the minimum in the nucleonic phase occurs very much below the minimum in the uniform phase.

The chiral restoration density in the uniform phase is thus not of any physical interest as matter will always be in the lower energy nucleonic phase and so the identification of nucleon as a quark droplet at the density at which the minimum occurs in the uniform phase is not viable. Clearly, the nucleon is a quark soliton of mass M =938 MeV and falls at the zero density limit in the nucleonic phase.

2) Here we shall consider another realization of the expectation value of $< \sigma >$ and $< \vec{\pi} >$ corresponding to neutral pion condensation. This phenomenon was first considered in the context of nuclear matter.

Such a phenomenon also occurs with our quark based chiral σ model and was first considered at the Mean Field Level by Kutschera and Broniowski in an important paper [13]. Working in the chiral limit they found that the pion condensed state has lower energy than the uniform symmetry breaking state (phase 2) we have just considered for all density. This is expected, as the ansatz for the PC phase is more general than for phase 2.

For the pion condensed (PC) phase the expectation values carry a particular space dependence

$$< \sigma > = FCos(\vec{q}.\vec{r}) \tag{8}$$

$$< \pi_3 > = FSin(\vec{q}.\vec{r}) \tag{9}$$

$$< \pi_1 > = 0 \tag{10}$$

$$< \pi_2 > = 0 \tag{11}$$

Note, when $|\vec{q}|$ goes to zero, we recover the uniform phase (2).

We briefly remark on some features of this phase:

(1) The 2 flavour PC state is quite different from the uniform phase: unlike the 2 flavour CRQM states considered in [2], it cannot be recovered from 3 flavour CRQM by taking the strange quark mass to infinity. As we shall see in the next sections, this gives a new feature - a maximum strange current quark mass for SQM to be the true ground state.

(2) The reason that the PC phase has energy lower than the uniform $< \sigma >$ condensate is perhaps best understood in the language of quarks and anti quarks. To make a condensate a quark and anti-quark must make a bound state and condense. For a uniform $< \sigma >$ condensate the q and $\bar{q}$ must have equal and opposite momentum. Therefore, as the quark density goes up the system can only couple a quark with $k > k_f$ and a $\bar{q}$ with the opposite momentum . This costs much energy so the condensate can only occur if k_f is small, at low density. On the other hand, the pion condensed state is not uniform. So at finite density, if we take a quark with $k = k_f$ the $\bar{q}$ can have momentum $k = |\vec{k}_f - \vec{q}|$, which is a much smaller energy cost.

(3) Since the pion condensate is a chirally broken phase, the chiral restoration shifts from very low density in the uniform phase to very high density: $\sim 10\rho_{nuc}$. This is a signature of this phase.

(4) Since this phase is always lower in energy than the uniform phase we go directly from the nucleonic phase to the PC phase completely bypassing the uniform phase, and thus all the interesting features and conjectures for the uniform phase are never realized.

(5) Another feature of this $\vec{\pi}$ condensate is that since we have a spin isospin polarization we can get a net magnetic moment in the ground state.

For all the details we refer the reader to [13] where we consider, in Mean Field Theory, the phases of 2 flavour quark matter in the $SU(2)_L x SU(2)_R$ chiral model above. We then extend the model to 3 flavours (u, d, s) to describe SQM.

The results are for 3 flavour quark matter with a general ansatz for the ground state that can access both, the the SBCS phases (including pion condensation) as well as the CRQM phase assumed in previous treatments (for example, in Ref. 2).

For 2 flavour (u,d) quark matter the pion condensed(PC) state is the preferred state for all density [14] - it is always lower in energy than the CRQM state.

For 3 flavours and with the current strange quark mass, m_s, less than about 200 MeV, the ground state is well described by the CRQM state used in Ref.2. But for higher m_s, it is the state with a pion condensate that is preferred. This puts a limit on m_s.

In Ref. 2, since all quark matter is calculated in the CRQM state, the transition from 3 flavour quark matter to 2 flavour quark matter is accomplished essentially by taking the limit, $m_s \to \infty$.

It is clear that with the appearance of the lower energy 2 flavour pion condensed (PC), this is no longer true. As we tune, m_s, upwards the transition to the 2 flavour PC (CSB) state occurs at a finite value of m_s.

5. Results and Conclusions

5.1. *Results*

I) 1) Our finding is that (without including 1 gluon exchange) the new PC ground state

i) limits the bounds on the bag pressure, B , allowing

$148MeV < B^{1/4} < 162.5MeV$

instead of the result of ref.[2]

$145MeV < B^{1/4} < 162.5MeV$

ii) it cuts down the allowed pararmeter space of the explicit or current strange quark mass

$m_s < 250$ MeV

2) With, $\alpha_{QCD} = 0.6$, and including 1 gluon exchange the new PC ground state, with some simplifying approximations

i) strongly limits the bounds on the bag pressure, B , allowing

$141.5(156.5)MeV < B^{1/4} < 150.3(166)MeV$

(where the result without brackets follows on using the expression for the interaction energy, E_I, as derived in ref.[2] and that in brackets uses, E_I, from Baym et al [15] (see Ref. 13)).

instead of the result of ref.[2], in the absence of the PC state,

$128.5MeV < B^{1/4} < 145.6MeV$

ii) it further cuts down the allowed pararmeter space of the explicit strange quark mass

$m_s < 150$ MeV

This is a rather punishing constraint

II) The bag pressure ,B,in our chiral model (the SU(2) version) is given by,

$B = \frac{\lambda^2}{4}(f_\pi)^4 = \frac{m_\sigma^2}{8} f_\pi^2$

What is different is that this is now determined from low energy phenomenology.

(i) f_π is the pion decay constant and is well known.

(ii) m_σ is the scalar mass and is poorly known.

Thus, we get a small window in B, which allows for strange quark matter as the true ground state. Now, this allowed range translates into a certain range of allowed values for, m_σ.

As can be seen from [13], for the case of SU(3) there is a modification

$B = \frac{3}{2}\frac{\lambda^2}{4}(f_\pi)^4 = \frac{3}{2}\frac{m_\sigma^2}{8} f_\pi^2$

For all cases considered by us the maximum value of $B^{1/4}$ is 166 MeV, which corresponds to, $m_\sigma = 680 MeV$. Such a value for the sigma mass may be a little too low in the context of the linear sigma model employed by us, as can be seen from the following.

Recently, Schechter et al [16], have made fits to the scalar channel scattering data to see how it may be fitted with increasing range in $\sqrt{s}$, by chiral perturbation theory and several resonances. They have also looked at this channel using just a linear sigma model. Their results indicate that for $\sqrt{s} < 800 MeV$, a reasonable fit to the data can be made using the linear sigma model with a sigma mass between, 700 - 800 MeV.

This establishes that the conditions for SQM to be the absolute ground state are such as to require $m_s < 150 Mev$ and $m_\sigma < 700 Mev$, both of which are close to being not admissible from data. Of course, this is within the framework of MFT in a chiral model.

5.2. *Neutron /Strange stars and the equation of state*

i) Strange stars require the absolute stability of SQM. Since this has been shown to be highly implausible so is then the existence of strange stars.

ii) This analysis also points to an interesting and hitherto unclaimed EOS for dense matter, where chiral symmetry is never restored at any density! Let us explain: a) We start with saturation nuclear matter at nuclear density and this persists till the nuclear matter gets squeezed into quark matter at moderately higher density, when a pion condensed state takes over. Since we have not investigated other condensates, for example, a charged pion running wave condesate or a kaon condensate, we cannot vouch for our neutral pion condensate being the best ground state. However, it is worth pointing out that all these states , that have lower energy than the chirally restored CRQM state, are chiral symmetry broken states.

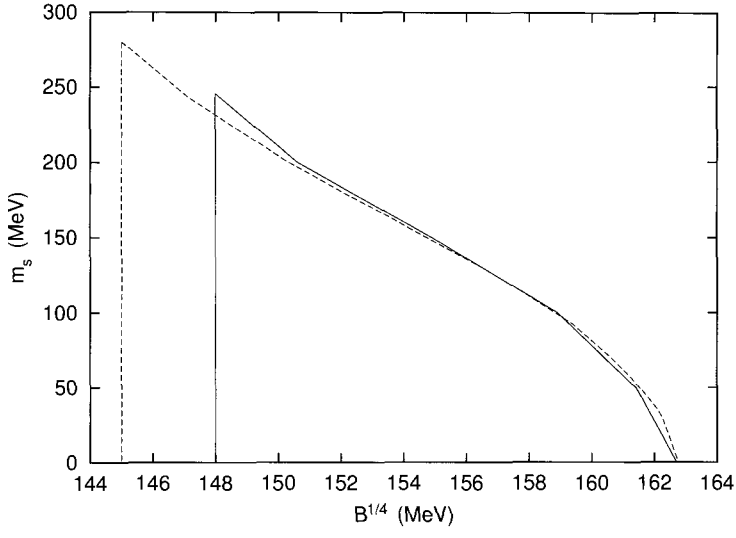

Figure 1. Allowed region in the bag constant-strange quark mass parameter plane for the Strange Quark Matter (SQM) ground state to be the absolute ground state of matter. Gluon exchange interaction is not included. The solid line shows the allowed window, taking into account the Pion Condensed (PC) phase reported in this paper. The region included within the curve is the allowed region. The dashed line shows the result for Chirally Restored Quark Matter (CRQM) from ref. [2]. The vertical left boundary for either case represents $E_B = 934$ MeV in 2-flavour matter and the curved line reresents $E_B = 930$ MeV in 3-flavour matter. The curve for CRQM shown here is a linear interpolation to 930 MeV from the results for 919 MeV and 939 MeV presented in ref. [2].

At even higher density the most likely state is a diquark condensate - a colour flavour locked (CFL) state - which can persist till arbitrarily high density. Such a ground state spontaneously breaks both chiral and colour symmetry. Diquark condensates are unlikely at moderately high density as they depend on the quark density of states and so the pion condensate is most likely at such densities. An important point to note is that, in any case, for quark matter we cannot have chirally restored SQM as it is unstable to the formation of diquark condensate. We will then make a transition from a PC state to a CFL state - both, spontaneously break chiral symmetry. We then arrive at the remarkable conclusion that chiral symmetry is never restored at any density - a situation to be contrasted with that at high temperature. This has profound implications.

ii) In neutron star interiors the central density is well beyond nuclear density. In this case we expect that the profile for star density will start

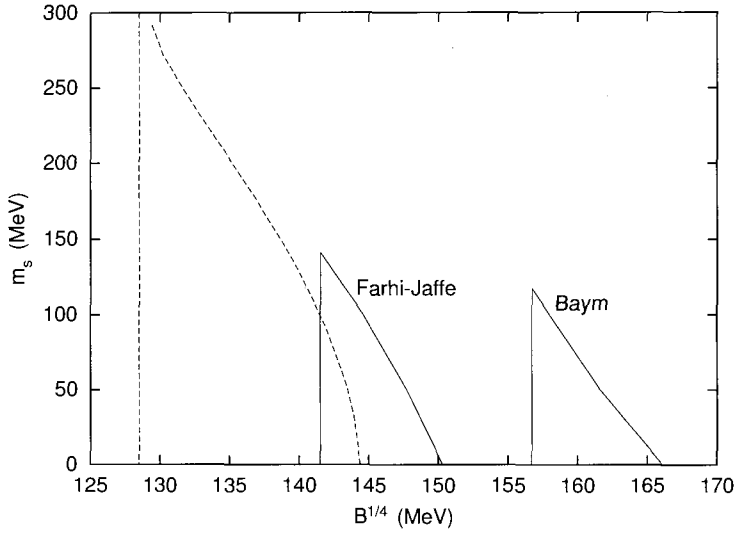

Figure 2. Similar to Figure 1, but with 1-gluon exchange included. The exchange energy is computed using two alternative prescriptions, by Farhi-Jaffe [2] and Baym [16], as indicated. The solid lines represent the constraints imposed by taking into account the PC phase in these two cases. The dashed line is for CRQM, obtained from the data presented by Farhi and Jaffe [2]. α_{QCD} is set to 0.6. The PC phase places a strong constraint on the strange quark mass if SQM should represent the absolute ground state of matter.

with the nucleonic EOS on the outside and go to a pion condensate in the interior and could well go to a a colour flavor locked state at the centre if the density there is large enough; though, this is unlikely if we have a pion condensate as its softness may result in smaller maximum mass.

A summary of the results without the one gluon exchange interaction appears in Fig. 1. For the case with the one gluon exchange interaction the results are summarized in Fig. 2.

6. Conclusions

We have found that the existence of a new and lower energy state of 2 flavour quark matter, the pion condensed state, has a significant effect on the window of opportunity for SQM to be the true ground state of matter.

In effect, as far as the existence of SQM as the true ground state is concerned, this analysis provides

i) A new and interesting constraint for the current mass of the strange quark. ii) Further, our results indicate that the window for SQM sets a constraint on the sigma mass used in our chiral model.

Both these constraints may not be admissable by the experimental data and thus point to the implausibility of SQM being the true ground state of matter.

In consequence, this points to the implausibility of strange stars. In conequence, this also almost eliminates the doomsday risk of the world being eaten up by strangelets produced at a heavy ion accelerator (see [17]).

Further, since this lower energy pion condensed state is favoured by the data, and CRQM quark matter is always unstable to the formation of a diquark condensate,this analysis provides the unexpected bonus that the phase diagram of QCD at finite density is such that chiral symmetry remains spontaeously broken at all density!

References

1. E. Witten, *Phys. Rev.* **D30**, 272 (1984).
2. E. Farhi and R.L. Jaffe, *Phys. Rev.* **D30**, 2379 (1984).
3. C. Alcock and A. Olinto, *Ann. Rev. Nucl. Part. Sci.* **38**, 161 (1988).
4. V. Soni, Mod. *Phys. Lett.* **A11**, 331 (1996), A. Manohar and H. Georgi, *Nucl. Phys.* **B234**, 203 (1984).
5. S. Kahana, G. Ripka and V. Soni, *Nucl. Phys.* **A415**, 351 (1984), M. C. Birse and M.K. Banerjee, *Phys. Lett.* **B134**, 284 (1984).
6. V. Soni, The nucleon and strongly interacting matter', Invited talk at DAE Symposium in Nuclear Physics Bombay, Dec 1992 and references therein.
7. M. C. Birse, Soliton Models in Nuclear Physics, Progress in Particle and Nuclear Phys. **25**, 1 (1991), and references therein.
8. see for example, R.Johnson, N. W. Park, J. Schechter and V. Soni and H. Weigel, *Phys. Rev.* **D42**, 2998 (1990), J. Stern and G. Clement, *Mod. Phys. Lett.* **A3**, 1657 (1988).
9. see for example, J. Stern and G. Clement, *Phys. Lett.* **B264**, 426 (1991), E.J. Eichten,I Hinchcliffe and C.Quigg, Fermilab-Pub 91/272 - T.
10. D. Diakonov, V. Petrov, P. Pobylitsa, M Polyakov and C. Weiss, *Nucl. Phys.* **B480**, 341 (1996), *Phys. Rev.* **D56**, 4069 (1997).
11. A. Gocksch, *Phys. Rev. Lett.* **67**, 1701 (1991).
12. V. Soni, *Phys. Lett.* **152B**, 231 (1985).
13. V. Soni and D. Bhattacharya, 'A new window on strange quark matter as the ground state of strongly interacting matter', preprint hep-ph/0309063.
14. M. Kutschera, W. Broniowski and A. Kotlorz, *Nucl. Phys.* **A516**, 566 (1990).
15. G. Baym and S. Chin, *Phys. Lett.* **62B**, 241 (1976), G. Baym in NORDITA lectures, 'Neutron Stars and the Properties of Matter at high density', (1977).

16. A. Abdel-Rehim, D. Black, A. H. Fariborz, S. Nazri and J. Schechter, preprint JLAB-THY-03-32, SU-4252-778, (May 2003).
17. Martin Rees in 'Our Final Century', published by William Heinemann, London (2003).

PROPERTIES OF NEUTRON STARS

M. H. VAN KERKWIJK
Department of Astronomy & Astrophysics,
60 Saint George Street,
Toronto, Ontario, M5S 3H8, Canada
E-mail: mhvk@astro.utoronto.ca

I review attempts made to determine the properties of neutron stars. I focus on constraints on the maximum mass that a neutron star can have, and on attempts to measure neutron-star radii. So far, there appears to be only one neutron star for which there is strong evidence that its mass is above the canonical $1.4\,M_\odot$, viz., Vela X-1, for which a mass close to $1.9\,M_\odot$ is found. Prospects for progress appear brightest for studies of systems in which the neutron star should have accreted substantial amounts of matter. While for individual systems the evidence that neutron stars can have high masses is weak, the ensemble appears to show that masses around $1.6\,M_\odot$ are possible. For the radius determination, most attempts have focussed on neutron stars in low-mass X-ray binaries in which accretion has temporarily shut down. These neutron stars are easiest to model, since they should have pure Hydrogen atmospheres and low magnetic fields. To obtain accurate radii, however, requires precise distances and very high quality data.

1. Trying to constrain the equation of state

The physics of matter at ultra-high density is not only of interest on its own accord, but also because of its astronomical implications: to understand the core collapse of massive stars, the supernova phenomenon, and the existence and properties of neutron stars, knowledge of the physics, as summarised in the equation of state (EOS), is required. As is clear from other contributions to these proceedings, quantum-chromodynamics calculations are not yet developed well enough to determine the densities at which, e.g., meson condensation and the transition between the hadron and quark-gluon phases occur. At densities slightly higher than nuclear and at high temperatures, the model predictions can be compared with the results of heavy-nuclei collision experiments. The substantial progress on this front is discussed elsewhere in these proceedings. For higher densities and low temperatures, however, no terrestrial experiments seem possible; the models can be compared only with neutron-star parameters. Recent

reviews of our knowledge of the EOS, and the use of neutron stars for constraining it, are given by Heiselberg & Pandharipande[11], and Lattimer & Prakash.[15,16]

Here, I focus on two possible ways to constrain the EOS: aiming to find the highest observed neutron-star mass, and to measure precise radii. The first part is an update of reviews I have given earlier.[31,32]

2. Maximum mass

Observationally, after spin periods, masses are perhaps the easiest bulk properties to determine. Their possible interest for constraining the EOS is that for any given EOS, there is a maximum mass a neutron star can have; beyond this, it would collapse to a black hole. For instance, for EOS with a phase transition at high densities, such as Kaon condensation,[5] only neutron stars with mass $< 1.5\,M_\odot$ could exist. This EOS would be excluded if a neutron star with a mass above this maximum were known to exist. Below, I first describe the constraints given by the very accurate masses derived from relativistic binary neutron stars, and next the less precise masses from X-ray binaries. I then discuss whether the narrow mass range implied by the most accurate masses implies a constraint on the EOS, or rather reflects the astrophysical processes by which neutron stars form. I conclude by briefly describing the situation for neutron stars for which on astronomical grounds one might expect that they have accreted a substantial amount, and hence have become more massive.

2.1. *Relativistic neutron-star binaries*

The most accurate mass determinations have come from radio timing studies of pulsars (see Thorsett & Chakrabarty[29] for an excellent review). The best among these are for pulsars that are in eccentric, short-period orbits with other neutron stars, in which several non-Keplerian effects on the orbit can be observed: the advance of periastron, the combined effect of variations in the second-order Doppler shift and gravitational redshift, the shape and amplitude of the Shapiro delay curve shown by the pulse arrival times as the pulsar passes behind its companion, and the decay of the orbit due to the emission of gravitational waves. The most famous of the double neutron-star binaries is the Hulse-Taylor pulsar, PSR B1913+16, for which $M_{\rm PSR} = 1.4411 \pm 0.0007\,M_\odot$ and $M_{\rm comp} = 1.3874 \pm 0.0007\,M_\odot$ was derived.[28,27] Almost as accurate masses have been inferred for PSR B1534+12, for which the pulsar and its companion were found to have very similar mass:[26] $M_{\rm PSR} = 1.3332 \pm 0.0010\,M_\odot$ and $M_{\rm comp} = 1.3452 \pm 0.0010\,M_\odot$.

To these two best-known systems, recently two further interesting binaries have been added. The first is PSR J1141−6545, for which $M_{\rm PSR} = 1.30 \pm 0.02\,M_\odot$ and $M_{\rm comp} = 0.99 \pm 0.02\,M_\odot$ was measured;[1] here, the companion is most likely a massive white dwarf.[a] Very recently (after the conference), the discovery of a neutron-star binary was announced in which both components are radio pulsars.[17] From this 'double-lined' radio pulsar binary, masses $M_{\rm PSR,1} = 1.337 \pm 0.005\,M_\odot$ and $M_{\rm PSR,2} = 1.250 \pm 0.005\,M_\odot$ were derived.

From the above, one sees that all these well-determined masses are in a relatively narrow range, between 1.25 and $1.44\,M_\odot$.

2.2. *The high-mass X-ray binary Vela X-1*

Neutron-star masses can also be determined for some binaries containing an accreting X-ray pulsar, from the amplitudes of the X-ray pulse delay and optical radial-velocity curves in combination with constraints on the inclination (the latter usually from the duration of the X-ray eclipse, if present). This method has been applied to about half a dozen systems.[13,36] The masses are generally not very precise, but are consistent with $\sim 1.4\,M_\odot$ in all but one case.

The one exception is the X-ray pulsar Vela X-1, which is in a 9-day orbit with the B0.5 Ib supergiant HD 77581. For this system, a rather higher mass of around $1.8\,M_\odot$ has consistently been found ever since the first detailed study in the late seventies.[37,35] A problem with this system, however, is that the measured radial-velocity orbit, on which the mass determination relies, shows strong deviations from a pure Keplerian radial-velocity curve. These deviations are correlated within one night, but not over longer periods. A possible cause could be that the varying tidal force exerted by the neutron star in its eccentric orbit excites high-order pulsation modes in the optical star which interfere constructively for short time intervals.

The velocity excursions appeared not to depend on orbital phase, and we hoped that, with sufficient observations, it would be possible to average

[a] Given that this system has an eccentric orbit, it seems certain that the white dwarf was formed before the supernova explosion that left the neutron star (and made the orbit eccentric). Likely, what happened is that both stars in the binary originally had masses too low to form a neutron star, but that as the originally more massive star evolved, a phase of mass transfer ensued in which the originally less massive star received sufficient material to push its mass over the limit required for neutron-star formation (for references, see citations in Bailes et al.[1]).

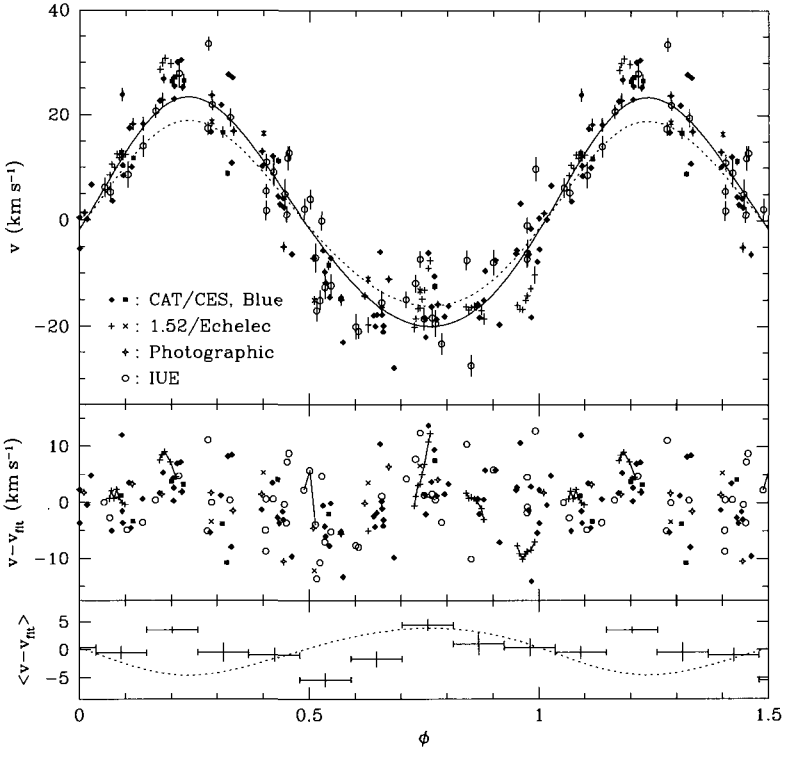

Figure 1. Radial-velocity measurements for HD 77581, the optical counterpart to Vela X-1. Overdrawn is the Keplerian curve that best fits the nightly averages of the data (solid line; $K_{\rm opt} = 21.7 \pm 1.6\,{\rm km\,s^{-1}}$), as well as the curve expected if the neutron star has a mass of $1.4\,M_\odot$ (dotted line; $K_{\rm opt} = 17.5\,{\rm km\,s^{-1}}$). The residuals to the best-fit are shown in the middle panel. For clarity, the error bars have been omitted. Points taken within one night are connected with lines. In the bottom panel, the residuals averaged in 9 phase bins are shown. The horizontal error bars indicate the size of the phase bins, and the vertical ones the error in the mean. The dotted line indicates the residuals expected for a $1.4\,M_\odot$ neutron star.

them out. For that purpose, we obtained about 150 spectra, taken in as many nights and covering more than 20 orbits, of the optical counterpart.[2] Unfortunately, we found that the average velocity curve does show systematic effects with orbital phase (see Fig. 1), which dominate our final uncertainty. While our best estimate still gives a high mass, of $1.86\,M_\odot$, the 2σ uncertainty of $0.33\,M_\odot$ does not allow us to exclude soft equations of state conclusively.

A different approach would be to try to obtain very dense coverage of the orbit, in the hope that one could model and remove the excursions. This approach was tried too,[21] and for the two weeks covered by the observations, it was found to be possible to model the velocity excursions as a fairly coherent, 2.18-d oscillation (in contrast to what was the case in earlier observations[35]). After removal, however, the systematic orbital-phase dependent effects that plagued our determination became apparent here too, and the final mass has roughly the same value, but also roughly the same uncertainty as the one described above.

2.3. *Physical or astrophysical implications?*

While we cannot draw a firm conclusion about the mass of Vela X-1, it is worth wondering how it could be the only neutron star with a mass so different from all others. I would argue one should be careful in taking the narrow mass range around $1.4\,M_\odot$ as evidence for an upper mass limit set by the EOS.[2] After all, for all EOS, neutron stars substantially *less* massive than $1.4\,M_\odot$ can exist, yet none are known. Could it be that the narrow range in mass simply reflects the formation mechanism, i.e., the physics of supernova explosions and the evolution of stars massive enough to reach core collapse? There certainly is precedent: white dwarfs are formed with masses mostly within a very narrow range around $0.6\ M_\odot$, well below their maximum (Chandrasekhar) mass.

Interestingly, from evolutionary calculations,[30] it is expected that single stars produce neutron stars with a bimodal mass distribution, with peaks at 1.27 and $1.76\ M_\odot$. For stars in binaries, only a single peak at $\sim 1.3\,M_\odot$ was found, but it is not clear whether this result will hold (S. Woosley, 2000, pers. communication). If not, could it be that the progenitor of Vela X-1 was a star that managed to produce a massive neutron star? If so, one may still wonder why no massive radio pulsars or pulsar companions have been found. This may be a selection effect:[2] all neutron stars with accurate masses are in binary neutron stars systems in close orbits, whose formation requires a common-envelope stage. During this stage, a merger can only be avoided if the initial orbit was very wide. Stars massive enough to form a massive neutron star, however, likely do not evolve through a red-giant phase, and a common-envelope phase would occur only for rather close orbits, for which the binary would merge.

2.4. *Trying for bias*

In considering the mass measurements discussed above, it should be noticed that for all neutron stars with good masses, it is expected that they accreted only little mass after their formation. Only neutron stars in low-mass X-ray binaries and radio pulsars with low-mass white dwarf companions are expected to have accreted substantial amounts of material. It may thus be worthwhile to try to bias oneself to more massive neutron stars by studying these.

For low-mass X-ray binaries, higher masses, of $\sim 2\,M_\odot$, have indeed been suggested; e.g., from dynamical measurements and lightcurve fitting for Cyg X-2,[19] and from inferences based on quasi-periodic oscillations.[40] These estimates, however, rely to greater or lesser extent on unproven assumptions.

The radio pulsars with white dwarf companions provide cleaner systems, for a number of reasons. First, most of the radio pulsars in these binaries spin very rapidly and stably, making them ideally suited for precision timing. Second, both components can safely be approximated as point masses for dynamical purposes, so that deviations from Keplerian motion can be readily interpreted. Third, by taking optical spectra of the white dwarf, it is possible to determine its radial-velocity curve, and thus obtain the mass ratio. Finally, from a model-atmosphere analysis of optical spectra, one can infer the surface gravity and, using the white-dwarf mass-radius relation, the mass. Combined with a mass ratio, this yields the pulsar mass.

In many of these systems, one expects the neutron star to have accreted a substantial amount of matter. This is because many of the white dwarf companions have masses of only $\sim 0.2\,M_\odot$. In order for their progenitors to have evolved off the main sequence in a Hubble time, the initial masses much have been at least $0.8\,M_\odot$. Hence, at least $0.6\,M_\odot$ was lost. From evolutionary considerations, one would expect much of this to have been accreted to the neutron star, as mass transfer should have been relatively slow and stable.

Despite the above expectations, initial results showed no evidence for such high masses.[29] Current results for four systems are shown in Fig. 2. One sees that for none of these, the mass measurements exclude $1.4\,M_\odot$ at high significance, but for all the best values are above it. This is true for a number of other systems as well.[18]

While the masses appear to be above the narrow range inferred from the relativistic binary pulsars, suggesting that some accretion has happened,

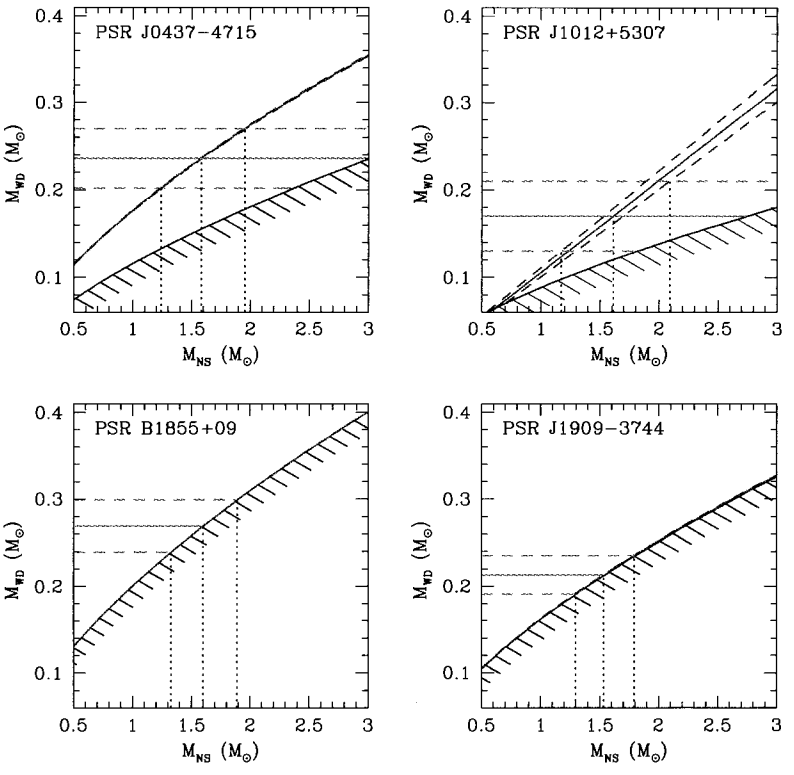

Figure 2. Constraints on the masses of four radio pulsars with white-dwarf companions.[38,33,7,14,18,12] In all panels, the solid line with hashing on the lower right reflects the limit set by the pulsar mass function. The horizontal lines reflect the limits on the companion mass, with the 2-σ uncertainties. For PSR J1012+5307, the mass is inferred from a fit to the optical spectrum, while for the other three sources it is measured from Shapiro delay. The Shapiro delay also implies inclinations very close to 90° (edge-on) for PSR B1855+09 and PSR J1909−3744. For PSR J0437−4715, the curved line is the constraint on the inclination, inferred from the change in aspect with which we view the system due to its proper motion. For PSR J1012+5307, the diagonal straight lines show the mass ratio and its 2-σ uncertainties, inferred from the radial-velocity amplitudes of the two components. The vertical lines show the resulting 2-σ constraints on the pulsar masses.

the masses are not as high as the expected $\sim 2\,M_\odot$. Could this reflect a hard limit set by the EOS? Unfortunately, there may also be a more mundane, astronomical explanation. The pulsars in these binaries have magnetic fields that are much weaker than those inferred for regular radio pulsars. On empirical grounds, it is believed this reduction is related to being in a binary, with the magnetic field being reduced somehow by the

accretion (for a review, see Phinney & Kulkarni[20]). If this is indeed the case, above some amount of accreted matter, the magnetic field may be reduced so far that no pulsar will be seen. This would thus lead one to find a upper limit to the mass of pulsars that accreted matter.

Even though the above may mean a low apparent upper limit to the mass distribution may not be very meaningful, the masses do appear to be higher than in other systems. At present, therefore, the radio pulsars with white dwarf companions still seem to be the most promising systems for obtaining precise and reliable masses that provide strong constraints on the EOS. Further radio timing observations, as well as optical spectroscopy, are underway.

3. Atmospheric modelling

Spectroscopic analysis of emission arising in the photosphere of a neutron star offers, in principle, the possibility of much stronger constraints. From models, the temperature and angular diameter could be inferred, which, combined with a distance, gives the radius. If absorption lines are present, also the gravitational redshift ($\Rightarrow M/R$) and pressure broadening ($\Rightarrow M/R^2$) can be measured. An accurate measurement of even just one of these may be useful, given the narrow range of observed neutron-star masses for neutron stars that did not accrete much after their formation.

In practice, most neutron stars are unsuitable: many have spectra contaminated or even dominated by poorly understood magnetospheric or accretion processes. Even without those, the strong magnetic fields present in many neutron stars imply that the microphysics (energy levels, radiative transfer, etc.) is complicated and that the temperature will in general not be uniform. Finally, most have atmospheres almost certainly composed of pure Hydrogen, since, if any is present, gravitational settling ensures that it will quickly float to the top.

3.1. *Quiescent emission from low-mass X-ray binaries*

The only neutron stars for which no pulsations are seen, and which therefore may not have significant magnetic fields, are those that reside in low-mass X-ray binaries. For some of these, the accretion is episodic, and when accretion turns off, one may be able to observe simple thermal emission from the surface.[6]

Given that the accreted matter contained Hydrogen, which will float to the top, the atmosphere should be composed of pure Hydrogen. This makes

the modelling relatively easy, even if it also implies likely no lines will be seen (small features may be visible due to continuing low-level accretion). Thus, the best one can hope for is to determine effective temperatures and angular diameters. If one has a distance, e.g., because the source is in a globular cluster, this will yield the radius. This may even be quite precise, as distances to globular clusters are becoming better and better.

A possible problem lies in the interpretation: one measures the radius as seen at infinity, $R_\infty = R/\sqrt{1-2GM/Rc^2}$, which, unfortunately, depends more strongly on the precise value of the mass than the radius itself. Since accretion has happened, one does not know the mass a priori. Nevertheless, significant constraints are possible. For instance, for many soft EOS, one finds $R_\infty < 14\,\mathrm{km}$ for neutron stars with any mass between 0.5 and the upper limit for those EOS, $\sim 1.6\,M_\odot$. Similarly, for the stiffer EOS, one finds $R_\infty > 15\,\mathrm{km}$ for any mass above $1.35\,M_\odot$.

Attempts to measure radii for neutron stars in low-mass X-ray binaries in quiescence have been made by a number of authors. Most work has been done for binaries in the field.[6,22,23,25,39] For these, one will need to obtain parallaxes to obtain meaningful radii. However, the observations also showed that the interpretation was not always as straightforward as hoped. First, for some sources, interstellar absorption cuts off a large part of the spectrum, making it difficult to measure the temperature accurately. Second, in the best studied source, Aql X-1, a non-thermal component was found, and even the thermal component was found to be variable on a relatively short timescale of months.[24] These complications shed some doubt on whether the observations are interpreted correctly. It also gives some hope, however: the non-thermal emission is likely due to residual accretion, and it may be possible to see the signature of that in lines from heavier elements.

More recently, the focus has shifted to sources in globular clusters, where the distances are known to fair precision. The best results have come from XMM, because of its large collecting area.[9,10] For the two sources studied in most detail, the uncertainty in the radius now seems dominated by the uncertainty in the distance; the uncertainty due to just the X-ray fitting appears to be below 0.5 km.

3.2. *X-ray bursts*

The X-ray emission of low-mass X-ray binaries is dominated by emission from the neutron-star surface not only in quiescence, when accretion is

absent, but also during so-called X-ray bursts. These X-ray bursts occur when the layer of freshly accreted matter becomes unstable to nuclear burning (usually of Helium; Hydrogen is burnt at least partially as matter accretes; for a review, see Bildsten[3]). The bursts typically last a few seconds, and occur every few hours.

In a very long, 335 ks *XMM* observation of the X-ray burst source EXO 0748−676, taken for calibration purposes, 28 X-ray bursts were observed. By analysing the summed spectra obtained during these bursts (which lasted a cumulative 3.2 ks), possible small absorption features were found, which could be identified with the $n = 2$ to 3 transition of Hydrogen- and Helium-like Iron,[8] for a gravitational redshift $z = 0.35$. It is not clear where the Iron originates. One might think it results from the nuclear fusion, and is brought to the surface, but an alternative explanation is that the metals observed are brought to the photosphere by continuing accretion.[4]

Unfortunately, while the results are extremely intriguing, they are very difficult to confirm, since observationally it is hard to get much higher quality data.

4. Conclusions and prospects

The pessimistic conclusion from the above would be that, since their discovery, neutron stars have not much advanced our understanding of the physics at extreme densities. Viewing the situation more positively, though, one sees that the mass determinations are now getting accurate enough to be interesting, especially for the radio pulsars with white dwarf companions. The precision will increase with further timing of the pulsars, helped by optical studies of the white dwarfs.

Furthermore, new avenues are explored in which the thermal emission is modelled and used to derive angular diameters and gravitational redshifts. The study of low-mass X-ray binaries in quiescence seems particularly promising, particularly once the distances settle down. For globular clusters, this is in progress, while for individual systems in the field it will come in the somewhat longer run, using direct parallax determinations with NASA's Space Interferometry Mission or ESA's GAIA, both expected to be launched in about ten years.

Finally, not mentioned in my talk or this write-up, there are a number of nearby neutron stars with what appear to be purely thermal spectra. Recently, for a number of these, absorption features have been detected, which are likely due to Hydrogen atmospheres in extremely strong magnetic

fields, 10^{13} to 10^{14} G.[34] In such fields, absorption might be due to proton cyclotron or neutral Hydrogen; with more than a single line, one may be able to solve for the field strength and the gravitational redshift. Several are close enough for parallax determinations; combined with angular diameters from atmospheric modelling, this might yield good radii.

Overall, the outlook seems fairly bright.

References

1. Bailes, M., Ord, S. M., Knight, H. S., & Hotan, A. W. 2003, *Astroph. J.* **595**, L49
2. Barziv, O., Kaper, L., van Kerkwijk, M. H., Telting, J., van Paradijs, J., 2001, *Astron. Astroph.* **377**, 925
3. Bildsten, L. 2000. In: Holt, S. S., & Zhang, W. W. (Eds) *Cosmic Explosions*, AIP, 359 (astro-ph/0001135)
4. Bildsten, L., Chang, P., & Paerels, F. 2003, *Astroph. J.* **591**, L29
5. Brown, G. E., & Bethe, H. A. 1994, *Astroph. J.* **423**, 659
6. Brown, E. F., Bildsten, L., & Rutledge, R. E. 1998, *Astroph. J.* **504**, L95
7. Callanan, P. J., Garnavich, P. M., & Koester, D. 1998, *Mon. Not. R. Astron. Soc.* **298**, 211
8. Cottam, J., Paerels, F., & Mendez, M. 2002, *Nature* **420**, 51
9. Gendre, B., Barret, D., & Webb, N. A. 2003a, *Astron. Astroph.* **400**, 521
10. Gendre, B., Barret, D., & Webb, N. 2003b, *Astron. Astroph.* **403**, L11
11. Heiselberg, H., & Pandharipande, V. 2000, *Ann. Rev. Nucl. & Part. Sci.* **50**, 481
12. Jacoby, B. A., Bailes, M., van Kerkwijk, M. H., Ord, S., Hotan, A., Kulkarni, S. R., & Anderson, S. B. 2003, *Astroph. J.* **599**, L99
13. Joss, P. C., & Rappaport, S. A. 1984, *Ann. Rev. Astron. Astroph.* **22**, 537
14. Kaspi, V. M., Taylor, J. H., & Ryba, M. 1994, *Astroph. J.* **428**, 713
15. Lattimer, J. M., & Prakash, M. 2000, *Phys. Rep.* **333**, 121
16. Lattimer, J. M., & Prakash, M. 2001, *Astroph. J.* **550**, 426
17. Lyne, A. G., et al. 2004, *Science* **303**, 1153
18. Nice, D. J., Splaver, E. M., & Stairs, I. H. 2003. To appear in: Camilo, F., & Gaensler, B. M. (eds), Proc. IAU Symp. 218, ASP Conf. Proc., in press (astro-ph/0311296)
19. Orosz, J. A., & Kuulkers, E. 1999, *Mon. Not. R. Astron. Soc.* **305**, 1320
20. Phinney, E. S. & Kulkarni, S. R. 1994, *Ann. Rev. Astron. Astroph.* **32**, 591
21. Quaintrell, H., Norton, A. J., Ash, T. D. C., Roche, P., Willems, B., Bedding, T. R., Baldry, I. K., & Fender, R. P. 2003, *Astron. Astroph.* **401**, 313
22. Rutledge, R. E., Bildsten, L., Brown, E. F., Pavlov, G. G., & Zavlin, V. E. 1999, *Astroph. J.* **514**, 945
23. Rutledge, R. E., Bildsten, L., Brown, E. F., Pavlov, G. G., & Zavlin, V. E. 2001, *Astroph. J.* **559**, 1054
24. Rutledge, R. E., Bildsten, L., Brown, E. F., Pavlov, G. G., & Zavlin, V. E. 2002a, *Astroph. J.* **577**, 346

25. Rutledge, R. E., Bildsten, L., Brown, E. F., Pavlov, G. G., Zavlin, V. E., & Ushomirsky, G. 2002b, *Astroph. J.* **580**, 413
26. Stairs, I. H., Thorsett, S. E., Taylor, J. H., & Wolszczan, A. 2002, *Astroph. J.* **581**, 501
27. Taylor, J. H. 1992, *Phil. Trans. R. Soc. London A* **341**, 117
28. Taylor, J. H., & Weisberg, J. M. 1989, *Astroph. J.* **345**, 434
29. Thorsett, S. E., & Chakrabarty, D., 1999, *Astroph. J.* **512**, 288
30. Timmes, F. X., Woosley, S. E., & Weaver, T. A. 1996, *Astroph. J.* **457**, 834
31. Van Kerkwijk, M.H., 2001a. In: Kaper, L., Van den Heuvel, E.P.J., & Woudt, P.A. (eds.) Proc. of the ESO Workshop "Black holes in binaries and galactic nuclei." Springer, Heidelberg (Germany), p. 39 (astro-ph/0001077)
32. Van Kerkwijk, M.H., 2001b. To appear in: Van den Heuvel, E.P.J., Kaper, L., & Rol, E. (eds), Proc. Jan van Paradijs Memorial Symposium. Astronomical Society of the Pacific, San Fransisco (astro-ph/0110336)
33. Van Kerkwijk, M. H., Bergeron, P., & Kulkarni, S. R. 1996, *Astroph. J.* **467**, L89
34. Van Kerkwijk, M.H., Kaplan, D.L., Durant, M., Kulkarni, S.R., & Paerels, F., 2004, *Astroph. J.*, accepted (astro-ph/0402418)
35. Van Kerkwijk, M. H., van Paradijs, J., Zuiderwijk, E. J., Hammerschlag-Hensberge, G., Kaper, L., & Sterken, C. S. 1995, *Astron. Astroph.* **303**, 483
36. Van Kerkwijk, M.H., van Paradijs, J., & Zuiderwijk, E.J. 1995, *Astron. Astroph.* **303**, 497
37. Van Paradijs, J., Zuiderwijk, E. J., Takens, R., Hammerschlag-Hensberge, G., Van den Heuvel, E. P. J., & De Loore C. 1977, *Astron. Astroph. Supp.* **30**, 195
38. Van Straten, W., Bailes, M., Britton, M., Kulkarni, S. R., Anderson, S. B., Manchester, R. N., & Sarkissian, J. 2001, *Nature* **412**, 158
39. Wijnands, R., Guainazzi, M., van der Klis, M., & Méndez, M. 2002, *Astroph. J.* **573**, L45
40. Zhang, W., Strohmayer, T. E., & Swank, J. H. 1997, *Astroph. J.* **482**, L167

NEUTRON STARS AND QUARK STARS

FRIDOLIN WEBER

Department of Physics, San Diego State University, 5500 Campanile Drive, San Diego, CA 92182-1233, USA

The tremendous densities reached in the centers of neutron stars provide a high pressure environment in which exciting particles processes are likely compete with each other and novel phases of matter may exist. The particle processes range from the generation of hyperons, to quark deconfinement, to the formation of kaon condensates and H-matter. Another striking possibility concerns the formation of absolutely stable strange quark matter. In the latter event all neutron stars could in fact be strange (quark matter) stars, which would be largely composed of pure quark matter possibly enveloped in a thin nuclear crust made up ordinary hadronic matter. This paper gives an overview of the properties of both classes of stars.

1. Introduction

Most neutron stars are spotted as pulsars by radio telescopes and X-ray satellites. They are more massive ($\sim 1.5\,M_\odot$) than our sun but are typically only about $\sim$ 10 kilometers across so that the matter in their centers is compressed to densities that are up to an order of magnitude higher than the density of atomic nuclei. A neutron star, therefore, provides a high-pressure environment in which numerous subatomic particle processes are expected to compete with each other and novel phases of matter–like the quark-gluon plasma being sought at the most powerful terrestrial particle colliders–could exist. Of key importance for the theoretical analysis of the properties of neutron stars is the equation of state (EoS), that is, the functional dependence of pressure on total energy density of neutron star matter. It forms the basis input quantity in Einstein's field equations, from which the properties of neutron stars and strange stars are computed.

2. Equation of State

The EoS of neutron star matter below neutron drip, which occurs at densities around $4 \times 10^{11}\,\mathrm{g/cm^3}$, and at densities above neutron drip but below the saturation density of nuclear matter is relatively well known. This

is to a less extent the case for the EoS in the vicinity of the saturation density of normal nuclear matter, $\rho_0 = 0.16$ fm^{-3} (energy density of $\epsilon_0 = 140$ MeV/fm^3). Finally the physical properties of matter at still higher densities are highly uncertain and the associated EoS is only very poorly known. The models derived for it differ considerably from one another with respect to the functional dependence of pressure on density, as can be seen in Fig 1. This has its origin in various sources which concern:

(1) The many-body technique used to determination the EoS.
(2) The model of the nucleon-nucleon interaction (non-relativistic two-nucleon interaction, phenomenological three-nucleon interaction, relativistic meson-exchange interaction).
(3) Relativistic (field theoretical) effects.
(4) The alteration of hadrons properties by immersion in dense matter.
(5) The treatment of neutron star matter as an electrically charge neutral system of particles in chemical equilibrium.
(6) The fundamental constituents of neutron star matter which may be:
    (a) Neutrons (n),
    (b) Neutrons and protons (p) in chemical equilibrium with electrons (e^-) and muons (μ^-),
    (c) Nucleons, hyperons ($\Sigma^{\pm,0}, \Lambda, \Xi^{0,-}$) and possibly more massive baryon states ($\Delta^{++,+,0,-}$),
    (d) Presence of boson condensates (π^- or K^-),
    (e) Formation of H dibaryons,
    (f) Phase transition of confined hadronic matter into the deconfined phase of (u, d, s) quarks and gluons.
(7) The true ground state of the strong interaction (strange quark matter versus nuclear matter).

3. Nuclear Matter

Nuclear matter is an idealized many body system made up of equal number of neutrons and protons. The interactions among them are generally treated within the following treatments:

(1) The semiclassical Thomas-Fermi method.[1,2,3,4]
(2) Schroedinger-based theories (i.e. variational approach, standard Monte Carlo, Quantum Monte Carlo, Green function Monte Carlo, hole line expansion (Brueckner theory), coupled cluster method, Green function method).[5,6,7,8]

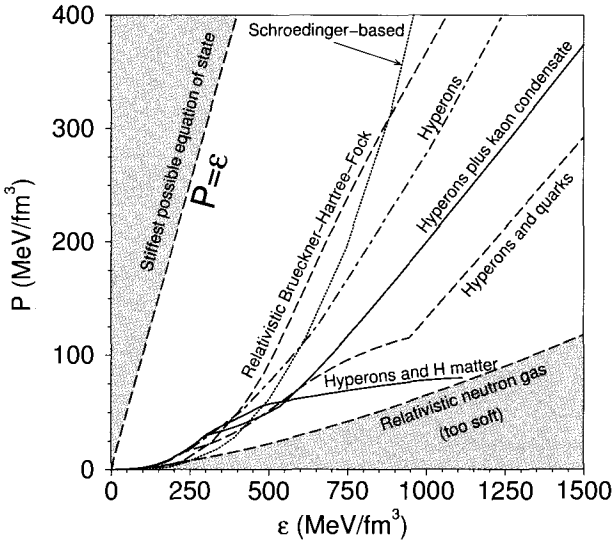

Figure 1. Models for the EoS of neutron star.

(3) Relativistic nuclear field theories solved for the Hartree, Hartree-Fock, or Brueckner-Hartree-Fock approximation.[9,10]

Any acceptable nuclear many-body calculation must reproduce the bulk properties of nuclear matter at saturation density, ρ_0, and finite nuclei. The nuclear matter properties are the binding energy E/A, effective nucleon mass $m_{\rm N}^*/m_{\rm N}$, incompressibility K, and symmetry energy $a_{\rm s}$. Table 1 shows these properties computed for numerous different many-body techniques as well as nuclear forces. Of the four, the value for the incompressibility carries the biggest uncertainty. Its value is currently believed to lie in the range between about 220 and 250 MeV. As can be seen from Table 1, several theoretical studies predict values considerably higher than that. Table 1 also shows the symmetry energy density derivative, L, and the slope, y, of the saturation curve of isospin asymmetric nuclear matter. These quantities are defined as[9,11]

$$L = 3\rho_0(\partial a_{\rm s}/\partial\rho)_{\rho_0}, \qquad y = -K a_{\rm s}\,(3\rho_0 L)^{-1}\,, \tag{1}$$

respectively. Evidently both L and y vary tremendously from one force to another.

Table 1. Saturation properties of nuclear matter.

Force	ρ_0 (fm^{-3})	E/A (MeV)	K (MeV)	a_s (MeV)	L (MeV)	y (MeV fm^3)
SI	0.155	−16.0	371	29.2	1.18	−19700
SII	0.148	−16.0	342	34.2	50.0	−524
SIII	0.145	−15.9	356	28.2	9.87	−2330
SIV	0.151	−16.0	325	31.2	63.5	−353
SV	0.155	−16.1	306	32.8	96.1	−224
SVI	0.144	−15.8	364	26.9	−7.38	3080
Ska	0.155	−16.0	263	32.9	74.6	−249
Skb	0.155	−16.0	263	23.9	47.5	−284
SG-0	0.168	−16.7	253	35.6	41.6	−430
SGI	0.154	−15.8	261	28.3	64.1	−250
SGII	0.158	−15.6	215	26.8	37.6	−322
SkM	0.160	−15.8	217	30.7	49.3	−281
SkM*	0.160	−15.8	217	30.0	45.8	−296
E	0.159	−16.1	334	27.6	−31.3	617
E_σ	0.163	−16.0	249	26.4	−36.9	364
Z	0.159	−16.0	330	26.8	−49.8	373
Z_σ	0.163	−15.9	233	26.7	−29.4	432
Z_σ^*	0.163	−16.0	235	28.8	−4.58	3030
R_σ	0.158	−15.6	238	30.6	85.7	−179
G_σ	0.158	−15.6	237	31.4	94.0	−167
MSkA	0.154	−16.0	314	30.4	57.2	−361
SkT6	0.161	−16.0	236	30.0	30.8	−475
SkP	0.163	−16.0	201	30.0	19.5	−632
SkSC4	0.161	−15.9	235	28.8	−2.17	6460
SkX	0.155	−16.1	271	31.1	33.2	−545
MSk7	0.158	−15.8	231	27.9	9.36	−1460
BSk1	0.157	−15.8	231	27.8	7.15	−1908
SLy4	0.160	−16.0	230	32.0	45.9	−335
SLy7	0.158	−15.9	230	32.0	47.2	−328
TM1	0.145	−16.3	281	37.9	114	−215
Bro A	0.174	−16.5	280	34.4	81.9	−225
Bro B	0.172	−15.7	249	32.8	90.2	−175
Bro C	0.170	−14.4	258	31.5	76.1	−209
$\mathrm{RHF}^{(1)}$	0.148	−15.8	610	28.9	132	−301
$\mathrm{RHF}^{(2)}$	0.148	−15.8	360	43.3	135	−260
$\mathrm{RHF}^{(3)}$	0.148	−15.8	460	38.6	138	−290
NL 1	0.152	−16.4	212	43.5	140	−145
NL-SH	0.146	−16.4	356	36.1	114	−257
FRDM	0.152	−16.3	240	32.7	–	–
ETFSI-1	0.161	−15.9	235	27.0	−9.29	1414

4. Neutron star matter

In the simplest conception, neutron star matter is made up of only neutrons. In a more accurate representation, however, because of chemical

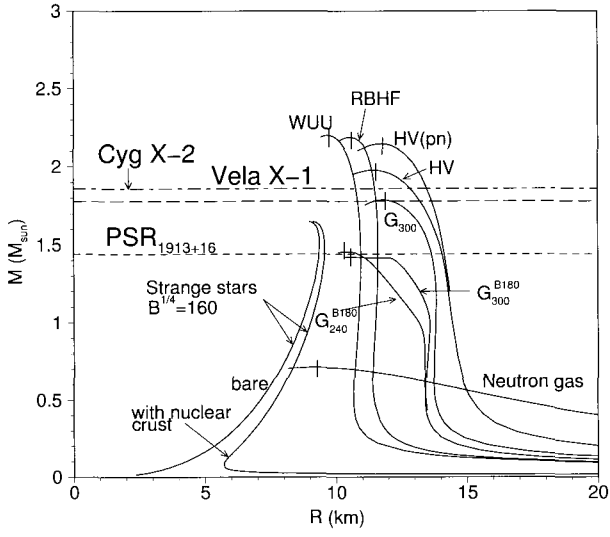

Figure 2. Neutron star mass versus radius for different EoS. The horizontal lines refer to the masses of Vela X-1 $(1.86 \pm 0.16\, M_\odot)$[12], Cyg X-2 $(1.78 \pm 0.23\, M_\odot)$[13], and PSR 1913+16 $(1.442 \pm 0.003\, M_\odot)$.[14]

equilibrium, such matter will consist of neutrons and protons whose charge is balanced by electrons and muons. Finally, additional hadronic states may make their appearance in neutron star matter at densities higher than a few times ρ_0, as will be discussed in this section. The uncertainties in the stellar composition together with the uncertainties in the many-body technique itself lead to theoretical predictions of neutron star properties that vary greatly with the underlying model for the EoS. This is illustrated for the mass-radius relationship of 'neutron' stars in Fig. 2.

4.1. *Hyperons*

At the densities in the interior of neutron stars, the neutron chemical potential, μ^n, exceeds the mass, modified by interactions, of various members of the baryon octet.[15] Hence, in addition to nucleons, neutron star matter is expected to have significant populations of hyperons and possibly more massive baryon states too. If so, pure neutron matter would constitute an excited state relative to hyperonic matter which, therefore, would quickly transform via the weak reaction

$$n \rightarrow p + e^- + \bar{\nu}_e \tag{2}$$

to the lower energy state. The chemical potentials associated with reaction (2) in equilibrium obey the relation

$$\mu^n = \mu^p + \mu^{e^-} , \tag{3}$$

where $\mu^{\bar{\nu}_e} = 0$ since (anti) neutrinos do not accumulate in neutron stars. (This is different for proto-neutron stars.[16]) Equation (3) is a special case of the general relation

$$\mu^\chi = B^\chi \mu^n - q^\chi \mu^{e^-} , \tag{4}$$

which holds in any system characterized by two conserved charges. These are in the case of neutron star matter electric charge, q^χ, and baryon number charge, B^χ. Application of Eq. (4) to the Λ hyperon ($B^\Lambda = 1$, $q^\Lambda = 0$), for instance, leads to

$$\mu^\Lambda = \mu^n . \tag{5}$$

Ignoring particle interactions the chemical potential of a relativistic particle of type χ is given by

$$\mu^\chi = \omega(k_{F_\chi}) \equiv \sqrt{m_\chi^2 + k_{F_\chi}^2} , \tag{6}$$

where $\omega(k_{F_\chi})$ is the single-particle energy of a particle χ moving with Fermi momentum k_{F_χ}. Substituting (6) into (5) leads to

$$k_{F_n} \geq \sqrt{m_\Lambda^2 - m_n^2} \simeq 3 \text{ fm}^{-1} \Rightarrow \rho_n \equiv \frac{{k_{F_n}}^3}{3\pi^2} \simeq 2\rho_0 , \tag{7}$$

where $m_\Lambda = 1116$ MeV and $m_n = 939$ MeV. That is, neutrons are replaced with Λ's in neutron star matter at densities just around twice the density of nuclear matter. This figure is only slightly altered by the inclusion of particle interactions.[15] Aside from chemical equilibrium, the condition of electric charge neutrality of neutron star matter, which reads

$$\sum_{\chi=p,\Sigma,\ldots;e^-,\mu^-} q^\chi \, k_{F_\chi}^3 + 3\pi^2 \, \rho_M \, \Theta(\mu^M - m_M) = 0 , \tag{8}$$

is of key importance for the composition of such matter too.

4.2. *Meson Condensation*

The last term in (8) accounts for the electric charges carried by condensed mesons of type M. The only mesons that may plausibly condense in neutron star matter are either the π^- (see, for instance, Ref. 17) or the currently more favored K^-.[18,19,20] The condensation of mesons other than these two

is unfavored because of electric charge reasons. Early estimates predicted the onset of charged pion condensation around $2\rho_0$. However, these estimates are very sensitive to the strength of the effective nucleon particle-hole repulsion in the isospin $T = 1$, spin $S = 1$ channel, described by the Landau Fermi-liquid parameter g' which tends to suppress the condensation mechanism.[21] Measurements in nuclei tend to indicate that the repulsion is too strong to permit condensation in nuclear matter.[22,23] Nevertheless, some authors argue to the contrary in the case of neutron star matter.[24,25]

Pion as well as kaon condensation would have two important effects on neutron stars. Firstly, condensates soften the EoS above the critical density for onset of condensation, which reduces the maximal possible neutron mass. At the same time, however, the central stellar density increases, because of the softening. Secondly, meson condensates would lead to neutrino luminosities which are considerably enhanced over those of normal (modified Urca process) neutron star matter, leading to dramatically different cooling histories of neutron stars.[9,26]

4.3. *Nucleon Matter*

Whether a meson of a certain type condenses in neutron star matter depends decisively on the meson's in-medium mass, m_M^*, since condensation can only occur if the meson energy equals the electron chemical potential. The condensation point would be given precisely by the bare mass if the meson did not interact with other hadrons. In the presence of interactions, however, the determination of the condensation point is considerably more complicated. In the case of K^- mesons, for instance, highly degenerated electrons can be replaced with kaons if the reaction

$$e^- \rightarrow K^- + \nu \tag{9}$$

becomes possible in neutron star matter. Information about the kaon's in-medium mass is provided by the K^- kinetic energy spectra extracted from Ni+Ni collisions at SIS energies measured by the KaoS collaboration at GSI.[27] An analysis of the KaoS data shows that the attraction from nuclear matter may bring the K^- mass down to $m_{K^-}^* \simeq 200$ MeV at $\rho \sim 3\,\rho_0$. For neutron-rich matter the relation[28,29,30,31]

$$m_{K^-}^*(\rho) \simeq m_{K^-}\left(1 - 0.2\,\frac{\rho}{\rho_0}\right) \tag{10}$$

was established with $m_K = 495$ MeV the K^- vacuum mass. Values around $m_{K^-}^* \simeq 200$ MeV lie in the vicinity of the electron chemical potential μ^e in

neutron star matter[9,10,15] so that the threshold condition for the onset of K^- condensation, $\mu^e = m_K^*$, which follows from Eq. (9), could be fulfilled in high-density neutron star matter. Equation (9) is followed by

$$n + e^- \rightarrow p + K^- + \nu\,, \tag{11}$$

with the neutrinos leaving a neutron star. By this conversion the nucleons in the cores of newly formed neutron stars can become half neutrons and half protons, which lowers the energy per baryon of the matter.[30] The relatively isospin symmetric composition achieved in this way resembles the one of atomic nuclei, which are made up of roughly equal numbers of neutrons and protons. Neutron star matter is therefore referred to in this scenario as nucleon matter, and neutron stars constructed for such an EoS as nucleon stars.[28,29,30,31]

4.4. *H-dibaryons*

A novel particle that could make its appearance in the center of a neutron star is the so-called H-dibaryon, a doubly strange six-quark composite with spin and isospin zero, and baryon number two.[32] In neutron star matter, which may contain a significant fraction of Λ hyperons, the Λ's could combine to form H-dibaryons which could give way to the formation of H-matter at densities somewhere between $3\,\epsilon_0$ and $6\,\epsilon_0$, depending on the in-medium properties of the H-dibaryon. H-matter could thus exist in the cores of moderately dense neutron stars.[33,34,35] If formed, however, H-matter may not remain dormant in the centers but, because of its instability against compression, could trigger the conversion of neutron stars into hypothetical strange stars.[35,36,37]

4.5. *Quark Deconfinement*

One item that came recently into particular focus concerns the possible quark-hadron phase transition of neutron star matter.[9,38,39] The phase transition is characterized by the conservation of baryon charge and electric charge. The Gibbs condition for phase equilibrium then is that the two associated chemical potentials μ^n and μ^e and pressure in the two phases be equal,[40]

$$P_{\rm H}(\mu^n, \mu^e, \{\chi\}, T) = P_{\rm Q}(\mu^n, \mu^e, T)\,. \tag{12}$$

$P_{\rm H}$ denoted the pressure of hadronic matter computed for a given hadronic Lagrangian $\mathcal{L}(\{\chi\})$, where $\{\chi\}$ denotes the field variables and Fermi momenta that characterize a solution to the equations of confined hadronic

matter. The pressure of quark matter, $P_{\rm Q}$, is obtainable from the bag model. The quark chemical potentials μ^u, μ^d, μ^s are related to the baryon and charge chemical potentials as

$$\mu^u = \frac{1}{3}\,\mu^n - \frac{2}{3}\,\mu^e\,, \qquad \mu^d = \mu^s = \frac{1}{3}\,\mu^n + \frac{1}{3}\,\mu^e\,. \tag{13}$$

Equation (12) is to be supplemented with the two global relations for conservation of baryon charge and electric charge within an unknown volume V containing A baryons. The first one is given by

$$\rho \equiv \frac{A}{V} = (1-\eta)\,\rho_{\rm H}(\mu^n, \mu^e, T) + \eta\,\rho_{\rm Q}(\mu^n, \mu^e, T)\,, \tag{14}$$

where $\eta \equiv V_{\rm Q}/V$ denotes the volume proportion of quark matter, $V_{\rm Q}$, in the unknown volume V, and $\rho_{\rm H}$ and $\rho_{\rm Q}$ are the baryon number densities of hadronic matter and quark matter. Global neutrality of electric charge within the volume V can be written as

$$0 = \frac{Q}{V} = (1-\eta)\,q_{\rm H}(\mu^n, \mu^e, T) + \eta\,q_{\rm Q}(\mu^n, \mu^e, T) + q_{\rm L}\,, \tag{15}$$

with q_i the electric charge densities of hadrons, quarks, and leptons. For a given temperature, T, Eqs. (12)–(15) serve to determine the two independent chemical potentials and the volume V for a specified volume fraction η of the quark phase in equilibrium with the hadronic phase. After completion $V_{\rm Q}$ is obtained as $V_{\rm Q} = \eta V$. Because of Eqs. (12)–(15), the chemical potentials depend on the proportion η of the phases in equilibrium, and hence so also all properties that depend on them, i.e. the energy densities, baryon and charge densities of each phase, and the common pressure. For the mixed phase, the volume proportion of quark matter varies from $0 \le \eta \le 1$, and the energy density is the linear combination of the two phases,

$$\epsilon = (1-\eta)\,\epsilon_{\rm H}(\mu^n, \mu^e, \{\chi\}, T) + \eta\,\epsilon_{\rm Q}(\mu^n, \mu^e, T)\,. \tag{16}$$

One model for the EoS computed along these lines is shown in Fig. 1 (labeled 'hyperons and quarks').[40] Possible astrophysical signals of quark deconfinement are discussed in Sect. 5 and in Refs. 9, 41, 42, 43 (see also this volume).

4.6. *Color Superconductivity of Quark Matter*

There has been much recent progress in our understanding of quark matter, culminating in the discovery that if quark matter exists it will be a color superconductor.[38,39,44,45] (See Rajagopal's contribution elsewhere in

this volume.) The phase diagram of such matter is very complex.[38,39] At asymptotic densities the ground state of QCD with a vanishing strange quark mass is the color-flavor locked (CFL) phase. This phase is electrically neutral in bulk for a significant range of chemical potentials and strange quark masses.[46] If the strange quark mass is heavy enough to be ignored, then up and down quarks may pair in the two-flavor superconducting (2SC) phase. Other possible condensation patters are the CFL-K^0 phase[47] and the color-spin locked (2SC+s) phase.[48] The magnitude of the gap energy lies between ~ 50 and 100 MeV. Color superconductivity thus modifies the EoS at the order $(\Delta/\mu)^2$ level, which is only a few percent. Such a small effect can be safely neglected in present determinations of models for the EoS of neutron star matter and strange star matter. This appears to be very different for phenomena involving the cooling by neutrino emission, the pattern of the arrival times of supernova neutrinos, the evolution of neutron star magnetic fields, rotational (r-mode) instabilities, and glitches in rotation frequencies of pulsars (see Refs. 39, 38, 49, 50, 51, 52, and references therein). Aside from neutron star properties, an additional test of color superconductivity may be provided by upcoming cosmic ray space experiments such as AMS [53] and ECCO.[54] As shown in Ref. 55, finite lumps of color-flavor locked strange quark matter (see Sect. 6), which should be present in cosmic rays if strange matter is the ground state of the strong interaction, turn out to be significantly more stable than strangelets without color-flavor locking for wide ranges of parameters. In addition, strangelets made of CFL strange matter obey a charge-mass relation of $Z/A \propto A^{-1/3}$, which differs significantly from the charge-mass relation of strangelets made of ordinary strange quark matter. In the latter case, Z/A would be constant for small baryon numbers A and $Z/A \propto A^{-2/3}$ for large A.[55,56,57] This difference may allow an experimental test of CFL locking in strange quark matter.[55]

5. Quark Deconfinement in Rotating Neutron Stars

Whether or not quark deconfinement occurs in neutron stars makes only very little difference to their static properties, such as the range of possible masses and radii, which renders the detection of quark matter in such objects extremely complicated. This turns out to be strikingly different for rotating neutron stars (i.e. pulsars) which develop quark matter cores in the course of spin-down. The reason being that as such stars spin down, because of the emission of magnetic dipole radiation and a wind of electron-

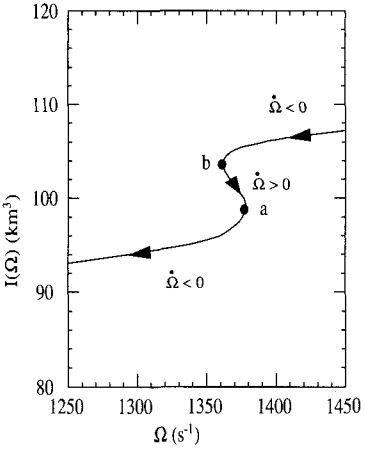

Figure 3. Moment of inertia, I, versus frequency. The generation of quark matter causes a backbending of I for frequencies between a and b [9,58].

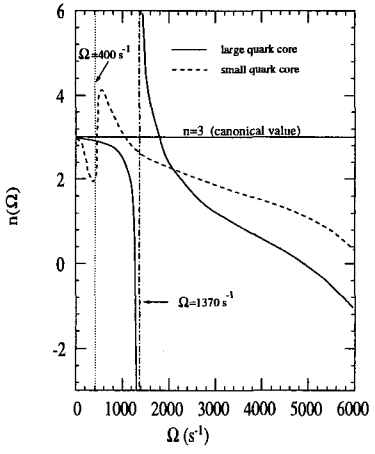

Figure 4. Anomaly in braking index, n, of a rotating neutron star caused by generation of quark matter.

positron pairs, they become more and more compressed. For some rotating neutron stars the mass and initial rotational frequency may be just such that the central density rises from below to above the critical density for dissolution of baryons into their quark constituents. This effects the star's moment of inertia dramatically,[58] as shown in Figure 3. Depending on the ratio at which quark and normal matter change with frequency, the moment of inertia can decrease very anomalously, and could even introduce an era of stellar spin-up lasting for $\sim 10^8$ years.[58] Since the dipole age of millisecond pulsars is about 10^9 years, one may estimate that roughly about 10% of the ~ 25 solitary millisecond pulsars presently known could be in the quark transition epoch and thus could be signaling the ongoing process of quark deconfinement. Changes in the moment of inertia reflect themselves in the braking index, n, of a rotating neutron star, as can be seen from ($I' \equiv \mathrm{d}I/\mathrm{d}\Omega$, $I'' \equiv \mathrm{d}^2I/\mathrm{d}\Omega^2$)

$$n(\Omega) \equiv \frac{\Omega\,\ddot{\Omega}}{\dot{\Omega}^2} = 3 - \frac{3\,I'\,\Omega + I''\,\Omega^2}{2\,I + I'\,\Omega}\,. \tag{17}$$

The right-hand-side of this expression reduces to the well-known canonical constant $n = 3$ if I is independent of frequency. Evidently, this is not the case for rapidly rotating neutron stars, and it fails completely for stars that experience pronounced internal changes (phase transitions) which alter the

moment of inertia significantly. Figure 4 illustrates this for the moment of inertia of the neutron star of Fig. 3. Because of the changes in I, caused by the gradual transition of hadronic matter into quark matter, the braking index deviates dramatically from 3 at the transition frequency, when pure quark matter is generated. Such dramatic anomalies in $n(\Omega)$ are not known for conventional neutron stars, because their moments of inertia appear to vary smoothly with Ω.[9] The future astrophysical observation of such anomalies in the braking behavior of pulsars may thus be interpreted as a signal for quark deconfinement in neutron stars.

Accreting x-ray neutron stars provide a very interesting contrast to the spin-down of isolated neutron stars discussed just above. These x-ray neutron stars are being spun up by the accretion of matter from a lower-mass ($M \lesssim 0.4 M_\odot$), less-dense companion. If the critical deconfinement density falls within that of canonical pulsars, quark matter will already exist in them but will be spun out of x-ray stars as their frequency increases during accretion. This scenario has been modeled in Refs. 42 and 59, and is discussed by Glendenning elsewhere in this volume.

6. Absolutely Stable Strange Quark Matter

As pointed out in Refs. 60, 61, 62, for a collection of more than a few hundred up, down, and strange quarks the energy of strange quark matter may be just as well below the energy of nuclear matter, $E/A = 930$ MeV. A simple estimate indicates that for strange quark matter $E/A = 4B\pi^2/\mu^3$, so that bag constants of $B = 57$ MeV/fm^3 (i.e. $B^{1/4} = 145$ MeV) and $B = 85$ MeV/fm^3 ($B^{1/4} = 160$ MeV) would place the energy per baryon of such matter at $E/A = 829$ MeV and 915 MeV, respectively, which correspond to strange quark matter which is absolutely bound with respect to nuclear matter.[63,64,65] If this were indeed the case, neutron star matter would be metastable with respect to strange quark matter, and all neutron stars should in fact be strange quark stars.[63,64,65] As briefly described in Sect. 4.6, strange quark matter is expected to be a color superconductor which, at extremely high densities, should be in the CFL phase. This phase is rigorously electrically neutral with no electrons required.[46] For sufficiently large strange quark masses, however, the low density regime of strange quark matter is rather expected to form a 2SC phase (or possibly other phases) in which electrons are present.[38,39] The presence of electrons causes the formation of an electric dipole layer on the surface of strange matter, which enables strange quark matter stars to carry crusts made of ordinary

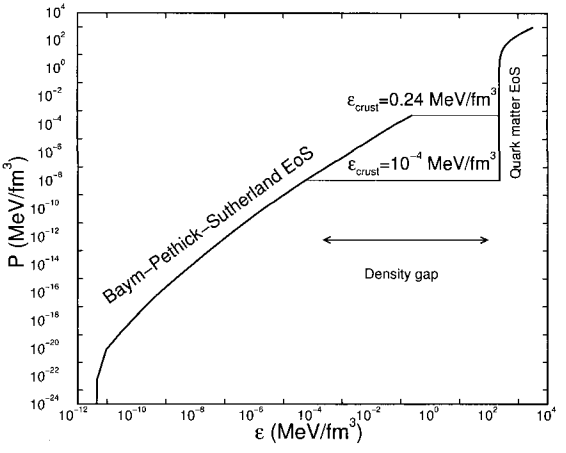

Figure 5. EoS of strange quark matter surrounded by nuclear matter. The maximal possible nuclear matter density is determined by neutron drip which occurs at $\epsilon_{\rm crust} = 0.24$ MeV/fm^3 (4.3×10^{11} g/cm^3). Any nuclear density that is smaller than that is possible. As an example, we show the EoS for a sample density of $\epsilon_{\rm crust} = 10^{-4}$ MeV/fm^3 (10^8 g/cm^3) too.

nuclear matter.[66,67,68] The maximal possible density at the base of the crust (inner crust density) is determined by neutron drip, which occurs at about 4×10^{11} g/cm^3. This somewhat complicated situation of the structure of strange matter enveloped in a (chemically equilibrated) nuclear crust can be represented by a proper choice for the EoS shown in Fig. 5.[69] The EoS is characterized by a discontinuity in density between strange quark matter and nuclear crust matter across the electric dipole gap where the pressure of the nuclear crust at its base equals the pressure of strange matter at its surface.[9,69]

Since the nuclear crust surrounding a strange star would be bound to the star by gravity rather than confinement, the mass-radius relationship of a strange matter star with a nuclear would be qualitatively similar to the one of purely gravitationally bound stars, that is neutron stars and white dwarfs, as illustrated in Fig. 2. The fact that strange stars with crusts tend to possess somewhat smaller radii than neutron stars leads to smaller mass shedding (Kepler) periods $P_{\rm K}$ for strange stars. This is obvious from the classical mass shedding expression $P_{\rm K} = 2\pi\sqrt{R^3/M}$ and has its correspondence in the full general relativistic case.[9] In more qualitative terms, it is found that, due to the smaller radii of strange stars, the com-

plete sequence of such objects and not just those close to the mass peak as is the case for neutron stars, can sustain extremely rapid rotation.[70] In particular, strange stars of a canonical pulsar mass around $1.45\,M_\odot$ have Kepler periods in the range of 0.55 msec $\lesssim P_K \lesssim$ 0.8 msec, depending on the thickness of the nuclear curst and the bag constant.[69,70] This range is to be compared with $P_K \sim 1$ msec obtained for standard (i.e., no phase transition) neutron stars of the same mass. Phase transitions in neutron stars, however, however, may lower this value down to Kepler periods typical of strange stars.[71]

As a last issue, I would like to mention the possible existence of a new class of white dwarfs–so called strange dwarfs–which could hide strange matter cores in their centers.[72] Until recently, only rather vague tests of the theoretical mass-radius relation of white dwarfs have been possible. This has changed because of the availability of new data emerging from the Hipparcos project.[73] These data allow the first accurate measurements of white dwarf distances and, as a result, establishing the mass-radius relation of such objects empirically.

References

1. W. D. Myers and W. J. Swiatecki, Ann. Phys. (N. Y.) **204** (1990) 401.
2. W. D. Myers and W. J. Swiatecki, Ann. Phys. (N. Y.) **211** (1991) 292.
3. W. D. Myers and W. J. Swiatecki, Nucl. Phys. **A601** (1996) 141.
4. K. Strobel, F. Weber, M. K. Weigel, and Ch. Schaab, Int. J. Mod. Phys. E **6**, No. 4 (1997) 669.
5. V. R. Pandharipande and R. B. Wiringa, Rev. Mod. Phys. **51** (1979) 821.
6. R. B. Wiringa, V. Fiks, and A. Fabrocini, Phys. Rev. C **38** (1988) 1010.
7. A. Akmal, V. R. Pandharipande, and D. G. Ravenhall, Phys. Rev. C **58** (1998) 1804.
8. H. Heiselberg and V. Pandharipande, Ann. Rev. Nucl. Part. Sci. **50** (2000) 481.
9. F. Weber, *Pulsars as Astrophysical Laboratories for Nuclear and Particle Physics* (IOP Publishing, Bristol, Great Britain, 1999).
10. S. Pal, M. Hanauske, I. Zakout, H. Stöcker, and W. Greiner, Phys. Rev. C **60** (1999) 015802.
11. K. Oyamatsu and K. Iida, Prog. Theor. Phys. **109** (2003) 631.
12. O. Barziv, L. Kaper, M. H. van Kerkwijk, J. H. Telting, and J. van Paradijs, A&A **377** (2001) 925.
13. J. A. Orosz and E. Kuulkers, Mon. Not. R. Astron. Soc. **305** (1999) 132.
14. J. H. Taylor and J. M. Weisberg, Astrophys. J. **345** (1989) 434.
15. N. K. Glendenning, Astrophys. J. **293** (1985) 470.
16. M. Prakash, I. Bombaci, M. Prakash, P. J. Ellis, J. M. Lattimer, and R. Knorren, Phys. Rep. **280** (1997) 1.

17. G. Baym, *Neutron Stars and the Physics of Matter at High Density*, in: Nuclear Physics with Heavy Ions and Mesons, Vol. 2, Les Houches, Session XXX, ed. by R. Balian, M. Rho and G. Ripka (North-Holland, Amsterdam, 1978) p. 745.
18. D. Kaplan and A. Nelson, Phys. Lett. **175B** (1986) 57.
19. G. E. Brown, K. Kubodera, and M. Rho, Phys. Lett. **192B** (1987) 273.
20. C.-H. Lee and M. Rho, *Kaon condensation in dense stellar matter*, Proc. of the International Symposium on Strangness and Quark Matter", ed. by G. Vassiliadis, A. Panagiotou, B. S. Kumar, and J. Madsen (World Scientific, Singapore, 1995) p. 283.
21. S.-O. Bäckman and W. Weise, *Pion condensation and the pion-nuclear interaction*, in: Mesons in Nuclei, Vol. III, ed. by M. Rho and D. Wilkinson (North-Holland, Amsterdam, 1979) p. 1095.
22. S. Barshay and G. E. Brown, Phys. Lett. **47B** (1973) 107.
23. G. E. Brown, K. Kubodera, D. Page, and P. Pizzochero, Phys. Rev. D **37** (1988) 2042.
24. T. Tatsumi and T. Muto, in: Nuclei in the Cosmos, ed. by H. Oberhummer and C. Rolfs (Springer-Verlag, Berlin, 1991).
25. H. Umeda, K. Nomoto, S. Tsuruta, T. Muto, and T. Tatsumi, *Neutron Star Cooling and Pion Condensation*, in: The Structure and Evolution of Neutron Stars, ed. by D. Pines, R. Tamagaki, and S. Tsuruta (Addison-Wesley, New York, 1992) p. 406.
26. Ch. Schaab, F. Weber, M. K. Weigel, and N. K. Glendenning, Nucl. Phys. **A605** (1996) 531.
27. R. Barth et al., Phys. Rev. Lett. **78** (1997) 4027.
28. G. Q. Li, C.-H. Lee, and G. E. Brown, Nucl. Phys. **A625** (1997) 372.
29. G. Q. Li, C.-H. Lee, and G. E. Brown, Phys. Rev. Lett. **79** (1997) 5214.
30. G. E. Brown, *Supernova Explosions, Black Holes and Nucleon Stars*, in: Proceedings of the Nuclear Physics Conference – INPC '95, ed. by S. Zuxun and X. Jincheng (World Scientific, Singapore, 1996) p. 623.
31. G. E. Brown, Phys. Bl. **53** (1997) 671.
32. R. L. Jaffe, Phys. Lett. **38** (1977) 195.
33. N. K. Glendenning and J. Schaffner-Bielich, Phys. Rev. C **58** (1998) 1298.
34. R. Tamagaki, Prog. Theor. Phys. **85** (1991) 321.
35. T. Sakai, J. Mori, A. J. Buchmann, K. Shimizu, and K. Yazaki, Nucl. Phys. **A625** (1997) 192.
36. A. Faessler, A. J. Buchmann, M. I. Krivoruchenko, and B. V. Martemyanov, Phys. Lett. **391B** (1997) 255.
37. A. Faessler, A. J. Buchmann, and M. I. Krivoruchenko, Phys. Rev. C **56** (1997) 1576.
38. M. Alford, Ann. Rev. Nucl. Part. Sci. **51** (2001) 131.
39. K. Rajagopal and F. Wilczek, *The Condensed Matter Physics of QCD*, At the Frontier of Particle Physics / Handbook of QCD, ed. M. Shifman, (World Scientific) (2001).
40. N. K. Glendenning, Phys. Rev. D **46** (1992) 1274.
41. F. Weber, J. Phys. G: Nucl. Part. Phys. **25** (1999) R195.

42. N. K. Glendenning and F. Weber, Lecture Notes in Physics **578**, (Springer-Verlag, Berlin, 2001), p. 305.
43. *Compact Stars in the QCD Phase Diagram*, Proc. of the Int. Conf., ed. R. Ouyed and F. Sannino, eConf C010815 (ISBN 87-7834-507-3).
44. M. Alford, K. Rajagopal, and F. Wilczek, Phys. Lett. **422B** (1998) 247.
45. R. Rapp, T. Schäfer, E. V. Shuryak, and M. Velkovsky, Phys. Rev. Lett. **81** (1998) 53.
46. K. Rajagopal and F. Wilczek, Phys. Rev. Lett. **86** (2001) 3492.
47. P. F. Bedaque and T. Schäfer, Nucl. Phys. **A697** (2002) 802.
48. T. Schäfer, Phys. Rev. D **62** (2000) 094007.
49. K. Rajagopal, Acta Physica Polonica B **31** (2000) 3021.
50. M. Alford, J. Bowers, and K. Rajagopal, Phys. Rev. D **63** (2001) 074016.
51. M. Alford, J. A. Bowers, and K. Rajagopal, J. Phys. G **27** (2001) 541.
52. D. Blaschke, D. M. Sedrakian, and K. M. Shahabasyan, A&A **350** (1999) L47.
53. The AMS home page is `http://ams.cern.ch`.
54. Information about ECCO can be found at `http://ultraman.berkeley.edu`.
55. J. Madsen, Phys. Rev. Lett. **87** (2001) 172003.
56. *Strange Quark Matter in Physics and Astrophysics*, Proc. of the International Workshop, ed. by J. Madsen and P. Haensel, Nucl. Phys. B (Proc. Suppl.) **24B** (1991).
57. J. Madsen, Lecture Notes in Physics **516** (1999) 162.
58. N. K. Glendenning, S. Pei, and F. Weber, Phys. Rev. Lett. **79** (1997) 1603.
59. N. K. Glendenning and F. Weber, Astrophys. J. **559** (2001) L119.
60. A. R. Bodmer, Phys. Rev. D **4** (1971) 1601.
61. E. Witten, Phys. Rev. D **30** (1984) 272.
62. H. Terazawa, INS-Report-338 (INS, Univ. of Tokyo, 1979); J. Phys. Soc. Japan, **58** (1989) 3555; **58** (1989) 4388; **59** (1990) 1199.
63. J. Madsen, Phys. Rev. Lett. **61** (1988) 2909.
64. J. Madsen, *Physics and Astrophysics of Strange Quark Matter*, Proc. of the 2nd International Conference on Physics and Astrophysics of Quark-Gluon Plasma, ed. by B. Sinha, Y. P. Viyogi, and S. Raha (World Scientific, Singapore, 1994) p. 186.
65. J. Madsen, AIP Conference Proc. 412, Big Sky, Montana, 1997, ed. by T. W. Donnelly (American Institute of Physics, New York, 1997) p. 999.
66. Ch. Kettner, F. Weber, M. K. Weigel, and N. K. Glendenning, Phys. Rev. D **51** (1995) 1440.
67. C. Alcock, E. Farhi, and A. V. Olinto, Astrophys. J. **310** (1986) 261.
68. C. Alcock and A. V. Olinto, Ann. Rev. Nucl. Part. Sci. **38** (1988) 161.
69. N. K. Glendenning and F. Weber, Astrophys. J. **400** (1992) 647.
70. N. K. Glendenning, Ch. Kettner, and F. Weber, Astrophys. J. **450** (1995) 253.
71. G. F. Burgio, H.-J. Schulze, and F. Weber, A&A **408** (2003) 675.
72. N. K. Glendenning, Ch. Kettner, and F. Weber, Phys. Rev. Lett. **74** (1995) 3519.
73. J. L. Provencal, H. L. Shipman, E. Hog, and P. Thejll, Astrophys. J. **494** (1998) 759.

This page is intentionally left blank

Dense Matter

This page is intentionally left blank

ROLE OF STRANGE QUARK MASS IN PAIRING PHENOMENA IN QCD*

HIROAKI ABUKI

Yukawa Institute for Theoretical Physics,
Kyoto University, Kyoto 606-8502, Japan
E-mail: abuki@yukawa.kyoto-u.ac.jp

We study the dynamical effect of strange quark mass as well as kinematical one on the color-flavor unlocking transition using a NJL model. Paying a special attention to the multiplicity of gap parameters, we derive an exact formula of the effective potential for 5-gap parameters. Based on this, we discuss that the unlocking transition might be of second order rather than of first order as is predicted by a simple kinematical criterion for the unlocking.

1. Introduction

The dynamics which quark-gluon matter exhibits under high baryon density is one of the most challenging and exciting problems in QCD [2,3,4]. A number of literatures have revealed the realization of the color-flavor locked (CFL) type of the pairing order [5] for sufficiently large quark number chemical potential [4,6,7,8]. In contrast to this solid fact, however, the phases for large, and realistic value of M_s^2/μ are still veiled in mystery, and so many phases and the associated phase transitions have been studied so far [9,10,11,12,13,14,15]. The unlocking transition from the CFL phase to the 2SC state is simplest one of the examples. This transition with increasing the value of M_s^2/μ is firstly investigated using Nambu–Jona-Lasinio (NJL) type effective models [9,10]. Their results show that the 1st order unlocking transition takes place at some critical M_s^c, and a simple kinematical picture for the critical mass works in quite satisfactory way. This criterion is based on the conjecture that the transition occurs when the mismatch of the Fermi momenta of light and strange quark becomes as large as the magnitude of

*Talk given at KIAS-APCTP Internatinal Symposium on Astro-Hadron Physics "*Compact Stars: Quest For New States of Dense Matter*", November 10-14, 2003, KIAS, Seoul, Korea. This talk is based on Ref. 1.

the gap. In Ref. 9, the expansion in flavor breaking parameter M_s^2/μ is used to the construction of the fermionic dispersions and the effective potential. On the other hand, in Ref. 10, the coupled gap equation is exactly solved with non-perturbative treatment of M_s. However, their construction of the effective potential is quite ambiguous and, as we shall show, possibly fails because of the multiplicity of gap parameters. Even though their results are in good accordance with each other, there still exist a possibility that the true solution is missed.

In this talk, we revisit the unlocking transition in more complete way than others [9,10], by making a proper use of the Pauli construction of the effective potential. In particular, we study how the CFL state and other states are realized in the multi-gap parameter space and how the potential gets distorted with increasing the value of M_s^2/μ. More complete analyses have been made in Ref. 1.

2. Coupled Gap Equation and Effective Potential

In this section, we present an outline for obtaining the gap equations and the effective potential with which we can determine the ground state of the system characterized by (μ, T, M_s) parameter.

Self-energies. We first introduce the color-flavor mixed quark base: $q^\alpha = \sum_{a,i} \left(\lambda_\alpha/\sqrt{2}\right)_a^i q_i^a$, where $\lambda_\alpha (\alpha = 1 \sim 8)$ are the Gell-Mann matrices and we defined $(\lambda^9)_i^a = \sqrt{\frac{2}{3}}\delta_i^a$. Then the Nambu-Gor'kov propagator in the 2-compnent quark field $Q = (q, \bar{q}^t)$ is written as

$$\boldsymbol{S}(q_0, \boldsymbol{q}) \equiv i\,\mathrm{F.T.}\langle T\{Q(x)\bar{Q}(0)\}\rangle = \begin{pmatrix} \not{q} + \not{\mu} - M & \Sigma(q_0, \boldsymbol{q}) \\ \gamma_0 \Sigma(q_0, \boldsymbol{q})^\dagger \gamma_0 & \not{q}^t - \not{\mu}^t + M \end{pmatrix}^{-1}. \quad (1)$$

$\Sigma(q_0, \boldsymbol{q})$ is off-diagonal self-energy which gives rise to gaps in the quasi-quark dispersion. M is the quark mass matrix in the color-flavor mixed base $M_{\alpha\beta} = \mathrm{tr}\left[\lambda_\alpha \hat{m} \lambda_\beta\right]/2$, where $\hat{m} = \mathrm{diag.}(0, 0, M_s)$ is mass matrix in flavor space. The pure CFL ansatz for the off-diagonal self-energy is expressed in the color-flavor mixed base as following,

$$\Sigma_{\alpha\beta}^{\mathrm{CFL}}(q_0, \boldsymbol{q}) = C\gamma_5 \otimes \begin{pmatrix} \Delta_8 \mathbf{1}_8 & \\ & \Delta_1 \end{pmatrix}. \quad (2)$$

Here, C is the charge conjugation matrix $C = i\gamma_2\gamma_0$. $C\gamma_5$ guarantees that the pairing takes place in the $J^P = 0^+$ channel. On the other hand, we would have the 2SC state with u-d pairing $\Sigma^{2\mathrm{SC}_{ud}} = -\epsilon_{ij}\epsilon^{ab3}\Delta_{2\mathrm{SC}} =$

$\Delta_A \epsilon_{ij}\epsilon^{ab3}$ for sufficiently large value of M_s, which is written as

$$\Sigma_{\alpha\beta}^{2\mathrm{SC}_{ud}}(q_0,\boldsymbol{q}) = C\gamma_5 \otimes \begin{pmatrix} \Delta_{2\mathrm{SC}}\mathbf{1}_3 & & \\ & \mathbf{0}_4 & \\ & & \begin{matrix} -\frac{1}{3}\Delta_{2\mathrm{SC}} & -\frac{\sqrt{2}}{3}\Delta_{2\mathrm{SC}} \\ -\frac{\sqrt{2}}{3}\Delta_{2\mathrm{SC}} & -\frac{2}{3}\Delta_{2\mathrm{SC}} \end{matrix} \end{pmatrix}, \tag{3}$$

in the color-flavor mixed base. From the two expressions for the 2SC and CFL phases, it is quite natural to expect the distorted CFL state (dCFL), the minimal interpolating pairing ansatz between those phases, for the small but finite strange quark mass [9,10],

$$\Sigma_{\alpha\beta}^{d\mathrm{CFL}}(q_0,\boldsymbol{q}) \overset{M_s \le M_s^c}{=} C\gamma_5 \otimes \begin{pmatrix} \Delta_{83}\mathbf{1}_3 & & \\ & \Delta_{82}\mathbf{1}_4 & \\ & & \begin{matrix} \Delta_{81} & \Delta \\ \Delta & \Delta_{11} \end{matrix} \end{pmatrix}. \tag{4}$$

In this parameterization, the $SU(3)_{C+V}$ symmetric CFL phase and $SU(2)_C \times SU(2)_L \times SU(2)_R$ symmetric 2SC phase are expressed only as different limits of the dCFL phase which is invariant under color flavor simultaneous rotation $SU(2)_{C+V}$. By introducing the 5-dimensional vector $\vec{\Delta} = (\Delta_{83}, \Delta_{82}, \Delta_{81}, \Delta, \Delta_{11})^t$, we can express the model space for the pure CFL state as $\vec{\Delta}_{\mathrm{CFL}} = (\Delta_8, \Delta_8, \Delta_8, 0, \Delta_1)^t$, which spans a 2-dimensional planer section, while the 2SC phase as the 1-parameter vector $\vec{\Delta}_{2\mathrm{SC}} = (\Delta_{2\mathrm{SC}}, 0, -\Delta_{2\mathrm{SC}}/3, -\sqrt{2}\Delta_{2\mathrm{SC}}/3, -2\Delta_{2\mathrm{SC}}/3)^t$.

Gap equations. The anomalous propagator is defined by the off-diagonal element of the Nambu-Gor'kov propagator, which takes the following form for our ansatz Eq. (4),

$$S_{12}^{\alpha\beta}(q) = i\mathrm{F.T.}\langle q^\alpha(x) q^\beta(0)\rangle = \gamma_5 C \otimes \begin{pmatrix} R_{83}\mathbf{1}_3 & & \\ & R_{82}\mathbf{1}_4 & \\ & & \begin{matrix} R_{81} & R \\ R & R_{11} \end{matrix} \end{pmatrix}. \tag{5}$$

$\{R_{83}, R_{82}, R_{81}, R, R_{11}\}$ are propagatores, which are complicated functions of $(q, \vec{\Delta}, \mu, M_s)$ [1]. The gap equation is obtained by using Feynman rule for the self consistency between proposed self-energy and the one-loop self-energy. In the case of NJL model with interaction vertex for one-gluon exchange, $\mathcal{L}_{\mathrm{int}} = (1/2)g^2\bar{q}\gamma_\mu t^a q \bar{q}\gamma^\mu t^a q$, we obtain

$$\Sigma_{\alpha\beta} = i4g^2 \int \frac{d^4q}{(2\pi)^4} (T^a)_{\gamma\alpha} S_{12}^{\gamma\delta}(q) (T^a)_{\delta\beta}. \tag{6}$$

Here, the bare vertex in the color-flavor mixed base is defined by $(T^a)_{\alpha\beta} = \mathrm{tr}\left[\lambda_\alpha \lambda_a \lambda_\beta\right]/4$. This integral matrix equation contains the following set of five equations.

$$\Delta_{83} = g^2 \frac{1}{12}\left(5\mathcal{R}_{83} - \mathcal{R}_{81} - 2\sqrt{2}\mathcal{R} - 2\mathcal{R}_{11}\right) \equiv g^2 K_{83}[\vec{\Delta}], \tag{7}$$

$$\Delta_{82} = g^2 \frac{1}{12}\left(2\mathcal{R}_{82} + 2\mathcal{R}_{81} + \sqrt{2}\mathcal{R} - 2\mathcal{R}_{11}\right) \equiv g^2 K_{82}[\vec{\Delta}], \tag{8}$$

$$\Delta_{81} = g^2 \frac{1}{12}\left(-3\mathcal{R}_{83} + 8\mathcal{R}_{82} - \mathcal{R}_{81} + 2\sqrt{2}\mathcal{R} - 2\mathcal{R}_{11}\right) \equiv g^2 K_{81}[\vec{\Delta}], \tag{9}$$

$$\Delta = g^2 \frac{\sqrt{2}}{12}\left(-3\mathcal{R}_{83} + 2\mathcal{R}_{82} + \mathcal{R}_{81} - \sqrt{2}\mathcal{R}\right) \equiv g^2 K[\vec{\Delta}], \tag{10}$$

$$\Delta_{11} = g^2 \frac{1}{6}\left(-3\mathcal{R}_{83} - 4\mathcal{R}_{82} - \mathcal{R}_{81}\right) \equiv g^2 K_{11}[\vec{\Delta}]. \tag{11}$$

Here, we have defined $\mathcal{R}$ by

$$\mathcal{R}_i(\vec{\Delta}; M_s) = i \int \frac{d^4q}{(2\pi)^4} \frac{1}{4} \mathrm{tr}\left[C\gamma_5 R_i(q; \vec{\Delta}, M_s)\right]. \tag{12}$$

Effective potential for multi-gap parameters. Here, we do not attempt to formulate the Pauli-construction of the effective potential, which is exactly done in Ref. 1. But instead, we illustrate how we would miss the true effective potential due to the multiplicity of gap parameters when it is constructed by the integration of the gap equation, and only show the correct procedure to obtain true one.

We might think that the derivative of the effective potential is

$$\frac{\partial \Omega_{\mathrm{eff}}}{\partial \Delta_i} \propto (\text{gap equation for } \Delta_i). \tag{13}$$

If so, the effective potential is constructed by

$$\Omega_{\mathrm{eff}}\left[\vec{\Delta}\right] \propto \sum_i \frac{\Delta_i^2}{2g^2} - \sum_i \int_0^1 dt \Delta_i K_i[t\vec{\Delta}]. \tag{14}$$

But this gives a false formula in the case that the many gap parameters exist and couple each other by different couplings.

Actually, the derivative of the effective potential coincides with some linear combination of the gap equation like

$$g^2 D_{ij}^{-1} \frac{\partial \Omega_{\mathrm{eff}}}{\partial \Delta_j} = A_{ij}(\Delta_j - g^2 K_j[\vec{\Delta}]), \tag{15}$$

where the diagonal matrix $D = \mathrm{diag.}(3, 4, 1, 2, 1)$ represents the degeneracies of the gap parameters, and the matrix A is relating the gap parameters $\vec{\Delta} = (\Delta_{83}, \Delta_{82}, \Delta_{81}, \Delta, \Delta_{11})$ and the corresponding condensates

$\vec{\phi} = (\phi_{83}, \phi_{82}, \phi_{81}, \phi, \phi_{11})$ as $4g^2\vec{\phi} = \hat{A}\vec{\Delta}$. For the detail of the definition $\vec{\phi}$ and the form of the matrix A, see Ref. 1. We can obtain the true formula for the effective potential as

$$\Omega_{\rm eff}[\vec{\Delta}] = \sum_{i,j} \frac{(DA)_{ij}}{2g^2}\Delta_i\Delta_j - \sum_{ij}\int_0^1 dt(DA)_{ij}\Delta_i K_j[t\vec{\Delta}]. \qquad (16)$$

Note that DA is real-valued symmetric matrix, whose eigenvalues are all real.

3. Numerical Results

Here, we present our numerical results. The cutoff parameter is set to $\Lambda = 800$MeV, and the coupling parameter g^2 is tuned to reproduce 400MeV for the constituent mass of quark at zero chemical potential [10].

3.1. *Solution of gap equation*

We display the solution of the coupled gap equation Eqs. (7)$\sim$(11). In FIG. 1(a), we show the eigenvalues of the original gap matrix Eq. (4) as functions of M_s. $(\Delta_{83}, \Delta_{82})$ are the gaps for iso-triplet and doublet modes. (χ_1, χ_2) are the eigenvalues of the iso-singlet mixing sector. According to the values of these parameters, the states are distinguished by

Gap parameters	Global Symmetry	States
$\Delta_{83} = \Delta_{82} = \chi_2$, $\chi_1 \neq 0$	$SU(3)_V$	CFL for $M_s = 0$
$\Delta_{83} = \chi_1$, $\Delta_{82} = \chi_2 = 0$	$SU(2)_L \times SU(2)_R$	2SC for $M_s > M_s^c$
otherwise	$SU(2)_V$	distorted CFL (dCFL)

It is surprising that the system seems to undergo continuous transition from the CFL to the 2SC, and actually stays in the distorted CFL (dCFL) phase even for $M_s > \mu = 400$ MeV. We will see later that even in our case, the 2SC is always a solution of the gap equation, but with higher energy than the CFL state. In FIG. 1(b), we display in FIG. 1, the gaps $(\Delta_{83}, \Delta_{82}, \chi_1, \chi_2)$ for $M_s = 250$ MeV as functions of temperature. We see that as the temperature is raised, the dCFL phase encounters the continuous transition to the 2SC state at $T = 35$MeV, and eventually the system undergoes 2nd order phase transition to the normal fermi-liquid at $T = 60$MeV.

3.2. *Effective potential for multi-gap parameter space*

We now study how these states are realized in the multi-gap parameter space by computing the effective potential with help of the formula Eq. (16).

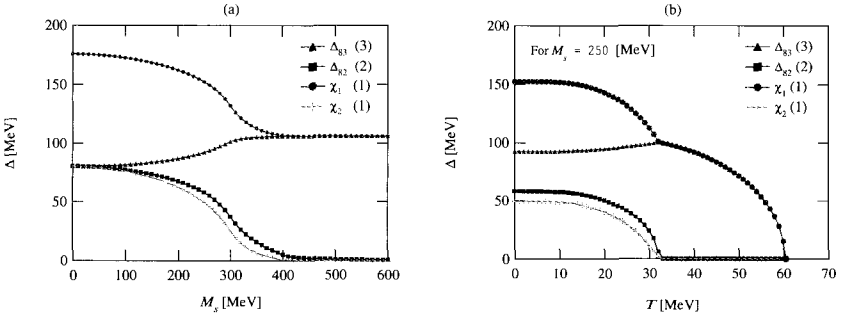

Figure 1. (a) Gaps are plotted as functions of M_s. (b) The temperature dependence of the gaps for $M_s = 250$ MeV.

Let us first introduce the vector

$$\vec{\Delta}(i,j) = \frac{(i-10)\vec{\Delta}_{\rm CFL} + (j-10)\vec{\Delta}_{\rm 2SC}}{50}, \tag{17}$$

with the CFL gap vector $\vec{\Delta}_{\rm CFL} = (80, 80, 80, 80, -175)$ and the 2SC gap vector $\vec{\Delta}_{\rm 2SC} = (106, 0, -35, -50, -70)$ for $Ms = 0$ (in the chiral limit). Eq. (17) define 2-dimensional planer section in the 5-dimensional gap parameter space, which includes the simple Fermi gas $(10, 10)$ with $\vec{\Delta} = \vec{\mathbf{0}}$, the CFL $(60, 10)$ and the 2SC $(10, 60)$. In FIG. 2, we show the contour plot of the effective potential $\Omega_{\rm eff}[\vec{\Delta}(i,j); M_s]$, for $M_s = 0$ MeV (a), 200 MeV (b), 300 MeV (c) and 400 MeV (d). We can see that the CFL state $(60, 10)$ looks the global minimum in this 2-parameter space (i, j) for $M_s = 0$ MeV. On the other hand, the 2SC state $(10, 60)$ is realized as a saddle point which is stable in the direction of the simple Fermi gas $(10, 10)$, but is unstable in the direction towards the CFL state $(60, 10)$. As the strange quark mass is increased to 200 MeV, the CFL minimum moves towards the 2SC point, and its condensation energy gets reduced, while the position and the energy of the 2SC state is unaffected by M_s. This minimum point $(55, 20)$ is expected to be located close to the distorted CFL dCFL state in the full 5-parameter space. The dCFL state gets distorted significantly towards the 2SC state at $M_s = 300$ MeV (FIG. 2(c)), and seems absorbed into the 2SC as the strange quark mass approaches the order of the chemical potential $\sim \mu$ of the system. We can conclude that the unlocking transition is not of 1st order. More detailed analyses made in Ref. 1 reveals that this transition is of 2nd order and indicates that the dCFL satate at low strange quark density is the Bose-Einstein condensation of tightly bound pairs rather than

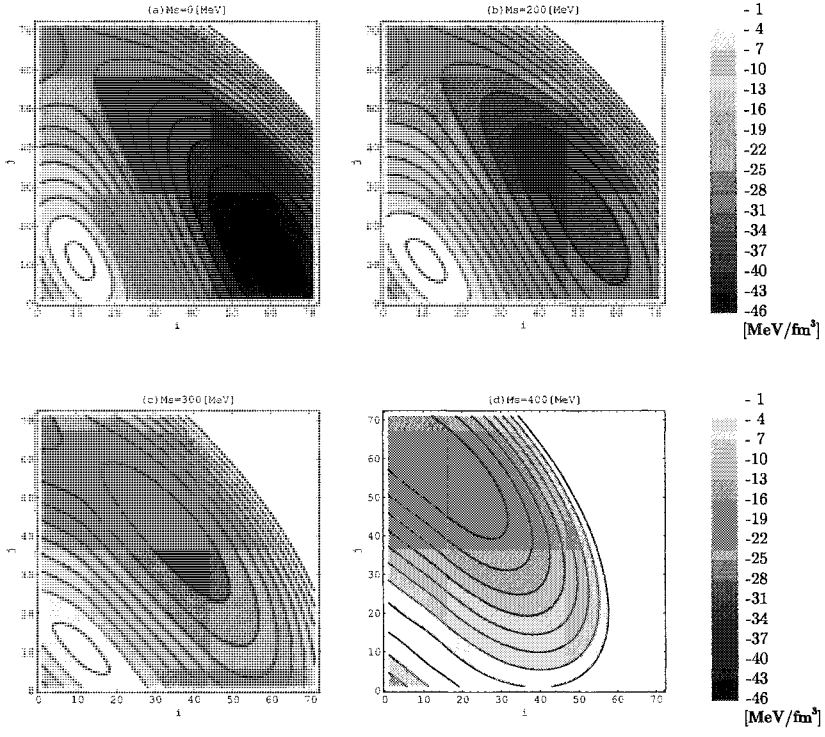

Figure 2. Contour plot of the effective potential $\Omega_{\rm eff}[\Delta(i,j)]$ where $\Delta(i,j)$ is defined by Eq. (17), for $M_s = 0$ MeV (a), $M_s = 200$ MeV (b), $M_s = 300$ MeV (c), and for $M_s = 400$ MeV (d).

the BCS state [16].

2SC as a solution of gap equation. What should be stressed here is that the 2SC stays at least a saddle point in the full model space irrespective of the value of M_s. This means that the 2SC is always a solution of the gap equation, and if we had missed in obtaining the correct effective potential, then we misunderstood it as the true ground state instead of the dCFL state for intermediate strange quark mass M_s.

Unstable CFL state? In FIG. 3(a), we plot the section of the effective potential surface FIG. 2(a) on the line linking the 2SC $(10, 60)$ $\vec{\Delta}_{t=0} = \vec{\Delta}_{\rm 2SC}$ and the CFL $(60, 10)$ $\vec{\Delta}_{t=1} = \vec{\Delta}_{\rm CFL}$. Both states are determined by solving the gap equation in 5-gap parameter space for $M_s = 0$ MeV. Now we address

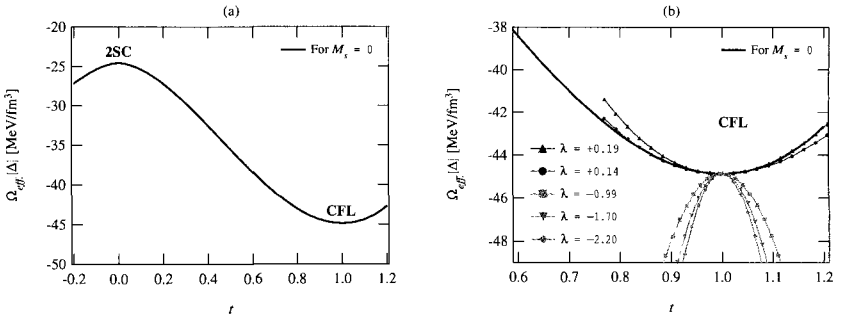

Figure 3. (a) The values of the effective potential on the 1-dimensional line connecting from the 2SC state $t = 0$ to the CFL state $t = 1$. (b) The bold line is just an enlargement of the potential curve for $M_s = 0$ in (a), and five set of the points (triangles, bold dots, squares, reflected triangles, lozenges) represent the potential curves in the directions of the eigenvectors belonging to the five eigenvalues $\lambda \cong (0.19, 0.14, -0.99, -1.70, -2.20)\mu^3$ of the Hessian curvature matrix at the CFL.

the question whether the CFL state is true global minimum even in the full model space or not. FIG. 3(b) shows us the answer for this question. Five potential curves are shown near the pure CFL for $M_s = 0$, each of which represents the potential curve in the direction of an eigenvector belonging to the corresponding eigenvalue λ of the Hessian curvature matrix at the CFL point $\frac{\partial^2\Omega}{\partial\Delta_i\partial\Delta_j}\Big|_{\vec{\Delta}=\vec{\Delta}_{\rm CFL}}$. What is surprising is that the CFL state is not the global minimum in the full model space. It is unstable in three out of five directions. These three directions correspond to the color-flavor sextet channels in which the interaction acts repulsive [1]. Also it should be noted that the color-flavor sextet gap parameters do not break any symmetry, thus are not the order parameter for the unlocking as is anticipated in their critical behaviour $\sim (1 - T/T_c)^{3/2}$ near critical temperature T_c in the chiral limit [17]. Anyway, because the effective potential becomes unbound once the sextet condensations are included, it makes no physical sense to include symmetric mean fields contribution [5,18,19] in the ansatz for the gap matrix. It is said that the sextet condensations are not induced within the mean field approximation, whereas those might be triggered by higher order fluctuation effects beyond the mean fields.

4. Conclusion

We have adopted the NJL model to study the phases of quark matter under high chemical potential. By making proper use of the Pauli-construction

method, we have derived the exact formula for the effective potential for multi-gap parameters. In particular, we have studied the unlocking phase transition from the CFL to the 2SC. We list main results below.

1. Second order phase transition. The unlocking transition is of continuous weak 2nd order. The 1st order unlocking never appear even at $T = 0$. This contradicts the simple kinematical picture for the color-flavor unlocking transition.

2. Toughness of the CFL state. The CFL state at $T = 0$ is much more robust against the increase of M_s than is predicted from the kinematical criterion, and the 2SC state is continuously connected from the dCFL state at the strange quark mass $M_s^c > \mu\,(\gg 2\sqrt{\mu\Delta_8(\mu, M_s = 0)})$.

3. The 2SC as a saddle point. 2SC state is always a saddle point, a solution of the gap equation, of the effective potential for any value of M_s, which is unstable in the direction towards the dCFL state, as well as three color-flavor sextet directions. The dCFL state, a solution of the gap equation with a larger condensation energy than the 2SC state approaches the 2SC saddle point as M_s approaches M_s^c.

4. Role of the sextet gap parameters. The dCFL state is also unstable in the directions for three color-flavor symmetric channels. This is attributed to the fact that the interaction is repulsive in these channels. We should not include the symmetric components of the gap parameter into our ansatz from the beginning, because no Cooper instability is present in these channels due to the absence of the attractive force. However, the effects of the sextet gaps on the anti-triplet sector are very small even if they are included. In this talk, we completely neglected the electric charge neutrality and also the color neutrality [20]. It would be interesting to include these effect into the gap equation, and to study how our dCFL phase is robust or fragile to be withdrawn by the neutrality condition. Also, we have ignored the usual chiral condensates in the vacuum. However, we have to include this effect to discuss the phase transitions in the lower chemical potential region. Studying phase transitions in this regime by improving our model along this line is also an interesting subject to be done in the future.

Acknowledgments

I am grateful to T. Kunihiro for stimulating discussions. I would also like to thank Deog-Ki Hong, Sung-Ah Cho and the other organizers and assistants for giving me an opportunity to give a talk at International Symposium on Astro-Hadron Physics and also for their hospitality during my stay at Seoul.

References

1. H. Abuki, arXiv:hep-ph/0401245.
2. D. Bailin and A. Love, Phys. Rep. **107**, 325 (1984),
3. M. Iwasaki and T. Iwado, Phys. Lett. B **350**, 163 (1995); M.G. Alford, K. Rajagopal and F. Wilczek, Phys. Lett. B **422**, 247 (1998); R. Rapp, T. Schäfer, E.V. Shuryak and M. Velkovsky, Phys. Rev. Lett. **81**, 53 (1998).
4. For reviews, see K. Rajagopal and F. Wilczek, arXiv:hep-ph/0011333; M.G. Alford, Ann. Rev. Nucl. Part. Sci. **51**, 131 (2001); T. Schäfer, arXiv:hep-ph/0304281; D.H. Rischke, arXiv:nucl-th/0305030.
5. M.G. Alford, K. Rajagopal and F. Wilczek, Nucl. Phys. B **537**, 443 (1999).
6. E. Shuster and D.T. Son, Nucl. Phys. B **573**, 434 (2000); B. Park, M. Rho, A. Wirzba and I. Zahed, Phys. Rev. D **62**, 034015 (2000).
7. T. Schäfer, Nucl. Phys. B **575**, 269 (2000).
8. S.D.H. Hsu, F. Sannino (Yale U.) and M. Schwetz (Boston U.), Mod. Phys. Lett. A **16** 1871, (2001).
9. T. Schäfer and F. Wilczek, Phys. Rev. D **60**, 074014 (1999).
10. M. Alford, J. Berges and K. Rajagopal, Nucl. Phys. B **558**, 219 (1999).
11. T. Schäfer, Phys. Rev. Lett. **85**, 5531 (2000);
12. M.G. Alford, J.A. Bowers and K. Rajagopal, Phys. Rev. D **63**, 074016 (2001).
13. I. Shovkovy and M. Huang, Phys. Lett. B **564**, 205 (2003); M. Huang and I. Shovkovy, arXiv:hep-ph/0307273.
14. E. Gubankova, W.V. Liu and F. Wilczek, Phys. Rev. Lett. **91**, 032001 (2003); M. Alford, C. Kouvaris and K. Rajagopal, arXiv:hep-ph/0311286.
15. K. Iida, T. Matsuura, M. Tachibana and T. Hatsuda, arXiv:hep-ph/0312363.
16. M. Matsuzaki, Phys. Rev. D **62**, 017501 (2000); H. Abuki, T. Hatsuda and K. Itakura, Phys. Rev. D **65**, 074014 (2002).
17. H. Abuki, Prog. Theor. Phys. **110**, 937 (2003).
18. I.A. Shovkovy and L.C.R. Wijewardhana, Phys. Lett. B **470**, 189 (1999).
19. R. Casalbuoni, R. Gatto, G. Nardulli and M. Ruggieri, Phys. Rev. D **68**, 034024 (2003).
20. K. Iida and G. Baym, Phys. Rev. D **63**, 074018 (2001). M. Alford and K. Rajagopal, JHEP **0206**, 031 (2002); A.W. Steiner, S. Reddy and M. Prakash, Phys. Rev. D **66**, 094007 (2002); F. Neumann, M. Buballa and M. Oertel, Nucl. Phys. A **714**, 481 (2003);

NUCLEAR MATTER AND THE TRANSITION TO QUARK MATTER IN AN EFFECTIVE QUARK THEORY

W. BENTZ AND T. HORIKAWA
Department of Physics, School of Science, Tokai University
Hiratsuka-shi, Kanagawa 259-1292, Japan

N. ISHII
The Institute of Physical and Chemical Research (RIKEN)
Hirosawa, Wako-shi, Saitama 351-0198, Japan

H. MINEO
Department of Physics, National Taiwan University
1 Roosevelt, Section 4, Taipei 10764, Taiwan
and
Institute of Physics, Academia Sinica
Taipei 11529, Taiwan

A. W. THOMAS
Special Research Center for the Subatomic Structure of Matter
and
Department of Physics and Mathematical Physics
The University of Adelaide
Adelaide, SA 5005, Australia

K. YAZAKI
Department of Physics, Tokyo Woman's Christian University
Suginami-ku, Tokyo 167-8585, Japan

We use an effective chiral quark theory to incorporate the nucleon structure into the description of nuclear matter, and use the resulting equation of state to discuss the EMC effect in nuclear matter. We also construct the equation of state for quark matter including the effect of color superconductivity, and describe the phase transition from nuclear matter to quark matter in the region of high baryon density.

1. Introduction

The question to what extent the properties of nuclear many body systems reflect the quark substructure of the single nucleon is an important research subject of intermediate energy hadronic physics. Directly related to this problem is the behavior of matter at high baryon densities, where one expects a phase transition to quark matter. In order to describe these phenomena reliably, one needs a theoretical framework which can account for not only for the quark substructure of the single nucleon, but also for (i) the properties of normal nuclear matter (NM), (ii) the medium modifications of nucleon properties, and (iii) the properties of high density quark matter (QM). It has been shown in recent works [1,2,3] that the Nambu-Jona-Lasinio (NJL) model [4] is a strong candidate for these purposes: Besides a covariant description of the nucleon as a quark-diquark bound state [5], it reproduces a saturating NM equation of state (EOS), the EMC effect in NM, and describes the transition to 2-flavor color superconducting QM. It is the purpose of this paper to discuss the most important results which we obtained in our studies of these three subjects.

The NJL model is characterized by a chiral symmetric contact interaction between quarks. Because of its simplicity, the relativistic Faddeev equation for the nucleon can be solved in the ladder approximation, taking into account the interactions in the scalar and axial vector diquark channels[5]. For our present investigations at finite density, however, we will restrict ourselves to the scalar diquark channel, and to a simple approximation to the Faddeev equation, where the momentum dependence of the quark exchange kernel is neglected[6]. The calculations presented in this paper are based on this "quark-diquark picture" of the single nucleon.

2. Description of nuclear matter

The effective (grand) potential for NM at zero temperature in the mean field approximation has the form [2]

$$V^{(NM)} = V_{\rm vac} + V_N + V_\omega \,, \tag{1}$$

where $V_{\rm vac}$ describes the polarization of the Dirac sea of quarks due to the presence of the valence nucleons, V_N arises from the Fermi motion of the valence nucleons depending on the nucleon mass $M_N(M)$, which is a solution of the quark-diquark bound state equation and depends on the constituent quark mass M, and V_ω is the contribution of the mean vector

field (V_0) acting on the quarks in NM. The conditions $\partial V^{(NM)}/\partial M = \partial V^{(NM)}/\partial V_0 = 0$ determine M and V_0 for fixed chemical potential μ.

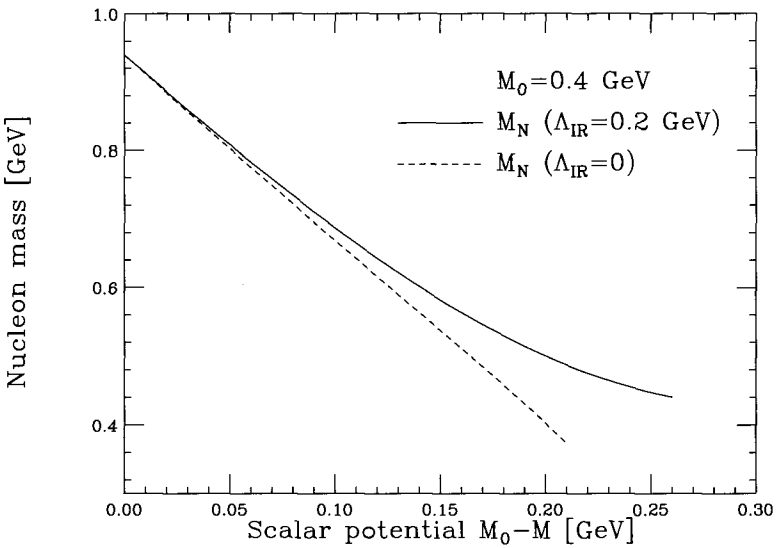

Figure 1. Nucleon mass as a function of the scalar potential for $\Lambda_{IR} = 0$ (dashed line) and $\Lambda_{IR} = 0.2$ GeV (solid line). M_0 is the constituent quark mass for zero density.

In effective meson-nucleon theories based on the linear realization of chiral symmetry, one often observes a collapse of the NM EOS because the σ mass decreases too rapidly as a function of the density [7]. It has been shown in Ref.[1], however, that the saturation properties of the NM EOS can be described if the quark structure of the nucleon is taken into account, provided that one eliminates the thresholds for the unphysical decay of the nucleon into quarks. This can be done, for example, in the proper time regularization scheme by introducing an infrared cut-off (Λ_{IR}) in addition to the ultraviolet one [8]. The elimination of the unphysical decay threshold then leads to a positive scalar polarizability [9] of the single nucleon, and this in turn gives rise to an effective $NN\sigma\sigma$ interaction which raises the σ meson mass and prevents the collapse.

These points are shown in Figs. 1 and 2. Fig. 1 shows the function $M_N(M)$, which is the solution of the quark-diquark bound state equation for the nucleon. For the case $\Lambda_{IR} = 0$, where the unphysical quark decay thresholds are present, one obtains an almost linear function. This is similar to the case of a point nucleon, and leads to the same kind of collapse as

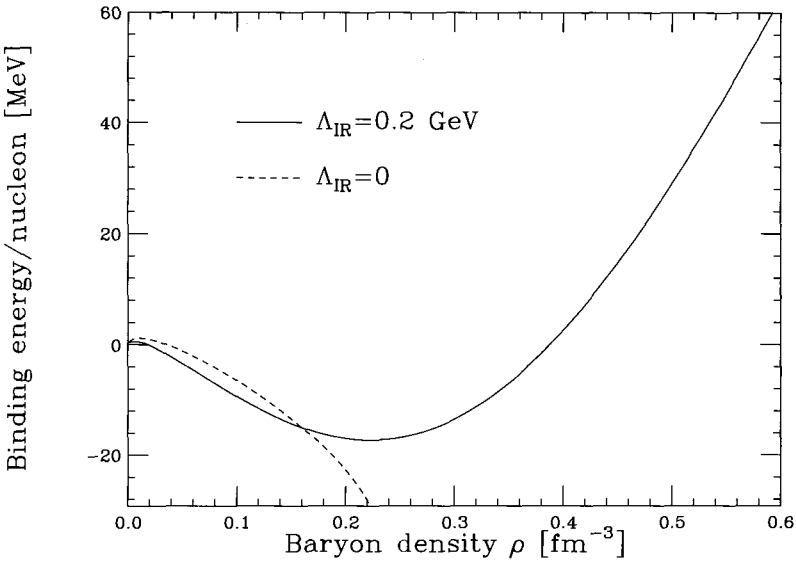

Figure 2. Binding energy per nucleon in NM as a function of the baryon density for $\Lambda_{\rm IR} = 0$ (dashed line) and $\Lambda_{\rm IR} = 0.2$ GeV (solid line).

observed in the linear sigma model, see the dashed line of Fig. 2. The elimination of unphysical quark decay thresholds by an infrared cut-off $\Lambda_{\rm IR}$, however, leads to a positive scalar polarizability (curvature of the function $M_N(M)$), which is clearly shown by the solid line in Fig. 1. This effect stabilizes the NM EOS, and leads to the saturation of the binding energy per nucleon, as shown by the solid line in Fig. 2. The saturation problem in effective chiral field theories can therefore be solved by taking into account the quark structure of the nucleon *and* a particular aspect of confinement physics, namely the absence of quark decay thresholds of the nucleon.

3. The EMC effect in nuclear matter

The isoscalar light cone momentum distribution ($f_{q/A} \equiv f_{u/A} + f_{d/A}$) of quarks per nucleon in a nucleus with mass number A is defined as[10]

$$f_{q/A}(x_A) = \frac{P_-}{A^2} \int \frac{{\rm d}w^-}{2\pi} e^{iP_- x_A w^-/A} < A, P|\overline{\psi}(0)\gamma^+\psi(w^-)|A, P > . \quad (2)$$

Here P^μ is the total 4-momentum of the nucleus and P_- its light cone "minus component", ψ is the quark field, and x_A is the Bjorken variable of the nucleus, which is equivalent to the fraction of the total P_- carried

by a quark times A. In the rest system of the nucleus (NM) we have $P_-/A = \epsilon_F/\sqrt{2}$, where ϵ_F is the Fermi energy (that is, the mass per nucleon or the chemical potential) of the nucleons.

The distribution (2) can be expressed as a convolution of the light cone momentum distributions of quarks in the nucleon and of nucleons in the nucleus[3]. For the evaluation of the quark distribution in the nucleon, we describe the nucleon as a bound state of a quark and a scalar diquark in the NJL model as in the previous section. The presence of the nuclear medium is taken into account via the same scalar and vector mean fields which were used to describe the EOS of NM. The most important relation of this approach, which shows the direct effect of the vector mean field on the quark distribution function, is as follows[3]:

$$f_{q/A}(x_A) = \frac{\epsilon_F}{E_F} f_{q/A0}(x'_A = \frac{\epsilon_F}{E_F} x_A - \frac{V_0}{E_F}). \tag{3}$$

Here the distribution without the explicit effect of the mean vector field is denoted as $f_{q/A0}(x'_A)$, and the nucleon Fermi energy has the form $\epsilon_F = E_F + 3V_0$, where $E_F = \sqrt{M_N^2 + p_F^2}$ and V_0 is the mean vector field as in sect.1.

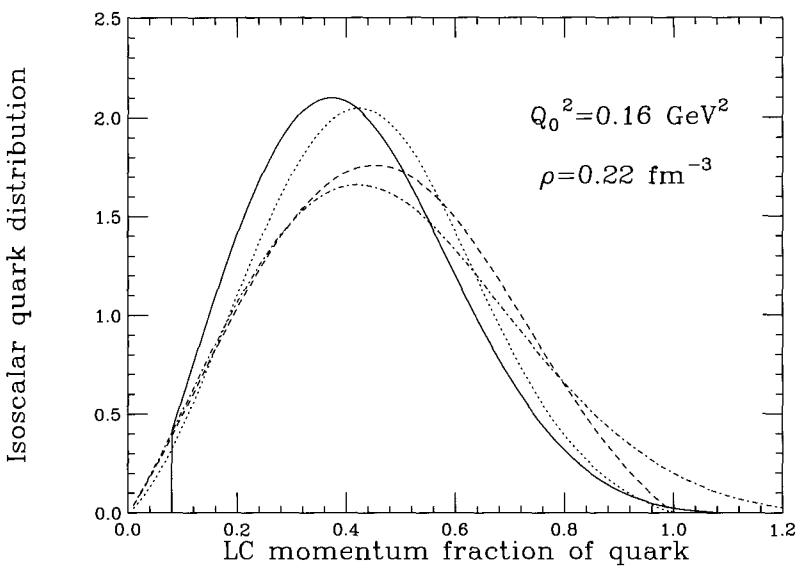

Figure 3. Sum of the up and down quark light cone momentum distributions at the low energy scale $Q_0^2 = 0.16$ GeV^2. For explanation of the lines, see text.

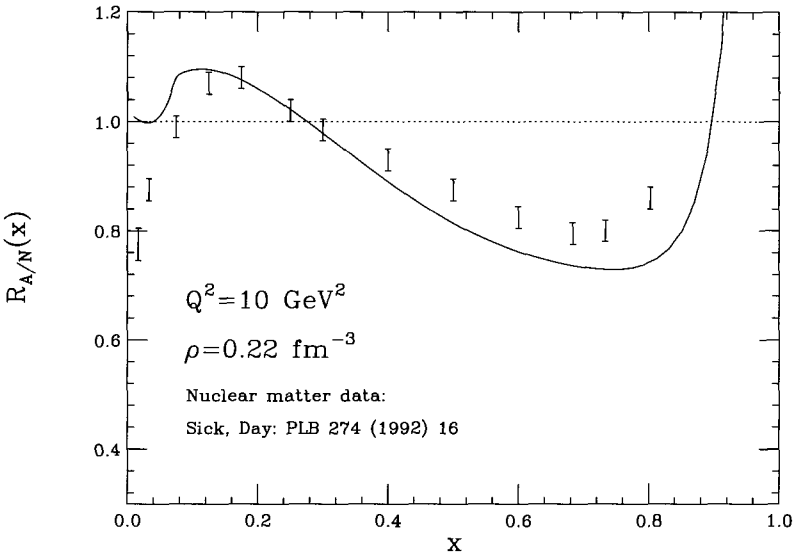

Figure 4. Ratio of the structure function per nucleon in isospin symmetric nuclear matter to the free isoscalar nucleon structure function at $Q^2 = 10$ GeV^2.

The actual calculation of $f_{q/A}$ therefore proceeds as follows: First we calculate the distribution for a free nucleon in the quark-diquark approach, then we replace the quark, diquark and nucleon masses by the effective ones according to the EOS of NM determined in sect.1, then we include the effect of the Fermi motion of nucleons with effective mass M_N, and finally we perform the scale transformation (3) to include the direct effect of the vector mean field. The results for these 4 steps are shown in Fig.3 at the saturation density of our NM EOS for the low energy scale $Q_0^2 = 0.16$ GeV^2. The dotted line shows the distribution in a free nucleon, which is consistent with the empirical parametrizations[11]. The dashed line shows the result when all masses are replaced by the effective ones, the dot-dashed line shows the result including the Fermi motion of nucleons without the direct effect of the mean vector field, and finally the solid line is obtained from the dot-dashed one by the scale transformation (3). We see that the direct effect of the mean vector field is to squeeze the quark distribution from both the small and the large side of the Bjorken variable. The mean vector field is therefore essential to describe the depletion in the valence quark region, and also leads to an enhancement for smaller values of the Bjorken variable. This is shown by the EMC ratio[12] in Fig. 4, which has

been obtained by performing the Q^2 evolution up to $Q^2 = 10$ GeV^2[13]. We see that the calculation can reproduce the main features of the EMC effect, namely the suppression at large x and the enhancement at smaller x.

4. Phase transition to color superconducting quark matter

The EOS of color superconducting QM in the mean field approximation has the form[2]

$$V^{(QM)} = V_{\rm vac} + V_Q + V_\Delta + V_\omega \,, \tag{4}$$

where $V_{\rm vac}$ describes the polarization of the Dirac sea of quarks due to the presence of the valence quarks, V_Q arises from the Fermi motion of the valence quarks without the effect of quark pairing, V_Δ arises from quark pairing in the scalar diquark channel and depends on the color superconducting gap (Δ)[14], and V_ω is the contribution of the mean vector field (V_0) in QM. The conditions $\partial V^{(QM)}/\partial M = \partial V^{(QM)}/\partial \Delta = \partial V^{(QM)}/\partial V_0 = 0$ determine M, Δ and V_0 for fixed chemical potential μ.

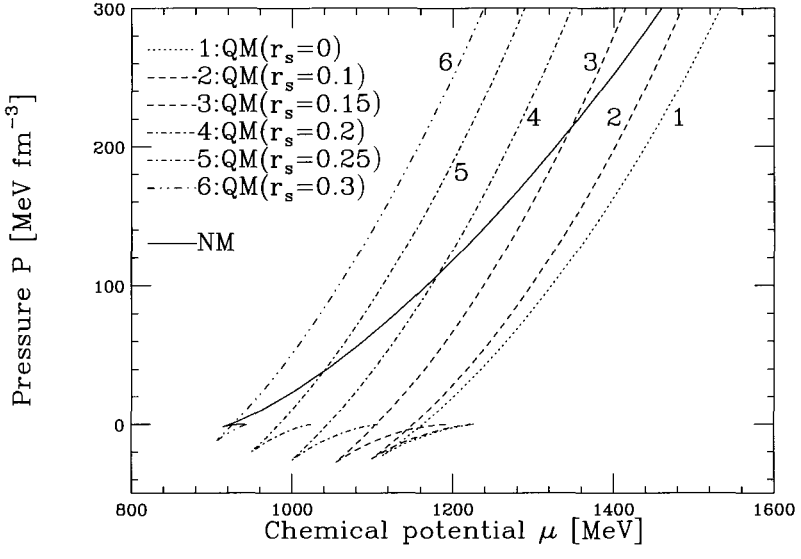

Figure 5. Pressure as function of chemical potential in NM (solid line), and in QM for several values of r_s, which is the ratio of the coupling constant in the scalar diquark channel to the one in the pionic channel.

Fig. 5 shows the EOS for QM with several values for the strength of the pairing interaction in the scalar diquark channel (r_s). Curve 1 corresponds

to normal, i.e., non-color superconducting, QM, and the other curves show the results for increasing strength of the pairing interaction. We also show the EOS for NM by the solid line.

It is clear from Fig. 5 that there is no phase transition from NM to normal QM in our model. The scalar diquark condensation, however, gives rise to a substantial softening of the QM EOS, and to a phase transition from NM to QM at a transition density which decreases with increasing strength of the pairing interaction.

We now assume a particular value of the coupling constant in the scalar diquark channel, which leads to reasonable transition densities, and investigate the nature of the phase transition more closely. Fig. 6 shows the resulting pressure of the ground state as a function of the baryon density for the case corresponding to $r_s = 0.2$ of Fig. 5. We obtain first order transitions from the vacuum (VAC) to NM, where in both phases chiral symmetry is broken and color symmetry is intact, and from NM to color superconducting QM, where in the latter phase chiral symmetry is largely restored and color symmetry is broken. The present calculation gives large color superconducting gaps in the QM phase ($\Delta > 200$ MeV), see ref.[2] for details.

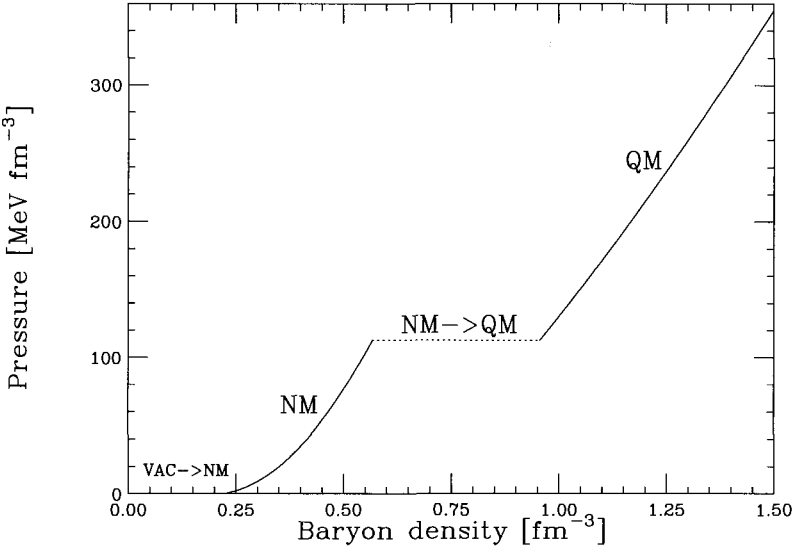

Figure 6. Pressure of the ground state of the system - vacuum (VAC), nuclear matter (NM) or superconducting quark matter (QM) - as function of the baryon density for $r_s = 0.2$. The mixed phases are also indicated.

5. Summary

Let us summarize the three most important points which we found in our investigations on the role of quark degrees of freedom in strongly interacting baryonic matter: First, the effects of quark substructure of the nucleons can solve the saturation problem in chiral many-body theories. The main difference to the point nucleon case is that the extended nucleon has a positive scalar polarizability, which leads to a curvature of the nucleon mass function $M_N(M)$, an in-medium sigma meson mass which depends only weakly on the density, and a saturation of the binding energy per nucleon. Second, the coupling of the mean vector field in nuclear matter to the quarks inside the nucleons influences the form of the quark light cone momentum distributions directly, besides its indirect influence through the equation of state of the system. This direct modification of the quark distribution is expressed by Eq.(3), and is the principal agent to explain the EMC effect in the framework of a mean field description of nuclear matter. Third, there is a phase transition from nuclear matter to quark matter, provided that the effects of scalar diquark condensation (color superconductivity) are taken into account. This phase transition is characterized by the restoration of chiral symmetry and the spontaneous breaking of color symmetry in the high density region.

Acknowledgments

This work is supported by the Grant in Aid for Scientific Research of the Japanese Ministry of Education, Culture, Sports and Technology, Project No. C2-13640298, the Australian Research Council and The University of Adelaide.

References

1. W. Bentz and A.W. Thomas, Nucl. Phys. **A 696** (2001) 138.
2. W. Bentz, T. Horikawa, N. Ishii and A.W. Thomas, Nucl. Phys. **A 720** (2003) 95.
3. H. Mineo, W. Bentz, N. Ishii, A.W. Thomas and K. Yazaki, nucl-th/0312097 (Nucl. Phys. **A**, in press).
4. Y. Nambu and G. Jona-Lasinio, Phys. Rev. **122** (1960) 345; **124** (1961) 246.
5. N. Ishii, W. Bentz and K. Yazaki, Nucl. Phys. **A 578** (1995) 617;
   M. Oettel, R. Alkofer and L. von Smekal, Eur. Phys. J. **A 8** (2000) 553.
6. A. Buck, R. Alkofer and H. Reinhardt, Phys. Lett. **B 286** (1992) 29.
7. J. Boguta, Phys. Lett. **B 120** (1983) 34;
   W. Bentz, L. G. Liu and A. Arima, Ann. Phys. **188** (1988) 61.

8. D. Ebert, T. Feldmann and H. Reinhardt, Phys. Lett. **B388** (1996), 154.
9. M. Birse and J. McGovern, Phys. Lett. **B 292** (1992) 242.
10. R.L. Jaffe, in *Proceedings of the 1985 Los Alamos School on Relativistic Dynamics and Quark Nuclear Physics*, edited by M.B. Johnson and A. Pickleseimer (Wiley, New York, 1985).
11. A.D. Martin, R.G. Roberts, W.J. Stirling and R.S. Thone (MRST2002), Eur. Phys. J. **C 28** (2003) 455.
12. J. Aubert *et al.*, Phys. Lett. **B 123** (1982) 275 ;
D.F. Geesaman, K. Saito and A.W. Thomas, Ann. Rev. Nucl. Part. Sci. **45** (1995) 337 ;
G. Piller and W. Weise, Phys. Rep. **330** (2000) 1. G.A. Miller and J. R. Smith, Phys. Rev. **C 65** (2002) 015211.
13. M. Miyama and S. Kumano, Comput. Phys. Commun. **94** (1996) 185.
14. D. Bailin and A. Love, Phys. Rep. **107** (1984) 325;
M. Alford, K. Rajagopal and F. Wilczek, Phys. Lett. **B422** (1998), 247;
T. Schäfer, Int. J. Mod. Phys. **B 15** (2001) 1474;
O. Kiriyama, S. Yasui and H. Toki, Int. J. Mod. Phys. **E 10** (2001) 501.

A NEW STATE OF MATTER AT HIGH TEMPERATURE AS "STICKY MOLASSES"

GERALD E. BROWN

Department of Physics and Astronomy,
State University of New York, Stony Brook, NY 11794, USA
E-mail: Ellen.Popenoe@sunysb.edu

CHANG-HWAN LEE

Department of Physics and
Nuclear Physics & Radiation Technology Institute (NuRI),
Pusan National University, Pusan 609-735, Korea
E-mail: clee@pusan.ac.kr

MANNQUE RHO

Service de Physique Théorique, CEA/Saclay, 91191 Gif-sur-Yvette, France,
Korea Institute for Advanced Study, Seoul 130-722, Korea
& Department of Physics, Hanyang University, Seoul 133-791, Korea
E-mail: rho@spht.saclay.cea.fr

The main objective of this work is to explore the evolution in the structure of the quark-antiquark bound states in going down in the chirally restored phase from the so-called "zero binding points" T_{zb} to the QCD critical temperature T_c at which the Nambu-Goldstone and Wigner-Weyl modes meet. In doing this, we adopt the idea recently introduced by Shuryak and Zahed for charmed $\bar{c}c$, light-quark $\bar{q}q$ mesons π, σ, ρ, A_1 and gluons that at T_{zb}, the quark-antiquark scattering length goes through ∞ at which conformal invariance is restored, thereby transforming the matter into a near perfect fluid behaving hydrodynamically, as found at RHIC. We name this new state of matter as "sticky molasses". We show that the binding of these states is accomplished by the combination of (i) the color Coulomb interaction, (ii) the relativistic effects, and (iii) the interaction induced by the instanton-anti-instanton molecules. The spin-spin forces turned out to be small. While near T_{zb} all mesons are large-size nonrelativistic objects bound by Coulomb attraction, near T_c they get much more tightly bound, with many-body collective interactions becoming important and making the σ and π masses approach zero (in the chiral limit). The wave function at the origin grows strongly with binding, and the near-local four-Fermi interactions induced by the instanton molecules play an increasingly more important role as the temperature moves downward toward T_c.

1. Introduction

The concept that hadronic states may survive in the high temperature phase of QCD, the quark-gluon plasma[1], has been known for some time. In particular, it was explored by Brown et al.[2,3]. The properties of (degenerate) π and σ resonances above T_c in the context of the NJL model was discussed earlier by Hatsuda and Kunihiro[4], and in the instanton liquid model by Schäfer and Shuryak [5]. Recently, lattice calculations [6,7] have shown that, contrary to the original suggestion by Matsui and Satz [8], the lowest charmonium states $J/\psi, \eta_c$ remain bound well above T_c. The estimates of the zero binding temperature for charmonium $T_{J/\psi}$ is now limited to the interval $2T_c > T_{J/\psi} > 1.6T_c$, where $T_c \approx 270\, MeV$ is that for quenched QCD. Similar results for light quark mesons exist but are less quantitative at the moment. However since the "quasiparticle" masses close to T_c are large, they must be similar to those for charmonium states.

In the chiral limit all states above the chiral restoration go into chiral multiplets. For quark quasiparticles this is also true, but although the chirality is conserved during their propagation, they are not massless and move slowly near T_c where their "chiral mass" $m = E(p \to 0)$ is large (~ 1 GeV).

RHIC experiments have found that hot/dense matter at temperatures above the critical value $T_c \approx 170\, MeV$ is *not* a weakly interacting gas of quasiparticles, as was widely expected. We envision it to be "sticky molasses." Indeed, RHIC data have demonstrated the existence of very robust collective flow phenomena, well described by ideal hydrodynamics. Most decisive in reaching this conclusion was the early measurement of the elliptic flow which showed that equilibration in the new state of matter above T_c set in in a time < 1 fm/c [9]. Furthermore, the first viscosity estimates [10] show surprisingly low values, suggesting that this matter is the most perfect liquid known. Indeed, the ratio of shear viscosity coefficient to the entropy is only $\eta/s \sim 0.1$, two orders of magnitude less than for water. Furthermore, it is comparable to predictions in the infinite coupling limit[11] (for N=4 SUSY YM theory) $\eta/s = 1/4\pi$, perhaps the lowest value possible.

Shuryak and Zahed[12] (hereafter referred to as SZ whenever unambiguous) have recently connected these two issues together. They have suggested that large rescattering cross sections apparently present in hot matter at RHIC are generated by resonances near the zero-binding lines. Indeed, at the point of zero binding the scattering length a of the two

constituents goes to ∞ and this provides low viscosity. This phenomenon is analogous to the elliptic flow observed in the expansion of trapped ^{6}Li atoms rendered possible by tuning the scattering length to very large values via a Feshbach resonance [13].

Near the zero-binding points, to be denoted by T_{zb}, introduced by SZ the binding is small and thus the description of the system can be simple and nonrelativistic. The binding comes about chiefly from the attractive Coulomb color electric field, as evidenced in lattice gauge calculation of Karsch and collaborators[6,14], and Asakawa and Hatsuda[7], as we shall detail. The instanton molecule interactions, which we describe below, are less important at these high temperatures ($T \sim 400$ MeV). All changes as one attempts (as we show below) to dicuss the more deeply bound states just above T_c.

In another work [15], Shuryak and Zahed have also found sets of highly relativistic bound light states in the strongly coupled N=4 supersymmetric Yang-Mills theory at finite temperature (already mentioned above in respect to viscosity). They suggested that the very strong Coulomb attraction can be balanced by high angular momentum, producing light states with masses $m \sim T$. Furthermore, the density of such states remains constant at arbitrarily large coupling. They argued that in this theory a transition from weak to strong coupling basically implies a smooth transition from a gas of quasiparticles to a gas of "dimers", without a phase transition. This is an important part of the overall emerging picture, relating strong coupling, viscosity and light bound states.

In this work we wish to construct the link between the chirally broken state of hadronic matter below T_c and the chirally restored mesonic, glueball state above T_c. Our objective is to understand and to work out in detail what exactly happens with hadronic states at temperatures between T_c and T_{zb}. One important new point is that these chirally restored hadrons are so small that the color charges are locked into the hadrons at such short distances (< 0.5 fm) that the Debye screening is unimportant. This is strictly true at $T \gtrsim T_c$, where there is very little free charge. In this temperature range the nonrelativistic treatment of SZ should be changed to a relativistic one.

The relativistic current-current interaction, ultimately related with the classical Ampere law, is about as important as the Coulomb one, effectively doubling the attraction (see section 2.1). We also found that the spin-spin forces discussed in 2.2 are truly negligible. In effect, with the help of the instanton molecule interaction, one can get the bound quark-antiquark

states down in energy, reaching the massless σ and π at T_c, so that a smooth transition can be made with the chiral breaking at $T < T_c$.

The non-pertubative interaction from the instanton molecules becomes very important. Let us remind the reader of the history of the issue. The nonperturbative gluon condensate, contributing to the dilatational charge or trace of the stress tensor $T_{\mu\mu} = \epsilon - 3p$, is not melted at T_c. In fact more than half of the vacuum gluon condensate value remains at T right above T_c. the hard glue or epoxy which explicitly breaks scale invariance but is unconnected with hadronic masses. The rate at which the epoxy is melted can be measured by lattice gauge simulations, and this tells us the rate at which the instanton molecules are broken up with increasing temperature[1].

As argued by Ilgenfritz and Shuryak [16], this phenomenon can be explained by breaking of the instanton ensemble into instanton molecules with zero topological charge. Such molecules generate a new form of effective multi-fermion effective interaction similar to the orignal NJL model. Brown et al.[17] (denoted as BGLR below) obtained the interaction induced by the instanton molecules above T_c by continuing the Nambu-Jona-Lasinio description upwards from below T_c.

Our present discussion of mesonic bound states should not be confused with quasi-hadronic states found in early lattice calculations[18] for quarks and antiquarks propagating in the space-like direction. Their spectrum, known as "screening masses" is generated mostly by "dynamical confinement" of the spatial Wilson loop which is a nonperturbative phenomenon seen via the lattice calculations. Similar effects will be given here by the instanton molecule interaction.

2. Binding of the $\bar{q}q$ states

2.1. *The Coulomb interaction and the relativistic effects*

At $T > T_c$ the charge is screened rather than confined [19], and so the potential has a general Debye form

$$V = \frac{\alpha_s(r,T)}{r} exp\left(-\frac{r}{R_D(T)}\right) \tag{1}$$

(Note that we use a (somewhat nonstandard) definition in which α_s absorbs the 4/3 color factor.) The general tenet of QCD tells us that the strength of the color Coulomb should run. We know that perturbatively it should run as

$$\alpha_s \sim \frac{1}{\log(Q/\Lambda_{\rm QCD})} \tag{2}$$

with $\Lambda_{QCD} \sim 0.25$ GeV. The issue is what happens when the coupling is no longer small. In vacuum we know that the electric field is ultimately confined to a string, producing a linear potential.

In the so-called "plasma phase" this does not happen, and SZ assumed that the charge runs to larger values, which may explain the weak binding at rather high T we discussed in the introduction. Lattice results produce potentials which, when fitted in the form $V(r) = -A\exp(-mr) + B$ with constant A, B indeed indicate that $A(T)$ grows above T_c by a large factor, before starting to decrease logariphmically at high T. The maximal value of the average coupling $max(A) \approx 1/2$. This is the value which will keep charmonium bound, as found by Asakawa and Hatsuda, up to $1.6T_c$[7].

Running of the coupling is not very important for this work in which we are mostly interested in deeply bound states related with short enough distances. Therefore we will simply keep it as a non-running constant, selecting some appropriate average value.

It is well known in the point charge Coulomb problem (QED) that when $Z\alpha$ is increased and the total energy reaches zero there is a singularity, preventing solutions for larger $Z\alpha$. In the problem of the "sparking of the vacuum" in relativistic heavy ion collisions, the solution of the problem was found by approximating the nuclei by a uniformly charged sphere; for a review of the history see Rafelski et al. [20]. As a result of such regularization, the bound electron level continues past zero to $-m$, at which point e^+e^- production becomes possible around the critical value of $Z_{cr} = 169$. In short, the problem of the point Coulomb charge could be taken care of by choosing a distributed electric field which began from zero at the origin.

In QCD the charge at the origin is switched off by asymptotic freedom, the coupling which runs to zero value at the origin. A cloud of virtual fields making the charge is thus "empty inside". We will model a resulting potential for the color Coulomb interaction by simply setting the electric field equal to zero at $r = 0$, letting it decrease (increase in attraction) going outward. We can most simply do this by choosing a charge distribution which is constant out to R, the radius of the meson. If the original $2m_q$ mass were to be lowered to zero by the color Coulomb interaction and instanton molecule interaction, then the radius of the final molecule will be

$$R \simeq \frac{\hbar}{2m_q}, \tag{3}$$

although the rms radius will be substantially greater with the instanton

molecule interactions playing the main role around T_c.

$$V = -\alpha_s \frac{1}{2R}\left(3 - \frac{r^2}{R^2}\right), \quad r < R$$
$$= -\alpha_s \frac{1}{r}, \quad r > R. \tag{4}$$

This V has the correct general characteristics. As noted above, the electric field $\vec{E}$ must be zero at $r = 0$. It is also easy to see that V must drop off as r^2/R^2 as the two spheres corresponding to the quark and antiquark wave functions are pulled apart. Precisely where the potential begins the $1/r$ behavior may well depend upon polarization effects of the charge, the $+$ and $-$ charges attracting each other, but it will be somewhere between R and $2R$, since the undisturbed wave functions of quark and antiquark cease to overlap here.

The $q\bar{q}$ system is similar to positronium in the equality of masses of the two constituents. Since the main term value is $m\alpha^2/4$, the 4, rather than 2 in hydrogen, coming from the reduced mass, one might think that the Coulomb, velocity-velocity and other interactions would have to be attractive and 8 times greater than this term value in order to bring the $2m_q$ in thermal masses to zero. However, this does not take into account the increase in reduced mass with α. Breit and Brown [21] found an $\alpha^2/4$ increase in the reduced mass with α, or 25% for $\alpha = 1$, to that order. It should be noted that in the Hund and Pilkuhn [22] prescription the reduced mass becomes $\mu = m_q^2/E$, which increases as E drops.

We first proceed to solve the Coulomb problem, noting that this gives us the solution to compare with the quenched lattice gauge simulations, which do not include quark loops.

Having laid out our procedure, we shall proceed with approximations. First of all, we ignore spin effects in getting a Klein-Gordon equation. The chirally restored one-body equation which has now left-right mixing is given by

$$(p_0 + \vec{\alpha} \cdot \vec{p})\psi = 0. \tag{5}$$

Expressing ψ in two-component wave functions Φ and Ψ, one has

$$p_0 \Phi = -\vec{\sigma} \cdot \vec{p} \Psi$$
$$p_0 \Psi = -\vec{\sigma} \cdot \vec{p} \Phi, \tag{6}$$

giving the chirally restored wave function on Ψ

$$\left(p_0 - \vec{\sigma} \cdot \vec{p} \frac{1}{p_0} \vec{\sigma} \cdot \vec{p}\right) \Psi = 0. \tag{7}$$

Here

$$p_0 = E_V = E + \alpha_s/r. \tag{8}$$

Neglecting spin effects, $\vec{\sigma} \cdot \vec{p}$ commutes with p_0, giving the Klein-Gordon equation $p_0^2 - \vec{p}^2 = 0$. We now introduce the effective (thermal) mass, so that the equations for quark and hole can be solved simultaneously following [22];

$$\left[(\epsilon - V(r))^2 - \mu^2 - \hat{p}^2\right] \psi(r) = 0 \tag{9}$$

where $\hat{p}$ is momentum operator, and the reduced energy and mass are $\epsilon = (E^2 - m_1^2 - m_2^2)/2E, \mu = m_1 m_2/E$ with $m_1 = m_2 = m_q$.

Furthermore from eq.(6),

$$\langle \vec{\alpha} \rangle = (\Psi^\dagger, \vec{\sigma}\Phi) + (\Phi^\dagger, \vec{\sigma}\Psi) = \frac{\vec{p}}{p_0} - \frac{i}{p_0}\langle[\vec{\sigma} \times \vec{p}]\rangle. \tag{10}$$

If $\vec{\sigma}$ is parallel to $\vec{p}$, as in states of good helicity, the second term does not contribute. From the chirally restored Dirac equation (5), ignoring spin effects such as the spin-orbit interaction which is zero in S-states we are considering, we find $p_0^2 = \vec{p}^2$.

Brown [23] showed that in a stationary state the EM interaction Hamiltonian between fermions is

$$H_{\rm int} = \frac{e^2}{r}\left(1 - \vec{\alpha}_1 \cdot \vec{\alpha}_2\right), \tag{11}$$

where the $\vec{\alpha}_{1,2}$ are the velocities. Applying (11) to the chirally restored domain of QCD, we expect

$$\begin{aligned} H_{\rm int} &= \frac{2\alpha_s}{r} \qquad \text{for } \vec{\alpha}_1 \cdot \vec{\alpha}_2 = -1 \\ &= 0 \qquad \text{for } \vec{\alpha}_1 \cdot \vec{\alpha}_2 = +1 \end{aligned} \tag{12}$$

2.2. *The spin-spin interaction*

The nonrelativistic form of the spin-spin interaction, in the delta-function form, may give an impression that it is maximal at the smallest distances. However this is not true, as becomes clear if the relativistic motion is included in full, and in fact at $r \to 0$ it is suppressed. At large r, when particle motion is slow, it is of course again suppressed, thus contributing mostly at some intermediate distances.

This fact is clear already from the derivation of the $1s$-state hyperfine splitting Fermi-Breit due to hyperfine interaction in hydrogen from 1930 [24]

given by

$$\delta H = \frac{2}{3}(\vec{\sigma}\cdot\vec{\mu})\int d^3r \frac{\psi^\dagger\psi}{r^2}\frac{d}{dr}\frac{e}{E+e^2/r+m}. \tag{13}$$

Note the complete denominator, which non-relativistically is just substituted by m alone, but in fact contains the potential and is singular at $r \to 0$. The derivative of the e^2/r in the denominator insured that the electric field was zero at $r = 0$. Here $\vec{\sigma}$ is the electron spin, $\vec{\mu}$ the proton magnetic moment. In eq (13) the derivative can then be turned around to act on $\psi^\dagger\psi$, and to order $\alpha = 1$ and with the e^2/r neglected in the denominator, one has

$$\delta H \simeq -\frac{8\pi}{3}(\vec{\sigma}\cdot\vec{\mu})\frac{e}{2m}\psi^2(0), \tag{14}$$

with ψ taken to be the nonrelativistic $1s$ wave function to lowest order in α.

The hyperfine structure is obtained by letting the first $\vec{p}$ in eq. (7) act on the p_0^{-1} and the second $\vec{p}$ go $\vec{p} + \sqrt{\alpha_s}\,\vec{A}$ with

$$\vec{A} = \frac{\vec{\mu}\times\vec{r}}{r^3} \tag{15}$$

with $\vec{\mu}$ the magnetic moment of the antiquark. One finds that the hyperfine structure is [24]

$$H_{\rm hfs} = \frac{1}{p_0^2}\sqrt{\alpha_s}\,\vec{\sigma}\cdot[\vec{E}\times\vec{A}] \tag{16}$$

where $\vec{E}$ is color electric field. Thus,

$$H_{\rm hfs} = \frac{\sqrt{\alpha_s}\,|\vec{E}|}{p_0^2}\left(\frac{\vec{\sigma}\cdot\vec{\mu}}{r^2} - \frac{\vec{\sigma}\cdot\vec{r}\,\vec{\mu}\cdot\vec{r}}{r^4}\right) = \frac{2}{3}\frac{\sqrt{\alpha_s}\,|\vec{E}|}{p_0^2}\frac{\vec{\sigma}\cdot\vec{\mu}}{r^2}. \tag{17}$$

where $|\vec{E}| = 2\alpha_s/r^2$. As in the hydrogen atom, the magnetic moments of quarks and antiquarks are

$$\mu_{q,\bar{q}} = \mp\frac{\sqrt{\alpha_s}}{p_0 + m_{q,\bar{q}}} \tag{18}$$

except that the Dirac mass $m_{q,\bar{q}} = 0$ and p_0, in which the potential is increased by a factor of 2 to take into account the velocity-velocity interaction, is now

$$p_0 = E + 2(\alpha_s/r) \tag{19}$$

for QCD so that in terms of the quark and antiquark magnetic moment operators,

$$H_{\rm hfs} = -\frac{2}{3}\frac{|\vec{E}|}{p_0 r^2}(\vec{\mu}_q \cdot \vec{\mu}_{\bar{q}}). \tag{20}$$

Of course, our p_0 for the chirally restored regime has substantial r dependence, whereas the e/r in the hydrogen atom is generally neglected, and $E+m$ is taken to be $2m$, so that $\mu_e = -e/2m_e$. From Fig. 1 it will be seen that (square of) the wave function is large just where α_s/r is large.

For rough estimates we use averages. We see that, as in Table 1, if E is to be brought down by $\sim 0.5m_q$ for the σ and π by the Coulomb interaction, then

$$2\langle \alpha_s/r \rangle \simeq \frac{1}{2}m_q \simeq \frac{1}{4}p_0 \tag{21}$$

so that with $\alpha_s \sim 0.5$,

$$\langle r^{-1} \rangle \simeq \frac{1}{2}m_q. \tag{22}$$

We next see that this is consistent with the spin splitting forming a fine structure of the two groups, the lower lying σ and π, and the slightly higher lying vectors and axial vectors. Using our above estimates, we obtain

$$\langle H_{\rm hfs} \rangle \simeq \frac{1}{24}\,\frac{1}{16}\vec{\sigma}_q \cdot \vec{\sigma}_{\bar{q}} m_q. \tag{23}$$

so that for the σ and π where $\vec{\sigma}_1 \cdot \vec{\sigma}_2 = -3$ we have

$$\langle H_{hfs} \rangle \sim -\frac{m_q}{128}, \tag{24}$$

the approximate equality holding when $\alpha_s = 0.5$. Note that the hyperfine effect is negligible for the $\alpha_s \sim 0.5$. Although formally eq. (23) looks like the hyperfine structure in the chirally broken sector, it is really completely different in makeup.

In our expression for $\langle H_{hfs} \rangle$ we have the r dependence as $(p_0 r)^{-4} r^{-1}$ and $p_0 r = 4$, basically because the Coulomb interaction lowers the π and σ only 1/4 of the way to zero mass. This explains most of the smallness of the spin-dependent interaction.

A recently renewed discussion of spin-spin and spin-orbit interactions in a relativistic bound states has been made by Shuryak and Zahed [25], who derived their form for both weak and strong coupling limits. Curiously enough, the spin-spin term changes sign between these two limits: perhaps this is another reason why at intermediate coupling considered in this work it happens to be so small.

2.3. *The resulting $\bar{q}q$ binding*

We first construct the bound states for $T \gtrsim T_c$, at temperature close enough to T_c so that we can take the running coupling constants at $T = T_c + \epsilon$. The fact that we are above T_c is important, because the $\Lambda_{\chi\mathrm{SB}} \sim 4\pi f_\pi \sim 1$ GeV which characterizes the broken symmetry state below T_c no longer sets the scale. Until we discover the relevant variables above T_c we are unable to find the scale that sets $\alpha_s = \frac{4}{3}\frac{g^2}{\hbar c}$, the color Coulomb coupling constant.

Following SZ [12], we adopt quark-antiquark bound states to be the relevant variables and specifically, the instanton molecule gas [26] as a convenient framework. In particular, Adami et al.[27], Koch and Brown[28], and BGLR [17] have shown that $\gtrsim 50\%$ of the gluon condensate is not melted at $T = T_c$. The assumption motivated by Ilgenfritz & Shuryak [16] is then that the glue that is left rearranges itself into gluon molecules around $T = T_c$, i.e., what BGLR call "epoxy". We have quantitatively determined couplings for the mesons in the instanton molecule gas by extending the lower energy NJL in the chiral symmetry breaking region up through T_c [17]. We set these couplings in order to fit Miller's [29] lattice gauge results for the melting of the soft glue.

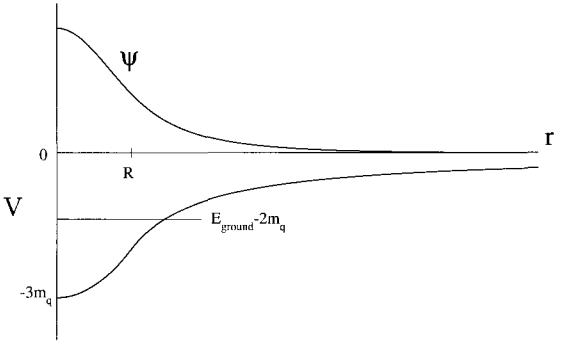

Figure 1. The color Coulomb potential V and the corresponding wave function ψ for relativistic Klein-Gordon case. The interaction eq. (4) with $R = \hbar/2m_q$ was used. The ground state energy with $\alpha_s = 1$ corresponds to $E_{\mathrm{ground}} = 0.645\ m_q$. The minimum of the potential at the origin is at $-3m_q$ here.

In Fig. 1 we show that if we choose $\alpha_s = 1$ (effectively $\alpha_s = 2$ by the doubling in Eq. (12)) as would be required to enter the strong coupling region considered by Shuryak and Zahed[30] we bring the meson mass down by $-1.36\ m_q$ from their unperturbed $2\ m_q$. However, we switch to the region of $\alpha_s \sim 0.5$, which is required by charmonium (intermediate coupling). In Table 1 we summarize the Coulomb binding for a few choices of α_s.

In the case of the instanton molecule interaction the coupling constant $G = 3.825\ \text{GeV}^{-2}$ is dimensionful, so that its contribution to the molecule energy scales as $G\ m_q^3$. (Since we take $\alpha_s = 0.5$ and will find that with inclusion of the velocity-velocity interaction the effective α_s will be 1, powers of α will not affect our answer. We will use $m_q = 1$ GeV, essentially the lattice result for $\frac{3}{2}T_c$ and $3T_c$[14], which works well in our schematic model.) Of course, in QCD the Polyakov line goes to zero at T_c, indicating an infinite quark mass below T_c; i.e., confinement. Just at T_c the logarithmically increasing confinement force will not play much of a role because the dynamic confinement holds the meson size to $\sim \hbar/m_q c$, or ~ 0.2 fm with our assumption of $m_q = 1$ GeV. (Later we shall see that the rms radius is ~ 0.3 fm.) Since we normalize the instanton molecule force, extrapolating it through T_c, and obtain the color Coulomb force from charmonium, our m_q is pretty well determined. However, our $m_q = 1$ GeV is for the unquenched system and at a temperature where the instanton molecules play an important role.

Given these caveats, we may still try to compare our Coulomb result with the lowest peak of Asakawa et al.[31] which is at ~ 2 GeV for $T = 1.4T_c \sim 0.38$ GeV and for Petreczky at $\lesssim 5T \sim 2.030$ GeV for $T = 1.5T_c \sim 0.406$ GeV where we used the Asakawa et al. T_c. We wish to note that: *(i)* These temperatures are in the region of temperatures estimated to be reached at RHIC, just following the color glass phase (which is estimated to last $\sim 1/3$ fm/c). Indeed, Kolb et al. begin hydrodynamics at $T = 360$ MeV. *(ii)* These are in the region of temperatures estimated by SZ[12] to be those for which bound mesons form. We find these mesons to be basically at zero binding, because the instanton molecule interactions although important at $T = T_c$ (unquenched) because of the smallness ($\sim 1/3$ fm) of the Coulomb $\bar{q}q$ states, will be unimportant at $T \sim 400$ MeV where the molecules are much bigger. In the lattice calculations the scalar, pseudoscalar, vector and axial-vector mesons come at the same energy.

Whereas there seems to be consistency between our estimates and the giant resonances of both Asakawa et al.[31] and of Petreczky[32], we should note that with the $m_q \sim 1.6$ GeV by Petreczky et al.[14] the mesons would

still be bound by ~ 1.2 GeV at $T = 1.5T_c$ (quenched). We do not think that the instanton molecules should play an important role at such a high (~ 400 MeV) temperature, so this seems to be a discrepancy. Such a high binding would seem to invalidate the SZ[12] need for the mesons to break up around this temperature. Earlier we have argued for a lower $m_q \sim 1$ GeV.

We are unable to extend our consideration to higher temperatures, where the situation may move towards the perturbative one, but we believe that lattice calculations do support our scenario that the QGP contains large component of bound mesons from $T \sim 170$ MeV up to $T \sim 400$ MeV.

Table 1. Binding energies from color Coulomb interaction and the corresponding rms radii for various α_s (effectively, $2\alpha_s$ including velocity-velocity interaction). 4-point interactions are calculated using the parameters obtained from color Coulomb interaction.

α_s	$\Delta E_{\text{Coulomb}}$ [GeV]	$\sqrt{\langle r^2 \rangle}$ [fm]	$\Delta E_{4-\text{point}}$[GeV]
0.50	−0.483	0.360	−0.994
0.55	−0.595	0.313	−1.385
0.60	−0.707	0.276	−1.834
1.00	−1.355	0.143	−7.574

For $\alpha_s = 0.5$, which is the value required to bind charmonium up through $T = 1.6T_c$, we find that the Coulomb interaction binds the molecule by ~ 0.5 GeV, the instanton molecule interaction by ~ 1.5 GeV. However, the finite size of the $\psi^\dagger\psi$ of the instanton zero mode could cut the latter down by an estimated $\sim 50\%$. As in the usual NJL, there will be higher order bubbles, which couple the Coulomb and instanton molecule effects. We draw the Coulomb molecule in Fig. 2, where the double lines denote the Furry representation (Coulomb eigenfunction for quark and antiquark in the molecule).

Figure 2. Coulomb molecule. The wavy line on the left represents the momentum transfer necessary to produce the molecule. The double line denotes the Furry representation, i.e., Coulomb eigenstate.

The four-point instanton molecule interaction is shown in Fig. 3. There will be higher-order effects as shown in Fig. 4, of the 4-point interaction

Figure 3. The four-point instanton molecule interaction between Coulomb eigenstates. The $(\bar{\psi}\psi)^2$ intersect at the thick point.

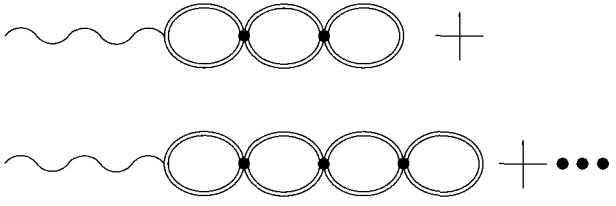

Figure 4. Higher order effects of four-point interaction.

used in higher-order between Coulomb eigenstates which always end in a 4-point interaction. The energy of the propagators has been lowered from the 2 GeV of the two noninteracting quarks to 1.5 GeV by the Coulomb interaction. The series beginning with terms in Figs. 2–4 is

$$\Delta E = -0.5\text{GeV} - 1\text{GeV}\, F - \frac{1(\text{GeV})^2 F^2}{1.5\text{GeV}} - \frac{1(\text{GeV})^3 F^3}{(1.5\text{GeV})^2} + \cdots$$
$$= -0.5\text{GeV} - \frac{1\text{GeV}F}{1 - \frac{1\text{GeV}F}{1.5\text{GeV}}}. \tag{25}$$

Now $\Delta E = -1.25$ GeV is accomplished for $F = 0.5$.

Working in the Furry representation, we have a -0.5 GeV shift already in the representation from the Coulomb wave functions. This means that we must obtain $\Delta E = -1.5$ GeV to compensate for the $2m_q = 2$ GeV, in order to bring the π and σ masses to zero. The four-point interaction is a constant, at a given temperature, so this problem is just the extended schematic model of nuclear vibrations (See Sec. V of Brown [33], where simple analytical solutions are given).

Our eq. (25) corresponds to the Tamm-Dancoff solution, summing loops going only forward in time. If ΔE decreases -0.75 GeV in this approximation, then when backward going graphs are added [1], ΔE will decrease by twice this amount [33], or the -1.5 GeV necessary to bring the π and σ energy to zero. Of course, forward and backward going loops are summed in the Bethe-Salpeter equation to give the NJL in the broken symmetry sector, but the actual summation is more complicated there, because the intermediate state energies are not degenerate. In the next section we shall show that the backward going graphs appear in lattice gauge calculations.

In detail, with our estimated $F = (0.75)^2$ and the 4-point energies from Table 1, our π and σ excitations without inclusion of backward going graphs are brought down 58% of the way from -0.5 GeV to -2 GeV; i.e., slightly too far. We have not made the adjustment down to 50%, because the uncertainties in our estimate of F, etc., do not warrant greater accuracy.

3. Conclusions

Shuryak and Zahed have discussed the formation of the mesonic bound states at higher temperatures, well above T_c. They pointed out that in the formation of the bound state, or any one of the molecular excited states, the quark-quark scattering length becomes infinite, similarly for the more strongly bound gluon-gluon states. In this way the nearly instantaneous equilibration found by RHIC can be explained. As we explained in the last section, lattice calculations seem to support the scenario of nearly bound scalar, pseudoscalar, vector and axial-vector excitation at $\sim 2T_c$ (~ 1.5 times the quenched T_c).

In this work we are able to construct a smooth transition from the chirally broken to the chirally restored sector in terms of continuity in the masses of the σ and π mesons, vanishing at $T \to T_c$. In doing so we had to include relativistic effects. One of them – the velocity-velocity term related to Amper law for the interacting currents – nearly doubles the effective coupling. The spin-spin term happen to be very small. The crucial part of strong binding in our picture of $\bar{q}q$ mesons (or molecules) is the quasi-local interaction due to instanton molecules (the "hard glue"). We found that the tight binding of these mesons near T_c enhences the wave function at the origin, and gives us additional understanding of the nonperturbative hard glue (epoxy) which is preserved at $T > T_c$.

Thus, we believe that the material formed in RHIC was at a temperature where although the matter is formally in a quark-gluon plasma phase, most of it is made of chirally restored mesons. Certainly this is not the weakly coupled quark-gluon plasma expected at high T.

Finally, in this paper we have focused on quantum mechanical binding effects in the vicinity of the critical temperature T_c coming down from above. Nice continuity in the spectra of the light-quark hadrons – e.g., the pions and the σ – across the phase boundary should also hold for other excitations such as the vector mesons ρ, ω, A_1 which lie slightly above π and σ because of quantum corrections. Since going below T_c from above involves a symmetry change from Wigner-Weyl to Nambu-Goldstone, there

is a phase transition and to address this issue, it would be necessary to treat the four-fermi interactions more carefully than in the pseudo-potential approximation adopted here. It seems plausible from the renormalization group point of view [34] that the four-fermi interactions generated by the instanton molecules – attractive in all channels – will not only trigger the quark pairs to condense, thereby spontaneously breaking chiral symmetry but also bring down the mass of the vector mesons, as the temperature approaches T_c from above. We will show in a future publication [35] how this phenomenon can take place in a schematic model.

Acknowledgments

GEB was partially supported by the US Department of Energy under Grant No. DE-FG02-88ER40388. CHL was supported by Pusan National University Grant.

References

1. G.E. Brown, C.-H. Lee, M. Rho, and E.V. Shuryak, hep-ph/0312175 *(denoted as BLRS).*
2. G.E. Brown, H.A. Bethe, and P.M. Pizzochero, Phys. Lett. **B263** (1991) 337.
3. G.E. Brown, A.D. Jackson, H.A. Bethe, and P.M. Pizzochero, Nucl. Phys. **A560** (1993) 1035.
4. T. Hatsuda and T. Kunihiro, hep-ph/0010039; Phys. Lett. **B145** (1984) 7; Phys. Rev. Lett. 55 (1985) 158; Prog. Theor. Phys. **74** (1985) 765.
5. T. Schafer and E. V. Shuryak, Phys. Lett. **B356** (1995) 147.
6. S. Datta, F. Karsch, P. Petreczky, and I. Wetzorke, Nucl. Phys. Proc. Suppl. **119** (2003) 487.
7. M. Asakawa and T. Hatsuda, "J/ψ and η_c in the deconfined plasma fom lattice QCD," hep-lat/0308034.
8. T. Matsui and H. Satz, Phys. Lett. **B178** (1986) 416.
9. D. Teaney, J. Lauret, and E. Shuryak, Phys. Rev. Lett. **86** (2001) 4783, see also nucl-th/0110037 (unpublished); P.F. Kolb, P. Huovinen, U.W. Heinz, and H. Heiselberg, Phys. Lett. **B500** (2001) 232.
10. D. Teaney, "The effects of viscosity on spectra, elliptic flow and HBT radii", nucl-th/0301099.
11. G. Policastro, D. T. Son and A. O. Starinets, Phys. Rev. Lett. **87** (2001) 081601.
12. E. Shuryak and I. Zahed, hep-ph/0307267.
13. K. M. O'Hara et al, Science **298** (2002) 2179; T. Bourdel et al, Phys. Rev. Lett. **91** (2003) 020402.
14. P. Petreczky, F. Karsch, E. Laermann, S. Stickan, I. Wetzorke, Nucl. Phys. Proc. Suppl. **106** (2002) 513; hep-lat/0110111.
15. E. Shuryak and I. Zahed, hep-th/0308073, Phys. Rev. D, in press.

16. E. M. Ilgenfritz and E. V. Shuryak, Phys. Lett. B **325** (1994) 263.
17. G.E. Brown, L. Grandchamp, C.-H. Lee, M. Rho, hep-ph/0308147.
18. C. DeTar, Phys. Rev. **D32** (1985) 276; **D37** (1987) 2378.
19. E V Shuryak, Zh.E.T.F **74** (1978) 408; Sov. Phys. JETP **47** (1978) 212
20. J. Rafelski, L.P. Fulcher, and A. Klein, Phys. Rept. **38C** (1978) 227.
21. G. Breit and G.E. Brown, Phys. Rev. **74** (1948) 1278.
22. V. Hund and H. Pilkuhn, J. Phys. **B33** (2000) 1617.
23. G.E. Brown, Phil. Mag. **43** (1952) 467.
24. E. Fermi, Z.f.Phys. **60** (1930) 320; G. Breit & W. Doermann, Phys. Rev. **36** (1930) 1732.
25. E. V. Shuryak and I. Zahed, hep-th/0310031.
26. T. Schäfer, E. V. Shuryak and J. J. M. Verbaarschot, Phys. Rev. D **51** (1995) 1267; Nucl. Phys., **B412** (1994) 143.
27. C. Adami, T. Hatsuda, and I. Zahed, Phys. Rev. **D43** (1991) 921.
28. V. Koch and G.E. Brown, Nucl. Phys. **A560** (1993) 345.
29. D.E. Miller, hep-ph/0008031.
30. E. Shuryak and I. Zahed, hep-th/0308073.
31. M. Asakawa, T. Hatsuda, and Y. Nakahara, Nucl. Phys. **A715** (2003) 863c.
32. P. Petreczky, hep-ph/0305189.
33. G.E. Brown, *"Unified Theory of Nucleon Models and Forces"*, 1967, North Holland Pub. Co., Amsterdam.
34. R. Shankar, Rev. Mod. Phys. **66** (1994) 129; J. Polchinski, *Recent Directions in Particle Theory: From Superstrings and Black Holes to the Standard Model*, edited by J. Harvey and J. Polchinski (World Scientific, Singapore, 1994) p235-274.
35. G.E. Brown, C.-H. Lee and M. Rho, "Chemical equilibration in relativistic heavy-ion collisions," to appear.

MODE SOFTENING NEAR THE CRITICAL POINT WITHIN EFFECTIVE APPROACHES TO QCD

H. FUJII

Institute of Physics, University of Tokyo, Komaba, Tokyo 153-8902, Japan
E-mail: hfujii@phys.c.u-tokyo.ac.jp

M. OHTANI

Radiation Laboratory, RIKEN, Wako, Saitama 351-0198, Japan
E-mail: ohtani@rarfaxp.riken.jp

We study the soft mode along the critical line in the phase diagram with the tricritical point, using the Nambu–Jona-Lasinio model. At the critical point with finite quark mass, the ordering density becomes a linear combination of the scalar, quark number and energy densities, and their susceptibilities diverge with the same exponent. Based on the conservation law, it is argued that the divergent susuceptibility of a conserved density must be accompanied by a critically–slowing hydrodynamic mode. The shift of the soft mode from the sigma meson to the hydrodynamic mode occurs at the tricritical point on the critical line.

1. Introduction

The phases of QCD have been explored by investigating the behavior of the quark condensate, the Polyakov loop and the color superconducting gap as functions of the temperature (T) and the quark chemical potential (μ). Among various possibilities on the phase structure, existence of a critical point (CP) as an endpoint of the first–order phase boundary has been theoretically suggested and discussed in the literature[1,2,3].

When we extend the phase space by taking the mass (m) of the u and d quarks as the third variable, we can study this CP from the viewpoint of the phase space T–μ–m with a tricritical point (TCP). The static properties of this phase diagram with the TCP is well described by the Ginzburg–Landau (GL) effective potential of the quark condensate σ expanded up to the σ^6 term.[4] First in the case of exact chiral symmetry $m = 0$ the T–μ plane must be devided into two domains of the symmetric and broken phases with a boundary *line*. Although the order of the singularity of this line is

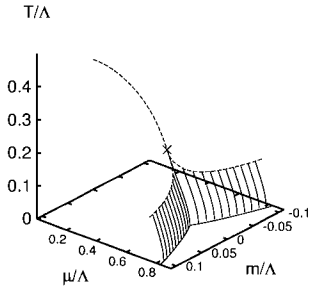

Figure 1. Phase diagram of the NJL model. The critical line is drawn in a dashed line. The first–order phase boundary forms a surface shown by hatch. The TCP is indicated by $\times$.

unknown in general, we *assume* the TCP where the order of the singularity shifts from the 2nd to the 1st order. Next, when the quark mass takes small but non–zero value, the 2nd order line disappears and the assumed TCP becomes a usual CP (see Fig. 1). In this consideration, the relation of this CP to the chiral symmetry is rather obscure.

Characteristic time scale of the system response becomes infinitely large at a CP, which is known as critical slowing down. The mode whose typical frequency vanishes at the CP is called "soft mode." In the conventional theory increase of this time scale of a soft mode is related to the divergence of the susceptibility at the CP. The most familiar example will be the sigma meson or the radial fluctuation of the quark condensate in the chiral critical transition[5].

In this talk we discuss the soft mode along the line of the CP within effective approaches to QCD.[6,7] We will point out that the soft mode associated with the CP at finite m must have hydrodynamic character. This argument is based on the conservation of the baryon number and energy densities, and therefore is very general. Near the TCP the critical mode is different between the symmetric and broken phases. Although we restrict ourselves to the result obtained in the Nambu–Jona-Lasinio (NJL) model here, we should stress that the same result can be reached within the time–dependent GL approach as well.[7]

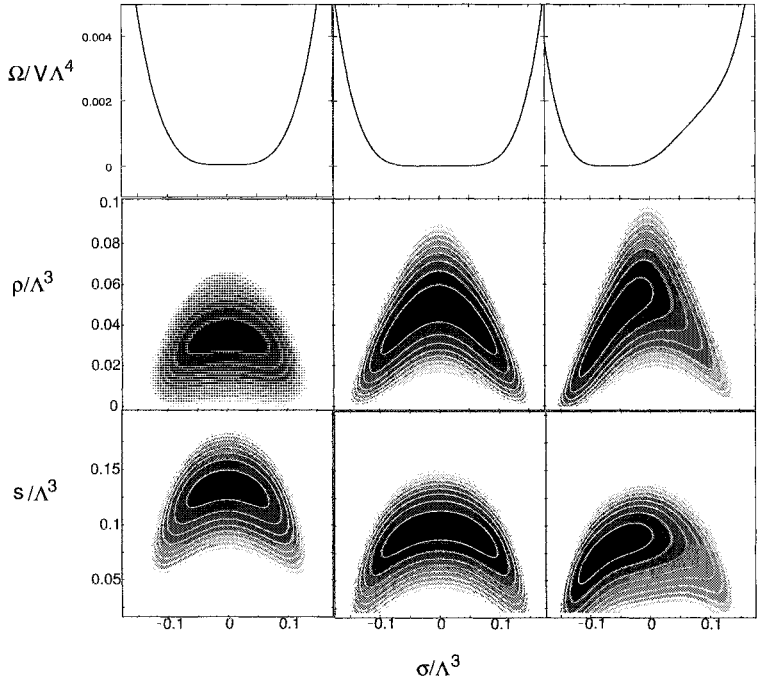

Figure 2. Effective potentials $\tilde{\Omega}$ with two ordering densities, σ–ρ and σ–s at critical poinsts, chiral CP (left), TCP (middle), CP (right). Those with the single ordering density (uppermost) are also shown.

2. Effective potential

We use the NJL model[8,9] $\mathcal{L} = \bar{q}(i\partial\!\!\!/ - m)q + g[(\bar{q}q)^2 + (\bar{q}i\gamma_5\tau^a q)^2]$, in the mean field approximation ($\langle\bar{q}q\rangle = \sigma$=const, $\langle\bar{q}i\gamma_5\tau^a q\rangle = \pi$=0). The thermodynamics is described by the effective potential,

$$\Omega(T,\mu,m;\sigma)/V = -\nu\int\frac{d^3k}{(2\pi)^3}[E - T\ln(1-n_+) - T\ln(1-n_-)] + \frac{1}{4g}(2g\sigma)^2, \tag{1}$$

where $n_\pm = (e^{\beta(E\mp\mu)}+1)^{-1}$, $E = \sqrt{M^2+\mathbf{k}^2}$, $M = m - 2g\sigma$, and $\nu = 2N_fN_c = 2\cdot 2\cdot 3 = 12$ with N_f and N_c the numbers of flavor and color, respectively. The true thermodynamic state is determined by the extremum condition, $\partial\Omega/\partial\sigma = 0$, and the corresponding grand potential is $\Omega(T,\mu,m)$. We define the model with the three-momentum cutoff Λ and with the coupling constant $g\Lambda^2 = 2.5$ which allows the TCP. In the following, all the

dimensionful quantities are expressed in the units of Λ.

It is useful to difine the GL effective potential $\tilde{\Omega}$ with two order parameters in studying the true flat direction.[7] It is numerically constructed as shown in Fig. 2 at the chiral CP with (T, μ)=(0.3419, 0.3), the TCP (0.20362, 0.49558) and a CP (0.1498, 0.5701) with $m = 0.01$ in the units of Λ.[6] The susceptibilities $\chi_{ij} = -\frac{1}{V}\partial^2\Omega/\partial i \partial j$ $(i, j = T, \mu, m)$ are equal to the inverse of the curvature matrix of the GL effective potential at the extremum point. Therefore the divergence of the susceptibilities at the critical point is related to the appearance of a flat direction in the GL effective potential.

At the chiral CP, the flat direction must be the scalar density σ due to symmetry (Fig. 2). The susceptibility of σ is divergent while those of the quark number density ρ and the entropy density s remain finite in the mean field approximation.

The σ^2 and σ^4 terms in the potential (1) vanish at the TCP. This fact results in the large fluctuation along the potential valley of $\tilde{\Omega}$ with two ordering densities (Fig. 2). The fluctuations of ρ and s become divergent at the TCP approached from the broken phase.[a] If we define a potential of *e.g.*, the quark density ρ by eliminating σ with $\partial\tilde{\Omega}(\sigma, \rho)/\partial\sigma = 0$, we see that the potential is flat on the lower density side of the critical density ρ_t at the TCP.[7]

On the other hand, at the CP with the explicit breaking $m \neq 0$ the proper ordering direction becomes a linear combination of σ, ρ and s (Fig. 2).[10,7,11] The susceptibilities of these densities diverge with the same exponent since all of them involve a fraction of the critical fluctuation of the proper ordering density. Here the σ direction is no longer special. One may choose equally well any of these densities as the ordering density in the static GL potential.

3. Susceptibility and spectral density

The susceptibility is obtained in the q–limit of the response function, which allows us to express the susceptibility as a sum of the spectral density:

$$\chi_{ij} = \chi_{ij}(0, \mathbf{q} \to 0) = \lim_{\mathbf{q}\to 0} \int \frac{d\omega}{2\pi} \frac{2\mathrm{Im}\chi_{ij}(\omega, \mathbf{q})}{\omega}. \qquad (i, j = m, \mu, T) \quad (2)$$

From this expression we see that divergence of the susceptibility is caused by spectral enhancement at $\omega = 0$ or mode softening, provided that the

[a]Note that the fluctuation of s is a linear combination of those of the quark number density and the energy density.

spectral density $2\mathrm{Im}\chi_{ij}(\omega, \mathbf{q})$ itself is integrable.

At the chiral CP, the divergence of the scalar susceptibility is generated by softening of the sigma meson mode, which is the chiral partner of the pion mode. However, we should recognize that there is no symmetry reason to expect the massless sigma at the CP with explicit symmetry breaking due to $m \neq 0$.

There is a strong constraint on the spectrum in the fluctuations of the conserved quantity: the modes contributing to the susceptibility of a conserved quantity have to be hydrodynamic, that is, the typical frequency must vanish as $\mathbf{q} \to \mathbf{0}$. Physically this is a consequence of the existence of the current $\mathbf{j}$ such that $\partial_t \rho + \nabla \cdot \mathbf{j} = 0$ for *e.g.*, the quark number density. Using the fact that the conserved density operator is commutative with the total Hamiltonian and the fluctuation–disspation theorem, we can express the susceptibility in another form,[8,7]

$$\chi_{ij} = \beta \lim_{\mathbf{q}\to 0} \int \frac{d\omega}{2\pi} \frac{2\mathrm{Im}\chi_{ij}(\omega, \mathbf{q})}{1 - e^{-\beta\omega}}. \tag{3}$$

These two expressions (2) and (3) coincide with each other if and only if $\lim_{\mathbf{q}\to\mathbf{0}} 2\mathrm{Im}\chi_{ij}(\omega, \mathbf{q}) = 2\pi\delta(\omega)\omega\chi_{ij}$. Hence, when the susceptibility of a conserved quantity diverges, there must be a hydrodynamic mode which shows critical slowing.

Finally we remark that the ω–limit of the response function $\chi_{ij}(\omega \to 0, \mathbf{0})$ has no contribution from the hydrodynamic mode spectrum.

4. Soft modes in the NJL model

The response functions in the random phase approximation are written as

$$\chi_{ij}(iq_4, \mathbf{q}) = \Pi_{ij}(iq_4, \mathbf{q}) + \Pi_{im}(iq_4, \mathbf{q}) \frac{1}{1 - 2g\Pi_{mm}(iq_4, \mathbf{q})} 2g\Pi_{mj}(iq_4, \mathbf{q}). \tag{4}$$

Here polarization functions are defined with the imaginary–time quark propagator $\mathcal{S}(\tilde{k}) = 1/(\tilde{k} + M)$ as

$$\Pi_{ij}(iq_4, \mathbf{q}) = -\int \frac{d^3k}{(2\pi)^3} T \sum_{n=-\infty}^{\infty} tr_{\mathrm{fcD}} \mathcal{S}(\tilde{k}) \Gamma \mathcal{S}(\tilde{k} - q) \Gamma', \tag{5}$$

where $q_4 = 2l\pi T$ ($l \in \mathbb{Z}$), $\tilde{k} = (\mathbf{k}, k_4 + i\mu)$ with $k_4 = -(2n+1)\pi T$, Γ is an appropriate Dirac matrix, and the traces are taken over the flavor, color and Dirac indices. $\Gamma = 1$ for the scalar, $i\gamma_4$ for the baryon number, and

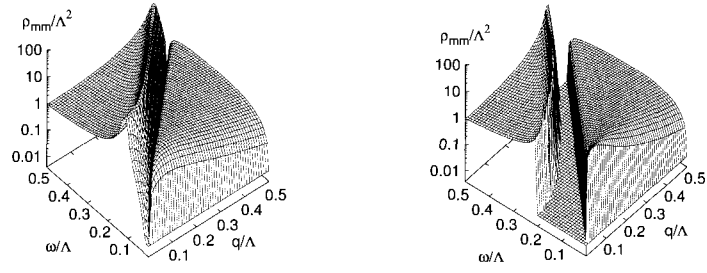

Figure 3. Spectral functions of the scalar channel above (Left, $T/\Lambda = 0.35$) and below (Right, $T/\Lambda = 0.339$) the chiral transition point with $\mu/\Lambda = 0.3$ in the ω–q plane.

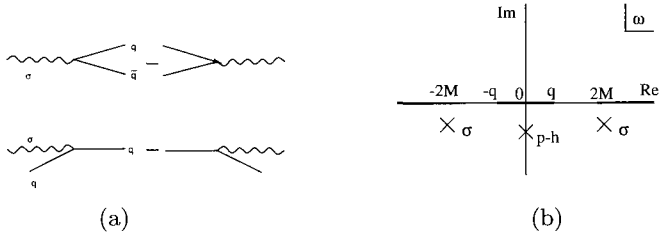

Figure 4. (a) Physical processes contributing to the spectrum with the detailed balance. (b) Analytic structure of the response function. The σ meson and p–h poles ($\times$) locate in the unphysical Riemann sheet.

$\mathcal{H}_{MF}$ for β with

$$\mathcal{H}_{MF} = -i\frac{1}{2}\boldsymbol{\gamma}\cdot\overleftrightarrow{\boldsymbol{\nabla}} + M + i\mu\gamma_4. \tag{6}$$

We deal with the response function of $\mathcal{H}_{MF}$ instead of the entropy because the entropy has no microscopic expression. The real–time response function is obtained from the imaginary–time propagator through the usual replacement $iq_4 \to q_0 + i\epsilon$ in the final expression.

The collective modes are generated by the infinite sum of the bubble diagrams in the NJL model. The spectral function $\rho_{mm}(\omega, \mathbf{q}) = 2\mathrm{Im}\chi_{mm}(\omega, \mathbf{q})$ of the scalar response function[5] just above and below the chiral critical point with fixed $\mu = \mu_c$ are shown in Fig. 3. The spectrum in the time–like region comes from the quark pair creation/annihilation while the spectrum in the space–like region is due to the absorption/emission of the scalar fluctuation

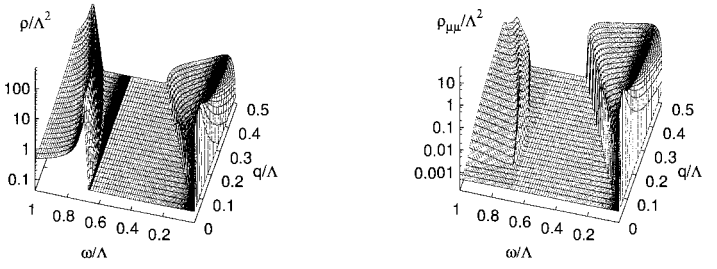

(a) (b)

Figure 5. Spectral functions of the scalar and the quark number susceptibilities at the CP with $m/\Lambda = 0.01$.

by a quark or an anti–quark. The latter particle–hole (p–h) process gives rise to the Landau damping of collective motion in medium. These physical processes are schematically shown in Fig. 4 (a). In the unphyscal Riemann sheet of ω (Fig. 4 (b)), we found two kinds of complex poles corresponding to the collective excitations of these processes. We shall call here the pole related with the time–like spectrum the sigma meson and the pole for the space–like one the p–h mode.

Approaching the chiral CP from the symmetric phase, we see in Fig. 3 (a) that the sigma meson mode becomes soft. Meanwhile the p–h mode does not show any particular enhancement. From the broken phase, on the other hand, the mass gap of the sigma meson mode is vanishing and the p–h mode spectrum also gets stronger at $\mathbf{q} = \mathbf{0}$ (Fig. 3 (b)).

At the critical point with $m/\Lambda = 0.01$ both the scalar and quark–number susceptibilities diverge. The scalar spectral function is shown in Fig. 5 (a). In this case the sigma meson has finite mass gap, which is set by the quark mass as $\sim 2M \sim m^{1/5}$. The p–h mode has the hydrodynamic character ($\omega \to 0$ as $\mathbf{q} \to \mathbf{0}$). We note that the strength of this mode is strongly enhanced at this critical point. In Fig. 5 (b), we show the specral function of the quark–number response function. It is clear that the divergence is caused solely by the p–h mode spectrum with hydrodynamic character, which is consistent with the general argument given in Sec. 3.

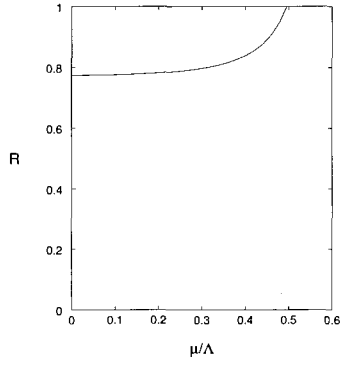

Figure 6. Ratio (7) of the spectral contribution along the chiral critical line in Fig. 1 approached from the broken phase. $R \to 1$ toward the TCP.

5. Change of the spectral contribution along the critial line

We know that the sigma meson mode is the soft mode associated with the chiral CP while we have seen that the p–h mode shows the critical slowing at the CP with finite quark mass m. Let us study the change of the critical eigenmode along the critical line as shown in a dashed line in Fig. 1, with defining the relative weight of the spectral contributions of the p–h mode to the total spectrum by

$$R \equiv \frac{\chi_{mm}(0, \mathbf{0}^+) - \chi_{mm}(0^+, \mathbf{0})}{\chi_{mm}(0, \mathbf{0}^+)}. \tag{7}$$

Here we used the fact that the difference between the q– and ω–limits of $\chi_{mm}(\omega, \mathbf{q})$ stems from the spectral contribution of the hydrodynamic mode. From the argument in Sec. 3, this ratio must be unity for the susceptibility of a conserved quantity, which can be confirmed explicitly.

We show the numerical result of R in Fig. 6. The ratio vanishes if the chiral CP or the TCP is approaced from the symmetric phase, which means that the critical divergence is generated by the sigma mode without any contribution from the p–h mode. From the broken phase, on the other hand, we see the finite portion of the divergence comes from the p–h mode spectrum in the chiral critical transition — even in the $\mu = 0$ case. Approaching the TCP along the critical line, we see that the contribution from the p–h mode increases and eventually saturates the spectral sum (2).

First one may ask why the p–h mode gives no contibution in the symmetric phase. This is because that the chirality and helicity is the same for

a massless quark and that the chirality flip in the scalar coupling requires the finite momentum transfer $\mathbf{q}$. In the broken phase, a massive quark with definite chirality has both helicity components, and therefore the p–h mode spectrum remains contributing to the susceptibility in the $\mathbf{q} \to \mathbf{0}$ limit.

Next we note that the mixing of this p–h spectrum in the susceptibility of ρ and s is possible in the broken phase through the coupling proportional to the condensate σ. This mixing gives rise to the finite gap of these susceptibilities across the *chiral* critical line. This fact implies that the p–h mode contribution must be of order of $1/\sigma^2 \to \infty$ in the scalar channel, to cancel the σ^2 factor from the coupling.

At the TCP approached from the broken phase with fixed μ, χ_{mm} diverges as $1/\sigma^4$ while $\chi_{\mu\mu}$ and χ_{TT} blow up as $1/\sigma^2$, which is easily confirmed within the Ginzburg–Landau approach. Only the p–h mode spectrum with hydrodynamic character can cause this divergence in the NJL model. The sigma meson mode in the NJL model provides the singularity of order $1/\sigma^2$ to χ_{mm} at the TCP approached from the broken phase. From the symmeric phase, where $\sigma \equiv 0$, there is no contribution from the p–h mode and the critical divergence at the TCP is completely provided by softening of the sigma meson. The $\chi_{\mu\mu}$ and χ_{TT} are finite there.

Along the critical line with finite quark masses $m \neq 0$, $\chi_{\mu\mu}$ and χ_{TT} as well as $\chi_{\mu\mu}$ diverge with the same exponent. Generally these divergence must come from softening of a hydrodynamic mode in the system because the baryon number and the energy are conserved quantities. We can prove this within the NJL model as well as the time-dependent GL approach.

6. Summary

We have seen that, unlike at the chiral CP, the ordering density at the CP with finite quark mass m is a linear combination of the scalar density, the baryon number density and the energy density, and that the susceptibilities of these density diverge there. Since the susceptibility of a conserved density solely comes from the hydrodynamic spectrum, the associated critical soft mode must be hydrodynamic. We identified the p–h mode in the NJL model as this critical mode. Recently it is explicitly argued that the dynamic unversality class of this point is the same as the liquid-gas critical point[11,12].

Experimentally, it is worthwhile to study the fluctuation of the conserved densities.[1] The correct evolution equation for the correlation length must be hydrodynamic one, which is slower than the sigma like motion. In this sense the growth of the correlation length in the heavy ion events

passing by the CP acquires a renewed interest.[13]

Along the critical line in the phase space of T–μ–m, we have studied the changeover of the associated soft mode from the sigma meson mode at the chiral CP to the p–h mode at the CP with $m \neq 0$. This shift occurs at the TCP, where the critical soft mode is different between the symmetric and broken phases. The dynamic classification of this TCP will be theoretically interesting.[7,11,12]

There is a speculated phase diagram of QCD in the space of T–μ–m–m_s,[14] in which we see several critical lines and surfaces. It seems important to keep the hydrodynamic viewpoint in mind when we study these criticalities.

Acknowledgments

One (H.F.) of the authors is grateful for the warm hospitality extended to him by KIAS. This work is supported in part by the Grants-in-Aid for Scientific Research of Monbu-kagaku-sho (No. 13440067).

References

1. For review, M.A. Stephanov, "QCD phase diagram and the critical point," arXiv:hep-ph/0402115.
2. M. Stephanov, K. Rajagopal and E.V. Shuryak, Phys. Rev. Lett. **81**, 4816 (1998).
3. M. Stephanov, K. Rajagopal and E.V. Shuryak, Phys. Rev. D **60**, 114028 (1999).
4. I. Lawrie and S. Sarbach, in *Phase Transitions and Critical Phenomena*, ed. by C. Domb and J. Lebowitz (Academic Press, NY, 1984), Vol. 9, pp. 1.
5. T. Hatsuda and T. Kunihiro, Phys. Rev. Lett.**55**, 158 (1985).
6. H. Fujii, Phys. Rev. D **67**, 094018 (2003).
7. H. Fujii and M. Ohtani, arXive:hep-ph/0401028; arXive:hep-ph/0402263.
8. T. Hatsuda and T. Kunihiro, Phys. Rept. **247**, 221 (1994).
9. S.P. Klevansky Rev. Mod. Phys. **64**, 649 (1992).
10. F. Karsch, E. Laermann and C. Schmidt, Phys. Lett. B **520**, 41 (2001).
11. D.T. Son and M.A. Stephanov, arXiv:hep-ph/0401052.
12. P.C. Hohenberg and B.I. Halperin, Rev. Mod. Phys. **49**, 435 (1977).
13. B. Berdnikov and K. Rajagopal, Phys. Rev. D **61**, 105017 (2000).
14. C. Schmidt, C. R. Allton, S. Ejiri, S. J. Hands, O. Kaczmarek, F. Karsch and E. Laermann, Nucl. Phys. Proc. Suppl. **119**, 517 (2003).

THERMAL PHASE TRANSITION OF DENSE QCD

T. HATSUDA

Department of Physics, The University of Tokyo,
Tokyo 113-0033, Japan

Using the Ginzburg-Landau (GL) free energy, we study the effects of thermal fluctuations of gluons and the diquark pairing field on the superconducting-to-normal state phase transition in a three-flavor color superconductor. At high baryon densities, the system becomes a Type I superconductor and the gluonic fluctuations dominate over diquark fluctuations. The thermal gluons induce a cubic term in the GL free energy, as well as large corrections to quadratic and quartic terms of the order parameter. The cubic term leads to a relatively strong first order transition in comparison to the very weak first order transitions in metallic Type I superconductors. The strength of the first order transition decreases with increasing baryon density. In addition, gluonic fluctuations lower the critical temperature of the first order transition. We derive explicit formulae for the critical temperature and the discontinuity of the order parameter at the critical point. The validity of the first order transition obtained in the one-loop approximation is also examined by estimating the size of the critical region.

1. Introduction

Degenerate quark matter at high baryon density is expected to undergo a phase transition to a color superconducting state.[1] The properties of color superconductors have been much studied in various approaches.[2,3,4,5,6] A major difference of color superconductors and metallic superconductors is that the former is a highly relativistic system in which the long-range magnetic interaction (dynamically screened only by Landau-damping[7]) is responsible for the formation of the non-standard form of the superconducting gap, Δ.[8] Despite this non-BCS feature of color superconductivity, the finite temperature transition in mean-field theory is of second order, with a BCS critical temperature $T_c \simeq 0.57\Delta$.[9]

In this article, we address the question of thermal fluctuations of the gluons and of the diquark pairing [10]. The similar thermal fluctuations were first studied in BCS superconductors in metals in Ref. 11, and in finite temperature field theory in Ref. 12. In metalic superconductors, Type I materials have a *weak* first order transition, characterized by a cubic term of

the order parameter in the GL free energy induced by the thermal photons. A similar mechanism can be expected in color superconductors.[2] However, there are some crucial differences from metallic superconductors. Firstly, the fluctuations of the diquark field alone may lead to a first order phase transition.[13,14] Secondly, thermal gluon fluctuations may induce a relatively *strong* first order transition, in contrast to the metallic case partly because of the relativistic nature of the quarks and partly because of the large coupling constant α_s.

We study the effects of fluctuations of the diquark and gluon fields on the phase transition via their effects on the GL free energy, emphasizing the relative importance of the diquark and gluon fluctuations, and of a theoretical treatment of gluon fluctuations that consistently keeps all terms of the same order. We estimate, semi-quantitatively, the strength of first order transition as well as the modification of the transition temperature. Unlike the conclusion of Ref. 2, we find that the first order transition becomes weak with increasing baryon density, and that the transition temperature is lowered from its mean-field value.

2. Ginzburg-Landau Free Energy

Let us consider a system of degenerate massless u, d, s quarks with a common Fermi momentum. The pairng gap of the quark of color b and flavor j with that of color c and flavor k in the $J^P = 0^+$ channel is written as ϕ_{bcjk}. By further assuming that the pairing takes place in the color-flavor antisymmetric channel which is expected to be the most attractive in the weak coupling, the gap is parametrized as[4,5] $\phi_{bcjk} = \epsilon_{abc}\epsilon_{ijk}(\mathbf{d})^i_a$. Under $G = SU(3)_c \times SU(3)_{L+R} \times U(1)_B$, $\mathbf{d}^i_a$ transforms as a vector and belongs to the $(3^*, 3^*)$ representation of $SU(3)_c$ and $SU(3)_{L+R}$.

The GL free energy in three spatial dimensions, written in terms of $\mathbf{d}^i_a(\mathbf{x})$, with coupling to the $SU(3)_c$ gluon gauge fields, reads [5]

$$S = \bar{\alpha}\sum_a |\mathbf{d}_a|^2 + \beta_1(\sum_a |\mathbf{d}_a|^2)^2 + \beta_2(\sum_{ab} |\mathbf{d}^*_a \cdot \mathbf{d}_b|)^2 \qquad (1)$$
$$+2\kappa_T \sum_a |(D_l\mathbf{d})_a|^2 + \frac{1}{4}G^\alpha_{lm}G^\alpha_{lm}.$$

The parameters $\bar{\alpha}$, β_1, and β_2 characterize the homogeneous part of the free energy, while κ_T is the stiffness parameter. Since $\mathbf{d}^i_a$ is antisymmetric in color space, the color-covariant derivative reads $(D_l\mathbf{d})_a = \partial_l\mathbf{d}_a + \frac{i}{2}gA^\alpha_l(\lambda^{\alpha *}\mathbf{d})_a$, where the $\lambda^{\alpha *}$ are the complex conjugates of the Gell-Mann matrices. G_{lm} is the spatial part of the gluon field-strength tensor.

The free energy density Eq.(1) may be interpreted as an $SU(3)_c \times SU(3)_f$ scalar field theory coupled to an $SU(3)_c$ gauge field in three-spatial dimensions. Eq. (1) is model independent and valid near the critical temperature of the second order transition.

Although the general analysis does not require specific values of the parameters in the GL free energy, it is useful to bear in mind their characteristic scales, as found in weak coupling:

$$\bar{\alpha} = 4N(\mu/3)\ln\left(\frac{T}{T_c}\right), \quad \beta_1 = \beta_2 = 3\kappa_T = \frac{7\zeta(3)}{8(\pi T_c)^2}N(\mu/3), \tag{2}$$

where $N(\mu/3) = (\mu/3)^2/(2\pi^2)$, $\zeta(3) = 1.2020\cdots$, μ the *baryon* chemical potential and T_c the critical temperature in the weak coupling.

The color-flavor locking (CFL) and isoscalar (IS) ordering in three-flavor matter are characterized as $\mathbf{d}_a^i = d\ \delta_{ai}$ (CFL), $d\ \delta_{a3}\delta_{i3}$ (IS), respectively. Since $\bar{\alpha}$ changes sign at the mean field T_c, it is useful to introduce the reduced tempetature as $\bar{\alpha} = \alpha_0(T - T_c)/T_c \equiv \alpha_0 t$. Whether the paired state just below T_c is CFL or IS depends on the values of β_1 and β_2. In the weak coupling limit where $\beta_1 = \beta_2$ and $\alpha_0 \sim \mu^2$, the CFL ordering is favored with $d_{\rm CFL} \sim T_c\sqrt{|t|}$ for $T \sim T_c$.

3. Fluctuation about the mean-field

Let us consider the effect of thermal fluctuations of the spin-zero diquark (scalar) field and the spin-one gluon fields about their mean values, in the Gaussian approximation. The fluctuations of the gauge fields at the same spatial coordinate, are given by the thermal average, $\langle \mathbf{A}^\alpha \mathbf{A}^\beta \rangle$, of the product of the gauge fields:

$$\langle \mathbf{A}^\alpha \mathbf{A}^\beta \rangle = 2\delta_{\alpha\beta}\, T \int_{|\mathbf{k}|<\Lambda} \frac{d^3k}{(2\pi)^3} \frac{1}{\mathbf{k}^2 + (m_A)^2_{\alpha\alpha}}, \tag{3}$$

where we have taken the Coulomb gauge $\nabla \cdot \mathbf{A} = 0$. The momentum Λ is an ultraviolet cutoff, which corresponds to an upper bound on the wave numbers of the classical thermal fluctuations with zero Matsubara frequency. This cutoff is inversely proportional to the size of the quark pairs ($\Lambda \sim d \sim T_c$).[17,11] In the following we take $\Lambda = T_c$ for simplicity. In Eq. (3), $(m_A)_{\alpha\beta}$ is the Meissner mass matrix. Its components are listed in Table 1.

In weak coupling, we have $m_A \sim g\mu\sqrt{|t|}$ for $T \sim T_c$. Since the Meissner mass is vanishingly small compared to $\Lambda \sim T_c$ near the second order critical

Table 1. The inverse squared correlation lengths of the scalar (d) and gauge (A) fluctuations, m_d^2 and m_A^2, together with the number of degenerate modes corresponding to each fluctuation.

	IS		CFL	
	$m_{d,A}^2$	degeneracy	$m_{d,A}^2$	degeneracy
d	$2(\beta_1+\beta_2)\ d^2/\kappa_T$	1	$2(3\beta_1+\beta_2)\ d^2/\kappa_T$	1
	$-\beta_2 d^2/\kappa_T$	8	$2\beta_2 d^2/\kappa_T$	8
	0	9	0	9
A	$\frac{4}{3}\kappa_T g^2 d^2$	1		
	$\kappa_T g^2 d^2$	4	$2\kappa_T g^2 d^2$	8
	0	3		

point, we may expand Eq. (3) in terms of $(m_A)_{\alpha\alpha}/T_c$ as

$$\langle \mathbf{A}^\alpha \mathbf{A}^\beta \rangle = \delta_{\alpha\beta} \frac{TT_c}{\pi^2} \left[1 - \frac{\pi}{2} \frac{(m_A)_{\alpha\alpha}}{T_c} + \left(\frac{(m_A)_{\alpha\alpha}}{T_c^2} \right)^2 + \cdots \right]. \tag{4}$$

One can similarly calculate the expectation value of the product of the fluctuations of the scalar diquark field.

The number of modes corresponding to a given correlation length is also indicated in Table 1. The ninefold massless scalar modes ($m_d = 0$) may be understood as follows. The IS state, characterized by $\mathbf{d}_a^i = \delta_{a3}\delta_{i3} d$, is invariant under $G' = SU(2)_c \times SU(2)_{L+R} \times U(1) \times U(1)$. Here the first $U(1)$ symmetry corresponds to a simultaneous rotation in baryon-color space, and the second to a simultaneous rotation in baryon-flavor space. Thus the number of Nambu-Goldstone bosons is dim[G]-dim[G'] $= 17 - 8 = 9$. The CFL state, characterized by $\mathbf{d}_a^i = d\delta_{ai}$, is invariant under $G' = SU(3)_{c+L+R}$. Thus one has $17 - 8 = 9$ Nambu-Goldstone bosons in this case too. Note that not all massless scalar modes with $m_d = 0$ in Table 1 are physical. Parts of them are absorbed in the longitudinal components of the gluon. As a result, only four scalar modes out of nine are physical in the IS state, while only one scalar mode is physical in the CFL state. However, as we show later, the physical massless modes do not modify the structure of the one-loop free energy. In weak coupling, the masses of the physical modes behave as $m_d \sim T_c\sqrt{|t|}$ for $T \sim T_c$.

As discussed in Refs. 11 and 17, the initial term in the expansion Eq. (4) proportional to TT_c simply shifts the critical temperature, T_c, of the second order transition. On the other hand, the terms proportional to $TT_c m_d$ and $TT_c m_A$ in Eq. (4) induce a cubic term of the order parameter in the GL potential, and thus generally drive the first order phase transition.[11] The terms $TT_c m_d^2$ and $TT_c m_A^2$ in Eq. (4) modify the coefficient of quadratic term of the order parameter in the GL potential, which turn out to be

important in determining the strength of the first order transition.

4. Critical region

Let us now discuss the critical regions for scalar and gauge fluctuations. In the immediate vicinity of T_c, fluctuations of the soft modes become significant, leading to a breakdown of the Gaussian approximation.[17] The temperature span of this critical region can be determined from standard scaling arguments near the critical point. For our problem, the typical spatial scales of scalar and gauge field fluctuations are m_d^{-1} and m_A^{-1}, respectively. Using these scales, we can thus define the "effective" coupling strengths among the soft modes for the scalar and gauge fields as $\beta_i T_c/(32\pi^2\kappa_T^2 m_d)$ and $g^2 T_c/(2\pi^2 m_A) = 2\alpha_s T_c/(\pi m_A)$, respectively. These coupling strengths should be small enough that the calculation of the free energy in a loop expansion is meaningful. Also the three dimensional effective theory for the soft modes is meaningful only when the masses of the soft mode are small enough compared to $\Lambda \sim T_c$. Combining the conditions discussed above, one finds necessary (but not sufficient) conditions for the Gaussian approximation to be valid,

$$\frac{|\beta_i|}{32\pi^2\kappa_T^2} T_c \ll m_d \ll T_c, \quad \frac{2\alpha_s}{\pi} T_c \ll m_A \ll T_c, \tag{5}$$

namely the temperature should be inside the appropriate region where the masses of the soft modes are not too small and not too large. Also the above equations imply that the coupling constants should be sufficiently small, $|\beta_i|/(32\pi^2\kappa_T^2) \ll 1$ and $2\alpha_s/\pi \ll 1$.

Let us introduce a ratio of the typical spatial scales of scalar and gauge field fluctuations

$$\kappa^2 \equiv \left(\frac{m_d}{m_A}\right)^2 \simeq \frac{|\beta_i|}{4\pi\alpha_s\kappa_T^2} \to \frac{10^3}{\alpha_s}\left(\frac{T_c}{\mu}\right)^2, \tag{6}$$

where the last equation is valid only in the weak coupling and a numerical coefficient of order unity is neglected. As we shall see later, the gauge (scalar) fluctuations are more important than the scalar (gauge) flucutations for $\kappa \ll 1 (\gg 1)$. In the weak coupling, κ is considerably smaller than unity.

The parameter κ defined in Eq. (6) has also the meaning of Ginzburg-Landau parameter[19] that distinguishes the type of color superconductor under an external chromomagnetic field; $\kappa = \delta/\xi$ where δ is the penetration depth, and ξ the coherence length. It was recently shown, by the explicit

calculation of the surface energy of a domain wall separating the normal and superconducting phases in the presence of an external magnetic field, that Type I color superconductor is realized for $\kappa_{\rm IS} < 1/\sqrt{2}$ in the IS state[5] and for $\kappa_{\rm CFL} < 0.589$ in the CFL state[20] with $\beta_1 = \beta_2$. As Eq. (6) indicates, $m_d \ll m_A$ is realized in the weak coupling. Therefore, the color superconductor is Type I at least at very high density. Whether the system is Type I or Type II at low densities is not known.

In the weak coupling limit, the Ginzburg criterion (the first of the inequalities in Eq. (5)) becomes

$$t \gg \epsilon_d \equiv 10^2 \left(\frac{T_c}{\mu}\right)^4, \quad t \gg \epsilon_A \equiv 10\alpha_s \left(\frac{T_c}{\mu}\right)^2. \tag{7}$$

where we have neglected unimportant numerical coefficients of order unity. In the weak coupling, the ratio T_c/μ is exponentially suppressed as $\exp(-3\pi^2/\sqrt{2}g)$. Therefore one finds $1 \gg \epsilon_A \gg \epsilon_d$ at high baryon density. Note also the relation $\kappa^2 \sim 10^{-2}\epsilon_d/\epsilon_A$; the relative sizes of the critical regions are related to the types of color superconductor.

We briefly summarize the results obtained so far. For a Type I color superconductor, as realized in the high density region, gluon fluctuations give the dominant correction to the free energy. In the one-loop approximation, the gluon fluctuations change the order of the phase transition from second to first, and modify the critical temperature to T_c^*. If the relative shift of the critical temperature $(T_c^* - T_c)/T_c$ is well outside the critical region dictated by Eq. (5), the Gaussian approximation is consistent. This situation is quite analogous to the first order transition in Type I metallic superconductor.[11]

On the other hand, in a Type II color superconductor, which may be realized in the low density region for T_c comparable to μ, scalar fluctuations are not at all negligible. Furthermore, the Gaussian approximation becomes highly questionable. A renormalization group analysis with an ϵ expansion shows that, even without gauge fields, scalar fluctuations alone induce a first order transition[14] in an $SU(n) \times SU(n)$ model with $n \geq 3$. Our model falls in this category when the coupling of the gauge field with the diquarks is neglected. A further complication for Type II color superconductors is that the non-Abelian self-coupling of the gauge field may not be negligible.

Once we take into account fluctuations of the order-parameter and the gauge fields, we need to consider the phase structure in the four dimensional $(\beta_1, \beta_2, \kappa_T, \alpha_s)$ space. Fig. 1 shows its projection onto the two dimensional (β, α_s) space with a constraint $\beta \equiv \beta_1 = \beta_2 = 3\kappa_T$. The CFL phase in the

weak coupling limit lies on this reduced space. The solid line in the figure is a boundary separating Type I and Type II color superconductors which is characterized by $\kappa = 1$ in Eq.(6). For the Gaussian approximation on the gauge field to be reliable, $2\alpha_s/\pi < 1$ should also be satisfied. Therefore, as long as we stay in the shaded region in the figure, the one-loop approximation taking into acount only the gauge field is reliable to study the effect of the thermal fluctuation. Also shown in the figure by the dashed line is a relation between α_s and β (both functions of μ) in the weak coupling. The weak coupling regime is found to be well inside the shaded area.

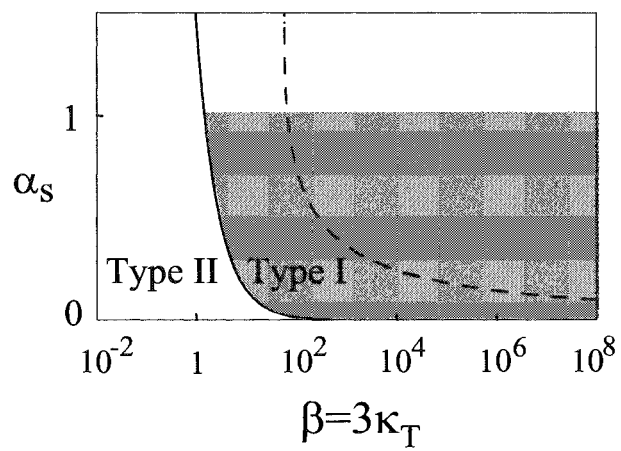

Figure 1. The phase structure in the two dimensional (β, α_s) space. The solid line characterized by $\kappa = 1$ is the boundary between Type I (right side) and Type II (left side) superconducting behavior. The dashed line shows α_s as a function of β, calculated in the weak coupling. The loop expansion for gauge field fluctuations is valid in the shaded area.

In Fig. 2, we show κ calculated in weak coupling. The dependences of μ on T_c and α_s are taken from the weak coupling results. The figure indicates that $\kappa \ll 1$ (Type I superconductor) is satisfied not only at high density but also at moderate densities, to the extent that one can rely on the extrapolation using the weak coupling formulae.

5. First order transition induced by gauge field

In this section, we assume a Type I color superconductor and evaluate the free energy of the CFL state up to the one-loop order, taking into account

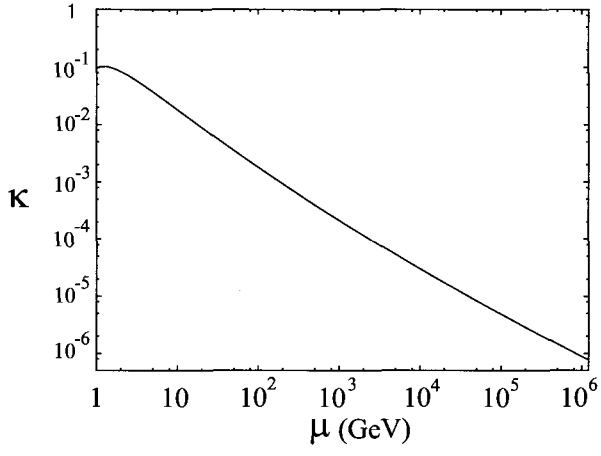

Figure 2. The parameter κ calculated as a function of μ in the weak coupling approximation.

only the gauge field fluctuations. The free energy difference between the superfluid and normal phases, $F_{\rm eff}(d)$, in this approximation reads, in the Coulomb gauge,

$$F_{\rm eff}(d) = S(d) + \frac{1}{2}\ln\det\left(\frac{\partial^2 S}{\partial \mathbf{A}^\alpha \partial \mathbf{A}^\beta}\right) - F_{\rm eff}(d=0) \tag{8}$$

$$= S(d) + T\sum_\alpha \left[a_2 (m_A)^2_{\alpha\alpha} - a_3 (m_A)^3_{\alpha\alpha} + a_4 (m_A)^4_{\alpha\alpha}\right], \tag{9}$$

$$\equiv 3\tilde{\alpha} d^2 - q d^3 + r d^4. \tag{10}$$

where $a_2 = T_c/(2\pi^2), a_3 = 1/(6\pi), a_4 = 1/(4\pi^2 T_c)$ and m_A is given in Table 1. At each order of the expansion of $F_{\rm eff}(d)$ in terms of d, dominant contribution comes from the modes with larger mass which is evident from Eq.(9).

The terms in Eq.(10) are explicitly written as

$$3\tilde{\alpha} d^2 = \left[3\bar{\alpha} + \frac{T T_c}{\pi^2}\left(32\pi\kappa_T \alpha_s\right)\right] d^2, \tag{11}$$

$$q d^3 = \left[\frac{T}{\pi}\frac{8\sqrt{2}}{3}\left(4\pi\kappa_T\alpha_s\right)^{\frac{3}{2}}\right] d^3, \tag{12}$$

$$r d^4 = \left[3(3\beta_1 + \beta_2) + \left(\frac{T}{T_c}\right) 128\kappa_T^2 \alpha_s^2\right] d^4. \tag{13}$$

The effects of gauge fluctuations are three-fold: First, they increase the

size of the quadratic term proportional to d^2. This increase implies that thermal fluctuations tend to make the superconducting phase less energetically favorable. Second, we find a cubic term with a negative coefficient, $-q$, which favors the superconducting phase. Furthermore, the second-order transition found in mean-field theory turns into a first order one due to this term, independent of the magnitude of μ. Finally, we find a positive correction to the quartic term from the fluctuations. Like the correction to the quadratic term, this term acts against the superconducting phase. The sum of these three corrections leads to a first order transition which is significantly stronger than the metallic superconductor, but is much weaker than that claimed in Ref. 2 where the quartic correction was neglected.

For later convenience, we define a "renormalized" critical temperature T_c' at which $\tilde{\alpha} = 0$. Then, one finds, $T_c'/T_c = [1 + (T_c^2/\alpha_0)(32\kappa_T\alpha_s/3\pi)]^{-1}$ and $\tilde{\alpha} = \alpha_0(T - T_c')/T_c' \equiv \alpha_0 t'$. The decrease of the renormalized critical temperature from the mean-field one ($T_c' < T_c$) is consistent with the fact that the contribution of the fluctuations to the quadratic term makes the superconducting state less favorable. On the other hand the true critical temperature of the first order transition, T_c^*, is the temperature where the free energy has two degenerate minima, $d = 0$ and $d = d^* \neq 0$. Then one finds

$$\frac{T_c^*}{T_c'} = 1 + \frac{q^2}{12\alpha_0 r}, \quad d^* = \frac{q}{2r}. \tag{14}$$

Due to the effect of the cubic term $-qd^3$ in the free energy which tends to stabilize the superconducting phase, the critical temperature of the first order transition is increased from T_c' as seen in Eq. (14). Thus the ratio T_c^*/T_c' is one of the measures of the strength of first order transition induced by the thermal gluons. One may also define another measure such as the jump of the diquark condensate at $T = T_c^*$ relative to its $T = 0$ value, d^*/d_0, where $d_0 = d(T = 0) = (\pi/e^\gamma)T_c$ with γ being the Euler constant. Using the formulae for β_i and κ_T in the weak coupling, we find the following estimates at high density;

$$\frac{T_c^*}{T_c} - 1 \sim -\frac{\alpha_s}{10^2}, \quad \frac{d^*}{d_0} \sim \frac{10}{\sqrt{\alpha_s}}\left(\frac{T_c}{\mu}\right) \sim 0.3\kappa, \tag{15}$$

The jump of the order parameter at the critical point, d^*/d_0, is at most a few percent level for $\mu > 1$ GeV, but is much larger than that expected in Type I metalic superconductors. Also, the first order transition becomes weaker logarithmically as μ increases, and approaches a second order transition at $\mu = \infty$. As we have mentioned, this is in contrast to

the result of Ref. 2 in which the first order transition becomes strong as μ increases. Such behavior is unreasonable because the coupling of gluons and diquarks becomes weak at high density due to the asymptotic freedom. The discrepancy between our result and that in Ref. 2 originates from the fact that thermal corrections to the quartic

term in the free energy were not taken into account in Ref. 2. As we approach to the baryon density close to the confinement-deconfinement transition, $\mu \sim 1$ GeV, the fluctuations of the scalar field as well as the non-Abelian interactions of the gluons neglected in our calculation become important. Therefore the results here may be modified qualitatively in such region. Study of the super-to-normal transition in the low density region remains an interesting open question.

Let us now discuss the reliability of the first order phase transition obtained in the weak coupling, from the point of view of the critical region examined in Sec. 4. The first inequalities in Eq. (5) can be interpreted as conditions for the size of $T - T_c$ or alternatively the conditions for the size of d: If $T_c^* - T_c$ or d^* is too small, critical fluctuations are not negligible and one cannot trust the result of the one-loop approximation. In the weak coupling, we have $t^* \equiv |T_c^* - T_c|/T_c \simeq 10^{-2}\alpha_s$ as well as $T_c/\mu \ll 1$, which implies that the conditions given in Eq.(7), $t^* \gg \epsilon_{A,d}$, are well satisfied. Namely the critical temperature of the first order transition is outside the critical region of the diquark and gauge fluctuations. Also, by substituting d^*/d_0 in Eq. (15) into the first inequalities in (5), one finds $\alpha_s/\beta \ll 1.6\ \pi^5$ and $\alpha_s \ll \pi^2/6$, which should be satisfied for the effective three-dimensional approach to be valid. They are in fact well satisfied, insofar as the couplings stay in the shaded region in Fig. 1.

6. Summary

We have discussed the effect of thermal fluctuations of diquarks and the gluons on the superconducting-to-normal phase transition in a three-flavor color superconductor. For this purpose, we adopted the Ginzburg-Landau free energy in three-spatial dimensions. The relative importance of the two types of fluctuations is controlled by κ, the ratio of the masses of the scalar field and the gluon just below the critical temperature; κ is also identified as the Ginzburg-Landau parameter which differentiates Type I and Type II color superconductors. In the high density regime where the weak coupling approximation is valid, the system is Type I and the gauge fluctuations dominate over the scalar fluctuation.

The thermal phase transition of Type I color superconductor, which is second order in the mean field theory, becomes first order due to the cubic term in the GL free energy. The first order transition weakens (strengthens) as the baryon density increases (decreases). This is in sharp contrast to that found in Ref. 2. The difference stems from the thermal correction to the quartic term missing in Ref. 2.

Our general considerations in this paper for Type I superconductor are valid insofar as the parameters in the Ginzburg-Landau free energy stay in the shaded area in Fig. 1, which corresponds to high density region. On the other hand, in the low density, strong coupling region, not only scalar fluctuations but also non-Abelian interactions among thermal gluons are not negligible. Furthermore, the strange quark mass plays an important role in the unlocking transition from the CFL state to the IS state [21]. The anti-quark pairing and the non-perturbative running of α_s at low momentum are also not negligible at low density.[22] These effects may change the nature of the phase transition at low density from what is realized at high densities. Lattice simulations of the $SU(3)_c \times SU(3)_{L+R} \times U(1)_B$ sigma-model + $SU(3)_c$ gauge field introduced in the present paper would be a good starting point to analyse the phase structure in the strong coupling region.

Acknowledgments

This work is based on a collabolation with T. Matsuura (Univ. of Tokyo), K. Iida (RIKEN) and G. Baym (Univ. of Illinois). It was partially by the Grants-in-Aid of the Japanese Ministry of Education, Culture, Sports, Science, and Technology (No. 15540254).

References

1. K. Rajagopal and F. Wilczek, hep-ph/0011333.
   M.G. Alford, *Ann. Rev. Nucl. Part. Sci.* **51**, 131 (2001).
2. D. Bailin and A. Love, *Phys. Rep.* **107**, 325 (1984).
   M. Iwasaki and T. Iwado, *Phys. Lett.* **B350**, 163 (1995).
3. M. Alford, K.Rajagopal, and F. Wilczek, *Phys. Lett.* **B422**, 247 (1998).
   R. Rapp, T. Schäfer, E. V. Shuryak and M. Velkovsky, *Phys. Rev. Lett.* **81**, 53 (1998).
4. K. Iida and G. Baym, *Phys. Rev.* **D63**, 074018 (2001); *Erratum Phys. Rev.* **D66**, 059903 (2002).
5. K. Iida and G. Baym, *Phys. Rev.* **D66**, 014015 (2002).
6. K. Iida and G. Baym, *Phys. Rev.* **D65**, 014022 (2002).
7. G. Baym, H. Monien, C. J. Pethick and D. G. Ravenhall, *Phys. Rev. Lett.* **64**, 1867 (1990).

8. D. T. Son, *Phys. Rev.* **D59**, 094019 (1999).
9. R. D. Pisarski and D. H. Rischke, *Phys. Rev.* **D61**, 074017 (2000).
10. T. Matsuura, K. Iida, T. Hatsuda and G. Baym, hep-ph/0312042, Phys. Rev. **D** (2004) in press.
11. B.I. Halperin, T.C. Lubensky and S.-k. Ma, *Phys. Rev. Lett.* **32**, 292 (1974).
12. G. Baym and G. Grinstein, *Phys. Rev.* **Dl5**, 2897 (1977).
13. R. D. Pisarski and D. H. Rischke, *Phys. Rev. Lett.* **83**, 37 (1999).
14. A.J. Paterson, *Nucl. Phys.* **B190**, 188 (1981).
15. M.G. Alford, J. Berges and K. Rajagopal, *Nucl. Phys.* **B558**, 219 (1999). T. Schäfer and F. Wilczek, *Phys. Rev.* **D60** 074014 (1999). H. Abuki, *Prog. Theor. Phys.* **110**, 937 (2003).
16. R.D. Pisarski, *Phys. Rev.* **C62**, 035202 (2000).
17. V.L. Ginzburg, *Fiz. Tverd. Tela* **2**, 2031 (1960) [*Sov. Phys. Solid State* **2**, 1824 (1961)].
18. W.E. Brown, J.T. Liu, and H.-c. Ren, *Phys. Rev.* **D62**, 054016 (2000).
19. V. L. Ginzburg and L. D. Landau, *Zh. Eksp. Theor. Fiz.* **20**, 1064 (1950). A.A. Abrikosov, *Zh. Eksp. Teor. Fiz.* **32**, 1442 (1957) [*Soviet Physics JETP* **5**, 1174 (1957)].
20. I. Giannakis and H-c. Ren, *Nucl. Phys.* **B669**, 462 (2003).
21. K. Iida, T. Matsuura, M. Tachibana and T. Hatsuda, hep-ph/0312363.
22. H. Abuki, T. Hatsuda and K. Itakura, *Phys. Rev.* **D65**, 074014 (2002).

PSEUDOGAP IN COLOR SUPERCONDUCTIVITY*

M. KITAZAWA

Department of Physics,
Kyoto University,
Kyoto, 606-8502, Japan
E-mail: masky@ruby.scphys.kyoto-u.ac.jp

We show that the pseudogap of the quark density of states is formed in hot quark matter as a precursory phenomenon of the color superconductivity on the basis of a low-energy effective theory. We clarify that the soft mode of the di-quark pair field gives rise to a peculiar behavior of the quark dispersion relation and a short life-time of the quasiparticles near the Fermi surface, both of which make a depression of the density of states of quarks. Our result suggests that the appearance of the pseudogap is a universal phenomenon of strong coupling superconductors, irrespective of the dimensionality. A brief comment is given on the behavior of the specific heat above the critical temperature.

1. Introduction

It is an intriguing subject in hadron physics to determine the phase structure of QCD at large chemical potential μ and relatively low temperature T. The recent renewed interest in the color superconductivity (CS)[3] stimulated intensive studies in these region, which in turn are revealing rich physics of the high density hadron/quark matter with CS[4].

Possible physical realizations of the CS in compact stars or ultrarelativistic heavy-ion collisions are also discussed actively. Here, note that these systems are at relatively low density ρ where the strong coupling nature of QCD may show up. The strong coupling may invalidate the mean-field approximation à la BCS theory[3], and make the so-called Ginzburg region so wide that precursory fluctuations of the pair field can have a prominent strength and may give rise to physically significant effects even above the critical temperature T_c[5].

*This talk is based on the work in collaboration with T. Koide, T. Kunihiro and Y. Nemoto[1] and the work with T. Kunihiro[2].

The existence of the large fluctuations suggests us that the CS may share some basic properties with the high-T_c superconductivity (HTSC) of cuprates rather than with the usual superconductivity in metals. One of the most characteristic phenomena of HTSC is the existence of the *pseudogap*, i.e., the anomalous depression of density of state (DOS) $N(\omega)$ as a function of the fermion energy ω around the Fermi surface above T_c. Although the mechanism of the pseudogap in HTSC is still controversial, precursory fluctuations of the pair field and the quasi-two dimensionality of the system seem to be basic ingredients to realize the pseudogap[6]. Interestingly enough, a pseudogap above T_c can be realized by the fluctuation of the pair field even in the three-dimensional nuclear matter at low densities[7]. Thus, one may naturally expect that although the relativistic kinematics may introduce additional complications, the pseudogap of the quark density of states exists as a precursory phenomenon of the CS at finite T. In this talk, we shall show that it is the case using a chiral model[1]. Our result also suggests that the appearance of the pseudogap is a universal phenomenon of strong coupling superconductors, irrespective of the dimensionality.

2. Formalism

To describe a system at relatively low T and ρ, it is appropriate to adopt a low-energy effective theory of QCD. Here we employ the Nambu-Jona-Lasinio model with the scalar-diquark interaction in the chiral limit,

$$L = \bar{\psi} i\partial\!\!\!/ \psi + G_C \sum_A (\bar{\psi} i\gamma_5 \tau_2 \lambda_A \psi^C)(\bar{\psi}^C i\gamma_5 \tau_2 \lambda_A \psi) + G_S[(\bar{\psi}\psi)^2 + (\bar{\psi} i\gamma_5 \vec{\tau}\psi)^2], \quad (1)$$

where $\psi^C \equiv C\bar{\psi}^T$, with $C = i\gamma_2\gamma_0$ being the charge conjugation operator. Here, τ_2 and λ_A mean the antisymmetric flavor SU(2) and color SU(3) matrices, respectively. The coupling G_S and the three dimensional momentum cutoff $\Lambda = 650$ MeV are determined so as to reproduce the physical quantities and we choose $G_C = 3.11\text{GeV}^{-2}$.

We neglect the gluon degrees of freedom, especially their fluctuation, which is known to make the CS phase transition first order in the weak coupling region[3]. However, nothing definite is known on the characteristics of the CS in the intermediate density region. In this work, simply assuming that the fluctuation of the pair field dominates that of the gluon field, we examine the effects of the precursory fluctuations of the diquark pair field on the quark sector in the T-matrix approximation (T-approximation[8]) [6,7].

The DOS $N(\omega)$ is given by

$$N(\omega) = 4 \int \frac{d^3\boldsymbol{k}}{(2\pi)^3} \mathrm{Tr}_{\mathrm{c,f}} \left[\rho_0(\boldsymbol{k},\omega)\right], \tag{2}$$

where $\rho_0 = (1/4)\mathrm{Tr}[\gamma_0 A]$ with $A(\boldsymbol{k},\omega) = -1/\pi \cdot \mathrm{Im}G^R(\boldsymbol{k},\omega)$ denoting the spectral function of a single quark. The retarded Green function G^R is given by the analytic continuation of the imaginary-time Green function $\tilde{G}$, which obeys the following Dyson-Schwinger equation

$$\tilde{G}(\boldsymbol{k},\omega_n) = \tilde{G}_0(\boldsymbol{k},\omega_n)\{1 + \tilde{\Sigma}(\boldsymbol{k},\omega_n)\tilde{G}(\boldsymbol{k},\omega_n)\}, \tag{3}$$

where $\tilde{G}_0(\boldsymbol{k},\omega_n) = [(i\omega_n+\mu)\gamma^0 - \boldsymbol{k}\cdot\boldsymbol{\gamma}]^{-1}$ and$\tilde{\Sigma}(\boldsymbol{k},\omega_n)$ denote the free Green function and the self-energy in the imaginary time with $\omega_n = (2n+1)\pi T$.

As was shown in our previous work[5], the fluctuating diquark pair field develops a collective mode (the *soft mode* of the CS) at T above but in the vicinity of T_c, in accordance with the Thouless criterion[9]. Our point in this work is that the soft mode in turn contributes to the self-energy of the quark field, thereby can modify the DOS so much to give rise to a pseudogap.

The quark self-energy $\tilde{\Sigma}$ owing to the soft mode may be obtained by the infinite series of the ring diagrams shown in Fig. 1;

$$\tilde{\Sigma}(\boldsymbol{k},\omega_n) = 8T \sum_{n_1} \int \frac{d^3\boldsymbol{k}_1}{(2\pi)^3} \tilde{\Xi}(\boldsymbol{k}+\boldsymbol{k}_1, \omega_n + \omega_{n_1}) \tilde{G}_0(\boldsymbol{k}_1, \omega_{n_1}), \tag{4}$$

$$\tilde{\Xi}(\boldsymbol{k},\nu_n) = -G_C \left(1 + G_C Q(\boldsymbol{k},\nu_n)\right)^{-1}, \tag{5}$$

with the lowest particle-particle correlation function $Q(\boldsymbol{k},\nu_n)$ [5] and $\nu_n = 2n\pi T$.

Inserting Eqs. (4) and (5) into Eq. (3) and performing the analytic continuation to the upper half of the complex energy plane, we obtain the retarded Green function, $G^R(\boldsymbol{k},\omega) = (G_0^{-1}(\boldsymbol{k},\omega+i\eta) - \Sigma^R(\boldsymbol{k},\omega))^{-1}$, with $\Sigma^R(\boldsymbol{k},\omega) = \tilde{\Sigma}(\boldsymbol{k},\omega_n)|_{i\omega_n=\omega+i\eta}$. Here, the self-energy Σ^R has the matrix structure $\Sigma^R(\boldsymbol{k},\omega) = \Sigma_0(\boldsymbol{k},\omega)\gamma^0 - \Sigma_{\mathrm{v}}(\boldsymbol{k},\omega)\hat{\boldsymbol{k}}\cdot\boldsymbol{\gamma} \equiv \gamma^0(\Sigma_-\Lambda_- + \Sigma_+\Lambda_+)$, where $\Lambda_\mp = (1 \pm \gamma^0\boldsymbol{\gamma}\cdot\hat{\boldsymbol{k}})/2$ denotes the projection operators onto the positive and negative energy states. $\Sigma_\mp = \Sigma_0 \mp \Sigma_{\mathrm{v}}$ represents the self-energies of the particles and anti-particles, respectively.

3. Numerical Results

Since $\rho_0(\boldsymbol{k},\omega)$ for $\omega > -\mu$ is well approximated solely by the positive-energy part, we see the characteristic properties of the quark self-energy

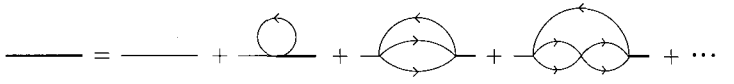

Figure 1. The Feynman diagrams representing the quark Green function.

Σ_-. We show the real and imaginary part of Σ_- at $\mu = 400\text{MeV}$ and the reduced temperature $\varepsilon \equiv (T - T_c)/T_c = 0.01$ in Fig. 2. From figure, one sees that $\text{Re}\Sigma_-$ has a rapid increase around $\omega = \mu - k$. The behavior of $\text{Re}\Sigma_-$ affects the quark dispersion relation $\omega = \omega(k)$, since it is given by $\omega(k) + \mu - |\boldsymbol{k}| - \text{Re}(\boldsymbol{k}, \omega(k)) = 0$. In particular, $\text{Re}\Sigma_-$ around $\omega = |\boldsymbol{k}| - \mu$ which is the dispersion relation of the free system is responsible for the dispersion relation. The rapid increase of $\text{Re}\Sigma_-$ near $\omega = |\boldsymbol{k}| - \mu$ appears around the Fermi energy $\omega = 0$ or the Fermi momentum $k = 400\text{MeV}$, which means that the dispersion relation is strongly affected around the Fermi surface. The rapid increase of $\text{Re}\Sigma_-$ implies the similar behavior of the dispersion relation, and hence there appears a rapid increase of $\omega(k)$ around the Fermi momentum $k = 400\text{MeV}$, although not shown because of the lack of space. Therefore, the DOS proportional to $(\partial\omega_-/\partial k)^{-1}$ becomes smaller near the Fermi surface, which suggests the existence of a pseudogap, provided that the imaginary part $\text{Im}\Sigma_-$ is neglected, which will be discussed below.

Figure 2 also shows that the peak of $|\text{Im}\Sigma_-|$ appears around $\omega = -k + \mu$. This means that the quasiparticles with this energy are dumped modes. In our approximation, $\text{Im}\Sigma_-$ describes a decay process of a quark to a hole and a diquark, q→h+(qq), as shown in Fig. 3, where the hole is on-shell with a free dispersion relation $\omega_h = \mu - |\boldsymbol{k}_h|$. The essential point for the pseudogap formation is that the above process is enhanced when the diquark (qq) makes a collective mode, which we have emphasized is the case; the diquark soft mode $(\text{qq})_{\text{soft}}$ has a prominent strength at small energy ω_s and momentum $\boldsymbol{k}_s$ near T_c. Owing to the energy-momentum conservation, the energy-momentum of the decaying particle $(\omega_p, \boldsymbol{k}_p)$ should satisfy $\omega_p + \omega_h = \omega_s \simeq 0$ and $\boldsymbol{k}_p + \boldsymbol{k}_h = \boldsymbol{k}_s \simeq 0$. It means that when the decaying particle has almost the same energy as a free quark has, $|\text{Im}\Sigma_-(\boldsymbol{k}, \omega)|$ has the largest value.

We show the spectral function $\rho_0(\boldsymbol{k}, \omega)$ in Fig. 4, at the same μ and ε as those in Fig. 2. One can see the quasiparticle peaks of the quarks and anti-quarks at $\omega = \omega(k) \approx k - \mu$ and $\omega = -k - \mu$, respectively. It should be noticed that the quasiparticle peak has a clear depression around

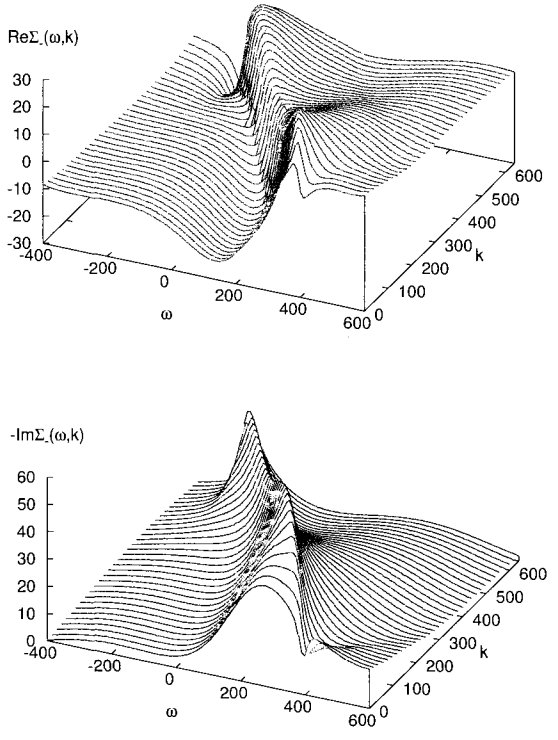

Figure 2. The quark self-energy $\Sigma_-(k,\omega)$ at $\mu = 400\text{MeV}$ and $\varepsilon \equiv (T - T_c)/T_c = 0.01$. Top and bottom panels show the real and imaginary parts of $\Sigma_-(k,\omega)$, respectively.

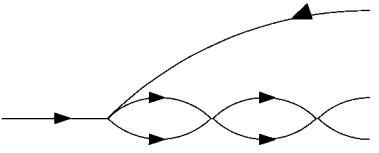

Figure 3. Decaying process of quarks in the T-approximation.

$\omega = 0$, i.e., the Fermi energy. The mechanism for the depression is easily understood in terms of the characteristic properties of $\text{Im}\Sigma_-$ mentioned

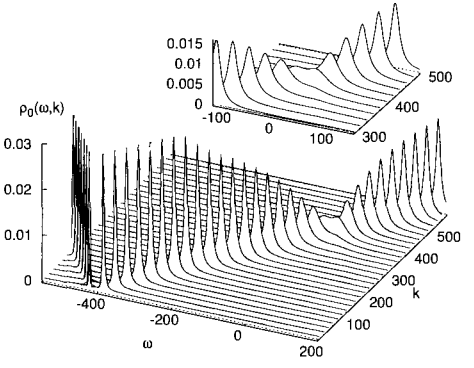

Figure 4. The spectral function ρ_0. There is a depression around $\omega = 0$, which is responsible for the pseudogap formation.

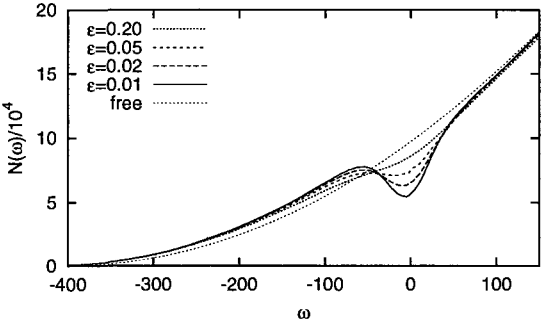

Figure 5. Density of state at $\mu = 400$MeV and various $\varepsilon \equiv (T - T_C)/T_C$. A clear pseudogap structure is seen, which survives up to $\varepsilon \approx 0.05$.

above: Since the peak of $\mathrm{Im}\Sigma_-(\boldsymbol{k}, \omega)$ manifest itself around $\omega = \mu - |\boldsymbol{k}|$, it coincides with the quasiparticle peak $\omega = \omega(k)$ around $\omega = 0$.

Integrating ρ_0, one obtains the DOS $N(\omega)$: Fig. 5 shows the DOS at $\mu = 400$MeV and various values of the reduced temperature ε together with that of the free quark system, $N_0(\omega)$. As anticipated, one can see a remarkable depression of $N(\omega)$, i.e., the *pseudogap*, around the Fermi energy $\omega = 0$; $N(\omega)/N_0(\omega)|_{\omega=0} \simeq 0.55$ at $\varepsilon = 0.01$. The clear pseudogap structure survives even at $\varepsilon = 0.05$. One may thus conclude that there is a pseudogap region within the QGP phase above T_c up to $T = (1.05 \sim 1.1)T_c$ at $\mu =$

400MeV, for instance. A numerical calculation shows that ε dependence of the width of the pseudogap region hardly changes for 320MeV$< \mu <$ 500MeV.

4. Specific Heat

The anomalous behavior of the DOS in the pseudogap region may affect various observables near T_c. In this section, we consider the behavior of the specific heat c_V near T_c as an example of such effects on observables. Although precise calculation for c_V is in progress[2], it is possible to give an intuitive discussion on the qualitative behavior of it from the behavior of the DOS.

As was shown above, the DOS $N(\omega)$ around the Fermi surface becomes smaller as temperature is lowered toward T_c. In particular, $N(\omega)$ decreases sharply near T_c while the Fermi-Dirac distribution function $f(\omega)$ remains almost the same. In this case, number of particles around the Fermi surface becomes smaller due to the decrease of the DOS in these region, and hence particles are emitted from the vicinity of the Fermi surface. Therefore, the energies corresponding to the particle emission are released around the Fermi surface as T is lowered. This energy release may lead to the anomalous enhancement of c_V near T_c, because the specific heat is the released energy from the system while the temperature is lowered by a unit temperature: Recall that the definition of c_V is the amount of energy required to raise the temperature of the system. In particular, one can expect that the enhancement of c_V becomes more remarkable as T approaches T_c since the decrease of the DOS around the Fermi energy becomes sharp as T is lowered toward T_c.

The behavior of c_V discussed above is reasonable in accordance with the fact that c_V is enhanced near T_c in the usual superconducting phase transitions on account of the enhancement of the pair fluctuations[9]. It should be noted, however, that the rather wide pseudogap region as we have shown above indicates that the anomalous behavior of the specific heat can manifest itself in the similar range of temperatures, $T = (1.05 \sim 1.1)T_c$. This temperature range is quite wide compared with the one in the usual metal superconductivity in which anomalous behavior of c_V is seen only in $\epsilon \lesssim 10^{-10}$. Thus, it might be possible to observe the anomalous enhancement of c_V as a signature of the phase transition of the CS in the observation of the compact stars; for example, in the cooling process of the proto neutron stars in the very early stage. It is also interesting that

Voskresensky estimated that c_V increases anomalously from $T \sim 2T_c$ based on a GL approach with parameters determined in the weak coupling limit[10]. This estimation of the temperature range is about one order larger than ours. The discussion on the origin of this difference will be given in our future work[2].

5. Conclusion

In this work, we have found that the pseudogap can be formed as a precursory phenomenon of the CS in a rather wide region of T above T_c. The rather wide region of It should be noted that our work is the first calculation to show the formation of the pseudogap in the relativistic framework.

We notice that the pseudogap region obtained in the present work is more than one order of magnitude wider in the unit of ε than in the nuclear matter[7] where the clear pseudogap is seen up to $\varepsilon \approx 0.0025$. This is just a reflection of the strong coupling nature of the QCD at intermediate density region. Our result obtained for a three-dimensional system tells us that a considerable pseudogap can be formed without the help of the low-dimensionality as in the HTSC and that the pseudogap phenomena in general may be universal in any strong coupling superconductivity.

References

1. M. Kitazawa, T. Koide, T. Kunihiro and Y. Nemoto, hep-ph/0309026.
2. M. Kitazawa, T. Kunihiro, in preparation.
3. D. Bailin and A. Love, Phys. Rept. **107**, 325 (1984); T. Matsuura, K. Iida, T. Hatsuda and G. Baym, hep-ph/0312042.
4. see, for reviews, K. Rajagopal and F. Wilczek, Chapter 35 in the Festschrift in honor of B. L. Ioffe, M. Shifman, ed., (World Scientific).
5. M. Kitazawa, T. Koide, T. Kunihiro and Y. Nemoto, Phys. Rev. D **65**, 091504(R) (2002).
6. See for example, Y. Yanase ,T. Judo, T. Nomura, H. Ikeda, T. Hotta and K. Yamada, Phys. Rep. **387**, 1 (2003); V. M. Loktev, R. M. Quick and S. G. Sharapov, Phys. Rept. **349**, 1 (2001).
7. A. Schnell, G. Ropke and P. Schuck, Phys. Rev. Lett. **83**, 1926 (1999).
8. L.P. Kadanoff and G. Baym, *Quantum statistical mechanics*,(W.A. Benjamin, 1962).
9. D. J. Thouless, Ann. Phys. **10**, 553 (1960).
10. D. N. Voskresensky, hep-ph/0306077.

ASPECTS OF HIGH DENSITY EFFECTIVE THEORY

DEOG KI HONG

Department of Physics,
Pusan National University,
Busan 609-735, Korea
E-mail: dkhong@pusan.ac.kr

We discuss the salient features of the high density effective theory (HDET) of QCD, elaborating more on the matching for vector-vector correlators and axial-vector-vector correlators, which are related to screening mass and axial anomaly, respectively. We then apply HDET to discuss various color-superconducting phases of dense QCD.

1. Introduction

As physics advances, its frontier has expanded. One of the frontiers under active exploration is matter at extreme conditions. Recent surprising data, obtained from heavy-ion collisions and compact stars such as neutron stars, and also some theoretical breakthroughs have stimulated active investigation in this field [1].

How does matter behave as we squeeze it extremely hard? This question is directly related to one of the fundamental questions in Nature; what are the fundamental building blocks of matter and how they interact. According to QCD, matter at high density is quark matter, since quarks interact weaker and weaker as they are put closer and closer.

At what temperature and density does the phase transition to quark matter occur? To determine the phase diagram of thermodynamic QCD is an outstanding problem. The phases of matter are being mapped out by colliding heavy-ions and by observing compact stars. Since QCD has only one intrinsic scale, $\Lambda_{\rm QCD}$, the phase transition of QCD matter should occur at that scale as matter is heated up or squeezed down. Indeed, recent lattice QCD calculations found the phase transition does occur at temperature around 175 MeV [2]. Even though lattice QCD has been quite successful at finite temperature but at zero density, it has not made much progress at finite density due to the notorious sign problem. The lattice calculation is

usually done in Euclidean space and Euclidean QCD with a chemical potential has a complex measure, which precludes use of importance samplings, the main technique in the Monte Carlo simulation for lattice calculations.

Lattice QCD at finite density is described by a partition function

$$Z(\mu) = \int \mathrm{d}A \det(M)\, e^{-S(A)}\,, \tag{1}$$

where $M = \gamma_E^\mu D_E^\mu + \mu\gamma_E^4$ is the Dirac operator of Euclidean QCD with a chemical potential μ. The eigenvalues of M are in general complex, since $\gamma_E^\mu D_E^\mu$ is anti-Hermitian while $\mu\gamma_E^4$ is Hermitian. For certain gauge fields such as $A^\mu(-x) = -A^\mu(x)$, M can be mapped into $M^\dagger$ by a similarity transformation and thus its determinant M is nonnegative. However, for generic fields $M \neq P^{-1}M^\dagger P$ and $\det(M)$ is complex.

Recently there have been some progress in lattice simulation at small chemical potential, using a re-weighting method, to find the phase line [3,4]. Another interesting progress in lattice simulation was made at very high density in [5,6], where it was shown that for QCD at high density the sign problem is either mild or absent, since the modes, responsible for the complexness of the Dirac determinant, decouple from dynamics or become irrelevant at high baryon density [7].

2. High Density Effective Theory

At low temperature or energy, most degrees of freedom of quark matter are irrelevant due to Pauli blocking. Only quasi-quarks near the Fermi surface are excited. Therefore, relevant modes for quark matter are quasi-quarks near the Fermi surface and the physical properties of quark matter like the symmetry of the ground state are determined by those modes. High density effective theory (HDET) [8,9] of QCD is an effective theory for such modes to describe the low-energy dynamics of quark matter.

To find out the modes near the Fermi surface, one needs to know the energy spectrum of QCD, which is very difficult in general since it is equivalent to solving QCD. However, at high density $\mu \gg \Lambda_{\mathrm{QCD}}$, quarks near the Fermi surface carry large momenta and the typical interaction involves a large momentum transfer. Therefore, due to the asymptotic freedom of QCD, the spectrum near the Fermi surface at high density looks very much like that of free fermion: $(\vec{\alpha}\cdot\vec{p} - \mu + \beta m)\,\psi_\pm = E_\pm\psi_\pm$, as shown in Fig. 1. We see that at low energy, $E < 2\mu$, the states near the Fermi surface ($|\vec{p}| \simeq p_F$), denoted as ψ_+, are easily excited while states deep in the Dirac sea, denoted as ψ_-, are hard to excite.

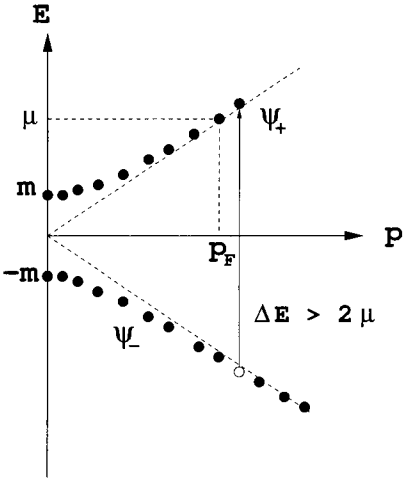

Figure 1. Energy spectrum of quarks at high density

At low energy, the typical momentum transfer by quarks near the Fermi surface is much smaller than the Fermi momentum. Therefore, similarly to the heavy quark effective theory, we may decompose the momentum of quarks near the Fermi surface as

$$p^\mu = \mu v^\mu + l^\mu, \tag{2}$$

where $v^\mu = (0, \vec{v}_F)$ and $\vec{v}_F$ is the Fermi velocity. For quark matter, the typical size of the residual momentum is $|l^\mu| \sim \Lambda_{\rm QCD}$, and the Fermi velocity of the quarks does not change for $\mu \gg \Lambda_{\rm QCD}$, when they are scattered off by soft gluons.

We now introduce patches to cover the Fermi surface, as shown in Fig. 2. The sizes of each patch are 2Λ in vertical direction to the Fermi surface and $2\Lambda_\perp$ in horizontal direction. The quarks in a patch are treated to carry a same Fermi velocity.

The energy of the quarks in the patch is given as

$$E = -\mu + \sqrt{p^2 + m^2} = \vec{l} \cdot \vec{v}_F + \frac{l^2}{2\mu} + O\left(\frac{1}{\mu^2}\right). \tag{3}$$

We see that at the leading order in $1/\mu$ expansion, the energy is independent of the residual momentum, $\vec{l}_\perp$, perpendicular to the Fermi velocity. In HDET, therefore, the perpendicular momentum labels the degeneracy and

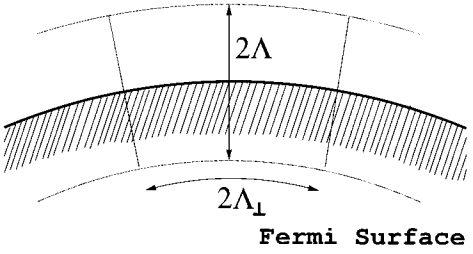

Figure 2. A patch covering the Fermi surface

should satisfy a normalization condition

$$\sum_{\text{patches}} \int_{\Lambda_\perp} \mathrm{d}^2 l_\perp = 4\pi p_F^2. \tag{4}$$

To identify the modes near the Fermi surface, we expand the quark field as

$$\Psi(x) = \sum_{\vec{v}_F} e^{-i\mu \vec{x}\cdot\vec{v}_F} \left[\psi_+(\vec{v}_F, x) + \psi_-(\vec{v}_F, x)\right], \tag{5}$$

where $\psi_\pm(\vec{v}_F, x)$ satisfies respectively

$$\frac{1 \pm \vec{\alpha}\cdot\hat{v}_F}{2}\psi_\pm = \psi_\pm. \tag{6}$$

Note that the projection operator $P_\pm = (1 \pm \vec{\alpha}\cdot\hat{v}_F)/2$ projects out the particle state, ψ_+, and the anti-particle state, ψ_- (or more precisely $\bar{\psi}_-$), from the Dirac spinor field Ψ. The quasi-quarks in a patch carries the residual momentum l^μ and is given as

$$\psi_+(\vec{v}_F, x) = \frac{1 + \vec{\alpha}\cdot\hat{v}_F}{2} e^{-i\mu\vec{v}_F\cdot\vec{x}}\psi(x) \tag{7}$$

The Lagrangian for quark fields becomes

$$\begin{aligned}\mathcal{L} &= \bar{\Psi}\left(i\not{D} + \mu\gamma^0\right)\Psi = \sum_{\vec{v}_F} \bar{\psi}(\vec{v}_F, x)\left(P_+ + P_-\right)\left(\mu\not{V} + \not{D}\right)\left(P_+ + P_-\right)\psi(\vec{v}_F, x) \\ &= \bar{\psi}_+\, i\not{D}_\parallel\, \psi_+ + \bar{\psi}_-(2\mu\gamma^0 + i\not{D}_\parallel)\psi_- + \left[\bar{\psi}_-\, i\not{D}_\perp\, \psi_+ + \text{h.c.}\right], \end{aligned} \tag{8}$$

where we neglected the quark mass term for simplicity and $V^\mu = (1, \vec{v}_F)$. The parallel component of the covariant derivative is $D_\parallel^\mu = V^\mu\, D\cdot V$ and

the perpendicular component $D_\perp = D - D_\parallel$. From the quark Lagrangian one can read off the propagators for $\psi_\pm(\vec{v}_F, x)$:

$$S_F^+ = P_+ \frac{i}{\not{l}_\parallel}, \quad S_F^- = P_- \frac{i\gamma^0}{2\mu}\left[1 - \frac{i\gamma^0 \not{l}_\parallel}{2\mu} + \cdots\right]. \tag{9}$$

We see indeed that in HDET the quarks near the Fermi surface or ψ_+ modes are the propagating modes, while ψ_- are not.

By integrating out ψ_- modes and the hard gluons, one obtains the high density effective theory of QCD. In general the integration results in nonlocal terms in the effective theory and one needs to expand them in powers of $1/\mu$. This is usually done by matching the one-light-particle irreducible amplitudes of the microscopic theory with those of the effective theory. For tree-level amplitudes, this is tantamount to eliminating the irrelevant modes, using the equations of motion.

$$\psi_-(\vec{v}_F, x) = -\frac{i\gamma^0}{2\mu + i\not{D}_\parallel} \not{D}_\perp \psi_+ = -\frac{i\gamma^0}{2\mu} \sum_{n=0}^{\infty} \left(-\frac{i\not{D}_\parallel}{2\mu}\right)^n \not{D}_\perp \psi_+ \,. \tag{10}$$

For instance, a one-light particle irreducible amplitude in QCD of two gluons and two quarks is matched as

$$\bar{\psi}_+ i \not{D}_\perp \psi_-(\vec{v}_F, x) \bar{\psi}_- i \not{D}_\perp \psi_+(\vec{v}_F, y) = \bar{\psi}_+ i \not{D}_\perp \left(-\frac{i\gamma^0}{2\mu}\right) i \not{D}_\perp \psi_+(\vec{v}_F, y)\,, \tag{11}$$

which is shown in Fig. 3. Similarly one can eliminate the hard gluons. In-

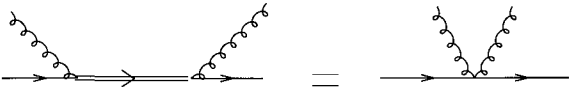

Figure 3. Tree-level matching: The double line denotes ψ_- modes and the single line ψ_+.

tegrating out hard gluons results in four-Fermi interactions of ψ_+ modes. (See Fig. 4.) One continues matching one-loop or higher-loop amplitudes. One interesting feature of HDET is that a new marginal operator arises at the one-loop matching, when incoming quarks are in Cooper-paring kinematics, namely when they have opposite Fermi velocities. As shown in Fig. 5, when the incoming quarks have opposite Fermi velocity, the amplitudes in HDET are ultra-violet divergent while QCD amplitudes are not.

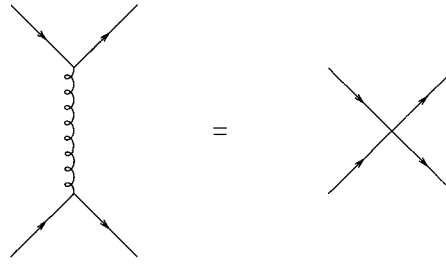

Figure 4. Tree-level matching: Four-Fermi interaction due to hard gluons

Therefore, one needs to introduce a four-Fermi operator as a counter term to remove the UV divergence. If we collect all the terms in the effective

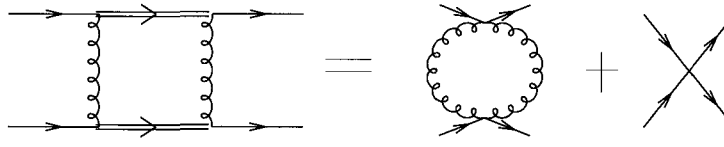

Figure 5. One-loop matching

theory, it has a systematic expansion in $1/\mu$ and coupling constants α_s as

$$\mathcal{L}_{\rm HDET} = b_1 \bar{\psi}_+ i\gamma_{\shortparallel}^{\mu} D_{\mu} \psi_+ - \frac{c_1}{2\mu} \bar{\psi}_+ \gamma^0 (\not{D}_{\perp})^2 \psi_+ \ + \ \cdots , \qquad (12)$$

where $b_1 = 1 + O(\alpha_s)$, $c_1 = 1 + O(\alpha_s), \cdots$. Note that HDET has a reparametrization invariance, similarly to heavy quark effective theory, which is due to the fact that the Fermi velocity of quarks in a patch is not uniquely determined. For a given quark momentum, the corresponding Fermi velocity is determined up to reparametrization; $\vec{v}_F \to \vec{v}_F + \delta\vec{l}_{\perp}/\mu$ and $\vec{l} \to \vec{l} - \delta\vec{l}$, where $\delta\vec{l}_{\perp}$ is a residual momentum perpendicular to the Fermi velocity. As in the heavy quark effective theory [10], the renormalization of higher-order operators are restricted due to the reparametrization invariance. For instance, $b_1 = c_1$ at all orders in α_s.

In order for the effective theory to be meaningful, it should have a consistent power-counting. We find the consistent counting in HDET to be

for $\Lambda_\perp = \Lambda$

$$\left(\frac{D_\parallel}{\mu}\right)^n \cdot \left(\frac{D_\perp}{\mu}\right)^m \cdot \psi_+^l \sim \left(\frac{\Lambda}{\mu}\right)^{n+m} \Lambda^{3l/2}. \tag{13}$$

To be consistent with the power counting, we impose in loop integration

$$\int_{\Lambda_\perp} \mathrm{d}^2 l_\perp \, l_\perp^n = 0 \quad \text{for} \quad n > 0. \tag{14}$$

So far we have restricted ourselves to operators containing quarks in the same patch. For operators with quarks in different patches, one has to be careful, since the loop integration might jeopardize the power-counting rules. Indeed, consistent counting is to sum up all the hard-loops, as shown by Schäfer [11].

3. More on matching

In HDET, the currents are given in terms of particles and holes but without antiparticles as

$$J^\mu = \sum_{\vec{v}_F} \bar{\psi}(\vec{v}_F, x)\gamma_\parallel^\mu \psi(\vec{v}_F, x) - \frac{1}{2\mu}\psi^\dagger(\vec{v}_F, x)\,[\gamma_\perp^\mu,\, i\not{D}_\perp]\,\psi(\vec{v}_F, x) + \cdots,$$

where the color indices are suppressed and we have reverted the notation ψ for ψ_+ henceforth. We find that the HDET current is not conserved unless one adds a counter term. Consider the current correlator

$$\langle J^\mu(x) J^\nu(y)\rangle = \frac{\delta^2 \Gamma_{\text{eff}}}{\delta A_\mu(x)\delta A_\nu(y)} = \int_p e^{-ip\cdot(x-y)} \Pi^{\mu\nu}(p) \tag{15}$$

where the vacuum polarization tensor

$$\Pi_{ab}^{\mu\nu}(p) = -\frac{iM^2}{2}\delta_{ab} \int \frac{\mathrm{d}\Omega_{\vec{v}_F}}{4\pi} \left(\frac{-2\vec{p}\cdot\vec{v}_F V^\mu V^\nu}{p\cdot V + i\epsilon \vec{p}\cdot\vec{v}_F}\right) \tag{16}$$

and $M^2 = N_f g_s^2 \mu^2/(2\pi^2)$. We see that the vacuum polarization tensor is not transverse, $p_\mu \Pi_{ab}^{\mu\nu}(p) \neq 0$, which means that the current is not conserved. The physical reason for this is that not only modes near the Fermi surface but also modes deep in the Fermi sea respond to external sources collectively. To recover the current conservation in the effective theory, we need to add the DeBye screening mass term due to ψ_- (See Fig. 6):

$$\Gamma^{\text{eff}} \mapsto \tilde{\Gamma}^{\text{eff}} = \Gamma^{\text{eff}} - \int_x \frac{M^2}{2} \sum_{\vec{v}_F} A_\mu A_\nu g_\perp^{\mu\nu}. \tag{17}$$

Then vacuum polarization tensor becomes

$$\Pi^{\mu\nu}(p) \mapsto \tilde{\Pi}^{\mu\nu}(p) = \Pi^{\mu\nu} - \frac{i}{2}\sum_{\vec{v}_F} g_{\perp}^{\mu\nu} M^2 \,. \tag{18}$$

The modified polarization tensor is now transverse, $p_\mu \tilde{\Pi}^{\mu\nu} = 0$.

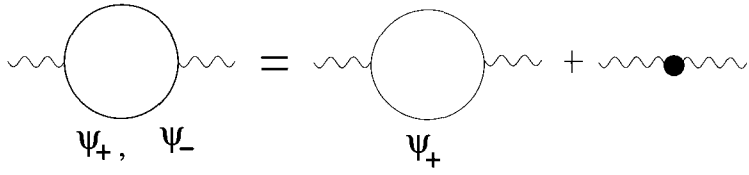

Figure 6. Matching two-point functions

Now, let us consider the divergence of axial currents in HDET, which is related to the axial anomaly and also to how the quark matter responds to external axial-current sources like electroweak probes.

It is easy to show that the axial anomaly in dense matter is independent of density or the chemical potential μ [12]. In general one may re-write the divergence of axial currents in dense QCD as follows:

$$\langle \partial_\mu J_5^\mu \rangle = \frac{g^2}{16\pi^2}\tilde{F}_{\mu\alpha}F^{\mu\alpha} + \Delta^{\alpha\beta}(\mu)A_\alpha A_\beta \,, \tag{19}$$

where the first term is the usual axial anomaly in vacuum and the second term is due to matter. However, one can explicitly calculate the second term, which is finite, to find $\Delta^{\alpha\beta}(\mu) = 0$. In HDET, the axial anomaly due to modes near the Fermi surface is given as

$$\sum_{\vec{v}_F}\int_{x,y} e^{ik_1\cdot x + ik_2\cdot y}\left\langle \partial_\mu J_5^\mu(\vec{v}_F,0)J^\alpha(\vec{v}_F,x)J^\beta(\vec{v}_F,y)\right\rangle \equiv \Delta_{\text{eff}}^{\alpha\beta} \tag{20}$$

By explicit calculation we find

$$\Delta_{\text{eff}}^{0i}(k_1,k_2) = -\frac{g^2}{12\pi^2}\left(\vec{k}_1\times\vec{k}_2\right)^i,\ \Delta_{\text{eff}}^{ij} = \frac{2g^2}{12\pi^2}\epsilon^{ijl}\left(k_{10}k_{2l} - k_{1l}k_{20}\right). \tag{21}$$

We see that the modes near the Fermi surface contributes only some parts of the axial anomaly. As in the vector current, the rest should come from modes in the deep Fermi sea and from anti-particles. To recover the full

axial anomaly we add a counter term (See Fig. 7), which is two thirds of the axial anomaly plus a Chern-Simons term:

$$\tilde{\Delta}^{\alpha\beta}_{\rm eff}(k_1,k_2)=\Delta^{\alpha\beta}_{\rm eff}+\frac{g^2}{6\pi^2}\epsilon^{\alpha\beta\rho\sigma}k_{1\rho}k_{2\sigma}+\frac{g^2}{12\pi^2}\epsilon^{\alpha\beta 0l}\left(k_{10}k_{2l}-k_{1l}k_{20}\right). \quad (22)$$

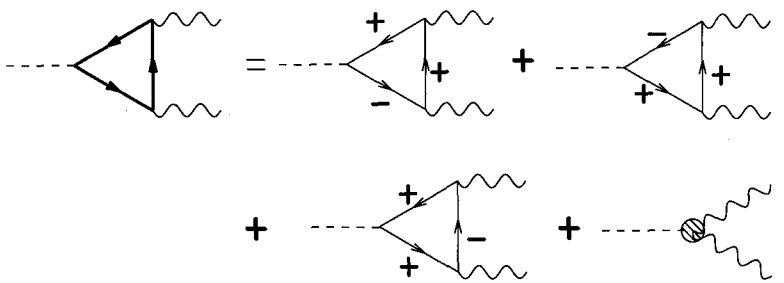

Figure 7. Matching axial anomaly. + denotes ψ_+ and − denotes ψ_-.

4. Color superconductivity in dense QCD

At high density, quarks in dense matter interact weakly with each other and form a Fermi sea, due to asymptotic freedom. When the energy is much less than the quark chemical potential ($E \ll \mu$), only the quarks near the Fermi surface are relevant. The dynamics of quarks near the Fermi surface is effectively one-dimensional, since excitations along the Fermi surface do not cost any energy. The momentum perpendicular to the Fermi momentum just labels the degeneracy, similarly to the perpendicular momentum of charged particle under external magnetic field. This dimensional reduction due to the presence of Fermi surface makes possible for quarks to form a Cooper pair for any arbitrary weak attraction, since the critical coupling for the condensation in (1+1) dimensions is zero, known as the Cooper theorem in condensed matter.

While, in the BCS theory, such attractive force for electron Cooper pair is provided by phonons, for dense quark matter, where phonons are absent, the gluon exchange interaction provides the attraction, as one-gluon exchange interaction is attractive in the color anti-triplet channel.[a] One

[a]There is also an attractive force between quarks and holes in the color octet channel:

therefore expects that color anti-triplet Cooper pairs will form and quark matter is color superconducting, which is indeed shown more than 20 years ago [14,15,16].

At intermediate density, quarks and gluons are strongly interacting and gluons are therefore presumably screened. Then, QCD at intermediate density may be modelled by four-Fermi interactions and higher-order terms by massive gluons.

$$\mathcal{L}_{\rm QCD}^{\rm eff} \ni \frac{G}{2}\bar{\psi}\psi\bar{\psi}\psi + \cdots , \tag{23}$$

where the ellipsis denotes higher-order terms induced by massive gluons. When the incoming quarks have opposite momenta, the four-Fermi interaction is marginally relevant, if attractive, and all others are irrelevant. As the renormalization group flows toward the Fermi surface, the attractive four-Fermi interaction is dominant and blows up, resulting in a Landau pole, which can be avoided only when a gap opens at the Fermi surface. This is precisely the Cooper-instability of the Fermi surface. The size of gap can be calculated by solving the gap equation, which is derived by the variational principle that the gap minimizes the vacuum energy:

$$0 = \frac{\partial V_{\rm BCS}(\Delta)}{\partial \Delta} = \frac{\Delta}{G} - i\int \frac{d^4k}{(2\pi)^4}\frac{\Delta}{k_0^2 - (\vec{k}\cdot\vec{v}_F)^2 - \Delta^2}, \tag{24}$$

which gives

$$\Delta = -iG\int \frac{d^4k}{(2\pi)^4}\frac{\Delta}{[(1+i\epsilon)k_0]^2 - (\vec{k}\cdot\vec{v}_F)^2 - \Delta^2}. \tag{25}$$

We note that the integrand in Eq. 25 does not depend on $k_\perp$, whose integration gives the density of states at the Fermi surface, and the $i\epsilon$ prescription is consistent with the Feynman propagator. The pole occurs at

$$k_0 = \pm\sqrt{(\vec{k}\cdot\vec{v}_F)^2 + \Delta^2} \mp i\epsilon \tag{26}$$

or in terms of full momentum $p = \mu v + k$ it occurs at

$$p_0 = \pm\sqrt{(|\vec{p}| - \mu)^2 + \Delta^2} \mp i\epsilon\,. \tag{27}$$

$\langle\bar{\psi}_i(-\vec{p})\psi_j(\vec{p})\rangle \neq 0$, which corresponds to a density wave. However, because of the momentum conservation, the density wave condensate does not enjoy the full Fermi surface degeneracy. Indeed, for QCD, the diquark condensate is energetically preferred to the density wave condensate [13].

We find the solution to the gap equation

$$\Delta_0 = 2\mu \exp\left(-\frac{\pi^2}{2G\mu^2}\right). \tag{28}$$

For generic parameters of dense QCD, the gap is estimated to be $10 \sim 100\,\mathrm{MeV}$ at the intermediate density. The free energy of the BCS state is given as

$$\begin{aligned} V_{\mathrm{BCS}}(\Delta_0) &= \int_0^{\Delta_0} \frac{\partial V_{\mathrm{BCS}}}{\partial \Delta} \mathrm{d}\Delta \\ &= \frac{4\mu^2}{G} \int_0^{x_0} \left(x + g^2 \ln x\right) dx = -\frac{\mu^2}{4\pi^2}\Delta_0^2, \end{aligned} \tag{29}$$

where $x = \Delta/(2\mu)$ and $g^2 = 2G\mu^2/\pi^2$. At high density magnetic gluons are not screened though electric gluons are screened [17,18,19]. The long-range pairing force mediated by magnetic gluons leads to the Eliashberg gap equation (See Fig. 8).

$$\Delta(p_0) = \frac{g_s^2}{36\pi^2} \int_{-\mu}^{\mu} dq_0 \frac{\Delta(q_0)}{\sqrt{q_0^2 + \Delta^2}} \ln\left(\frac{\bar{\Lambda}}{|p_0 - q_0|}\right), \tag{30}$$

where $\bar{\Lambda} = 4\mu/\pi \cdot (\mu/M)^5 e^{3/2\xi}$ and ξ is a gauge parameter. Due to the

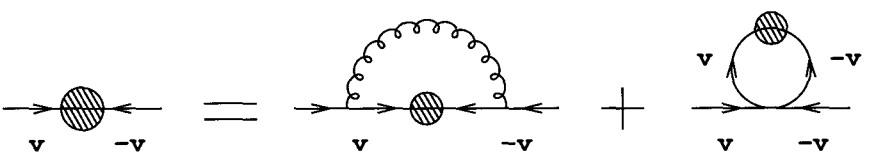

Figure 8. Eliashberg equation at high density.

unscreened but Landau-damped gluons, there is an extra (infrared) logarithmic divergence in the gap equation, when the incoming quark momentum is collinear with the gluon momentum. The Cooper-pair gap at high density is found to be [19,20]

$$\Delta_0 = \frac{2^7\pi^4}{N_f^{5/2}} e^{3\xi/2+1} \cdot \frac{\mu}{g_s^5} \exp\left(-\frac{3\pi^2}{\sqrt{2}g_s}\right).$$

The numerical prefactor of the gap is not complete, since the contributions from subleading corrections to the gap equation that lead to logarithmic

divergences, such as the wavefunction renormalization and the vertex corrections, are not taken into account. Recently, however, the contributions to the prefactor, coming from the vertex corrections and the wavefunction renormalization for quarks were calculated by finding a (nonlocal) gauge [21], where the quark wavefunction is not renormalized for all momenta, $Z(p) = 1$. At the nonlocal gauge, $\xi \simeq 1/3$. The subleading corrections therefore increase the leading-order gap at the Coulomb gauge by about two thirds.

5. Quark matter under stress

It is quite likely to find dense quark matter inside compact stars like neutron stars. However, when we study the quark matter in compact stars, we need to take into account not only the charge and color neutrality of compact stars and but also the mass of the strange quark, which is not negligible at the intermediate density. By the neutrality condition and the strange quark mass, the quarks with different quantum numbers in general have different chemical potentials and different Fermi momenta. When the difference in the chemical potential becomes too large the Cooper-pairs breaks or other exotic phases like kaon condensation or crystalline phase is more preferred to the BCS phase.

Let us consider for example the pairing between up and strange quarks in chemical equilibrium. The energy spectrum of up quarks is given as

$$E = -\mu \pm |\vec{p}|, \tag{31}$$

while the energy of strange quarks of mass M_s becomes

$$E = -\mu \pm \sqrt{|\vec{p}|^2 + M_s^2}\,. \tag{32}$$

The Fermi sea of up and strange quarks is shown in Fig. 9. Because of the strange quarks mass, they have different Fermi momenta. Note that the Cooper-pairing occurs for quarks with same but opposite momenta. Therefore, at least one of the pairing quarks should be excited away from the Fermi surface, costing some energy. Let us suppose that the Cooper-pair gap opens at $|\vec{p}| = \bar{p}$ between two Fermi surfaces, $p_F^s \le \bar{p} \le p_F^u$.

To describe such pairing, we consider small fluctuations of up and strange quarks near $\bar{p}$. The energy of such fluctuations of up and down quarks is respectively

$$E_u = -\mu + |\bar{p} + \vec{l}\,| \simeq -\delta\mu^u + \vec{v}_u \cdot \vec{l}, \qquad E_s \simeq -\delta\mu^s + \vec{v}_s \cdot \vec{l}, \tag{33}$$

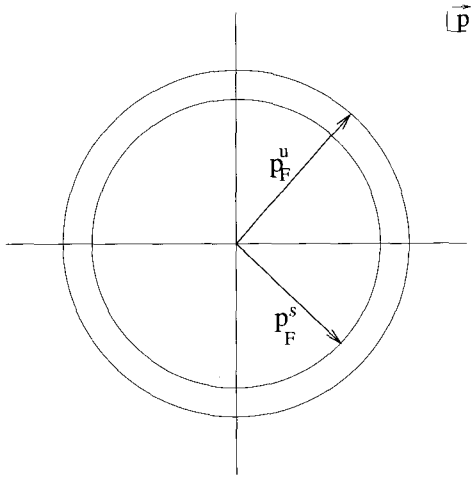

Figure 9. Fermi sea of up and strange quarks.

where $\delta\mu^u = \mu - \bar{p}$ and $\delta\mu^s = \mu - \sqrt{\bar{p}^2 + M_s^2}$. $\vec{v}_u$ and $\vec{v}_s$ are the velocities of up and strange quarks at $|\vec{p}| = \bar{p}$. Let Δ be the BCS gap for the u, s pairing. Then, the Lagrangian for the u, s quarks is given as

$$\mathcal{L} = \bar{u}\left(i\,\partial\!\!\!/ + \mu\gamma^0\right) u + \bar{s}_c\left(i\,\partial\!\!\!/ - \mu\gamma^0 - M_s\right) s_c - \Delta\,\bar{s}_c\,u + \text{h.c.} + \mathcal{L}_{\text{int}}, \quad (34)$$

where s_c is the charge conjugate field of s quark. In HDET, the Lagrangian becomes

$$\mathcal{L}_{\text{HDET}} = u^\dagger\left(iV_u \cdot \partial + \delta\mu^u\right) u + s_c^\dagger\left(i\bar{V}_s \cdot \partial - \delta\mu^s\right) s_c - \Delta\bar{s}_c\,u + \cdots, \quad (35)$$

where $V_u = (1, \vec{v}_u)$ and $\bar{V}_s = (1, -\vec{v}_s)$. The Cooper-pair gap equation is then

$$\Delta(p) = \int_l \frac{i\Delta(l)\,K(p-l)}{[(1+i\epsilon)l_0 - \vec{l}\cdot\vec{v}_u + \delta\mu^u][(1+i\epsilon)l_0 + \vec{l}\cdot\vec{v}_s - \delta\mu^u] - \Delta^2}, \quad (36)$$

where K is the kernel for the gap equation and is a constant for the four-Fermi interaction. By examining the pole structure, we see that the Cooper-pair gap does not exist when

$$-\delta\mu^u\delta\mu^s > \frac{\Delta^2}{4}. \quad (37)$$

Only when $-\delta\mu^u\delta\mu^s < \Delta^2/4$, one can shift $l_0 \to l_0' = l_0 + \delta\mu^u$ or $l_0 \to l_0' = l_0 - \delta\mu^s$ without altering the pole structure. Note that the gap becomes

biggest when $\delta\mu^u = -\delta\mu^s (\equiv \delta\mu)$, which determines the pairing momentum to be

$$\bar{p} = \mu - \frac{M_s^2}{4\mu}. \tag{38}$$

If $\delta\mu < \Delta/2$ or $\Delta > M_s^2/(2\mu)$, the solution to the Cooper-pair gap exists. The gap equation then can be written as, shifting l_0, in Euclidean space

$$\Delta(p) = \int \frac{\mathrm{d}^4 l}{(2\pi)^4} \frac{\Delta(l)}{l_\parallel^2 + \Delta^2} K(l-p), \tag{39}$$

where $l_\parallel^2 = l_0^2 + c^2(\vec{l}\cdot\hat{v})^2$ and $c^2 = \bar{p}/\sqrt{\bar{p}^2 + M_s^2}$. In HDET, one can easily see that the Cooper-pair gap closes if the effective chemical potential difference, $2\delta\mu$, due to an external stress, exceeds the Cooper-pair gap when there is no stress. One should note that even before the Cooper-pair gap closes other gap may open as shown by many authors [22,23,24]. But, one needs to compare the free energy of each phases to find the true ground state for quark matter under stress.

Acknowledgements

The author wishes to thank Mark Alford, Philippe de Forcrand, Simon Hands, Krishna Rajagopal, Francesco Sannino, Thomas Schäfer, Chaejun Song, and Y. J. Sohn for useful discussions. The author is thankful especially to Steve Hsu for the critical discussions and for wonderful collaborations. This work is supported by Korea Research Foundation Grant (KRF-2003-041-C00073).

References

1. K. Rajagopal and F. Wilczek, arXiv:hep-ph/0011333; D. K. Hong, Acta Phys. Polon. B **32**, 1253 (2001) [arXiv:hep-ph/0101025]; M. G. Alford, Ann. Rev. Nucl. Part. Sci. **51**, 131 (2001) [arXiv:hep-ph/0102047]; S. D. H. Hsu, arXiv:hep-ph/0003140. T. Schafer, arXiv:hep-ph/0304281. D. H. Rischke, arXiv:nucl-th/0305030.
2. F. Karsch, E. Laermann and A. Peikert, Nucl. Phys. B **605**, 579 (2001) [arXiv:hep-lat/0012023]; F. Karsch, E. Laermann, A. Peikert, C. Schmidt and S. Stickan, arXiv:hep-lat/0010027; F. Karsch, Nucl. Phys. A **698**, 199 (2002) [arXiv:hep-ph/0103314].
3. Z. Fodor and S. D. Katz, Phys. Lett. B **534**, 87 (2002) [arXiv:hep-lat/0104001]; JHEP **0203**, 014 (2002) [arXiv:hep-lat/0106002].
4. C. R. Allton *et al.*, Phys. Rev. D **66**, 074507 (2002) [arXiv:hep-lat/0204010]; P. de Forcrand and O. Philipsen, arXiv:hep-lat/0209084; M. D'Elia and M. P. Lombardo, Phys. Rev. D **67**, 014505 (2003) [arXiv:hep-lat/0209146].

5. D. K. Hong and S. D. Hsu, Phys. Rev. D **66**, 071501 (2002) [arXiv:hep-ph/0202236].
6. D. K. Hong and S. D. Hsu, Phys. Rev. D **68**, 034011 (2003) [arXiv:hep-ph/0304156].
7. For more discussions, see D. K. Hong and S. D. H. Hsu, "The fermion sign problem and high density effective theory," arXiv:hep-ph/0402002 (these proceedings).
8. D. K. Hong, Phys. Lett. B **473**, 118 (2000) [arXiv:hep-ph/9812510];
9. D. K. Hong, Nucl. Phys. B **582**, 451 (2000) [arXiv:hep-ph/9905523].
10. M. Luke and A. V. Manohar, Phys. Lett. B **286** (1992) 348.
11. T. Schafer, Nucl. Phys. A **728**, 251 (2003) [arXiv:hep-ph/0307074]; T. Schafer, arXiv:hep-ph/0310176.
12. D. K. Hong, B. I. Hur, Y. J. Son and T.-S. park, to appear.
13. E. Shuster and D. T. Son, Nucl. Phys. B **573**, 434 (2000) [arXiv:hep-ph/9905448]. B. Y. Park, M. Rho, A. Wirzba and I. Zahed, Phys. Rev. D **62**, 034015 (2000) [arXiv:hep-ph/9910347].
14. F. Barrois, Nucl. Phys. **B129** (1977) 390.
15. S. C. Frautschi, *Asymptotic freedom and color superconductivity in dense quark matter*, in: Proceedings of the Workshop on Hadronic Matter at Extreme Energy Density, N. Cabibbo, Editor, Erice, Italy (1978).
16. D. Bailin and A. Love, Phys. Rept. **107** (1984) 325.
17. G. Baym, H. Monien and C. J. Pethick, In "Hirschegg 1988, Proceedings, Gross properties of nuclei and nuclear excitations" 128-132; C. J. Pethick, G. Baym and H. Monien, Nucl. Phys. A **498**, 313C (1989).
18. R. D. Pisarski and D. H. Rischke, Phys. Rev. Lett. **83**, 37 (1999) [arXiv:nucl-th/9811104].
19. D. T. Son, Phys. Rev. D **59**, 094019 (1999) [arXiv:hep-ph/9812287].
20. D. K. Hong, V. A. Miransky, I. A. Shovkovy and L. C. R. Wijewardhana, Phys. Rev. D **61**, 056001 (2000) [Erratum-ibid. D **62**, 059903 (2000)] [arXiv:hep-ph/9906478]; T. Schafer and F. Wilczek, Phys. Rev. D **60**, 114033 (1999) [arXiv:hep-ph/9906512]; R. D. Pisarski and D. H. Rischke, Phys. Rev. D **61**, 051501 (2000) [arXiv:nucl-th/9907041]; W. E. Brown, J. T. Liu and H. c. Ren, Phys. Rev. D **61**, 114012 (2000) [arXiv:hep-ph/9908248].
21. D. K. Hong, T. Lee, D. P. Min, D. Seo and C. Song, Phys. Lett. B **565**, 153 (2003) [arXiv:hep-ph/0303181].
22. M. G. Alford, J. A. Bowers and K. Rajagopal, Phys. Rev. D **63**, 074016 (2001) [arXiv:hep-ph/0008208]; M. Alford, C. Kouvaris and K. Rajagopal, arXiv:hep-ph/0311286; R. Casalbuoni, R. Gatto, M. Mannarelli and G. Nardulli, Phys. Lett. B **511**, 218 (2001) [arXiv:hep-ph/0101326].
23. P. F. Bedaque and T. Schafer, Nucl. Phys. A **697**, 802 (2002) [arXiv:hep-ph/0105150]; D. B. Kaplan and S. Reddy, Phys. Rev. D **65**, 054042 (2002) [arXiv:hep-ph/0107265].
24. I. Shovkovy and M. Huang, Phys. Lett. B **564** (2003) 205 [arXiv:hep-ph/0302142].

MODEL INDEPENDENT SUM RULES FOR STRANGE FORM FACTORS

SOON-TAE HONG*

Department of Science Education
Ewha Womans University, Seoul 120-750 Korea
E-mail: soonhong@ewha.ac.kr

We study chiral models with SU(3) group structure such as Skyrmion and chiral bag to yield theoretical predictions of proton strange form factor comparable to the recent experimental data of the SAMPLE Collaboration. For these predictions we formulate model independent sum rules for proton strange form factor in terms of baryon octet magnetic moments. We also investigate the Becci-Rouet-Stora-Tyutin symmetries associated with the Stückelberg coordinates, ghosts and anti-ghosts involved in the Skyrmion model.

1. Introduction

There have been many interesting developments concerning the strange flavor structures in the nucleon and the hyperons. Especially, the internal structure of the nucleon is still a subject of great interest to both experimentalists and theorists. In 1933, Frisch and Stern [1] performed the first measurement of the magnetic moment of the proton and obtained the earliest experimental evidence for the internal structure of the nucleon. However, it wasn't until 40 years later that the quark structure of the nucleon was directly observed in deep inelastic electron scattering experiments and we still lack a quantitative theoretical understanding of these properties including the magnetic moments.

Recently, the SAMPLE Collaboration reported the experimental data of the proton strange magnetic form factor through parity violating electron scattering at a small momentum transfer $Q_S^2 = 0.1$ $(\mathrm{GeV/c})^2$ [2]

$$G_M^s(Q_S^2) = +0.14 \pm 0.29 \text{ (stat)} \pm 0.31 \text{ (sys) n.m..} \qquad (1)$$

*Work partially supported by the Korea Science and Engineering Foundation grant R01-2000-00015.

On the other hand, baryons were described by topological solitons [3,4,5,6,7] and the MIT bag model [8] was later unified with the Skyrmion model to yield the chiral bag model (CBM) [9], which then includes the pion cloud degrees of freedom and the chiral invariance consistently. Moreover, the soliton was exploited to yield superqualiton [10] in color flavor locking phase [11].

The QCD is the basic underlying theory of strong interaction, from which low energy hadron physics should be attainable. Moreover, for hadron structure calculations, the coupling constant g is not a relevant expansion parameter of QCD. Long ago, 't Hooft noted that $1/N_c$ could be regarded as expansion parameter of QCD [12] where N_c is the number of colors and gN_c^2 is kept constant. The properties of large N_c limit of the QCD can be satisfied by the meson sector of the nonlinear sigma model such as the Skyrmion model.

In this paper, we will study the chiral models such as the Skyrmion and chiral bag to yield theoretical predictions of proton strange form factor comparable to the recent experimental data of the SAMPLE Collaboration. To do this, we will formulate the model independent sum rules for the proton strange form factor in terms of the baryon octet magnetic moments. We will also investigate the Becci-Rouet-Stora-Tyutin (BRST) symmetries associated with the Stückelberg coordinates, ghosts and anti-ghosts involved in the Skyrmion model.

2. BRST symmetries of Skyrmion in improved Dirac quantization

Now, in order to study the hadron physics phenomenology, we treat $1/N_c$ as expansion parameter of QCD, so that the properties of large N_c limit of the QCD can be satisfied by the SU(3) Skyrmion model whose Lagrangian is of the form [4]

$$L = \int \mathrm{d}^3x \left[-\frac{f_\pi^2}{4}\mathrm{tr}(l_\mu l^\mu) + \frac{1}{32e^2}\mathrm{tr}[l_\mu, l_\nu]^2 \right] + L_{WZW} \tag{2}$$

where $l_\mu = U^\dagger \partial_\mu U$ and $U \in \mathrm{SU}(3)$ is described by pseudoscalar meson fields π_a $(a = 1, 2, ..., 8)$ and the topological aspects can be included via the WZW action [4]. Assuming maximal symmetry, we introduce the hedgehog ansatz U_0 embedded in the SU(2) isospin subgroup of SU(3) to yield the topological charge

$$Q = -\frac{1}{2\pi}\chi_E(\theta - \sin\theta\cos\theta) = 1 \tag{3}$$

where θ is the chiral angle and χ_E is the Euler characteristic being an inter two in the spherical bag surface.

In order to define the spin and isospin we can quantize, in the SU(2) Skyrmion for instance, the zero modes via

$$U_0 \rightarrow AU_0A^\dagger \tag{4}$$

and

$$A(t) = a^0 + i\vec{a}\cdot\vec{\tau}, \tag{5}$$

with a^μ being the collective coordinates. We can then obtain the Lagrangian

$$L = -m_0 + 2i_1\dot{a}^\mu\dot{a}^\mu \tag{6}$$

where the static mass m_0 and the moment of inertia i_1 are calculable in the Skyrmion model. Introducing the canonical momenta π^μ we can obtain the canonical Hamiltonian

$$H = m_0 + \frac{1}{8i_1}\pi^\mu\pi^\mu. \tag{7}$$

Note that the second-class geometrical constraints

$$\begin{aligned}\Omega_1 &= a^\mu a^\mu - 1 \approx 0,\\ \Omega_2 &= a^\mu\pi^\mu \approx 0\end{aligned} \tag{8}$$

should be treated via the Dirac brackets [13]. However, in the Dirac quantization, we have difficulties in finding the canonically conjugate pair, which were later overcome [14] by introducing pair of auxiliary Stückelberg fields θ and π_θ with

$$\{\theta, \pi_\theta\} = 1. \tag{9}$$

In the Skyrmion the first-class constraints

$$\begin{aligned}\tilde{\Omega}_1 &= a^\mu a^\mu - 1 + 2\theta,\\ \tilde{\Omega}_2 &= a^\mu\pi^\mu - a^\mu a^\mu\pi_\theta\end{aligned} \tag{10}$$

were constructed [15] to satisfy the strongly involutive Lie algebra

$$\{\tilde{\Omega}_1, \tilde{\Omega}_2\} = 0. \tag{11}$$

Similarly, the first-class Hamiltonian was formulated to yield the baryon mass spectrum

$$m_B = m_0 + \frac{1}{2i_1}\left[J(J+1) + \frac{1}{4}\right] \tag{12}$$

with the isospin quantum number J. Here note that an additional global shift is due to the Weyl ordering correction. Following the BRST quantization scheme [16] with (anti)ghost and their Lagrangian multiplier fields, we obtain the BRST symmetric Lagrangian [15],

$$L_{eff} = -m_0 + \frac{2i_1\dot{a}^\mu\dot{a}^\mu}{1-2\theta} - \frac{2i_1\dot{\theta}^2}{(1-2\theta)^2} - \frac{\dot{\theta}\dot{b}}{1-2\theta}$$
$$-2i_1(1-2\theta)^2(b+2\bar{c}c)^2 + \dot{\bar{c}}\dot{c} \tag{13}$$

invariant under the transformations,

$$\delta_\lambda a^\mu = \lambda a^\mu c, \quad \delta_\lambda\theta = -\lambda(1-2\theta)c,$$
$$\delta_\lambda\bar{c} = -\lambda b, \quad \delta_\lambda c = \delta_\lambda b = 0. \tag{14}$$

(For more details of the BRST quantization of the SU(2) and SU(3) Skyrmions, see Ref. [15] and Ref. [17], respectively.)

3. Model independent sum rules and proton strange form factors

Next, we consider the CBM which is a hybrid of two different models: the MIT bag model at infinite bag radius on one hand and Skyrmion model at vanishing radius on the other hand. (The explicit CBM Lagrangian is given in Ref. [7] for instance.) In the CBM the total topological charge Q in (3) is now splitted into the meson and quark pieces to satisfy the Cheshire cat principle [18]. Moreover, the quark fractional charge is given by sum of integer one (from valence quarks) and the quark vacuum contribution, which is also rewritten in terms of the eta invariant [19].

In the collective quantization of the CBM, we explicitly obtain the proton magnetic moment [20,21]

$$\mu_p = \frac{1}{90}(9I_1 + 24I_2 + 12I_3 + 16I_4 - 4I_5) + \frac{2I_6}{1125}(9I_1 + 4I_2 - 8I_3) \tag{15}$$

with the inertia parameters I_n $(n = 1, ..., 6)$ calculable in the CBM. Similarly we construct the baryon octet magnetic moments to reproduce the Coleman-Glashow sum rules [22,21] such as U-spin symmetries,

$$\mu_{\Sigma^+} = \mu_p, \quad \mu_{\Xi^0} = \mu_n, \quad \mu_{\Xi^-} = \mu_{\Sigma^-}. \tag{16}$$

Now we define the Dirac and Pauli EM form factors via

$$\langle p+q|\hat{V}^\mu|p\rangle = \bar{u}(p+q)\left[F_{1B}(q^2)\gamma^\mu + \frac{i}{2m_B}F_{2B}(q^2)\sigma^{\mu\nu}q_\nu\right]u(p) \tag{17}$$

Table 1. The baryon octet strange form factors

Input	$F^s_{2N}(0)$	$F^s_{2\Lambda}(0)$	$F^s_{2\Xi}(0)$	$F^s_{2\Sigma}(0)$
CBM	0.30	0.49	0.25	−1.54
Exp	0.32	1.42	1.10	−1.10

where q is momentum transfer and $\sigma^{\mu\nu} = \frac{i}{2}(\gamma^\mu\gamma^\nu - \gamma^\nu\gamma^\mu)$ and m_B is baryon mass. The Sachs form factors are then given by

$$G_M = F_{1B} + F_{2B}, \quad G_E = F_{1B} + \frac{q^2}{4m_B^2}F_{2B}, \tag{18}$$

so that, at zero momentum transfer, the Pauli strange form factor is identical to the Sachs strange form factor:

$$F^s_{2B}(0) = G^s_M(0). \tag{19}$$

In the SAMPLE experiment, they measured the neutral weak form factor

$$G_M^{Z,p} = \left(\frac{1}{4} - \sin^2\theta_W\right)G_M^p - \frac{1}{4}G_M^n - \frac{1}{4}G_M^s \tag{20}$$

with G_M^p and G_M^n being the proton and neutron Sachs form factors, to predict the proton strange form factor (1) which is positive value contrary to the negative values from most of the model calculations except the predictions [20,23] of the SU(3) CBM and the recent predictions of the chiral quark soliton model [24] and the chiral perturbation theory [25,26]. (See Ref. [7] for more details.)

In the CBM the proton strange form factor is given by [20]

$$\begin{aligned} F^s_{2N}(0) = &\frac{1}{60}(21I_1 - 4I_2 - 2I_3 - 4I_4 - 2I_5) \\ &+\frac{I_6}{2250}(-129I_1 + 76I_2 - 52I_3) \end{aligned} \tag{21}$$

which, after some algebra with the other baryon octet strange form factors, yields the sum rule for the proton strange form factor in terms of the baryon octet magnetic moments only (for the other baryon sum rules see Ref. [27])

$$F^s_{2N}(0) = \mu_p - \mu_{\Xi^-} - (\mu_p + \mu_n) - \frac{1}{3}(\mu_{\Sigma^+} - \mu_{\Xi^0}) + \frac{4}{3}(\mu_n - \mu_{\Sigma^-}). \tag{22}$$

Explicitly calculating the inertia parameters I_n numerically in (21), we predict the proton strange form factor, 0.30 n.m. as shown in Table 1.

Moreover, exploiting the experimental data for the baryon octet magnetic moments in (22) we obtain

$$F_{2N}^{s}(0) = G_{M}^{s}(0) = 0.32 \text{ n.m.}. \tag{23}$$

On the other hand, the quantities $G_{E,M}^{Z}$ in (20) for the proton can be determined via elastic parity-violating electron scattering to yield the experimental data $G_{M}^{s}(Q_{S}^{2}) = +0.14 \pm 0.29$ (stat) ± 0.31 (sys) n.m. [2] for the proton strange magnetic form factor. Here one notes that the prediction for the proton strange form factor (23) obtained from the sum rule (22) is comparable to the SAMPLE data and is shown in Table 1, together with those of the other baryon strange form factors. Moreover, from the relation (20) at zero momentum transfer, the neutral weak magnetic moment of the nucleon can be written in terms of the nucleon magnetic moments and the proton strange form factor [28]

$$4\mu_{p}^{Z} = \mu_{p} - \mu_{n} - 4\sin^{2}\theta_{W}\mu_{p} - F_{2N}^{s}(0). \tag{24}$$

4. Conclusions

In conclusion, we discussed the SAMPLE experiments in the topological solitons such as the Skymion and chiral models to predict baryon strange form factors by constructing the model independent sum rules for the proton strange form factor in terms of the baryon octet magnetic moments. We also exploited the improved Dirac quantization scheme to investigate the BRST symmetries associated with the Stückelberg coordinates, ghosts and anti-ghosts involved in the Skyrmion model.

References

1. R. Frisch and O. Stern, *Z. Physik* **85**, 4 (1933).
2. R. Hasty et al., *Science* **290**, 2117 (2000); R.D. McKeown, *Phys. Lett.* **B219**, 140 (1989).
3. T.H.R. Skyrme, *Proc. Roy. Soc.* **A260**, 127 (1961).
4. G.S. Adkins, C.R. Nappi and E. Witten, *Nucl. Phys.* **B228**, 552 (1983); E. Witten, *Nucl. Phys.* **B223**, 422 (1983); **B223**, 433 (1983).
5. M. Rho, A.S. Goldhaber and G.E. Brown, *Phys. Rev. Lett.* **51**, 747 (1983).
6. S.T. Hong, *Phys. Lett.* **B417**, 211 (1998).
7. S.T. Hong and Y.J. Park, *Phys. Rep.* **358**, 143 (2002).
8. A. Chodos, R.L. Jaffe, K. Johnson and C.B. Thorn, *Phys. Rev.* **D10**, 10 (1974).
9. G.E. Brown and M. Rho, *Phys. Lett.* **B82**, 177 (1979).
10. D.K. Hong, M. Rho and I. Zahed, *Phys. Lett.* **B468**, 261 (1999); D.K. Hong, S.T. Hong and Y.J. Park, *Phys. Lett.* **B499**, 125 (2001).

11. K. Rajagopal and F. Wilczek, *Handbook of QCD*, ed. M. Shifman (World Scientific, 2001), and references therein.
12. G. 't Hooft, *Nucl. Phys.* **B72**, 462 (1974).
13. P.A.M. Dirac, *Lectures in Quantum Mechanics* (Yeshiva University, New York, 1964).
14. I.A. Batalin and E.S. Fradkin, *Phys. Lett.* **B180**, 157 (1986); I.A. Batalin and I.V. Tyutin, *Int. J. Mod. Phys.* **A6**, 3255 (1991).
15. S.T. Hong and Y.J. Park, *Phys. Rev.* **D59**, 114026 (1999).
16. C. Becci, A. Rouet and R. Stora, *Ann. Phys.* **98**, 287 (1976); I.V. Tyutin, Lebedev Preprint 39 (1975).
17. S.T. Hong and Y.J. Park, *Phys. Rev.* **D63**, 054018 (2000).
18. M.A. Nowak, M. Rho, I. Zahed, *Chiral Nuclear Dynamics* (World Scientific, Singapore, 1996), and references therein.
19. M.F. Atiyah, V. Patodi and I. Singer, *Math. Proc. Camb. Phil. Soc.* **77**, 43 (1975).
20. S.T. Hong and B.Y. Park, *Nucl. Phys.* **A561**, 525 (1993).
21. S.T. Hong and G.E. Brown, *Nucl. Phys.* **A564**, 491 (1993).
22. S. Coleman and S.L. Glashow, *Phys. Rev. Lett.* **6**, 423 (1961).
23. S.T. Hong, B.Y. Park and D.P. Min, *Phys. Lett.* **B414**, 229 (1997).
24. H.C. Kim, M. Praszalowicz, M.V. Polyakov and K. Goeke, *Phys. Rev.* **D58**, 114027 (1998).
25. Ulf-G. Meissner, *Nucl. Phys.* **A666-A667**, 51 (2000);
26. C.M. Maekawa and U. van Kolck, *Phys. Lett.* **B478**, 73 (2000); U. van Kolck et al., *Phys. Lett.* **B488**, 167 (2000).
27. S.T. Hong, `hep-ph/0111470`.
28. R.D. McKeown, *Prog. Part. Nucl. Phys.* **44**, 313 (2000).

THE FERMION SIGN PROBLEM AND HIGH DENSITY EFFECTIVE THEORY

D. K. HONG*
Department of Physics,
Pusan National University,
Pusan 609-735, Korea
E-mail: dkhong@pusan.ac.kr

S. D. H. HSU†
Institute of Theoretical Science
University of Oregon,
Eugene, OR 97403-5203
E-mail: hsu@duende.uoregon.edu

We investigate the positivity of the Euclidean path integral measure for low-energy modes in dense fermionic matter. We show that the sign problem usually associated with fermions is absent if one considers only low-energy degrees of freedom. We describe a method for simulating dense QCD on the lattice and give a proof using rigorous inequalities that the color-flavor locked (CFL) phase is the true vacuum of three flavor, massless QCD.

1. Introduction

Euclidean quantum chromodynamics (QCD) with a non-zero chemical potential has a complex measure, which has made lattice simulation particularly difficult[1]. (Lattice simulation of the QCD phase boundary at finite density[2,3] has been a topic of recent interest.) This problem is often referred to as the sign problem, because, by appropriately grouping terms, quantities such as the partition function can be written as a sum over real, but potentially negative, terms. (That this grouping can be accomplished

*Work partially supported by the academic research fund of the Ministry of Education, Republic of Korea, Project KRF-2000-015-DP0069, and the USA-Korea Cooperative Science Program, NSF 9982164.
†Work partially supported by the U.S. Deptartment of Energy, DE-FG06-85ER40224 and the USA-Korea Cooperative Science Program, NSF 9982164.

is in many systems a consequence of a discrete symmetry such as parity or time-reversal invariance.) Indeterminate signs are enough to preclude use of importance sampling, the main technique for speeding up Monte Carlo integration. It is important to note that while the sign problem often arises in systems of fermions, it is neither inevitable nor inescapable. For example, in QCD at zero chemical potential and in the Hubbard model at half filling one can organize the sum so that terms are real and positive.

Analytical work in color superconductivity[4] has demonstrated a rich phase structure at high density, and stimulated interest in QCD at nonzero baryon density. Several experiments have been proposed to probe matter at density of a few times nuclear matter density[5]. Even rudimentary information about the behavior of dense matter would be useful to the experimental program, as well as to the study of compact astrophysical objects such as neutron stars. Recently[6], we showed that QCD near a Fermi surface has positive, semi-definite measure. In the limit of low energies, the contribution of the remaining modes far from the Fermi surface can be systematically expanded, using a high density effective theory previously introduced by one of us[7,8]. This effective theory is sufficient to study phenomena like color superconductivity, although quantities like the equation of state may be largely determined by dynamics deep in the Fermi sea.

The expansion about the Fermi surface is in powers of $1/\mu$, where μ is the chemical potential. For this expansion to be controlled, the ultraviolet cutoff of our effective theory must be less than μ, or equivalently the scale of the physics of interest must be small relative to the chemical potential. In QCD at asymptotic density, the superconducting gap is exponentially small, so this condition is satisfied. However, it is also quite possible that at intermediate densities (e.g., those inside a neutron star) the gap is somewhat smaller than μ, providing us with an additional small dimensionless parameter. Even if this is not the case, the power expansion of the effective theory is qualitatively different from the usual perturbation in α_s, and therefore worth exploring.

2. Example: (1+1) Dimensions and Beyond

We begin with an example that illustrates the basic ideas in a simple setting. Consider the Euclidean (1+1) action of non-relativistic fermions interacting with a gauge field A

$$S = \int d\tau dx \; \psi_\sigma^\star \left[(-\partial_\tau + i\phi + \epsilon_F) \; - \; \epsilon(-i\partial_x + A) \right] \psi_\sigma \qquad (1)$$

where $\epsilon(p)$ is the energy as a function of momentum (e.g. $\epsilon(p) \approx \frac{p^2}{2m} + \cdots$). In (1) and below we may consider it as a function of the operator $(-i\partial_x + A)$. The dispersion relation in the presence of the chemical potential ϵ_F is: $E(p) = \epsilon(p) - \epsilon_F$, and a low energy mode must have momentum close to $\pm p_F$, where $\epsilon(\pm p_F) = \epsilon_F$. The Fermi surface in (1+1) dimensions is reduced to the two points $p = \pm p_F$. Near these points we have

$$E(p \pm p_F) \approx \pm\, v_F p \quad , \tag{2}$$

where $v_F = \partial E/\partial p|_{p_F}$ is the Fermi velocity.

The action (1) is not obviously positive. In fact, the operator in brackets $[\ \cdots\ ]$ clearly has Hermitian as well as anti-Hermitian components, and hence complex eigenvalues.

Let us assume that the gauge field has small amplitude and is slowly varying relative to the scale p_F. We will extract the slowly varying component of the fermion field to construct a low energy effective theory involving quasiparticles and gauge fields. This effective theory will have positive, semi-definite determinant.

First, we extract the quasiparticle modes (we suppress the spin index in what follows)

$$\psi(x,\tau) = \psi_L e^{+ip_F x} \ + \ \psi_R e^{-ip_F x} \quad , \tag{3}$$

where the functions $\psi_{L,R}$ are slowly varying. To simplify the action, we use the identity

$$e^{\pm ip_F x}\ E(-i\partial_x + A)\ e^{\mp ip_F x}\ \psi(x) \approx \pm\, v_F(-i\partial_x + A)\psi(x) \quad , \tag{4}$$

to obtain[a]

$$S_{\text{eff}} = \int d\tau dx \left[\psi_L^\dagger(-\partial_\tau + i\phi + i\partial_x - A)\psi_L \ + \ \psi_R^*(-\partial_\tau + i\phi - i\partial_x + A)\psi_R\right]. \tag{5}$$

We can write this in a more familiar form by introducing the Euclidean (1+1) gamma matrices $\gamma_{0,1,2}$, which are Hermitian and can be taken as $\gamma_i = \sigma_i$ where $\vec{\sigma}$ are the Pauli matrices. Using $\psi_{L,R} = \frac{1}{2}(1 \pm \gamma_2)\psi$ we obtain

$$S_{\text{eff}} = \int d\tau dx\ \bar{\psi}\gamma^\mu(\partial_\mu + iA_\mu)\psi \ \equiv \ \int d\tau dx\ \bar{\psi} \not{D} \psi \quad . \tag{6}$$

[a]For simplicity we set $v_F = 1$. Alternatively it could be absorbed in the definition of the spatial γ_1 as in QCD below.

Since the gamma matrices are Hermitian, and the operator $(\partial_\mu + iA_\mu)$ is anti-Hermitian, the operator $\not{D}$ in (6) has purely imaginary eigenvalues. However, because γ_2 anticommutes with $\not{D}$, the eigenvalues come in conjugate pairs: given $\not{D}\,\phi = \lambda\phi$, we have

$$\not{D}\,(\gamma_2\phi) = -\gamma_2 \not{D}\,\phi = -\gamma_2\lambda\phi = -\lambda(\gamma_2\phi_n) \quad .$$

Hence the determinant $\det \not{D} = \prod \lambda^*\lambda$ is real and positive semi-definite.

Thus, by considering only the low-energy modes near the Fermi points of the original model (1), we obtain an effective theory with desirable positivity properties. Note that it is necessary that the interactions (in this case, the background gauge field A) not couple strongly the low-energy modes to fast modes which are far from the Fermi points. This is a reasonable approximation in many physical situations, where it is the interactions among quasiparticles that are of primary interest. In what follows, we will apply this basic idea to more complex models such as QCD.

It is straightforward to go beyond (1+1) dimensions. Consider an electron system, described by

$$L = \psi^\dagger \left[i\partial_t - \epsilon(\vec{p}) \right] \psi + \mu\psi^\dagger\psi, \tag{7}$$

where $\epsilon(\vec{p})$ is the electron energy, a function of momentum $\vec{p}$. It is interesting to note that the non-relativistic system already has a sign problem even at the zero density, $\mu = 0$, though the free case does not suffer this, thanks to the separation of variables. In fact, it is quite unusual to have a system like vacuum QCD which has no sign problem. In Euclidean space the electron determinant is

$$M = -\partial_\tau - \epsilon(\vec{p}) + \mu. \tag{8}$$

The first term in operator (8) is anti-Hermitian, while the rest are Hermitian. Since there is no constant matrix P in the spin space that satisfies $M^\dagger = P\,M\,P^{-1}$, it has a sign problem in general.

Let us decompose the fermion momentum as

$$\vec{p} = \vec{p}_F + \vec{l}. \tag{9}$$

Again, the Fermi momentum is defined to be a momentum at which the energy equals to the chemical potential at zero temperature: $\mu = \epsilon(p_F)$, and the Fermi velocity is defined as

$$\vec{v}_F = \left. \frac{\partial\epsilon(p)}{\partial\vec{p}} \right|_{p=p_F} . \tag{10}$$

If we are interested in low energies, $\left|\vec{l}\right| \ll p_F$, we may integrate out the fast modes to get an effective operator,

$$M_{\rm EFT} = -\partial_\tau - \vec{v}_F \cdot \vec{l}, \tag{11}$$

which has complex eigenvalues. However, when we include the $-\vec{v}_F$ sector, we have $M_{\rm EFT}(\vec{v}_F) M_{\rm EFT}(-\vec{v}_F) \leq 0$ (i.e., has real negative eigenvalues), assuming $\epsilon(\vec{p}) = \epsilon(-\vec{p})$. We again see that the sign problem in the electron system is alleviated in the low-energy effective theory.

3. QCD

Let us recall why the measure of dense QCD is complex in Euclidean space. We use the following analytic continuation of the Dirac Lagrangian to Euclidean space:

$$x_0 \to -ix_E^4, \quad x_i \to x_E^i \; ; \; \gamma_0 \to \gamma_E^4, \quad \gamma_i \to i\gamma_E^i \quad . \tag{12}$$

The Euclidean gamma matrices satisfy

$$\gamma_E^{\mu\,\dagger} = \gamma_E^\mu \quad , \quad \{\gamma_E^\mu, \gamma_E^\nu\} = 2\delta^{\mu\nu}. \tag{13}$$

The Dirac-conjugated field, $\bar{\psi} = \psi^\dagger \gamma^0$, is mapped into a field, still denoted as $\bar{\psi}$, which is independent of ψ and transforms as $\psi^\dagger$ under $SO(4)$. Then, the grand canonical partition function for QCD is

$$Z(\mu) = \int {\rm d}A_\mu \det(M)\, e^{-S(A_\mu)}, \tag{14}$$

where $S(A_\mu)$ is the positive semi-definite gauge action, and the Dirac operator

$$M = \gamma_E^\mu D_E^\mu + \mu \gamma_E^4, \tag{15}$$

where $D_E = \partial_E + iA_E$ is the analytic continuation of the covariant derivative. The Hermitian conjugate of the Dirac operator is

$$M^\dagger = -\gamma_E^\mu D_E^\mu + \mu \gamma_E^4 \quad . \tag{16}$$

The first term in (15) is anti-Hermitian, while the second is Hermitian, hence the generally complex eigenvalues. When $\mu = 0$, the eigenvalues are purely imaginary, but come in conjugate pairs (λ, λ^*) [b], so the resulting determinant is real and positive semi-definite:

$$\det {\rm M} = \prod \lambda^* \lambda \geq 0 \quad . \tag{17}$$

[b] As before, note that γ_5 anti-commutes with M, so if $M\phi = \lambda\phi$, then $M\gamma_5\phi = -\gamma_5 M\phi = -\lambda\gamma_5\phi$.

In what follows we investigate the positivity properties of an effective theory describing only modes near the Fermi surface. To low energy modes, the curvature of the Fermi surface is not evident, and the positivity of the usual Dirac sea determinant is recovered.

A system of degenerate quarks with a net baryon number asymmetry is described by the QCD Lagrangian density with a chemical potential μ,

$$L_{\rm QCD} = \bar{\psi} i \not{D} \psi - \frac{1}{4} F^a_{\mu\nu} F^{a\mu\nu} + \mu \bar{\psi} \gamma_0 \psi, \tag{18}$$

where the covariant derivative $D_\mu = \partial_\mu + iA_\mu$ and we neglect the quark mass for simplicity.

At high density ($\mu \gg \Lambda_{\rm QCD}$), due to asymptotic freedom the energy spectrum of quarks near the Fermi surface is approximately given by a free Dirac eigenvalue equation,

$$(\vec{\alpha} \cdot \vec{p} - \mu)\, \psi_\pm = E_\pm \psi_\pm, \tag{19}$$

where $\vec{\alpha} = \gamma_0 \vec{\gamma}$ and $\psi_\pm$ denote the energy eigenfunctions with eigenvalues $E_\pm = -\mu \pm |\vec{p}|$, respectively. At low energy $E < \mu$, the states ψ_+ near the Fermi surface, $|\vec{p}| \sim \mu$, are easily excited but ψ_-, which correspond to the states in the Dirac sea, are completely decoupled due to the presence of the energy gap μ provided by the Fermi sea. Therefore the appropriate degrees of freedom at low energy consist of gluons and ψ_+ only.

Now, we wish to construct an effective theory describing the dynamics of ψ_+ by integrating out modes whose energy is greater than μ. Consider a quark near the Fermi surface, whose momentum is close to $\mu \vec{v}_F$. Without loss of generality, we may decompose the momentum of a quark into a Fermi momentum and a residual momentum as

$$p_\mu = \mu v_\mu + l_\mu, \tag{20}$$

where $v^\mu = (0, \vec{v}_F)$. Since the quark energy is given as

$$E = -\mu + \sqrt{(l_\parallel + \mu)^2 + l_\perp^2}, \tag{21}$$

the residual momentum should satisfy $(l_\parallel + \mu)^2 + l_\perp^2 \leq 4\mu^2$ with $\vec{l}_\parallel = \vec{v}_F \vec{l} \cdot \vec{v}_F$ and $\vec{l}_\perp = \vec{l} - \vec{l}_\parallel$.

To describe the small excitations of the quark with Fermi momentum, $\mu \vec{v}_F$, we decompose the quark fields as

$$\psi(x) = e^{i\mu \vec{v}_F \cdot \vec{x}} \left[\psi_+(\vec{v}_F, x) + \psi_-(\vec{v}_F, x) \right], \tag{22}$$

where

$$\psi_\pm(\vec{v}_F, x) = P_\pm(\vec{v}_F) e^{-i\mu \vec{v}_F \cdot \vec{x}} \psi(x) \quad \text{with} \quad P_\pm(\vec{v}_F) \equiv \frac{1 \pm \vec{\alpha} \cdot \vec{v}_F}{2}. \tag{23}$$

The quark Lagrangian in Eq. (18) then becomes

$$\begin{aligned}\bar{\psi}\left(i\not{D}+\mu\gamma^0\right)\psi &= \bar{\psi}_+(\vec{v}_F,x)i\gamma_\parallel^\mu D_\mu\psi_+(\vec{v}_F,x)\\ &+\bar{\psi}_-(\vec{v}_F,x)\gamma^0\left(2\mu+i\bar{D}_\parallel\right)\psi_-(\vec{v}_F,x)\\ &+\left[\bar{\psi}_-(\vec{v}_F,x)i\not{D}_\perp\psi_+(\vec{v}_F,x)+\text{h.c.}\right]\end{aligned}\tag{24}$$

where $\gamma_\parallel^\mu \equiv (\gamma^0, \vec{v}_F\vec{v}_F\cdot\vec{\gamma})$, $\gamma_\perp^\mu = \gamma^\mu - \gamma_\parallel^\mu$, $\bar{D}_\parallel = \bar{V}^\mu D_\mu$ with $V^\mu = (1,\vec{v}_F)$, $\bar{V}^\mu = (1,-\vec{v}_F)$, and $\not{D}_\perp = \gamma_\perp^\mu D_\mu$.

At low energy, we integrate out all the "fast" modes ψ_- and derive the low energy effective Lagrangian by matching all the one-light-particle irreducible amplitudes containing gluons and ψ_+ in loop expansion. The effects of fast modes will appear in the quantum corrections to the couplings of low energy interactions. At tree-level, the matching is equivalent to eliminating ψ_- in terms of equations of motion:

$$\psi_-(\vec{v}_F,x) = -\frac{i\gamma^0}{2\mu+iD_\parallel}\not{D}_\perp\psi_+(\vec{v}_F,x) = -\frac{i\gamma^0}{2\mu}\sum_{n=0}^{\infty}\left(-\frac{iD_\parallel}{2\mu}\right)^n\not{D}_\perp\psi_+(\vec{v}_F,x).\tag{25}$$

Therefore, the tree-level Lagrangian for ψ_+ becomes

$$L_{\text{eff}}^0 = \bar{\psi}_+ i\gamma_\parallel^\mu D_\mu\psi_+ - \frac{1}{2\mu}\bar{\psi}_+\gamma^0(\not{D}_\perp)^2\psi_+ \;+\; \cdots,\tag{26}$$

where the ellipsis denotes terms with higher derivatives.

Consider the first term in our effective Lagrangian, which when continued to Euclidean space yields the operator

$$M_{\text{eft}} = \gamma_\parallel^E\cdot D(A).\tag{27}$$

M_{eft} is anti-Hermitian and it anti-commutes with γ_5, so it leads to a positive semi-definite determinant. However, note that the Dirac operator is not well defined in the space of $\psi_+(\vec{v}_F,x)$ (for fixed v_F), since it maps $\psi_+(\vec{v}_F,x)$ into $\psi_+(-\vec{v}_F,x)$:

$$i\not{D}_\parallel P_+\psi = P_- i\not{D}_\parallel\psi.\tag{28}$$

Since $P_-(\vec{v}_F) = P_+(-\vec{v}_F)$, $i\not{D}\,\psi_+(\vec{v}_F,x)$ are $\psi_+(-\vec{v}_F,x)$ modes, or fluctuations of a quark with momentum $-\mu\vec{v}_F$.

Thus far we have considered the quark velocity as a parameter labelling different sectors of the quark field. This is similar to the approach of heavy quark effective theory (HQET)[9], in which the velocity of the heavy charm or bottom quark is almost conserved due to the hierarchy of scales between the heavy quark mass and the QCD scale. However, this approach contains

an ambiguity often referred to as "reparameterization invariance", related to the non-uniqueness of the decomposition (20) of quark momenta into a large and residual component. In the dense QCD case, two $\psi(v_F, x)$ modes whose values of v_F are not very different may actually represent the same degrees of freedom of the original quark field. In what follows we give a different formulation which describes *all* velocity modes of the quark field, and is suitable for defining the quasiparticle determinant.

First, a more precise definition of the breakup of the quark field into Fermi surface modes. Using the momentum operator in a position eigenstate basis: $\vec{p} = -i\vec{\partial}$, we construct the Fermi velocity operator:

$$\vec{v} = \frac{-i}{\sqrt{-\nabla^2}} \frac{\partial}{\partial \vec{x}} \quad , \tag{29}$$

which is Hermitian, and a unit vector.

Using the velocity operator, we define the projection operators $P_\pm$ as before and break up the quark field as, $\psi(x) = \psi_+(x) + \psi_-(x)$, with $\psi_\pm = P_\pm \psi$. By leaving $\vec{v}$ as an operator we can work in coordinate space without introducing the HQET-inspired velocity Fourier transform which introduces v_F as a parameter. If we expand the quark field in the eigenstates of the velocity operators, we recover the previous formalism with all Fermi velocities summed up.

The leading low-energy part of the quark action is given by

$$L_+ = \bar{\psi} P_-(v) \left(i\partial\!\!\!/ - A\!\!\!/ + \mu\gamma_0 \right) P_+(v) \psi \quad . \tag{30}$$

As before, we define the fields ψ_+ to absorb the large Fermi momentum:

$$\psi_+(x) = e^{-i\mu \vec{x}\cdot\vec{v}} P_+(v) \psi(x). \tag{31}$$

Let us denote the eigenvalue v obtained by acting on the field ψ (which has momentum of order μ) as v_l (or v "large"), whereas eigenvalues obtained by acting on the effective field theory modes ψ_+ are denoted v_r (or v "residual"). If the original quark mode had momentum p with $|p| > \mu$ (i.e. was a particle), then v_l and v_r are parallel, whereas if $|p| < \mu$ (as for a hole) then v_r and v_l are anti-parallel. In the first case, we have $P_+(v_l) = P_+(v_r)$ whereas in the second case $P_+(v_l) = P_-(v_r)$. Thus, the residual modes ψ_+ can satisfy either of $P_\pm(v_r)\psi_+ = \psi_+$, depending on whether the original ψ mode from which it was derived was a particle or a hole. In fact, ψ_+ modes can also satisfy either of $P_\pm(v_l)\psi_+ = \psi_+$ since they can originate from ψ modes with momentum $\sim +\mu v$ as well as $-\mu v$ (both are present in the

original measure: $D\bar{\psi}\, D\psi$). So, the functional measure for ψ_+ modes contains all possible spinor functions – the only restriction is on the momenta: $|l_0|, |\vec{l}| < \Lambda$, where Λ is the cutoff.

In light of the ambiguity between v_l and v_r, the equation $\psi = e^{+i\mu x\cdot v}\psi_+$ must be modified to

$$\psi = \exp\left(+i\mu x\cdot v\ \alpha\cdot v\right)\psi_+ = \exp\left(+i\mu x\cdot v_r\ \alpha\cdot v_r\right)\psi_+ \quad , \tag{32}$$

where the factor of $\alpha\cdot v_r$ corrects the sign in the momentum shift if v_r and v_l are anti-parallel. In general, any expression with two powers of v is unaffected by this ambiguity. For notational simplicity we define a local operator

$$X \equiv \mu\, x\cdot v\ \alpha\cdot v = \mu\frac{\alpha^i x^j}{\nabla^2}\frac{\partial^2}{\partial x^i \partial x^j}. \tag{33}$$

Taking this into account, we obtain the following action:

$$L_+ = \bar{\psi}_+ e^{-iX}\left(i\partial\!\!\!/ - A\!\!\!/ + \mu\gamma_0\right)e^{+iX}\psi_+ \quad . \tag{34}$$

We treat the $A\!\!\!/$ term separately from $i\partial\!\!\!/ + \mu\gamma_0$ since the former does not commute with X, while the latter does. Continuing to Euclidean space, and using the identity $P_-\gamma_\mu P_+ = \gamma_\mu^{\|} P_+$, we obtain

$$L_+ = \bar{\psi}_+\gamma_{\|}^{\mu}\left(\partial^\mu + iA_+^\mu\right)\psi_+ \quad , \tag{35}$$

where

$$A_+^\mu = e^{-iX}\ A^\mu\ e^{+iX} \quad , \tag{36}$$

and all γ matrices are Euclidean. The term containing A cannot be fully simplified because $[v, A] \neq 0$. Physically, this is because the gauge field carries momentum and can deflect the quark velocity. The redefined ψ_+ modes are functions only of the residual momenta l, and the exponential factors in the A term reflect the fact that the gluon originally couples to the quark field ψ, not the residual mode ψ_+.

The kinetic term in (35) can be simplified to

$$\gamma_{\|}^{\mu}\partial^\mu = \gamma^\mu\partial^\mu \tag{37}$$

since $v\cdot\partial\, v\cdot\gamma = \partial\cdot\gamma$. The action (35) is the most general dimension 4 term with the rotational, gauge invariance[c] and projection properties

[c] If we simultaneously gauge transform A_+ and ψ_+ in (35) the result is invariant. There is a simple relation between the gauge transform of the + fields and that of the original fields: $U_+(x) = U(x)e^{iX}$. Of course, the momentum-space support of the + gauge transform must be limited to modes less than the cutoff Λ.

appropriate to quark quasiparticles. Therefore, it is a general consequence of any Fermi liquid description of quark-like excitations.

The operator in (35) is anti-Hermitian and leads to a positive, semi-definite determinant since it anti-commutes with γ_5. The corrections given in (26) are all Hermitian, so higher orders in the $1/\mu$ expansion may re-introduce complexity. The structure of the leading term plus corrections is anti-Hermitian plus Hermitian, just as in the original QCD Dirac Lagrangian with chemical potential.

By integrating out the fast modes, the Euclidean QCD partition function can be rewritten as

$$Z(\mu) = \int \mathrm{d}A_+ \ \det M_{\mathrm{eff}}(A_+) e^{-S_{\mathrm{eff}}(A_+)}. \tag{38}$$

The leading terms in the effective action for gluons (these terms are generated when we match our effective theory, with energy cutoff Λ, to QCD) also contribute only real, positive terms to the partition function:

$$S_{\mathrm{eff}}(A) = \int \mathrm{d}^4 x_E \left(\frac{1}{4} F^a_{\mu\nu} F^a_{\mu\nu} + \frac{M^2}{16\pi} \sum_{\vec{v}_F} A^a_{\perp\mu} A^a_{\perp\mu} \right) \geq 0, \tag{39}$$

where $A_\perp = A - A_\parallel$ and the Debye screening mass is $M = \sqrt{N_f/(2\pi^2)} g_s \mu$. Note that Landau damping is due to softer quark modes which have not been integrated out, and therefore do not contribute to matching.

Although the HDET only describes low-energy modes, it still contains Cooper pairing interactions. This is because Cooper pairing, in which the quasiparticles have nearly equal and opposite momenta, is induced by gluonic interactions with small energy and momentum transfer. That is, although a gluon exchange (or other interaction) which causes a large angular deflection of a quasiparticle

$$|\vec{p}\rangle \to |\vec{p}\,'\rangle$$

must involve a large momentum transfer, and hence is not part of the effective theory, a Cooper pairing interaction

$$|\vec{p}, -\vec{p}\rangle \to |\vec{p}\,', -\vec{p}\,'\rangle$$

only involves a small energy and momentum transfer, even if the angle between $\vec{p}$ and $\vec{p}\,'$ is large. Hence, it is described by the leading order interaction between soft gluons and quarks in the effective theory (35).

4. Lattice Simulation

The goal of this section is to give a method for simulating QCD at finite density. We will consider a chemical potential μ much larger than $\Lambda_{\rm QCD}$ throughout, and divide the functional integral over quark excitations into two parts: (I) modes within a shell of width Λ of the Fermi surface, and (II) modes which are further than Λ from the Fermi surface. We will assume the hierarchy

$$\mu >> \Lambda >> \Lambda_{\rm QCD} \quad . \tag{40}$$

The quark determinant in region (I) is well approximated by the determinant of the leading operator in high density effective theory (HDET) as long as the first inequality in (40) is satisfied. As discussed in the previous section, it is positive and real.

Here we will show that the contributions to the effective action for the gauge field from quark modes in region (II) are small and vanish as the Λ grows large compared to $\Lambda_{\rm QCD}$.

First consider the theory in Minkowski space. The Dirac operator is

$$M = i\not{D} + \mu\gamma_0 \tag{41}$$

and the Dirac equation can be written as

$$i\partial_0\psi = H\psi \tag{42}$$

with

$$H = i\alpha\cdot\partial - \mu \tag{43}$$

a Hermitian operator. The break up into regions (I) and (II) proceeds naturally in terms of energy eigenvalues of H (or l_0 in the HDET notation). The low-lying modes in region (I) are particle states with spatial momenta satisfying $|\vec{p}| \approx \mu$.

The analytic continuation of region (I) to Euclidean space leads to the HDET determinant considered previously.

Modes in region (II) all have large energy eigenvalues, at least as large as Λ. In considering their effect on physics at the scale $\Lambda_{\rm QCD}$, we can integrate them out in favor of local operators suppressed by powers of $\Lambda_{\rm QCD}/\Lambda$.

To make this concrete, consider the effective action for gauge fields with field strengths $F_{\mu\nu}$ of order $\Lambda_{\rm QCD}$. The quark contribution to this effective action is simply the logarithm of the determinant we wish to compute. It can be expanded diagrammatically in graphs with external gauge field lines connected to a single quark loop. Restricting to region (II), we require that

the quark modes in the loop have large H eigenvalues. Evaluating such graphs leads only to operators which are local in the external fields $A_\mu(x)$.

The resulting renormalizable (dimension 4) operator is the finite density equivalent of $F_{\mu\nu}^2$, except that due to the breaking of Lorentz invariance it contains separate time- and space-like components which represent the contribution of high-energy modes to the renormalization of the coupling constant, and Debye screening. These effects do not introduce a complex component when continued to Euclidean space.

Higher dimension operators, which involve additional powers of $F_{\mu\nu}$ or covariant derivatives D_μ are suppressed by the scale Λ. These are presumably the source of complex terms introduced to the effective action. However, due to the $1/\Lambda$ suppression they are dominated by the contribution from the low-lying modes in region (I), which is necessarily non-local, but real.

The logarithm of the Euclidean quark determinant will have the form:

$$\ln \det M \sim O(\mu^4) + (\text{non} - \text{local}, \text{real}) + O(\frac{1}{\Lambda})(\text{local}, \text{complex}) \quad , \quad (44)$$

where the first term is the (real, constant) free energy of non-interacting quarks, the second term is from the positive determinant in region (I) and the last term is the suppressed, complex contribution from region (II). Only the last two terms depend on the gauge field $A_\mu(x)$

On the lattice, one can use the dominant dependence of $\det M$ on the first and second terms to do importance sampling. In order to keep the complex higher dimension operators (last term in (44)) small, it is important that the gauge field strengths are kept smaller than Λ^2. One can impose this condition by using two different lattice spacings, a_g for the gluons and $a_{\rm det}$ for the quarks, with $a_g > a_{\rm det}$. The determinant is calculated on the finer $a_{\rm det}$ lattice, and is a function of plaquettes which are obtained by interpolation from the plaquettes on the coarser a_g lattice. Interpolation can be defined in a natural way, since each lattice link variable $U_{x\mu}$ is an element of the gauge group, and one can connect any two points g_1, g_2 on the group manifold in a linear fashion: $g(t) = g_1 + t(g_2 - g_1)$, $0 \leq t \leq 1$.

5. Inequalities and Anomaly Matching

Positivity of the measure allows for rigorous QCD inequalities at asymptotic density. For example, inequalities among masses of bound states can be obtained using bounds on bare quasiparticle propagators. One subtlety that arises is that a quark mass term does not lead to a quasiparticle gap

(the mass term just shifts the Fermi surface). Hence, for technical reasons the proof of non-breaking of vector symmetries[10] must be modified. (Naive application of the Vafa-Witten theorem would preclude the breaking of baryon number that is observed in the color-flavor-locked (CFL) phase[11]). A quasiparticle gap can be inserted by hand to regulate the bare propagator, but it will explicitly violate baryon number. However, following the logic of the Vafa-Witten proof, any symmetries which are preserved by the regulator gap cannot be broken spontaneously. One can, for example, still conclude that isospin symmetry is never spontaneously broken (although see below for a related subtlety). In the case of three flavors, one can introduce a regulator d with the color and flavor structure of the CFL gap to show rigorously that none of the symmetries of the CFL phase are broken at asymptotic density. On the other hand, by applying anomaly matching conditions[12], we can prove that the $SU(3)_A$ symmetries *are* broken. We therefore conclude that the CFL phase is the true ground state for three light flavors at asymptotic density, a result that was first established by explicit calculation[13,8,14].

To examine the long-distance behavior of the vector current, we note that its correlator in a given background gauge field A can be written as

$$\left\langle J_\mu^a(\vec{v}_F,x)J_\nu^b(\vec{v}_F,y)\right\rangle^A = -\mathrm{Tr}\,\gamma_\mu T^a S^A(x,y;d)\gamma_\nu T^b S^A(y,x;d),$$

where the $SU(N_f)$ flavor current $J_\mu^a(\vec{v}_F,x) = \bar{\psi}_+(\vec{v}_F,x)\gamma_\mu T^a\psi_+(\vec{v}_F,x)$. The propagator with $SU(3)_V$-invariant IR regulator d is given as

$$S^A(x,y;d) = \langle x|\,\frac{1}{M}\,|y\rangle = \int_0^\infty \mathrm{d}\tau\,\langle x|\,e^{-i\tau(-iM)}\,|y\rangle$$

where with $D = \partial + iA$

$$M = \gamma_0\begin{pmatrix} D\cdot V & d \\ d^\dagger & D\cdot\bar{V}\end{pmatrix} \tag{45}$$

Since the eigenvalues of M are bounded from below by d, we have

$$\left|\langle x|\,\frac{1}{M}\,|y\rangle\right| \le \int_R^\infty \mathrm{d}\tau\, e^{-d\tau}\sqrt{\langle x|x\rangle}\sqrt{\langle y|y\rangle} = \frac{e^{-dR}}{d}\sqrt{\langle x|x\rangle}\sqrt{\langle y|y\rangle}, \tag{46}$$

where $R \equiv |x-y|$. The current correlators fall off rapidly as $R\to\infty$;

$$\left|\int \mathrm{d}A_+ \det M_{\mathrm{eff}}(A)\; e^{-S_{\mathrm{eff}}}\left\langle J_\mu^A(\vec{v}_F,x)J_\nu^B(\vec{v}_F,y)\right\rangle^{A_+}\right|$$

$$\le \int_{A_+}\left|\left\langle J_\mu^A(\vec{v}_F,x)J_\nu^B(\vec{v}_F,y)\right\rangle^{A_+}\right| \le \frac{e^{-2dR}}{d^2}\int_{A_+}|\langle x|x\rangle|\,|\langle y|y\rangle|\,, \tag{47}$$

where we used the Schwartz inequality in the first inequality, since the measure of the effective theory is now positive, and equation (46) in the second inequality. The IR regulated vector currents do not create massless modes out of the vacuum or Fermi sea, which implies that there is no Nambu-Goldstone mode in the $SU(3)_V$ channel. Therefore, for three massless flavors $SU(3)_V$ has to be unbroken as in CFL. The rigorous result provides a non-trivial check on explicit calculations, and applies to any system in which the quasiparticle dynamics have positive measure. The case with non-zero quark masses is complicated, and requires careful consideration of the order of limits[6].

6. Conclusion

The low-energy physics of dense fermionic matter, ranging from quark matter to electronic systems, is controlled by modes near the Fermi surface. An effective Lagrangian describing the low-energy modes can be given in a systematic expansion in powers of the energy scale over the chemical potential. The leading term in this expansion has a simple form, and we have shown that it leads to a real, positive Euclidean path integral measure.

This observation opens the door to importance sampling in Monte Carlo simulations of dense matter systems. The key requirement is that the interactions do not strongly couple the low-energy modes to modes far from the Fermi surface. QCD at high density satisfies this requirement, as do all asymptotically free models. Electronic systems in which the important interactions involve momentum transfer less than the Fermi energy are in this category, although some idealized models such as the Hubbard model are not. We have given some proposals for how the positive effective theory might be simulated numerically. Ultimately, we hope that actual practitioners will develop even more practical methods.

Finally, positivity has analytical applications as well, since it allows the use of rigorous inequalities. In QCD we obtain restrictions on symmetry breaking patterns at high density. Similar restrictions can probably be obtained for electronic systems with suitable interactions.

References

1. See, for instance, S. Hands, *Nucl. Phys. Proc. Suppl.* **106**, 142 (2002) [arXiv:hep-lat/0109034]; I. M. Barbour, S. E. Morrison, E. G. Klepfish, J. B. Kogut and M. P. Lombardo, *Nucl. Phys. Proc. Suppl.* **60A**, 220 (1998) [arXiv:hep-lat/9705042]; M. G. Alford, *Nucl. Phys. Proc. Suppl.* **73**, 161 (1999) [arXiv:hep-lat/9809166].

2. Z. Fodor and S. D. Katz, *Phys. Lett.* **B534**, 87 (2002) [arXiv:hep-lat/0104001]; JHEP **0203**, 014 (2002) [arXiv:hep-lat/0106002].
3. C. R. Allton *et al.*, *Phys. Rev.* **D66**, 074507 (2002) [arXiv:hep-lat/0204010]; P. de Forcrand and O. Philipsen, arXiv:hep-lat/0209084; M. D'Elia and M. P. Lombardo, *Phys. Rev.* **D67**, 014505 (2003) [arXiv:hep-lat/0209146].
4. For reviews, see D. K. Hong, *Acta Phys. Polon.* **B32**, 1253 (2001) [arXiv:hep-ph/0101025]; S. D. H. Hsu, [arXiv:hep-ph/0003140], Proceedings of the TMU-Yale Meeting on Dynamics of Gauge Fields, Tokyo, 1999; M. Alford, [arXiv:hep-ph/0102047]; K. Rajagopal and F. Wilczek, [arXiv:hep-ph/0011333].
5. For Japanese Hadronic Facilities, see "Expression of Interest for Nuclear/Hadron Phys. Exp. at the 50-GeV PS," http://psux1.kek.jp/50GeV-PS/EOI-nucl-hadron.pdf; For HADES at GSI, see http://www-hades.gsi.de/.
6. D. K. Hong and S. D. H. Hsu, *Phys. Rev.* **D66**, 071501 (2002) [arXiv:hep-ph/0202236]; *Phys. Rev.* **D68**, 034011 (2003), [arXiv:hep-ph/0304156];[arXiv:hep-lat/0309103], To appear in the proceedings of 21st International Symposium on Lattice Field Theory (LATTICE 2003), Tsukuba, Ibaraki, Japan, 15-19 Jul 2003.
7. D. K. Hong, *Phys. Lett.* **B473**, 118 (2000) [hep-ph/9812510].
8. D. K. Hong, *Nucl. Phys.* **B582**, 451 (2000) [hep-ph/9905523].
9. N. Isgur and M. B. Wise, *Phys. Lett.* **B232**, 113 (1989); *ibid.* **B237**, 527 (1990); H. Georgi, *Phys. Lett.* **B240**, 447 (1990).
10. C. Vafa and E. Witten, *Phys. Rev. Lett.* **53**, 535 (1984); *Nucl. Phys.* **B234**, 173 (1984).
11. M. G. Alford, K. Rajagopal and F. Wilczek, *Nucl. Phys.* **B537**, 443 (1999) [arXiv:hep-ph/9804403].
12. S. D. Hsu, F. Sannino and M. Schwetz, *Mod. Phys. Lett.* **A16**, 1871 (2001) [arXiv:hep-ph/0006059]; F. Sannino, *Phys. Lett.* **B480** (2000) 280 [arXiv:hep-ph/0002277]; arXiv:hep-ph/0301035.
13. N. Evans, J. Hormuzdiar, S. D. Hsu and M. Schwetz, *Nucl. Phys.* **B581**, 391 (2000) [arXiv:hep-ph/9910313].
14. T. Schafer, *Nucl. Phys.* **B575**, 269 (2000) [arXiv:hep-ph/9909574]; I. A. Shovkovy and L. C. Wijewardhana, *Phys. Lett.* **B470**, 189 (1999) [arXiv:hep-ph/9910225].
15. P. F. Bedaque and T. Schafer, *Nucl. Phys.* **A697**, 802 (2002) [arXiv:hep-ph/0105150]; D. B. Kaplan and S. Reddy, *Phys. Rev.* **D65**, 054042 (2002) [arXiv:hep-ph/0107265].
16. D. K. Hong, T. Lee and D. P. Min, *Phys. Lett.* **B477**, 137 (2000) [arXiv:hep-ph/9912531]; D. K. Hong, *Phys. Rev.* **D62**, 091501 (2000) [arXiv:hep-ph/0006105].

DYNAMICAL THEORY OF DISORIENTED CHIRAL CONDENSATES AT QCD PHASE TRANSITION

SANG PYO KIM

Department of Physics,
Kunsan National University,
Kunsan 573-701, Korea
E-mail: sangkim@kunsan.ac.kr

We apply the canonical quantum field theory based on the Liouville-von Neumann equation to the nonequilibrium linear sigma model. Particular emphasis is put on the mechanism for domain growth of disoriented chiral condensates due to long wavelength modes and its scaling behavior. Scattering effects, decoherence and emergence of order parameter are also discussed beyond the Hartree approximation.

1. Introduction

The high density and temperature state of hadronic matter consists of quark-gluon plasma and would have occurred in the early universe or may be realizable in heavy ion collision experiments. In QCD with two massless quarks, the chiral symmetry $SU(2)_L \times SU(2)_R$ at high temperatures spontaneously breaks down to $SU(2)_{L+R}$ at lower temperatures by the quark-antiquark condensate $\langle \bar{q}^i_L q_{Rj} \rangle = \sigma \delta^i_j + i\vec{\pi} \cdot \vec{\tau}^i_j$, an order parameter. The field $\phi_a = (\sigma, \vec{\pi})$ respects $O(4)$ rotations and thus belongs to the universality class of a four component isotropic Heisenberg antiferromagnet.[1] The effective theory of the QCD phase transition is described by the linear sigma model[2] or equally by a mean-field theory of Polyakov loops and/or by the glueball fields for the hadronic states of QCD.[3]

In QCD the $SU(2)$ phase transition would probably be a second order whereas the $SU(3)$ phase transition would be a weakly first order. In relativistic heavy ion collisions, hot and high dense regions are made, where the chiral symmetry would be restored, and as the regions cool, the quark-gluon plasma would undergo the second order phase transition. In second order phase transitions, as temperature approaches a critical temperature, the correlation length cannot grow indefinitely and must be frozen due to

causality.[4] However, the cooling process may be fast enough for the kinematic time scale of quench to be smaller than thermal relaxation time scale. The rapid expansion of the quark-gluon plasma enforces a rapid quench and results in a phase transition far from equilibrium (nonequilibrium). In such a nonequilibrium phase transition domains (regions of misaligned vacuum) develop due to the instability of long wavelength modes.

Another possible candidate for the QCD phase transition is Centauri events in comic rays.[5] Anomalously large event-by-event fluctuations have been observed in the ratio of charged to neutral pions and thus require a new theory or interpretation. The disoriented chiral condensate (DCC) of classical pion fields was introduced as one of the proposed mechanisms for coherent emission of pions from a large domain.[6] If the QCD phase transition proceeds in equilibrium, all directions of $\vec{\pi}$ are equally probable and domains of size $1/T_c$ cannot explain the anomalous production of pions of a certain kind. Rajagopal and Wilczek advocated the nonequilibrium QCD phase transition through a quench for DCC domain growth, where unstable long wavelength modes of pions are exponentially amplified.[2]

In this talk, we adopt a recently introduced canonical field method to elaborate the nonequilibrium QCD phase transition based on the linear sigma model. The quench process is imitated by a mass squared that changes signs during a finite quench time.[7,8,9] We particularly focus on the dynamical process of domain formation from long wavelength modes of pions growing exponentially during an instability period and on the scaling behavior of domains size. The scaling behavior of domains has been found through simulations in condensed matter systems and cosmology. We further discuss the effects of direct scatterings among each pion field modes on domains size and on decohering long wavelength modes and emergence of an order parameter.

2. Nonequilibrium Linear Sigma Model

The effective theory of QCD phase transition with two massless quarks is described by the quark-antiquark condensate $\langle \bar{q}q \rangle$, which, in turn, defines $\phi_a = (\sigma, \vec{\pi})$, $\vec{\pi}$ being the pion field. The quark mass m_q provides a symmetry breaking external field to an, otherwise, $O(4)$ symmetric field theory at high temperatures. To include a quench, we may write the linear sigma model[10] in the form

$$L = \int d^3x \left[\frac{1}{2} \partial_\mu \phi^a \partial^\nu \phi_a - \frac{\lambda}{4} (\phi^a \phi_a)^2 - \frac{1}{2} m^2(t) \phi^a \phi_a + H\sigma \right]. \qquad (1)$$

The time-dependent quench process has been imitated by the symmetry breaking mass squared $m^2(t)$, which changes signs during the phase transition. In this sense Eq. (1) is the nonequilibrium linear sigma model. As H does not affect much the instability of long wavelength modes during the phase transition, we assume $H = 0$ for simplicity reason.

To illustrate how nonequilibrium phase transitions in general affect formation of domains, we consider a simple field model with a quench time scale.[7] The simple model motivated by the nonequilibrium linear sigma model is given by the potential

$$V(\phi_a) = \frac{m^2(t)}{2}\phi^a\phi_a + \frac{\lambda}{4}(\phi^a\phi_a)^2, \tag{2}$$

with the mass squared

$$m^2(t) = m_1^2 - m_0^2 \tanh\Big(\frac{t}{\tau}\Big), \quad (m_0^2 > m_1^2). \tag{3}$$

In the limit of zero quench time ($\tau = 0$), we obtain the instantaneous (sudden) quench. Now finite temperature field theory[11] cannot be applied to this model when the quench time scale τ is smaller than relaxation time scale. Further, in the second order phase transitions, long wavelength modes grow exponentially during rolling over the barrier. Finite temperature field theory does not properly take into account dynamical processes of phase transitions.

One therefore needs some nonequilibrium quantum field theory when the kinematic time scale is smaller than thermal relaxation time scale so that finite temperature field theory cannot be applied. There are several methods for nonequilibrium quantum fields such as the closed-time path integral[12] and the functional Schrödinger-picture.[13] Recently there has been developed a canonical method based on the quantum Liouville-von Neumann equation, which provides all time-dependent Fock states at the leading order.[7,8] The new canonical method is equivalent, at leading order, to the time-dependent Hartree approximation, but it can go beyond the Hartree approximation since any perturbation method can be readily applied to these Fock states.

As a nonlinear theory, the linear sigma model has defied yet any nonperturbative solution in a closed form. We can, at best, rely on perturbation methods. The Hartree approximation, though being a perturbation scheme, includes some part of nonperturbative effects at the lowest order.[14,15] In the Hartree approximation, dividing the σ field into a background field $\phi(t)$ and its quantum fluctuation $\chi(\mathbf{x}, t)$, and using the Hartree factorization,[14]

we obtain the truncated Hamiltonian for the linear sigma model

$$H_0 = \int d^3x \left[\frac{\pi_\chi^2}{2} + \frac{\pi_{\vec{\pi}}^2}{2} + \frac{(\nabla\chi)^2}{2} + \frac{(\nabla\vec{\pi})^2}{2} + h_\phi(t)\chi + \frac{m_\chi^2(t)}{2}\chi^2 + \frac{m_{\vec{\pi}}^2}{2}\vec{\pi}^2 \right], \quad (4)$$

where the effective couplings are

$$\begin{aligned} h_\phi(t) &= \phi(t)[m^2(t) + 4\lambda\phi^2(t) + 4\lambda\langle\vec{\pi}^2\rangle], \\ m_\chi^2(t) &= m^2(t) + 4\lambda\phi^2(t) + 4\lambda\langle\vec{\pi}^2\rangle, \\ m_{\vec{\pi}}^2(t) &= m^2(t) + 12\lambda\phi^2(t) + 4\lambda\langle\vec{\pi}^2\rangle. \end{aligned} \quad (5)$$

3. DCC Domain Growth

Quantum dynamics of DCC can be further approximated by an exactly solvable model now motivated by the linear sigma model (1) or the Hartree approximation (4). The model Hamiltonian for the pion field ϕ_a is[16]

$$H_0(t) = \int d^3x \left[\frac{1}{2}\pi^a\pi_a + \frac{1}{2}(\nabla\phi^a \cdot \nabla\phi_a)^2 + \frac{1}{2}m^2(t)\phi^a\phi_a \right]. \quad (6)$$

Note that all pion fields are decoupled from each other since the nonlinear term is neglected at this moment. In terms of the Fourier cosine and sine modes

$$\phi_{\mathbf{k}}^{(+)}(t) = \frac{1}{2}[\phi_{\mathbf{k}}(t) + \phi_{-\mathbf{k}}(t)], \quad \phi_{\mathbf{k}}^{(-)}(t) = \frac{i}{2}[\phi_{\mathbf{k}}(t) - \phi_{-\mathbf{k}}(t)], \quad (7)$$

and with a compact notations $\alpha = \{(\pm), \mathbf{k}\}$, the Hamiltonian becomes a sum of decoupled time-dependent oscillators

$$H_0(t) = \sum_{a\alpha} \frac{1}{2}\pi_{a\alpha}^2 + \frac{1}{2}\omega_\alpha^2(t)\phi_{a\alpha}^2, \quad (\omega_\alpha^2(t) = \mathbf{k}^2 + m^2(t)). \quad (8)$$

Then quantum states of the pion field are found by the time-dependent creation and annihilation operators[7,8]

$$\begin{aligned} \hat{a}_{a\alpha}^\dagger(t) &= -i[\varphi_{a\alpha}(t)\hat{\pi}_{a\alpha} - \dot{\varphi}_{a\alpha}(t)\hat{\phi}_{a\alpha}], \\ \hat{a}_{a\alpha}(t) &= i[\varphi_{a\alpha}^*(t)\hat{\pi}_{a\alpha} - \dot{\varphi}_{a\alpha}^*(t)\hat{\phi}_{a\alpha}], \end{aligned} \quad (9)$$

where $\hat{\pi}_{a\alpha}$ and $\hat{\phi}_{a\alpha}$ are Schrödinger operators. Note that these operators do not diagonalize the Hamiltonian (8), but satisfy the Liouville-von Neumann equations

$$i\frac{\partial}{\partial t}\hat{a}_{a\alpha}^\dagger(t) + [\hat{a}_{a\alpha}^\dagger(t), \hat{H}_{a\alpha}(t)] = 0, \quad i\frac{\partial}{\partial t}\hat{a}_{a\alpha}(t) + [\hat{a}_{a\alpha}(t), \hat{H}_{a\alpha}(t)] = 0, \quad (10)$$

which lead to mean-field equations for the auxiliary field variables

$$\ddot{\varphi}_{a\alpha}(t) + \omega_\alpha^2(t)\varphi_{a\alpha}(t) = 0. \quad (11)$$

In fact, these operators satisfy the equal time commutation relations

$$[\hat{a}_{a\alpha}(t), \hat{a}^{\dagger}_{b\beta}(t)] = \delta_{ab}\delta_{\alpha\beta}, \tag{12}$$

with the aid of the Wronskian condition

$$\dot{\varphi}^{*}_{a\alpha}\varphi_{a\alpha} - \varphi^{*}_{a\alpha}\dot{\varphi}_{a\alpha} = i. \tag{13}$$

The Fock space for each pion field mode consists of number states defined as

$$\hat{N}_{a\alpha}(t)|n_{a\alpha}, t\rangle_0 \equiv \hat{a}^{\dagger}_{a\alpha}(t)\hat{a}_{a\alpha}(t)|n_{a\alpha}, t\rangle_0 = n_{a\alpha}|n_{a\alpha}, t\rangle_0. \tag{14}$$

We should note that these are exact quantum states of the time-dependent Schrödinger equation for the Hamiltonian (6) or (8). The quantum state of the pion field itself is then a product of each mode state for each pion field. Of a particular interest is the Gaussian vacuum state of the pion field

$$|0, t\rangle_0 = \prod_{a\alpha} |0_{a\alpha}, t\rangle_0. \tag{15}$$

Now the Green function for the pion field is simply given by

$$G_0(\mathbf{x}, t; \mathbf{x}', t') = \prod_{a\alpha} G_{0a\alpha}(\phi_{a\alpha}, t; \phi'_{a\alpha}, t'), \tag{16}$$

where the $(a\alpha)$-mode Green function takes the form

$$G_{0a\alpha}(\phi_{a\alpha}, t; \phi'_{a\alpha}, t') = \sum_{n_{a\alpha}} \langle \phi_{a\alpha}|n_{a\alpha}, t\rangle_0 \; {}_0\langle n_{a\alpha}, t'|\phi'_{a\alpha}\rangle. \tag{17}$$

To study formation of domains during a nonequilibrium quench process, we consider the smooth finite quench (3). The free field theory (6) is then exactly solvable,[7] and is a good approximation for the linear sigma model as long as $|m^2(t)|$ is larger than $|\phi(t)|$ and $\langle\vec{\pi}\rangle^2 = \sum_{b\beta} \varphi^{*}_{b\beta}\varphi_{b\beta}$. Far before the phase transition, each mode is stable and oscillates around the true vacuum with the solution

$$\varphi_{a\alpha i}(t) = \frac{1}{\sqrt{2\omega_{\alpha i}}} e^{-i\omega_{\alpha i}t}, \quad \omega_{\alpha i} = \sqrt{\mathbf{k}^2 + m_i^2}. \tag{18}$$

The two-point correlation function for each component of pion field is the Green function at equal times

$$G_{0a}(\mathbf{x}, \mathbf{x}', t) = \langle \hat{\phi}_a(\mathbf{x}, t)\hat{\phi}_a(\mathbf{x}', t)\rangle_0 = G_{0a}(\mathbf{x}, t; \mathbf{x}', t) \tag{19}$$

with respect to the Gaussian vacuum or thermal equilibrium.

On the other hand, after the phase transition ($m^2 = -m_f^2 = -(m_0^2 - m_1^2)$), the long wavelength modes with $k < m_f$ become unstable and exponentially grow, whereas short wavelength modes with $k > m_f$ are still

stable and oscillate around the false vacuum. Far after the phase transition, the unstable long wavelength modes have the asymptotic solutions

$$\varphi_{a\alpha f} = \frac{\mu_{\mathbf{k}}}{\sqrt{2}(m_f^2 - \mathbf{k}^2)^{1/2}} e^{(m_f^2 - \mathbf{k}^2)^{1/2} t} + \frac{\nu_{\mathbf{k}}}{\sqrt{2}(m_f^2 - \mathbf{k}^2)^{1/2}} e^{-(m_f^2 - \mathbf{k}^2)^{1/2} t}. \tag{20}$$

Here $\mu_{\mathbf{k}}$ and $\nu_{\mathbf{k}}$ depend on the quench process and satisfy the relation $|\mu_{\mathbf{k}}|^2 - |\nu_{\mathbf{k}}|^2 = 1$. The correlation function is then dominated by the exponentially growing part

$$G_{0af}(\mathbf{x}, t; \mathbf{x}', t) \simeq \int_0^{m_f} \frac{d^3\mathbf{k}}{(2\pi)^3} e^{i\mathbf{k}\cdot(\mathbf{x}-\mathbf{x}')} |\mu_{\mathbf{k}}|^2 \frac{e^{2\sqrt{m_f^2 - \mathbf{k}^2}\, t}}{2(\mathbf{k}^2 - m_f^2)}. \tag{21}$$

Using the exact solutions,[7] we obtain the two-point thermal correlation function for each pion field at the intermediate stage of the quench ($-\tau < t < \tau$)

$$G_{0aT}(r, t) \simeq G_{0aT}(0, t) \frac{\sin\left(\frac{\sqrt{\tau t}}{m_0} r\right)}{\frac{\sqrt{\tau t}}{m_0} r} \exp\left(-\frac{r^2}{8\frac{\sqrt{\tau t}}{m_0}}\right). \tag{22}$$

It follows that domains obey a scaling relation for the correlation length

$$\xi_D(t) = 2\left(\frac{2\tau t}{m_0^2}\right)^{1/4}. \tag{23}$$

The power 1/4 has been found in numerical simulations.[17] At the later stage far after the quench ($t \gg \tau$), domains still show the Cahn-Allen scaling behavior but with a different power

$$\xi_D(t) = 2\left(\frac{2\tilde{t}}{m_f}\right)^{1/2}, \quad \tilde{t} = t - \frac{\tau^3}{8}[\zeta(3) - 1](m_i^2 + m_f^2). \tag{24}$$

The scaling relation for the instantaneous quench is obtained by letting $\tau = 0$ in Eq. (24). A kind of resonance has also been observed in the correlation function with simple poles at

$$\tau = \frac{n}{(m_f^2 - \mathbf{k}^2)^{1/2}}, \quad (n = 1, 2, 3, \cdots). \tag{25}$$

This structure implies certain adjusted quench rates τ may lead to sufficiently large domains.[7]

4. Scattering, Decoherence and Order Parameter

The tree level approximation in Sec. 3 does take into account neither any interaction among different modes of each pion field nor the interaction between pions. Similarly the Hartree approximation includes only mean-field effects among modes and pion fields and thus neglects any direct scatterings among modes. To go beyond the Hartree approximation we may use the formalism in Ref. 8. The wave functional for the Schrödinger equation can be expressed in terms of the Green function (kernel or propagator) as

$$\Psi(\mathbf{x},t) = \int G(\mathbf{x},t;\mathbf{x}_0,t_0)\Psi(\mathbf{x}_0,t_0)d\mathbf{x}_0 dt_0. \tag{26}$$

As the linear sigma model is nonlinear, we use a perturbation method. We divide the Hamiltonian

$$H(t) = H_0(t) + \lambda H_P(t), \tag{27}$$

into an exactly solvable (quadratic) Gaussian and a perturbation part

$$\begin{aligned} H_0 &= \frac{1}{2}\pi_\phi^a \pi_{\phi a} + \frac{1}{2}(\nabla\phi^a \cdot \nabla\phi_a)^2 + \frac{1}{2}(m^2 + 9\lambda\langle\phi^b\phi_b\rangle)\phi^a\phi_a, \\ H_P &= \frac{1}{4}(\phi^a\phi_a)^2 - \frac{9}{2}\langle\phi^b\phi_b\rangle\phi^a\phi_a. \end{aligned} \tag{28}$$

Then in terms of the Green function for $\hat{H}_0$ in Sec. 3,

$$\Big(i\frac{\partial}{\partial t} - \hat{H}_0(\mathbf{x},t)\Big)G_0(\mathbf{x},t;\mathbf{x}',t') = \delta(\mathbf{x}-\mathbf{x}')\delta(t-t'), \tag{29}$$

we write the wave functional as

$$\Psi(\mathbf{x},t) = \Psi_0(\mathbf{x},t) + \lambda\int G_0(\mathbf{x},t;\mathbf{x}',t')\hat{H}_P(\mathbf{x}',t')\Psi(\mathbf{x}',t')d\mathbf{x}'dt', \tag{30}$$

and finally obtain the wave functional of the form

$$\begin{aligned} \Psi(1) = \Psi_0(1) &+ \lambda\int G_0(1,2)\hat{H}_P(2)\Psi_0(2) \\ &+\lambda^2\int\int G_0(1,2)\hat{H}_P(2)G_0(2,3)\hat{H}_P(3)\Psi_0(3) + \cdots, \end{aligned} \tag{31}$$

where (i) denotes $(\mathbf{x}_i,t_i)$ and Ψ_0 is a wave functional for $\hat{H}_0$. This method goes beyond the Hartree approximation and gives us the wave functional in a series of λ

$$\Psi(\mathbf{x},t) = \Psi_0(\mathbf{x},t) + \sum_{n=1}\lambda^n\Psi_0^{(n)}. \tag{32}$$

The term $\Psi_0^{(n)}$ comes from nth order correction of H_P.

We now give a few remarks on the effects on DCC formation of the non-Gaussian (beyond the Hartree) approximation. First, the nonlinear correction due to $\Psi_0^{(n)}$ enhances the correlation length for domains by a factor[9]

$$\frac{\xi_{Dn}}{\xi_D} = (2n+1)^{1/2}. \tag{33}$$

Higher order correction terms begin to grow provided that the duration of instability is long enough before crossing the inflection point. This condition may be provided by the quench time scale that is comparatively large but still smaller than relaxation time scale. Under this condition, significantly large DCC domains may lead to observable effects in heavy ion collisions or high energy cosmic rays. Second, the higher order correction terms in Eq. (32) include direct scattering effects. The direct scattering can be shown obviously in Eq. (31), where the Green function is simply given by

$$G_0(\mathbf{x},t;\mathbf{x}',t') = \sum_{q=0}^{\infty} \Psi_q(\mathbf{x},t)\Psi_q^*(\mathbf{x}',t') \tag{34}$$

with Ψ_q being the Fock states of H_0. Thus the nonlinear perturbation H_P scatters $\Psi_{a\alpha q}$ into $\Psi_{b\beta p}$, and vice versa. In particular, direct scatterings with short wavelength modes (environment or noise) would lead to decoherence of long wavelength modes. Therefore, long wavelength modes achieve not only classical correlation but also decoherence[18] and long wavelength modes emerge as a classical order parameter.

5. Conclusion

The QCD with two massless quarks would undergo a second order phase transition. The effective theory for the QCD phase transition is the linear sigma model for the quark-antiquark condensate, that is, the sigma and pion fields. Under a rapid cooling process, the QCD phase transition proceeds far from equilibrium (nonequilibrium). In this talk we focused on the dynamical process of the nonequilibrium phase transition and its implications on DCC domain growth.

The most prominent feature of nonequilibrium second order phase transitions is the instability of long wavelength modes. These modes begin to grow exponentially at the onset of phase transition while rolling over the barrier from the false vacuum to the true vacuum. Therefore, this nonequilibrium dynamical process leads to large domains of disoriented chiral condensate, regions of misaligned vacuum. On the contrary, domains formed

from thermal equilibrium have small sizes determined by thermal energy and are randomly oriented in isospin space.

Using the nonequilibrium linear sigma model with a smooth finite, we observed that DCC domains grow according to some power-law scaling relations. We found the power $t^{1/4}$ for the scaling behavior in the intermediate stage and the Cahn-Allen scaling power $t^{1/2}$ at the later stage of phase transition. However, in the Hartree approximation, exponentially growing long wavelength modes contribute $\lambda\langle\vec{\pi}^2\rangle$, which in turn attenuates the instability. The instability completely stops when $\lambda\langle\vec{\pi}^2\rangle$ dominates over m_f^2. Therefore, domains grow for a limited time and reach a typical size of $1 \sim 2$ fm in the Hartree approximation.[14] This size of DCC domain may not be large enough to lead to any significant observation.

It was shown that higher order quantum corrections increase the domains size by additional factors $(2n+1)^{1/2}$ if the duration of instability is long enough to make higher order terms grow. The longer is the quench time, the larger domains are. However, relaxation time scale gives a limitation on domain growth through instability, because thermal equilibration competes with instability when the quench time is comparable to relaxation time. This non-Gaussian effects on DCC domains may lead to observations in heavy ion collisions and high energy cosmic rays. This mechanism should be distinguished from the anomaly enhanced domain formation.[19]

Acknowledgments

The author would like to thank K. Rajagopal for useful discussions. This work is supported by Korea Research Foundation under grant No. KRF-2003-041-C20053.

References

1. R. Pisarski and F. Wilczek, *Phys. Rev.* **D29**, 338 (1984); F. Wilczek, *Int. J. Mod. Phys.* **A7**, 3911 (1992).
2. K. Rajagopal and F. Wilczek, *Nucl. Phys.* **B399**, 395 (1993); **B404**, 577 (1993).
3. R. D. Pisarski, *Nucl. Phys.* **A702**, 151 (2002); *Phys. Rev.* **D62**, 111501(R) (2000); F. Sannino, *Phys. Rev.* **D66**, 034013 (2002).
4. T. W. B. Kibble, *J. Phys.* **A9**, 1387 (1976); W. H. Zurek, *Nature* **317**, 505 (1985).
5. C. M. Lattes, Y. Fujimoto, and S. Hasegawa, *Phys. Rept.* **65**, 151 (1980).
6. A. Anselm, *Phys. Lett.* **B217**, 169 (1988); A. Anselm and M. G. Ryskin, *Phys. Lett.* **B266**, 482 (1991).

7. S. P. Kim and C. H. Lee, *Phys. Rev.* **D62**, 125020 (2000); S. P. Kim, S. Sengupta, and F. C. Khanna, *Phys. Rev.* **D64**, 105026 (2001).
8. S. Sengupta, F. C. Khanna, and S. P. Kim, *Phys. Rev.* **D68**, 105014 (2003); S. P. Kim, *Dynamical Theory of Phase Transitions and Topological Defect Formation in the Early Universe*, hep-ph/0401095.
9. S. P. Kim and F. C. Khanna, *Non-Gaussian Effects on Domain Growth*, hep-ph/0011115 (unpublished).
10. M. Gell-Mann and M. Levy, *Nuovo Cimento* **16**, (705) (1960).
11. L. Dolan and R. Jackiw, *Phys. Rev.* **D9**, 3320 (1974).
12. J. Schwinger, *J. Math. Phys.* **2**, 407 (1961); L. V. Keldysh, *Sov. Phys. JETP* **20**, 1018 (1965).
13. K. Freese, C. T. Hill, and M. Mueller, *Nucl Phys.* **B 255**, 693 (1985); A. Ringwald, Phys. Rev. D **36**, 2598 (1987); O. Éboli, R. Jackiw, and S.-Y. Pi, *Phys. Rev.* **D37**, 3557 (1988).
14. D. Boyanovsky, D.-S. Lee, and A. Singh, *Phys. Rev.* **D48**, 800 (1993); D. Boyanovsky, H. J. de Vega, and R. Holman, *Phys. Rev.* **D51**, 734 (1995).
15. F. Cooper, Y. Kluger, E. Mottola, and J. P. Paz, *Phys. Rev.* **D51**, 2377 (1995).
16. R. D. Amado and I. I. Kogan, *Phys. Rev.* **D51**, 190 (1995); R. Randrup, *Phys. Rev. Lett.* **77**, 1226 (1996); *Phys. Rev.* **D55**, 1188 (1997); *Heavy Ion Phys.* **9**, 289 (1999); *Phys. Rev.* **C62**, 064905 (2000).
17. G. Holzwarth and J. Klomfass, *Phys. Rev.* **D66**, 045032 (2002).
18. F. C. Lombardo, F. D. Mazzitelli, and R. J. Rivers, *Phys. Lett.* **B523**, 317 (2001); S. P. Kim and C. H. Lee, *Phys. Rev.* **D65**, 045013 (2002). F. C. Lombardo, F. D. Mazzitelli, and R. J. Rivers, *Nucl. Phys.* **B672**, 462 (2003).
19. M. Asakawa, H. Minakata, and B. Müller, *Phys. Rev.* **D58**, 094011 (1998); *Phys. Rev.* **C65**, 057901 (2002).

NEW RESULTS FROM BELLE*

YOUNGJOON KWON
Institute of Physics & Applied Physics
Yonsei University
Seoul 120-749, Korea
E-mail: yjkwon63@yonsei.ac.kr

In this paper, some of the new results from the Belle experiment are reviewed. In particular, we report new measurements on the CP violation in $B \to \phi K_S$ and related modes. We also present Belle's new measurements on the recently discovered unusual hadrons states $D_{sJ}(2317)$, $D_{sJ}(2457)$, and $X(3872)$.

1. Introduction

The Belle experiment is one of the two "B-Factory" experiments currently running in the world. The main goal of a B-factory is to first observe and establish CP violation in B-decays and then to precisely measure the CP violation angles of the Unitarity Triangle, as well as the lengths of its sides. With these measurements, we want to either confirm the Kobayashi-Maskawa model[1] for the mechanism of CP violation or find evidence of physics beyond the Standard Model. In this paper, we present a new result on the time-dependent CP violation in $b \to s\bar{s}s$ decays, in particular $B \to phiK_S$.

Since the initial state of the collision process $e^+e^- \to \Upsilon(4S) \to B\bar{B}$ is cleanly known, the kinematics of B decay products are very tightly constrained. This helps Belle to observe unusual hadron states and study their properties. In this paper, we will present Belle's new results on the recently discovered unusual hadron states $D_{sJ}(2317)$, $D_{sJ}(2457)$, and $X(3872)$

This paper is organized as follows. In the next section, we briefly describe the experimental apparatus: KEKB accelerator and the Belle detector. In section 3, we present the new CP violation results in $B \to K_S\phi$ and

*This work is supported by bk21 from krf and chep src from kosef.

related modes. In section 4, experimental results on recently observed new hadron states are described.

2. KEKB and Belle

KEKB [2] is an asymmetric e^+e^- collider, which consists of 8 GeV e^- and 3.5 GeV e^+ storage rings and an injection linear accelerator for them. It has one interaction point where the e^+ and e^- beams collide with a finite crossing angle of 22 mrad. The collider has been operated with peak beam currents of 1470 mA(e^+) and 1130 mA(e^-) (as of February, 2004), giving a peak luminosity of $1.1\times10^{34}/\mathrm{cm}^2/\mathrm{sec}$, exceeding the target luminosity $10^{34}/\mathrm{cm}^2/\mathrm{sec}$. Due to the energy asymmetry, the $\Upsilon(4S)$ and its daughter B-pair are produced with $\beta\gamma$ =0.425 along the electron beam direction (z direction) in the laboratory frame. The average distance between the two decay vertices of B mesons is approximately 200 μm. A total integrated luminosity of 140 fb^{-1} was accumulated during the period between October 1999 and the end of July 2003, corresponding to 152 million $B\bar{B}$ pair events.

Belle is an international collaboration consisting of ~300 physicists from ~50 institutes in 14 countries. The Belle detector [3] is a general purpose large solid angle magnetic spectrometer surrounding the interaction point. Charged particle tracking is done by a silicon vertex detector (SVD) and a central drift chamber (CDC). The SVD consists of three layers of double-sided silicon strip detectors (DSSD) at radii of 3.0, 4.5 and 6.0 cm. The CDC is a small-cell cylindrical drift chamber consisting of 50 layers of anode wires (18 stereo wire layers), covering $17^\circ < \theta_{lab} < 150^\circ$. The CDC is operated with a $He(50\%)+C_2H_6(50\%)$ mixture. The CDC also provides measurements of the energy loss with a resolution of $\sigma(dE/dx)$=6.9%.

Particle identification is done by three detectors: dE/dx measurements in the CDC, time-of-flight counters (TOF) and aerogel Cherenkov counters (ACC). The TOF system consists of 128 plastic scintillators. The time resolution is 95 psec (rms) which provides $\pi^\pm/K^\pm$ separation up to 1.5 GeV. The ACC consists of 1188 aerogel blocks with refractive indices of between 1.01 and 1.03, depending on the polar angle. By combining information from these detectors, the efficiency for $K^\pm$ identification is about 90% and the π fake rate is 6% with the requirement $P(K/\pi) > 0.6$. The electromagnetic calorimeter (ECL) consists of 8736 CsI(Tl) crystal blocks, 16.1 radiation length thick, and covering the same angular region as CDC. Electron identification in Belle is based on a combination of dE/dx measurements in the CDC, the response of the ACC, and the position, shape

and total energy (i.e. E/p) of its associated CsI shower. The outermost detector, for the measurement of $\mu^{\pm}$ and K_L (KLM), consists of 14 layers of iron (4.7 cm thick) absorbers alternating with resistive plate counters (RPC).

3. CP violation in $b \to s\bar{s}s$ decays

In the standard model (SM), CP violation arises from an irreducible phase, the Kobayashi-Maskawa (KM) phase [1], in the weak-interaction quark-mixing matrix. In particular, the SM predicts CP asymmetries in the time-dependent rates for B^0 and $\overline{B}^0$ decays to a common CP eigenstate f_{CP} [4]. Recent measurements of the CP-violation parameter $\sin 2\phi_1$ by the Belle [5] and BaBar [6] collaborations established CP violation in $B^0 \to J/\psi K^0_S$ and related decay modes, which are governed by the $b \to c\bar{c}s$ transition, at a level consistent with KM expectations.

Despite this success, many tests remain before one can conclude that the KM phase is the only source of CP violation. The $B^0 \to \phi K^0_S$ decay, which is dominated by the $b \to s\bar{s}s$ transition, is sensitive to new CP-violating phases from physics beyond the SM [7]. The other charmless decays $B^0 \to K^+K^-K^0_S$ and $B^0 \to \eta' K^0_S$, which are mediated by $b \to s\bar{s}s$, $s\bar{u}u$ and $s\bar{d}d$ transitions, also provide additional information. Since the SM predicts that measurements of CP violation in these charmless modes should also yield $\sin 2\phi_1$ to a good approximation [8,9], a significant deviation in the time-dependent CP asymmetry in these modes from what is observed in $b \to c\bar{c}s$ decays would be evidence for a new CP-violating phase.

In the decay chain $\Upsilon(4S) \to B^0\overline{B}^0 \to f_{CP}f_{\rm tag}$, where one of the B mesons decays at time t_{CP} to a final state f_{CP} and the other decays at time $t_{\rm tag}$ to a final state $f_{\rm tag}$ that distinguishes between B^0 and $\overline{B}^0$, the decay rate has a time dependence given by [4]

$$P(\Delta t) = \frac{e^{-|\Delta t|/\tau_{B^0}}}{4\tau_{B^0}}\left\{1 + q \cdot [S\sin(\Delta m_d \Delta t) + A\cos(\Delta m_d \Delta t)]\right\}, \qquad (1)$$

where τ_{B^0} is the B^0 lifetime, Δm_d is the mass difference between the two B^0 mass eigenstates, $\Delta t = t_{CP} - t_{\rm tag}$, and the b-flavor charge $q = +1$ (-1) when the tagging B meson is a B^0 ($\overline{B}^0$). S and A are CP-violation parameters; to a good approximation, the SM predicts $S = -\xi_f \sin 2\phi_1$, where $\xi_f = +1(-1)$ corresponds to CP-even (-odd) final states, and $A = 0$ for both $b \to c\bar{c}s$ and $b \to s\bar{s}s$ transitions. In this paper, we report a measurement incorporating an event sample with integrated luminosity of 140 fb^{-1} (152 million $B\overline{B}$ pairs).

We reconstruct B^0 decays to ϕK^0_S and $\eta' K^0_S$ final states for $\xi_f = -1$, and $B^0 \to K^+K^-K^0_S$ decays that are a mixture of $\xi_f = +1$ and -1. K^+K^- pairs that are consistent with $\phi \to K^+K^-$ decay are excluded from the $B^0 \to K^+K^-K^0_S$ sample. We find that the $K^+K^-K^0_S$ state is primarily $\xi_f = +1$; a measurement of the $\xi_f = +1$ fraction with a 140 fb^{-1} data set yields $1.03 \pm 0.15(\mathrm{stat}) \pm 0.05(\mathrm{syst})$, which is consistent with the previous result [9]. In the following determination of S and A, we fix $\xi_f = +1$ for this mode. The intermediate meson states are reconstructed from the following decay chains: $\eta' \to \rho^0(\to \pi^+\pi^-)\gamma$ or $\eta' \to \pi^+\pi^-\eta(\to \gamma\gamma)$, $K^0_S \to \pi^+\pi^-$, and $\phi \to K^+K^-$. We reject K^+K^- pairs that are consistent with $D^0 \to K^+K^-$, $\chi_{c0} \to K^+K^-$, or $J/\psi \to K^+K^-$ decay. $D^+ \to K^0_S K^+$ candidates are also removed. We use the same η' selection criteria as those used in our previously published analyses [10,11].

For reconstructed $B \to f_{CP}$ candidates, we identify B meson decays using the energy difference $\Delta E \equiv E_B^{\mathrm{cms}} - E_{\mathrm{beam}}^{\mathrm{cms}}$ and the beam-energy constrained mass $M_{\mathrm{bc}} \equiv \sqrt{(E_{\mathrm{beam}}^{\mathrm{cms}})^2 - (p_B^{\mathrm{cms}})^2}$, where $E_{\mathrm{beam}}^{\mathrm{cms}}$ is the beam energy in the cms, and E_B^{cms} and p_B^{cms} are the cms energy and momentum of the reconstructed B candidate, respectively. Figure 1 shows the M_{bc} distributions for the reconstructed B candidates that have ΔE values within the signal region.

We use events outside the signal region as well as a large MC sample to study the background components.

The b-flavor of the accompanying B meson is identified from inclusive properties of particles that are not associated with the reconstructed $B^0 \to f_{CP}$ decay [5]. We use two parameters, q and r, to represent the tagging information. The first, q, is already defined in Eq. (1). The parameter r is an event-by-event, MC-determined flavor-tagging dilution factor that ranges from $r = 0$ for no flavor discrimination to $r = 1$ for unambiguous flavor assignment. It is used only to sort data into six r intervals. The wrong tag fractions for the six r intervals, w_l $(l = 1, 6)$, and differences between B^0 and $\overline{B}^0$ decays, Δw_l, are determined from the data; we use the same values that were used for the $\sin 2\phi_1$ measurement [12].

We determine S and A for each mode by performing an unbinned maximum-likelihood fit to the observed Δt distribution. The probability density function (PDF) expected for the signal distribution, $P_{\mathrm{sig}}(\Delta t; S, A, q, w_l, \Delta w_l)$, is given by Eq. (1) incorporating the effect of incorrect flavor assignment. The distribution is convolved with the proper-time interval resolution function $R_{\mathrm{sig}}(\Delta t)$ [12], which takes into account the finite vertex resolution. Table 1 gives the fit values of $-\xi_f S$ and A.

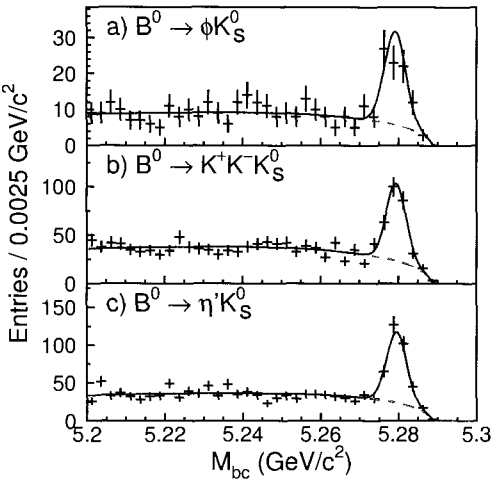

Figure 1. The $M_{\rm bc}$ distributions for (a) $B^0 \to \phi K^0_S$, (b) $B^0 \to K^+K^-K^0_S$, and (c) $B^0 \to \eta' K^0_S$ within the ΔE signal region. Solid curves show the fit to signal plus background distributions, and dashed curves show the background contributions.

Table 1. Results of the fits to the Δt distributions. The first errors are statistical and the second errors are systematic. The third error for the $K^+K^-K^0_S$ mode arises from the uncertainty in the fraction of the CP-odd component.

Mode	$-\xi_f S$ (= $\sin 2\phi_1$ in the SM)	A (= 0 in the SM)
ϕK^0_S	$-0.96 \pm 0.50^{+0.09}_{-0.11}$	$-0.15 \pm 0.29 \pm 0.07$
$K^+K^-K^0_S$	$+0.51 \pm 0.26 \pm 0.05^{+0.18}_{-0.00}$	$-0.17 \pm 0.16 \pm 0.04$
$\eta' K^0_S$	$+0.43 \pm 0.27 \pm 0.05$	$-0.01 \pm 0.16 \pm 0.04$

We obtain values consistent with the present world average of $\sin 2\phi_1 = +0.731 \pm 0.056$ [13] in the $B^0 \to K^+K^-K^0_S$ and $\eta' K^0_S$ decays, while a negative value is observed in $B^0 \to \phi K^0_S$ decay.

We define the raw asymmetry in each Δt bin by $A \equiv (N_{q\xi_f=-1} - N_{q\xi_f=+1})/(N_{q\xi_f=-1} + N_{q\xi_f=+1})$, where $N_{q\xi_f=+1(-1)}$ is the number of observed candidates with $q\xi_f = +1(-1)$. Figures 2(a-f) show the raw asymmetries in two regions of the flavor-tagging parameter r. While the numbers of events in the two regions are similar, the effective tagging efficiency is much larger and the background dilution is smaller in the region $0.5 < r \leq 1.0$. The observed CP asymmetry for $B^0 \to \phi K^0_S$ in the region

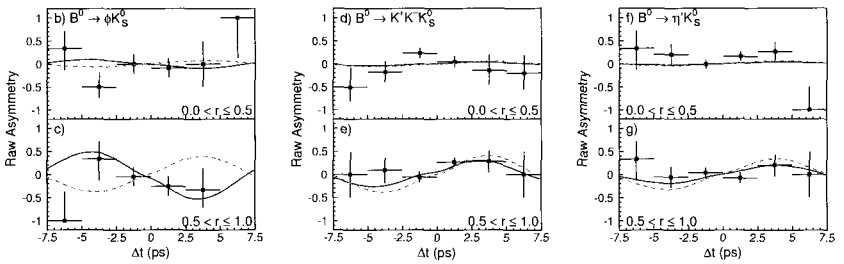

Figure 2. (a) The asymmetry, A, in each Δt bin for $B^0 \to \phi K^0_S$ with $0 < r \leq 0.5$, (b) with $0.5 < r \leq 1.0$, (c) for $B^0 \to K^+K^-K^0_S$ with $0 < r \leq 0.5$, (d) with $0.5 < r \leq 1.0$, (e) for $B^0 \to \eta' K^0_S$ with $0 < r \leq 0.5$, and (f) with $0.5 < r \leq 1.0$, respectively. The solid curves show the result of the unbinned maximum-likelihood fit. The dashed curves show the SM expectation with $\sin 2\phi_1 = +0.731$ and $A = 0$.

$0.5 < r \leq 1.0$ [Fig. 2(b)] indicates the difference from the SM expectation (dashed curve). Note that these projections onto the Δt axis do not take into account event-by-event information (such as the signal fraction, the wrong tag fraction and the vertex resolution), which is used in the unbinned maximum-likelihood fit.

The dominant sources of systematic error for the $B^0 \to \phi K^0_S$ mode are a possible fit bias for the input S value near the physical boundary ($^{+0.06}_{-0.00}$ for S), the uncertainties in the $B^0 \to K^+K^-K^0_S$ and $f_0(980)K^0_S$ background fractions ($^{+0.00}_{-0.08}$ for S and ± 0.04 for A), in the other background fractions (± 0.05 for S and ± 0.04 for A), and in the vertex reconstruction (± 0.02 for S and ± 0.05 for A). Other contributions come from uncertainties in the background Δt distribution, wrong tag fractions, τ_{B^0}, and Δm_d. We add each contribution in quadrature to obtain the total systematic uncertainty. We find that the dominant sources are uncertainties from the background fractions and from the vertex reconstruction.

We use the Feldman-Cousins frequentist approach [14] to determine the statistical significance of the observed deviation from the SM expectation in $B^0 \to \phi K^0_S$. From 1-dimensional confidence intervals for S with A set at zero, the case with $S = +0.731$ is ruled out at 99.95% confidence level, equivalent to 3.5σ significance for Gaussian errors.

4. Unusual hadron states

4.1. *Properties of D_{sJ}*

Recently a new $D_s\pi^0$ resonance with a mass of 2317 MeV/c^2 and a very narrow width was observed by the BaBar collaboration [15]. A natural

interpretation is that this is a P-wave $c\bar{s}$ quark state that is below the DK threshold, which accounts for the small width [16]. This interpretation is supported by the observation of a $D_s^*\pi^0$ resonance [17] by the CLEO collaboration [18] and Belle collaboration [19]. All groups observe these states in inclusive e^+e^- processes. The mass difference between the two observed states is consistent with the expected hyperfine splitting of the P-wave D_s meson doublet with total light-quark angular momentum $j = 1/2$ [16]. However, the masses of these states are considerably below potential model expectations [20], and are nearly the same as those of the corresponding $c\bar{u}$ states recently measured by Belle [21]. The low mass values have caused speculation that these states may be more exotic than a simple $q\bar{q}$ meson system [22,23,24,25,26]. To clarify the nature of these states, it is necessary to determine their quantum numbers and decay branching fractions.

Belle searched for new decays of these states, which we refer to as D_{sJ}. Figure 3(a) shows the $\Delta M(D_s^+\gamma) = M(D_s^+\gamma) - M_{D_s^+}$ distribution. Here photons are required to have energies greater than 600 MeV in the CM and those that form a π^0 when combined with another photon in the event are not used. A clear peak near $\Delta M(D_s^+\gamma) \sim 490\,\mathrm{MeV}/c^2$, corresponding to the $D_{sJ}(2457)$, is observed. No peak is found in the $D_{sJ}(2317)$ region. The D_s^+ sideband distribution, shown as a histogram, shows no structure. We fit the distribution with a double Gaussian for the signal, which is determined from the MC, and a third-order polynomial for the background. The fit yields 152 ± 18 (stat) events and a ΔM peak at $491.0 \pm 1.3(\mathrm{stat}) \pm 1.9(\mathrm{syst})\,\mathrm{MeV}/c^2$ (corresponding to $M = 2459.5 \pm 1.3(\mathrm{stat}) \pm 2.0(\mathrm{syst})\,\mathrm{MeV}/c^2$). The $D_{sJ}(2457)$ mass determined here is consistent with the value determined from $D_s^*\pi^0$ decays.

Using the detection efficiency of 10.2% for the $D_s^+\gamma$ decay mode, we determine the branching fraction ratio

$$\frac{\mathcal{B}(D_{sJ}^+(2457) \to D_s^+\gamma)}{\mathcal{B}(D_{sJ}^+(2457) \to D_s^{*+}\pi^0)} = 0.55 \pm 0.13(\mathrm{stat}) \pm 0.08(\mathrm{syst}).$$

The existence of the $D_{sJ}(2457) \to D_s\gamma$ mode rules out the $0^\pm$ quantum number assignments for the $D_{sJ}(2457)$ state. For the $D_{sJ}(2317)$, we obtain the upper limit

$$\frac{\mathcal{B}(D_{sJ}^+(2317) \to D_s^+\gamma)}{\mathcal{B}(D_{sJ}^+(2317) \to D_s\pi^0)} \leq 0.05\ (90\%\ \mathrm{C.L.}).$$

From the $M(D_s^{*+}\gamma) = M(D_s^{*+}\gamma) - M_{D_s^{*+}}$ distribution, we determine the

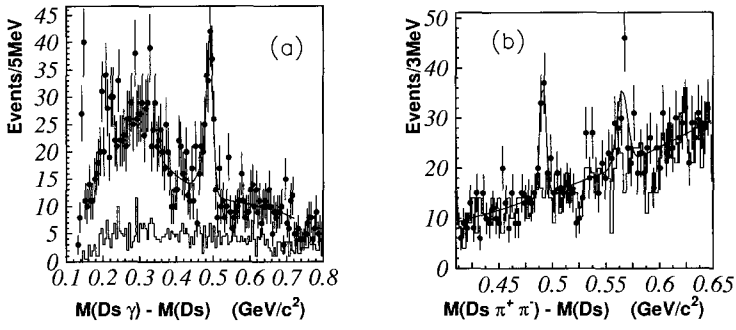

Figure 3. (a) The $\Delta M(D_s^+\gamma)$ distribution. The curve is a fit using a double Gaussian for the signal and a third-order polynomial for the background. (b) The $\Delta M(D_s^+\pi^+\pi^-)$ distribution. The curve is a fit using Gaussian for the signals and a third-order polynomial for the background.

upper limits

$$\frac{\mathcal{B}(D_{sJ}^+(2317) \to D_s^{*+}\gamma)}{\mathcal{B}(D_{sJ}^+(2317) \to D_s\pi^0)} \leq 0.18 \text{ (90\% C.L.)} \quad \text{and}$$

$$\frac{\mathcal{B}(D_{sJ}^+(2457) \to D_s^{*+}\gamma)}{\mathcal{B}(D_{sJ}^+(2457) \to D_s^{*+}\pi^0)} \leq 0.31 \text{ (90\% C.L.)}.$$

Figure 3(b) shows the $\Delta M(D_s^+\pi^+\pi^-) = M(D_s^+\pi^+\pi^-) - M_{D_s^+}$ distribution. For pions, we require at least one of them to have momentum greater than $300\,\mathrm{MeV}/c$ in the CM, one with $P(K/\pi) < 0.1$ and other with $P(K/\pi) < 0.9$, and $|M(\pi^+\pi^-) - M_{K_S}| \geq 15\,\mathrm{MeV}/c^2$. A clear peak near $\Delta M(D_s^+\pi^+\pi^-) \sim 490\,\mathrm{MeV}/c^2$, corresponding to the $D_{sJ}(2457)$, is observed. Evidence of an additional peak near $\Delta M(D_s^+\pi^+\pi^-) \sim 570\,\mathrm{MeV}/c^2$ corresponding to $D_{s1}(2536)$ is also visible. No peak is found in the $D_{sJ}(2317)$ region. The D_s^+ sideband distribution, shown as a histogram, shows no structure. We fit the distribution with Gaussians for the signals, which are determined from the MC, and a third-order polynomial for the background. The fit yields 59.7 ± 11.5(stat) events and a ΔM peak at 491.4 ± 0.9(stat) $\pm$ 1.5(syst) MeV/c^2 (corresponding to $M = 2459.9 \pm 0.9$(stat) $\pm$ 1.6(syst) MeV/c^2) for $D_{sJ}(2457)$, and 56.5 ± 13.4(stat) events for $D_{s1}(2536)$. The statistical significance is 5.7σ for $D_{sJ}(2457)$, and 4.5σ for $D_{s1}(2536)$. This is the first observation of the $D_{sJ}(2457) \to D_s^+\pi^+\pi^-$ decay mode.

The existence of the $D_{sJ}(2457) \to D_s\pi^+\pi^-$ mode also rules out the 0^+ assignment for $D_{sJ}(2457)$. Using the detection efficiency of 15.8% for the $D_s\pi^+\pi^-$ decay mode, we determine the branching fraction ratio

$$\frac{\mathcal{B}(D_{sJ}^+(2457) \to D_s^+\pi^+\pi^-)}{\mathcal{B}(D_{sJ}^+(2457) \to D_s^{*+}\pi^0)} = 0.14 \pm 0.04(\text{stat}) \pm 0.02(\text{syst}),$$

where the systematic error is dominated by the systematic uncertainty of the $D_{sJ}(2457) \to D_s^{*+}\pi^0$ yield. We establish the upper limit

$$\frac{\mathcal{B}(D_{sJ}^+(2317) \to D_s^+\pi^+\pi^-)}{\mathcal{B}(D_{sJ}^+(2317) \to D_s^+\pi^0)} \leq 4 \times 10^{-3} \text{ (90\% C.L.)}.$$

In summary, we observe radiative and dipion decays of the $D_{sJ}(2457)$ and set upper limits on the corresponding decays of the $D_{sJ}(2317)$. We determine the $D_{sJ}(2317)$ and $D_{sJ}(2457)$ masses from their decays to $D_s^+\pi^0$ and $D_s^{*+}\pi^0$, respectively, and set an upper limit on the decay of $D_{sJ}(2457)$ to $D_s^+\pi^0$. These results are consistent with the spin-parity assignments for the $D_{sJ}(2317)$ and $D_{sJ}(2457)$ of 0^+ and 1^+, respectively.

In order to clarify the nature of the D_{sJ} states, it is useful to search for these states in exclusive B decay processes. The well-defined initial state of B mesons can help identify the quantum numbers of the D_{sJ} states. We search for exclusive decays of the type $B \to \bar{D}D_{sJ}$, which are expected to be the dominant exclusive D_{sJ} production mechanism in B decays. Because of the known properties of the parent B meson, angular analyses of these decays can unambiguously determine the D_{sJ} quantum numbers. Moreover, since QCD sum rules in HQET predict that P-wave mesons with $j = 1/2$ should be more readily produced in B decays than mesons with $j = 3/2$ [27], the observation of $B \to \bar{D}D_{sJ}$ would provide additional support for the P-wave nature of these states as well as serving as a check of these predictions.

The ΔE and D_{sJ} candidate's invariant mass ($M(D_{sJ})$) distributions for $B \to \bar{D}D_{sJ}$ candidates are presented in Fig. 4, where all $\bar{D}^0$ and D^- decay modes are combined. Each distribution is the projection of the signal region of the other parameter; distributions for events in the $M(D_{sJ})$ and ΔE sidebands are shown as crosshatched histograms. Clear signals are observed for the $DD_{sJ}(2317)[D_s\pi^0]$ and $DD_{sJ}(2457)[D_s^*\pi^0, D_s\gamma]$ final states. The measured masses for the $D_{sJ}(2317)$ and $D_{sJ}(2457)$ are $(2319.8 \pm 2.1 \pm 2.0)$ MeV/c^2 and $(2459.2 \pm 1.6 \pm 2.0)$ MeV/c^2 respectively. The fitted widths are consistent with those expected for D_{sJ} mesons of zero intrinsic width. The systematic error in the D_{sJ} mass is expected to come from the photon energy scale.

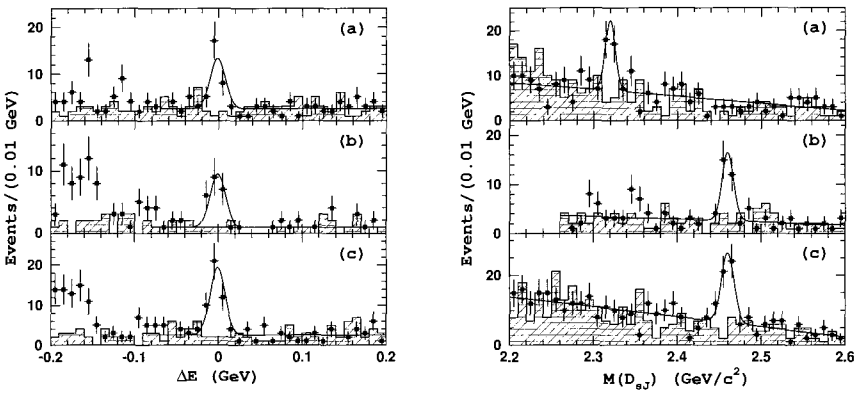

Figure 4. ΔE (left) and $M(D_{sJ})$ (right) distributions for the $B \to \bar{D} D_{sJ}$ candidates: (a) $D_{sJ}(2317) \to D_s\pi^0$, (b) $D_{sJ}(2457) \to D_s^*\pi^0$ and (c) $D_{sJ}(2457) \to D_s\gamma$. Points with errors represent the experimental data, crosshatched histograms show the sidebands and curves are the results of the fits.

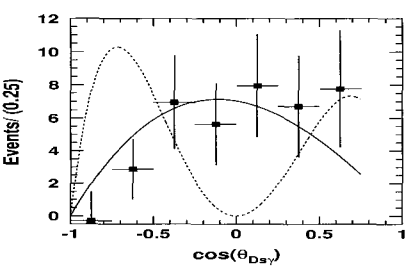

Figure 5. The $D_{sJ}(2457) \to D_s\gamma$ helicity distribution. The points with error bars are the results of fits to the ΔE spectra for experimental events. Solid and dashed curves are MC predictions for the $J = 1$ and $J = 2$ hypotheses, respectively. The highest bin has no events because of the cut on the $D\gamma$ invariant mass.

We also study the helicity distribution for the $D_{sJ}(2457) \to D_s\gamma$ decay. The helicity angle $\theta_{D_s\gamma}$ is defined as the angle between the $D_{sJ}(2457)$ momentum in the B meson rest frame and the D_s momentum in the $D_{sJ}(2457)$ rest frame. The $\theta_{D_s\gamma}$ distribution in the data (Fig. 5) is consistent with MC expectations for the $J = 1$ hypothesis for the $D_{sJ}(2457)$ (χ^2/n.d.f$= 5/6$), and contradicts the $J = 2$ hypothesis (χ^2/n.d.f.$= 44/6$). The $J = 0$ hypothesis is already ruled out by the conservation of angular momentum and parity in $D_{sJ}(2457) \to D_s\gamma$.

4.2. *Observation of X(3872)*

A major experimental issue for the $c\bar{c}$ charmonium particle system is the existence of as yet unestablished charmonium states that are expected to be below threshold for decays to open charm and, thus, narrow. These include the $n = 1$ singlet P state, the $J^{PC} = 1^{+-}$ $1^1\mathrm{P}_{c1}$, and possibly the $n = 1$ singlet and triplet spin-2 D states, i.e. the $J^{PC} = 2^{-+}$ $1^1\mathrm{D}_{c2}$ and $J^{PC} = 2^{--}$ $1^3\mathrm{D}_{c2}$, all of which are narrow if their masses are below the $D\bar{D}^*$ threshold. The observation of these states and the determination of their masses would provide useful information about the spin dependence of the charmonium potential.

In addition to charmonium states, some authors have predicted the existence of $D^{(*)}\bar{D}^{(*)}$ "molecular charmonium" states [28] and $c\bar{c}g$ "hybrid charmonium" states [29]. If such states exist with masses below the relevant open charm threshold, they are expected to be narrow and to have large branching fractions to low-lying $c\bar{c}$ charmonium states.

The large B meson samples produced at B-factories provide excellent opportunities to search for new charmonium states. In this paper, in particular, we report on an experimental study of the $\pi^+\pi^- J/\psi$ and $\gamma\chi_{c1}$ mass spectra from exclusive $B^+ \to K^+\pi^+\pi^- J/\psi$ and $K^+\gamma\chi_{c1}$ decays. Candidate $B^+ \to K^+\pi^+\pi^- J/\psi$ mesons are reconstructed using the energy difference ΔE and the beam-energy constrained mass M_{bc}. The signal region is defined as 5.271 GeV $< M_{\mathrm{bc}} <$ 5.289 GeV and $|\Delta E| < 0.030$ GeV.

Figure 6(a) shows the distribution of $\Delta M \equiv M(\pi^+\pi^-\ell^+\ell^-) - M(\ell^+\ell^-)$ for events in the ΔE-M_{bc} signal region. Here a large peak corresponding to

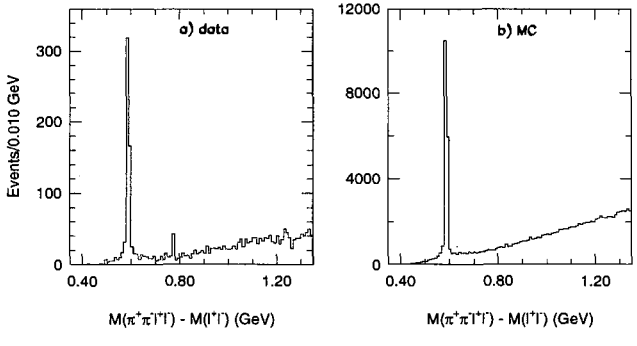

Figure 6. Distribution of $M(\pi^+\pi^-\ell^+\ell^-) - M(\ell^+\ell^-)$ for selected events in the ΔE-M_{bc} signal region for **(a)** Belle data and **(b)** generic $B\bar{B}$ MC events .

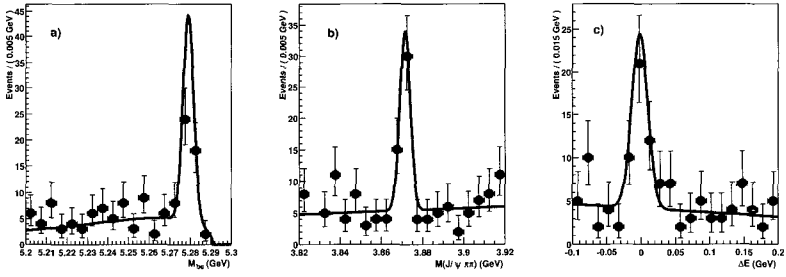

Figure 7. Signal-band projections of **(a)** $M_{\rm bc}$, **(b)** $M_{\pi^+\pi^- J/\psi}$ and **(c)** ΔE for the $X(3872) \to \pi^+\pi^- J/\psi$ signal region with the results of the unbinned fit superimposed.

Table 2. Results of the fits to the ψ' and $M = 3872$ MeV regions. The errors are statistical only.

Quantity	ψ' region	$M = 3872$ MeV region
Signal events	489 ± 23	35.7 ± 6.8
$M^{\rm meas}_{\pi^+\pi^- J/\psi}$ peak	3685.5 ± 0.2 MeV	3871.5 ± 0.6 MeV
$\sigma_{M\pi^+\pi^- J/\psi}$	3.3 ± 0.2 MeV	2.5 ± 0.5 MeV

$\psi' \to \pi^+\pi^- J/\psi$ is evident at 0.589 GeV. In addition there is a significant spike in the distribution at 0.775 GeV. Figure 6(b) shows the same distribution for a large sample of generic $B\bar{B}$ Monte Carlo (MC) events. Except for the prominent ψ' peak, the distribution is smooth and featureless. The spike at $\Delta M = 0.775$ GeV corresponds to a mass near 3872 MeV.

Figures 7(a), (b) and (c) show the $M_{\rm bc}$, $M_{\pi^+\pi^- J/\psi}$, and ΔE signal-band projections for the $M = 3872$ MeV signal region, respectively. The superimposed curves indicate the results of the fit. There are clear peaks with consistent yields in all three quantities. The signal yield of 35.7 ± 6.8 events has a statistical significance of 10.3σ, determined from $\sqrt{-2\ln(\mathcal{L}_0/\mathcal{L}_{\rm max})}$, where $\mathcal{L}_{\rm max}$ and $\mathcal{L}_0$ are the likelihood values for the best-fit and for zero-signal-yield, respectively. The results of the fits are presented in Table 2. In the following we refer to this as the $X(3872)$.

We determine the mass of the signal peak relative to the well measured ψ' mass:

$$M_X = M_X^{\rm meas} - M_{\psi'}^{\rm meas} + M_{\psi'}^{\rm PDG} = 3872.0 \pm 0.6 \pm 0.5 \text{ MeV}.$$

Here the first error is statistical and the second systematic. Since we use the precisely known value of the ψ' mass as a reference, the systematic

error is small. The $M_{\psi'}$ measurement, which is referenced to the J/ψ mass that is 589 MeV away, is -0.5 ± 0.2 MeV from its world-average value [30]. Variation of the mass scale from $M_{\psi'}$ to M_X requires an extrapolation of only 186 MeV and, thus, can safely be expected to be less than this amount. We assign 0.5 MeV as the systematic error on the mass.

The measured width of the $X(3872)$ peak is $\sigma = 2.5 \pm 0.5$ MeV, which is consistent with the MC-determined resolution and the value obtained from the fit to the ψ' signal. To determine an upper limit on the total width, we repeated the fits using a resolution-broadened Breit-Wigner (BW) function to represent the signal. This fit gives a BW width parameter that is consistent with zero: $\Gamma = 1.4 \pm 0.7$ MeV. From this we infer a 90% confidence level (CL) upper limit of $\Gamma < 2.3$ MeV.

We determine a ratio of product branching fractions for $B^+ \to K^+X(3872)$, $X(3872) \to \pi^+\pi^- J/\psi$ and $B^+ \to K^+\psi'$, $\psi' \to \pi^+\pi^- J/\psi$ to be

$$\frac{Br(B^+ \to K^+X(3872)) \times Br(X(3872) \to \pi^+\pi^- J/\psi)}{Br(B^+ \to K^+\psi') \times Br(\psi' \to \pi^+\pi^- J/\psi)} = 0.063 \pm 0.012 \pm 0.007.$$

Here the systematic error is mainly due to the uncertainties in the efficiency for the $X(3872) \to \pi^+\pi^- J/\psi$ channel, which is estimated with MC simulations that use different models for the decay.

4.3. *Conclusions*

In this paper, some of the new results from the Belle experiment are reviewed. Improved measurements of CP-violation parameters for $B^0 \to \phi K^0_S$, $K^+K^-K^0_S$ and $\eta' K^0_S$ decays are obtained. These charmless decays are sensitive to possible new CP-violating phases. A 3.5σ deviation from the Standard Model (SM) is observed for $B^0 \to \phi K^0_S$. The result suggests that there is a large CP-violating phase in its decay amplitude, which cannot be explained by the SM.

Several new results on unusual hadron states have been obtained by Belle . In particular, the new narrow charm-strange states $D_{sJ}(2317)$ and $D_{sJ}(2457)$ which are discovered by BaBar and CLEO, respectively, are confirmed by Belle. New radiative and dipion decays of $D_{sJ}(2457)$ are observed by Belle, which helps determine the spin-parity of D_{sJ} states. Belle has also observed D_{sJ} states in B decays for the first time. In addition, Belle has observed a strong signal for a state that decays to $\pi^+\pi^- J/\psi$ with $M = 3872 \pm 0.6 \pm 0.5$ MeV and $\Gamma < 2.3$ MeV (90% C.L.).

Acknowledgments

The author thanks the staffs of KEKB accelerator group for delivering world-best luminosity performance as well as colleagues of the Belle group for a wonderfully performed experimental collaboration. He also acknowledges the financial supports from the CHEP SRC program of KOSEF and the BK21 program of KRF.

References

1. M. Kobayashi and T. Maskawa, Prog. Theor. Phys. **49**, 652 (1973).
2. S. Kurokawa and E. Kikutani *et al.*, Nucl. Instrum. Methods A **499**, 1 (2003).
3. Belle Collaboration, A. Abashian *et al.*, Nucl. Instrum. Methods A **479**, 117 (2002).
4. A. B. Carter and A. I. Sanda, Phys. Rev. D **23**, 1567 (1981); I. I. Bigi and A. I. Sanda, Nucl. Phys. **B193**, 85 (1981).
5. Belle Collaboration, K. Abe *et al.*, Phys. Rev. Lett. **87**, 091802 (2001); Phys. Rev. D **66**, 032007 (2002); Phys. Rev. D **66**, 071102 (2002).
6. BaBar Collaboration, B. Aubert *et al.*, Phys. Rev. Lett. **87**, 091801 (2001); Phys. Rev. D **66**, 032003 (2002); Phys. Rev. Lett. **89**, 201802 (2002).
7. Y. Grossman and M. P. Worah, Phys. Lett. B **395**, 241 (1997).
8. D. London and A. Soni, Phys. Lett. B **407**, 61 (1997); Y. Grossman, G. Isidori and M. P. Worah, Phys. Rev. D **58**, 057504 (1998).
9. Belle Collaboration, A. Garmash *et al.*, hep-ex/0307082.
10. Belle Collaboration, K. Abe *et al.*, Phys. Rev. D **67**, 031102 (2003).
11. Belle Collaboration, K.-F. Chen and K. Hara *et al.*, Phys. Lett. B **54 6**, 196 (2002).
12. Belle Collaboration, K. Abe *et al.*, hep-ex/0308036.
13. Particle Data Group, K. Hagiwara *et al.*, Particle Listings in the 2003 Review of Particle Physics, http://www-pdg.lbl.gov/2003/contents_listings.html.
14. G. J. Feldman and R. D. Cousins, Phys. Rev. D **57**, 3873 (1998).
15. BaBar Collaboration, B. Aubert *et al.*, Phys. Rev. Lett. **90**, 242001 (2003).
16. W. Bardeen, E. Eichten and C. Hill, Phys. Rev. D **68**, 054024 (2003).
17. In the heavy c-quark mass limit, one expects two doublets of $c\bar{s}$ states with quantum numbers $J^P = 0^+$, 1^+ and 1^+, 2^+. The second one has been observed in $D^{(*)}K$ decays.
18. CLEO Collaboration, D. Besson *et al.*, Phys. Rev. D **68**, 032002 (2003).
19. Belle Collaboration, K. Abe *et al.*, EPS contribution paper, BELLE-CONF-0340, hep-ex/0307052.
20. J. Bartelt and S. Shukla, Ann. Rev. Nucl. Part. Sci. **45**, 133 (1995).
21. Belle Collaboration, K. Abe *et al.*, hep-ex/0307021, submitted to Phys. Rev. D.
22. R. Cahn and D. Jackson, Phys. Rev. D **68**, 037502 (2003).
23. T. Barnes, F. Close and H. Lipkin, Phys. Rev. D **68**, 054006 (2003).
24. E. Beveren and G. Rupp, Phys. Rev. Lett. **91**, 012003 (2003).
25. H. Cheng and W. Hou, Phys. Lett. B **566**, 193 (2003).

26. P. Colangelo and F. Fazio, Phys. Lett. B **570**, 180 (2003).
27. A. Yaouanc *et al.*, Phys. Lett. B **520**, 59 (2001).
28. See, for example, M. Bander, G.L. Shaw and P. Thomas, Phys. Rev. Lett. **36**, 695 (1977); M.B. Voloshin and L.B. Okun, JETP Lett. **23**, 333 (1976); A. De Rujula, H. Georgi and S.L. Glashow, Phys. Rev. Lett. **38**, 317 (1977); N.A. Törnqvist, Z. Phys. **C61**, 525 (1994); and A.V. Manohar and M.B. Wise, Nucl. Phys. **B339**, 17 (1993).
29. See, for example, S. Godfrey and J. Napolitano, Rev. Mod. Phys. **71**, 1411 (1999), and reference cited therein.
30. We use the PDG 2002 average value of $M_{\psi'} - M_{J/\psi} = 589.07 \pm 0.13$ MeV. A recent more precise measurement of $589.194 \pm 0.027 \pm 0.011$ MeV has recently been reported by V.M. Aulchenko *et al.* (KEDR Collaboration), hep-ex/0306050.

TOPOLOGICAL STRUCTURE OF DENSE HADRONIC MATTER

BYUNG-YOON PARK

Department of Physics, Chungnam National University, Daejon 305-764, Korea
E-mail: bypark@cnu.ac.kr

HEE-JUNG LEE AND VICENTE VENTO

Departament de Física Teòrica and Institut de Física Corpuscular
Universitat de València and Consejo Superior de Investigaciones Científicas
E-46100 Burjassot (València), Spain
E-mail: hjlee@phya.snu.ac.kr, Vicente.Vento@uv.es

JOON-IL KIM AND DONG-PIL MIN

Department of Physics, Seoul National University, Seoul 151-742, Korea
E-mail: jikim@phya.snu.ac.kr, dpmin@phya.snu.ac.kr

MANNQUE RHO

Department of Physics, Hanyang University, Seoul 133-791, Korea,
School of Physics, Korea Institute for Advanced Study, Seoul 130-722, Korea,
and
Service de Physique Théorique, CE Saclay
91191 Gif-sur-Yvette, France
E-mail: rho@spht.saclay.cea.fr

We present a summary of work done on dense hadronic matter, based on the Skyrme model, which provides a unified approach to high density, valid in the large N_c limit. In our picture, dense hadronic matter is described by the *classical* soliton configuration with minimum energy for the given baryon number density. By incorporating the meson fluctuations on such ground state we obtain an effective Lagrangian for meson dynamics in a dense medium. Our starting point has been the Skyrme model defined in terms of pions, thereafter we have extended and improved the model by incorporating other degrees of freedom such as dilaton, kaons and vector mesons.

1. Introduction

At high temperature and/or density, hadrons are expected to possess properties that are very different from those at normal conditions. Understanding the properties of hadrons in such extreme conditions is currently an important issue not only in nuclear and particle physics but also in many other related fields such as astrophysics. Data from the high energy heavy ion colliders, astronomical observations on compact stars and some theoretical developments have shown that the phase diagram of hadronic matter is far richer and more interesting than initially expected. Lattice QCD calculations have been carried out successfully at high temperature, however similar calculations at high density have not yet been possible[1]. Theoretical developments have unveiled such interesting QCD phases as color superconductivity[2]. Moreover effective theories can be derived for these extreme conditions, using macroscopic degrees of freedom, by matching them to QCD at a scale close to the chiral scale $\Lambda_\chi \sim 4\pi f_\pi \sim 1$ GeV[3].

We have followed a different path to dense matter studies by using as our starting point a model Lagrangian, in the spirit of Skyrme, which describes hadronic matter and meson dynamics respecting the symmetries of QCD. The parameters of the model are fixed by meson dynamics at *zero* baryon number density. *À la* Skyrme[4], baryons arise from a soliton solution, the skyrmion, with the topological winding number describing the baryon number. In our scheme dense matter is approximated by a system of skyrmions with a given baryon number density whose ground state arises as a crystal configuration[5,6]. Starting from this ground state our approach provides insight on the intrinsic in-medium dependence of meson dynamics. We have studied (i) the in-medium properties of the mesons and (ii) the role of the other degrees of freedom besides pions in the description of matter as it becomes denser[7,8,9,10,11,12].

2. Model Lagrangians

The original Skyrme model Lagrangian[4] reads

$$L_\pi = -\frac{f_\pi^2}{4}\mathrm{Tr}(L_\mu L^\mu) + \frac{1}{32e^2}\mathrm{Tr}[L_\mu, L_\nu]^2 + \frac{f_\pi^2 m_\pi^2}{4}\mathrm{Tr}(U + U^\dagger - 2), \qquad (1)$$

where $L_\mu = U^\dagger \partial_\mu U$ and $U = \exp(i\vec{\tau}\cdot\vec{\pi}) \in SU(2)$ is a nonlinear realization of the pion fields, f_π the decay constant and m_π the pion mass . The second term with e, the Skyrme parameter, was introduced to stabilize the soliton solution.

The dilaton field χ was incorporated in the model to make it consistent with the scale anomaly of QCD[13]. The Lagrangian (1) then becomes

$$\begin{aligned} L_{\pi\chi} = & -\frac{f_\pi^2}{4}\left(\frac{\chi}{f_\chi}\right)^2 \mathrm{Tr}(L_\mu L^\mu) + \frac{1}{32e^2}\mathrm{Tr}[L_\mu, L_\nu]^2 \\ & + \frac{f_\pi^2 m_\pi^2}{4}\left(\frac{\chi}{f_\chi}\right)^3 \mathrm{Tr}(U + U^\dagger - 2) \\ & + \tfrac{1}{2}\partial_\mu\chi\partial^\mu\chi - V(\chi), \end{aligned} \tag{2}$$

Note the different powers of (χ/f_χ) in front of each term. The last line is the Lagrangian for the free dilaton field, where $V(\chi) = (m_\chi^2 f_\chi^2/4)((\chi/f_\chi)^4(\ln(\chi/f_\chi) - \frac{1}{4}) - \frac{1}{4})$, m_χ is the dilaton mass and f_χ its decay constant.

The vector mesons, ρ and ω, can be incorporated into the Lagrangian as dynamical gauge bosons of a hidden local gauge symmetry which requires the doubling of the degrees of freedom as $U = \xi_L^\dagger \xi_R$. This Lagrangian reads[14]

$$\begin{aligned} L_{\pi\chi\rho\omega} = & -\frac{f_\pi^2}{4}\left(\frac{\chi}{f_\chi}\right)^2 \mathrm{Tr}(L_\mu L^\mu) + \frac{f_\pi^2 m_\pi^2}{4}\left(\frac{\chi}{f_\chi}\right)^3 \mathrm{Tr}(U + U^\dagger - 2) \\ & - \frac{f_\pi^2}{4} a \left(\frac{\chi}{f_\chi}\right)^2 \mathrm{Tr}[\xi_L \partial_\mu \xi_L^\dagger + \xi_R \partial_\mu \xi_R^\dagger + i(g/2)(\vec{\tau}\cdot\vec{\rho}_\mu + \omega_\mu)]^2 \\ & + \tfrac{3}{2} g \omega_\mu B^\mu \\ & - \tfrac{1}{4}\vec{\rho}_{\mu\nu}\cdot\vec{\rho}^{\mu\nu} - \tfrac{1}{4}\omega_{\mu\nu}\omega^{\mu\nu} + \tfrac{1}{2}\partial_\mu\chi\partial^\mu\chi - V(\chi), \end{aligned} \tag{3}$$

with $\vec{\rho}_{\mu\nu} = \partial_\mu\vec{\rho}_\nu - \partial_\nu\vec{\rho}_\mu + g\vec{\rho}_\mu \times \vec{\rho}_\nu$, $\omega_{\mu\nu} = \partial_\mu\omega_\nu - \partial_\nu\omega_\mu$, and where B_μ is the *topological* baryon number current. The quartic Skyrme term of (1) is not present, because its stabilizing role is played here by the vector mesons.

3. In-Medium Pion Dynamics

In order to explain our basic strategy, we start with the Skyrme model (1). Table 1 serves to generalize the discussion to other models. The vacuum solution of (1) in the $B = 0$ sector is $U = 1$. Fluctuations on top of this vacuum describe pion dynamics. The Lagrangian supports solitons with nontrivial topological structures. The $B = 1$ soliton solution with lowest energy is a "hedgehog" , $U^{B=1} = \exp(i\vec{\tau}\cdot\hat{r}F(r))$ with the boundary condition for the profile function $F(r)$, $F(0) = \pi$ and $F(\infty) = 0$. The two-skyrmion system has lowest energy when one on the skyrmions is rotated relatively to the other in isospin space, by an angle π, about an axis perpendicular to the line joining their centers. Therefore, skyrmion matter has the lowest energy in an FCC (face centered cubic) single skyrmion crystal structure, where the skyrmions at the nearest site are relatively oriented

in such a low energy configuration and $U(\vec{r})$ has the symmetry structure described in Table 1.

For a given baryon number density, the lowest energy configuration can be found numerically by varying the field values at points of a discrete mesh[5] or by adjusting the coefficients of the Fourier series expansion for the fields with specific symmetries[6].

We show in Figure 1 the energy per baryon E/B of skyrmion matter and σ, the average value of $\frac{1}{2}\mathrm{Tr}U = \phi_0^\pi$ over space, as a function of the FCC single skyrmion crystal size parameter L. Dimensionless units are used for E/B (in units of $6\pi^2 f_\pi/e$) and L(in units of $(ef_\pi)^{-1}$). For massless pions, for a value of $L \sim 3.8$ the slope of E/B changes indicating that the system undergoes a first order phase transition. If we look into the actual baryon number distributions (see figures in the small boxes), we see that the system changes from the FCC single skyrmion crystal to a CC half-skyrmion crystal. In the former phase, a well-localized single skyrmion is located at each FCC lattice site where $\phi_0^\pi = -1$. In the latter phase, one half of the baryon number carried by the single skyrmion is concentrated at each FCC site while the other is concentrated on the links where $\phi_0^\pi = +1$. Both "half-skyrmions" centered at the points where $\phi_0^\pi = \pm 1$ can hardly be distinguished and therefore they form a CC crystal. This phase transition

Table 1. Summary of the properties of the $B = 0$ vacuum solution,the hedgehog Ansatz for the $B = 1$ skyrmion, the symmetries of the FCC single skyrmion crystal for pions, dilaton and vector mesons.

	pion & rho	dilaton & omega
vacuum	$U = 1,\ \rho_\mu^a = 0$	$\chi = f_\chi,\ \omega_\mu = 0$
hedgehog	$U = \exp(i\vec{\tau}\cdot\hat{r}F(r))$ $\rho_i^a = \varepsilon_{aip}\hat{r}_p G(r)/gr$	$\chi = \chi(r)$ $\omega_0 = \omega(r)$
boundary condition	$F(0) = \pi \quad F(\infty) = 0$ $G(0) = -2 \quad G(\infty) = 0$	$\omega'(0) = 0\ \omega(\infty) = 0$ $\chi'(0) = 0\ \chi(\infty) = 0$
reflection(1) (yz-plane)	$(\phi_0^{\pi,\rho}, -\phi_1^{\pi,\rho}, \phi_2^{\pi,\rho}, \phi_3^{\pi,\rho})^*$	$\chi,\ \omega$
3-fold axis rotation(2)	$(\phi_0^{\pi,\rho}, \phi_2^{\pi,\rho}, \phi_3^{\pi,\rho}, \phi_1^{\pi,\rho})$	$\chi,\ \omega$
4-fold axis rotation(3)	$(\phi_0^{\pi,\rho}, \phi_1^{\pi,\rho}, \phi_3^{\pi,\rho}, -\phi_2^{\pi,\rho})$	$\chi,\ \omega$
FCC translation(4)	$(\phi_0^{\pi,\rho}, -\phi_1^{\pi,\rho}, -\phi_2^{\pi,\rho}, \phi_3^{\pi,\rho})$	$\chi,\ \omega$
Ansatz for fluctuations	$U = \sqrt{U_\pi}U_M\sqrt{U_\pi}$ $\rho_\mu^a = \rho_\mu^{a,M} + \tilde{\rho}_\mu^a$	$\chi = \chi_M + \tilde{\chi}$ $\omega_\mu = \omega_{\mu,M} + \tilde{\omega}_\mu$

$^*U = \phi_0^\pi + i\vec{\tau}\cdot\vec{\phi}^\pi,\ \rho_i^a = \varepsilon_{abc}\phi_b^\rho\partial_i\phi_b^\rho/(1+\phi_0^\rho)$
$(x,y,z) \to$ (1) $(-x,y,z)$, (2) (y,z,x), (3) $(x,z,-y)$, (4) $(x+L, y+L, z)$

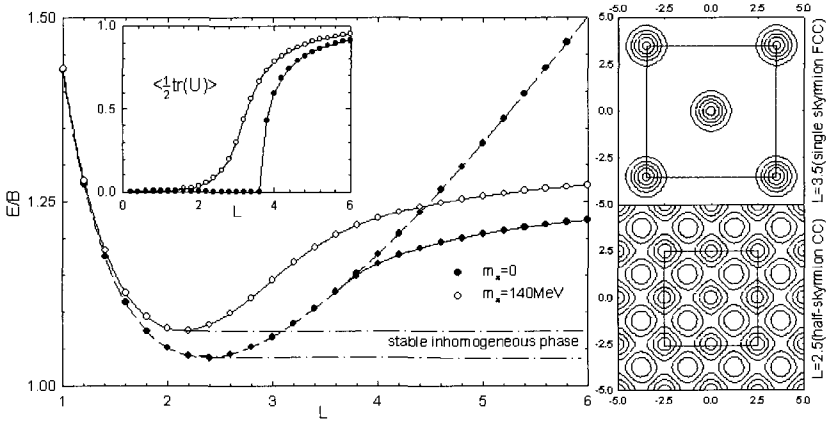

Figure 1. This figure shows the energy per skyrmion and the average value of $\sigma = \langle \frac{1}{2}\mathrm{Tr}(U) \rangle$ as a function of the FCC crystal parameter L (in units of $(ef_\pi)^{-1}$). The figures in the small boxes correspond to samples of the baryon number distribution on the xy-plane ($z = 0$). The corresponding FCC boxes are drawn by a square.

can be seen more apparently in the quantity $\langle \frac{1}{2}\mathrm{Tr}U \rangle$ (see the inset figure). In the literature[5], the vanishing of σ is often interpreted as the restoration of the chiral symmetry.

If we turn on the pion mass (results shown in the figure by open circles), we see no sudden change in the slope of E/B but at sufficiently high baryon number density skyrmion matter behaves as in an approximate half-skyrmion phase.

The phase to the left of the minimum, referred to in our work as "homogeneous", is described by a crystal configuration. The phase to the right of the minimum, which we called "inhomogeneous", because the pressure $P \equiv \partial E/\partial V$ is negative and therefore skyrmion matter is unstable against condensation of the skyrmions into dense lumps leaving large volumes of space empty.

We incorporate the pion fluctuations through the Ansatz

$$U(\vec{r}, t) = \sqrt{U_\pi} U_M(\vec{r}) \sqrt{U_\pi}, \tag{4}$$

where $U_M(\vec{r})$ describes the background baryonic matter and $U_\pi = \exp(i\tau_a \tilde{\pi}_a / f_\pi)$ describes the fluctuating pions. Substitution of this Ansatz

into (1) leads to

$$L_\pi^{B\neq 0} = \tfrac{1}{2}G_{ab}(\vec{r})\partial_\mu\tilde{\pi}^a\partial^\mu\tilde{\pi}_b + \tfrac{1}{4}m_\pi^2\mathrm{Tr}(U_M)\tilde{\pi}_a\tilde{\pi}_a \\ -\partial_\mu\tilde{\pi}_a A_a^\mu(\vec{r}) - \varepsilon_{abc}\tilde{\pi}_a\partial_\mu\tilde{\pi}_b V_c^\mu(\vec{r}) + \cdots, \tag{5}$$

where we have expanded up to the second order in the fluctuating fields. Eq.(5) describes the dynamics of the pion in the dense medium. $G_{ab}(\vec{r})$, $V_\mu^a(\vec{r})$ and $A_\mu^a(\vec{r})$ are the interaction potentials appearing due to background matter.

As a first approximation let's average the potentials over space. Due to the reflection symmetries of the background matter, $\langle V_\mu^a\rangle = \langle A_\mu^a\rangle = 0$, $\langle G_{ab}\rangle = \langle 1 - \phi_a^\pi\phi_b^\pi\rangle \equiv Z_\pi^2\delta_{ab}$ and $\langle\phi_0^\pi\rangle \equiv \sigma$. Thus, the Lagrangian becomes

$$L_\pi^{B\neq 0} = \tfrac{1}{2}Z_\pi^2\partial_\mu\tilde{\pi}^a\partial^\mu\tilde{\pi}_a + \tfrac{1}{2}m_\pi^2\sigma\tilde{\pi}_a\tilde{\pi}_a. \tag{6}$$

The factor Z_π in front of the kinetic term can be absorbed into the renormalization of the pion fields as

$$\tilde{\pi}_a \to \tilde{\pi}' = Z_\pi\tilde{\pi}_a. \tag{7}$$

In terms of this newly defined fields $\tilde{\pi}'_a$, the Lagrangian can be rewritten as

$$L_\pi^{B\neq 0} = \tfrac{1}{2}\partial_\mu\tilde{\pi}'_a\partial^\mu\tilde{\pi}'_a + \tfrac{1}{2}m_\pi^2(\sigma/Z_\pi^2)\tilde{\pi}'_a\tilde{\pi}'_a. \tag{8}$$

This implies that the pions effective mass in the medium is given by

$$m_\pi^* = m_\pi\sqrt{\sigma}/Z_\pi. \tag{9}$$

Furthermore, we may reinterpret the wave function renormalization factor Z_π as the ratio between the *in-medium* decay constant and the free space one,

$$f_\pi^*/f_\pi = Z_\pi. \tag{10}$$

The results on these in-medium quantities (9) and (10) are presented in Figure 2 as a function of the baryon number density. The scales are strongly dependent on the the parameters f_π and e, e.g. the density units in ρ could change considerably, and therefore the shown numbers should not be taken as definitive. However, the qualitative behavior will remain unchanged. In particular, the dependence on the baryon number density showing approximate scaling with the Skyrme parameter e as $\sim e^{-3}$ is a solid statement.

In Figure 2, we show that at low densities $m_\pi^*/m_\pi \sim 1$, while at higher density the ratio decreases down to zero. The density dependence does not appear linear in ρ, since the classical background leads automatically to higher powers in the density dependence. At higher densities, powers

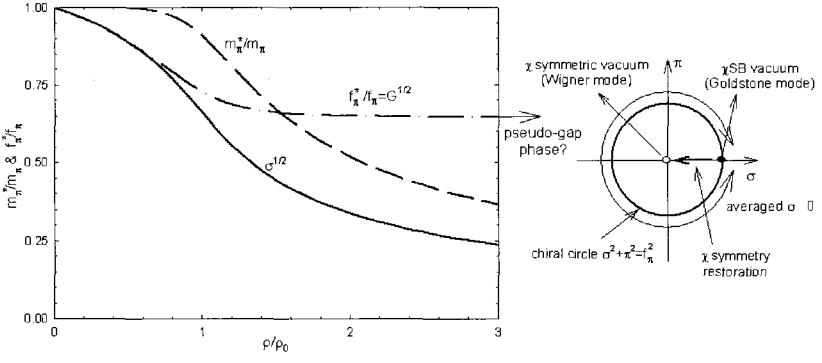

Figure 2. We show the effective pion mass and decay constant in the dense medium as a function of the baryon number density. The dependence on the baryon number density approximately scales with the Skyrme parameter e as $\sim e^{-3}$. The right figure illustrates a pseudo-gap scenario.

greater than one in ρ come to play important roles. As the density increases the decay constant f_π^* decreases, which can be interpreted as a partial restoration of the chiral symmetry in the medium. However, the ratio f_π^*/f_π only decreases up to ~ 0.65 remaining constant thereafter. This non vanishing of the pion decay constant, despite the vanishing of σ, indicates that we may be describing a phase which is not in the standard Wigner-Weyl symmetry. It may be a pseudo-gap phase where the gap is non-zero though chiral symmetry is restored, resembling what might be happening in the normal phase of high T_c superconductivity[16]. The pseudo-gap phase is schematically illustrated in Figure 2.

The pseudo-gap phase may be an artifact of the model with only pions. If we have only pion degrees of freedom which are realized non-linearly through the phase of U, they must live on the chiral circle and the pseudo-gap phenomenon might appear.

However if we introduce a dilaton field χ, as in (2), we see that it may shrink the chiral circle to a point and the conventional Wigner-Weyl symmetry appears [9]. To illustrate this we take the χ field constant, $\chi/f_\chi = X$. In baryon free space the vacuum of the dilaton field is the minimum point of $V(\chi)$ and is $X = 1$. However, for the dense baryonic matter, the ground state should be the minimum of E/B, the energy per baryon expressed as

$$E/B(X) = X^2(E_2/B) + (E_4/B) + X^3(E_m/B) + (2L^3)V(X). \qquad (11)$$

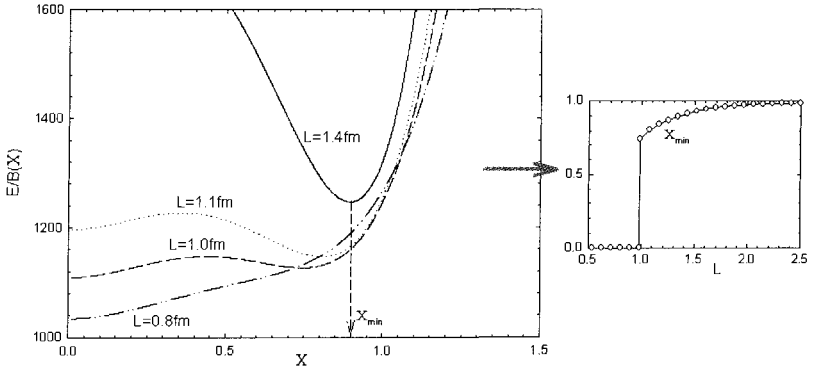

Figure 3. The effective potential $E/B(X)$ as a function of the constant scalar field X for various L.

Here, E_2, E_4 and E_m are the contributions from the skyrmion field configurations of the given baryon number density through the kinetic term, Skyrme term and mass term of the Skyrme Lagrangian, respectively. Couplings to dilaton matter terms contributes with other effective potentials which will modify the value of X at which E/B has a minimum further.

Shown in Figure 3 is E/B as function of X for various FCC length parameters, where we have substituted for E_2/B, E_4/B and E_m/B the values that led to Figure 1. At low density (large L), the minimum of the *effective* potential $E/B(X)$ is shifted slightly away from $X = 1$. As the density increases, $E/B(X)$ starts developing another minimum at $X = 0$ which was an unstable extremum in free space. At $L \sim 1$ fm, the newly developed minimum can compete with the one near $X \sim 1$. At higher density, the minimum gets shifted to $X = 0$. The figure in the small box presents the resulting values of X_{min} as a function of L. There we see an explicit manifestation of a first order phase transition. This mechanism corresponds to reformulating BR-scaling[15] in a more accurate way.

One can perform a more rigorous treatment by allowing the space dependence in $\chi_M(\vec{r})$ (with the symmetries summarized in Table 1), which leads basically to the same physics except for small quantitative difference. The most essential new ingredient is that the static dilaton field for dense matter vanishes identically *all over the space* in the half-skyrmion phase.

By incorporating the fluctuations of pions and dilaton, as summarized in Table 1, we obtain as before the Lagrangian for the dynamics of these

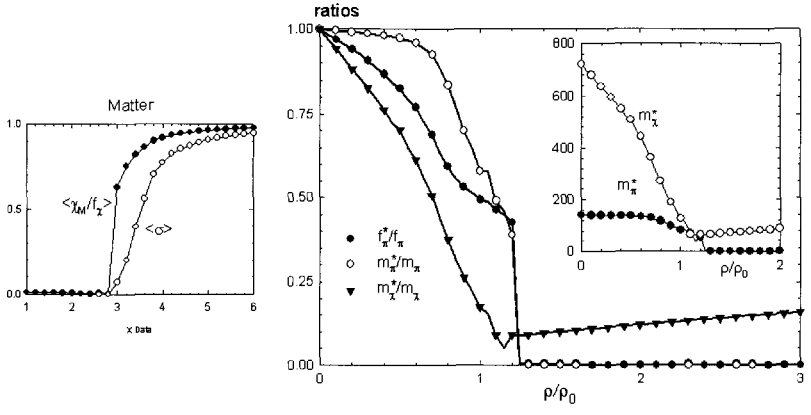

Figure 4. In medium properties of the pion and dilaton fluctuations as a function of the baryon number density. In the inset figure, the pion and dilaton masses are presented in the actual energy scale. The numerical results on the average values of χ_M and σ of the background matter are presented in the small figure on the left hand side.

particles

$$L(U,\chi) = L_{\mathrm{M},\pi} + L_{\mathrm{M},\chi} + L_{\mathrm{M},\pi\chi}, \tag{12}$$

where we have put the subscript "M" to denote that it describes the *in-medium* dynamics. Explicitly, each term can be expressed as

$$\begin{aligned} L_{\mathrm{M},\pi} = {} & \tfrac{1}{2}G_{ab}(\vec{r})\partial_\mu\tilde{\pi}_a\partial^\mu\tilde{\pi}_b - \tfrac{1}{2}S(\vec{r})\tilde{\pi}_a^2 \\ & + \epsilon_{abc}\partial_\mu\tilde{\pi}_a\tilde{\pi}_b V_c^i(\vec{r}) \end{aligned} \tag{12a}$$

$$L_{\mathrm{M},\chi} = \frac{1}{2}\partial_\mu\tilde{\chi}\partial^\mu\tilde{\chi} - \frac{1}{2}M(\vec{r})\tilde{\chi}^2, \tag{12b}$$

$$L_{\mathrm{M},\chi\pi} = P_a^i(\vec{r})\tilde{\chi}\partial^i\tilde{\pi}_a + Q_a(\vec{r})\tilde{\chi}\tilde{\pi}^a. \tag{12c}$$

Here, $G_{ab}(\vec{r})$, $S(\vec{r})$, $V_c^i(\vec{r})$, $M(\vec{r})$, $P_a^i(\vec{r})$ and $Q_a(\vec{r})$ are the effective potentials provided to the fluctuating fields by the background fields $U_M(\vec{r})$ and $\chi_M(\vec{r})$ (For the details, see Ref.[9]).

By applying the same approximation, i.e taking the average values for the effective potentials over the space, we can estimate the medium effects on the properties of the fluctuating fields. As for the pion, we are led to a Lagrangian similar to (6), where Z_π and σ take the average values with the additional factors $(\chi_M/f_\chi)^2$ and $(\chi_M/f_\chi)^3$, respectively. Since χ_M vanishes in the chiral symmetry restored phase, the ratio f_π^*/f_π now

vanishes. However, even in the chirally restored phase, with $\langle\sigma\rangle = \langle\chi_M\rangle = 0$, $\langle M\rangle$ does not vanish due to the background $U_M(\vec{r})$ couplings to $\tilde{\chi}$. In Figure 4 we show the ratios of the in-medium parameters relative to their free-space values.

The phenomenon discussed above is closely related to "Brown-Rho" scaling [15]. In the description of Ref.[15], the density dependence comes solely from the change in the mean field χ^* where the corresponding change in the skyrmion structure has been ignored. Our present result corrects this fact and gives a precise meaning to the scaling relation of Ref.[15].

We can treat the background interactions more systematically following the *perturbative* scheme we have developed. We decompose the Lagrangian into an unperturbed part, L_0, and an interaction part, L_I. This leads to a Hamiltonian split also in two parts

$$H = H_0 + H_I. \tag{13}$$

The free propagators are defined by H_0 and the interaction potentials appearing due to H_I are summarized in Figure 5. In Figure 5, $G^{ab}(\vec{\ell})$, for example, is the Fourier transform of the local potential $G^{ab}(\vec{r})$:

$$G^{ab}(\vec{\ell}) = \frac{1}{V_{\rm box}} \int_{\rm box} d^3r e^{i\vec{\ell}\cdot\vec{r}} G^{ab}(\vec{r}), \tag{14}$$

where the integration is over a unit box of the crystal and $V_{\rm box}$ is its volume. Due to the periodic structure of the crystal only discrete values of the momentum are allowed.

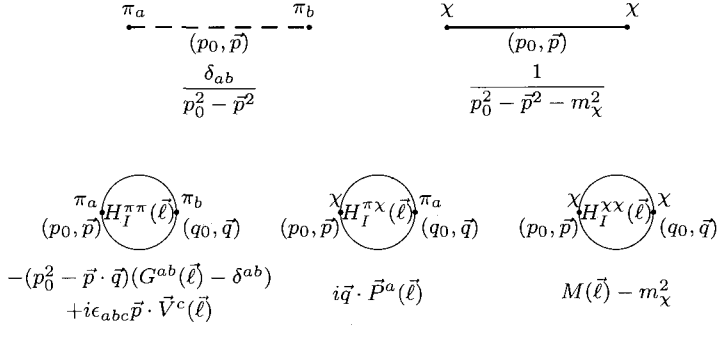

Figure 5. Free propagators and interactions for the pion and the scalar fields in the presence of background skyrmion matter. The energy-momentum conservation delta functions are not shown.

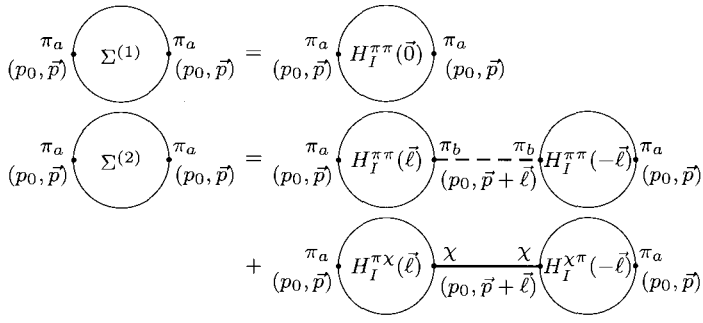

Figure 6. Diagrams used to evaluate the self-energy of the π_a propagation up to second order in the interaction. Here, b runs over $1, 2, 3$ and the intermediate states run over all $\vec{\ell} \neq 0$.

We show in Figure 6 the diagrams used to evaluate the self-energy. Only the diagrams for $\Sigma_{\pi_a \pi_b}$ appear. The symmetry structure of skyrmion matter allows a non vanishing self-energy only for $a = b$. To first order, $\Sigma^{(1)}$ is nothing but $H_I(\vec{\ell} = \vec{0})$. Since $H_{\pi\chi}(\vec{0}) = 0$, no mixing between the fluctuating pions and the fluctuating scalar occurs. Thus, the pion propagator for $\tilde{\pi}_a$ can be expressed as

$$\frac{1}{p_0^2 - \vec{p}^2 - \Sigma^{(1)}(p_0, \vec{p})} = \frac{1}{G^{aa}(\vec{0})(p_0^2 - \vec{p}^2)}. \tag{15}$$

where we have used that the self energy to this order is $\Sigma^{(1)}_{\pi_a \pi_a}(p_0, \vec{p}) = -p^2(G_{aa}(\vec{0}) - 1)$. The superscript "(1)" means that the quantities are evaluated to first order.

Since Lorentz symmetry is broken by the medium, the general form of the *in-medium* propagator can be written as

$$\frac{1}{Z_t^{-1} p_0^2 - Z_s^{-1} \vec{p}^2}, \tag{16}$$

with $Z_{t,s}^{-1} = (f_{t,s}/f_\pi)^2$ and the "pion velocity" in medium is given as $v_\pi^2 = Z_t/Z_s$. Comparing with this, we obtain $f_t = f_s = f_\pi \sqrt{G_{aa}(\vec{0})}$. Since $G_{aa}(\vec{0})$ is nothing but the average of $G^{aa}(\vec{r})$ over the space, our calculation thus far reproduces the naive approximations discussed above. To the same order, the self-energy of the scalar field is $\Sigma^{(1)}_{\chi\chi} = M(\vec{0}) - m_\chi^2$. Since it is constant, this self-energy modifies just the scalar mass from the free value m_χ to $\sqrt{M(\vec{0})}$.

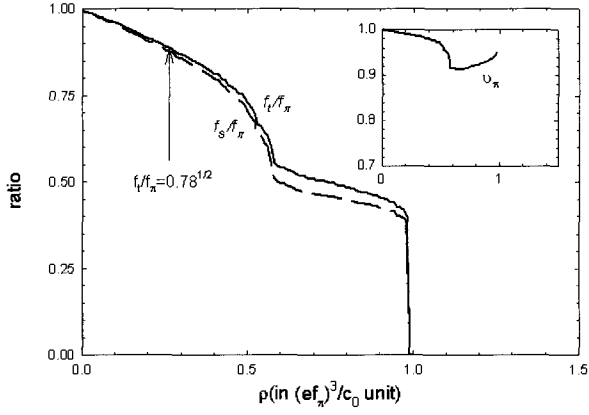

Figure 7. f_t and f_s as a function of skyrmion matter density in arbitrary units for the chiral limit, $m_\pi = 0$ and $m_\chi = 720$ MeV. The in medium pion velocity appears as function of matter density in the small box. The arrow indicates the point at which the observed ratio in pionic nuclei (at $\rho \approx 0.6\rho_0$) is located.

Now, the second order diagrams shown in Figure 6 can be calculated similarly. Again, in spite of the $\pi - \chi$ coupling term in the interaction Lagrangian (12), $\Sigma^{(2)}_{\chi\pi_a}$ vanishes so that the pion propagator and the scalar propagator can be simply written as

$$\frac{1}{p_0^2 - \vec{p}^2 - \Sigma^{(1+2)}_{\pi_b\pi_a}}, \qquad \frac{1}{p_0^2 - \vec{p}^2 - m_\chi^2 - \Sigma^{(1+2)}_{\chi\chi}}, \tag{17}$$

respectively.

The p_0 and $\vec{p}$ dependence of $\Sigma^{(2)}$ is not so simple as that of $\Sigma^{(1)}$. By assuming that energy and momentum are small, we may expand the self-energy $\Sigma_{\pi_a\pi_b}$ in powers of p_0 and $\vec{p}$. Then, we can express the propagator in the form of (16), but Z_s gets some corrections terms from the second order diagram. The corrections are negative definite so that the pion velocity becomes $v_\pi < 1$.

The results of our calculation are shown in Figure 7. We show the decay constants f_t and f_s in units of f_π as a function of the density measured in a dimensional unit. The inset figure is their ratio, i.e. the in-medium pion velocity v_π. To second order the contribution to f_s/f_π turns out to be small, and thus the pion velocity stays $v_\pi \sim 1$. The lowest value is about ~ 0.9. Furthermore, for the pions at higher matter densities, the internal propagator provides an extra suppression because L scales as $\rho^{1/3}$. Once

we pass the density at which the pion velocity has its minimum, the pion velocity increases with density and approaches 1. When the background matter is in the half-skyrmion phase, $\chi_0(\vec{r})$ vanishes identically and so do all the local potentials. Thus, both f_t and f_s vanish. Moreover, their difference is proportional to the square of the potentials and vanishes faster. This fact explains the asymptotic behavior $v_\pi \to 1$ in Figure 7. This result is very similar to that of Ref. [17] found in heat bath, where the pion velocity approaches 1 while both the spatial and temporal pion decay constants vanish at $T = T_c$.

4. Vector mesons

At higher density and/or temperature we need more degrees of freedom such as the ρ and ω vector mesons. The same procedure can be repeated with the vector mesons using the Lagrangian (3). The lowest energy FCC skyrmion crystal configuration can be found by requiring the symmetries given in Table 1 to the pion, dilaton, rho and omega fields. The numerical results are presented in Figure 8.

In the $\pi\rho\chi$ model, as the density of the system increases (L decreases), E/B changes slightly. Its value is close to the energy of a single skyrmion up to densities larger than ρ_0 ($L \sim 1.43$). because the size of the skyrmion is very small and the skyrmions in the lattice only interact at very high densities when their tails overlap.

In the absence of the ω the dilaton field plays as before an important role. Skyrmion matter undergoes an abrupt phase transition at the density at which the expectation value of the dilaton field vanishes $\langle\chi\rangle = 0$.

In the $\pi\rho\omega\chi$ model, the situation changes dramatically, because the ω provides not only a strong repulsion between the skyrmions but also an intermediate range attraction. In both the $\pi\rho\omega$ and the $\pi\rho\omega\chi$ models, at high density, the interaction reduces E/B to 85% of the $B = 1$ skyrmion mass. This value should be compared with 94% in the $\pi\rho$ model. In the $\pi\rho\chi$-model, E/B goes down to 74% of the $B = 1$ skyrmion mass, but in this case it is due to the dramatic behavior of the dilaton field.

In the $\pi\rho\omega\chi$ model the role of the dilaton field is suppressed. It provides only a small attraction at intermediate densities. Moreover, the phase transition towards its vanishing expectation value, $\langle\chi\rangle = 0$, does not take place. Instead, its value grows at high density!

The reason for this can be found in the role played by omega in (3). In the static configuration, omega produces a potential, whose source is the

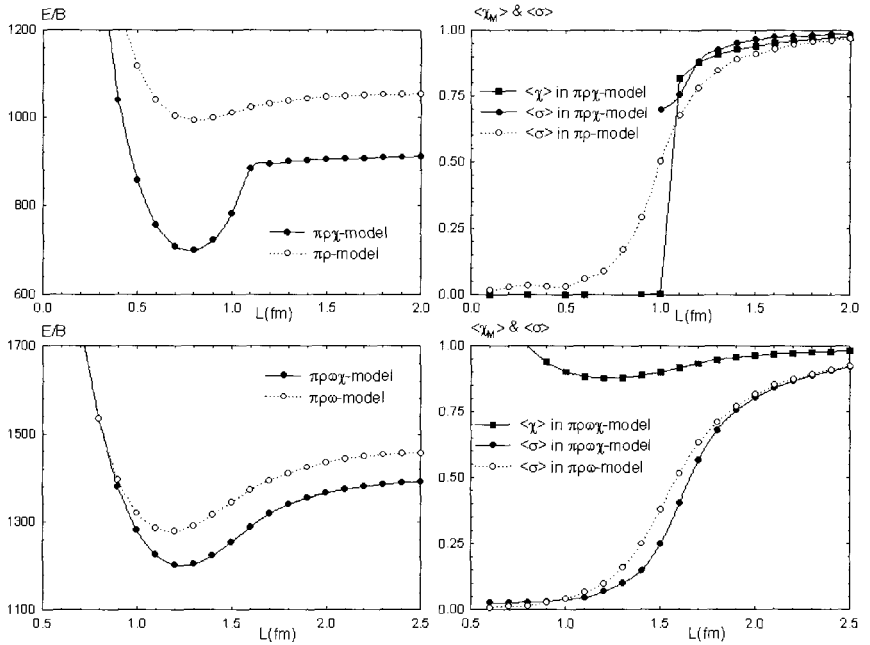

Figure 8. E/B and the average values of the fields over the space as a function of L.

baryon number density, which mediates the self-interaction energy of the baryon number distribution. Thus, unless it is screened properly by the omega mass, the periodic source filling infinite space will lead to an infinite self-energy. To reduce the energy of the system, the effective ω mass must grow at high density, for which χ must grow too. Note the factor $(\chi/f_\chi)^2$ in the omega mass term in Lagrangian (3).

5. Summary

We have developed a unified approach to dense matter in the Skyrme philosophy, where systems of baryons and mesons can be described by a single Lagrangian. In our approach dense baryonic matter is approximated by skyrmion matter in the lowest energy configuration for a given baryon number density. By incorporating in it fluctuating mesons we can get some insights on meson dynamics in a dense medium. Our approach enables us to study this dynamics beyond the first order in the baryon number density. One can continue to work in this direction by incorporating more degrees

of freedom, by improving the way of treating matter beyond the crystal solution, and so on.

However, before closing the presentation, we must clearly lay down the scope of our work. We do not claim that the results obtained at present describe reality. The most fundamental problem we phase is that our "ground state" for matter is a crystal not a Fermi liquid. Our aim has been to assume a state for matter, given by a classical solution of a theory considered to be valid at large N_c, and have studied the implications for its excitations. Our work should be taken as representing the first step towards a more realistic treatment of a dense matter theory.

Acknowledgments

H.-J. Lee, B.-Y. Park and V. Vento are grateful for the hospitality extended to them by KIAS. This work was partially supported by grants MCyT-FIS2004-05616-C02-01 and GV-GRUPOS03/094 (VV) and KOSEF Grant R01-1999-000-00017-0 (BYP & DPM).

References

1. For a review, see, for example, T. DeGrand, "Lattice QCD at the end of 2003", hep-ph/0312241; also see T. Hatsuda in this proceedings.
2. See, for instance, D. K. Hong, in this proceedings.
3. M. Harada and K. Yamawaki, Phys. Rep. **381**, 1 (2003), hep-ph/0302103.
4. T. H. R. Skyrme, Nucl. Phys. **31**, 556 (1962).
5. I. Klebanov, Nucl. Phys. **B262**, 133 (1985); G. E. Brown, A. D. Jackson and E. Wüst, Nucl. Phys. **A468**, 450 (1985); A. S. Goldhaber and N. S. Manton, Phys. Lett. **B198**, 231 (1987); A. D. Jackson and J. J. M. Verbaarschot, Nucl. Phys. **A501**, 419 (1988); L. Castillejo, P. S. J. Jones, A. D. Jackson, J. J. M. Verbaarschot and A. Jackson, Nucl. Phys. **501**, 801 (1989).
6. M. Kugler and S. Shtrikman, Phys. Lett. **B208**, 491 (1988); Phys. Rev. **D40**, 3421 (1989).
7. B.-Y. Park, D.-P. Min, M. Rho and V. Vento, Nucl.Phys. **A707**, 381 (2002), nucl-th/0201014.
8. H.-J. Lee, B.-Y. Park, D.-P. Min, M. Rho and V. Vento, Nucl.Phys. **A723**, 427 (2003), hep-ph/0302019.
9. H.-J. Lee, B.-Y. Park, M. Rho and V. Vento, Nucl. Phys. **A726**, 69 (2003), hep-ph/0304066.
10. H.-J. Lee, B.-Y. Park, M. Rho and V. Vento, "Pion Velocity in Dense Skyrmion Matter", hep-ph/0307111, submitted to Phys. Lett. **B**.
11. B.-Y. Park, M. Rho and V. Vento, "Vector Mesons and Dence Skyrmion Matter", hep-ph/0310087, submitted to Nucl. Phys. **A**.
12. J.-I. Kim, B.-Y. Park, D.-P. Min, M. Rho, V. Vento, in preparation.

13. J. Ellis and J. Lanik, Phys. Lett. **B150**, 289 (1985).
14. M. Bando, T. Kugo, S. Uehara, K. Yamawaki and T. Yanagida, Phys. Rev. Lett. **54**, 1215 (1985); Phys. Rep. **164**, 217 (1988); Ulf-G. Meissner, Phys. Rep. **161**, 213 (1988).
15. G.E. Brown and M. Rho, Phys. Rev. Lett. **66**, 2720 (1991).
16. See e.g. M. Frantz, Z. Tesanovic and O. Vafec, Phys. Rev. **B66**, 054535 (2002), cond-mat/0203333.
17. M. Harada, Y. Kim, M. Rho and C. Sasaki, "Effective degrees of freedom at chiral restoration and the vector manifestation in HLS theory, Nucl. Phys. **A**, in press, hep-ph/0308237; M. Harada, Y. Kim, M. Rho and C. Sasaki, Nucl. Phys **A727**, 437 (2003), hep-ph/0207012.

CHIRAL SYMMETRY OF HEAVY-LIGHT-QUARK HADRONS IN HOT/DENSE MATTER*

MANNQUE RHO

Service de Physique Théorique, CEA/Saclay, 91191 Gif-sur-Yvette, France,
Korea Institute for Advanced Study, Seoul 130-722, Korea
& Department of Physics, Hanyang University, Seoul 133-791, Korea
E-mail: rho@spht.saclay.cea.fr

The recent discoveries by the BaBar and CLEO II collaborations on the splitting between D_s and $\bar{D}_s$ which exhibited surprises in the structure of heavy-light-quark systems are connected – via the Harada-Yamawaki "vector manifestation" of hidden local symmetry – to chiral symmetry restoration expected to take place at some critical temperature T_c in heavy-ion collisions or at some critical density n_c in the deep interior of compact stars, the main theme of this symposium. This unexpected connection exemplifies the diversity of astro-hadronic phenomena discussed in this meeting.

1. Foreword

This is the last talk of this Symposium and as such it is supposed to conclude it. What distinguishes this meeting from other meetings of a similar scope is the diversity of the topics covered, ranging from hadron/particle physics to astrophysics, but with a common objective, that is, to explore the extreme state of matter in high density or/and high temperature. Given the diversity and the exploratory stage of the development, it would be presumptuous of me to make any conclusion on any subtopic of the meeting, not to mention the totality, so what I will do is to present to you yet another surprising development that at first sight might appear unrelated to the main theme of the meeting but as it turns out, has an uncanny connection to what we have been discussing throughout this meeting.

What I shall present here is a combination of the work I did with Maciej A. Nowak and Ismail Zahed a decade ago [1] and the work I did very

*The concluding talk at the KIAS-APCTP Symposium in Astro-Hadron Physics "Compact Stars: Quest for New States of Dense Matter," November 10-14, 2003, Seoul, Korea.

recently with Masayasu Harada and Chihiro Sasaki [2]. The question I will address here is: *Do the recent discoveries on the structure of heavy-light-quark mesons by the BaBar, CLEO and Belle collaborations that we have just heard have any ramifications on what we have been discussing in this meeting, i.e., the structure of compact stars and the early Universe?* My answer is: *Yes, if the chiral phase transition predicted in QCD has significant influence on them.*

2. The BaBar, CLEO and Belle Discoveries

On April 12th 2003, the BaBar collaboration announced a narrow peak of mass 2.317GeV $/c^2$ that decays into $D_s^+\pi^0$ [3]. On May 12th 2003, the CLEO II collaboration confirmed the BaBar result, and also observed a second narrow peak of mass 2.46 GeV$/c^2$ in the final $D_s^{*+}\pi^0$ state [4]. Subsequently both states were confirmed by the Belle collaboration [5]. The experimental results were surprising since such states were expected neither to lie below DK and D^*K thresholds nor to be so narrow. These observations have recently generated a flurry of theoretical activities. The excitement surrounding these developments was nicely summarized by Nowak [6].

Remarkably, however, the existence of this type of states was theoretically predicted more than a decade ago [1,7] based on the combination of chiral symmetry of light quarks and heavy-quark symmetry of heavy quarks. What is relevant in my discussion in this meeting is the suggestion made in [8] that the splitting of the chiral doublers carries a direct information on the light-quark condensate $\langle\bar{q}q\rangle$ and can therefore be a litmus indicator for chiral symmetry property of the medium in which the chiral doubling phenomenon is observed. In particular, if one measures the splitting in hot or dense matter, then as the chiral phase transition point generically denoted $[pt]_\chi$ (such as the critical temperature T_c or density n_c) is approached, the splitting should disappear in the chiral limit. This could then be an ideal tool to map out the chiral phase structure of hot/dense matter.

3. Chiral Doubling Starting From the "Vector Manifestation (VM)"

The standard approach to hot/dense-matter physics starts with a Lagrangian for cold/dilute matter for which one has both experimental and theoretical control and then drives the system to a hot/dense environment so as to bring it to a phase transition. This is what is being done in heavy-ion collisions and in compact-star physics heard in this meeting. This was

the idea proposed by Nowak, Rho and Zahed in [8] for heavy-light mesons in medium. The idea of Harada, Sasaki and myself [2] is to go in the opposite direction: Instead of going from zero temperature/density to high temperature/density, that is, "bottom-up", we will go "top-down". This is because we think we have a theory which is well-defined at the critical point $[pt]_\chi$ although whether that theory is directly related to QCD is yet to be verified. Our task then is to simply assume that this description of $[pt]_\chi$ has something to do with that of QCD and then deduce the chiral doubling of heavy-light hadrons. This strategy seems to work amazingly well, giving credence to the notion of the "vector manifestation (VM)" of chiral symmetry at chiral restoration introduced by Harada and Yamawaki [9].

3.1. *The Vector Manifestation of Hidden Local Symmetry*

To make the discussion as simple as possible, I shall take in the light-quark sector all the current quark masses to be zero, the so-called chiral limit. The experiments that brought surprises involve the strange quark whose current quark mass is comparable to the strong interaction scale, namely, the pion decay constant $F_\pi \sim 93$ MeV, so to make a quantitative comparison with experiments, one would have to worry about the explicit breaking of chiral symmetry. However I believe that the qualitative feature can be captured in the chiral limit.

Now up to the transition point $[pt]_\chi$, that is, in the chiral symmetry broken phase, the relevant degrees of freedom are hadrons. In the standard way of doing things, one assumes that the only relevant degrees of freedom are the pions with other degrees of freedom such as vector mesons, baryons etc. considered to be too heavy to be relevant to the chiral phase transition. This is the picture typically given by the linear sigma model. The key point in my discussion which departs from the conventional picture is that not just the pions but also the vector mesons, namely, the ρ mesons, are quite relevant. Now how does one "see" this? One cannot see it if one has a Lagrangian with the pions and massive vector mesons coupled in the usual way which is consistent with the global symmetry but not local gauge invariant because of the vector-meson mass. With such a Lagrangian it is not easy – although not impossible – to go toward $[pt]_\chi$: There is no systematic way to compute loop corrections. In fact, there is no easy way to see whether the theory without local gauge invariance breaks down and if so, locate at what point it does so. There is however a "trick" to make the theory locate, and work up to, the break-down point. That

is to introduce hidden local symmetry and make the theory local-gauge invariant [10]. The authors in Ref.[10] call it "fake" symmetry but it has the advantage of endowing the vector mesons with a chiral power counting [9].

To illustrate the idea, consider the chiral $G \equiv SU(3)_L \times SU(3)_R$ symmetry appropriate to three-flavor QCD. The symmetry G is spontaneously broken in the vacuum to $H \equiv SU(3)_{L+R}$, so the coordinates of the system are given by the coset space G/H parameterized by the Sugawara field $U = e^{i\pi/f}$ where π is the Nambu-Goldstone pion field. In the absence of other fields than pions, we have the well-known chiral perturbation development à la Gasser and Leutwyler. In this pion-only chiral perturbation theory, the vector mesons ρ can be introduced in consistency with the assumed symmetry. In fact there are several different ways of doing this but they are all physically equivalent, provided they are limited to tree order or the next-to-leading order in chiral perturbation. See [9] for a clear discussion on this point. The massive vectors so introduced do not, however, render themselves to a systematic chiral perturbation treatment beyond the tree order. This means that such a theory is powerless as one moves toward the $[pt]_\chi$ point. In my opinion, works purporting to describe chiral properties of hot/dense matter away from the vacuum without resorting to this strategy all suffer from this defect and cannot be trusted. This difficulty is beautifully circumvented if the nonlinearly realized chiral symmetry G/H is gauged to linear $G_{global} \times H_{local}$ as recently worked out by Harada and Yamawaki. If one fixes the gauge to unitary gauge, one then recovers the same theory without gauge invariance.

Harada and Yamawaki [9] have shown that in hidden local symmetry theory that exploits the above strategy with pions and ρ mesons as the relevant degrees of freedom and where a consistent chiral perturbation can be effectuated, the vector mesons are found to play an *essential role* at $[pt]_\chi$ since the mass of the vector meson mass goes to zero in proportion to the quark condensate $\langle\bar{q}q\rangle$. In fact by matching the HLS theory to QCD at a matching scale Λ_M above the vector meson mass, they show by one-loop renormalization-group equation involving the vector mesons as well pions that $[pt]_\chi$ corresponds to the vector manifestation (VM) fixed point at which the local gauge coupling g goes to zero and the ratio $a \equiv F_\sigma^2/F_\pi^2$ (where σ are the scalar Goldstone bosons arising from the spontaneous breaking of the gauge symmetry) goes to 1.

Up to date, there are no proofs – lattice or otherwise – for or against that the vector mass goes to zero at $[pt]_\chi$. In many conference talks (e.g., QM2004), one frequently sees view-graphs in which the ρ and a_1 masses

come together at the critical temperature T_c but at non-zero value above the degenerate π and σ. A recent study of chemical equilibration in RHIC experiments shows that this is most probably incorrect [11] in hot matter: Both the $\pi - \sigma$ complex and the $\rho - a_1$ complex should become massless at T_c. Real-time lattice calculations in temperature should ultimately be able to validate or invalidate this scenario: The screening mass measured on lattice in hot matter does not carry the relevant information. In the absence of evidence either for or against it, we will simply assume that the VM is realized at the chiral transition point and see whether the result we obtain gives an a posteriori consistency check, if not a proof, of the assumption.

The presence of the VM at the chiral transition point $[pt]_\chi$ implies a scenario that is quite different from the standard one based on the linear sigma model invoked to describe two-flavor chiral restoration. For instance, the pion velocity at $[pt]_\chi$ is predicted to be near the velocity of light with the vector mesons at VM [12] whereas the linear sigma model predicts it to be zero [13].

3.2. *From the VM Fixed Point to the Nambu-Goldstone Phase*

Consider the heavy-light-quark, $Q\bar{q}$, mesons where Q is the heavy quark and q is the light quark. Again for simplicity, I shall take the mass of Q to be infinite – and as mentioned, that of q to be zero. Let us imagine that we are at the VM fixed point. In constructing the Lagrangian for the light-quark system, the relevant variables are the HLS 1-forms for the light mesons,

$$\alpha_{R(L)\mu} = \frac{1}{i}\partial_\mu \xi_{\mathrm{R(L)}} \cdot \xi^\dagger_{[\mathrm{R(L)}]} \tag{1}$$

which transform under $SU(3)_L \times SU(3)_R$ as $\alpha_{R(L)\mu} \to R(L)\,\alpha_{R(L)\mu}[R(L)]^\dagger$ with $R(L) \in SU(3)_R(SU(3)_L)$. Since the gauge coupling g is zero at the fixed point, the HLS gauge bosons are massless and their transverse components decouple from the system. Two matrix valued variables $\xi_{L,R}$ are parameterized as $\xi_{L,R} = \exp[i\phi_{L,R}]$. Here the combination $(\phi_R + \phi_L)/2$ corresponds to the longitudinal components of the vector mesons ρ (the ρ meson and its flavor partners) in the broken phase, while the combination $(\phi_R - \phi_L)/2$ corresponds to the pseudoscalar Nambu-Goldstone bosons π (the pion and its flavor partners). With these 1-forms and since

$a = (F_\sigma/F_\pi)^2 = 1$, the light-quark HLS at the VM takes the simple form,

$$\mathcal{L}^*_{\rm light} = \frac{1}{2}F_\pi^2 {\rm tr}[\alpha_{R\mu}\alpha_R^\mu + \alpha_{L\mu}\alpha_L^\mu], \tag{2}$$

with the star representing the VM fixed point and F_π denoting the bare pion decay constant. The physical pion decay constant f_π vanishes at the VM fixed point by the quadratic divergence although the bare one is non-zero [9].

For the heavy mesons, one introduces the right and left fluctuation fields $\mathcal{H}_R$ and $\mathcal{H}_L$ that transform under $SU(3)_L \times SU(3)_R$ as $\mathcal{H}_{R(L)} \to \mathcal{H}_{R(L)}R^\dagger(L^\dagger)$. The fixed point Lagrangian for the heavy mesons in the presence of the light mesons takes the form

$$\begin{aligned}\mathcal{L}^*_{\rm heavy} = &-{\rm tr}\left[\mathcal{H}_R i v_\mu \partial^\mu \bar{\mathcal{H}}_R\right] - {\rm tr}\left[\mathcal{H}_L i v_\mu \partial^\mu \bar{\mathcal{H}}_L\right] + m_0 {\rm tr}\left[\mathcal{H}_R\bar{\mathcal{H}}_R + \mathcal{H}_L\bar{\mathcal{H}}_L\right] \\ &+2k\,{\rm tr}\left[\mathcal{H}_R\alpha_{R\mu}\gamma^\mu\frac{1+\gamma_5}{2}\bar{\mathcal{H}}_R + \mathcal{H}_L\alpha_{L\mu}\gamma^\mu\frac{1-\gamma_5}{2}\bar{\mathcal{H}}_L\right],\end{aligned} \tag{3}$$

where v_μ is the velocity of the heavy meson, m_0 represents the mass generated by the interaction between heavy quark and the "pion cloud" surrounding the heavy quark, and k is a real constant to be determined.

Next we need to consider the modification to the VM Lagrangian generated by the spontaneous breaking of chiral symmetry. The gauge coupling constant becomes non-zero, $g \neq 0$, so the derivatives in the HLS 1-forms become the covariant derivatives. Then $\alpha_{L\mu}$ and $\alpha_{R\mu}$ are covariantized:

$$\begin{aligned}&\partial_\mu \to D_\mu = \partial_\mu - ig\rho_\mu, \\ &\alpha_{R\mu} \to \hat{\alpha}_{R\mu}, \quad \alpha_{L\mu} \to \hat{\alpha}_{L\mu}.\end{aligned} \tag{4}$$

These 1-forms transform as $\hat{\alpha}_{R(L)\mu} \to h\,\hat{\alpha}_{R(L)\mu}h^\dagger$ with $h \in [SU(3)_V]_{\rm local}$. Apart from the kinetic-energy term $\mathcal{L}_{\rho{\rm kin}} = -\frac{1}{2}{\rm tr}\left[\rho_{\mu\nu}\rho^{\mu\nu}\right]$, there may be other terms, such as e.g., $(a-1)F_\pi^2{\rm tr}[\hat{\alpha}_{L\mu}\hat{\alpha}_R^\mu]$ which vanishes at the fixed point with $a = 1$. Although generally $a \neq 1$ in the broken phase, $a = 1$ gives a variety of physical quantities in good agreement with experiment in matter-free space, as shown in [9]. A detailed analysis in preparation for publication [14] shows that in the present problem, at the one-loop level that we consider, there are no $(a-1)$ corrections. Therefore we can safely set $a = 1$ in what follows. In the heavy sector, chiral-symmetry breaking will generate the term

$$\mathcal{L}_{\chi{\rm SB}} = \frac{1}{2}\Delta M\,{\rm tr}\left[\mathcal{H}_L\bar{\mathcal{H}}_R + \mathcal{H}_R\bar{\mathcal{H}}_L\right], \tag{5}$$

with $\mathcal{H}_{R(L)}$ transforming under the HLS as $\mathcal{H}_{R(L)} \to \mathcal{H}_{R(L)}h^\dagger$. Here ΔM is the *bare* parameter corresponding to the mass splitting between the two multiplets and can be determined by matching the EFT with QCD.

The main finding of this approach is that ΔM comes out to be proportional to the quark condensate, i.e., $\Delta M \sim \langle \bar{q}q \rangle$.

In order to compute the mass splitting between D and $\tilde{D}$ [a], we need to go to the corresponding fields in parity eigenstate, H (odd-parity) and G (even-parity) as defined, e.g., in [8];

$$\mathcal{H}_{R,L} = \frac{1}{\sqrt{2}}\left[G \mp iH\gamma_5\right]. \tag{6}$$

We shall denote the corresponding masses as $M_{H,G}$. They are given by

$$\begin{aligned} M_H &= -m_0 - \frac{1}{2}\Delta M \ , \\ M_G &= -m_0 + \frac{1}{2}\Delta M \ . \end{aligned} \tag{7}$$

The mass splitting between G and H is therefore given by ΔM:

$$M_G - M_H = \Delta M \ . \tag{8}$$

The next step in the calculation is to determine ΔM at the matching point in terms of QCD variables. We shall do this for the pseudoscalar and scalar correlators for $D(0^-)$ and $\tilde{D}(0^+)$, respectively. The axial-vector and vector current correlators can similarly be analyzed for $D(1^-)$ and $\tilde{D}(1^+)$. In the EFT sector, the correlators are expressed as

$$\begin{aligned} G_P(Q^2) &= \frac{F_D^2 M_D^4}{M_D^2 + Q^2}, \\ G_S(Q^2) &= \frac{F_{\tilde{D}}^2 M_{\tilde{D}}^4}{M_{\tilde{D}}^2 + Q^2}, \end{aligned} \tag{9}$$

where F_D ($F_{\tilde{D}}$) denotes the D-meson ($\tilde{D}$-meson) decay constant and the space-like momentum $Q^2 = (M_D + \Lambda)^2$ with Λ being the matching scale. If we ignore the difference between F_D and $F_{\tilde{D}}$ which can be justified by the QCD sum rule analysis [15], then we get

$$\Delta_{SP}(Q^2) \equiv G_S(Q^2) - G_P(Q^2) \simeq \frac{3F_D^2 M_D^3}{M_D^2 + Q^2}\Delta M_D. \tag{10}$$

[a] Although we are referring specifically to the D mesons, our discussion generically applies to all heavy-light mesons.

In the QCD sector, the correlators G_S and G_P are given by the operator product expansion (OPE) as [15]

$$\begin{aligned} G_S(Q^2) &= G(Q^2)\big|_{\text{pert}} \\ &\quad + \frac{m_H^2}{m_H^2+Q^2}\left[- m_H\langle\bar{q}q\rangle + \frac{\alpha_s}{12\pi}\langle G^{\mu\nu}G_{\mu\nu}\rangle\right], \\ G_P(Q^2) &= G(Q^2)\big|_{\text{pert}} \\ &\quad + \frac{m_H^2}{m_H^2+Q^2}\left[m_H\langle\bar{q}q\rangle + \frac{\alpha_s}{12\pi}\langle G^{\mu\nu}G_{\mu\nu}\rangle\right], \end{aligned} \tag{11}$$

where m_H is the heavy-quark mass. To the accuracy we are aiming at, the OPE can be truncated at $\mathcal{O}(1/Q^2)$. The explicit expression for the perturbative contribution $G(Q^2)\big|_{\text{pert}}$ is available in the literature but we do not need it since it drops out in the difference. From these correlators, the Δ_{SP} becomes

$$\Delta_{SP}(Q^2) = -\frac{2m_H^3}{m_H^2+Q^2}\langle\bar{q}q\rangle. \tag{12}$$

Equating Eq. (10) to Eq. (12) and neglecting the difference $(m_H - M_D)$, we obtain the following matching condition:

$$3F_D^2\,\Delta M_D \simeq -2\langle\bar{q}q\rangle. \tag{13}$$

Thus at the matching scale, the splitting is

$$\Delta M_D \simeq -\frac{2}{3}\frac{\langle\bar{q}q\rangle}{F_D^2}. \tag{14}$$

As announced, the splitting is indeed proportional to the light-quark condensate. Let us denote the ΔM_D determined at the scale Λ as ΔM_{bare} which will figure in the numerical calculation.

Given the splitting ΔM_{bare} at the scale Λ, we need to decimate down to the physical scale. This amounts to making quantum corrections to the correlators written in terms of the bare quantities or more specifically to $\mathcal{L}_{\chi\text{SB}}$ in Eq. (5). This calculation turns out to be surprisingly simple for $a = 1$. For $a = 1$, ϕ_L does not mix with ϕ_R in the light sector, and hence ϕ_L couples to only $\mathcal{H}_L$ and ϕ_R to only $\mathcal{H}_R$. As a result $\mathcal{H}_{L(R)}$ cannot connect to $\mathcal{H}_{R(L)}$ by the exchange of ϕ_L or ϕ_R. Only the ρ-loop links between the fields with different chiralities as shown in Fig. 1.

This term contributes to the two-point function as

$$\Pi_{LR}\Big|_{\text{div}} = -\frac{1}{2}\Delta M\, C_2(N_f)\,\frac{g^2}{2\pi^2}\left(1-2k-k^2\right)\ln\Lambda, \tag{15}$$

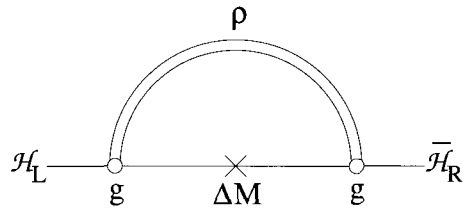

Figure 1. Diagram contributing to the mass difference.

where $C_2(N_f)$ is the second Casimir defined by $(T_a)_{ij}(T_a)_{jl} = C_2(N_f)\delta_{il}$ with i, j and l denoting the flavor indices of the light quarks. This divergence is renormalized by the bare contribution of the form $\Pi_{LR,\mathrm{bare}} = \frac{1}{2}\Delta M_{\mathrm{bare}}$. Thus the renormalization-group equation (RGE) takes the form

$$\mu\frac{d\,\Delta M}{d\mu} = C_2(N_f)\,\frac{g^2}{2\pi^2}\Big(1 - 2k - k^2\Big)\Delta M. \tag{16}$$

For simplicity, we may neglect the scale dependence in g and k. Then the solution to the RGE for ΔM is

$$\Delta M = \Delta M_{\mathrm{bare}}\exp\Big[-C_2(N_f)\,\frac{g^2}{2\pi^2}\Big(1 - 2k - k^2\Big)\ln\frac{\Lambda}{\mu}\Big]. \tag{17}$$

This is our main result. This shows unequivocally that the mass splitting is dictated by the *bare* splitting ΔM_{bare} proportional to $\langle\bar{q}q\rangle$ corrected by the quantum effect given by $C_{\mathrm{quantum}} = \exp\Big[-C_2(N_f)\,\frac{g^2}{2\pi^2}\Big(1 - 2k - k^2\Big)\ln\frac{\Lambda}{\mu}\Big]$.

4. Prediction

4.1. ΔM

In the chiral limit, one can make a neat prediction on the splitting ΔM. There are no free parameters here.

I shall not attempt any error analysis and merely quote the semi-quantitative estimate arrived at in [2]. The second Casimir for three flavors is $C_2(N_f = 3) = 4/3$; the constant k can be extracted from $D^* \to D\pi$ decay [16] and comes out to be $k \simeq 0.59$. By taking $\mu = m_\rho = 771\,\mathrm{MeV}$, $\Lambda = 1.1\,\mathrm{GeV}$ and $g = g(m_\rho) = 6.27$ determined through the Wilsonian matching [9], we find that the quantum effect increases the mass splitting by about 60%, i.e., $C_{\mathrm{quantum}} \approx 1.6$. It turns out [14] that this result is quite stable against the matching scale Λ. Taking the value for F_D, $F_D \simeq 0.205$ GeV, and that for $\langle\bar{q}q\rangle$, $\langle\bar{q}q\rangle = -(0.243\,\mathrm{GeV})^3$ from the literature [17] as

typical ones, we find from (14)

$$\Delta M_{\rm bare} \simeq 0.23 \text{ GeV} \tag{18}$$

so that

$$\Delta M \simeq 0.37 \text{ GeV}. \tag{19}$$

This should be compared with the constituent quark mass $\simeq m_N/3$ where m_N is the nucleon mass. This is consist with what was observed in the experiments [3,4]. Of course, in comparing with experiments, particularly the BaBar/CLEO experiments, we need to take into account the flavor symmetry breaking which is not yet systematically investigated in the framework discussed here. But the point is that it is the quark condensate that carries the main imprint of the splitting. Another point of interest in the result is that the bare splitting depends on the heavy-meson decay constant. This suggests that the splitting may show heavy-quark flavor dependence. This could be checked with experiments once a systematic heavy-quark expansion (which is not done here) is carried out.

4.2. *Implications*

There is an obvious implication on heavy-light baryons that can be obtained as skyrmions [19,20] from the heavy-light mesonic Lagrangian. One expects off-hand that the chiral doubling splitting in heavy-light baryons would also be given by the ρ-exchange graph and hence will likewise be proportional to the light-quark condensate. Another exciting avenue would be to look at pentaquarks as skyrmions in this HLS/VM-implemented theory with a heavy quark replacing the strange quark in the recently observed Θ^+ baryon which is generating lots of activities nowadays. It would be interesting to expose the contribution to the heavy penaquark mass that bears directly on chiral symmetry as in the heavy-light mesons.

Suppose future experiments do show that in hot/dense matter, the splitting in heavy-light mesons or baryons gets reduced as temperature/density goes up in such a way as to be consistent with the vanishing splitting at the critical point in the chiral limit. An attractive interpretation of such an observation is that one is realizing the VM at $[pt]_\chi$, and hence the ρ meson mass does go to zero at the phase transition as predicted in a different context a long time ago [18]. Furthermore a recent striking development [11] on the phase structure of hot matter near T_c suggests that massive excitations in the ρ channel above T_c in the form of an instanton liquid go massless at

T_c as do the pion and the scalar σ. Lattice confirmation of this phenomenon would be highly desirable.

5. Concluding Remarks

This is a "concluding" talk in more than one sense. It is the last talk in this Symposium and is also most likely the last talk in this series of astro-hadron physics I have been helping develop in KIAS. So let me add a few of my personal remarks here.

In early 1990's, with a small group of young – as well as less young – theorists in hadronic physics in Korea I initiated a concerted effort to understand how hadronic physics involved in the strong interactions of matter can be merged into certain aspect of astrophysical phenomena that are thought to be produced under extreme conditions of temperature and/or density, a new field of research which we called "astro-hadron physics." The first international meeting in Korea bearing that name – funded by APCTP – was held at Seoul National University in 1997. With the advent of Korea Institute for Advanced Study (KIAS) originally conceived with the primary purpose of generating and developing original, innovative research activities in Korea that could be brought to the forefront of the world, the activity in astro-hadron physics was taken up at KIAS in the precise spirit of the institute's objective. With the influx of a large number of bright visitors from abroad, the activity has met with success. This then led to the first KIAS astrophysics meeting in 2000 in which astro-hadron physics figured importantly in bringing together such explosive astrophysical processes as supernovae, gamma-ray burst, black-hole formations with such explosive laboratory processes as relativistic heavy-ion collisions. The so-called hadronic phase diagram shown at this meeting was quite barren with most of the areas unexplored or empty, with little overlap between what the astronomers were observing and what the laboratory experimenters were measuring. Since then, the phase map has rapidly filled up, as we witnessed in this meeting, with measurements coming from various terrestrial laboratories (CERN, RHIC...) and from satellite observatories (Chandra, RXTE ...). This meeting is clearly a timely one to start establishing crucial connections between the two sources and synthesizing a coherent picture that will ultimately expose the structure of the novel form of matter searched for in extreme conditions of temperature and/or density.

Although this may be – at least for the time being – the last meeting of the series here at KIAS, the activity in this field should, and surely will, go

on, if not here, then elsewhere in this country. With the advent of JPARC in Japan in tandem with that of SIS 300 at GSI in Germany together with forthcoming satellite observatories, this field is poised to develop strongly in this Asian Pacific area. It would be a pity if Korea with her early start were to miss out in this exciting new development. What I discussed in my talk together with the discovery of the novel structure in pentaquark systems promise clearly that there will be surprises and breakthroughs in store in this field.

Acknowledgments

I would like to thank Masayasu Harada, Maciek Nowak, Chihiro Sasaki and Ismail Zahed for most enjoyable collaborations on which my talk was based.

References

1. M.A. Nowak, M. Rho and I. Zahed, *Phys. Rev.* **D48**, 4370 (1992) [arXiv:hep-ph/9209272].
2. M. Harada, M. Rho and C. Sasaki, "Chiral doubling of heavy-light hadrons and the vector manifestation of hidden local symmetry," arXiv:hep-ph/0312182.
3. BABAR Collaboration, B. Aubert et al., *Phys. Rev. Lett.* **90**, 242001 (2003) [arXiV:hep-ex/0304021].
4. CLEO Collaboration, D. Besson et al., *Phys. Rev.* **D68**, 032002 (2003) [arXiv:hep-ex/0305100].
5. BELLE Coll., P. Krokovny et al., *Phys. Rev. Lett.* **91**, 262002 (2003) [arXiv:hep-ex/0308019].
6. M.A. Nowak, "Chiral doublings of heavy-light hadrons: New charmed mesons discovered by BABAR, CLEO and BELLE," hep-ph/0311154.
7. W.A. Bardeen and C. T. Hill, *Phys. Rev.* **D49**, 409 (1994) [arXiv:hep-ph/9304265].
8. M. A. Nowak, M. Rho and I. Zahed, "Chiral doubling of heavy-light hadrons: BaBar 2317-MeV/c^2 and CLEO 2463-MeV/c^2 discoveries," arXiv:hep-ph/0307102.
9. See for review M. Harada and K. Yamawaki, *Phys. Rept.* **381**, 1 (2003) [arXiv:hep-ph/0302103].
10. See, e.g., N. Arkani-Hamed, H. Gerogi and M.D. Schwartz, *Ann. Phys.* **305**, 96 (2003) [arXiv:hep-th/0210184].
11. G.E. Brown, C.-H. Lee and M. Rho, "Chemical equilibration in relativistic heavy ion collisions," to appear.
12. M. Harada, Y. Kim, M. Rho and C. Sasaki , *Nucl.Phys.* **A730**, 379 (2004) [arXiv:hep-ph/0308237].
13. D. T. Son and Stephanov, *Phys. Rev.* **D66**, 070611 (2002).
14. M. Harada, M. Rho and C. Sasaki, in preparation.

15. S. Narison, *Phys. Lett.* **B210**, 238 (1988).
16. K. Hagiwara *et al.* [Particle Data Group Collaboration], *Phys. Rev.* D **66**, 010001 (2002).
17. S. Narison, hep-ph/0307248.
18. G. E. Brown and M. Rho, *Phys. Rev. Lett.* **66**, 2720 (1991).
19. M. Rho, D.O. Riska and N.N. Scoccola, *Z. Phys.* **A341**, 343 (1992).
20. E. Jenkins, A.V. Manohar and M.B. Wise, *Nucl. Phys.* **B396**, 27 (1993).

EFFECTIVE LAGRANGIANS FOR QCD: DECONFINEMENT AND CHIRAL SYMMETRY RESTORATION

ÁGNES MÓCSY

Institut für Theoretische Physik, J.W. Goethe-Universität, Postfach 11 19 32 60054 Frankfurt am Main, Germany
E-mail: mocsy@th.physik.uni-frankfurt.de

FRANCESCO SANNINO*

NORDITA & The Niels Bohr Institute, Blegdamsvej 17 2100 Copenhagen O, Denmark
* *Speaker at the conference.*
E-mail: francesco.sannino@nbi.dk

KIMMO TUOMINEN

University of Jyväskylä, Department of Physics, P.O. Box 35, 40014 Jyväskylän Yliopisto, Finland
E-mail: kimmo.tuominen@phys.jyu.fi

Effective Lagrangians for Quantum Chromodynamics (QCD) especially suited for understanding deconfinement and chiral symmetry restoration at non-zero temperature and matter density are reviewed. These effective theories allow one to study generic properties of phase transitions using non-order parameter fields without loosing the information encoded in the true order parameter. For the pure gauge theory we demonstrate that near the deconfining phase transition the center group symmetry is naturally linked to the conformal anomaly. Another relevant outcome is that when the theory contains also quarks we can explain the intertwining of chiral symmetry restoration and deconfinement for QCD with matter fields either in the fundamental or in the adjoint representation of the gauge group. As a test of our general approach we show that our results are applicable also at non-zero baryon chemical potential. We also predict new testable substructures to be present in the phase diagram of quarks in the adjoint representation of the gauge group. Here we provide some new insights on the large N limit of gauge theories by investigating the hadronic world. We propose that the world of infinite N should already be well described when $N = 6$ for QCD with two and three light flavors. Finally, we suggest possible future applications of our results for heavy ion collisions.

1. Introduction

Symmetries, anomalous and exact, are used to constrain effective Lagrangian theories . The latter are applicable to any region of Quantum Chromodynamics (QCD) or QCD-like phase diagram, whenever the relevant degrees of freedom and the associated symmetries are known. To decide in which phase a strongly interacting theory can be one uses experimental inputs, model computations, such as Nambu-Jona Lasinio model, and/or computer simulations. Exact non-perturbative constraints, like anomaly matching conditions, are another elegant and powerful way to help deciding among the phases that a strongly interacting theory (vector- and chiral-like) can be in. The original idea of t'Hooft has been extended [1,2,3] to strongly interacting gauge theories at non-zero chemical potential.

A number of novel effective Lagrangians have been used in the literature to describe QCD and similar theories at zero temperature (see [4] for a review). At zero temperature and quark chemical potential some non-perturbative quantitative predictions about the spectrum and the vacuum properties of QCD with one Dirac flavor have been made through an effective Lagrangian able to interpolate from super Yang-Mills to QCD [5]. These predictions can be tested via lattice simulations. These results are also linked to a different type of $1/N$ expansion around the supersymmetric limit [6], in which the fermions transform according to the two index anti-symmetric representation of the gauge group. This expansion in the inverse number of colors may very well be more convergent then the ordinary $1/N$ expansion. Here fermions remain in the fundamental representation of the gauge group, while increasing the number of colors. In [7] the existence of a critical number of colors has been identified. For and above this number of colors the low energy $\pi - \pi$ scattering amplitude, computed from the sum of the current algebra and vector meson terms, is crossing symmetric and unitary at leading order in a $1/N$ expansion. This critical number of colors is $N = 6$, and is insensitive to the explicit breaking of chiral symmetry, meaning that ordinary $1/N$ corrections for the real world are large. These results are supported by the findings in [8]. As an important outcome, our results are consistent with the expectation that the low lying sigma state, $\sigma(560)$, is not a $q\bar{q}$ object [9,10,11,12]. Its implications are on the physics of chiral symmetry restoration, since this state should not be considered as the chiral partner of the pion, as it is at times assumed in literature. While we expect large $1/N$ corrections for $N = 3$, for six or more colors and with two or three flavors the physics should be well described by the

large number of colors limit, for which a number of properties can be diagrammatically deduced [13]. $SU(6)$ gauge theories are currently explored by lattice simulations [14]. Encouraged by the findings in the hadronic world [7,8,11], we predict a transition from the world of infinite N to the world of small N already for $N = 6$ with two flavors, and possibly with three flavors as well. Some ideas on $N =$ infinity at non-zero temperature are also available [15].

Deconfinement and chiral symmetry restoration at finite temperature, quark chemical potential or number of flavors has attracted much interest [16,21,18]. Here we discuss recently developed effective Lagrangians for QCD, relevant for gaining insight on the deconfinement and/or chiral symmetry restoration problem at non-zero temperature and matter density. Our goal is to provide a unifying point of view in which different models can be seen as different description of the same physics.

We first consider the effective theory unifying two apparently very different sectors of a Yang-Mills theory at non-zero temperature [19]: the hadronic sector and the Polyakov loop. This theory is able to communicate the information about the center group symmetry to the hadronic states. It also provides the link between deconfinement and conformal anomaly. Then, discussion of effective Lagrangians for strongly interacting theories with matter fields will follow. Via these theories we offer a simple interpretation for the intertwining between chiral symmetry restoration and deconfinement in QCD with matter fields in the fundamental and in the adjoint representation of the gauge group, as function of temperature and/or chemical potential. We also show that the most relevant term is a trilinear interaction between the singlet field and the order parameter. This term differentiates between different fermion representations, and it has been neglected previously in the literature [20,21,22]. Finally, we suggest possible applications.

2. Heavy Fields and Phase Transitions

Phase transition dynamics and the associated critical behavior are best investigated using order parameters. These are the degrees of freedom whose correlation length diverges when approaching the phase transition. However, the choice of the order parameters is not always obvious. Furthermore, even if the order parameter can be formally constructed, often this may be hard, or even impossible to be detected directly experimentally. A time honored example is the Polyakov loop in gauge theories. A true order parameter is zero in the symmetric phase, and has a finite value in the

symmetry broken phase. In what follows we term order parameter field a field whose expectation value is a true order parameter. Any field whose expectation value does not have this kind of behavior we call non-order parameter field. We consider non-order parameter fields which are singlets under the symmetry transformation acting on the order parameter.

One can ask some simple questions: Given a system consisting of an order parameter and singlet field(s), what can we learn about the phase transition by monitoring the singlet field? Can we identify the onset of the phase transition without referring to the order parameter? We show here that there is a clear and universal characteristic behavior of the singlet field, induced by the order parameter close to the phase transition. Our considerations are universal, and as such, can be carried over to virtually any phase transition once the symmetries of the order parameter are identified. We explicitly consider the cases of Z_2 symmetry, which is of relevance for the pure Yang–Mills gauge theory with two colors, and $SU(4)$, which is of relevance for the effective theories of two color QCD with two quark flavors in either the fundamental or adjoint representation of the gauge group.

Lattice simulations of the pure Yang-Mills gauge theory [27,37,38] already confirm our prediction.

For QCD with quarks lattice simulations pose the following interesting puzzle: Why, for matter in the fundamental representation deconfinement and chiral symmetry restoration appear to be linked with a single phase transition observed at a given critical temperature, while for matter in the adjoint representation there are two phase transitions, well separated in temperature? Our effective Lagrangian description can offer a simple unifying way of addressing this puzzle.

3. From the Polyakov Loop to the Glueballs

At non-zero temperature the pure $SU(N)$ Yang-Mills theory possesses a global Z_N symmetry. This symmetry is intact at low temperatures and is broken at high temperatures. The associated order parameter is the Polyakov loop, which is the trace of the thermal Wilson line. Under the action of Z_N the Polyakov loop transforms as $\ell \to z\ell$ with $z \in Z_N$.

The condensation of Polyakov loops is associated to deconfinement, since the potential $V(\vec{x}, T)$ at a given temperature T between static fundamental charges is related to the Polyakov loop:

$$\exp(-V(\vec{x}, T)/T) \equiv \langle \ell(\vec{0})\ell^\dagger(\vec{x})\rangle \underset{|\vec{x}|\to\infty}{\longrightarrow} |\ell|^2 \quad ,$$

For $T < T_c$ the static quarks experience a linearly rising potential

$$V(\vec{x}, T) = \sigma(T) \, |x| \, , \tag{1}$$

where $\sigma(T)$ is the string tension. For $T > T_c$ the potential is no longer a confining one:

$$V(\vec{x}, T) \propto k(T) \, , \tag{2}$$

and it does not depend on the distance between the static sources.

Close to T_c, using age-old arguments by Landau, the mean field effective potential is

$$V(\ell) = T^4 \mathcal{F}(\ell) \, , \tag{3}$$

where $\mathcal{F}(\ell)$ is a Z_N-invariant polynomial in ℓ . It was Svetitsky and Yaffe [23,24,25] who provided the first reliable non-perturbative study of the critical behavior of Yang-Mills theories, as well as the above form for the effective potential. The idea of describing the Yang-Mills pressure using directly a mean field theory of Polyakov loops has been recently advocated by Pisarski [26]. This model has since been used in several phenomenological studies [20,21]. The scale dimension is set by the temperature. Physical states (i.e. hadrons), however, do not carry any charge under Z_N . In order for a hadronic state to know about the center group symmetry this must communicate with the Polyakov loop.

In the following, we consider as representative of the hadronic spectrum the lightest scalar glueball. At zero temperature a well known effective theory constrained by the trace anomaly has been constructed in [30], using the potential of the form

$$H \ln \frac{H}{\Lambda^4} \, . \tag{4}$$

The glueball field H is related to $G^a_{\mu\nu} \, G^{\mu\nu,a}$, where $G^{\mu\nu,a}$ is the gluon field strength and $a = 1, \ldots, N^2 - 1$ the gauge indices. This potential encodes the basic properties of the Yang–Mills vacuum at $T = 0$ [31], and has also been used at non-zero density [32] and temperature [33,34]. As we increase the temperature the Polyakov loop becomes a well defined object. We stress that previously in the literature the Yang-Mills pressure has been described by either glueball theories [33] and their generalizations [35], or directly with the Polyakov loop model [20]. In effective glueball theories a possible drop at T_c of the *non-perturbative* contribution to the gluon condensate has been often considered as an indication of deconfinement [33,32]. However, since the gluon condensate is not an order parameter for the center group symmetry

there is, a priori, no guarantee that such a drop, even if observed, should appear at the same critical temperature. Furthermore, the glueball theory by construction is blind to the number of colors. This explains why it always predicts a first order phase transition independent of the number of colors of the underlying Yang-Mills theory one wants to describe [21]. The Polyakov model, on the other hand, has automatically built in the knowledge about the number of colors, but looses contact with a simple physical picture in terms of hadronic states.

We will now show, by marrying these two theories, that: i) The drop of the non-perturbative part of the gluon condensate *must* happen exactly at the deconfining phase transition [19], partially justifying glueball models; ii) Information about the order of the transition is now encoded in a nontrivial way in the profile of the condensate drop.

We constructed the following general potential using all of the relevant symmetries, i.e. trace anomaly, Z_N invariance, and analyticity of the interaction term between the glueball field and the Polyakov loop[19]

$$V(\ell, H) = H \ln \frac{H}{\Lambda^4} + V_T(H) + H\mathcal{P}(\ell) + T^4\mathcal{F}(\ell)\,. \tag{5}$$

$V_T(H)$ is the intrinsic temperature dependence of the glueball gas. This we can neglect, since the glueball is heavy near the phase transition. The most general interaction term compatible with the saturation of the trace anomaly is $H\mathcal{P}(\ell)$, where $\mathcal{P}(\ell)$ is a Z_N symmetric polynomial in ℓ . In the static limit we can use the equation of motion for the H field to integrate this out in terms of ℓ field, yielding the functional relation $H \equiv H(\ell)$. This shows that the center group symmetry is transferred to the singlet sector of the theory. However, we find it more illuminating to keep both fields. For two colors we take

$$\begin{aligned}\mathcal{F}(\ell) &= a_1\ell^2 + a_2\ell^4 + \mathcal{O}(\ell^6)\,,\\ \mathcal{P}(\ell) &= b_1\ell^2 + \mathcal{O}(\ell^4)\,.\end{aligned}$$

The coefficients a_2 and b_1 are assumed to be positive and independent of the temperature, while $a_1(T) = \alpha(T - T_*)$, with $\alpha > 0$. Solving for the minimum, one finds that below T_c the two fields are completely decoupled and

$$\langle \ell \rangle = 0, \quad \langle H \rangle = \Lambda^4/e\,. \tag{6}$$

As the critical temperature $T_c = T_* + \frac{b_1}{e\alpha}\frac{\Lambda^4}{T_c^3}$ is reached, the symmetry is spontaneously broken, and the Polyakov loop obtains a non-zero

expectation value, which affects also the one for H:

$$\langle \ell \rangle \propto \frac{\Delta T}{T_c}, \quad \langle H \rangle = \frac{\Lambda^4}{e} \exp\left[-2b_1 \langle \ell \rangle^2\right] . \tag{7}$$

For three colors the essential modification is the inclusion of the ℓ^3 and ℓ^{*3} terms into the Polyakov loop potential $\mathcal{F}$. The interaction potential becomes $\mathcal{P} \propto |\ell|^2$. Cubic terms render the transition first order, and thus the change in both the Polyakov loop and the glueball becomes discontinuous. Once more we deduce that the change in the order parameter ℓ induces a change in the expectation value of the non-order parameter field. The behavior in these two cases is shown in figure 1. In conclusion, not only

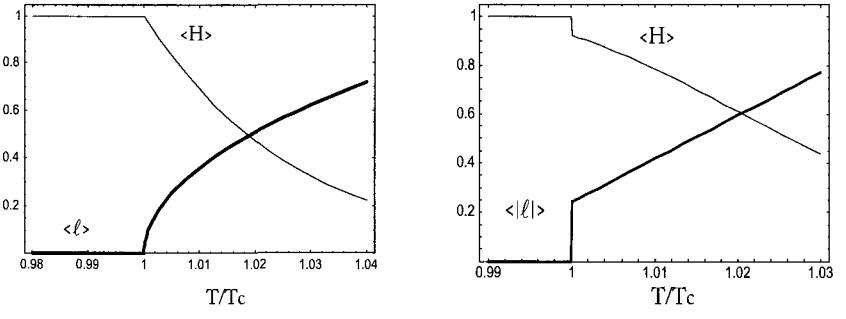

Figure 1. Expectation values of the fields as function of temperature. Left panel: two color theory (2nd order transition). Right panel: three color theory (1st order transition).

the drop of the non-perturbative part of the gluon condensate knows about the Yang-Mills phase transition, but also that the drop occurs at T_c . Furthermore, the profile of the gluon condensate as function of temperature encodes the information on the order of the phase transition. With this theory we unified two apparently very different pictures of the deconfining phase transition.

4. Chiral Symmetry versus Confinement

Consider now adding quarks into the Yang-Mills theory. Lattice results for quarks in the fundamental representation of the gauge group [39] indicate that as chiral symmetry is restored, the expectation value of the Polyakov loop rises, signalling deconfinement. Figure 2 illustrates that the critical

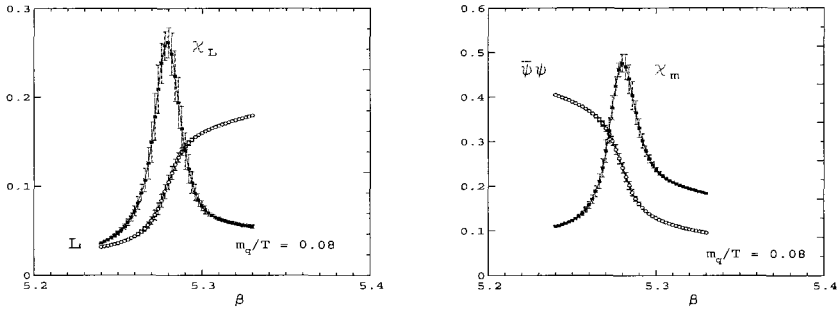

Figure 2. The Polyakov loop (left panel) and the chiral condensate (right panel), with the corresponding susceptibilities, as determined on the lattice with quarks in the fundamental representation. From [39].

temperature[a] of deconfinement and of chiral symmetry restoration coincide, $T_{\rm chiral} = T_{\rm deconf}$. We further learn from lattice that for quarks in the adjoint representation this is not the case, as shown in Fig. 3 taken from [40]. Here $T_{\rm chiral} \simeq 8T_{\rm deconf}$. Note, that even if the two transitions happen

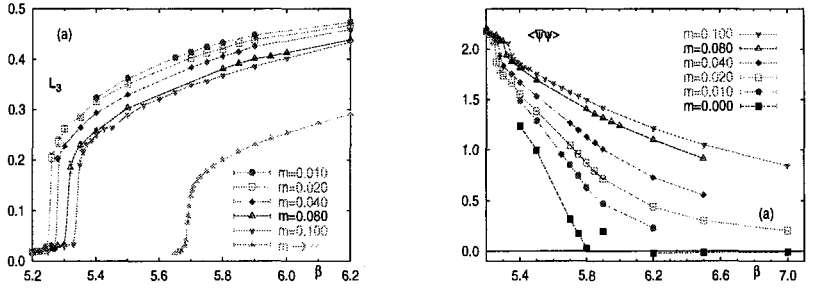

Figure 3. Behavior of the Polyakov loop (left panel) and of the chiral condensate (right panel) as determined on the lattice with quarks in the adjoint representation. From [40].

separately, the chiral condensate knows about deconfinement, as the jump in its behavior at $T_{\rm deconf}$ indicates.

Lattice simulations are already available for two color QCD at nonzero baryon chemical potential [41], and observe deconfinement for 2 color QCD and 8 continuum flavors at $\mu \neq 0$. Figure 4 illustrates the rise

[a]The (pseudo) critical temperatures are identified from the peak position of the corresponding susceptibilities, also shown in figure 2.

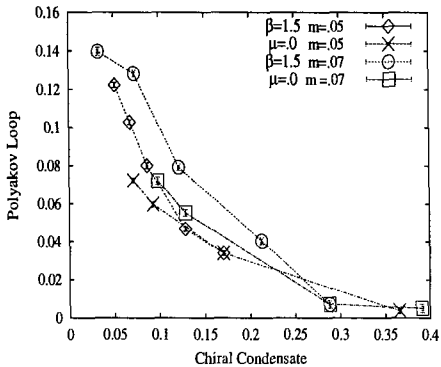

Figure 4. Polyakov loop versus chiral condensate for two color QCD and 8 continuum flavors at non-zero baryon chemical potential as determined on the lattice. From [41].

in the Polyakov loop when the chiral condensate vanishes. The two phase transitions happen at the same value of the chemical potential, $\mu_{\rm chiral} = \mu_d$.

Our goal is to provide a simple unified way to describe all of these features. This is possible thanks to a crucial interaction term [27,28,29], which has been neglected in previous phenomenological investigations [20,21,22].

The quark representation with respect to the gauge group is significant [42]. When quarks are in the fundamental representation the Z_N symmetry is not exact for any finite value of the quark mass. When, on the other hand, quarks are in the adjoint representation of the gauge group the center group symmetry is intact. Chiral symmetry is also explicitly broken by the quark mass. In the non-perturbative regime we do not know the amount of Z_N breaking (unless a fit to lattice data [43] is performed [44]). Thus, we cannot establish which symmetry is more broken for a given quark mass. Fortunately, at least theoretically, we can take limits in the QCD parameter space, allowing for exact statements, independent of the lattice results. When chiral symmetry is exact, i.e. quark masses are zero, for any number of flavors and colors, Z_N is not a symmetry and the only order parameter is the chiral condensate ($\bar{q}q \sim \sigma$). We demonstrate, that due to the presence of a relevant Z_N symmetry breaking term the Polyakov loop[b] has an induced critical behavior driven by the chiral transition. This term is the most relevant term differentiating among fermion representations. We expect

[b] χ is the canonically normalized field associated with the Polyakov loop. The subscript χ refers to the Polyakov loop, not to chiral symmetry. These have the subscript σ.

that its inclusion drastically affects phenomenological predictions [20,21], and their implications for heavy ion collision experiments.

If Z_N symmetry is only softly broken one might expect another transition for deconfinement [45,46,47]. The main motivation for having advocated, in the past, two independent phase transitions is related to the possibility of two independent scales in QCD: one associated to chiral symmetry breaking and the other associated to deconfinement. As explained above, lattice results now dismiss this possibility. If quark masses are smaller than the confining scale of the theory and barring *accidental* dynamical suppression we expect that by comparing the ratios

$$m_{\rm q}/\Lambda \quad \text{for chiral breaking} \quad \text{and} \quad N_f/N \quad \text{for } \mathrm{Z_N} \text{ breaking},$$

we can have a rough estimate of which symmetry is more broken. For chiral symmetry one could use also $m_\pi/4\pi F_\pi$. We expect the Z_N breaking term to be a more complicated function of number of flavors, colors and quark masses $f(N_f, N_c, m_{\rm q}/\Lambda)$. A two phase transitions scenario is still possible in QCD with fixed number of flavors of massless quarks, in the limit of large number of colors, $N_f/N \ll 1$. This is unnatural for $N_f \sim N$.

We now study the two color theory with N_f flavors in the chiral limit. The rational behind this choice is that at the same time, with minor modification of the effective Lagrangian, we can discuss the fundamental and adjoint representations at non-zero temperature or quark chemical potential. The generalization to three colors is straightforward at non-zero temperature, while a bit more involved for the quark chemical potential.

4.1. *Fundamental Representation*

The global symmetry group for two colors is $SU(2N_f)$. After chiral symmetry breaking has occurred, $SU(2N_f) \to Sp(2N_f)$, the degrees of freedom in the chiral sector of the effective theory are $2N_f^2 - N_f - 1$ Goldstone fields π^a , and a scalar field σ. For $N_f = 2$ the potential is [48,49]:

$$V_{\rm ch}[\sigma, \pi^a] = \frac{m^2}{2}\mathrm{Tr}\left[M^\dagger M\right] + \lambda_1 \mathrm{Tr}\left[M^\dagger M\right]^2 + \frac{\lambda_2}{4}\mathrm{Tr}\left[M^\dagger M M^\dagger M\right] \quad (8)$$

with $2\,M = \sigma + i\,2\sqrt{2}\pi^a\,X^a$, $a = 1, \ldots, 5$ and $X^a \in \mathcal{A}(SU(4)) - \mathcal{A}(Sp(4))$. The generators X^a are given by equations (A.5) and (A.6) of [48]. The Polyakov loop χ is now a heavy field, singlet under chiral symmetry. Its contribution to the potential in the absence of the Z_2 symmetry is

$$V_\chi[\chi] = g_0\chi + \frac{m_\chi^2}{2}\chi^2 + \frac{g_3}{3}\chi^3 + \frac{g_4}{4}\chi^4 . \quad (9)$$

To complete the effective theory we introduce interaction terms allowed by chiral symmetry

$$V_{\rm int}[\chi,\sigma,\pi^a] = \left(g_1\chi + g_2\chi^2\right) {\rm Tr}\left[M^\dagger M\right] = \left(g_1\chi + g_2\chi^2\right)\left(\sigma^2 + \pi^a\pi^a\right) . \tag{10}$$

The g_1 term plays a fundamental role. This is the term we previously emphasized. For $T < T_{c\sigma}$ chiral symmetry is spontaneously broken, the σ acquires a non-zero expectation value (adopt usual $\langle\pi\rangle = 0$), which in turn induces a change in $\langle\chi\rangle$. The extremum of the linearized potential is at

$$\langle\sigma\rangle^2 \simeq -\frac{m_\sigma^2}{\lambda} , \qquad m_\sigma^2 \simeq m^2 + 2g_1\langle\chi\rangle, \tag{11}$$

$$\langle\chi\rangle \simeq \chi_0 - \frac{g_1}{m_\chi^2}\langle\sigma\rangle^2 , \quad \chi_0 \simeq -\frac{g_0}{m_\chi^2} , \tag{12}$$

where $\lambda = \lambda_1 + \lambda_2$. Equation (12) hold near the phase transition, where σ is small. m_σ^2 is the full coefficient of the σ^2 term in the tree-level Lagrangian which, due to the coupling between χ and σ, also depends on $\langle\chi\rangle$. Spontaneous chiral symmetry breaking appears for $m_\sigma^2 < 0$. In this regime the positive mass squared is $M_\sigma^2 = 2\lambda\langle\sigma^2\rangle$. Near $T_{\rm c}$ the mass of the order parameter field is assumed to posses the generic behavior $m_\sigma^2 \sim (T - T_{\rm c})^\nu$. Equation (12) shows that for $g_1 > 0$ and $g_0 < 0$ the expectation value of χ behaves oppositely to that of σ : As the chiral condensate starts to decrease towards chiral symmetry restoration, the expectation value of the Polyakov loop starts to increase, signaling the onset of deconfinement. This is illustrated in the left panel of figure 5. When applying the analysis presented in [27,28], the general behavior of the spatial two-point correlator of the Polyakov loop can be determined. Near the transition point, in the broken phase, the χ two-point function is dominated by the infrared divergent σ-loop. We find a drop in the screening mass of the Polyakov loop at the phase transition. When approaching the transition from the unbroken phase we find again a drop in the screening mass of the Polyakov loop (this is actually the string tension) close to the phase transition. We deduce for this drop, the variation of the χ mass with respect to the tree level mass, $\Delta m_\chi^2(T) = m_\chi^2(T) - m_\chi^2$, using a large N framework motivated resummation [28]:

$$\Delta m_\chi^2(T) = -\frac{2g_1^2(1+N_\pi)}{8\pi\, m_\sigma + (1+N_\pi)3\lambda} , \quad T > T_{c\sigma} \tag{13}$$

$$\Delta m_\chi^2(T) = -\frac{2g_1^2}{8\pi\, M_\sigma + 3\lambda} , \qquad T < T_{c\sigma} . \tag{14}$$

From the above equations one finds that the screening mass of the Polyakov loop is continuous and finite at $T_{c\sigma}$, and $\Delta m_\chi^2(T_{c\sigma}) = -2g_1^2/(3\lambda)$, independent of N_π , the number of pions. Please find a detailed discussion regarding the necessity for and distinction between different resummation schemes in [28]. We emphasize that this analysis is not restricted to the chiral/deconfining transition. The entanglement between the order parameter and the non-order parameter field is universal.

4.2. *Adjoint Representation*

Consider now two color QCD with two massless Dirac quark flavors in the adjoint representation. Here the global symmetry is $SU(2N_f)$ which breaks via a bilinear quark condensate to $O(2N_f)$. The number of Goldstone bosons is $2N_f^2 + N_f - 1$. We take $N_f = 2$. There are two exact order parameter fields: the chiral σ field and the Polyakov loop χ . Since the relevant interaction term $g_1\chi\sigma^2$ is now forbidden, one might expect no efficient information transfer between the fields. While respecting general expectations the following analysis suggests the presence of a new and more elaborated structure which future lattice data can clarify. The chiral part of the potential is given by (8) with $2\,M = \sigma + i\,2\sqrt{2}\pi^a\,X^a$, $a = 1, \ldots, 9$ and $X^a \in \mathcal{A}(SU(4)) - \mathcal{A}(O(4))$. X^a are the generators provided explicitly in equations (A.3) and (A.5) of [48]. The now Z_2 symmetric potential for the Polyakov loop is

$$V_\chi[\chi] = \frac{m_{0\chi}^2}{2}\chi^2 + \frac{g_4}{4}\chi^4\,, \tag{15}$$

and the only interaction term allowed by symmetries is

$$V_{\rm int}[\chi, \sigma, \pi] = g_2\chi^2\,{\rm Tr}\left[M^\dagger M\right] = g_2\chi^2(\sigma^2 + \pi^a\pi^a)\,. \tag{16}$$

The effective Lagrangian does not know which transition happens first, but this is irrelevant for the validity of our general results. Consider the physical case in which deconfinement happens first, $T_{c\chi} < T < T_{c\sigma}$ both symmetries are broken, and the expectation values of the two order parameter fields are linked to each other:

$$\begin{aligned}
\langle\sigma\rangle^2 &= -\frac{1}{\lambda}\left(m^2 + 2g_2\langle\chi\rangle^2\right) \equiv -\frac{m_\sigma^2}{\lambda}\,,\\
\langle\chi\rangle^2 &= -\frac{1}{g_4}\left(m_{0\chi}^2 + 2g_2\langle\sigma\rangle^2\right) \equiv -\frac{m_\chi^2}{g_4}\,.
\end{aligned} \tag{17}$$

The coupling g_2 is taken to be positive. In the neighborhood of the two transitions, $T_{c\chi}$ and $T_{c\sigma}$, we find the qualitative situation illustrated in

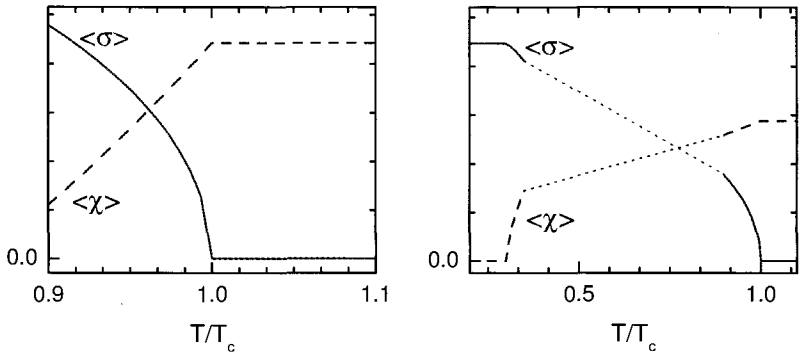

Figure 5. Left panel: Expectation values of the Polyakov loop and chiral condensate close to the chiral phase transition as a function of temperature, with massless quarks in the fundamental representation. Right panel: Same as in left panel, for massless quarks in the adjoint representation and $T_{c\chi} \ll T_{c\sigma}$ (see discussion in the text).

the right panel of figure 5. On both sides of $T_{c\chi}$ the relevant interaction term $g_2\langle\sigma\rangle\sigma\chi^2$ emerges, leading to a one-loop contribution to the static two-point function of the σ field $\propto \langle\sigma\rangle^2/m_\chi$. Near the deconfinement transition $m_\chi \to 0$ yielding an infrared sensitive screening mass for σ. Similarly, on both sides of $T_{c\sigma}$ the interaction term $\langle\chi\rangle\chi\sigma^2$ is generated, leading to the infrared sensitive contribution $\propto \langle\chi\rangle^2/m_\sigma$ to the χ two-point function. We conclude, that when $T_{c\chi} \ll T_{c\sigma}$, the two order parameter fields, a priori unrelated, do feel each other near the respective phase transitions. We thus predict the existence of substructures near these transitions, when considering fermions in the adjoint representation. Searching for such hidden behaviors in lattice simulations would help to further understand the nature of phase transitions in QCD.

The analysis can be extended for phase transitions driven by a chemical potential. In fact, for two color QCD this is straightforward. When considering fermions in the pseudoreal representation there is a phase transition from a quark-antiquark condensate to a diquark condensate [50]. We hence predict, in two color QCD, that when diquarks form for $\mu = m_\pi$, the Polyakov loop feels the presence of the phase transition exactly in the same manner as it feels when considering the temperature driven phase transition. Such a situation is supported by recent lattice simulations [41].

5. Conclusions and Outlook

We have shown how deconfinement (i.e. a rise in the Polyakov loop) is a consequence of chiral symmetry restoration in the presence of massless fermions in the fundamental presentation. In nature quarks have small, but non-zero masses, which makes chiral symmetry only approximate. Nevertheless, the picture presented here still holds: confinement is driven by the dynamics of the chiral transition in the chiral limit. The argument can be extended even further: If quark masses were very large then chiral symmetry would be badly broken, and could not be used to characterize the phase transition. But in such a case the Z_2 symmetry becomes more exact, and by reversing the roles of the protagonists in the previous discussion, we would find that the Z_2 breaking drives the (approximate) restoration of chiral symmetry. Which of the underlying symmetries demands and which amends can be determined directly from the critical behavior of the spatial correlators of hadrons or of the Polyakov loop [27,28]. With quarks in the adjoint representation we investigated the physical scenario in which chiral symmetry is restored after deconfinement sets in. In this case we have pointed to the existence of an interesting structure: There are still two distinct phase transitions, but since the fields are now entangled, the transitions are not independent. This entanglement is shown at the level of expectation values and spatial correlators of the fields. More specifically, the spatial correlator of the field which is not at its critical temperature will in any case feel the phase transition measured by the other field. Lattice simulations will play an important role in checking these predictions. The results presented here are not limited to describing the chiral/deconfining phase transition and can readily be used to understand phase transitions sharing similar features. Furthermore, the effective Lagrangians presented here can be immediately used, following [20,21], to study the physics at RHIC. We expect the new trilinear term [28], essential for our understanding of the relation between confinement and chiral symmetry breaking [29], to play a role also for the physics of heavy ion collisions.

Acknowledgments

We thank P. Damgaard, A. Jackson, J. Kapusta, J. Schechter and B. Tomasik for discussions and careful reading of the manuscript. We thank P. Petreczky and R. Pisarski for insightful discussions. F.S. thanks the organizers for having arranged such an interesting and stimulating conference.

References

1. F. Sannino, Phys. Lett. B **480**, 280 (2000) [arXiv:hep-ph/0002277].
2. S. D. H. Hsu, F. Sannino and M. Schwetz, Mod. Phys. Lett. A **16**, 1871 (2001) [arXiv:hep-ph/0006059].
3. F. Sannino, "Anomaly matching and low energy theories at high matter density," Proceedings for the conference on the Electroweak and Strong Matter, Heidelberg, 2001. arXiv:hep-ph/0301035.
4. F. Sannino, *Effective Lagrangians for QCD, Duality and Exact Results* arXiv:hep-ph/0312375.
5. F. Sannino and M. Shifman, *Effective Lagrangians for orientifold theories*, arXiv:hep-th/0309252.
6. A. Armoni, M. Shifman and G. Veneziano, Phys. Rev. Lett. **91**, 191601 (2003) [arXiv:hep-th/0307097].
7. M. Harada, F. Sannino and J. Schechter, arXiv:hep-ph/0309206. See also references therein related to the σ particle.
8. M. Uehara, arXiv:hep-ph/0401037.
9. R. L. Jaffe, Phys. Rev. D **15**, 267 (1977).
10. D. Black, A. H. Fariborz, F. Sannino and J. Schechter, Phys. Rev. D **59**, 074026 (1999) [arXiv:hep-ph/9808415].
11. J. R. Pelaez, arXiv:hep-ph/0309292.
12. M. Uehara, arXiv:hep-ph/0308241.
13. E. Witten, Nucl. Phys. B **160**, 57 (1979).
14. B. Lucini, M. Teper and U. Wenger, arXiv:hep-lat/0309170.
15. R. D. Pisarski and M. Tytgat, arXiv:hep-ph/9702340.
16. An incomplete list: A. M. Polyakov, Phys. Lett. B **72**, 477 (1978); G. 't Hooft, Nucl. Phys. B **138**, 1 (1978); A. Casher, Phys. Lett. B **83**, 395 (1979); C. Adami, T. Hatsuda and I. Zahed, Phys. Rev. D **43**, 921 (1991); G. E. Brown, A. D. Jackson, H. A. Bethe and P. M. Pizzochero, Nucl. Phys. A **560**, 1035 (1993); F. Wilczek, Int. J. Mod. Phys. A **7**, 3911 (1992) [Erratum-ibid. A **7**, 6951 (1992)]; G. E. Brown, L. Grandchamp, C. H. Lee and M. Rho, arXiv:hep-ph/0308147; S. Digal, E. Laermann and H. Satz, Nucl. Phys. A **702**, 159 (2002);
17. O.Scavenius, A.Mocsy, I.N.Mishustin and D.H.Rischke, Phys. Rev. C **64**, 045202 (2001);
18. F. Sannino, N. Marchal and W. Schafer, Phys. Rev. D **66**, 016007 (2002) [arXiv:hep-ph/0202248]; Y. Hatta and K. Fukushima, arXiv:hep-ph/0307068; K. Fukushima, arXiv:hep-ph/0310121.
19. F. Sannino, Phys. Rev. D **66**, 034013 (2002) [arXiv:hep-ph/0204174].
20. A. Dumitru and R. D. Pisarski, Phys. Lett. B **504**, 282 (2001) [arXiv:hep-ph/0010083].
21. O. Scavenius, A. Dumitru and J. T. Lenaghan, Phys. Rev. C **66**, 034903 (2002) [arXiv:hep-ph/0201079]; O. Scavenius, A. Dumitru and A. D. Jackson, Phys. Rev. Lett. **87**, 182302 (2001) [arXiv:hep-ph/0103219].
22. D. H. Rischke, arXiv:nucl-th/0305030.
23. B. Svetitsky and L. G. Yaffe, Nucl. Phys. B **210**, 423 (1982)

24. L. G. Yaffe and B. Svetitsky, Phys. Rev. D **26**, 963 (1982).
25. B. Svetitsky, Nucl. Phys. A **418**, 477C (1984).
26. R. D. Pisarski, Phys. Rev. D **62**, 111501 (2000) [arXiv:hep-ph/0006205].
27. A. Mocsy, F. Sannino and K. Tuominen, Phys. Rev. Lett. **91**, 092004 (2003) [arXiv:hep-ph/0301229].
28. A. Mocsy, F. Sannino and K. Tuominen, *Induced universal properties and deconfinement*, arXiv:hep-ph/0306069.
29. A. Mocsy, F. Sannino and K. Tuominen, *Confinement versus chiral symmetry*, arXiv:hep-ph/0308135.
30. J. Schechter, Phys. Rev. D **21**, 3393 (1980); A. A. Migdal and M. A. Shifman, Phys. Lett. B **114**, 445 (1982).
31. F. Sannino and J. Schechter, Phys. Rev. D **57**, 170 (1998) [arXiv:hep-th/9708113] and see references therein; F. Sannino and J. Schechter, Phys. Rev. D **60**, 056004 (1999) [arXiv:hep-ph/9903359].
32. G. E. Brown and M. Rho, Phys. Rept. **363**, 85 (2002) [arXiv:hep-ph/0103102].
33. N. O. Agasian, JETP Lett. **57** (1993) 208 [Pisma Zh. Eksp. Teor. Fiz. **57** (1993) 200].
34. G. W. Carter, O. Scavenius, I. N. Mishustin and P. J. Ellis, Phys. Rev. C **61**, 045206 (2000) [arXiv:nucl-th/9812014].
35. N. O. Agasian and S. M. Fedorov, "Hadron resonance gas and nonperturbative QCD vacuum at finite temperature," arXiv:hep-ph/0310249.
36. A. Mocsy, F. Sannino and K. Tuominen, in preparation.
37. P. Bacilieri *et al.*, Phys. Lett. B **220**, 607 (1989).
38. S. Datta and S. Gupta, arXiv:hep-ph/9809382.
39. F. Karsch, Lect. Notes Phys. **583**, 209 (2002) [arXiv:hep-lat/0106019].
40. F. Karsch and M. Lutgemeier, Nucl. Phys. B **550**, 449 (1999) [arXiv:hep-lat/9812023].
41. B. Alles, M. D'Elia, M. P. Lombardo and M. Pepe, arXiv:hep-lat/0210039.
42. T. Banks and A. Ukawa, Nucl. Phys. B **225**, 145 (1983).
43. F. Karsch, E. Laermann and A. Peikert, Nucl. Phys. B **605**, 579 (2001) [arXiv:hep-lat/0012023].
44. A. Dumitru, D. Roder and J. Ruppert, arXiv:hep-ph/0311119.
45. E. V. Shuryak, Phys. Lett. B **107**, 103 (1981).
46. R. D. Pisarski, Phys. Lett. B **110**, 155 (1982).
47. A. Manohar and H. Georgi, Nucl. Phys. B **234**, 189 (1984).
48. T. Appelquist, P. S. Rodrigues da Silva and F. Sannino, Phys. Rev. D **60**, 116007 (1999). For the anomaly terms see: Z. Y. Duan, P. S. Rodrigues da Silva and F. Sannino, Nucl. Phys. B **592**, 371 (2001) [arXiv:hep-ph/0001303].
49. J. T. Lenaghan, F. Sannino and K. Splittorff, Phys. Rev. D **65**, 054002 (2002).
50. For a review on 2 color QCD see S. Hands, Nucl. Phys. Proc. Suppl. **106**, 142 (2002).

PION VELOCITY NEAR THE CHIRAL PHASE TRANSITION*

CHIHIRO SASAKI

Department of Physics, Nagoya University, Nagoya, 464-8602, JAPAN

We study the pion velocity near the critical temperature T_c of chiral symmetry restoration in QCD. Using the hidden local symmetry (HLS) model as the effective field theory, where the chiral symmetry restoration is realized as the vector manifestation (VM), we show that the pion velocity for $T \to T_c$ receives neither quantum nor (thermal) hadronic corrections at the critical temperature even when we start from the bare theory with Lorentz symmetry breaking. We show that this is related to a new fixed point structure originated in the VM. Further we match at a matching scale the axial-vector current correlator in the HLS with the one in the operator product expansion for QCD, and present the matching condition to determine the bare pion velocity. We find that the pion velocity is close to the speed of light, $v_\pi(T) = 0.83 - 0.99$.

1. Introduction

Chiral symmetry in QCD is expected to be restored under some extreme conditions such as large number of flavor N_f and high temperature and/or density. In hadronic sector, the chiral symmetry restoration is described by various effective field theories (EFTs) based on the chiral symmetry [3].

By using the hidden local symmetry (HLS) model [4] as an EFT and performing the Wilsonian matching which is one of the methods that determine the bare theory from the underlying QCD [5], the vector manifestation (VM) in hot or dense matter was formulated in Refs. 6, 7. In the VM, the massless vector meson becomes the chiral partner of pion at the critical point [8 a]. There, the *intrinsic temperature or density dependences of the parameters* of the HLS Lagrangian, which are obtained by integrating out the high

*Talk given at KIAS-APCTP International Symposium on Astro-Hadron Physics, November 10-14, 2003, KIAS, Seoul, Korea. This talk is based on the works done in Refs. 1 and 2.

[a] As studied in Ref. 15 in detail, the VM is defined only as a limit with bare parameters approaching the VM fixed point from the broken phase.

energy modes (i.e., the quarks and gluons above the matching scale) in hot and/or dense matter, play the essential roles to realize the chiral symmetry restoration consistently. That the vector meson mass vanishes at the critical temperature/density supports the in-medium scaling of the vector meson proposed by Brown and Rho, Brown-Rho scaling [9], and has qualitatively important influences on the properties of hadrons in medium.

In the analysis done in Ref. 10, it was shown that the effect of Lorentz symmetry breaking to the bare parameters caused by the intrinsic temperature dependence through the Wilsonian matching are small [10,11]. Starting from the bare Lagrangian with Lorentz invariance, it was presented that the pion velocity approaches the speed of light at the critical temperature [10], although in low temperature region ($T \ll T_c$) the pion velocity deviates from the speed of light due to hadronic corrections [11].

However there do exist the Lorentz non-invariant effects in bare EFT anyway due to the intrinsic temperaure and/or density effects. Further the Lorentz non-invariance might be enhanced through the renormalization group equations (RGEs), even if effects of Lorentz symmetry breaking at the bare level are small. Thus it is important to investigate how Lorentz non-invariance at bare level influences physical quantities.

In this talk, we pick up the pion velocity at the critical temperature and study the quantum and hadronic thermal effects based on the VM. The pion velocity is one of the important quantities since it controls the pion propagation in medium through a dispersion relation. We show the non-renormalization property on the pion velocity v_π, which is protected by the VM, and estimate the value of v_π near the critical temperature.

2. Model Based on the Hidden Local Symmetry

In this section, we show the HLS Lagrangian at leading order including the effects of Lorentz non-invariance.

The HLS model is based on the $G_{\rm global} \times H_{\rm local}$ symmetry, where $G = SU(N_f)_L \times SU(N_f)_R$ is the chiral symmetry and $H = SU(N_f)_V$ is the HLS. The basic quantities are the HLS gauge boson V_μ and two matrix valued variables $\xi_L(x)$ and $\xi_R(x)$ which transform as $\xi_{L,R}(x) \to \xi'_{L,R}(x) = h(x)\xi_{L,R}(x)g^\dagger_{L,R}$, where $h(x) \in H_{\rm local}$ and $g_{L,R} \in [SU(N_f)_{\rm L,R}]_{\rm global}$. These variables are parameterized as [b] $\xi_{L,R}(x) = e^{i\sigma(x)/F^t_\sigma} e^{\mp i\pi(x)/F^t_\pi}$, where

[b]The wave function renormalization constant of the pion field is given by the temporal component of the pion decay constant [1,12]. Thus we normalize π and σ by F^t_π and F^t_σ respectively.

$\pi = \pi^a T_a$ denotes the pseudoscalar Nambu-Goldstone bosons associated with the spontaneous symmetry breaking of $G_{\rm global}$ chiral symmetry, and $\sigma = \sigma^a T_a$ denotes the Nambu-Goldstone bosons associated with the spontaneous breaking of $H_{\rm local}$. This σ is absorbed into the HLS gauge boson through the Higgs mechanism, and then the vector meson acquires its mass. F_π^t and F_σ^t denote the temporal components of the decay constant of π and σ, respectively. The covariant derivative of ξ_L is given by

$$D_\mu \xi_L = \partial_\mu \xi_L - i V_\mu \xi_L + i \xi_L \mathcal{L}_\mu, \tag{1}$$

and the covariant derivative of ξ_R is obtained by the replacement of $\mathcal{L}_\mu$ with $\mathcal{R}_\mu$ in the above where V_μ is the gauge field of $H_{\rm local}$, and $\mathcal{L}_\mu$ and $\mathcal{R}_\mu$ are the external gauge fields introduced by gauging $G_{\rm global}$ symmetry. In terms of $\mathcal{L}_\mu$ and $\mathcal{R}_\mu$, we define the external axial-vector and vector fields as $\mathcal{A}_\mu = (\mathcal{R}_\mu - \mathcal{L}_\mu)/2$ and $\mathcal{V}_\mu = (\mathcal{R}_\mu + \mathcal{L}_\mu)/2$.

In the HLS model it is possible to perform the derivative expansion systematically [13,14,15]. In the chiral perturbation theory (ChPT) with HLS, the vector meson mass is to be considered as small compared with the chiral symmetry breaking scale Λ_χ, by assigning $\mathcal{O}(p)$ to the HLS gauge coupling, $g \sim \mathcal{O}(p)$ [13,14]. (For details of the ChPT with HLS, see Ref. 15.) The leading order Lagrangian with Lorentz non-invariance can be written as [7]

$$\begin{aligned}
\mathcal{L} = & \left[(F_\pi^t)^2 u_\mu u_\nu + F_\pi^t F_\pi^s \left(g_{\mu\nu} - u_\mu u_\nu \right) \right] {\rm tr} \left[\hat{\alpha}_\perp^\mu \hat{\alpha}_\perp^\nu \right] \\
& + \left[(F_\sigma^t)^2 u_\mu u_\nu + F_\sigma^t F_\sigma^s \left(g_{\mu\nu} - u_\mu u_\nu \right) \right] {\rm tr} \left[\hat{\alpha}_\parallel^\mu \hat{\alpha}_\parallel^\nu \right] \\
& + \left[-\frac{1}{g_L^2} u_\mu u_\alpha g_{\nu\beta} - \frac{1}{2 g_T^2} \left(g_{\mu\alpha} g_{\nu\beta} - 2 u_\mu u_\alpha g_{\nu\beta} \right) \right] {\rm tr} \left[V^{\mu\nu} V^{\alpha\beta} \right] ,
\end{aligned} \tag{2}$$

where

$$\hat{\alpha}_{\perp,\parallel}^\mu = \frac{1}{2i} \left[D^\mu \xi_R \cdot \xi_R^\dagger \mp D^\mu \xi_L \cdot \xi_L^\dagger \right]. \tag{3}$$

Here F_π^s denote the spatial pion decay constant and similarly F_σ^s for the σ. The rest frame of the medium is specified by $u^\mu = (1, \vec{0})$ and $V_{\mu\nu}$ is the field strength of V_μ. g_L and g_T correspond in medium to the HLS gauge coupling g. The parametric π and σ velocities are defined by [16]

$$V_\pi^2 = F_\pi^s / F_\pi^t, \qquad V_\sigma^2 = F_\sigma^s / F_\sigma^t. \tag{4}$$

3. Vector Manifestation Conditions

In this section, we start from the HLS Lagrangian with Lorentz non-invariance, and requiring that the axial-vector current correlator be equal to the vector current correlator at the critical point, we present the conditions satisfied at the critical point.

Concept of the matching in the Wilsonian sense is based on the following assumptions: The bare Lagrangian of the effective field theory (EFT) $\mathcal{L}_{\rm bare}$ is defined at a suitable matching scale Λ. Generating functional derived from $\mathcal{L}_{\rm bare}$ leads to the same Green's function as that derived from the generating functional of QCD at Λ. In other words, the bare parameters are obtained after integrating out the high energy modes, i.e., the quarks and gluons above Λ. When we integrate out the high energy modes in hot matter, the bare parameters have a certain temperature dependence, *intrinsic temperature dependence*, converted from QCD to the EFT. The intrinsic temperature dependence is nothing but the signature that hadrons have an internal structure constructed from quarks and gluons. In the following, we describe the chiral symmetry restoration based on the point of view that *the bare HLS theory is defined from the underlying QCD.* We note that the Lorentz non-invariance appears in bare HLS theory as a result of including the intrinsic temperature dependences. Once the temperature dependence of the bare parameters is determined through the matching with QCD mentioned above, from the RGEs the parameters appearing in the hadronic corrections pick up the intrinsic thermal effects.

Now we consider the matching near the critical temperature. The axial-vector and vector current correlators at bare level are constructed in terms of bare parameters and are expanded in terms of the longitudinal and transverse projection operators $P^{\mu\nu}_{L,T}$: $G^{\mu\nu}_{A,V} = P^{\mu\nu}_{L} G^{L}_{A,V} + P^{\mu\nu}_{T} G^{T}_{A,V}$. At the chiral phase transition point, the axial-vector and vector current correlators must agree with each other, i.e., chiral symmetry restoration is characterized by the following conditions: $G^{L}_{A(\rm HLS)} - G^{L}_{V(\rm HLS)} \to 0$ and $G^{T}_{A(\rm HLS)} - G^{T}_{V(\rm HLS)} \to 0$ for $T \to T_c$. In Ref. 7, it was shown that they are satisfied for any values of p_0 and $\bar{p}$ around the matching scale only if the following conditions are met: $(g_{L,\rm bare}, g_{T,\rm bare}, a^{t}_{\rm bare}, a^{s}_{\rm bare}) \to (0,0,1,1)$ for $T \to T_c$. This implies that at bare level the longitudinal mode of the vector meson becomes the real NG boson and couples to the vector current correlator, while the transverse mode decouples.

In Ref. 1, we have shown that $(g_L, a^t, a^s) = (0,1,1)$ is a fixed point of the RGEs and satisfied in any energy scale. Thus the VM condition is given

by

$$(g_L, a^t, a^s) \to (0, 1, 1) \quad \text{for} \quad T \to T_c. \tag{5}$$

The vector meson mass is never generated at the critical temperature since the quantum correction to M_ρ^2 is proportional to g_L^2. Because of $g_L \to 0$, the transverse vector meson at the critical point, in any energy scale, decouples from the vector current correlator. The VM condition for a^t and a^s leads to the equality between the π and σ (i.e., longitudinal vector meson) velocities:

$$\left(V_\pi / V_\sigma\right)^4 = \left(F_\pi^s F_\sigma^t / F_\sigma^s F_\pi^t\right)^2 = a^t / a^s \overset{T \to T_c}{\to} 1. \tag{6}$$

This is easily understood from a point of view of the VM since the longitudinal vector meson becomes the chiral partner of pion. We note that this condition $V_\sigma = V_\pi$ holds independently of the value of the bare pion velocity which is to be determined through the Wilsonian matching.

4. Non-renormalization Property on the Pion Velocity

As we have seen in the previous section, the dropping mass of vector meson can be realized as the VM which is formulated by using the HLS theory. Then what is the prediction of the VM? Recently it was proven that the non-renormalization property on the pion velocity which is protected by the VM [1]. In the following, we show that this can be understood based on the idea of chiral partners.

Before going to the critical temperature T_c, let us consider the situation away from T_c. Starting from the bare pion velocity $V_{\pi,\mathrm{bare}}^2 = F_{\pi,\mathrm{bare}}^s / F_{\pi,\mathrm{bare}}^t$ and including quantum and hadronic corrections into the parameters through the diagrams shown in Fig. 1. Away from T_c, there exists the

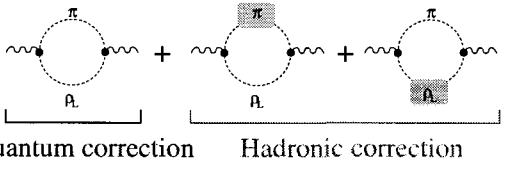

Figure 1. Diagrams for contribution to the pion velocity. Center (right) diagram denotes the interaction between the pion (vector meson) and heat bath.

hadronic thermal correction to the pion velocity [11]:

$$v_\pi^2(T) \simeq V_\pi^2 - N_f \frac{2\pi^2}{15} \frac{T^4}{(F_\pi^t)^2 M_\rho^2} \qquad \text{for} \quad T < T_c, \tag{7}$$

where the contribution of the massive σ (i.e., the longitudinal mode of massive vector meson) is suppressed owing to the Boltzmann factor $\exp[-M_\rho/T]$, and then only the pion loop contributes to the pion velocity.

On the other hand, when we approach the critical temperature, the vector meson mass goes to zero due to the VM. Thus $\exp[-M_\rho/T]$ is no longer the suppression factor. As a result, the hadronic correction in the pion velocity is absent due to the exact cancellation between the contribution of pion and that of its chiral partner σ. Similarly the quantum correction generated from the pion loop is exactly cancelled by that from the σ loop. Accordingly we conclude

$$v_\pi(T) = V_{\pi,\mathrm{bare}}(T) \qquad \text{for} \quad T \to T_c, \tag{8}$$

i.e., *the pion velocity in the limit $T \to T_c$ receives neither hadronic nor quantum corrections due to the protection by the VM.* This implies that $(g_L, a^t, a^s, V_\pi) = (0, 1, 1, \text{any})$ forms a fixed line for four RGEs of g_L, a^t, a^s and V_π. When one point on this fixed line is selected through the matching procedure as done in Ref. 2, namely the value of $V_{\pi,\mathrm{bare}}$ is fixed, the present result implies that the point does not move in a subspace of the parameters. Approaching the restoration point of chiral symmetry, the physical pion velocity itself flows into the fixed point.

5. Matching Conditions on the Bare Pion Velocity

One possible way to determine the bare parameters is the Wilsonian matching proposed in Ref. 5 which is done by matching the axial-vector and vector current correlators derived from the HLS with those by the operator product expansion (OPE) in QCD at the matching scale Λ. In this section, we present the matching conditions to determine the bare pion velocity including the effect of Lorentz symmetry breaking at the bare level following Ref. 2.

In the EFT sector, pion couples to the longitudinal part of the axial-vector current correlator G_A^L. We regard $G_A^{L,T}$ as functions of $-q^2$ and $|\vec{q}|^2$ instead of q_0 and $\vec{q}$, and expand G_A^L in a Taylor series around $\bar{q} = |\vec{q}| = 0$ in $\bar{q}^2/(-q^2)$ as follows:

$$G_A^L(-q^2, \bar{q}^2) = G_A^{L(0)}(-q^2) + G_A^{L(1)}(-q^2)\bar{q}^2 + \cdots . \tag{9}$$

Expanding the axial-vector current correlator derived from the HLS theory

$G_A^{(\mathrm{HLS})L}$ in terms of $\bar{q}^2/(-q^2)$, we obtain

$$G_A^{(\mathrm{HLS})L(0)}(-q^2) = \frac{F^t_{\pi,\mathrm{bare}} F^s_{\pi,\mathrm{bare}}}{-q^2} - 2z^L_{2,\mathrm{bare}}\,, \tag{10}$$

$$G_A^{(\mathrm{HLS})L(1)}(-q^2) = \frac{F^t_{\pi,\mathrm{bare}} F^s_{\pi,\mathrm{bare}}(1 - V^2_{\pi,\mathrm{bare}})}{(-q^2)^2}, \tag{11}$$

where $z^L_{2,\mathrm{bare}}$ is the parameter of the higher order term.

On the other hand, the axial-vector current correlator obtained from the OPE is given by [17,18,19]

$$\begin{aligned} G_A^{\mu\nu}(q_0,\bar{q}) = (q^\mu q^\nu - g^{\mu\nu}q^2)\frac{-1}{4}\Bigg[& \frac{1}{2\pi^2}\left(1+\frac{\alpha_s}{\pi}\right)\ln\left(\frac{Q^2}{\mu^2}\right) + \frac{1}{6Q^4}\left\langle \frac{\alpha_s}{\pi}G^2\right\rangle_T \\ & - \frac{2\pi\alpha_s}{Q^6}\left\langle \left(\bar{u}\gamma_\mu\gamma_5\lambda^a u - \bar{d}\gamma_\mu\gamma_5\lambda^a d\right)^2\right\rangle_T \\ & - \frac{4\pi\alpha_s}{9Q^6}\left\langle \left(\bar{u}\gamma_\mu\lambda^a u + \bar{d}\gamma_\mu\lambda^a d\right)\sum_q^{u,d,s}\bar{q}\gamma^\mu\lambda^a q\right\rangle_T\Bigg] \\ & + [-g^{\mu\nu}q^{\mu_1}q^{\mu_2} + g^{\mu\mu_1}q^\nu q^{\mu_2} + q^\mu q^{\mu_1}g^{\nu\mu_2} + g^{\mu\mu_1}g^{\nu\mu_2}Q^2] \\ & \times [\frac{4}{Q^4}A^{4,2}_{\mu_1\mu_2} + \frac{16}{Q^8}q^{\mu_3}q^{\mu_4}A^{6,2}_{\mu_1\mu_2\mu_3\mu_4}]\,, \end{aligned} \tag{12}$$

where $Q^2 = -q^2$, $\tau = d - s$ denotes the twist, and $s = 2k$ is the number of spin indices of the operator of dimension d. In the above expression, we restrict ourselves to contributions from the twist 2 ($\tau = 2$) operators [c]. $A^{2k+\tau,\tau}_{\mu_1\cdots\mu_{2k}}$ is the residual Wilson coefficient times matrix element of dimension d and twist τ. The general tensor structure of the matrix element of $A^{2k+\tau,\tau}_{\mu_1\cdots\mu_{2k}}$ is given in Ref. 17.

Now we proceed to estimate the pion velocity by matching to QCD. We require the following matching conditions at $Q^2 = \Lambda^2$:

$$\begin{aligned} & Q^2\frac{d}{dQ^2}G_A^{(\mathrm{HLS})L(0)}(Q^2) = Q^2\frac{d}{dQ^2}G_A^{(\mathrm{OPE})L(0)}(Q^2), \\ & G_A^{(\mathrm{HLS})L(1)}(Q^2) = G_A^{(\mathrm{OPE})L(1)}(Q^2). \end{aligned} \tag{13}$$

[c]The higher the twist of operators becomes, the more these operators are suppressed since the dimensions of such operators become higher and the power of $1/Q^2$ appear.

They lead to the conditions on the bare pion decay constants as

$$\frac{F^t_{\pi,\mathrm{bare}}F^s_{\pi,\mathrm{bare}}}{\Lambda^2} = \frac{1}{8\pi^2}\left[\left(1+\frac{\alpha_s}{\pi}\right) + \frac{2\pi^2}{3}\frac{\left\langle\frac{\alpha_s}{\pi}G^2\right\rangle_T}{\Lambda^4} + \pi^3\frac{1408}{27}\frac{\alpha_s\langle\bar{q}q\rangle_T^2}{\Lambda^6}\right]$$
$$+ \frac{\pi^2}{15}\frac{T^4}{\Lambda^4}A^\pi_{4,2} - \frac{16\pi^4}{21}\frac{T^6}{\Lambda^6}A^\pi_{6,4} \equiv G_0,$$
$$\frac{F^t_{\pi,\mathrm{bare}}F^s_{\pi,\mathrm{bare}}(1-V^2_{\mathrm{bare}})}{\Lambda^2} = \frac{32}{105}\pi^4\frac{T^6}{\Lambda^6}A^\pi_{6,4}, \tag{14}$$

where we use the dilute pion-gas approximation in order to evaluate the matrix element $\langle\mathcal{O}\rangle_T$ [17] in the low temperature region. From these conditions, we obtain the following matching condition to determine the deviation of the bare pion velocity from the speed of light in the low temperature region:

$$\delta_{\mathrm{bare}} \equiv 1 - V^2_{\pi,\mathrm{bare}} = \frac{1}{G_0}\frac{32}{105}\pi^4\frac{T^6}{\Lambda^6}A^\pi_4. \tag{15}$$

This implies that the intrinsic temperature dependence starts from the $\mathcal{O}(T^6)$ contribution. On the other hand, the hadronic thermal correction to the pion velocity starts from the $\mathcal{O}(T^4)$ [see Eq. (7)]. Thus the hadronic thermal effect is dominant in low temperature region.

6. Pion Velocity near the Critical Temperature

In this section, we extend the matching condition valid at low temperature, Eq. (15), to near the critical temperature, and determine the bare pion velocity at T_c.

As is discussed in Ref. 2, we should in principle evaluate the matrix elements in terms of QCD variables only in order for performing the Wilsonian matching, which is as yet unavailable from model-independent QCD calculations. Therefore, we make an estimation by extending the dilute gas approximation adopted in the QCD sum-rule analysis in the low-temperature region to the critical temperature with including all the light degrees of freedom expected in the VM. In the HLS/VM theory, both the longitudinal and transverse vector mesons become massless at the critical temperature since the HLS gauge coupling constant g_L vanishes. At the critical point, the longitudinal vector meson which becomes the NG boson σ couples to the vector current whereas the transverse vector mesons decouple from the theory because of the vanishing g_L. Thus we assume that thermal fluctuations of the system are dominated near T_c not only by the pions but also by the longitudinal vector mesons. We evaluate the thermal matrix elements of the non-scalar operators in the OPE, by extending the thermal pion gas

approximation employed in Ref. 17 to the longitudinal vector mesons that figure in our approach. This is feasible since at the critical temperature, we expect the equality $A_4^\rho(T_c) = A_4^\pi(T_c)$ to hold as the massless longitudinal vector meson is the chiral partner of the pion in the VM. It should be noted that, although we use the dilute gas approximation, the treatment here is already beyond the low-temperature approximation because the contribution from vector meson is negligible in the low-temperature region. Since we treat the pion as a massless particle in the present analysis, it is reasonable to take $A_4^\pi(T) \simeq A_4^\pi(T=0)$. We therefore use

$$A_4^\rho(T) \simeq A_4^\pi(T) \simeq A_4^\pi(T=0) \quad \text{for} \quad T \simeq T_c. \tag{16}$$

Therefore from Eq. (15), we obtain the deviation $\delta_{\rm bare}$ as

$$\delta_{\rm bare} = 1 - V_{\pi,\rm bare}^2 = \frac{1}{G_0}\frac{32}{105}\pi^4\frac{T^6}{\Lambda^6}\left[A_4^\pi + A_4^\rho\right]. \tag{17}$$

This is the matching condition to be used for determining the value of the bare pion velocity near the critical temperature.

Let us make a rough estimate of $\delta_{\rm bare}$. For the range of matching scale ($\Lambda = 0.8 - 1.1\,\mathrm{GeV}$), that of QCD scale ($\Lambda_{QCD} = 0.30 - 0.45\,\mathrm{GeV}$) and critical temperature ($T_c = 0.15 - 0.20\,\mathrm{GeV}$), we get

$$\delta_{\rm bare}(T_c) = 0.0061 - 0.29\,. \tag{18}$$

Thus we obtain the *bare* pion velocity as $V_{\pi,\rm bare}(T_c) = 0.83 - 0.99$. Finally thanks to the non-renormalization property, i.e., $v_\pi(T_c) = V_{\pi,\rm bare}(T_c)$ given in Eq. (8), we arrive at the physical pion velocity at chiral restoration:

$$v_\pi(T_c) = 0.83 - 0.99\,, \tag{19}$$

to be close to the speed of light.

7. Summary

In this talk, we started from the Lorentz non-invariant HLS Lagrangian at bare level and studied the pion velocity at the critical temperature based on the VM. We showed that *the pion velocity does not receive either quantum or hadronic corrections in the limit* $T \to T_c$, which is protected by the VM. This non-renormalization property means that it suffices to compute the pion velocity at the level of bare HLS Lagrangian at the matching scale to arrive at the *physical* pion velocity at the critical temperature of chiral symmetry restoration. We derived the matching condition on the *bare* pion velocity and finally we found that the pion velocity near T_c is close to the speed of light, $v_\pi(T) = 0.83 - 0.99$.

This is in contrast to the result obtaied from the chiral theory [20], where the relevent degree of freedom near T_c is only the pion. Their result is that the pion velocity becomes zero for $T \to T_c$. Therefore from the experimental data, we may be able to distinguish which picture is correct, $v_\pi \sim 1$ or $v_\pi \to 0$.

Acknowledgment

The author would like to thank Professor Masayasu Harada, Doctor Youngman Kim and Professor Mannque Rho for many useful discussions and comments. This work is supported in part by the 21st Century COE Program of Nagoya University provided by Japan Society for the Promotion of Science (15COEG01).

References

1. C. Sasaki, "A new fixed point originated in the vector manifestation," arXiv:hep-ph/0306005.
2. M. Harada, Y. Kim, M. Rho and C. Sasaki, Nucl. Phys. A. **730**, 379 (2004).
3. T. Hatsuda and T. Kunihiro, Phys. Rept. **247**, 221 (1994); R. D. Pisarski, arXiv:hep-ph/9503330; G. E. Brown and M. Rho, Phys. Rept. **269**, 333 (1996); G. E. Brown and M. Rho, Phys. Rept. **363**, 85 (2002); T. Hatsuda, H. Shiomi and H. Kuwabara, Prog. Theor. Phys. **95**, 1009 (1996); R. Rapp and J. Wambach, Adv. Nucl. Phys. **25**, 1 (2000); F. Wilczek, arXiv:hep-ph/0003183.
4. M. Bando, T. Kugo, S. Uehara, K. Yamawaki and T. Yanagida, Phys. Rev. Lett. **54**, 1215 (1985); M. Bando, T. Kugo and K. Yamawaki, Phys. Rept. **164**, 217 (1988).
5. M. Harada and K. Yamawaki, Phys. Rev. D **64**, 014023 (2001).
6. M. Harada and C. Sasaki, Phys. Lett. B **537**, 280 (2002).
7. M. Harada, Y. Kim and M. Rho, Phys. Rev. D **66**, 016003 (2002).
8. M. Harada and K. Yamawaki, Phys. Rev. Lett. **86**, 757 (2001).
9. G. E. Brown and M. Rho, Phys. Rev. Lett. **66**, 2720 (1991).
10. M. Harada, Y. Kim, M. Rho and C. Sasaki, Nucl. Phys. A **727**, 437 (2003).
11. M. Harada and C. Sasaki, arXiv:hep-ph/0304282; C. Sasaki, arXiv:hep-ph/0304298.
12. U. G. Meissner, J. A. Oller and A. Wirzba, Annals Phys. **297**, 27 (2002).
13. H. Georgi, Phys. Rev. Lett. **63** (1989) 1917; Nucl. Phys. B **331**, 311 (1990).
14. M. Tanabashi, Phys. Lett. B **316**, 534 (1993).
15. M. Harada and K. Yamawaki, Phys. Rept. **381**, 1 (2003).
16. R. D. Pisarski and M. Tytgat, Phys. Rev. D **54**, 2989 (1996).
17. T. Hatsuda, Y. Koike and S. H. Lee, Nucl. Phys. B **394** (1993) 221.
18. S. Leupold and U. Mosel, Phys. Rev. C **58**, 2939 (1998).
19. B. Friman, S. H. Lee and H. C. Kim, Nucl. Phys. A **653**, 91 (1999).
20. D. T. Son and M. A. Stephanov, Phys. Rev. Lett. **88**, 202302 (2002); Phys. Rev. D **66**, 076011 (2002).

EFFECTIVE THEORY OF SUPERFLUID QUARK MATTER

THOMAS SCHÄFER
Department of Physics, North Carolina State University, Raleigh, NC 27695
and Riken-BNL Research Center, Brookhaven National Laboratory, Upton, NY 11973

We provide a brief introduction to the high density effective theory of QCD. As an application, we consider the instanton correction to the perturbatively generated gap in the color superconducting phase. We show that the instanton correction becomes large for $\mu \sim 1.25$ GeV in $N_f = 2$ QCD, and for $\mu \sim 750$ MeV in $N_f = 3$ QCD with a massive strange quark. We also study some other numerical issues related to the magnitude of the gap. We find, in particular, that a renormalization group improved gap equation does not give results that are substantially different from a gap equation with a fixed coupling.

1. Introduction

Over the last several years we have seen rapid progress in the theoretical study of very dense hadronic matter. Many new phases of strongly interacting matter, such as color superconducting quark matter and color-flavor locked matter have been predicted [1,2,3,4,5]. Reviews of these developments can be found in [6,7,8,9,10]. Exotic phases of matter at high baryon density may be realized in nature in the cores of neutron stars. In order to study this possibility quantitatively we would like to develop a systematic framework that will allow us to determine the exact nature of the phase diagram as a function of the density, temperature, the quark masses, and the lepton chemical potentials, and to compute the low energy properties of these phases. In this contribution we give a brief review of an attempt to use effective field theory methods to address this problem.

2. High Density Effective Theory

At high baryon density the relevant degrees of freedom are particle and hole excitations which move with the Fermi velocity v. Since the momentum $p \sim v\mu$ is large, typical soft scatterings cannot change the momentum by

very much. An effective field theory of particles and holes in QCD is given by [11,12]

$$L = \sum_v \psi_v^\dagger (iv \cdot D)\psi_v - \frac{1}{4} G^a_{\mu\nu} G^a_{\mu\nu} + \ldots, \tag{1}$$

where $v_\mu = (1, \vec{v})$. The field describes particles and holes with momenta $p = \mu\vec{v} + l$, where $l \ll \mu$. We will write $l = l_0 + l_\parallel + l_\perp$ with $\vec{l}_\parallel = \vec{v}(\vec{l} \cdot \vec{v})$ and $\vec{l}_\perp = \vec{l} - \vec{l}_\parallel$. In order to take into account the entire Fermi surface we have to cover the Fermi surface with patches labeled by the local Fermi velocity. The number of these patches is $n_v \sim (\mu^2/\Lambda_\perp^2)$ where $\Lambda_\perp \ll \mu$ is the cutoff on the transverse momenta $l_\perp$.

Higher order terms are suppressed by powers of $1/\mu$. As usual we have to consider all possible terms allowed by the symmetries of the underlying theory. At $O(1/\mu)$ we have

$$L = \sum_v \left\{ -\frac{1}{2\mu} \psi_v^\dagger D_\perp^2 \psi_v - g\psi_v^\dagger \frac{\sigma^{\mu\nu} G^\perp_{\mu\nu}}{4\mu} \psi_v \right\}. \tag{2}$$

At higher order in $1/\mu$ there is an infinite tower of operators of the form $\mu^{-n} \psi_v^\dagger D_\perp^{2n_1} (\bar{v} \cdot D)^{n_2} \psi_v$ with $\bar{v} = (1, -\vec{v})$ and $n = 2n_1 + n_2 - 1$. At $O(1/\mu^2)$ the effective theory contains four-fermion operators [13]

$$\begin{aligned} L = \frac{1}{\mu^2} \sum_{v_i} \sum_{\Gamma,\Gamma'} & c^{\Gamma\Gamma'}(\vec{v}_1 \cdot \vec{v}_2, \vec{v}_1 \cdot \vec{v}_3, \vec{v}_2 \cdot \vec{v}_3) \\ & \cdot \left(\psi_{v_1} \Gamma \psi_{v_2}\right) \left(\psi_{v_3}^\dagger \Gamma' \psi_{v_4}^\dagger\right) \delta(v_1 + v_2 - v_3 - v_4). \end{aligned} \tag{3}$$

There are two types of operators that are compatible with the restriction $v_1 + v_2 = v_3 + v_4$. The first possibility is that both the incoming and outgoing fermion momenta are back-to-back. This corresponds to the BCS interaction

$$L = \frac{1}{\mu^2} \sum_{v,v'} \sum_{\Gamma,\Gamma'} V_l^{\Gamma\Gamma'} R_l^{\Gamma\Gamma'}(\vec{v} \cdot \vec{v}') \left(\psi_v \Gamma \psi_{-v}\right) \left(\psi_{v'}^\dagger \Gamma' \psi_{-v'}^\dagger\right), \tag{4}$$

where $\vec{v} \cdot \vec{v}' = \cos\theta$ is the scattering angle and $R_l^{\Gamma\Gamma'}(\vec{v} \cdot \vec{v}')$ is a set of orthogonal polynomials. The second possibility is that the final momenta are equal to the initial momenta up to a rotation around the axis defined by the sum of the incoming momenta. The relevant four-fermion operator is

$$L = \frac{1}{\mu^2} \sum_{v,v',\phi} \sum_{\Gamma,\Gamma'} F_l^{\Gamma\Gamma'}(\phi) R_l^{\Gamma\Gamma'}(\vec{v} \cdot \vec{v}') \left(\psi_v \Gamma \psi_{v'}\right) \left(\psi_{\tilde{v}}^\dagger \Gamma' \psi_{\tilde{v}'}^\dagger\right), \tag{5}$$

where $\tilde{v}, \tilde{v}'$ are the vectors obtained from v, v' by a rotation around $v_{tot} = v + v'$ by the angle ϕ.

The four-fermion operators in the effective theory can be determined by matching moments of quark-quark scattering amplitudes between QCD and the effective theory. The matching conditions involve on-shell scattering amplitudes in BCS and forward kinematics. The scattering amplitude in the effective theory contains almost collinear gluon exchanges which do not change the velocity label of the quarks as well as four-fermion operators which correspond to scattering involving different patches on the Fermi surface. There are several contributions in the microscopic theory that are absorbed into four-fermion operators in the effective theory. Examples are large angle scatterings [13] and non-perturbative instanton effects [14].

3. Power Counting

In this section we briefly discuss the power counting in the high density effective theory. We will denote the small scale by $l \ll \mu$. We first discuss the scaling properties of a generic operator. We assume that $v \cdot D$ scales as l, ψ_v scales as $l^{3/2}$, A_μ scales as l, and $\vec{D}_\perp, \bar{v} \cdot D \sim l$. Complication arise because not all loop diagrams scale as l^4. In fermion loops sums over patches and integrals over transverse momenta can combine to give integrals that are proportional to the surface area of the Fermi sphere,

$$\frac{1}{2\pi} \sum_{\vec{v}} \int \frac{d^2 l_\perp}{(2\pi)^2} = \frac{\mu^2}{2\pi^2} \int \frac{d\Omega}{4\pi}. \tag{6}$$

These loop integrals scale as l^2, not l^4. In the following we will refer to loops that scale as l^2 as "hard loops" and loops that scale as l^4 as "soft loops". In order to take this distinction into account we define V_k^S and V_k^H to be the number of soft and hard vertices of scaling dimension k. A vertex is called soft if it contains no fermion lines. In order to determine the l counting of a general diagram in the effective theory we remove all gluon lines from the graph, see Fig. 1. We denote the number of connected pieces of the remaining graph by N_C. Using Euler identities for both the initial and the reduced graph we find that the diagram scales as l^δ with

$$\delta = \sum_i \left[(k-4) V_k^S + (k-2-f_k) V_k^H \right] + E_Q + 4 - 2N_C. \tag{7}$$

Here, f_k denotes the number of fermion fields in a hard vertex, and E_Q is the number of external quark lines. We observe that in general the scaling

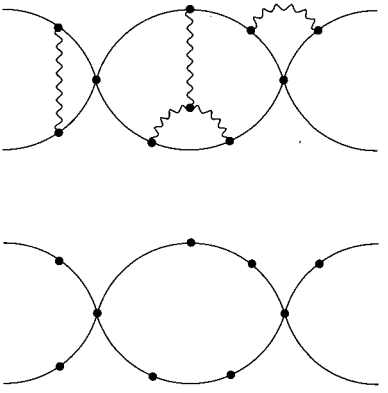

Figure 1. Counting hard loops in the effective field theory. If all (soft) gluon lines are removed the remaining fermionic loops contain sums over the velocity index.

dimension δ increases with the number of higher order vertices, but there are two important exceptions.

First we observe that the number of disconnected fermion loops, N_C, reduces the power δ. Each disconnected loop contains at least one power of the coupling constant, g, for every soft vertex. As a result, fermion loop insertions in gluon n-point functions spoil the power counting if the gluon momenta satisfy $l \sim g\mu$. This implies that for $l < g\mu$ the high density effective theory becomes non-perturbative and fermion loops in gluon n-point functions have to be resummed. The generating functional for hard dense loops in gluon n-point functions is given by [15,16]

$$L_{HDL} = -m^2 \int \frac{d\Omega}{4\pi} \mathrm{Tr}\, G_{\mu\alpha} \frac{\hat{P}^\alpha \hat{P}^\beta}{(\hat{P}\cdot D)^2} G^\mu_\beta, \tag{8}$$

where $m^2 = N_f g^2 \mu^2/(4\pi^2)$ and the angular integral corresponds to an average over the direction of $\hat{P}_\alpha = (1, \hat{p})$. For momenta $l < g\mu$ we have to add L_{HDL} to L_{HDET}. In order not to over-count diagrams we have to remove at the same time all diagrams that become disconnected if all soft gluon lines are deleted. Note that the high density effective theory is different from the standard hard dense loop approximation, because hard loops are resummed only in gluon Green functions, but not in quark Green functions or quark-gluon vertex functions.

The second observation is that the power counting for hard vertices is modified by a factor that counts the number of fermion lines in the vertex. It is easy to see that four-fermion operators without extra derivatives are

leading order ($k - 2 - f_k = 0$), but terms with more than four fermion fields, or extra derivatives, are suppressed. This result is familiar from the effective field theory analysis of theories with short range interactions [17,18].

4. Color Superconductivity

In the last section we saw that hard loops lead to non-perturbative effects in the effective theory that require resummation at the scale $l \sim g\mu$. In addition to that, there are logarithmic divergences that have to be resummed at exponentially small scales $l \sim \mu \exp(-c/g)$. The most important effect of this type is the BCS instability in the quark-quark scattering amplitude. This instability leads to the formation of a gap in the single particle spectrum. We can take this effect into account in the high density effective theory by including a tree level gap term

$$L = \Delta\, R_l^\Gamma(\vec{v}\cdot\hat{\Delta})\psi_{-v}\sigma_2\Gamma\psi_v + h.c.. \tag{9}$$

The Dirac matrix Γ and the angular factor $R_l^\Gamma(x)$ determine the helicity and partial wave channel. The magnitude of the gap is determined variationally, by requiring the free energy to be stationary order by order in perturbation theory.

At leading order in the high density effective theory the variational principle for the gap Δ gives the Dyson-Schwinger equation

$$\Delta(p_4) = \frac{2g^2}{3}\int \frac{d^4q}{(2\pi)^4}\frac{\Delta(q_4)}{q_4^2 + l_q^2 + \Delta(q_4)^2} v_\mu v_\nu D_{\mu\nu}(p-q), \tag{10}$$

where we have restricted ourselves to angular momentum zero and the color anti-symmetric $[\bar{3}]$ channel. $D_{\mu\nu}$ is the hard dense loop resummed gluon propagator. We also note that equ. (10) only contains collinear exchanges. According to the arguments give in Sect. 3 four-fermion operators are of leading order in the HDET power counting. However, even though collinear exchanges and four-fermion operators have the same power of l, collinear exchanges are enhanced by a logarithm of the small scale. As a consequence, we can treat four-fermion operators as a perturbation.

Sine the electric interaction is screened it is possible to absorb electric gluon exchanges into four-fermion operators. At leading order in the high density theory the gap equation is completely determined by the collinear divergence in the magnetic gluon exchange interaction. This IR divergence is independent of the helicity and angular momentum channel. We have

$$\Delta(p_4) = \frac{g^2}{18\pi^2}\int_0^{\Lambda_\parallel} dq_4 \frac{\Delta(q_4)}{\sqrt{q_4^2 + \Delta(q_4)^2}} \log\left(\frac{\Lambda_\perp}{|p_4^2 - q_4^2|^{1/2}}\right). \tag{11}$$

The leading logarithmic behavior is independent of the ratio of the cutoffs and we can set $\Lambda_\parallel = \Lambda_\perp = \Lambda$. We introduce the dimensionless variables variables $x = \log(2\Lambda/(q_4 + \epsilon_q))$ and $y = \log(2\Lambda/(p_4 + \epsilon_p)$ where $\epsilon_q = (q_4^2 + \Delta(q_4))^{1/2}$. In terms of dimensionless variables the gap equation is given by

$$\Delta(y) = \frac{g^2}{18\pi^2} \int_0^{x_0} dx\, \Delta(x) K(x,y), \tag{12}$$

where $x_0 = \log(2\Lambda/\Delta_0)$ and $K(x,y)$ is the kernel of the integral equation. At leading order we can use the approximation $K(x,y) = \min(x,y)$. We can perform an additional rescaling $x = x_0\bar{x}$, $y = x_0\bar{y}$. Since the leading order kernel is homogeneous in x and y we can write the gap equation as an eigenvalue equation

$$\Delta(\bar{y}) = x_0^2 \frac{g^2}{18\pi^2} \int_0^1 d\bar{x}\, \Delta(\bar{x}) K(\bar{x},\bar{y}), \tag{13}$$

where the gap function is subject to the boundary conditions $\Delta(0) = 0$ and $\Delta'(1) = 0$. This integral equation has the solutions [19]

$$\Delta_n(\bar{x}) = \Delta_{n,0} \sin\left(\frac{g}{3\sqrt{2}\pi} x_{0,n} \bar{x}\right), \quad x_{0,n} = (2n+1)\frac{3\pi^2}{\sqrt{2}g}. \tag{14}$$

The physical solution corresponds to $n = 0$ which gives the largest gap, $\Delta_0 = 2\Lambda \exp(-3\pi^2/(\sqrt{2}g))$. Solutions with $n \neq 0$ have smaller gaps and are not global minima of the free energy.

5. Higher Order Corrections to the Gap

The high density effective field theory enables us to perform a systematic expansion of the kernel of the gap equation in powers of the small scale and the coupling constant. It is not so obvious, however, how to solve the gap equation for more complicated kernels, and how the perturbative expansion of the kernel is related to the expansion of the solution of the gap equation.

For this purpose it is useful to develop a perturbative method for solving the gap equation [20,13]. We can write the kernel of the gap equation as $K(x,y) = K_0(x,y) + \delta K(x,y)$, where $K_0(x,y)$ contains the leading IR divergence and $\delta K(x,y)$ is a perturbation. We expand both the gap function $\Delta(x)$ and the eigenvalue x_0 order by order δK,

$$\Delta(\bar{x}) = \Delta^{(0)}(\bar{x}) + \Delta^{(1)}(\bar{x}) + \Delta^{(2)}(\bar{x}) + \ldots, \tag{15}$$

$$\bar{x}_0 = \bar{x}_0^{(0)} + \bar{x}_0^{(1)} + \bar{x}_0^{(2)} + \ldots, \tag{16}$$

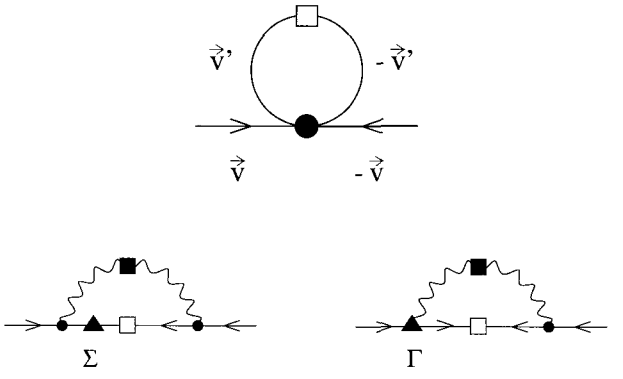

Figure 2. Higher order corrections to the gap equation in the high density effective theory. The diagrams shown in this figure correspond to four-fermion operators, fermion self-energy corrections, and vertex corrections.

where we have defined $\bar{x}_0^2 = g^2 x_0^2/(18\pi^2)$. The expansion coefficients can be found using the fact that the unperturbed solutions given in equ. (14) form an orthogonal set of eigenfunctions of K_0. The resulting expressions for $\bar{x}_0^{(i)}$ and $\Delta^{(i)}(\bar{x})$ are very similar to Rayleigh-Schroedinger perturbation theory. At first order we have

$$\bar{x}_0^{(1)} = -\frac{1}{2}\left(\bar{x}_0^{(0)}\right)^2 \int_0^1 d\bar{x} \int_0^1 d\bar{y}\, \Delta_0^{(0)}(\bar{x}) \delta\bar{K}(x_0\bar{x}, x_0\bar{y}) \Delta_0^{(0)}(\bar{y}), \qquad (17)$$

$$c_k^{(1)} = \frac{\bar{x}_0^{(0)}}{1 - \left(\frac{1}{2k+1}\right)^2} \int_0^1 d\bar{x} \int_0^1 d\bar{y}\, \Delta_0^{(0)}(\bar{x}) \delta\bar{K}(x_0\bar{x}, x_0\bar{y}) \Delta_k^{(0)}(\bar{y}), \qquad (18)$$

with $\Delta^{(1)}(x) = \sum c_k^{(1)} \Delta_k^{(0)}(x)$ and $\delta\bar{K} = g/(3\sqrt{2}\pi)\delta K$.

We can now study the role of various corrections to the kernel. The simplest contribution arises from four-fermion operators. We find

$$\delta K(x_0\bar{x}, x_0\bar{y}) = \log(b), \qquad b = \frac{512\pi^4\mu}{g^5\Lambda}\left(\frac{2}{N_f}\right)^{\frac{5}{2}}. \qquad (19)$$

This contribution does not change the shape of the gap function but it gives an $O(g)$ correction to the eigenvalue $\bar{x}_0$. This corresponds to a constant pre-exponential factor, $\Delta^{(1)} = b\Delta^{(0)}$. An important advantage of the effective field theory method is that this factor is manifestly independent of the choice of gauge. The gauge independence of the pre-exponential factor is related to the fact that this coefficient is determined by four-fermion

operators in the effective theory, and that these operators are determined by on-shell matching conditions.

Another effect that contributes to the eigenvalue at $O(g)$ is the fermion self energy [20,21]. A one-loop calculation in the high density effective theory gives [22,23,24,25,26]

$$\Sigma(p_4) = \frac{g^2 C_F}{12\pi^2} p_4 \log\left(\frac{\Lambda}{p_4}\right). \tag{20}$$

The correction to the kernel of the gap equation is

$$\delta\bar{K}(x_0\bar{x}, x_0\bar{y}) = -\frac{g^2}{9\pi^2}\,(\bar{x}_0\bar{x})\,K_0(x_0\bar{x}, x_0\bar{y}), \tag{21}$$

and the shift in the eigenvalue is given by

$$\bar{x}_0^{(1)} = -\frac{1}{2}\left(\bar{x}_0^{(0)}\right)^2 \langle 0|\delta\bar{K}|0\rangle = \frac{4+\pi^2}{8}\frac{g}{3\sqrt{2}\pi}, \tag{22}$$

where $\langle 0|\delta\bar{K}|0\rangle$ denotes the matrix element of the kernel between unperturbed gap functions, see equ. (17). At this order in g, there is no contribution from the quark-gluon vertex correction. Note that the quark self energy correction makes an $O(g)$ correction to the eigenvalue, even though it is an $O(g^2)$ correction to the kernel. This is related to the logarithmic divergence in the self energy. The perturbative expansion of $\bar{x}_0$ is of the form

$$\bar{x}_0 \sim g\log(\Delta) = O(g^0) + O(g\log(g)) + O(g) + \ldots. \tag{23}$$

Brown et al. argued that equ. (22) completes the $O(g)$ term. At this order the spin zero gap in the 2SC phase of $N_f = 2$ QCD is [21,27,13]

$$\Delta = 512\pi^4 \mu g^{-5} e^{-\frac{4+\pi^2}{8}} e^{-\frac{3\pi^2}{\sqrt{2}g}}. \tag{24}$$

In other spin or flavor channels the relevant four fermion operators are different and the pre-exponential factor is modified [5,21,28,29]. In the CFL phase of $N_f = 3$ QCD the gap is suppressed by a factor $(2/3)^{5/2}2^{-1/3}$.

6. Instanton Correction

In this section we shall focus on the correction to the perturbatively generated gap parameter which is due to instantons. If the density is very large instanton effects are exponentially small as compared to perturbative interactions. In this regime instantons are important for physical observables, like the mass of the $U(1)_A$ Goldstone mode, that receive no contribution

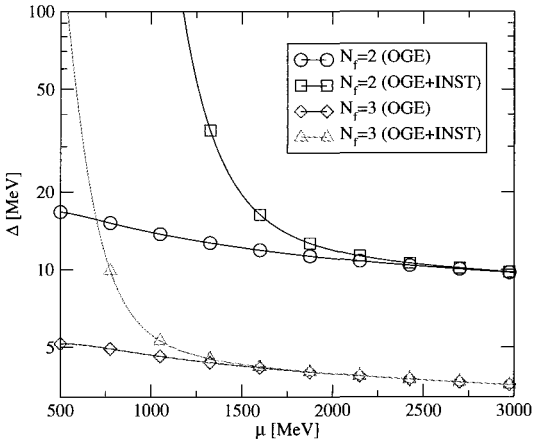

Figure 3. Instanton correction to the perturbatively generated gap in QCD with $N_f = 2$ and $N_f = 2 + 1$ flavors. We show the gap with and without instanton corrections. In the $N_f = 2 + 1$ case we have used $m_s = 150$ MeV.

from perturbative interactions, but they make no significant contribution to the gap. As the density is lowered instanton effects grow. In the following we will use the methods described in the last section in order to determine the scale at which instanton contributions to the gap become important.

Instantons induce a chirality changing four-fermion operator. In QCD with $N_f = 3$ flavors and $m_{u,d} \ll m_s$ we have

$$L = \int n(\rho,\mu)d\rho \frac{2(2\pi\rho)^4\rho^3}{4(N_c^2-1)} m_s \epsilon_{f_1 f_2}\epsilon_{g_1 g_2}\left(\frac{2N_c-1}{2N_c}(\bar\psi_{R,f_1}\psi_{L,g_1})(\bar\psi_{R,f_2}\psi_{L,g_2})\right.$$
$$\left. -\frac{1}{8N_c}(\bar\psi_{R,f_1}\sigma_{\mu\nu}\psi_{L,g_1})(\bar\psi_{R,f_2}\sigma_{\mu\nu}\psi_{L,g_2}) + (L\leftrightarrow R)\right), \qquad (25)$$

where the sum over flavors runs over up and down quarks only, $f_{1,2} = g_{1,2} = (u,d)$, and the instanton size distribution $n(\rho,\mu)$ is given by

$$n(\rho,\mu) = C_N \left(\frac{8\pi^2}{g^2}\right)^{2N_c} \rho^{-5}\exp\left[-\frac{8\pi^2}{g(\rho)^2}\right]\exp\left[-N_f\rho^2\mu^2\right], \qquad (26)$$

$$C_N = \frac{0.466\exp(-1.679N_c)1.34^{N_f}}{(N_c-1)!(N_c-2)!}, \qquad (27)$$

$$\frac{8\pi^2}{g^2(\rho)} = -b\log(\rho\Lambda), \qquad b = \frac{11}{3}N_c - \frac{2}{3}N_f\,. \qquad (28)$$

Note that equ. (25) is an effective interaction for quarks near the Fermi surface. In particular, there are no form factors that have to be included.

We also observe that the integration over sizes is cut off at $\rho \sim \mu^{-1}$. As a consequence, instanton effects are of order $\exp(-8\pi^2/g^2(\mu)) \sim (\Lambda_{QCD}/\mu)^b$. In addition to the four-fermion vertex given in equ. (25) instantons also induce a six-fermion operator. This operator has important physical effects, but it does not contribute to the gap to leading order in the effective interaction, so we will not consider it here. In QCD with $N_f = 2$ massless flavors instantons induce a four-fermion operator which can be obtained from equ. (25) by making the replacement $m_s\rho \to 1$.

We can now compute the instanton correction to the kernel of the gap equation. In the three flavor case we find $\delta K_I = \log(b_I)$ with $\log(b_I) = 9G_I/g^2$ and

$$G_I(N_f{=}3) = \frac{C_N}{\mu^2}\left(\frac{m_s}{\mu}\right)\left(\frac{\Lambda_{QCD}}{\mu}\right)^{\beta_0}\left(\frac{8\pi^2}{g^2}\right)^{2N_c} \cdot \frac{(2\pi)^2}{2(N_c^2-1)}\frac{4(N_c+1)}{N_c}\frac{\Gamma\left(\frac{\beta_0+3}{2}\right)}{2N_f^{(\beta_0+3)/2}}, \qquad (29)$$

where $\beta_0 = 11N_c/3 - 2N_f/3$ is the first coefficient of the beta function. In the two flavor case we get

$$G_I(N_f{=}2) = \frac{C_N}{\mu^2}\left(\frac{\Lambda_{QCD}}{\mu}\right)^{\beta_0}\left(\frac{8\pi^2}{g^2}\right)^{2N_c} \cdot \frac{(2\pi)^2}{2(N_c^2-1)}\frac{4(N_c+1)}{N_c}\frac{\Gamma\left(\frac{\beta_0}{2}+1\right)}{2N_f^{(\beta_0/2+1)}}. \qquad (30)$$

We note that the main difference is a suppression factor (m_s/μ) in the $N_f = 3$ flavor case. Numerical results are shown in Fig. 3. We observe that the instanton correction becomes large for $\mu \sim 1250$ MeV in $N_f = 2$ QCD and for $\mu \sim 750$ MeV in the realistic case of QCD with three flavors and a massive strange quark.

We should note that the fact that the instanton correction to the gap is on the order of 100% does not necessarily invalidate the perturbative expansion. As explained in the previous section, the quantity that is being expanded is not the gap Δ, but $\log(\mu/\Delta)$. In Fig. 4 we compare the size of the leading order $O(1/g)$ term, the sub-leading $O(\log(g))$ and $O(1)$ terms, as well as the instanton contribution to the logarithm of the gap in $N_f = 3$ QCD. We observe that exponentially small instanton contributions start to dominate over all other contact terms for $\mu \sim 600$ MeV.

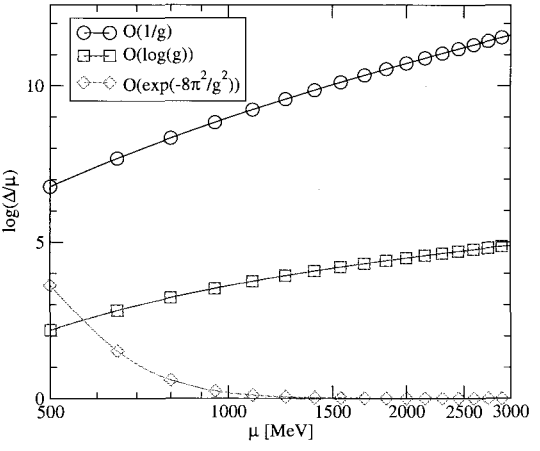

Figure 4. This figure shows successive terms in the perturbative expansion of $\log(\mu/\Delta)$ in QCD with $N_f = 3$ flavors.

For $\mu \sim 500$ MeV the instanton term becomes comparable to the leading $O(1/g)$ term and we can no longer consider instantons effects to be a small correction. In this regime it probably makes more sense to do an instanton calculation and consider perturbative gluon exchanges as a correction. This is the approach originally suggested in [3,4]. We should note, however, that for $\mu < 500$ MeV the instanton calculation requires some phenomenological input because the instanton size distribution equ. (26) is no longer reliably calculable.

Ideally, we would like to check perturbative calculations of the gap against numerical calculations on the lattice. While this cannot be done in the realistic case of QCD with $N_c = 3$ colors, the comparison is possible for QCD with $N_c = 2$ colors and an even number of flavors, or for QCD with $N_c = 3$ colors and a non-zero chemical potential for isospin rather than baryon number. In both of these cases it is also possible to separate the perturbative and instanton contributions by measuring both the gap and the mass of the $U(1)_A$ Goldstone boson [30].

7. Numerical Estimates

In this section we shall address a few more issues related to the magnitude of the gap. We will estimate the size of certain higher order corrections using numerical solutions of the gap equation. The first problem we wish to study is the importance of the fermion self energy correction. In Sect. 5 we saw

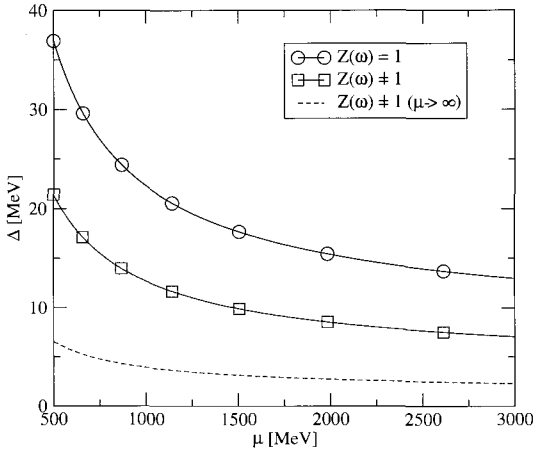

Figure 5. Numerical solution of the perturbative gap equation. We show the results with and without the fermion self energy included. We also show the asymptotic result, which corresponds to a reduction of the gap by a factor $\exp(-(\pi^2+4)/8) \simeq 0.18$.

that at asymptotically large chemical potential non-Fermi liquid effects in the fermion self energy reduce the gap by a factor $\exp(-(\pi^2+4)/8) \simeq 0.18$. In order to study the problem at moderate densities we consider the gap equation

$$\Delta(p_4) = \frac{g^2}{18\pi^2}\int_0^\mu dq_4\, Z(q_4)\frac{\Delta(q_4)}{\sqrt{q_4^2+\Delta(q_4)^2}}\log\left(\frac{b_0\mu}{|p_4^2-q_4^2|^{1/2}}\right), \qquad (31)$$

with

$$Z(q_4) = \left(1+\frac{g^2}{9\pi^2}\log\left(\frac{m_D}{q_4}\right)\right)^{-1} \qquad (32)$$

and $b_0 = 256\pi^4 g^{-5}$. If the density is very large then the scale inside the logarithm in equ. (32) does not matter. For our numerical estimates we have used the electric screening mass which is the scale suggested by one-loop calculations [24].

Numerical results are shown in Fig. 5. We observe that the gap is indeed reduced by the effects of fermion wave function renormalization, but at moderate density the reduction is smaller as compared to the asymptotic result. This is related to the fact that for $\mu \sim 500$ MeV and $\Delta \sim 50$ MeV the logarithm $\log(m_D/\Delta)$, which is formally $O(1/g)$, is numerically not very large.

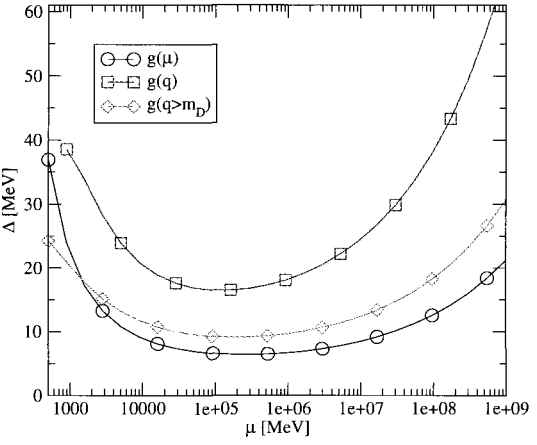

Figure 6. Numerical solution of the gap equation with running coupling constant effects included. We show the result with a fixed coupling $g = g(\mu)$, with a coupling that runs as a function of the momentum transfer as long as the momentum is larger than the electric screening scale, and a coupling that runs as a function of the momentum without any restrictions.

The second issue we wish to address is the role of running coupling constant effects in the gap equation [31]. For the numerical estimates presented in the last section we have used the weak coupling result equ. (24) with the coupling constant evaluated at the scale μ. It is easy to see that variation in the scale correspond to $O(g^2)$ corrections, which is of the same order as other terms that have been neglected.

In order to estimate the size of these effects we consider the gap equation

$$\Delta(p_4) = \int_0^{\mu} dq_4 \left\{ \frac{g^2(m_D)}{18\pi^2} \log\left(\frac{m_D^3 + \Lambda_M^3}{\Lambda_M^3} \right) + 2\log\left(\left[\frac{g^2(2\mu)}{g^2(m_D)} \right]^{4/(3\beta_0)} \right) \right\} \cdot Z(q_4) \frac{\Delta(q_4)}{\sqrt{q_4^2 + \Delta(q_4)^2}}, \tag{33}$$

where $\Lambda_M = (\pi m_D^2 |p_4 \pm q_4|/4)^{1/3}$ is the scale that characterizes magnetic gluon exchanges. For momenta above the electric screening scale we have used the one-loop running coupling at the scale set by the momentum transfer. For momenta below the screening scale the coupling is frozen. In the language if the high density effective theory this means that the we have performed the matching at the electric screening scale. The four-fermion operator acquires an anomalous dimension which is equal to the QCD beta function [32]. Below the electric screening scale the gluonic interaction is

effectively three-dimensional and does not run.

In Fig. 6 we show results obtained by solving equ. (33) numerically. For comparison we also show results obtained by solving a gap equation in which the coupling is allowed to run all the way down to the magnetic scale $(m_D^2\Delta)^{1/3}$. This approximation was suggested by Beane et al. [31]. We observe that for a moderate chemical potential $\mu \sim 500$ MeV the running coupling constant does not lead to very large effects. The reason is that there is no large hierarchy between the scales m_D and μ. If the chemical potential is very large, $\mu \sim 10$ GeV, the gap is increased by about 50%. This effect slowly disappears at asymptotically large chemical potential. The situation is different in case of the gap equation proposed by Beane et al. In that case the gap equation involves an extra large logarithm $\log(\mu/\Delta)$ and the pre-exponential factor in the asymptotic solution is modified [31].

8. Conclusions

We discussed an effective field theory for QCD at high baryon density. We studied, in particular, the problem of power counting in the high density effective theory. We showed that the power counting is complicated by "hard dense loops", i.e. loop diagrams that involve the large scale μ^2 and proposed a power counting that takes these effects into account. The modified l counting implies that hard dense loops in gluon n-point functions have to be resummed below the scale $g\mu$, and that four fermion operators are leading order in the HDET power counting.

We used the high density effective theory to study the size of instanton corrections to the gap in superfluid quark matter. We found that instanton effects are very large in the regime $\mu \sim 500$ MeV which is of physical interest. We argued that numerical calculation in QCD with $N_c = 2$ colors, or QCD with $N_c = 3$ colors and non-zero isospin chemical potential, will of great help in determining the gap in $N_c = 3$ QCD at non-zero baryon density. We also studied a renormalization group improved gap equation. We find no significant corrections as compared to a gap equation with a fixed coupling.

Acknowledgments: This work was supported in part by US DOE grant DE-FG-88ER40388.

References

1. D. Bailin and A. Love, Phys. Rept. **107**, 325 (1984).
2. M. Alford, K. Rajagopal and F. Wilczek, Phys. Lett. **B422**, 247 (1998), [hep-ph/9711395].

3. R. Rapp, T. Schäfer, E. V. Shuryak and M. Velkovsky, Phys. Rev. Lett. **81**, 53 (1998), [hep-ph/9711396].
4. M. Alford, K. Rajagopal and F. Wilczek, Nucl. Phys. **B537**, 443 (1999), [hep-ph/9804403].
5. T. Schäfer, Nucl. Phys. B **575**, 269 (2000), [hep-ph/9909574].
6. K. Rajagopal and F. Wilczek, The condensed matter physics of QCD, in: Festschrift in honor of B.L. Ioffe, 'At the Frontier of Particle Physics / Handbook of QCD', M. Shifman, ed., World Scientific, Singapore, [hep-ph/0011333].
7. M. Alford, Ann. Rev. Nucl. Part. Sci. **51**, 131 (2001), [hep-ph/0102047].
8. G. Nardulli, Riv. Nuovo Cim. **25N3**, 1 (2002), [hep-ph/0202037].
9. T. Schäfer, Quark Matter, BARC workshop on Quarks and Mesons; to appear in the proceedings, hep-ph/0304281.
10. D. H. Rischke, Prog. Part. Nucl. Phys. in press, nucl-th/0305030.
11. D. K. Hong, Phys. Lett. B **473**, 118 (2000), [hep-ph/9812510].
12. D. K. Hong, Nucl. Phys. B **582**, 451 (2000), [hep-ph/9905523].
13. T. Schäfer, Nucl. Phys. A **728**, 251 (2003) [hep-ph/0307074].
14. T. Schäfer, Phys. Rev. D **65**, 094033 (2002), [hep-ph/0201189].
15. E. Braaten and R. D. Pisarski, Phys. Rev. D **45**, 1827 (1992).
16. E. Braaten, Can. J. Phys. **71**, 215 (1993), [hep-ph/9303261].
17. R. Shankar, Rev. Mod. Phys. **66**, 129 (1994).
18. J. Polchinski, hep-th/9210046.
19. D. T. Son, Phys. Rev. D **59**, 094019 (1999), [hep-ph/9812287].
20. W. E. Brown, J. T. Liu and H. C. Ren, Phys. Rev. **D61**, 114012 (2000), [hep-ph/9908248].
21. W. E. Brown, J. T. Liu and H. C. Ren, Phys. Rev. D **62**, 054016 (2000), [hep-ph/9912409].
22. B. Vanderheyden and J. Y. Ollitrault, Phys. Rev. D **56**, 5108 (1997), [hep-ph/9611415].
23. W. E. Brown, J. T. Liu and H. c. Ren, Phys. Rev. D **62**, 054013 (2000), [hep-ph/0003199].
24. C. Manuel, Phys. Rev. D **62**, 076009 (2000), [hep-ph/0005040].
25. C. Manuel, Phys. Rev. D **62**, 114008 (2000), [hep-ph/0006106].
26. D. Boyanovsky and H. J. de Vega, Phys. Rev. D **63**, 034016 (2001), [hep-ph/0009172].
27. Q. Wang and D. H. Rischke, Phys. Rev. D **65**, 054005 (2002), [nucl-th/0110016].
28. T. Schäfer, Phys. Rev. D **62**, 094007 (2000), [hep-ph/0006034].
29. A. Schmitt, Q. Wang and D. H. Rischke, Phys. Rev. D **66**, 114010 (2002), [nucl-th/0209050].
30. T. Schafer, Phys. Rev. D **67**, 074502 (2003) [hep-lat/0211035].
31. S. R. Beane, P. F. Bedaque and M. J. Savage, Nucl. Phys. A **688**, 931 (2001) [nucl-th/0004013].
32. T. Schäfer, in preparation.

AXIAL ANOMALY IN DENSE QCD

DEOG KI HONG, BEONG IK HUR, YOUNG JIN SOHN
Department of Physics,
Pusan National University,
Busan 609-735, Korea
E-mail: dkhong@pnu.edu

TAE-SUN PARK
Department of Physics, KIAS
Seoul 207-43, Korea
E-mail: tspark@kias.re.kr

By explicit calculations, we show that the axial anomaly does not depend on the chemical potential in dense QCD. We also calculated the axial anomaly in the high density effective theory of QCD to find that the anomaly matching leads to additional operators in the effective theory.

1. Introduction

New emergent phenomena often appear at extreme conditions, unseen at normal circumstances. At extreme density, a density higher than the nuclear density, $\rho = 0.16\ \mathrm{fm}^{-3}$, which might be reached in the core of compact stars like neutron stars or in the relativistic heavy ion collision(RHIC), the asymptotic freedom of QCD predicts quark matter. The ground state of matter turns out to be a color superconducting state with rather rich phase structures[1].

Not only in compact stars but also in collider experiments, photon can be a useful probe to newly proposed phases of quark matter, since it can propagate into a color superconductor and interact easily with its low-energy excitations[2]. It is therefore quite important to find out how quark matter responds to external electromagnetic probes. In this talk, we consider among others the axial anomaly in quark matter, which is relevant to the anomalous decay of pions into two photons.

It is well-known that the axial vector currents is not conserved due to quantum effects in regularizing the ultraviolet divergences. When there is no matter, the divergence of the axial vector current is given as[3]

$$\langle \partial_\mu J_5^\mu \rangle = \frac{e^2}{16\pi^2} \epsilon^{\mu\nu\alpha\beta} F_{\mu\nu} F^{\alpha\beta}. \tag{1}$$

Since hot and dense matter does not change the structure of ultraviolet divergences, one expects that the anomaly is independent of temperature and density. However, since the Lorentz symmetry is broken in medium, there could be other terms besides the Pontriagin index, contributing to the axial anomaly. A prime candidate is the Chern-Simons term,

$$\langle \partial_\mu J_5^\mu \rangle \propto \epsilon^{ijk} A_i F_{jk} \tag{2}$$

which is invariant under rotations and gauge transformations. As discussed in the case of finite temperature[4], the anomaly condition

$$q^\mu T_{\mu\alpha\beta} = \frac{i}{2\pi^2} \epsilon_{\alpha\beta\rho\sigma} k_1^\rho k_2^\sigma \tag{3}$$

does not necessarily imply the singularity of the axial-vector-vector current correlator $T_{\mu\alpha\beta} = \langle J_\mu J_\alpha J_\beta^5 \rangle$ at $q^2 = 0$ in medium.

2. Axial Anomaly in Full QCD

The axial-anomaly(AA) can be studied the divergence of the following three-point function,

$$T_{\mu\nu\lambda}(k_1, k_2) = i \int d^4x_1 \int d^4x_2 \, \langle 0 | T J_\mu(x_1) J_\nu(x_2) J_\lambda^5(0) | 0 \rangle \, e^{ik_1 \cdot x_1 + ik_2 \cdot x_2} \tag{4}$$

where $J_\mu(x) = \bar{\psi}(x) \gamma_\mu \psi(x)$ and $J_\mu^5(x) = \bar{\psi}(x) \gamma_\mu \gamma_5 \psi(x)$ denote the vector and axial-vector current, respectively, and $\psi(x)$ is the quark field. At the tree-level, Ward identities read as $k_1^\mu T_{\mu\nu\lambda}(k_1, k_2) = k_2^\nu T_{\mu\nu\lambda}(k_1, k_2) = 0$ and $(k_1 + k_2)^\lambda T_{\mu\nu\lambda}(k_1, k_2) = 0$. Here and hereafter, we neglect quark masses. In free space, it has been known that we cannot satisfy all the Ward identities simultaneously due to quantum fluctuations; Requiring the vector Ward identities to be preserved, we have

$$\Delta_{\mu\nu}(k_1, k_2) \equiv (k_1 + k_2)^\lambda T_{\mu\nu\lambda}(k_1, k_2) = \frac{i}{2\pi^2} \epsilon^{\mu\nu\alpha\beta} k_{1\alpha} k_{2\beta}. \tag{5}$$

In this section, we will prove that this equation holds even in matter.

Let us begin with writing QCD Lagrangian with the chemical potential μ,

$$\mathcal{L}_{QCD} = \bar{\psi}(x)(i \not{D} - m + \mu\gamma_0)\psi(x) - \frac{1}{4}(G_{\mu\nu}^a)^2. \tag{6}$$

The corresponding free quark propagator reads

$$S_F(p;\mu) \equiv -i \int d^4x\, e^{ip\cdot x}\, \langle 0|T\psi(x)\bar{\psi}(0)|0\rangle$$
$$= \frac{1}{(1+i\epsilon)p_0\gamma^0 - \vec{p}\cdot\vec{\gamma} + \mu\gamma^0 - m}, \tag{7}$$

where ϵ is the positive infinitesimal.

The anomaly amplitude $\Delta^{\mu\nu}$ in QCD reads

$$\Delta^{\mu\nu}(\mu) = -\int \frac{d^4p}{(2\pi)^4} \mathrm{tr}\left[S_F(p;\mu)\ \not{q}\gamma_5 S_F(p-q;\mu)\,\gamma^\nu\, S_F(p-k_1;\mu)\,\gamma^\mu\right]$$
$$+(\mu\leftrightarrow\nu,\ k_1\leftrightarrow k_2) \tag{8}$$

where $q^\mu \equiv (k_1+k_2)^\mu$. As mentioned, the loop-integral is linearly divergent and a care is needed in doing the regularization. To amuse this, let us review the usual trick in evaluating the anomaly in free-space,

$$\not{q}\gamma_5 = \gamma_5(\not{p} - \not{q} - m) + (\not{p} - m)\gamma_5 + 2m\gamma_5 - \{\not{p},\ \gamma_5\}\,. \tag{9}$$

The contributions from the first two terms are identical but with opposite sign, provided that the integral is invariant under the change of variable, $p^\mu \to p^\mu + a^\mu$. If translational invariance is imposed in evaluating loop integrals, the contributions from the first two terms cancel each other exactly. The third term is proportional to the quark mass, and gives us vanishing contribution when we put m to be zero. But if use Pauli-Villars regularization which introduces fictitious quark field with a large mass M, the contribution from the third term cannot be neglected and actually account for the axial-anomaly in this regularization. Finally the last term vanishes identically when $D = 4$, D is the spacetime dimension.[a] Thus, there would be no AA if there is a regularization that has [1] translational invariance, [2] defined in $D = 4$ and [3] can be evaluated with vanishing quark masses. In reality, there is no such a regularization, and gives us the non-vanishing AA. For example, in CO, there is no translational invariance and the first two terms give us the AA. In DR, the last term is non-zero. In PV, we need to consider the limit of large quark mass since $\Delta^{\mu\nu}_{PV} = \lim_{M\to\infty}[\Delta^{\mu\nu}(m) - \Delta^{\mu\nu}(M)]$.

In sharp contrary to the free-space case, we observe that the medium modification

$$\bar{\Delta}^{\mu\nu}(\mu) \equiv \Delta^{\mu\nu}(\mu) - \Delta^{\mu\nu}(0) = \int_0^\mu d\mu' \frac{\partial}{\partial\mu'}\Delta^{\mu\nu}(\mu') \tag{10}$$

[a] Even in $D \neq 4$, $\{\not{q}, \gamma_5\}$ equals to zero since q^μ is a tangent vector lying in $1+3$ dimension.

is UV-finite and can be evaluated without any regulator. To show this, let us rewrite (8) using the change of variable[b],

$$p^\mu \to p'^\mu \equiv p^\mu + u^\mu \mu, \tag{11}$$

where $u^\mu \equiv (1, \vec{0})$. We then observe, omitting primes on p,

$$\begin{aligned} S_F(p - u\mu; \mu) &= (\not{p} + m) D_F(p; \mu), \\ D_F(p; \mu) &= \frac{1}{p^2 - m^2 + i\epsilon p_0 (p_0 - \mu)}. \end{aligned} \tag{12}$$

We further note that

$$\frac{\partial}{\partial \mu} D_F(p; \mu) = 2\pi i\, \delta(p^2 - m^2)\delta(p^0 - \mu) = 2\pi i\, \frac{\delta(p^0 - E_p)\delta(E_p - \mu)}{2E_p} \tag{13}$$

where $E_p \equiv \sqrt{\vec{p}^2 + m^2}$. That is, derivation with respect to μ makes the loop integral into an angle integration, which is UV-finite.

For an explicit proof, we consider $m = 0$ case. In (9), only the first two terms survive and gives us

$$\begin{aligned} &\mathrm{tr}[\not{p}\ \not{q}\gamma_5 (\not{p} - \not{q})\gamma^\nu (\not{p} - \not{k}_1)\gamma^\mu] \\ &= -4i\epsilon^{\mu\nu\alpha\beta} \left[p^2 k_{2\alpha}(p - k_1)_\beta + (p - q)^2 k_{1\alpha} p_\beta\right]. \end{aligned} \tag{14}$$

We thus have

$$\begin{aligned} \frac{\partial}{\partial \mu}\Delta^{\mu\nu}(\mu) &= 4i\epsilon^{\mu\nu\alpha\beta} \int \frac{d^4p}{(2\pi)^4} \frac{\partial}{\partial \mu} \Big[k_{2\alpha}(p - k_1)_\beta D_F(p - q; \mu) D_F(p - k_1; \mu) \\ &\qquad + k_{1\alpha} p_\beta D_F(p; \mu) D_F(p - k_1; \mu)\Big] \\ &\quad + (\mu \leftrightarrow \nu,\ k_1 \leftrightarrow k_2) \\ &= 4i\epsilon^{\mu\nu\alpha\beta} \int \frac{d^4p}{(2\pi)^4} 2\pi i\, \frac{\delta(p^0 - E_p)\delta(E_p - \mu)}{2E_p} \\ &\qquad \cdot \left(k_{2\alpha} p_\beta \left[D_F(p + k_2; \mu) + D_F(p - k_2; \mu)\right]\right. \\ &\qquad \left. + k_{1\alpha} p_\beta \left[D_F(p + k_1; \mu) + D_F(p - k_1; \mu)\right]\right) \\ &\quad + (\mu \leftrightarrow \nu,\ k_1 \leftrightarrow k_2). \end{aligned} \tag{15}$$

Being odd under $\mu \leftrightarrow \nu$ while even under $k_1 \leftrightarrow k_2$, they cancel exactly with the crossing terms,

$$\frac{\partial}{\partial \mu}\Delta^{\mu\nu}(\mu) = 0. \tag{16}$$

[b]Here one can say that we are using dimensional regularization which guarantees the translational invariance.

Inserting the AA in free-space, we have

$$\Delta^{\mu\nu}(\mu) = \frac{i}{2\pi^2}\epsilon^{\mu\nu\alpha\beta}k_{1\alpha}k_{2\beta}, \tag{17}$$

which is independent of μ.

3. Axial Anomaly in High Density Effective Theory

We can do the same calculation using high density effective theory(HDET) which is constructed by integrating out "fast" modes whose energy is higher than the chemical potential energy $E > \mu$ [5]. In calculating the triangle diagram which is linearly divergent one has to regularize it. There are many methods of regularization. One of them is the Pauli-Villars regularization in which a new field with large mass is introduced. However, the introduction of a fictitious field having large mass may cause some discrepancies in the effective theory. The most convenient way of regularizing a Feynman diagram is the dimensional regularization. Obviously γ_5 is defined only in 4-dimensional space-time. Thus we define a gamma matrix γ_s, a substitute for γ_5, as a product of all gamma matrices in a general dimension in order to satisfy key properties of projection operators in HDET.

$$\gamma_\parallel^\mu P_\pm = P_\mp \gamma_\parallel^\mu, \qquad \gamma_\perp^\mu P_\pm = P_\pm \gamma_\perp^\mu, \tag{18}$$

where the projection operators and gamma matrices parallel(perpendicular) to the Fermi velocity are given by

$$\begin{aligned} P_\pm &= \frac{1 \pm \gamma_s \vec{\gamma}\cdot\vec{v_1}\vec{\gamma}\cdot\vec{v_2}}{2}, \quad \vec{v}_F = \vec{v}_1 \times \vec{v}_2 \\ \gamma_\parallel^\mu &= (\gamma_0,\ \vec{v}_F\vec{v}_F\cdot\vec{\gamma}), \quad \gamma_\perp^\mu = \gamma^\mu - \gamma_\parallel^\mu \end{aligned} \tag{19}$$

$\vec{v}_1$ and $\vec{v}_2$ are defined to be an orthonormal set of unit vectors on the surface of the 2-dimensional Fermi sphere. In HDET quark field with momentum close to the Fermi momentum can be viewed as a composite of two components with different energy,

$$\psi(x) = e^{i\mu\vec{v}_F\cdot\vec{x}}\psi_+(\vec{v}_F, x) + e^{i\mu\vec{v}_F\cdot\vec{x}}\psi_-(\vec{v}_F, x) \tag{20}$$

where ψ_+ modes correspond to quarks near the Fermi momentum, while ψ_- modes correspond to antiquarks which are irrelevant at the energy of our interest due to the presence of the large Fermi sphere. Then the Lagrangian for quarks becomes

$$\begin{aligned} &\bar{\psi}(i\not{D} + \mu\gamma^0)\psi(x) \\ &= \bar{\psi}_+(\vec{v}_F, x)i\gamma_\parallel^\mu D_\mu\psi_+(\vec{v}_F, x) + \bar{\psi}_-(\vec{v}_F, x)\gamma^0(2\mu + iD_\parallel)\psi_-(\vec{v}_F, x) \\ &+ \bar{\psi}_-(\vec{v}_F, x)i\gamma_\perp D_\mu\psi_+(\vec{v}_F, x) + \bar{\psi}_+(\vec{v}_F, x)i\gamma_\perp D_\mu\psi_-(\vec{v}_F, x) \end{aligned} \tag{21}$$

where we have used (18) and $D_{\|} = \bar{V}^{\mu} D_{\mu}$ with $\bar{V}^{\mu} = (1, -\vec{v}_F)$ and $V^{\mu} = (1, \vec{v}_F)$.

The axial current is expanded in terms of powers of $\frac{1}{\mu}$.

$$\langle \partial_{\mu} J_5^{\mu} \rangle = \mu^2 \Delta_{(2)} + \mu \Delta_{(1)} + \Delta_{(0)} + \frac{1}{\mu} \Delta_{(-1)} + \cdots \tag{22}$$

Consider the anomaly amplitude of order of μ^2, $\Delta_{(2)}$ which corresponds to the triangle diagram with three intermediate fermions ψ_+.

$$\begin{aligned}
\Delta_{(2)}^{\alpha\beta} &= -(-ie)^2 \int \frac{d^4 l}{(2\pi)^4} \mathrm{tr}[\not{q} \gamma_5 S_F^+(l + k_2) \gamma^{\beta} S_F^+(l) \gamma^{\alpha} S_F^+(l - k_1)] \\
&\quad + (\alpha \leftrightarrow \beta, \quad k_1 \leftrightarrow k_2) \\
&= -(-ie)^2 \int \frac{d^4 l}{(2\pi)^4} \mathrm{tr} \left[\not{q}_{\|} \gamma_5 P_+^0 \frac{i}{(\not{l} + \not{k}_2)_{\|}^2} \gamma^{\beta} \frac{i}{\not{l}_{\|}^2} \gamma^{\alpha} \frac{i}{(\not{l} - \not{k}_1)_{\|}^2} \right] \\
&\quad + (\alpha \leftrightarrow \beta, \quad k_1 \leftrightarrow k_2) \\
&= 0
\end{aligned} \tag{23}$$

where $S_F^+(l)$ is the propagator for ψ_+ and it can be obtained from (21).

$$S_F^+(l) = P_+ \frac{i}{\not{l}_{\|}} \tag{24}$$

One can expand the propagator for ψ_- in terms of $\frac{1}{\mu}$ and calculate the anomaly amplitudes order by order like (22).

$$S_F^-(l) = P_- \frac{i\gamma^0}{2\mu} \left[1 - \frac{i\gamma^0 \not{l}_{\|}}{2\mu} + \cdots \right] \equiv S_F^{-\prime} + S_F^{-\prime\prime} + \cdots \tag{25}$$

We have seen that the term proportional to μ^2 does not contribute to the axial anomaly. Using the first term in (25), $S_F^{-\prime}$, we obtain the next-leading terms

$$\begin{aligned}
\Delta_{(1)a}^{\alpha\beta} &= -ie^2 \int \frac{d^4 l}{(2\pi)^4} \mathrm{tr} \left[\not{q} \gamma_5 S_F^+(l - k_1) \gamma^{\alpha} S_F^{-\prime} \gamma^{\beta} S_F^+(l + k_2) \right] \\
&\quad + (\alpha \leftrightarrow \beta, \quad k_1 \leftrightarrow k_2) \\
&= 0 \\
\Delta_{(1)b}^{\alpha\beta} &= 0 = \Delta_{(1)c}^{\alpha\beta}
\end{aligned} \tag{26}$$

where the subcripts a, b, c denote three triangle diagrams according to the possible fermion line for ψ_-. Therefore there is no axial anomaly up to order of μ which is consistent with the argument in Section **2**. Similarly

if we adopt the second term as the ψ_- propagator from (25), we get the anomaly amplitudes as

$$\begin{aligned}\Delta^{\alpha\beta}_{(0)a} &= -ie^2 \int \frac{d^4l}{(2\pi)^4} \mathrm{tr}\left[\not{A}\gamma_5 S_F^+(l-k_1)\gamma^\alpha S_F^{-\prime\prime}\gamma^\beta S_F^+(l+k_2)\right] \\ &\quad +(\alpha \leftrightarrow \beta,\ \ k_1 \leftrightarrow k_2) \\ &= \frac{ie^2}{6\pi^2}\delta^{\alpha i}\delta^{\beta j}k_{1\mu}k_{2\nu}\epsilon^{i\beta\mu j} \end{aligned} \tag{27}$$

where i, j means the spatial components of Dirac indices. Summing all the contributions at this order gives the axial anomaly

$$\Delta^{\alpha\beta}_{(0)} = \Delta^{\alpha\beta}_{(0)a} + \Delta^{\alpha\beta}_{(0)b} + \Delta^{\alpha\beta}_{(0)c} \tag{28}$$

$$\Delta^{0i}_{(0)} = \frac{1}{3}\Delta^{0i}_{\mathrm{full}}, \quad \Delta^{ij}_{(0)} = \frac{2}{3}\Delta^{ij}_{\mathrm{full}} \tag{29}$$

Note that the amplitudes computed using HDET differ by some factors from calculations in full theory. We find that in effective theory additional operators are needed for anomaly matching.

References

1. For reviews, see D.K. Hong, *Acta Phys. Polon.* B **32**, 1253 (2001) [arXiv:hep-ph/0101025]; M. Alford, hep-ph/0102047; K. Rajagopal and F. Wilczek, hep-ph/0011333; S.D.H. Hsu, hep-ph/0003140.
2. C. Manuel and K. Rajagopal, hep-ph/0107211; P. Jaikumar, R. Rapp and I. Zahed, hep-ph/0112308.
3. J.S. Bell and R. Jackiw, *Nuovo Cim.* A **60**, 47 (1969); S.L. Adler, *Phys. Rev.* **177**, 2426 (1969).
4. H. Itoyama and A.H. Mueller, *Nucl. Phys.* B **218**, 349 (1983); Y.L. Liu and G.J. Ni, *Phys. Rev.* D **45**, 1378 (1992); A. Gomez Nicola and R.F. Alvarez-Estrada, *Int. J. Mod. Phys.* A **9**, 1423 (1994).
5. D.K. Hong, *Phys. Lett.* B **473**, 118 (2000); D.K. Hong, *Nucl. Phys.* B **582**, 451 (2000).

ANDREEV REFLECTION IN COLOR SUPERCONDUCTIVITY

M. SADZIKOWSKI
H. Niewodniczański Institute of Nuclear Physics
Radzikowskiego 152, 31-342 Kraków, Poland

M. TACHIBANA
Theoretical Physics Laboratory, RIKEN
2-1 Hirosawa Wako, Saitama 351-0198, Japan

In this paper we discuss the phenomenon of the Andreev reflection of quarks at the interface between different types of QCD phases, appeared in QCD at asymptotically high densities.

1. Introduction

Quantum Chromodynamics is a non-abelian quantum field theory describing interactions between quarks and gluons. It describes the effect of confinement at low energy [1] and asymptotic freedom at high energy [2] compared to the QCD scale $\Lambda_{QCD} \sim 200$ MeV. The only known systematic approach to low energy QCD are lattice calculations. The physics of the high energy QCD can be controled by the perturbation analysis in strong coupling constant. There are three different types of phenomena of strong interactions which one can hope to describe in the perturbative regime: high energy scattering processes, high temperature and high baryon density systems. Especially the high baryon density quark matter at low temperatures is expected to exist in the cores of the compact stars [3]. Unfortunately, here also the densities are not high enough for direct perturbative calculations (by many orders of magnitude). Then the only possible approches are based on universal features of the phase transitions and models. The lattice approach fails at non-zero density physics because of the sign problem.

In this paper we focus on the high baryon density phases at $T = 0$. Since long ago one expected supeconducting phenomena in this kinematical region [4]. However only recently there have been a new interest in the

subject because new features were found in the theory [5,6,7]. If the energy scale is set by the quark chemical potential μ one can expect that at high enough densities there are a gas of free quarks and gluons. However the interaction between quarks mediated by the one-gluon exchange is attractive in the color $\bar{\mathbf{3}}$ channel. This leads to the well known phenomenon of the Cooper instability of the Fermi sea and finally results in the creation of a new vacuum - the condensate of Cooper pairs. This is the version of the BCS theory of superconductivity [8] applied to the interacting quark matter. The picture is generally correct, however somehow oversimplified. There are subtle but important differences between BCS theory and superconductivity in QCD which follow from the non-abelian character of the interation in quark-quark scattering (eg. [7]). The review of the whole subject can be found in [9]. Despite of some differences the high density QCD shares a lot of features with condensed matter systems.

Our subject of interest are scattering processes at the interfaces between different types of QCD phases. These are the analogs of the Andreev reflection [10] in condensed matter systems. This reflection appears at the junction between conductors and superconductors. In the case of dense QCD the role of conductor is played by the free Fermi gas of quarks and superconductor is 2SC or CFL phases of QCD. In this paper we consider the interface between 2SC and CFL phase. We shall show that this interface is the most general in a sense that it already contains the other cases: free quarks/2SC [11] and more: 2SC/2SC' and one only peculiar to 2SC/CFL. The case of free quarks/CFL interface [12] has to be considered independently.

2. Superconductivity in QCD

The perturbative approach to high density QCD is well established at much higher densities than one can expect in the cores of the compact stars. Thus the use of models are inevitable in the description of interesting physics. This is the approach we chose in this paper. The one gluon exchange suggests that the diquark condensate is created in color and flavor antisymmetric scalar channel. Similar feature one can also find using instanton-based models. The effective hamiltonian describing quark interaction with the pseudoscalar condensate at the high baryon density can be written in the general form (for the review see [9]):

$$H = \int d^3x \left[\sum_{a,i} \psi_a^{i\,\dagger}(-i\vec{\alpha}\cdot\vec{\nabla} - \mu)\psi_a^i + \sum_{a,b,i,j} \Delta_{ab}^{ij\,*}(\psi_a^{i\,T} C\gamma_5 \psi_b^j) + \text{h.c} \right] \quad (1)$$

where ψ_a^i are Dirac bispinors, a, b color indices, i, j flavor indices, C the charge conjugation matrix and μ is the quark chemical potential. At zero temperature the condensate Δ_{ab}^{ij} is a vacuum expectation value of the 2-point field correlator:

$$\langle \psi_a^{iT} C\gamma_5 \psi_b^j \rangle = \Delta_{ab}^{ij} \tag{2}$$

In the case of two flavors, the gap matrix (2) becomes:

$$\Delta_{ab}^{ij} = \tilde{\Delta}\epsilon^{ij}\epsilon_{ab3} \tag{3}$$

where the third direction in color space was chosen arbitrarily. This combination breaks gauge symmetry $SU(3)_c \to SU(2)_c$ whereas chiral symmetry $SU(2)_L \times SU(2)_R$ remains untouched. This is the 2SC phase. The Cooper pairs are created between the quarks of different two colors and flavors and third color quarks are unpaired. The lowest energy excitations are of course unpaird quarks. The quasiparticles are separeted by the gap $\tilde{\Delta}$ from the vacuum. The value of the gap depends on the model and is usualy in the range $50 - 150$ MeV.

For the case of three flavors the gap parameter takes the form[a]:

$$\Delta_{ab}^{ij} = \Delta\epsilon^{ijk}\epsilon_{kab}. \tag{4}$$

This is color-flavor locked (CFL) phase. The gauge symmetry and global chiral symmetry are broken according to the scheme $SU(3)_c \times SU(3)_L \times SU(3)_R \to SU(3)_{L+R+c}$. The baryon $U(1)$ symmetry is also broken. All quarks are gapped in Cooper pairs with different colors and flavors. The lowest excitations are nine Nambu-Goldstone bosons related to the spontaneous symmetry breaking of global symmetries. There is also additional Nambu-Goldstone boson connected to the breaking of restored axial symmetry $U_A(1)$. The value of the gap is model dependent of the order of the 2SC gap but usualy slightly smaller.

[a]There is also a small admixture of the condensate in color symmetric **6** channel but we neglect it in our considerations.

The gap matrix can be written in general as:

$$\Delta_{ij}^{ab} = \begin{pmatrix} 0 & \Delta_{ud} & \Delta_{us} & & & & & & \\ \Delta_{ud} & 0 & \Delta_{ds} & & & & & & \\ \Delta_{us} & \Delta_{ds} & 0 & & & & & & \\ & & & 0 & -\Delta_{ud} & & & & \\ & & & -\Delta_{ud} & 0 & & & & \\ & & & & & 0 & -\Delta_{us} & & \\ & & & & & -\Delta_{us} & 0 & & \\ & & & & & & & 0 & -\Delta_{ds} \\ & & & & & & & -\Delta_{ds} & 0 \end{pmatrix} \tag{5}$$

in the basis

$$(u_{red}, d_{green}, s_{blue}, d_{red}, u_{green}, s_{red}, u_{blue}, s_{green}, d_{blue}), \tag{6}$$

where:

$$\Delta_{us} = \Delta_{ds} = 0,\ \Delta_{ud} = \tilde{\Delta} \quad \text{for 2SC} \tag{7}$$

$$\Delta_{us} = \Delta_{ds} = \Delta_{ud} = \Delta, \quad \text{for CFL} \tag{8}$$

¿From the gap matrix structre one can easily recognize the (u_{red}, d_{green}), (u_{green}, u_{red}) pairings in 2SC phase. The quasiparticle excitations are two doublet representations of the remaining unbroken symmetry $SU(2)_L \times SU(2)_c$ of given chirality L. The second similar set exists for oposite chirality. The unpaird quarks are singlets under color rotations $SU(2)_c$ and doublets under chiral symmetries. All of the excitations have the same gap $\tilde{\Delta}$. The detail wave-functions of quasiparticle are given in Appendix B. For the CFL phase we have pairings: (d_{red}, u_{green}), (s_{red}, u_{blue}), (s_{green}, d_{blue}) similar to the 2SC and the combination of $(u_{red}, d_{green}, s_{blue})$ which is essentialy new for the CFL phase. After diagonalization of the matrix we can find 8 excitations with the gap Δ and one excitation with the gap 2Δ. These are octet and singlet representations of the unbroken $SU(3)_{L+R+c}$ symmetry.

3. Andreev reflection in superconducting QCD

In this section, let us consider the Andreev reflection at the interface consisting of two different superconductors in QCD, that is, the 2SC/CFL interface since we find it is the most general case among the possible interfaces. As is obvious from the expression of the gap matrix (5) with the conditions (7) and (8), there are three kinds of possibilities of the quark scatterings at this interface.

- (s_{red}, u_{blue}) and/or (s_{green}, d_{blue}): in this case, the Andreev reflection is similar to QGP/2SC because strange quark as well as blue up and down quarks are unpaired in the 2SC phase. This interface has already been studied [11].
- (d_{red}, u_{green}): in this case, the reflection is 2SC/2SC' - like because the gap of each phase is, in general, different.
- $(u_{red}, d_{green}, s_{blue})$: in this case, the reflection is a mixture of (QGP-2SC)/CFL interface. This happens because in the 2SC phase the u_{red}, d_{green} quarks are paired whereas strange quarks remain free.

Since the last two cases are specific to the 2SC/CFL interface and have not been studied so far, let us restrict our consideration into those cases. The comparison to other possibilities would be given at the end of this section.

Let us start with the 2SC/2SC' case. Physical setup we are interested in is that the interface is placed at $z = 0$ in space. For $z < 0$, we have 2SC phase and for $z > 0$, CFL phase and we provide the boundary condition that matches the wavefunctions at $z = 0$.

For $z < 0$, the wavefunction takes the form as (below we put $m = 0$ for simplicity)

$$\Psi_<(z) = \begin{pmatrix} e^{i\frac{\delta_s}{2}}\sqrt{\frac{E+\lambda}{2E}}\varphi^u_{\uparrow R} \\ e^{-i\frac{\delta_s}{2}}\sqrt{\frac{E-\lambda}{2E}}h^{d\dagger \mathrm{T}}_{\downarrow L} \end{pmatrix} e^{ik_1 z - iEt} + A \begin{pmatrix} e^{i\frac{\delta_s}{2}}\sqrt{\frac{E+\lambda}{2E}}\varphi^u_{\uparrow R} \\ e^{-i\frac{\delta_s}{2}}\sqrt{\frac{E-\lambda}{2E}}h^{d\dagger \mathrm{T}}_{\downarrow L} \end{pmatrix} \times e^{-ik_1 z - iEt} + B \begin{pmatrix} e^{i\frac{\delta_s}{2}}\sqrt{\frac{E-\lambda}{2E}}\varphi^u_{\uparrow R} \\ e^{-i\frac{\delta_s}{2}}\sqrt{\frac{E+\lambda}{2E}}h^{d\dagger \mathrm{T}}_{\downarrow L} \end{pmatrix} e^{-ik_2 z - iEt}, \tag{9}$$

while for $z > 0$,

$$\Psi_>(z) = C \begin{pmatrix} e^{i\frac{\delta_c}{2}}\sqrt{\frac{E+\xi}{2E}}\varphi^u_{\uparrow R} \\ e^{-i\frac{\delta_c}{2}}\sqrt{\frac{E-\xi}{2E}}h^{d\dagger \mathrm{T}}_{\downarrow L} \end{pmatrix} e^{ip_1 z - iEt} + D \begin{pmatrix} e^{i\frac{\delta_c}{2}}\sqrt{\frac{E-\xi}{2E}}\varphi^u_{\uparrow R} \\ e^{-i\frac{\delta_c}{2}}\sqrt{\frac{E+\xi}{2E}}h^{d\dagger \mathrm{T}}_{\downarrow L} \end{pmatrix} e^{ip_2 z - iEt}, \tag{10}$$

where $k_1 = \mu + \lambda, k_2 = -\mu + \lambda, p_1 = \mu + \xi$ and $p_2 = -\mu + \xi$. $\xi \equiv \sqrt{E^2 - \Delta^2}$ and $\lambda \equiv \sqrt{E^2 - \tilde{\Delta}^2}$. $\tilde{\Delta}$ is the gap in the 2SC phase. The angles δ_s and δ_c are phases of the gap parameters in 2SC and CFL superconductors respectively. The bispinors φ_R, h_L are desribed in Appendix A of Ref.[14].

By matching these wavefunctions at $z = 0$, we find the results as follows;

$$
\begin{aligned}
A &= 0, \\
B &= \frac{\sqrt{(E-\xi)(E+\lambda)}e^{i\alpha} - \sqrt{(E+\xi)(E-\lambda)}}{\sqrt{(E+\xi)(E+\lambda)} - \sqrt{(E-\xi)(E-\lambda)}e^{i\alpha}} + O(1/\mu), \\
C &= \frac{2\lambda e^{i\frac{\alpha}{2}}}{\sqrt{(E+\xi)(E+\lambda)} - \sqrt{(E-\xi)(E-\lambda)}e^{i\alpha}} + O(1/\mu), \\
D &= 0,
\end{aligned} \tag{11}
$$

where $\alpha = \delta_s - \delta_c$ is a phase difference of the gaps crossing the interface. Note here that the coefficients A and D exactly vanish in the massless limit. First of all, the transition and reflection coefficients, when $E > \Delta, \tilde{\Delta}$, are given by the formulae:

$$
\begin{aligned}
T &= \frac{\xi}{\lambda}|C|^2 = \frac{4\lambda\xi}{(E+\xi)(E+\lambda)}\frac{1}{1+r^2-2r\cos\alpha}. \\
R &= 1 - T
\end{aligned} \tag{12}
$$

where

$$
r = \sqrt{\frac{(E-\lambda)(E-\xi)}{(E+\lambda)(E+\xi)}} \tag{13}
$$

whereas for $\Delta < E < \tilde{\Delta}$, $T = 0$ and of course $R = 1$. The conserved current is defined as $j = \psi_>^\dagger \vec{\alpha}\psi_> = \psi_<^\dagger \vec{\alpha}\psi_<$ and coincides at both sides of the interface:

$$
j = \begin{cases} 0 & \text{for} \quad \Delta > E > \tilde{\Delta} \\ 2\mu\frac{\xi}{E}\frac{4\lambda^2}{(E+\xi)(E+\lambda)(1+r^2-2r\cos\alpha)} & \text{for} \quad E > \Delta, \tilde{\Delta} \end{cases} \tag{14}
$$

The coefficients and currents depend on the phase difference α of the gap parameters. We suggest that this combination is a gauge invariant quantity. Indeed in the case of $U(1)$ superconductors α variable is responsible for many interesting physical phenomena like, for example, the Josephson effect.

Let us move to the case (QGP - 2SC)/CFL interface (the mixed case). In this case, the basis of the wavefunction must be

$$
\begin{pmatrix} \psi^u_{red} \\ \psi^d_{green} \\ \psi^s_{blue} \\ \psi^{u\dagger \mathrm{T}}_{red} \\ \psi^{d\dagger \mathrm{T}}_{green} \\ \psi^{s\dagger \mathrm{T}}_{blue} \end{pmatrix} \tag{15}
$$

In the 2SC side, the wavefunction takes the form [14]:

$$\Psi_<(z) \equiv \begin{pmatrix} e^{i\frac{\delta_s}{2}}\sqrt{\frac{E+\lambda}{2E}}\varphi^u_{\uparrow R} \\ 0 \\ 0 \\ 0 \\ e^{-i\frac{\delta_s}{2}}\sqrt{\frac{E-\lambda}{2E}}h^{d\dagger \mathrm{T}}_{\downarrow L} \\ 0 \end{pmatrix} e^{ik_1 z}$$

$$+ A \begin{pmatrix} e^{i\frac{\delta_s}{2}}\sqrt{\frac{E+\lambda}{2E}}\varphi^u_{\uparrow R} \\ 0 \\ 0 \\ 0 \\ e^{-i\frac{\delta_s}{2}}\sqrt{\frac{E-\lambda}{2E}}h^{d\dagger \mathrm{T}}_{\downarrow L} \\ 0 \end{pmatrix} e^{-ik_1 z} + B \begin{pmatrix} e^{i\frac{\delta_s}{2}}\sqrt{\frac{E-\lambda}{2E}}\varphi^u_{\uparrow R} \\ 0 \\ 0 \\ 0 \\ e^{-i\frac{\delta_s}{2}}\sqrt{\frac{E+\lambda}{2E}}h^{d\dagger \mathrm{T}}_{\downarrow L} \\ 0 \end{pmatrix} e^{-ik_2 z}$$

$$+ C \begin{pmatrix} 0 \\ e^{i\frac{\delta_s}{2}}\sqrt{\frac{E+\lambda}{2E}}\varphi^d_{\uparrow R} \\ 0 \\ e^{-i\frac{\delta_s}{2}}\sqrt{\frac{E-\lambda}{2E}}h^{u\dagger \mathrm{T}}_{\downarrow L} \\ 0 \\ 0 \end{pmatrix} e^{-ik_1 z} + D \begin{pmatrix} 0 \\ e^{i\frac{\delta_s}{2}}\sqrt{\frac{E-\lambda}{2E}}\varphi^d_{\uparrow R} \\ 0 \\ e^{-i\frac{\delta_s}{2}}\sqrt{\frac{E+\lambda}{2E}}h^{u\dagger \mathrm{T}}_{\downarrow L} \\ 0 \\ 0 \end{pmatrix} e^{-ik_2 z}$$

$$+ F \begin{pmatrix} 0 \\ 0 \\ \varphi^s_{\uparrow R} \\ 0 \\ 0 \\ 0 \end{pmatrix} e^{-ik_3 z} + G \begin{pmatrix} 0 \\ 0 \\ 0 \\ 0 \\ 0 \\ h^{s\dagger \mathrm{T}}_{\downarrow L} \end{pmatrix} e^{-ik_4 z}, \qquad (16)$$

The first wavefunction describes the incoming quasiparticle, second and third the reflected quasiparticles of the same kind. The next two wavefunctions are quasiparticles of the second kind whereas the last two describe the posssibility of the reflection of the unpaired strange quark. The momenta of the strange quark and hole are $k_3 = \mu + E$ and $k_4 = -\mu + E$, the others were already given previously. On the other hand, for $z > 0$, we have the wavefunction given by the formula in Appendix C of [14]. In the massless limit we consider here the momenta in the wave function are given by $q_1 = \mu + \xi$, $q_2 = -\mu + \xi$, $p_1 = \mu + \zeta$ and $p_2 = -\mu + \zeta$. Solving the boundary condition which connects $\Psi_<(z)$ with $\Psi_>(z)$, we find the

following results (the phase $\exp(i\delta_s/2)$ was absorbed into the redefinition of constants G, H, K and N):

$$
\begin{aligned}
B &= -l + \frac{2e^{i\alpha}(e^{i\alpha}lx(x-2z)+x+z)\lambda}{(1-e^{i\alpha}lx)(3+e^{i\alpha}x(x-2z))(E+\lambda)} \\
D &= -\frac{2e^{i\alpha}(2x-z)\lambda}{(1-e^{i\alpha}lx)(3+e^{i\alpha}l(x-2z))(E+\lambda)} \\
G &= \frac{\lambda}{E}\sqrt{\frac{2E}{E+\lambda}}\frac{(x+z)e^{-i\delta_c}}{3+e^{i\alpha}l(x-2z)} \\
H &= -\frac{\lambda}{E}\sqrt{\frac{2E}{E+\lambda}}\frac{x(1+l(x-z)e^{i\alpha})e^{-i\delta_c}}{(1-e^{i\alpha}lx)(3+e^{i\alpha}l(x-2z))} \\
K &= \frac{\lambda}{E}\sqrt{\frac{2E}{E+\lambda}}\frac{xe^{-i\delta_c}}{3+e^{i\alpha}l(x-2z)} \\
N &= \frac{\lambda}{E}\sqrt{\frac{2E}{E+\lambda}}\frac{ze^{-i\delta_c}}{3+e^{i\alpha}l(x-2z)}
\end{aligned}
\tag{17}
$$

where

$$
x = \sqrt{\frac{E-\xi}{E+\xi}},\ l = \sqrt{\frac{E-\lambda}{E+\lambda}},\ x = \sqrt{\frac{E-\zeta}{E+\zeta}}, \tag{18}
$$

Other coefficients (A, C, D, F, J, L and P) vanish. Let us notice that the modulus square of the above coefficients depends only on the phase difference α crossing the interface. Similarly to the case of 2SC/2SC' junction this quantity we consider is gauge independent.

The probability current for $z < 0$ and $E > \tilde{\Delta}, 2\Delta$ is

$$
j \equiv \Psi_<^\dagger \vec{\alpha} \Psi_< = 2\mu[\frac{\xi}{E}(1-|B|^2-|D|^2)-|G|^2]. \tag{19}
$$

The analytical result is not given by short expression thus we rather show the current dependence on the energy in the Fig. 1 for generic set of parameters. Let us notice that the current starts at energy $E = \Delta$ and then rises linearly up to the point $E = 2\Delta$ where there is a jump. This behaviour is expected because below the gap there is no probability current and at the energy twice the gap additional current appears from the singlet excitation in the CFL phase.

4. Conclusions

In this paper we consider the general structure of the Andreev reflection between two superconductors 2SC and CFL in the high density QCD. We also

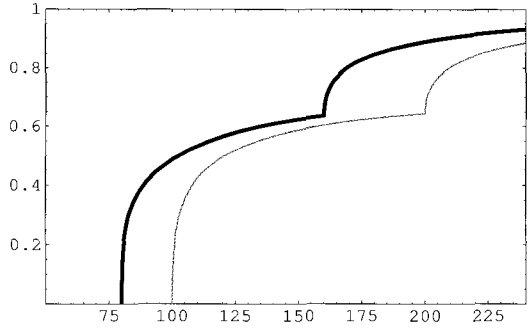

Figure 1. Dependence of the probability current (19) as a function of energy E [MeV] for two sets of parameters: $\Delta = 80$ MeV, $\tilde{\Delta} = 60$ MeV (black curve) and $\Delta = 100$ MeV, $\tilde{\Delta} = 60$ MeV (gray curve).

give the review of the Andreev reflection between QGP/2SC and QGP/CFL phases.

The essence of the AR stems from the peculiar behaviour of particles which hit the interface. If the energy of the incoming particle from the conductor side is below the energy gap in superconductor then the hole is reflected from the interface. The energy and momentum[b] are conserved, however, there is an apparent violation of the charge conservation. This last effect stems from the fact that the superconductor serves as an infinite suply of Cooper pairs. At the microscopic level charge is conserved, of course. The Andreev reflection can be understood as follows: the incoming particle takes another particle from the Fermi sea and creates a Cooper pair which dissolves in the condensate. Then the hole is left in the conductor with the appropriate kinematics constaraind by energy and momentum conservation.

So far, the only known place one can expect the color superconductors are the cores of protoneutron or Neutron Stars. Any subtle effects of Andreev reflection that happen inside these objects far away from our laboratories may be never observed. However there is at least one possibility one can imagine. The Andreev reflection affects the transport properties at the interfaces. If the protoneutron stars go through the first order phase transitions between QGP or/and 2SC or/and CFL phases during their history cooling then one can expect the mixed phase to be present in the core

[b]The momentum conservation is violated at the $O(1/E_F)$ level and can be neglected in the first approximation.

of the stars. In this situation the Andreev reflection influences the dynamics of the bubbles grow between different phases. These in turn influence the neutrino emission. Thus the time dependence of neutrino luminosity from supernovae can carry the information of the Andreev processes which took place inside the protoneutron stars. These intriguing possibilities require more attention.

Acknowledgments

M.T was supported by RIKEN Special Postdoctral Researchers Grant No.A12-52010.

References

1. For example, see Proceedings of *Quantum Chromodynamics and Color Confinement*, edited by H. Suganuma et al. (World Scientific, 2001).
2. D. Gross and F. Wilczek, Phys. Rev. Lett. **30** (1973) 1343; H.D. Politzer, Phys. Rev. Lett. **30** (1973) 1346.
3. G. Baym and S.A. Chin, Phus. Lett **B62** (1976) 241; G. Chaplin and M. Nauenberg, Nature **264** (1976) 235; Phys. Rev. **D16** (1977) 456; B.D. Keister and L.S. Kisslinger, Phys. Lett **B64** (1976) 117; W. B. Fechner and P.C. Joss, Nature **274** (1978) 347.
4. F. Barrois, Nucl. Phys. **B129** (1977) 390; D. Bailin and A. Love, Nucl. Phys. **B190** (1981) 175; Nucl. Phys. **B190** (1981) 751; Nucl. Phys. **B205** (1982) 119; Phys. Rep. **107** (1984) 325.
5. M. Alford, K. Rajagopal and F. Wilczek, Phys. Lett. **B422** (1998) 247; R. Rapp, T. Schäfer, E. Shuryak and M. Velkovsky, Phys. Rev. Lett. **81** (1998) 53.
6. M. Alford, K. Rajagopal and F. Wilczek, Nucl. Phys. **B537** (1999) 443.
7. D. Son, Phys. Rev. **D59** (1999) 094019.
8. J. Bardeen, L.N. Cooper and J.R. Schrieffer, Phys. Rev. **106** (1957) 162; bf 108 (1957) 1175.
9. K. Rajagopal and F. Wilczek, Chap. 35 in "At the Frontier of Particle Physics/ andbook of QCD", M. Shifman ed. (World Scientific) [hep-ph/0011333].
10. A.F. Andreev, Zh. Eksp. Teor. Fiz. **46** (1964) 1823.
11. M. Sadzikowski, Acta Phys. Pol. **B33** (2002) 1601.
12. M. Sadzikowski and M. Tachibana, Phys. Rev. **D66**, 045024 (2002).
13. N. N. Bogoliubov, Zh. Exp. Teor. Fiz **34** (1958) 58, 73 (JETP **34** (1958) 41, 51); Y. Nambu, Phys. Rev. **117** (1960) 648; P. G. de Gennes, *"Superconductivity of Metals and Alloys"* (Addison-Wesley, New York, 1992).
14. M. Sadzikowski and M. Tachibana, Acta. Phys. Pol. **B33**, 4141 (2002)

QUEST FOR DENSE AND COLD NUCLEAR BOUND SYSTEMS MEDIATED BY K^- MESONS

TOSHIMITSU YAMAZAKI
RI Beam Science Laboratory, RIKEN
Hirosawa 2-1, Wako-shi, Saitama-ken, 351-0198 Japan
E-mail: yamazaki@nucl.phys.s.u-tokyo.ac.jp

AKINOBU DOTÉ AND YOSHINORI AKAISHI
Institute of Particle and Nuclear Studies, KEK,
Tsukuba, Ibaraki 305-0801, Japan

Recently, strongly bound $\bar{K}$ nuclear systems have been predicted, which are shown to have large binding energies about 100 MeV for single-$\bar{K}$ systems and 200 MeV for double-$\bar{K}$ systems. Since these $\bar{K}$ bound nuclei are predicted to have enormous nucleon densities, several times as much as the normal nuclear density, they provide a unique playground for studying possible quark-gluon structure in dense, cold and microscopic nuclear systems. We discuss this new paradigm and offer various experimental ways to search for such interesting objects that should be deeply related to chiral symmetry restoration, hadron masses, kaon condensation and strange matter.

1. Introduction

Recently, exotic nuclear systems involving a $\bar{K}$ (K^- or $\bar{K}^0$) as a constituent have been predicted[1,2,3,4,5,6] based on phenomenologically constructed $\bar{K}N$ interactions (hereafter referred to as AY), which reproduce low-energy $\bar{K}N$ scattering data[7], kaonic hydrogen atom data[8] and the binding energy and decay width of $\Lambda(1405)$. The $\bar{K}N$ interactions are characterized by a strongly attractive $I = 0$ part, which is responsible for the deep bound state of $\Lambda(1405)$, but is fully reconciled with the "repulsive-like" low-energy scattering lengths and kaonic hydrogen level shift. These empirically based bare $\bar{K}N$ interactions are consistent with theoretical predictions based on a chiral SU(3) effective Lagrangian[9]. Whereas these bare interactions lead to a shallow K^- optical potential for *continuum states in infinite nuclear matter*[10,11], they persist to be strong for *isolated bound states of finite nuclei*, despite a prevailing claim for non-existence of kaonic nuclear states[12].

The effective interactions derived in Ref.[1] were examined and tested by comparing with exact few-body calculations using the bare interactions.

The strongly attractive K^--p interaction was shown to cause not only enormous binding of K^- in proton-rich nuclei, but also shrinkage of $\bar{K}$-bound nuclei. The calculated bound states in ppnK^-, ppnnK^- and ^{8}BeK^- lie below the $\Sigma\pi$ emission threshold, which is the main decay channel of K^-N, and thus, are predicted to have narrow decay widths. These few-body treatments have been further extended to more complex systems by the method of Antisymmetrized Molecular Dynamics (AMD)[3,4,5], which is now capable of calculating the structure with density distributions of individual constituent particles in an *ab initio* way without *a priori* assumption about the structure. The predicted $\bar{K}$ bound states have central nucleon densities ($\rho(0)$), 4-9 times as much as the normal nuclear density ($\rho_0 = 0.17$ fm^{-3}), with large binding energies ($E_K \approx 100$ MeV). Such strongly bound compact systems can be called "$\bar{K}$ nuclear clusters".

Since the predicted nucleon densities very much exceed the nucleon compaction limit, $\rho_c \approx 1/v_N \approx 2.3\rho_0$, with $v_N \approx 2.5$ fm^3 being the nucleon volume, it may be questionable to apply the hadronic $\bar{K}N$ and NN interactions to such dense systems. Although the $\bar{K}$ clusters are expected to be in deconfined quark-gluon states[13,14,15,16], there is no theoretical treatment available on "dense and cold" microscopic systems. Thus, it is vitally important to pursue experimental strategies to search for $\bar{K}$ clusters and to examine their properties, in which we take the predicted binding energies and widths as a guiding reference; an observed deviation from predicted values will bring us important implications.

2. Single-$\bar{K}$ nuclear systems

The strongly attractive force of p + K^- in the $I = 0$ channel plays an essential role in the following consideration[1]. When another proton is added to $\Lambda(1405)$, the "atomic" p + K^- system is changed to a "molecular" system, p + p + K^-, where the K^- behaves as a glue to combine two protons. The predicted ppK^- system has a binding energy ($E_K = 48$ MeV) and a width ($\Gamma_K = 61$ MeV)[2]. It is shown to have a p-p rms distance of 1.90 fm, close to the normal inter-nucleon distance. No such strong binding is expected for pnK^- and nnK^-.

We performed four-body variational calculation using the Tamagaki potential (OPEG)[17] as a bare NN interaction and the AY $\bar{K}N$ interaction as a bare $\bar{K}N$ interaction. We also constructed effective $\bar{K}$ interactions using

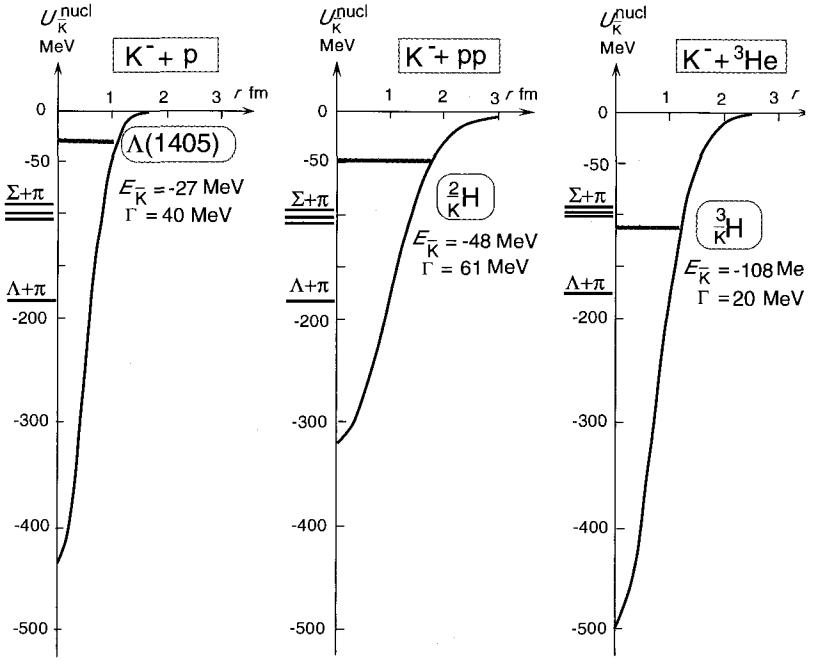

Figure 1. Calculated $\bar{K}N$ and $\bar{K}$-nucleus potentials and bound levels: $\Lambda(1405)$, $^{2}_{\bar{K}}H$ and $^{3}_{\bar{K}}H$ for K^-p, K^-pp and K^-ppn systems, respectively[2]. The nuclear contraction effect is taken into account. The shaded zones indicate the widths. The $\Sigma\pi$ and $\Lambda\pi$ emission thresholds are also shown.

the g-matrix method. In the ppnK^- and ppnnK^- systems drastic changes of the binding energy and width occur. The first effect is a shrinkage of the nucleus ^{3}He and ^{4}He due to the strong attraction of K^-. Although it is somewhat counterbalanced by the strong nuclear incompressibility, the equilibrium size of the system is substantially smaller. The binding energy is predicted to be so large that the state lies below the emission threshold of $\Sigma+\pi$, which is the main decay channel of K^-+N. This situation makes the width of the state narrow. The predicted total binding energy of ppnK^- is 118 MeV and the width is 21 MeV, much smaller than that of $\Lambda(1405)$. The potential energies of K^- in the p + K^-, pp + K^- and ppn + K^- systems are shown in Fig. 1.

The AMD calculation is now capable of producing the spatial distributions of p, n and K^- in strongly bound kaonic systems. Fig. 2 shows the result of ^{8}Be + K^-, where K^- shrinks drastically the two alpha particles to

two mini-alpha clusters. Fig. 3 shows density contours of ppnK$^-$, pppK$^-$ and pppnK$^-$.

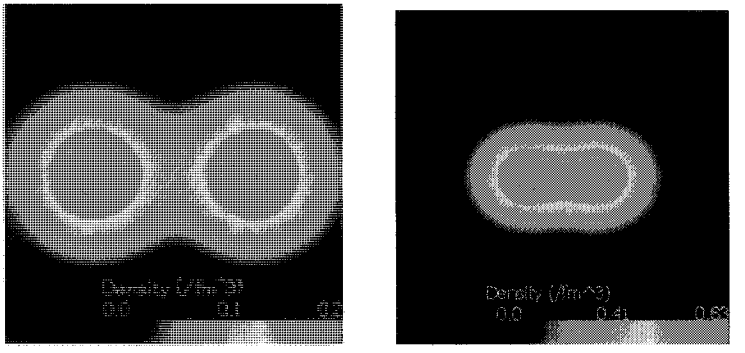

(a) ^{8}Be (b) ^{8}BeK$^-$

Figure 2. Calculated density contours of ^{8}BeK$^-$[4]. Comparison of the density distributions of (a) ordinary ^{8}Be and (b) ^{8}BeK$^-$ is shown in the size of 7 by 7 fm.

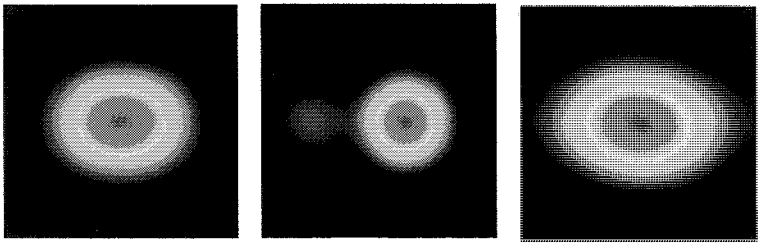

Figure 3. Density contours of the nucleon distributions of (left) ppnK$^-$, (middle) pppK$^-$ and (right) pppnK$^-$ nuclei: 3fm × 3fm.

2.1. *Double-$\bar{K}$ systems*

We extended the same theoretical treatments to double-$\bar{K}$ systems[6]. First, we performed four-body variational calculation on ppK$^-$K$^-$, where we neglected the $\bar{K}$-$\bar{K}$ interaction simply because of lack of information. The binding energy and width obtained in this system are $E_K = 117$ MeV and $\Gamma_K = 35$ MeV, with a p-p rms distance very much reduced to 1.3 fm. Thus, the addition of a $\bar{K}$ increases the binding energy and the nucleon density. We found from an AMD calculation that the double-$\bar{K}$ cluster

($ppnK^-K^-$) is more tightly bound than the dense single-$\bar{K}$ cluster ($ppnK^-$), as shown in Fig. 4, where we present the density contours of ^{3}He, $ppnK^-$ and $ppnK^-K^-$. The central nucleon density reaches $\rho(0) \sim 1.5$ fm^{-3} for $ppnK^-$ and ~ 1.5 fm^{-3} for $ppnK^-K^-$. We summarize these results in Table 1 together with the results on single-$\bar{K}$ clusters[4,5,6].

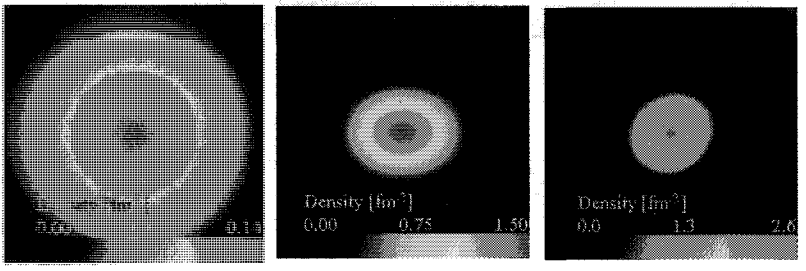

Figure 4. Calculated density contours of (left) ^{3}He, (middle) $ppnK^-$ and (right) $ppnK^-K^-$.

Table 1. Summary of predicted $\bar{K}$ clusters. M: total mass [MeV]. E_K: total binding energy [MeV]. Γ_K: decay width [MeV]. $\rho(0)$: nucleon density at the center of the system [fm^{-3}]. $R_{\rm rms}$: root-mean-square radius of the nucleon system [fm]. k_p and k_K: rms internal momenta [fm^{-1}] of p and K^-, respectively. The calculated binding energies are subject to an increase by ≈ 10 MeV, when the relativistic effect on K^- is taken into account.

$\bar{K}$ cluster	Mc^2 [MeV]	E_K [MeV]	Γ_K [MeV]	$\rho(0)$ [fm^{-3}]	$R_{\rm rms}$ [fm]	k_p [fm^{-1}]	k_K [fm^{-1}]
ppK^-	2322	48	61	0.52	0.99	1.49	1.18
$pppK^-$	3211	97	13	1.56	0.81		
$ppnK^-$	3192	118	21	1.50	0.72		
$ppppK^-$	4171	75	162	1.68	0.95		
$pppnK^-$	4135	113	26	1.29	0.97		
$ppnnK^-$	4135	114	34		1.12		
ppK^-K^-	2747	117	35				
$ppnK^-K^-$	3582	221	37	2.97	0.69		
$pppnK^-K^-$	4511	230	61	2.33	0.73		

2.2. *Unified view of $S = -1$ nuclear systems*

We point out that the kaonic bound states are "Feshbach resonance" states embedded in the continuum, belonging to the $S = -1$ sector of nuclear excitation. A unified view is given in Fig. 5 in the case of $A = 4$.

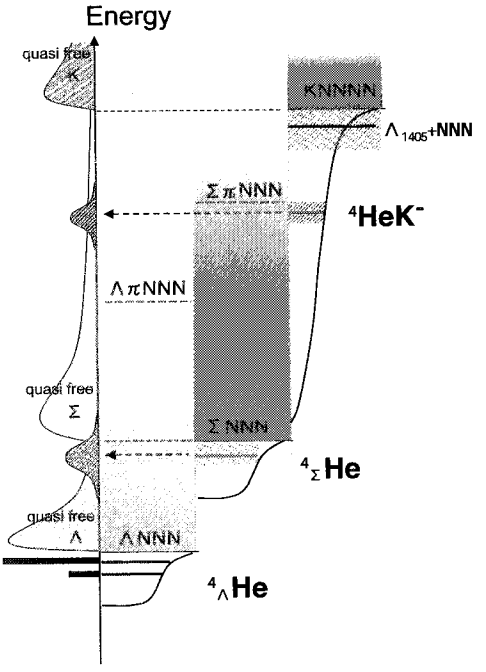

Figure 5. A unified view of the $S = -1$ sector of nuclear excitation as Feshbach resonances. In the case of $A = 4$.

3. Direct reactions to populate $\bar{K}$ nuclei

3.1. *(stopped K^-,n)*

The ppnK$^-$ system can be populated by ^{4}He(stopped K$^-$, n) reaction, in which the "Auger neutron" serves as an indicator of the bound state[1]. An experiment has been carried out at KEK, indicating a candidate for the predicted bound state with a mass of $M \sim 3140$ MeV and a total binding energy of ~ 170 MeV [18], as shown in Fig. 6. This value is significantly larger than the predicted value of 118 MeV, suggesting that the $\bar{K}$N interaction in this nuclear system may be enhanced over the bare one by 17 %.

3.2. *(K^-, N) reaction*

The reaction of (K^-, N) can be used to populate $\bar{K}$ bound states, in which the incoming $\bar{K}$ knocks out one of the target nucleons and stops in the nucleus[19].

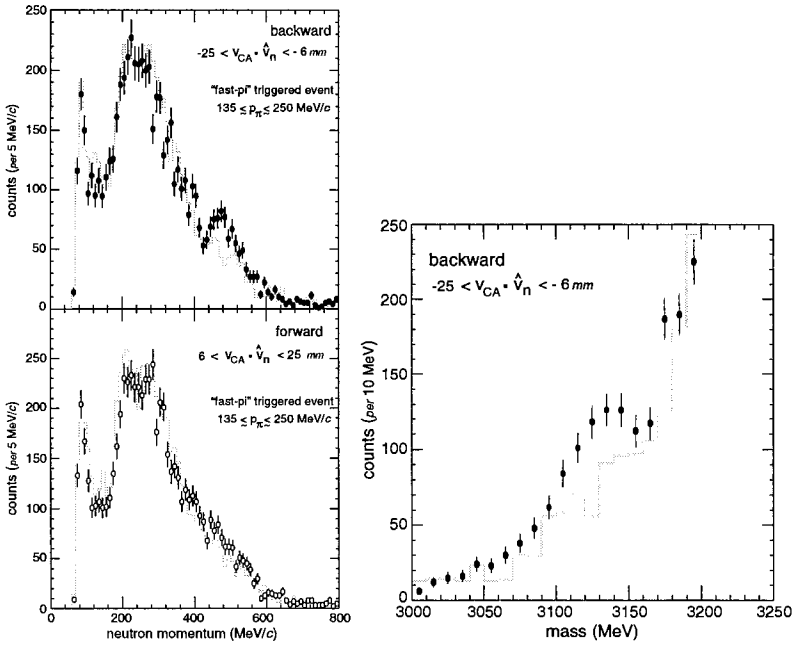

Figure 6. The first indication of a deeply bound kaonic state of ppnK$^-$ populated in the ^{4}He(stopped K$^-$,n) reaction. (Left) The momentum spectra of neutrons tagged by backward (upper) and forward (lower) fast pions, showing a peak at $p_n \sim 480$ MeV. (Right) Corresponding energy spectrum, showing a mass of ~ 3140 MeV (total binding energy of 170 MeV). From Iwasaki *et al.*[18].

3.3. *(K^-, π^-) and (π^{+-}, K^{+0}) reactions*

Various exotic $\bar{\text{K}}$ nuclei can be populated in *strangeness exchange reactions* such as (K^-, π^-) and $(\pi^{+,-}, K^{0,+})$. Table 2 lists kaonic nuclei to be produced.

Table 2. Various reactions to produce exotic $\bar{\text{K}}$ bound systems

				(K^-, π^-)			
	(K^-, p)	(K^-, n)	(π^-, K^0)	(π^+, K^+)	(π^+, K^0)	(p, K^+)	(p, K^0)
ΔQ	-2	-1	-1	0	+1	0	+1
Target							
p	-	-	Λ, Λ^*	Σ^+, Σ^{+*}	-	ppK^-	-
$[n]$	-	-	Σ^-, Σ^{-*}	pnK^-	ppK^-		
d	-	Λ, Λ^*	pnK^-	ppK^-	-	$ppnK^-$	$pppK^-$
^{3}He	pnK^-	ppK^-	$ppnK^-$	$pppK^-$	-	$pppnK^-$	$ppppK^-$
^{4}He	$pnnK^-$	$ppnK^-$	$ppnnK^-$	$pppnK^-$	$ppppK^-$	$pppnnK^-$	$ppppnK^-$

The spectral shape of the bound-K^- region populated in direct reactions, (K^-, π^-) and (π^+, K^+), was calculated based on the Λ^* doorway model[2,20]. In this treatment the formation of kaonic systems proceeds via the elementary production of $\Lambda(1405)$ by $n(K^-, \pi^-)\Lambda^*$ and $n(\pi^+, K^+)\Lambda^*$, which is then melted to form koanic states. The results for (π^+, K^+) and (π^-, K^0) on targets of d, ^{3}He and ^{4}He are shown in Fig. 7. The dense kaonic states produced from ^{3}He and ^{4}He are shown to be well separated from the huge "quasi-free" continuum. On the other hands, the ppK$^-$ state is broader in the natural width and closer in energy to the $\Lambda(1405)$ threshold, and thus its broad peak is partially separated from the quasi-free continuum. We need an efficient tagging to enhance the bound-state peak.

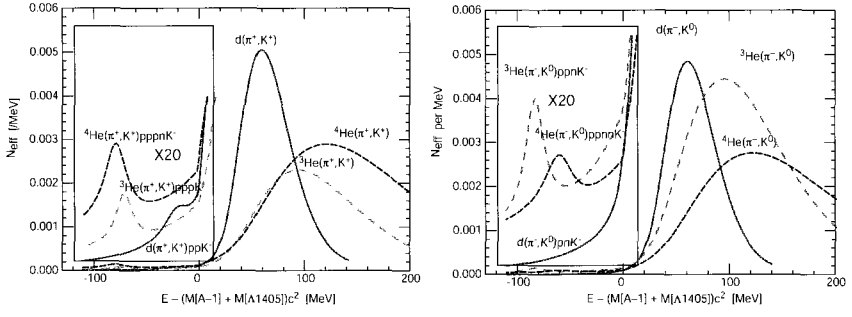

Figure 7. Spectra ($N_{\rm eff}$) of (π^+,K$^+$) and (π^-,K^0) at p_π = 1.5 GeV/c on d, ^{3}He and ^{4}He as functions of $E_K - [M(A-1) + M(\Lambda_{1405})]c^2$. Calculated based on the Λ^* doorway model[20].

3.4. *$\bar{K}$ clusters from compound $\bar{K}$ states*

The "quasi-free" component involves excited continuum compound states of K$^-$ nuclear systems, which immediately emit nucleons and end up in kaonic bound states. This is similar to the known situation in hyperfragment formation[21,22]. Such a "decay-channel" spectroscopy is even more feasible for kaonic bound states, because of their strong binding and characteristic decay channels from which invariant-mass spectra can be easily reconstructed.

The decay modes that can be detected are:

$$pppK^- \rightarrow p + p + \Lambda \quad (1)$$

$$ppnK^- \rightarrow d + \Lambda \quad (2)$$

$$pppnK^- \rightarrow d + p + \Lambda \quad (3)$$

The production cross sections of hyperfragments from continuum compound process were calculated by Sano *et al.*[23]. The same method can be extended to the case of $\bar{K}$ fragments.

4. $\bar{K}$ CLUSTERS AS RESIDUES IN HEAVY-ION COLLISIONS

4.1. *Evolution of* $\bar{K}$ *clusters as deep trapping centers*

The K^- mesons born in a fireball of heavy-ion collisions produce extra-deep and localized self-trapping potentials, which are intermittently accommodated by a few correlated nucleons (notably, p^2, p^2n (^{3}He) and p^2n^2 (^{4}He)). Since $\bar{K}$ clusters once produced are hardly destroyed by further collisions because of their extremely large binding energies compared to the temperature, we expect a cascade evolution of $\bar{K}$ clusters, as shown in Fig. 8. These processes occur as *collisional capture processes*, when aided by surrounding nucleons, which transfer energies and momenta to form $\bar{K}$ clusters efficiently.

4.2. *Direct formation of* $\bar{K}$ *clusters from QGP*

In central collisions of relativistic heavy ions, a dense and hot fireball is produced. When the temperature of a primordial fireball exceeds a QCD transition temperature ($T > 150$ MeV) it is expected to be in quark-gluon plasma (QGP). Since the $\bar{K}$ clusters are by themselves dense, and are likely to be in a deconfined quark-gluon phase, as in QGP, they will be spontaneously formed in a self-organized way, like clusterized islands, remaining in a cooling and expanding hadron-gas medium throughout the freeze-out phase, as schematically shown in Fig. 9. Here, the s quarks in a primordial QGP act as seeds for $\bar{K}$ clusters.

Recently, it was shown that particle emission data including strange particles are well accounted for by a hadro-chemical equilibrium model in terms of the freeze-out temperature, the baryon chemical potential and the fireball volume as parameters[24,25,26]. In this model all particles (or states) are treated on equal footing, and the yields of various $\bar{K}$ clusters have been calculated by Andronic *et al.*[27], as discussed in the next section.

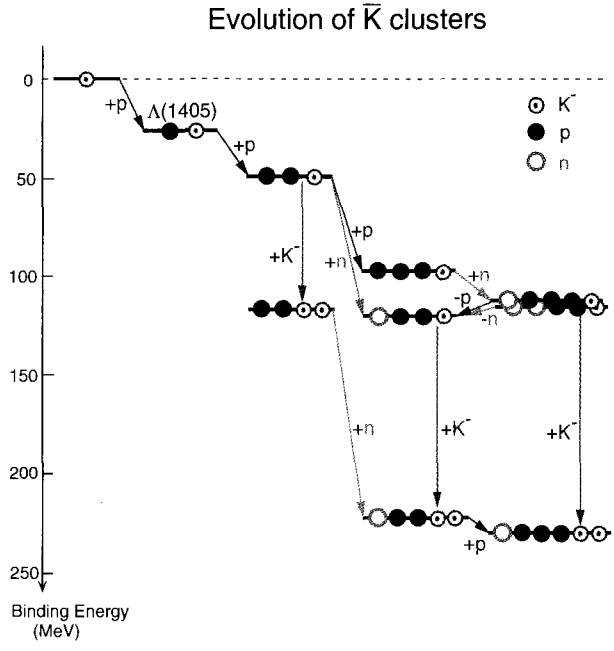

Figure 8. Cascade evolution of $\bar{K}$ clusters as deep traps in heavy-ion collisions. The calculated binding energies are shown.

5. $\bar{K}$-CLUSTER INVARIANT-MASS SPECTROSCOPY

Eventually, the $\bar{K}$ clusters formed in heavy-ion collisions decay via strong interactions by their own intrinsic decay modes. The condition to observe the free decay of a $\bar{K}$ cluster with a decay width Γ_K is

$$\tau_K = \hbar/\Gamma_K > \tau_f, \tag{4}$$

where τ_f is the freeze-out time. For the predicted decay width of $\Gamma_K \approx 20$ MeV, $\tau_K \approx 10$ fm/c, which is marginally longer than the calculated freeze-out time, $\tau_f \sim 5$ fm/c[28,29,30,31]. Thus, most $\bar{K}$ clusters formed in (and before) the freeze-out phase are likely to survive and undergo free decays.

The unique signature for $\bar{K}$ cluster formation is a clear peak to be revealed in invariant-mass spectra of its decay particles, provided that all of the decay particles with their energies and momenta are correctly identified. This method applies to limited cases, where $\bar{K}$ clusters can decay to

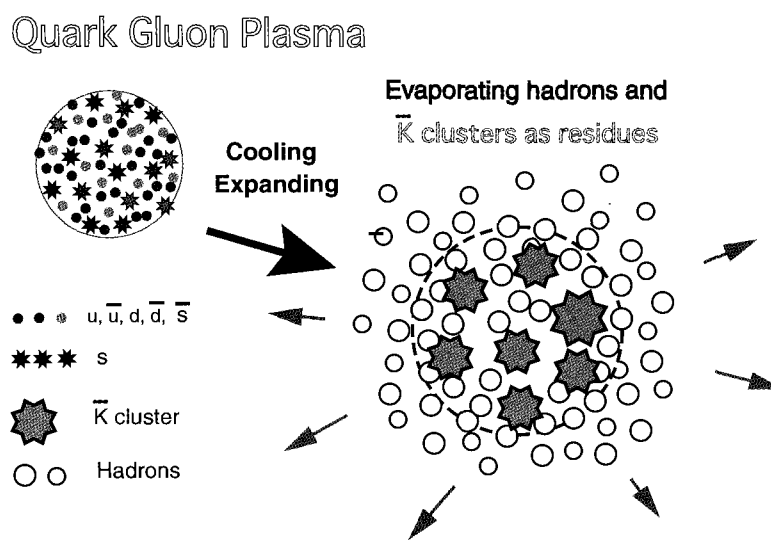

Figure 9. Quark gluon plasma and its transition to evaporating hadron gases with heavy and dense residues of $\bar{K}$ clusters.

trackable particles, such as

$$i)\ ppK^- \rightarrow \Lambda + p, \tag{5}$$

$$ii)\ ppnK^- \rightarrow \Lambda + d, \tag{6}$$

$$iii)\ pppK^- \rightarrow \Lambda + p + p, \tag{7}$$

$$vi)\ ppK^-K^- \rightarrow \Lambda + \Lambda, \tag{8}$$

$$vii)\ pppK^-K^- \rightarrow \Lambda + \Lambda + p. \tag{9}$$

These decay processes are energetically the most favoured, though their branching ratios are not known. The "decay-channel spectroscopy" *ii*) on ppnK$^-$ is being examined by Herrmann[32] by using the experimental data of Λ and d, obtained from the FOPI detector of GSI[33]. This can be compared with a recent result of the "entrance-channel spectroscopy" performed at KEK[18].

Recent calculations of Andronic *et al.*[27] based on a hadron-gas model[24] give $Y(ppnK^-) \sim 3 \times 10^{-3}$ per total charged pion, or ~ 0.06 per collision, when the incident energy is 2 GeV/u. It is interesting to note that this yield is larger than $Y(K^-)$. This means that, even if the decay branching to $\Lambda + d$ is 0.1, the $ppnK^- \rightarrow \Lambda + d$ signal can be identified with a ratio of $R \sim 0.02$ over a large combinatorial background.

Once single-$\bar{K}$ clusters are found, the next step will be to pursue double-$\bar{K}$ clusters. Here, we need a fireball with a large multiplicity of strangeness. Recently, abundant productions of Λ are observed at the RHIC energy by PHENIX[34] and STAR[35]. The future accelerator at GSI will provide 30-40 GeV/u heavy-ions[36], which is suitable for double-$\bar{K}$-cluster invariant-mass spectroscopy in view of the large baryon density to be achieved in collisions, and also of abundant strangeness production. The calculated yield of the double-$\bar{K}$ cluster, ppK^-K^-, has a maximum at the c.m. collision energy of $\sqrt{s} = 5 - 10$ GeV/u (the incident energy around 30 GeV/u), and amounts to $Y(ppK^-K^-) \sim 2\times10^{-4}$ per total charged pion, or ~ 0.01 per collision[27]. In view of such a large yield the invariant-mass spectroscopy for $\Lambda + \Lambda$ may also be feasible.

6. TOWARD COLD AND DENSE NUCLEAR MATTER

6.1. *Multi-$\bar{K}$ nuclear systems as a precursor to strange matter*

We can conceive of a further extension of the double-$\bar{K}$ systems to multi-$\bar{K}$ nuclear matter. Whereas the nucleons and hyperons are hard to compress, presumably because of the Pauli repulsion in the quark sector, multi-$\bar{K}$ systems, such as $(pK^-)^m n^n$, become self-compressed dense matter without the aid of gravity. A speculated diagram of strange nuclear matter is shown in Fig. 10. The characteristic feature of $\bar{K}$ in producing dense nuclear systems may be intuitively understood as a result of the non-existence of Pauli blocking in the (u, d) quark sector by implanting K^-, since K^- is composed of $s\bar{u}$. Here, kaon condensation may also play an essential role[37,38]. The $\bar{K}$ matter with a large $\bar{K}$ fraction ($K^-/N \sim 1$) may be more stable than the corresponding non-strange matter[6].

6.2. *Chiral symmetry restoration and phase transition to quark phases*

So far, the present treatment does not contain the effect of chiral symmetry restoration at high density. If the $\bar{K}N$ interaction is increased along with a restoration of the chiral symmetry in accordance with the Tomozawa-Weinberg relation[39,40], similar to an effect recently observed in the πN interaction in a nuclear medium[41], the K^- energy line in Fig. 10 bends downward with the increase of ρ; the $\bar{K}$ clusters may be more bound and denser, and the $\bar{K}$ matter may become more stable. If we take the first

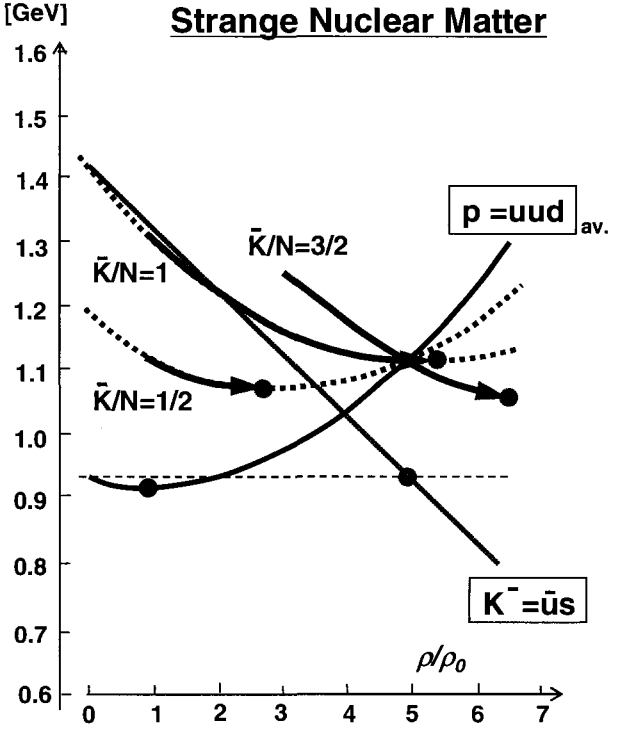

Figure 10. Speculated diagram for the density dependences of the bound-state energies of various baryon composite systems $(pK^-)^m n^n$. The $\bar{K}N$ energy is represented by the red straight line, where no effect of chiral symmetry restoration is invoked. The nuclear compression is represented by the black curve and the total energies for representative fractions of K^-/N (=1/2, 1 and 3/2) are depicted by respective curves.

indication of the KEK experiment, it implies a 17% enhancement of the $\bar{K}N$ interaction. The $\bar{K}$ (or s-quark) clusters, which we propose to study experimentally, will provide not only a unique playground to study possible quark-gluon phases of dense and bound nuclear systems, but also an important access toward the understanding of strange matter and stars.

7. Acknowledgement

We would like to thank Prof. P. Kienle, N. Herrmann, M. Iwasaki and R.S. Hayano for the helpful discussion. This work is supported by the Grant-in-Aid of Japanese Monbukagakusho.

References

1. Y. Akaishi and T. Yamazaki, Phys. Rev. **C 65** (2002) 044005.
2. T. Yamazaki and Y. Akaishi, Phys. Lett. **B 535** (2002) 70.
3. A. Doté, H. Horiuchi, Y. Akaishi and T. Yamazaki, Prog. Theor. Phys. Suppl. **146** (2002) 508.
4. A. Doté, H. Horiuchi, Y. Akaishi and T. Yamazaki, nucl-th/0207085, Phys. Lett. B, in press.
5. A. Doté, H. Horiuchi, Y. Akaishi and T. Yamazaki, nucl-th/0309062; submitted to Phys. Rev. C.
6. T. Yamazaki, A. Doté and Y. Akaishi, Phys. Lett. **B587** (2004) 167..
7. A. D. Martin, Nucl. Phys. **B 179** (1981) 33.
8. M. Iwasaki *et al.*, Phys. Rev. Lett. **78** (1997) 3067; T. M. Ito *et al.*, Phys. Rev. **C 58** (1998) 2366.
9. T. Waas, N. Kaiser, and W. Weise, Phys. Lett. **B 365** (1996) 12; Phys. Lett. **B 379** (1996) 34; N. Kaiser, P. B. Siegel, and W. Weise, Nucl. Phys. **A594** (1995) 325; W. Weise, Nucl. Phys. **A610** (1996) 35.
10. M. Lutz, Phys. Lett. **B 426** (1998) 12.
11. A. Ramos and E. Oset, Nucl. Phys. **A 671** (2000) 481.
12. A. Cieply, E. Friedman, A. Gal and J. Mares, Nucl. Phys. **A 696** (2001) 173.
13. T. Hatsuda and T. Kunihiro, Phys. Rev. Lett. **55** (1985) 158; Phys. Reports **247** (1994) 221.
14. W. Weise, Nucl. Phys. **A553** (1993) 59c.
15. K. Rajagopal, Nucl. Phys. **A661** (1999) 150c; M. Alford, K. Rajagopal and F. Wilczek, Phys. Lett. **B422** (1998) 247; R. Rapp, T. Schäfer, E.V. Shuryak and M. Velkovsky, Phys. Rev. Lett. **81** (1998) 53.
16. H. Heiselberg and V. Pandharipande, Annu. Rev. Nucl. Part. Sci. **50** (2000) 481.
17. R. Tamagaki, Prog. Theor. Phys. **39** (1968) 91.
18. M. Iwasaki *et al.*, nucl-ex/0310018, submitted to Phys. Lett. B.; T. Suzuki *et al.*, Proc. Int. Conf. HYP2003.
19. T. Kishimoto, Phys. Rev. Lett. **83** (1999) 4701.
20. Y. Akaishi, prepared for publication.
21. T. Yamazaki, Nuovo Cimento **103** (1989) 78.
22. H. Tamura *et al.*, Phys. Rev. **C40** (1989) 483.
23. M. Sano, M. Wakai and Y. Yamamoto, Prog. Theor. Phys. **87** (1992) 957; Y. Yamamoto, M. Wakai, T. Fukuda and M. Sano, Prog. Theor. Phys. **88** (1992) 1163.
24. P. Braun-Munzinger, J. Stachel, J.P. Wessels and N. Xu, Phys. Lett. **B 344** (1995) 43; P. Braun-Munzinger, I. Heppe and J. Stachel, Phys. Lett. **B 465** (1999) 15.
25. J. Cleymans and K. Redlich, Phys. Rev. Lett. **81** (1998) 5284; Phys. Rev. **C 60** (1999) 054908.
26. R. Stock, Phys. Lett. **B 456** (1999) 277.
27. A. Andronic *et al.*, in preparation; A. Andronic and P. Braun-Munzinger, private communication (2003).

28. S.A. Bass, C. Hartnack, H. Stöcker and W. Greiner, Phys. Rev. **C 51** (1995) 3343; S.A. Bass *et al.*, Prog. Part. Nucl. Phys. **41** (1998) 255.
29. W. Cassing and E. Bratkovskaya, Phys. Rep. **308** (1999) 65.
30. B. Friman, W. Nörenberg and V.D. Toneev, Eur. Phys. J. **A3** (1998) 165
31. B-A. Li, Phys. Rev. **C61** (2000) 021903(R).
32. N. Herrmann, private comm. (2003).
33. B. Hong *et al.*, Phys. Rev. **C 57** (1998) 244.; R. Kutsche, Dissertation, GSI DISS.2000-05.
34. K. Adcox *et al.*, Phys. Rev. Lett. **89** (2002) 092302.
35. C. Adler *et al.*, Phys. Rev. Lett. **89** (2002) 132301.
36. An International Accelerator Facility for Beams of Ions and Antiprotons: Conceptual Design Report, GSI, 2003.
37. D.B. Kaplan and A.E. Nelson, Phys. Lett. **B175** (1986) 57.
38. G.E. Brown, C.H. Lee, M. Rho and V. Thorsson, Nucl. Phys. **A567** (1994) 937; G.E. Brown, *ibid.* **A574** (1994) 217c; G.E. Brown and M. Rho, Phys. Rep. **269** (1996) 333.
39. Y. Tomozawa, Nuovo Cimento **A 46** (1966) 707.
40. S. Weinberg, Phys. Rev. Lett. **17** (1966) 616.
41. K. Suzuki *et al.*, Phys. Rev. Lett. **92** (2004) 072302; P. Kienle and T. Yamazaki, Prog. Part. Nucl. Phys. **52** (2004) 85.

STABILITY OF STRANGELETS WITH CHIRAL SYMMETRY BREAKING

S. YASUI, A. HOSAKA AND H. TOKI

Research Center for Nuclear Physics , Osaka University,
10-1, Mihogaoka, Ibaraki, Osaka, Japan
E-mail: yasui@senri.rcnp.osaka-u.ac.jp,
hosaka@senri.rcnp.osaka-u.ac.jp,
toki@senri.rcnp.osaka-u.ac.jp

O. KIRIYAMA

Research Center for Nanodevices and Systems, Hiroshima University
Higashi-Hiroshima, Hiroshima, Japan
E-mail: kiriyama@sxsys.hiroshima-u.ac.jp

We investigate the stability of strangelets in a chiral effective model. We focus on the effects of the chiral symmetry breaking in the strangelets by using the NJL model as an effective theory of QCD. The self-bound quark droplets are formulated by implementing the confinement picture in the MIT bag model. It is shown that the strangelets are not absolutely stable due to the chiral symmetry breaking and the large current mass as compared with light flavor. The observable quantities (the charge-mass ratios, the radii) of the strangelets are discussed to compare them with observed data in heavy ion collisions and/or in cosmic rays.

1. Introduction

The finite density quark matter is expected to give us the rich structures. Recently, the physics of the strangeness show us interesting phenomena, for example, the deeply bound state of kaonic nuclei[1] and the experimental observation of the Θ^+ ($uudd\bar{s}$) particles[2]. Concerning the quark matter, some decades ago, it was pointed out that the strange matter could be the true ground state of finite density QCD matter due to the increase of the number of degrees of freedom.[3] [4] [5] In the MIT bag model, it was shown that the bulk strange matter had a possibility to be more stable than the normal nuclear matter. The stability of the bulk strange matter would lead

the stability of finite lumps of strange matter which were called strangelets.[a] The strangelets are exotic quark states different from the ordinary nuclei. They are expected to be observed in heavy ion collisions and in cosmic rays as heavy particles with small charge-mass ratios. In order to identify such particles, it is necessary to predict observable quantities (charge-mass ratios and radii) of the strangelets. For the study the realistic strangelets, it is necessary to consider chiral symmetry breaking, which plays important roles in the low energy QCD physics. Our purpose is to investigate the stability of the strangelets and obtain the observable quantities in a chiral effective theory.

2. Strangelets

2.1. *The NJL model with the MIT bag boundary condition*

The bulk quark matter is described by the NJL model as an effective theory of QCD.[6] In fact, the NJL model explains spontaneous chiral symmetry breaking in the hadronic vacuum and reproduces many properties of hadrons. Many authors have discussed the stability of the bulk quark matter with the chiral symmetry breaking in the NJL model. It was discussed that the bulk strange matter is not favored due to the chiral symmetry breaking in the strange flavor.[7] Our interest here is to study the stability of finite lumps of quark matter with chiral symmetry breaking and strange flavor. In contrast with the bulk quark matter, we cannot neglect effects of confinement of quarks in the quark droplets. It is known that the NJL model cannot give an explanation of the confinement of the quarks. In order to confine quarks in the quark droplets in the NJL model, we assume the boundary condition of the MIT bag model.[8] Therefore we consider the following lagrangian;

$$L=\bar{\psi}(i\partial\!\!\!/-m^0)\psi+G\sum_{a=0}^{8}\left[\left(\bar{\psi}\frac{\lambda^a}{2}\psi\right)^2+\left(\bar{\psi}i\gamma_5\frac{\lambda^a}{2}\psi\right)^2\right]-M\bar{\psi}\psi\theta(r-R), \quad (1)$$

where ψ is the quark field, $m^0=\mathrm{diag}(m_u^0, m_d^0, m_s^0)$ is current mass matrix, $\lambda^a/2$ generators of $U(3)$ and G the coupling constant. The first term is the kinetic term and the second term is the NJL interaction, which has the symmetry $U(3)_L\times U(3)_R$. The last term represents the confinement of

[a]In general, the lumps or droplets of finite volume size of quark matter are called quark droplets. In this definition, the strangelets are quark droplets including not only u and d quarks, but also s quarks.

quarks in the bag with radius R. The mass parameter M is set infinity after all the calculations to confine quarks in the bag. The radius R is obtained by minimizing the total energy of the strangelet. The inside of the bag is the (chirally restored or broken) quark matter phase, and the outside is the baryonic vacuum phase, where chiral symmetry is broken.

The boundary condition makes the calculations in the quark droplets complicated rather than the bulk quark matter due to the discretized energy levels in the droplets. In principle, we can calculate the energy density and the number density by summation of all the energy levels occupied by the quarks. In order to simplify numerical calculations, we perform momentum integration in the energy density and the number density by multiple reflection expansion (MRE) in the quark propagater.[9 10] The state density in the momentum space is corrected by the function

$$\rho_{MRE}(p,m,R) = 1 + \frac{6\pi^2}{pR} f_S(p/m) + \frac{12\pi^2}{(pR)^2} f_C(p/m) + \cdots , \tag{2}$$

where p and m are the momentum and the dynamical mass of the quark and R is the radius of a quark droplet. f_S and f_C are universal functions given by

$$\begin{aligned} f_S(x) &= -\frac{1}{8\pi}(1 - \frac{2}{\pi}\arctan x), \\ f_C(x) &= \frac{1}{12\pi^2}[1 - \frac{3x}{2}(\frac{\pi}{2} - \arctan x)]. \end{aligned} \tag{3}$$

The second and third terms in Eq. (2) represent the corrections by the surface and the curvature of the droplet. Though it is not possible for the MRE method to include the shell structure by the discrete levels in the quark droplets, it is known that the MRE approximation reproduces the results obtained by the direct summation over the discrete levels for the quark droplets with baryon number $A > 10$.

2.2. *Energy density in the quark droplet*

The energy density in the quark droplets with the radius R is obtained from the lagrangian Eq. (1) by the mean field approximation.

$$\begin{aligned} \epsilon = \sum_{f=u,d,s} \Bigg[& \nu \int_0^{p_f^F} \sqrt{p^2 + m_f^2}\, \rho_{MRE}(p, m_f, R) \frac{p^2 dp}{2\pi^2} \\ & + \frac{(m_f - m_f^0)^2}{4G} - \nu \int_0^{\Lambda} \sqrt{p^2 + m_f^2}\, \rho_{MRE}(p, m_f, R) \frac{p^2 dp}{2\pi^2} \Bigg] - \epsilon_0, \end{aligned} \tag{4}$$

where m_f and p_f^F are the dynamical mass and the Fermi momentum of flavor f, Λ is a cut-off parameter and $\nu = 6$ is the degrees of degeneracy of spin and color. The last term stands for the energy density in the bulk vacuum given by

$$\epsilon_0 = \sum_{f=u,d,s} \left[\frac{(m_f^* - m_f^0)^2}{4G} - \nu \int_0^\Lambda \sqrt{p^2 + m_f^{*2}} \rho_{MRE}(p, m_f^*, R) \frac{p^2 dp}{2\pi^2} \right], \quad (5)$$

where m_f^* is quark mass of flavor f in the baryonic vacuum. The boundary condition in the MIT bag model is included in the momentum integration by MRE approximation Eq. (2). The Fermi momentum p_f^F is obtained by

$$\nu \int_0^{p_f^F} \rho_{MRE}(p, m_f, R) \frac{p^2 dp}{2\pi^2} = n_f, \quad (6)$$

where $n_f = N_f/V$ is the quark number density. ($V = \frac{4\pi}{3} R^3$ is the volume of the droplet.) The quark mass m_f in the quark droplet is determined by the Schwinger-Dyson equation which is given by the derivative of the energy density Eq. (4) by the quark mass m_f; $\partial\epsilon/\partial m_f = 0$.

In our study, the parameters are fixed as $m_u^0 = m_d^0 = 5.9$ MeV, $\Lambda = 0.6$ GeV and $G\Lambda^2 = 4.7$ to reproduce the averaged mass $m_{N+\Delta} = 1.134$ GeV of the nucleon and Δ, the pion mass $m_\pi = 0.139$ GeV and the pion decay constant $f_\pi = 93$ MeV in the vacuum. The mass $m_{N+\Delta}$ is related with the constituent quark mass by $m_{N+\Delta} = 3m_u^*$. We suppose the isospin symmetry in the u and d flavors. The strange current mass m_s^0 is then a free parameter, for which we take $m_s^0 = 0.1$ GeV. In actual calculations, we include the zero point energy in the quark droplets. It is known that the static energy α/R has to be subtracted from the total energy of the bag (quark droplet) in the MIT bag model, where $\alpha \sim 2.04$. We compare the energy of the quark droplets with several strangeness fraction $r_s = N_s/N_q$ to investigate the stability for the weak processes, where N_s is the number of the strange quarks and N_q is the quark number which is obtained as $N_q = A/3$ once the baryon number A is given. We keep the strangeness fraction r_s as a parameter. The ud droplets and the electrically neutral strangelets with equal number of quarks in each flavor corresponds to $r_s = 0$ and 0.33 respectively. Then the total energy E in the quark droplets with the radius R, the baryon number A and the strangeness fraction r_s is written

as

$$E = \sum_{f=u,d,s} \left[\frac{(m_f - m_f^0)^2}{4G} + \nu \int_\Lambda^{p_f^F} \sqrt{p^2 + m_f^2} \rho_{MRE}(p, m_f, R) \frac{p^2 dp}{2\pi^2} \right] V \quad (7)$$
$$-\epsilon_0 V + E_c - \frac{\alpha}{R},$$

where E_c is Coulomb energy. For simplicity, the Coulomb energy E_c is not considered in our discussions.

The minimization of the energy of the quark droplets are performed by fixing the baryon number A and the strangeness fraction r_s of the quark droplet with the radius R. Then the Fermi momentum p_f^F in the flavor f is obtained from Eq. (6). After that, we obtain the quark mass m_f in the quark droplets by the SD equation The energy and the radius of the quark droplets are given by $\partial E/\partial R = 0$ from Eq. (8).

3. Numerical results

3.1. *Restoration of chiral symmetry in the cavity vacuum*

In order to see the chiral symmetry of the cavity vacuum (the bag without valence quarks), the quark mass m in the cavity vacuum is shown in Fig. 1. As the radius of the cavity becomes small, there is a first order chiral phase transition. For example, the critical radius is 14 fm for massless quarks (see also Fig. 2). When chiral symmetry of the strange flavor is restored in the quark droplets and the mass of the s quarks is equal to the current mass, it would be energetically favorable to generate the s quarks from the u quarks by the weak decay in the ud droplets. Namely we have a possibility that the strangelets are absolutely stable when the radius of the quark droplets is sufficiently small.

3.2. *The absolute stability of quark droplets*

Now we compare the stability of the bulk quark matter and the quark droplets. Here we separate the discussions of the stability for the strong and weak forces to make the points clear, since the time scale of them are different. The energies per baryon number ϵ/n_B in quark droplets with fixed baryon number A and the strangeness fraction r_s are shown as function of the baryon number density n_B in Figs. 3 and 4 for the strangeness fraction $r_s = 0$ (ud droplet) and 0.33 (strangelet) respectively. The energy per baryon number in the vacuum $n_B = 0$ corresponds to the baryon mass in the vacuum. Concerning the bulk quark matter, we see the

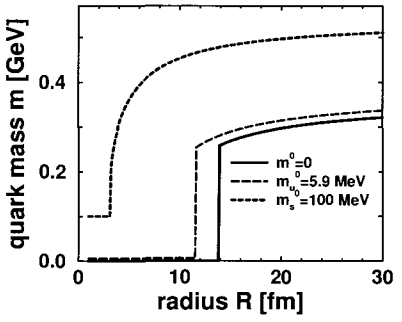

Figure 1. The quark mass m in the cavity vacuum with the radius R.

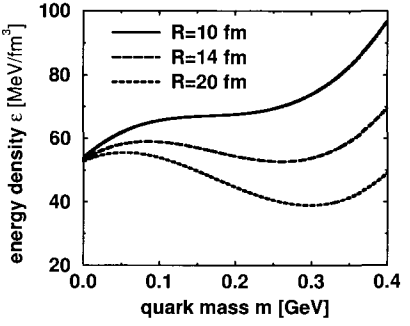

Figure 2. The energy density as function of the dynamical quark mass in the cavity vacuum with several radii. The current mass is set as $m^0 = 0$.

absolute stability of the bulk quark matter at the baryon number density $2.57\, n_B^0$ and $4.27\, n_B^0$ for $r_s = 0$ and 0.33 respectively by comparing ϵ/n_B in vacuum and at finite density. The energy gains are 19.4 MeV and 21.7 MeV for $r_s = 0$ and 0.33 respectively. Though the quark matter with any strangeness fractions is stable against the baryonic vacuum, the strange matter at the local minimum is not stable against the ud quark matter at the local minimum.

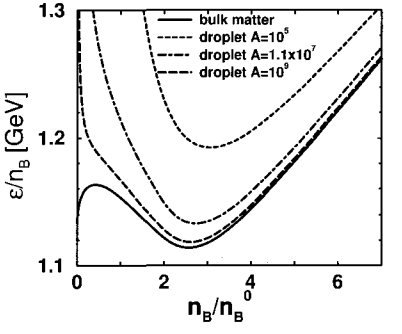

Figure 3. The energy per baryon number as function of the baryon number density with the strangeness fraction $r_s = 0$ (ud matter). The bulk quark matter and the quark droplets with various baryon number are compared.

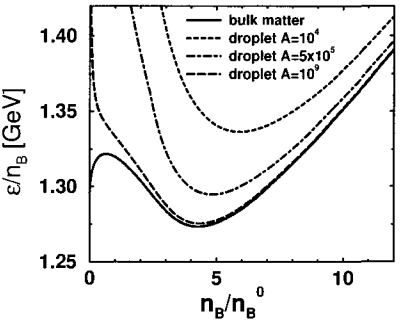

Figure 4. The same figure as Fig. 3, but with the strangeness fraction $r_s = 0.33$ (strangelet).

3.3. *The investigation of stability of strangelets*

Let us turn to the stability of the quark droplets. We see the local minima in the energy per baryon number in Figs. 3 and 4. It is recognized that energy per baryon number in the quark droplet increases as the baryon number decreases. In the *ud* droplet (Fig. 3), when the baryon number is smaller than the critical baryon number 1.1×10^7, then the energy per baryon number at the minimum is larger than the single baryon mass in the baryonic vacuum. The *ud* droplets with baryon number $A < 1.1 \times 10^7$ are not absolutely stable against the hadronization, while the *ud* droplets with $A > 1.1 \times 10^7$ are absolutely stable. This result is not changed qualitatively in the strangelets (Fig. 4) , provided that the critical baryon number is 5.0×10^5 for $r_s = 0.33$.

We have seen that the cavity vacuum with a small size restore chiral symmetry breaking as shown in Figs. 1. From this result, we can expect that the dynamical mass of the strange quark becomes small due to the restoration of the chiral symmetry breaking in the small quark droplets, which would lead absolute stability of the strangelets as compared with the *ud* droplets with small baryon number.

We plot the energy per baryon number E/A as a function of the baryon number A in a quark droplet with several strangeness fractions r_s in Fig. 5. As we expected, the strangelets ($r_s = 0.33$) are more stable than *ud* droplets for the small baryon number $A < 1.1 \times 10^3$. In fact, chiral symmetry breaking of the strange flavor is restored in the strangelets with $A < 1.1 \times 10^3$ as shown in Fig. 6. Generally, it is known that the strange quarks are generated in the quark matter, when the chemical potential μ_u of the u quarks are larger than the mass m_s, by the weak decay; $u \to s + e^+ + \nu_e$. Actually, in Fig. 7, we see $\mu_u > m_s$ in the *ud* droplets with $A < 1.1 \times 10^3$. However the strangelets which are more stable than the *ud* droplets are not absolutely stable against the strong decay to the hadrons, since the energy of such strangelets is larger than the mass of the baryons.

Though the strangelets with baryon number $A > 5.0 \times 10^5$ are not stable as compared to the *ud* droplets, they have a possibility to have a long life time. The life time τ of the weak decay of s quarks is estimated as about 10^{-7} sec. in the MIT bag model.[11] [12] It is expected that the total decay time to change all the s quarks into the u quarks in the strangelets takes more time when there are many strange quarks. Concerning the strong decay of unstable quark droplets with small baryon number, such quark droplets could have long life time to observe them in the heavy ion

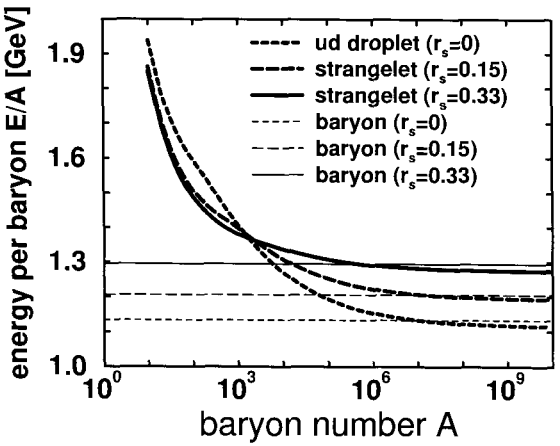

Figure 5. The energy per baryon number E/A in quark droplets with several strangeness fraction $r_s = 0$, 0.15, 0.33 as function of the baryon number A.

collisions. The transition amplitude from the quark droplets to hadrons must be suppressed, when the uniform quark wave functions in the quark droplet have to be localized to form the baryon wave functions.

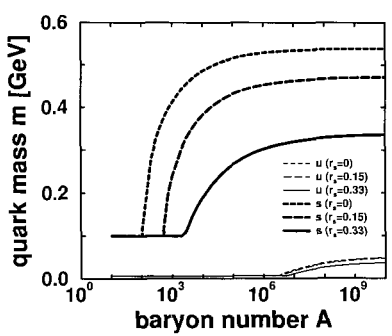

Figure 6. The quark mass of the u and s quarks in the quark droplets with various strangeness fraction $r_s = 0$, 0.15, 0.33.

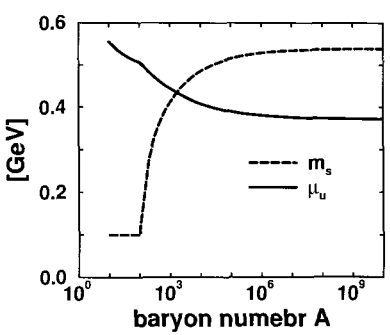

Figure 7. The chemical potential of the u quark and the dynamical mass m_s of the s quark in the ud droplet.

We have to be careful for using our model in the quark droplets with small radii. The last term in our lagrangian Eq. 1 breaks explicitly chiral symmetry, which would not change our result that the quark droplets with large baryon number is absolutely stable. On contrast, concerning the

quark droplets with small baryon number, we need to consider this problem seriously. One performance is to introduce meson fields around the bag to keep chiral symmetry on the surface. For further understanding, we need to discuss the possible decay modes of the unstable quark droplets, the effects of the color superconductivity[13] [14] and so on.

4. Conclusion

We discussed the stability of the quark droplets with chiral symmetry breaking by the NJL model supplemented by the boundary condition of the MIT bag model. The vacuum of the cavity with small radius restores chiral symmetry breaking. When the baryon number is sufficient large $A > 1.1 \times 10^7$ and $A > 5.0 \times 10^5$ for the strangeness fraction $r = 0$ and 0.33 respectively due to the boundary condition of the finite system, we found the absolute stability of the droplets against the baryons. The quark droplets with small baryon number is not stable against ordinary nuclei. Though the strangelets with large baryon number are unstable against the *ud* droplets, there is still a possibility that such strangelets have a long life time since the weak decay is considered to be suppressed in the strangelets with many baryon number.

Acknowledgments

We would like to thank S. Raha and N. Sandulescu for fruitful discussions about the strangelets at the beginning of this study. We also express our thanks to T. Itahashi for several discussions on the experiments of the strangelets.

References

1. Y. Akaishi and T. Yamazaki, *Phys. Rev.* **C65**, 044005 (2002).
2. T. Nakano *et al.* , *Phys. Rev. Lett.* **91**, 012002 (2003).
3. J. Madsen, astro-phy/9809032
4. E. Witten, *Phys. Rev.* **D30**, 272 (1984).
5. E. Fahri and R. L. Jaffe, *Phys. Rev.* **D30**, 2379 (1984).
6. S. P. Klevansky, *Rev. Mod. Phys.* **64**, 649 (1992); T. Hatsuda and T. Kunihiro, *Phys. Rept.* **247**, 221 (1994).
7. M. Buballa and M. Oertel , *Phys. Lett.* **B457**, 261 (1999).
8. O. Kiriyama and A. Hosaka, *Phys. Rev.* **D67**, 085010 (2003).
9. R. Balian and C. Bloch, *Ann. Phys.* **60**, 401 (1970); T. H. Hansson and R. L. Jaffe, *Ann. Phys.* **151**, 204 (1983)

10. E. P. Gilson and R. L. Jaffe, *Phys. Rev. Lett.* **71**, 332 (1993); J. Madsen, *Phys. Rev. Lett.* **70**, 391 (1993); *Phys. Rev.* **D47**, 5156 (1993); *Phys. Rev.* **D50**, 3328 (1994).
11. S. A. Chin and K. Kerman, *Phys. Rev. Lett.* **43**, 1292 (1979).
12. M. S. Berger and R. L. Jaffe, *Phys. Rev.* **C35**, 213 (1987).
13. J. Madsen, *Phys. Rev. Lett.* **87**, 172003 (2001).
14. O. Kiriyama, hep-ph/0401075.

Neutrinos

This page is intentionally left blank

ENERGY RELEASE DUE TO ANTINEUTRINO UNTRAPPING FROM HOT QUARK STARS*

D. N. AGUILERA, †

Fachbereich Physik, Universität Rostock, Universitätsplatz 1, D–18051 Rostock, Germany

Instituto de Física Rosario, Bv. 27 de febrero 210 bis, 2000 Rosario, Argentina

E-mail: deborah@darss.mpg.uni-rostock.de

D. BLASCHKE

Fachbereich Physik, Universität Rostock, Universitätsplatz 1, D–18051 Rostock, Germany

Bogoliubov Laboratory for Theoretical Physics, JINR Dubna, 141980 Dubna, Russia

email: david@thsun1.jinr.ru

H. GRIGORIAN

Fachbereich Physik, Universität Rostock, Universitätsplatz 1, D–18051 Rostock, Germany

Department of Physics, Yerevan State University, Alex Manoogian Str. 1, 375025 Yerevan, Armenia

email: hovik@darss.mpg.uni-rostock.de

An equation of state for 2-flavor quark matter (QM) with diquark condensation under the conditions for compact stars -β-equilibrium, charge and color neutrality- is presented. Trapped antineutrinos prevent the formation of the diquark condensate at moderate densities above a critical value of the antineutrino chemical potential $\mu^c_{\bar{\nu}_e}$. The following consequences are presented: 1) The star develops a 2-phase structure ($\mu_{\bar{\nu}_e} \geq \mu^c_{\bar{\nu}_e}$): a color superconducting QM core and a normal QM shell. 2)During the cooling, when the temperature is small enough ($T < 1$ MeV) the antineutrino mean free path becomes larger than the thickness of the normal QM shell and the antineutrinos get untrapped in a sudden burst. The energy release is estimated as $\simeq 10^{52}$ erg and an antineutrino pulse is expected to be observed.

*Conference Proceedings of the KIAS-APCTP International Symposium in Astro-Hadron Physics Compact Stars: Quest for New States of Dense Matter

†Work partially supported by Landesgraduiertenförderung von Mecklenburg- Vorpommern, Germany and by the Virtual Institute of the Helmholtz Association "Dense Hadronic Matter and QCD Phase Transition" under grant No. VH-V1-041.

1. Introduction

It has been proposed that cold dense quark matter should be in a superconducting state with the formation of a diquark condensate[1,2]. The consequences of the diquark condensation for the configuration and the cooling behaviour of compact stars have been broadly studied [3,4,5,6] and the question if this phase can be detected by the signatures still remains [7].

Also the engine for the most energetic phenomena in the universe like supernova explosions and gamma ray burst does not have a satisfactory explanation yet [8]and it has been proposed that the energy involved could be related with the occurence of the color superdonductivity phase [9,10].

Since the pairing energy gap in quark matter is of the order of the Fermi energy, the diquark condensation gives a considerable contribution to the equation of state (EoS) that is estimated of the order of $(\Delta/\mu)^2$. Disregarding relativistic effects, the total binding energy release in the core of a cooling protoneutron star has been estimated as $(\Delta/\mu)^2 M_{\rm core} \simeq 10^{52}$ erg. But, if relativistic effects are considered, the gravitational mass defect of the cooling star decreases when diquark condensation is included and there is no explosive process [6] possible since the color superconductivity transition is second order.

In this work a new mechanism of releasing the energy in an explosive way is presented (for the original idea see [11]). During the collapse of a protoneutron star antineutrinos are produced by the β-processes and remain trapped due to the small mean free path. This increases the asymmetry in the system and therefore the diquark condensation is inhibited at moderate densities. So, a two-phase structure developes in the star: a superconducting interior and a sorrounding shell of normal quark matter, the latter being opaque to antineutrinos for $T \geq 1$ MeV [12]. In the cooling process the antineutrino mean free path increases above the size of this normal matter shell and an outburst of neutrinos occurs releasing an energy of about $10^{51} - 10^{52}$ erg. This first order phase transition leads to an explosive phenomenon in which a pulse of antineutrinos could be observed.

1.1. *Equation of state for 2-flavour quark matter*

A nonlocal chiral quark model for 2-flavour $\{u, d\}$ and three color $\{r, b, g\}$ superconducting (2SC) quark matter in the mean field approximation is used, for details see [6,13]. The order parameters are the mass gap ϕ_f and the diquark gap Δ for the chiral and superconducting phase transitions respectively. As in [13], the following chemical potentials are introduced:

$\mu_q = (\mu_u + \mu_d)/2$ for quark number, $\mu_I = (\mu_u - \mu_d)/2$ for isospin asymmetry and μ_8 for color charge asymmetry. We consider that the deviation in the color space $\mu_8 \ll \mu_q$, so we neglect the effect of considering μ_8.

The quark thermodynamic potential is expresed as [14]

$$\begin{aligned}
&\Omega_q(\phi, \Delta; \mu_q, \mu_I, T) + \Omega_{vac} = \frac{\phi^2}{4G_1} + \frac{\Delta^2}{4G_2} \\
&-\frac{2}{2\pi^2}\int_0^\infty dq q^2 (N_c - 2)\{2E_\phi + \omega\left[E_\phi - \mu_q - \mu_I, T\right] \\
&+\omega\left[E_\phi - \mu_q + \mu_I, T\right] + \omega\left[E_\phi + \mu_q - \mu_I, T\right] + \omega\left[E_\phi + \mu_q + \mu_I, T\right]\} \\
&-\frac{4}{2\pi^2}\int_0^\infty dq q^2 \{E_+ + E_- + \omega[E_\phi^- - \mu_I, T] \\
&+\omega[E_\phi^- + \mu_I, T] + \omega[E_\phi^+ - \mu_I, T] + \omega[E_\phi^+ + \mu_I, T]\}
\end{aligned} \tag{1}$$

with

$$\omega[E, T] = T \ln\left[1 + \exp\left(-E/T\right)\right] \ . \tag{2}$$

The dispersion relations for the quarks of unpaired and paired colors are respectively,

$$E_\phi{}^2 = q^2 + \left(m + F^2(q)\phi\right)^2 \tag{3}$$

$$E_\phi^{\pm 2} = (E_\phi \pm \mu)^2 + F^4(\bar{q})\Delta^2 \tag{4}$$

The interaction between the quarks is implemented via a Gaussian form-factor function $F(q)$ in the momentum space (Gaussian types give stable hybrid configurations [7]) as $F(q) = \exp(-q^2/\Lambda^2)$.

The parameters $\Lambda = 1.025$ GeV, $G_1 = 3.761\ \Lambda^2$ and $m_u = m_d = m = 2.41$ MeV are fixed by the pion mass, pion decay constant and the constituent quark mass at $T = \mu = 0$ [15]. The constant G_2 is a free parameter of the approach and is fixed as $G_2 = 0.86\ G_1$.

1.1.1. *Stellar matter conditions*

The stellar matter in the interior of the compact stars consists of u and d quarks and leptons (electrons e^- and antineutrinos $\bar{\nu}_e$) under the following conditions

- β-equilibrium $\quad d \longleftrightarrow u + e^- + \bar{\nu}_e, \qquad \mu_e + \mu_{\bar{\nu}_e} = -2\mu_I,$
- Charge neutrality $\quad \frac{2}{3}n_u - \frac{1}{3}n_d - n_e = 0, \qquad n_B + n_I - 2n_e = 0,$
- Color neutrality $\quad n_8 = 0, \qquad 2n_{qr} - n_{qb} = 0,$

where $n_j = \left.\frac{\partial\Omega}{\partial\mu_j}\right|_{T,\phi=\phi_0,\Delta=\Delta_0}$ are the number densities corresponding to the chemical potential μ_j defined above.

The lepton contributions ($l = e, \bar{\nu}_e$) as ideal Fermi gases

$$\Omega_l(\mu, T) = -\frac{1}{12\pi^2}\mu^4 - \frac{1}{6}\mu^2 T^2 - \frac{7}{180}\pi^2 T^4 \tag{5}$$

are added to the quark thermodynamical potential

$$\Omega(\phi, \Delta; \mu_q, \mu_I, \mu_e, T) = \Omega_q(\phi, \Delta; \mu_q, \mu_I, T) + \Omega_e(\mu_e, T) + \Omega_{\bar{\nu}_e}(\mu_{\bar{\nu}_e}, T). \tag{6}$$

The baryon chemical potential $\mu_B = 3\mu_q - \mu_I$ is introduced as the conjugate of the baryon number density n_B.

The Ω function can have several minima in the ϕ, Δ plane, an example is shown is Fig. 1. The global minimum represents the stable equilibrium of the system and the minima search is perfomed solving the gap equations

$$\left.\frac{\partial\Omega}{\partial\phi}\right|_{\phi=\phi_0;\Delta=\Delta_0} = \left.\frac{\partial\Omega}{\partial\Delta}\right|_{\phi=\phi_0;\Delta=\Delta_0} = 0 \tag{7}$$

under the conditions that are mentioned above for the stellar interior.

The thermodynamics of the system, e.g. pressure P, energy density ϵ, number density n and entropy density s, is defined via this global minimum

$$\Omega(\phi_0, \Delta_0; \mu_B, \mu_I, T) = \epsilon - Ts - \mu_B n_B - \mu_I n_I = -P\ . \tag{8}$$

To fulfill the charge neutrality condition (see Fig. 2, right) a mixed phase between a subphase with diquark condensation (subscript $\Delta > 0$) and normal quark matter subphase (subscript $\Delta = 0$) is defined via the Glendenning construction. The Gibbs condition for equilibrium at fixed T and μ_B is that the pressure of the subphases should be the same

$$P = P^{\Delta>0}(\mu_B, \mu_I, \mu_e, T) = P^{\Delta=0}(\mu_B, \mu_I, \mu_e, T)\ . \tag{9}$$

The volume fraction χ that is occupied by the subphase with diquark condensation is defined by the charge Q in the subphases,

$$\chi = Q_{\Delta>0}/(Q_{\Delta>0} - Q_{\Delta=0})\ , \tag{10}$$

and is plotted on the right panel in Fig. 2 for different antineutrino chemical potentials as a function of μ_B. In the same way, the number

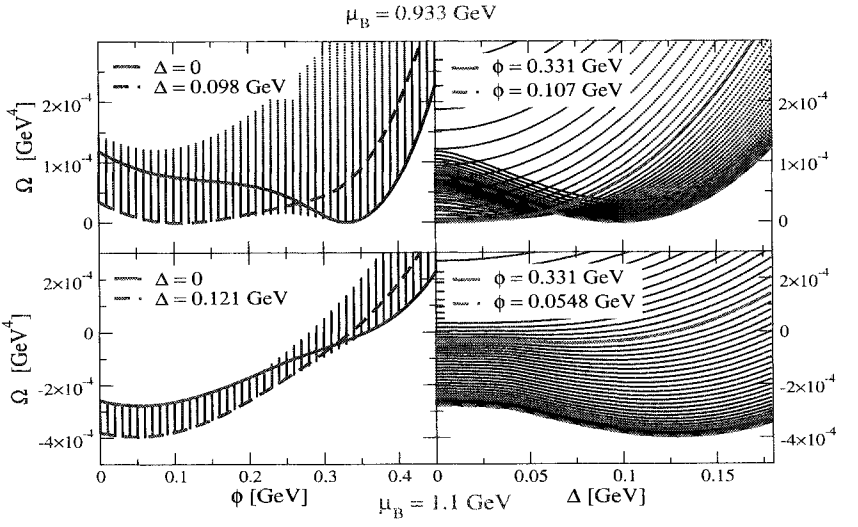

Figure 1. Cuts of the thermodynamic potential $\Omega(\phi, \Delta; \mu_B, \mu_I, T = 0)$ in the planes $\Delta = const$ (on the left) and $\phi = const$ (on the right) for two different constant values of μ_B and the corresponding μ_I. For $\mu_B = 933$ MeV (upper panel) two degenerate minima can coexist at the values: $\phi = 331$ MeV, $\Delta = 0$ (solid lines) and $\phi = 107$ MeV, $\Delta = 98$ MeV (dashed lines). For $\mu_B = 1100$ MeV (lower panel) the minimum with a nonvanishing diquark $\Delta = 121$ MeV and $\phi = 54.8$ MeV (dashed lines) is preferable. This corresponds to a first order transition from the vacuum to a superconducting phase. In this example $G_2/G_1 = 1$ was taken.

densities for the different particle species j and the energy density are given by

$$n_j = \chi n_{j_{\Delta>0}} + (1-\chi) n_{j_{\Delta=0}} \ , \tag{11}$$

$$\epsilon = \chi \epsilon_{\Delta>0} + (1-\chi)\epsilon_{\Delta=0} \ . \tag{12}$$

1.1.2. *Equation of state with trapped antineutrinos*

Increasing the antineutrino chemical potential $\mu_{\bar{\nu}_e}$ increases the asymmetry in the system and this shifts the onset of the superconducting phase transition to higher densities.

Above a critical value of $\mu_{\bar{\nu}_e} \geq \mu^c_{\bar{\nu}_e} \simeq 30$ MeV (see critical value in Fig. 2, on the left) first a normal quark matter phase occurs and then the phase transition to superconducting matter takes place, see Fig. 3, on the left.

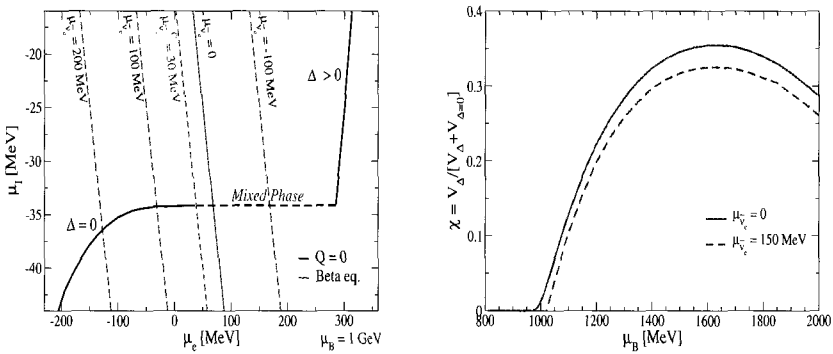

Figure 2. **Left**: Solutions of the gap equations and the charge neutrality condition (solid black line) in the μ_I vs. μ_e plane. Two branches are shown: states with diquark condensation on the upper right ($\Delta > 0$) and states from normal quark matter ($\Delta = 0$) on the lower left. The plateau in between corresponds to a mixed phase. The lines for the β-equilibrium condition are also shown (solid and dashed red lines) for different values of the (anti)-neutrino chemical potential. The stellar matter should satisfy both conditions (intersection of the corresponding lines) and therefore for $\mu_{\bar{\nu}_e} = 0$ a mixed phase is preferable. **Right**:Volume fraction χ of the phase with nonvanishing diquark condensate obtained by a Glendenning construction of a charge-neutral mixed phase. Results are shown for two different values of $\mu_{\bar{\nu}_e}$.

The consequences for the equation of state can be seen on the right of the Fig. 3: the onset of the superconductivity in quark matter is shifted to higher densities and the equation of state becames harder.

1.2. *Quark stars and antineutrino trapping*

The configurations for the quark stars are obtained by solving the Tolman-Oppenheimer-Volkoff equations for a set of central quark number densities n_q for which the stars are stable.

In Fig. 4 the configurations for different antineutrino chemical potentials are shown. The equations of state with trapped antineutrinos are softer and therefore this allows more compact configurations. The presence of antineutrinos tends to increase the mass of the star for a given central density.

A reference configuration with total baryon number $N_B = 1.51\ N_\odot$ (where $N_\odot$ is the total baryon number of the sun) is chosen and the case with (configurations A and B in Fig. 4) and without antineutrinos (f in Fig. 4) are compared. A mass defect can be calculated between the

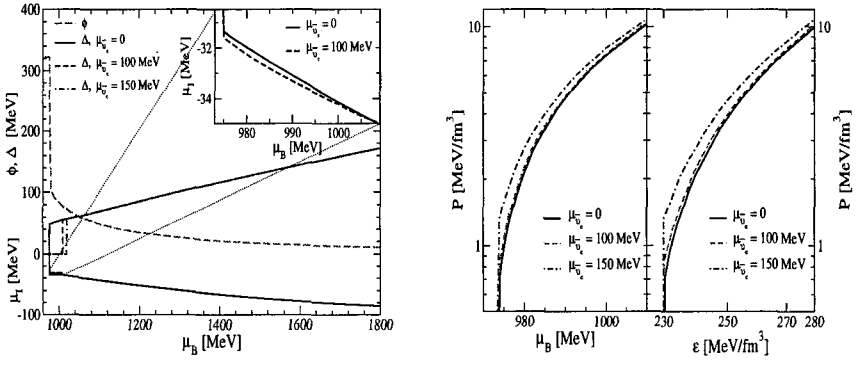

Figure 3. **Left**: Solutions of the gap equations and μ_I as a function of μ_B. Increasing the antineutrino chemical potential increases the asymmetry in the system and the superconducting phase is inhibited at moderates densities. **Right**: Equation of state for different values of $\mu_{\bar{\nu}_e}$ of trapped antineutrinos. As $\mu_{\bar{\nu}_e}$ increases the equation of state becomes harder.

configurations with and without trapped antineutrinos at constant total baryon number and the result is shown on the right panel of Fig. 4). The mass defect could be interpreted as an energy release if the configurations A, B with antineutrinos are initial states and the configuration f without them is the final state of a protoneutron star evolution.

1.2.1. *Protoneutron star evolution with antineutrino trapping*

After the collapse of a protoneutron star the star cools down by surface emission of photons and antineutrinos. Antineutrinos are trapped because they were generated by the direct β-process in the hot and dense matter and could not escape due to their small mean free path. The region of the star where the temperature falls below the density dependent critical value for diquark condensation, will transform to the color superconducting state which is almost transparent to (anti)neutrinos. But nevertheless due to the trapped antineutrinos there is a dilute normal quark matter shell which prevents neutrino escape from the superconducting bulk of the star, see Fig. 5 and Fig. 6. The criterion for the neutrino untrapping transition is to cool the star below a temperature of about 1 MeV when the mean free path of neutrinos becomes larger than the shell radius [16]. If at this temperature the antineutrino chemical potential is still large then the neutrinos can escape in a sudden outburst. If it is small then there will be only a gradual increase

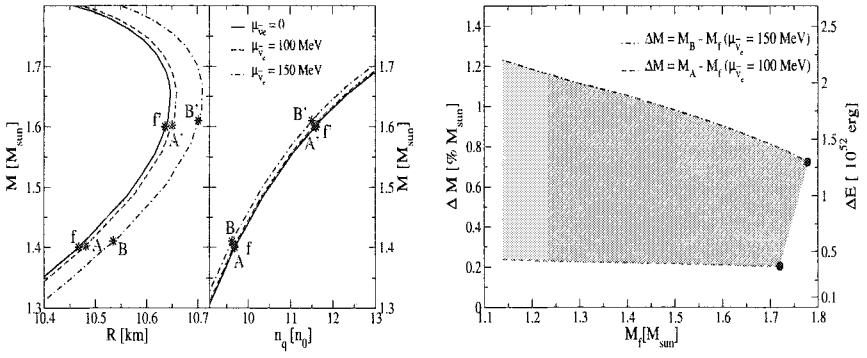

Figure 4. **Left**: Quark star configurations for different antineutrino chemical potentials $\mu_{\bar{\nu}_e} = 0,\ 100,\ 150$ MeV. The total mass M in solar masses ($M_{\rm sun} \equiv M_\odot$ in the text) is shown as a function of the radius R (left panel) and of the central number density n_q in units of the nuclear saturation density n_0 (right panel). Asterisks denote two different sets of configurations (A,B,f) and (A',B',f') with a fixed total baryon number of the set. **Right**: Mass defect ΔM and corresponding energy release ΔE due to antineutrino untrapping as a function of the mass of the final state M_f. The shaded region is defined by the estimates for the upper and lower limits of the antineutrino chemical potential in the initial state $\mu_{\bar{\nu}_e} = 150$ MeV (dashed-dotted line) and $\mu_{\bar{\nu}_e} = 100$ MeV (dashed line), respectively.

in the luminosity. An estimate for the possible release of energy within the outburst scenario can be given via the mass defect defined in the previous subsection between an initial configuration with trapped neutrinos (state A or B) and a final configuration without neutrinos (state f).

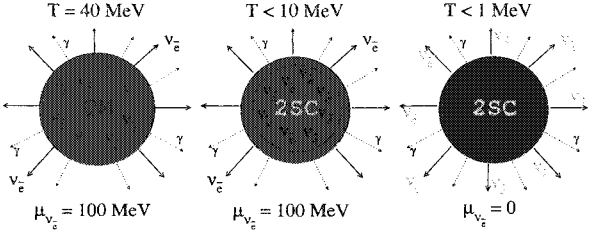

Figure 5. Left graph: Quark star cooling by antineutrino and photon emission from the surface. Middle graph: Two-phase structure developes due to the trapped antineutrinos: a normal quark matter shell and a superconducting interior. Right graph: Antineutrino untrapping and burst-type release of energy.

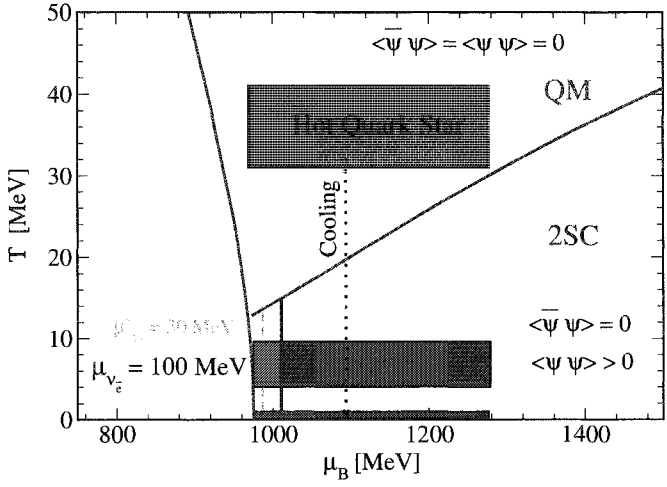

Figure 6. Star evolution corresponding to Fig. 5 plotted in the phase diagram

2. Conclusions

The effects of trapped antineutrinos on the diquark condensates in quark star configurations are investigated. At fixed baryon number the energy release in the antineutrino untrapping transition is of the order of 10^{52} erg. This is a first order transition and leads to an explosive release of energy that could help to explain energetic phenomena in the universe like gamma ray bursts or supernova explosions.

Acknowledgments

D.N.A and D.B. thank the organizers of the KIAS-APCTP International Symposium in Astro-Hadron Physics of Compact Stars for their invitation and in particular D.K. Hong and the staff of the Department of Physics at Pusan National Univertity for their hospitality and interest in this work. D.N.A acknowledges the DAAD-HOST programm D/03/31497 and the local Department of Physics for the financial support of the visit to Pusan University. The authors enjoyed the wonderful atmosphere and lively discussions with all colleagues during the conference.

References

1. M. Alford, J. A. Bowers and K. Rajagopal, J. Phys. G **27** (2001) 541 [Lect. Notes Phys. **578** (2001) 235] [arXiv:hep-ph/0009357].
2. D. Blaschke, N. K. Glendenning and A. Sedrakian, "Physics Of Neutron Star Interiors." Springer Lecture Notes in Physics **578** (2001). *Prepared for ECT* International Workshop on Physics of Neutron Star Interiors (NSI00), Trento, Italy, 19 Jun - 7 Jul 2000*
3. D. Blaschke, T. Klahn and D. N. Voskresensky, Astrophys. J. **533** (2000) 406 [arXiv:astro-ph/9908334].
4. D. Page, M. Prakash, J. M. Lattimer and A. Steiner, Phys. Rev. Lett. **85** (2000) 2048 [arXiv:hep-ph/0005094].
5. D. Blaschke, H. Grigorian and D. N. Voskresensky, Astron. Astrophys. **368** (2001) 561 [arXiv:astro-ph/0009120].
6. D. Blaschke, S. Fredriksson, H. Grigorian and A. M. Oztas, [arXiv:nucl-th/0301002].
7. D. Blaschke, H. Grigorian, D. N. Aguilera, S. Yasui and H. Toki, AIP Conf. Proc. **660** (2003) 209 [arXiv:hep-ph/0301087].
8. T. Piran and E. Nakar, arXiv:astro-ph/0202403.
9. R. Ouyed and F. Sannino, Astron. Astrophys. **387** (2000) 725 [arXiv:astro-ph/0103022].
10. D. K. Hong, S. D. H. Hsu and F. Sannino, Phys. Lett. B **516**, (2001) 362 [arXiv:hep-ph/0107017].
11. D. Aguilera, D. Blaschke and H. Grigorian, [arXiv:astro-ph/0212237].
12. S. Reddy, M. Prakash and J. M. Lattimer, Phys. Rev. D **58** (1998) 013009 [arXiv:astro-ph/9710115].
13. H. Grigorian, D. Blaschke and D. N. Aguilera, arXiv:astro-ph/0303518.
14. O. Kiriyama, S. Yasui and H. Toki, Int. J. Mod. Phys. E **10** (2001) 501 [arXiv:hep-ph/0105170].
15. S. M. Schmidt, D. Blaschke and Y. L. Kalinovsky, Phys. Rev. C **50** (1994) 435.
16. M. Prakash, J. M. Lattimer, R. F. Sawyer and R. R. Volkas, Ann. Rev. Nucl. Part. Sci. **51** (2001) 295 [arXiv:astro-ph/0103095].

COOLING DELAY FOR PROTOQUARK STARS DUE TO NEUTRINO TRAPPING*

J. BERDERMANN

Fachbereich Physik, Universität Rostock, D–18051 Rostock, Germany
E-mail: jens@darss.mpg.uni-rostock.de

D. BLASCHKE

Fachbereich Physik, Universität Rostock, D–18051 Rostock, Germany
Bogoliubov Laboratory for Theoretical Physics, JINR Dubna, 141980 Dubna, Russia

H. GRIGORIAN

Fachbereich Physik, Universität Rostock, D–18051 Rostock, Germany
Department of Physics, Yerevan State University, 375025 Yerevan, Armenia

The influence of neutrino trapping (NT) on the early cooling evolution of hot proto quark stars (PQS) with initial temperatures in the range $T \sim 40$ MeV is studied. Within a simplified model for the neutrino transport it is shown that the time for reaching neutrino opacity temperature of $T_{opac} \sim 1$ MeV is about 10 sec. This is an order of magnitude larger than without NT and of the same order as the duration long gamma ray bursts.

1. Introduction

Gamma ray bursts (GRBs) are among the most intriguing phenomena in the Universe, see [1] and references therein. If the energy is emitted isotropically, the measured energy release is of the order of $10^{53} \div 10^{54}$ erg and it is a puzzle to explain the engine of a GRB. However, there is now a compelling evidence that the gamma ray emission is not isotropic, but displays a jet-like geometry. When the emission is collimated within a narrow beam a smaller energy, of the order of 10^{52} erg, would be sufficient for the GRBs [2] but their sources are not yet understood. There is growing evidence for

*Conference Proceedings of the KIAS-APCTP International Symposium in Astro-Hadron Physics; Compact Stars: Quest for New States of Dense Matter

a connection of GRBs to supernovae now from emission features in some GRB afterglows, e.g. GRB 990707 [3], GRB 991216 [4], GRB 000214 [5] and, most recently GRB 030329 [6]. As in the realm of a supernova explosion a compact star is likely to be born, it has been conjectured (see [7] and references therein) that a phase transition from hadronic to deconfined quark matter might power the GRB. However, although the energy release might be in the right order of magnitude, the collapse timescale is too short ($\sim$ several ms) to explain long GRBs with a duration of several tens of seconds. Recently, it has been suggested [7] that the deconfinement transition in a compact star might be an example for a nucleation process of quark matter droplets which is a quantum tunneling process between metastable states, with a sufficient delay, depending on the surface tension of the quark matter droplet. This approach has been criticized [8] since during the supernova collapse the protoneutron star can be heated up to temperatures of the order of the Fermi energy $T \sim \varepsilon_F \approx 30 \div 40$ MeV so that the thermal fluctuations would dominate over quantum ones and make the phase transition sufficiently fast without the delay claimed in Ref. [7].

In the present contribution we consider the cooling evolution of a hot protoneutron star above the neutrino opacity temperature $T_{opac} \sim 1$ MeV [9], so that the neutrino mean free path is by orders of magnitude smaller than the size of the star. As it has recently been estimated [10] and also reported at this conference [11], the neutrino untrapping transition occuring when the star cools below T_{opac} might serve as an engine of a GRB. The question to be considered here is whether the energy release by neutrino emission can be sufficiently delayed due to neutrino trapping so that the typical duration of a long GRB could be explained.

2. Early cooling evolution

During the collapse of the progenitor star the density increases in its very interior from the densities of the iron core to those at and above the deconfinement transition. For this huge interval of densities, part of which we display in Fig. 1, matter can undergo several phase transitions. During these processes, like leptonization and deleptonization, neutrinos and antineutrinos are produced in weak interactions which eventually could also be trapped during the early stages of the evolution when the temperatures are expected to be much higher than T_{opac}. The cooling process for such a PQS is investigated in this contribution, where we use a simplified model of a homogeneous PQS structure and an approximate global thermal evolution.

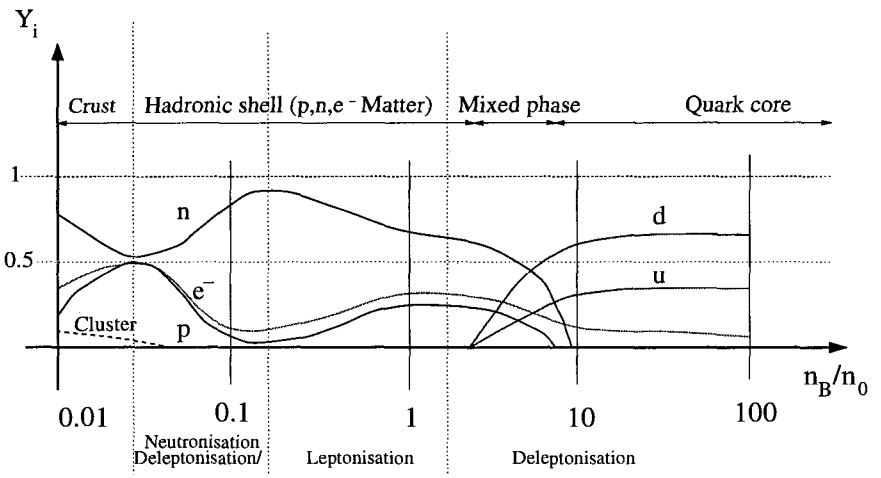

Figure 1. Schematic representation of the evolution of the composition of compact star matter with increasing density. $Y_i = n_i/n_B$ is the fraction of particles of species i per baryon and n_B/n_0 is the baryon density in units of the nuclear saturation density ($n_0 = 0.16$ fm^{-3}).

If the star cools below T_{opac} by surface-radiation, neutrinos could escape in a sudden outburst. For brevity, saying neutrino means both neutrino and antineutrino.

The loss of energy in a homogeneous system due to emission is given by

$$\frac{dU(T)}{dt} = -\epsilon_\nu(T) \cdot V \ . \tag{1}$$

Here the photon emissivity has been neglected since neutrinos dominate the cooling evolution of a PQS for temperatures well above 10^6 K. For the cooling behaviour of a star from a given initial-temperature T_i to a final temperature T_f with the luminosity $L(T) = -\epsilon_\nu(T) \cdot V$ follows

$$\triangle t = -\int_{T_i}^{T_f} \frac{C_v(T) \cdot dT}{L(T)} \ . \tag{2}$$

The luminosity $L(T) = L_\nu^V(T) + L_\nu^O(T)$ is explained more in detail in Section 3 and the specific heat $C_v(T)$ can be derived from the thermal energy $U(T)$ for relativistic quark matter [12]

$$C_v(T) = \frac{dU}{dT} = 1.8 \times 10^{48} \left(\frac{M}{M_\odot}\right) \cdot \left(\frac{n_B}{n_0}\right)^{-1/3} T_9 \ \text{erg}. \tag{3}$$

Here M is the mass of the star in units of the solar one and n_B is the baryon density of the star for a homogeneous mass distribution in units of the nuclear saturation density $n_0 = 0.16$ fm^{-3}. For the temperature we use the standard notation $T_9 = T/10^9$ K.

The emissivity for the direct URCA process in normal quark matter is given by

$$\epsilon_\nu^{URCA}(T) \simeq \frac{914}{315}\pi^2 G_F^2 \cos^2\theta_c \alpha_s \; n_B (3Y_d \; Y_u \; Y_e)^{\frac{1}{3}} \; T^6, \tag{4}$$

where G_F is the Fermi constant of the weak interaction, α_s is the strong coupling constant and θ_c the Cabbibo angle. We have introduced the fractions of the particle species i as $Y_i = n_i/n_B$ and the baryon density in terms of up and down quark densities is $n_B = (n_u + n_d)/3$. The neutrino mean free path (MFP) has the expression [13]

$$\lambda(T) = \frac{(6\pi)^{\frac{1}{3}}}{12 G_F^2 \cos^2\theta_c} \frac{Y_\nu^{\frac{1}{3}}}{Y_u^{\frac{2}{3}} Y_e} n_B^{-\frac{4}{3}} \left[1 + \frac{1}{2}\left(\frac{3Y_e}{Y_u}\right)^{\frac{1}{3}} + \frac{1}{10}\left(\frac{3Y_e}{Y_u}\right)^{\frac{2}{3}}\right]^{-1} \times [(E_\nu - \mu_\nu)^2 + (\pi T)^2]^{-1}. \tag{5}$$

Using the PQS matter constraints of charge neutrality $\frac{2}{3}n_u - \frac{1}{3}n_d - n_e = 0$ and β-equilibrium for the case of trapped neutrinos $\mu_\nu = \mu_u + \mu_e - \mu_d$, we can express all particle fractions Y_i via Y_e. In our model calculation we choose $Y_e = 0.001$ and approximate $E_\nu \simeq T$. For the above choice of parameters, the temperature dependence of the MFP is shown in Fig. 2 and the emissivity in Fig. 3, respectively.

3. Emissivity and luminosity of PQS

The emissivity ϵ_ν^{URCA} for the direct URCA-process in quark-matter Eq. (4) has to be modified for temperatures, at which the star is opaque to neutrinos. Due to the trapping of the neutrinos their emissivity is modified by a factor which takes into account the probability that the neutrino created at a distance r from the center can leave the star in the direction given by the angle α. The effective emissivity is given by a product of the emissivity for the direct URCA process and an exponential suppression factor

$$\bar{\epsilon}_\nu(r, \alpha; T) = \exp\left[-l(r, \alpha)/\lambda(T)\right] \cdot \epsilon_\nu^{URCA}(T) \; , \tag{6}$$

where $l(r, \alpha)$ is the distance from the neutrino creation point to the star surface, which for a spherically symmetric star with radius R is given by

$$l(r, \alpha) = \sqrt{R^2 - r^2 \sin^2\alpha} - r \; \cos\alpha. \tag{7}$$

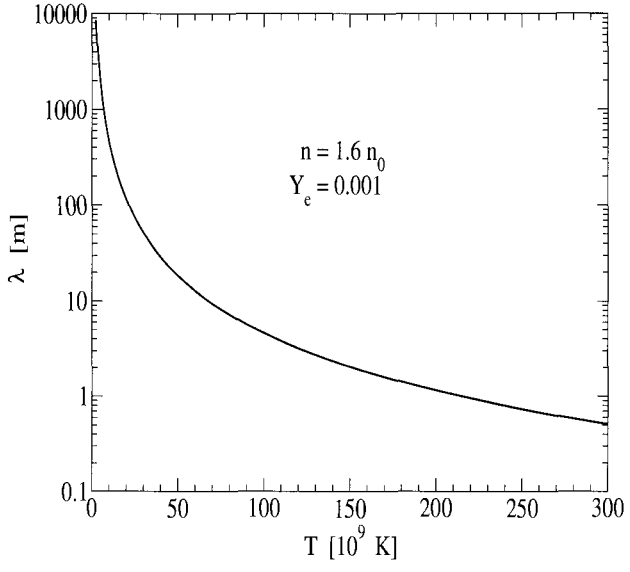

Figure 2. The neutrino MFP as a function of the temperature for given baryon density and electron fraction.

We average over all possible neutrino directions

$$\bar{\epsilon}_\nu(r;T) = \frac{1}{\pi}\int_0^\pi d\alpha\ \bar{\epsilon}_\nu(r,\alpha;T)\ , \tag{8}$$

and integrate over all distances r up to the star radius R in order to obtain the total luminosity for neutrino emission from the star volume

$$L_\nu^V(T) = 4\pi\int_0^R dr\ r^2\cdot\bar{\epsilon}_\nu(r;T)\ . \tag{9}$$

As long as the temperatures are high enough, $T \gtrsim 1$ MeV, there is a spherical inner star region, from where practically no neutrinos escape so that their number is quasi conserved and can be defined by a finite chemical potential μ_ν. This region extends up to a distance R_S from the center. The radius R_S of the neutrinosphere is a function of the temperature and moves towards the center during the cooling evolution, see Fig. 4. In calculating the bulk neutrino luminosity of a PQS during the trapping era, we can restrict the integration in Eq. (9) to the region between the neutrinosphere

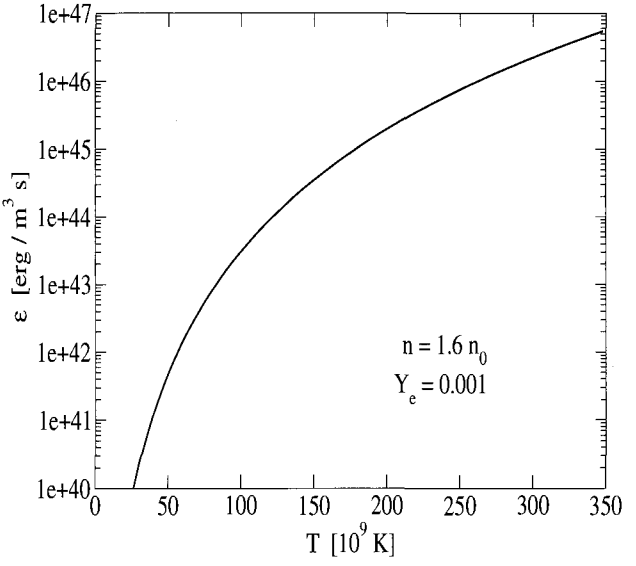

Figure 3. Temperature dependence of the neutrino emissivity for the URCA process for given baryon density and electron fraction.

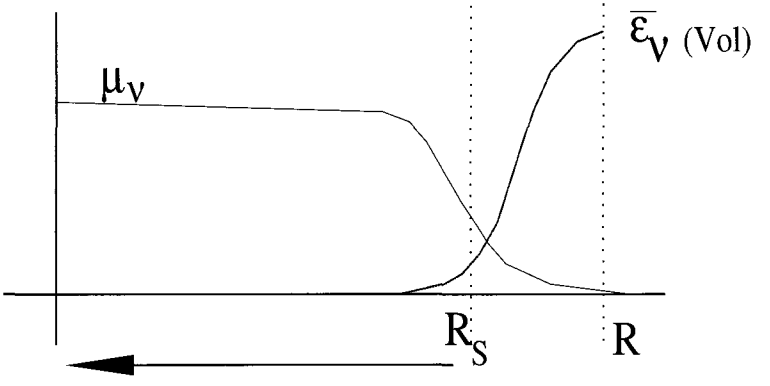

Figure 4. Evolution of the neutrinosphere.

and the surface of the star. Besides the bulk luminosity we have additional neutrino radiation just from the neutrinosphere which can be taken into

account by the generalized blackbody radiation formula

$$L_{\bar{\nu}}^{O}(T) = 4\pi R_S^2 \cdot \left(\frac{\mu_\nu^4}{4\pi^2} + \frac{\mu_\nu^2\, T^2}{2} + \frac{7\pi^2\, T^4}{60} \right) , \tag{10}$$

which we denote as inner surface luminosity. From the evolution of R_S with time we can characterize the untrapping transition of neutrinos as a burst-type phenomenon or a smooth fading. In Fig. 5 we compare the

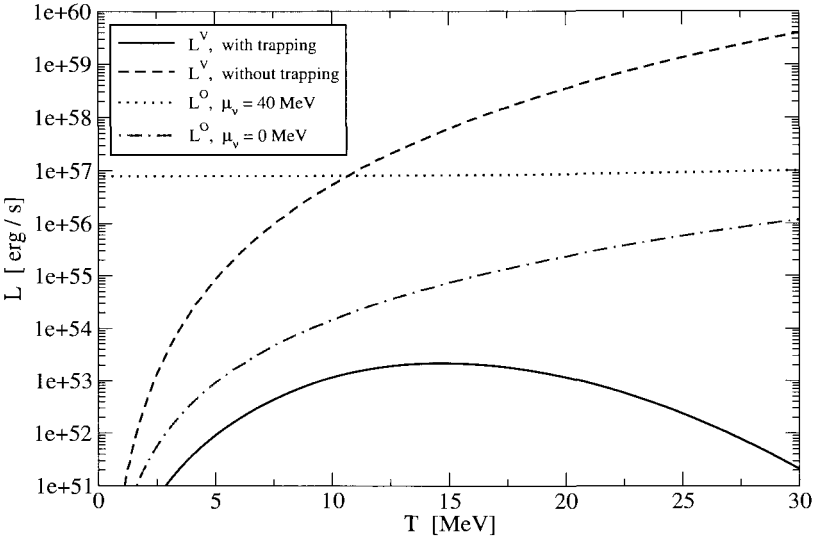

Figure 5. Temperature dependence of the bulk and inner surface neutrino luminosities.

temperature dependence of the bulk and inner surface luminosities. These results show that the trapping of the neutrinos changes the luminosities by about 6 orders of magnitude within the trapping regime. Moreover, for the trapping case, in contrast to the untrapped bulk emission, the bulk luminosity has a maximum at 10^{53} erg/s for temperatures around 15 MeV. Due to this particuliar behavior of the bulk luminosity in the neutrino trapping regime we expect that for initial temperatures much higher than 30 MeV there is not only a quantitative change in the cooling evolution but rather a qualitative change in the temporal evolution of the energy release.

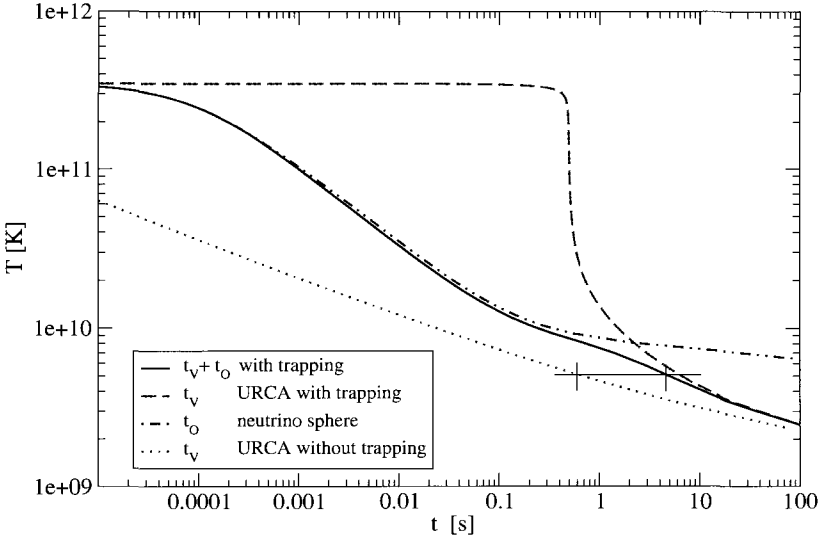

Figure 6. Cooling behavior of a protoneutron star with initial temperature $T_i = 30$ MeV and $R = 12$ km.

4. Results

In Fig. 6 we show the cooling curves of a PQS for an initial temperature of $T_i = 30$ MeV and a star radius of $R = 12$ km. The solid line corresponds to a cooler in the trapping regime including all effects discussed above. The other curves correspond to limiting cases, in particular to the case without trapping (dotted line), the case with trapping but without surface emission (dashed line) and the emission from the inner sphere only (dash-dotted line). The comparison shows that at the vicinity of the total untrapping regime for $T = 0.6$ MeV the time delay of the cooling with trapping amounts to a factor of ten. If one will neglect the inner surface emission of the neutrinos, then the neutrino release will not only be delayed but also occur within a sudden burst.

5. Outlook

The investigation of the effects of neutrino trapping on PQS evolution is only in its beginning. We have outlined a simple model for the study of spherical neutrino emission from a hot PQS with and without trapping.

Detailed investigations have to be conducted in order to make firm conclusions whether the hot neutrino trapping scenario could shed light into the mysteries of GRBs and the GRB supernova connection. We underline two observations made in this report:

- The main thermal energy of the star is released in a time interval, which is of the order of the duration of long GRB's ($\sim$ 10 s).
- The amount of energy which can be released in the cooling of a homogeneous PQS depends much on the initial temperature which is unknown and might for the PQS scenario be up to one order of magnitude larger than for the canonical protoneutron star scenario.

This latter observation can have significant implications for the early cooling evolution after a supernova collapse due to the strong temperature dependence of the dominating URCA process on the one hand and the large effective absorption of bulk emissivity on the other. Note that we have omitted here the possible effects of finite thermal conductivity which could make the separation of the neutrinosphere from the bulk emission zone even stronger and enhance the eventual temporal structure in the cooling evolution. First estimates show that the neutrino release can occur within a burst [10] and provided the conversion process to gamma rays is effective enough [14], an interesting PQS-GRB scenario emerges which can include a beaming mechanism due to the formation of a vortex lattice in a strongly magnetized superconducting PQS [15].

Acknowledgments

J.B. and D.B. thank the organizers of the KIAS-APCTP International Symposium on Astro-Hadron Physics of Compact Stars and DAAD-HOST programm D/03/31497 for the financial support of their conference participation and a study visit to Pusan University. The authors thank the colleagues for their interest in this work and useful discussions during the conference. H.G. acknowledges the support of the Virtual Institute VH-VI-041 of the Helmholtz Association for "Dense hadronic Matter and QCD Phase Transition".

References

1. T. Piran, Phys. Rep. **314**, 575 (1999); ibid **333**, 529 (2000).
2. D.A. Frayl et al., Astrophys. J., **562**, L55 (2001).
3. L. Amati et al., Science, **290**, 953 (2000); Astron. & Astrophys. **390**, 81 (2002).

4. L. Piro, et al., Astrophys. J., **514**, L73 (1999); Science, **290**, 955 (2000).
5. L.A. Antonelli et al., Astrophys. J. **545**, L39 (2000).
6. J.P.U. Fynbo et al., arXiv:astro-ph/0402264.
7. Z. Berezhiani, I. Bombaci, A. Drago, F. Frontera, and A. Lavagno, Astrophys. J., **586**, 1250 (2003).
8. D.N. Voskresensky, private communication.
9. S. Reddy, M. Prakash, and J.M. Lattimer, Phys. Rev. **D 58**, 013009 (1998).
10. D.Aguilera, D. Blaschke, and H. Grigorian, Astron. & Astrophys., **416**, 991 (2004).
11. D. Aguilera, D. Blaschke, and H. Grigorian, arXiv:astro-ph/0402073, these proceedings.
12. S. L. Shapiro, S. A. Teukolsky *Black Holes, White Dwarfs and Neutron Stars* 1983 by John Wiley & Sons, Inc.
13. N. Iwamoto, Ann. Phys. **141**, 1, (1982).
14. P. Haensel, B. Paczynski and P. Amsterdamski, Astrophys. J. **375** (1991) 209.
15. J. Berdermann, D. Blaschke, H. Grigorian, D.K. Hong and D.N. Voskresensky, in preparation.

COOLING OF NEUTRON STARS WITH COLOR SUPERCONDUCTING QUARK CORES*

D. BLASCHKE

Fachbereich Physik, Universität Rostock, D–18051 Rostock, Germany
Bogoliubov Laboratory for Theoretical Physics, JINR Dubna, 141980 Dubna, Russia
email: david@thsun1.jinr.ru

D. N. VOSKRESENSKY

Theory Division, GSI mbH, D–64291 Darmstadt, Germany
Moscow Institute for Physics and Engineering, 115409 Moscow, Russia

H. GRIGORIAN

FB Physik, Universität Rostock, D–18051 Rostock, Germany
Department of Physics, Yerevan State University, Alex Manoogian Str. 1, 375025 Yerevan, Armenia

We show that within a recently developed nonlocal, chiral quark model the critical densities for a phase transition to color superconducting quark matter under neutron star conditions can be low enough that these phases occur in compact star configurations with masses below 1.4 $M_\odot$. We study the cooling of these objects in isolation for different values of the gravitational mass and thus different composition and structure of the interior. Our equation of state allows for a 2SC phase with a large quark gap $\Delta \sim 100$ MeV for u and d quarks of two colors, a normal quark matter phase and their coexistence in a mixed phase within the hybrid star interior. We argue that, if the phases with unpaired quarks were allowed, the corresponding hybrid stars would cool too fast to describe the neutron star cooling data existing by today. We incorporate other attractive channels permitting a weak pairing of the residual quarks which remained unpaired in the 2SC phase and demonstrate that the model does not contradict the cooling data if the weak pairing gaps are of the order of 0.1 MeV.

*Conference Proceedings of the KIAS-APCTP International Symposium in Astro-Hadron Physics Compact Stars: Quest for New States of Dense Matter

1. Introduction

In the recent paper [1], hereafter BGV, we have reinvestigated the cooling of neutron stars (NS) within a purely hadron model, i.e., ignoring the possibility of quark cores in NS interiors. We have demonstrated that the NS cooling data available by today can be well explained within the *"Nuclear medium cooling scenario"*, i.e., if one includes medium effects in the emissivity and takes into account a suppression of the $3P_2$ neutron gap. In a subsequent work [2] we have shown that this result does not exclude the possibility that neutron stars might possess large quark matter cores that extend up to more than half of the star radius. Such a hybrid structure gives room for a whole variety of additional scenarios of compact star cooling which fall into two classes: either nuclear and quark matter phases have similar cooling behavior (homgeneous cooling) or the faster cooling of the one phase is compensated by the slower cooling of the other (inhomogeneous cooling). In the present contribution we will report on our results within the former, homgeneous cooling scenario of hybrid stars and what implications the comparison with present-day cooling data may provide for the EoS and transport properties of quark matter.

2. Color superconductivity

The quark-quark interaction in the color anti-triplet channel is attractive driving the pairing with a large zero-temperature pairing gap $\Delta \sim 100$ MeV for the quark chemical potential $\mu_q \sim (300 \div 500)$ MeV, cf. [3,4], see review [5] and Refs therein. The attraction comes either from the one-gluon exchange, or from a non-perturbative 4-point interaction motivated by instantons [6] or from non-perturbative gluon propagators [7]. Various phases are possible. The so called 2-flavor color superconductivity (2SC) phase allows for unpaired quarks of one color, say blue. There may also exist a color-flavor locked (CFL) phase [8] for not too large values of the dymanical strange quark mass or other words for very large values of the baryon chemical potential [9], where the color superconductivity (CSC) is complete in the sense that the diquark condensation produces a gap for quarks of all three colors and flavors. The value of the gap is of the same order of magnitude as that in the two-flavor case. There exist other attractive quark pairing channels for quarks that can't participate in 2SC and CFL pairing. These weak pairing channels are characterized by gaps typically in the interval ~ 10 keV $\div 1$ MeV, and a prominent example which will be used in the present work is the spin-1 pairing channel of single color diquarks in the

isospin singlet state, also named as color-spin locking (CSL) phase.

The high-density phases of QCD at low temperatures may exist in the interiors of hybrid stars affecting their cooling, rotation and magnetic field evolution, cf. [11,12,13,14,15].

3. Hybrid stars

In describing the hadronic part of the hybrid star we exploit the Argonne $V18+\delta v+UIX^*$ model of the EoS given in [16], which is based on the most recent models for the nucleon-nucleon interaction with the inclusion of a parameterized three-body force and relativistic boost corrections. Actually we adopt here an analytic parameterization of this model by Heiselberg and Hjorth-Jensen [17], hereafter HHJ. The latter uses a compressional part with the incompressibility $K \simeq 240$ MeV, and a symmetry energy fitted to the data around nuclear saturation density that smoothly incorporates causality at high densities. The density dependence of the symmetry energy is very important since it determines the value of the threshold density for the DU process ($n_c^{\rm DU}$). The HHJ EoS fits the symmetry energy to the original Argonne $V18 + \delta v + UIX^*$ model yielding $n_c^{\rm DU} \simeq 5.19\ n_0$ ($M_c^{\rm DU} \simeq 1.839\ M_\odot$).

The 2SC phase occurs at lower baryon densities than the CFL phase, see [18,19]. For applications to compact stars the omission of the strange quark flavor is justified by the fact that central chemical potentials in star configurations do barely reach the threshold value at which the mass gap for strange quarks breaks down and they appear in the system [22].

We will focus on the model of the quark EoS developed in [23]. The Gaussian, Lorentzian and NJL type cutoff formfactors were studied. The Lorentzian interpolates between a soft (Gaussian type, $\alpha \sim 2$), and a hard (NJL, $\alpha > 30$) depending on the value of the parameter α. We will further work out two possibilities of the Gaussian and the Lorentzian formfactors.

In some density interval at the first order phase transition there may appear the region of the mixed phase, see [21]. Ref. [21] disregarded finite size effects, such as surface tension and charge screening. Refs [24] on the example of the hadron-quark mixed phase have demonstrated that finite size effects might play a crucial role substantially narrowing the region of the mixed phase or even forbidding its appearance. Therefore we omit the possibility of the hadron-quark mixed phase in our model where the quark phase arises by the Maxwell construction. For the case of the Gaussian formfactor the quark core appears for $n > n_c = 0.34\text{fm}^{-3}$ ($M > 0.852\ M_\odot$),

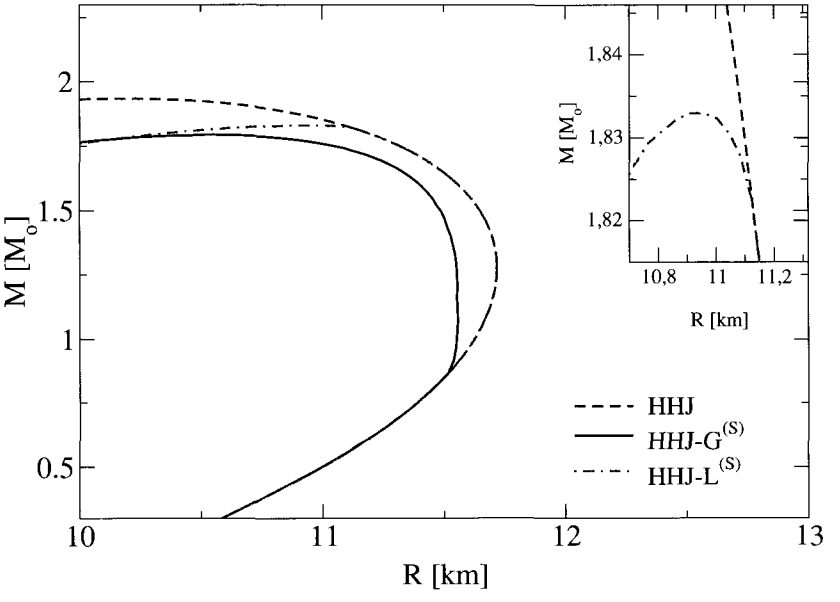

Figure 1. Mass - radius relations for compact star configurations with different EoS: purely hadronic star with HHJ EoS (dashed line), stable hybrid stars with HHJ - $SM_G^{(S)}$ EoS (solid line) and with HHJ - $SM_L^{(S)}$ EoS (dash-dotted line).

for the Lorentzian formfactor $n > n_c = 0.80\text{fm}^{-3}$ ($M > 1.81\ M_\odot$). In the following, we will not further discuss the Lorentzian case which gives a marginal quark core in a small mass range only, see Fig. 1.

A large difference between chemical potentials of u and d quarks forbids the pure 2SC phase, cf. [23]. The CFL phase is still not permitted at such densities. Ignoring the possibility of a weak coupling we have two possibilities: either the quark matter for $n > n_c$ is in the normal phase, or there appears a region of the 2SC – normal quark mixed phase. Following [21], Ref. [22] considered the latter possibility disregarding finite size effects and has found the possibility of a wide region (for Gaussian formfactor) of the 2SC – normal quark mixed phase instead of a pure 2SC phase. In the given case arguments of [24] are relaxed since the surface tension on the 2SC – normal quark boundary should be much less compared to that for the quark – hadron boundary. Indeed, the surface tension is proportional to

the difference of the energies of two phases, being very small in the given case, $\propto (\Delta/\mu_q)^2 \ll 1$.

In Fig. 1 we present the mass-radius relation for hybrid stars with HHJ vs. SM EoS. Two sets of configurations given by Gaussian (solid lines) and Lorentzian (dash-dotted lines) formfactors are stable, see also Ref. [23], where similar results for the nonlinear Walecka model EoS (RMF) have been found.

If one switches on the possibility of the weak coupling, e.g. the CSL pairing channel, see [10,19,20] all the quarks in the normal phase may acquire a corresponding spin-1 pairing gap, typically $\Delta \sim 10$ keV $\div 10$ MeV. In such a way all the quarks may get paired, either strongly in the 2SC channel or weakly in the CSL one.

4. Cooling

For the calculation of the cooling of the hadron part of the hybrid star we adopt the same model as in BGV. The main processes are medium modified Urca (MMU) and pair breaking and formation (PBF) processes. The HHJ EoS was adopted. In Fig. 2 (Fig. 20 of BGV) we show the cooling of different NS calculated within the hadron model of BGV. We use a fit-law for the relation between surface and interior temperatures, see BGV. Possibilities of the pion condensation and of the other so called exotic processes are for simplicity suppressed. Direct Urca is irrelevant in this model up to very large NS mass $M > 1.839\ M_\odot$. $1S_0$ neutron and proton gaps are taken the same as in paper [25], whereas $3P_2$ neutron gap is suppressed by the factor 0.1, see Fig. 4 of BGV.

For the calculation of the cooling of the quark part of the hybrid star we are basing on the model [13]. We include the most efficient processes: the quark direct Urca (QDU) processes on unpaired quarks, the quark modified Urca (QMU), the quark bremsstrahlung (QB), the electron bremsstrahlung (EB) Following [26] we include the emissivity of the quark pair formation and breaking (QPFB) processes. The specific heat incorporates the quark contribution, the electron contribution and the gluon-photon contribution. In the CSL phase [20] the specific heat is proportional to T^2. This new term does not significantly affect the total specific heat since the main contribution comes from electrons. The heat conductivity contains quark, electron and gluon terms.

We are basing on the picture presented in Fig. 2 and add the contribution of the quark core. For the Lorentzian formfactor the quark core

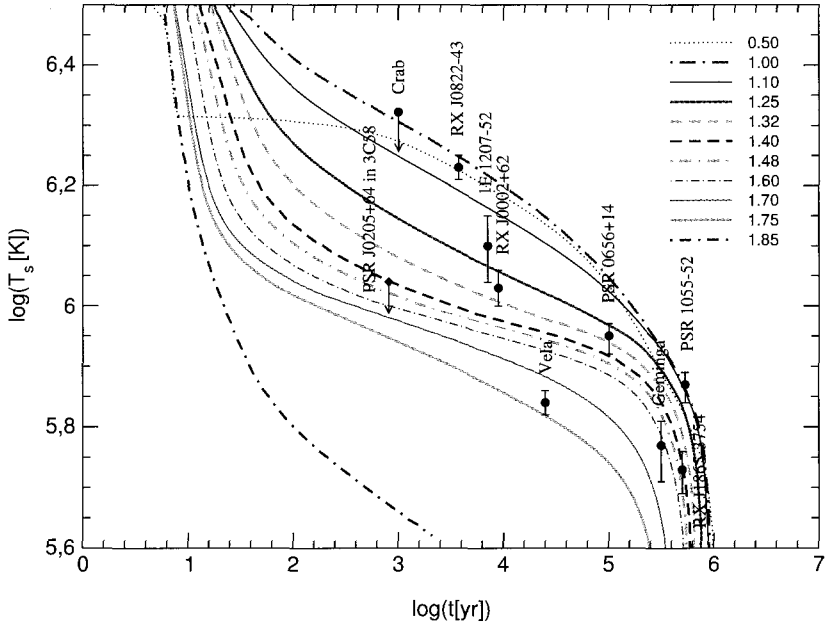

Figure 2. Cooling curves according to the nuclear medium cooling scenario, see Fig. 20 of BGV. The labels correspond to the gravitational masses of the configurations in units of the solar mass.

appears only for $M > 1.81\ M_\odot$, see Fig. 1. The existing cooling data are not affected, thereby.

For the Gaussian formfactor the quark core occurs already for $M > 0.852\ M_\odot$ according to the model [23], see Fig. 1. Most of the relevant NS configurations (see Fig. 2) are then affected by the presence of the quark core. First we check the possibility of the 2SC+ normal quark phases.

Fig. 3 shows the cooling curves calculated with the Gaussian ansatz. The variation of zero temperature gaps for the strong pairing of quarks within 2SC phase in the interval $\Delta \sim 20 \div 200$ MeV only slightly affects the results. The main cooling process is the QDU process on normal quarks. We see that the presence of normal quarks leads to too fast cooling. The data could be explained only if all the masses lie in a very narrow interval ($0.82 < M/M_\odot < 0.90$ in our case). The existence of only a very narrow

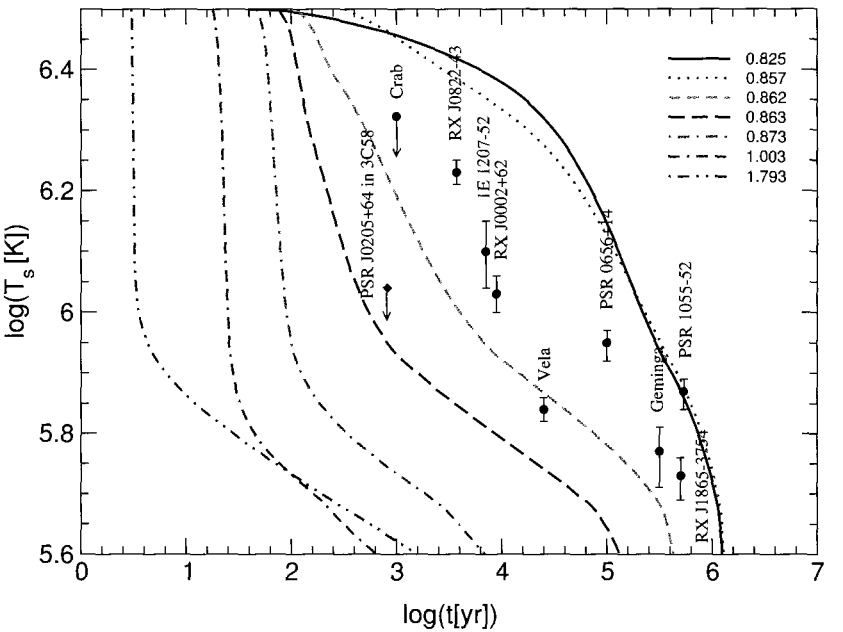

Figure 3. Cooling curves for hybrid star configurations with Gaussian quark matter core in the 2SC phase. The labels correspond to the gravitational masses of the configurations in units of the solar mass.

mass interval in which the data can be fitted seems us unrealistic as by itself as from the point of view of the observation of the NS with different masses: $M \simeq 1.41\ M_\odot$ and $M \simeq 1.25\ M_\odot$, cf. [27]. Thus the data can't be satisfactorily explained.

In Fig. 4 we permit the weak pairing for all quarks which were assumed to be unpaired. We use $\Delta \simeq 1$ MeV for the corresponding quark gap. Fig. 4 demonstrates too slow cooling.

In Fig. 5 we again allow for the weak pairing of those quarks which were assumed to be unpaired in Fig. 3, but now we use $\Delta = 50$ keV for the corresponding CSL quark gap. The data are appropriately fitted. The "slow cooling" data are explained by the cooling of NS either without quark core ($M \sim 0.5\ M_\odot$, see Fig. 2) or with a quark core. Although the majority of experimental cooling points are covered by NS masses in a very narrow

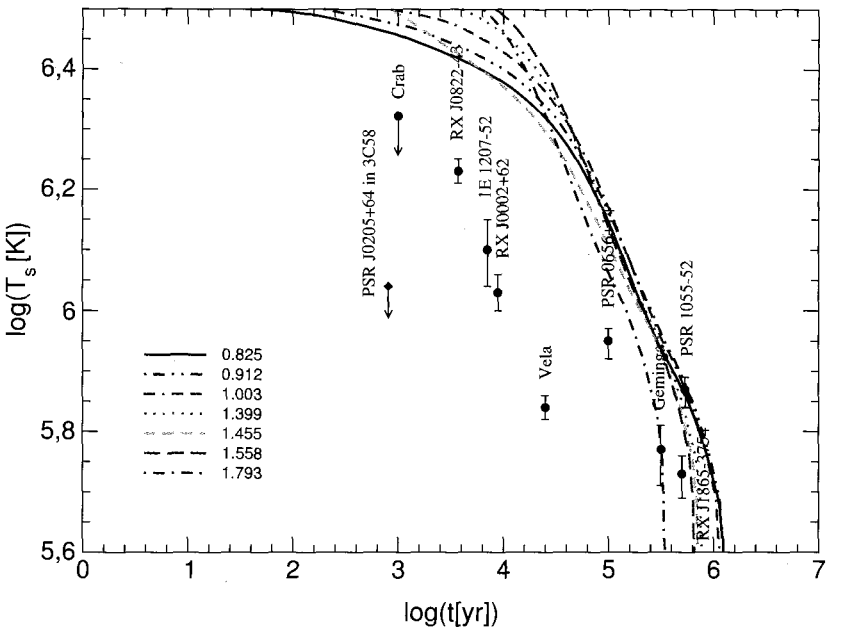

Figure 4. Cooling curves for hybrid star configurations with Gaussian quark matter core in the 2SC+CSL phase. The weak pairing gap is 1 MeV. The labels correspond to the gravitational masses of the configurations in units of the solar mass.

mass interval $M = 0.86 \div 0.87\ M_\odot$ the difference with Fig. 3 is crucial. We see that with the higher masses, up to 1.6 $M_\odot$ one may cover the rapid cooling point (Vela). Besides, the variation of parameters allows to shift all the curves up what permits to essentially broaden the mass interval that would cover the data. E.g. with the so called Tsuruta law for the $T_s - T_{in}$ relation the corresponding mass interval is $M = 0.86 \div 1.79\ M_\odot$. With these remarks we showed that the 2SC+CSL+hadron scenario allows to fit the data as well as the purely hadronic scenario, see [1]. To be more realistic one should further inlcude density dependences of the gaps what we intend to do in the forthcoming publication.

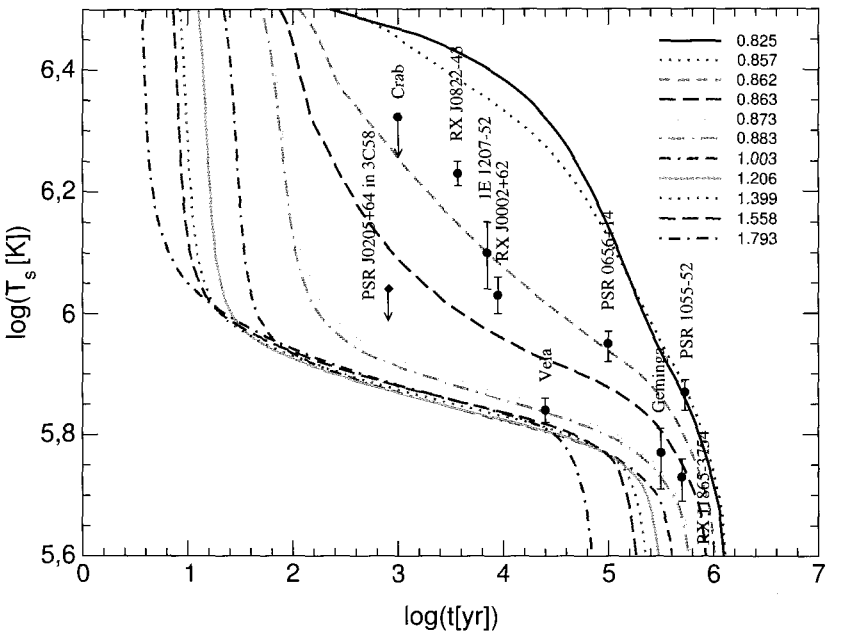

Figure 5. Same as Fig. 4 but with a weak pairing gap of 50 keV.

Conclusion

Concluding, we demonstrated that the present day cooling data can be explained not only by a purely hadronic structure of NS interiors but also by a hybrid one with a complex pairing pattern, where quarks are partly strongly paired within the 2SC channel, and partly weakly paired within the CSL channel with gaps $\Delta \lesssim 50$ keV. We conclude also that our choice of a density-independent weak pairing gap could be the reason why the mass interval for explaining slow and intermediate cooling data is very narrow. As it is well-known that the CSL gap should have a strong density dependence [20], the fastening of the cooling by increasing the star masses should be partly compensated for by the corresponding increase of the weak pairing gap. Corresponding calculations are under way.

Acknowledgement

H.G. and D.V. acknowledge the hospitality and support of Rostock University. The work of H.G. has been supported in part by the Virtual Institute of the Helmholtz Association under grant No. VH-VI-041, that of D.V. has been supported in part by DFG grant No. 436 RUS 17/117/03 and by RFBR grant NNIO-03-02-04008. D.B. thanks the organizers of the workshop, in particular D.-K. Hong and C.-H. Lee, for their invitation and support.

References

1. D. Blaschke, H. Grigorian, and D.N. Voskresensky, Cooling of Neutron Stars. Hadronic Model, arXiv:astro-ph/0403170
2. D. Blaschke, H. Grigorian, and D.N. Voskresensky, Cooling of Neutron Stars. Hybrid Model with 2SC and CSL Quark Matter Phases, Preprint MPG-VT-UR 247/04 (2004).
3. M. Alford, K. Rajagopal, and F. Wilczek, Phys. Lett. **B 422**, 247 (1998).
4. R. Rapp, T. Schäfer, E.V. Shuryak, and M. Velkovsky, Phys. Rev. Lett. **81**, 53 (1998).
5. K. Rajagopal, and F. Wilczek, "The Condensed Matter Physics of QCD", in: B.L. Ioffe Festschrift *At the Frontier of article Physics / Handbook of QCD*, vol. 3, edited by M. Shifman, World Scientific, Singapore, 2001, p. 2061
6. D. Diakonov, H. Forkel, and M. Lutz, Phys. Lett. **B 373**, 147 (1996); G.W. Carter, and D. Diakonov, Phys. Rev. **D 60**, 016004 (1999); R. Rapp, E. Shuryak, and I. Zahed, Phys. Rev. **D 63**, 034008 (2001).
7. D. Blaschke, and C.D. Roberts, Nucl. Phys. **A 642**, 197 (1998); J.C.R. Bloch, C.D. Roberts, and S.M. Schmidt, Phys. Rev. **C 60**, 65208 (1999).
8. M. Alford, K. Rajagopal, and F. Wilczek, Nucl. Phys. **B 357**, 443 (1999); T. Schäfer, and F. Wilczek, Phys. Rev. Lett. **82**, 3956 (1999).
9. M. Alford, J. Berges, and K. Rajagopal, Nucl. Phys. **B 558**, 219 (1999).
10. M. Alford, J. Bowers, J. Cheyne, and G.A. Cowan, Phys. Rev. **D 67**, 054018 (2003).
11. D. Blaschke, T. Klähn, and D.N. Voskresensky, Astrophys. J. **533**, 406 (2000).
12. D. Page, M. Prakash, J.M. Lattimer and A. Steiner, Phys. Rev. Lett. **85** 2048 (2000).
13. D. Blaschke, H. Grigorian, and D.N. Voskresensky, Astron. & Astrophys. **368**, 561 (2001).
14. D. Blaschke, D. M. Sedrakian, and K. M. Shahabasian, Astron. & Astrophys. **350**, L47 (1999); D.M. Sedrakian, D. Blaschke, K.M. Shahabasyan, and D.N. Voskresensky, Astrofizika **44**, 443 (2001).
15. K. Iida, and G. Baym, Phys. Rev. **D 63**, 074018 (2001); Phys. Rev. **D 65**, 014022 (2002); Phys. Rev. **D 66**, 014015 (2002).
16. A. Akmal, V.R. Pandharipande, and D.G. Ravenhall, Phys. Rev. **C 58**, 1804

(1998).
17. H. Heiselberg, and M. Hjorth-Jensen, Astrophys. J. **525**, L45 (1999).
18. A.W. Steiner, S. Reddy, and M. Prakash, Phys. Rev. **D 66**, 094007 (2002).
19. F. Neumann, M. Buballa, and M. Oertel, Nucl. Phys. **A714**, 481 (2003).
20. M. Buballa, J. Hosek and M. Oertel, Phys. Rev. Lett. **90** (2003) 182002
21. N.K. Glendenning, Phys. Rev. **D 46** 1274 (1992); N.K. Glendenning, Phys. Rep. **342**, 393 (2001).
22. C. Gocke, D. Blaschke, A. Khalatyan, and H. Grigorian, arXiv:hep-ph/0104183.
23. D. Blaschke, S. Fredriksson, H. Grigorian, and A. Öztas, Nucl. Phys. **A** (2004), in press; [arXiv:nucl-th/0301002]; H. Grigorian, D. Blaschke, and D.N. Aguilera, [arXiv:astro-ph/0303518].
24. D.N. Voskresensky, M. Yasuhira, and T. Tatsumi, Phys. Lett. **B 541**, 93 (2002); Nucl. Phys. **A 723**, 291 (2002).
25. T. Takatsuka, and R. Tamagaki, arXiv:nucl-th/0402011.
26. P. Jaikumar, and M. Prakash, Phys. Lett. **B 516**, 345 (2001).
27. A.G. Lyne, et al., arXiv:astro-ph/0401086.

NEUTRINO OSCILLATION EXPERIMENTS: SUPER-KAMIOKANDE, K2K AND THE JPARC NEUTRINO PROJECT

TAKAAKI KAJITA

Research Center for Cosmic Neutrinos, Institute for Cosmic Ray Research, Univ. of Tokyo, Kashiwa-no-ha 5-1-5, Kashiwa, Chiba 277-8582 Japan
E-mail: kajita@icrr.u-tokyo.ac.jp

Neutrino oscillations have been studied using various neutrino sources including solar, atmospheric, reactor and accelerator neutrinos. Our understanding on neutrino masses and mixing angles has been improved significantly by recent experiments. This report mainly discusses the present status and the future prospect of our understanding of neutrino masses and mixing angles that are related to larger Δm^2.

1. Introduction

Neutrinos are known to be much lighter than any other quarks or charged leptons. Study of neutrino masses and mixing angles is one of a few ways to explore physics beyond the standard model of particle physics, since small neutrino masses are related to physics in very high energy scales [1,2]. Small neutrino masses can be studied by neutrino flavor oscillations. For simplicity, we consider two-flavor neutrino oscillations. If neutrinos are massive, the flavor eigenstates, ν_α and ν_β, are expressed as combinations of the mass eigenstates, ν_i and ν_j. The probability for a neutrino produced in a flavor state ν_α to be observed in a flavor state ν_β after traveling a distance L through the vacuum is:

$$P(\nu_\alpha \to \nu_\beta) = \sin^2 2\theta_{ij} \sin^2 \left(\frac{1.27 \Delta m^2_{ij}(\mathrm{eV}^2) L(\mathrm{km})}{E_\nu(\mathrm{GeV})} \right), \qquad (1)$$

where E_ν is the neutrino energy, θ_{ij} is the mixing angle between the flavor eigenstates and the mass eigenstates, and $\Delta m^2_{ij} = m^2_{\nu j} - m^2_{\nu i}$.

The above description has to be generalized to three-flavor oscillations. In the three-flavor oscillation framework, neutrino oscillations are parameterized by three mixing angles (θ_{12}, θ_{23}, and θ_{13}), three mass squared

differences (Δm^2_{12}, Δm^2_{23}, and Δm^2_{13}; among the three Δm^2's, only two are independent) and one CP phase (δ). However, if a neutrino mass hierarchy is assumed, the three Δm^2's are approximated by two Δm^2's, and neutrino oscillation lengths are significantly different for the two Δm^2's. One $\Delta m^2(\Delta m^2_{12})$ is related to solar neutrino experiments and the KamLAND reactor experiment. The other $\Delta m^2(\Delta m^2_{23})$ is related to atmospheric, reactor and long baseline neutrino oscillation experiments. It is known that it is approximately correct to assume two-flavor oscillations for analyses of the present neutrino oscillation data. Therefore, in this article, we mostly discuss two flavor neutrino oscillations assuming two significantly different Δm^2's. We mostly discuss experiments related to larger Δm^2. Especially, emphasis will be made on the atmospheric neutrino results from Super-Kamiokande, the K2K results and the sensitivity in JPARC-Kamioka neutrino project.

2. Present data

2.1. *Atmospheric neutrino experiments*

The strongest evidence for $\nu_\mu \rightarrow \nu_\tau$ oscillation to date is given by atmospheric neutrino data from Super-Kamiokande [3]. The atmospheric neutrino flux is predicted to be up-down symmetric for the neutrino energies above a few GeV where the geomagnetic field effect can be neglected. On the other hand, neutrino oscillations with Δm^2 of about $3\times10^{-3}\mathrm{eV}^2$ predict a significant deficit of upward-going neutrino events. The first convincing evidence for oscillations was discovered by the zenith angle dependent deficit for muon neutrino events [3] (see also Ref. [4] for an earlier result.) Atmospheric neutrino experiments determine the $\nu_\mu \rightarrow \nu_\tau$ neutrino oscillation parameters utilizing the zenith angle and energy dependent deficit of muon neutrino events.

Recently, Super-Kamiokande has updated their neutrino interaction Monte Carlo simulation based on the K2K neutrino data. The detector Monte Carlo simulation and the event reconstruction have also been improved. In addition, a recent flux model based on a three dimensional calculation method [5] is used. Figure 1 shows the zenith angle distributions for various data samples from Super-Kamiokande. The zenith angle and energy dependent deficit of muon neutrino events is clearly seen. Consistent results have been obtained from Kamiokande [6], Soudan-2 [7] and MACRO [8].

The allowed regions of $\nu_\mu \rightarrow \nu_\tau$ oscillation parameters from these experiments are shown in Figure 2. The allowed regions from various experiments

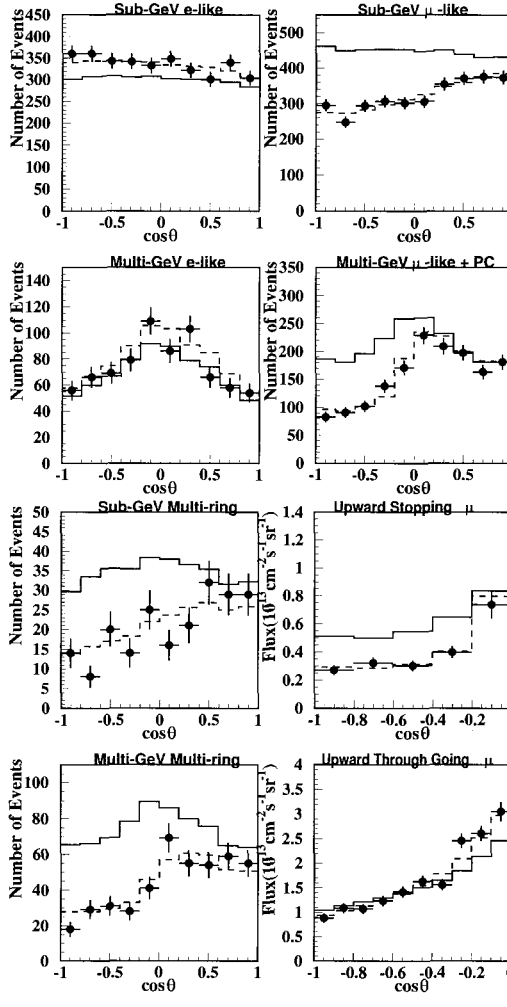

Figure 1. Zenith angle distributions observed in Super-Kamiokande. The detector exposure is 1489 days (92 kton·yr) for fully-contained (FC) and partially-contained (PC) events, 1646 days for upward stopping muon and through going muon events. Events denoted by "sub-GeV" ("multi-GeV") have their visible energies lower than (higher than) 1.3 GeV. $\cos\Theta$ =1(−1) means down-going (up-going). The solid histograms show the prediction without neutrino oscillations. The dotted histograms show the prediction with $\nu_\mu \rightarrow \nu_\tau$ oscillations (Δm^2_{23} =2.0×10^{-3} eV^2, $\sin^2 2\theta_{23}$ =1.0). In the oscillation prediction, various uncertainty parameters such as the absolute normalization are adjusted to give the best fit to the data.

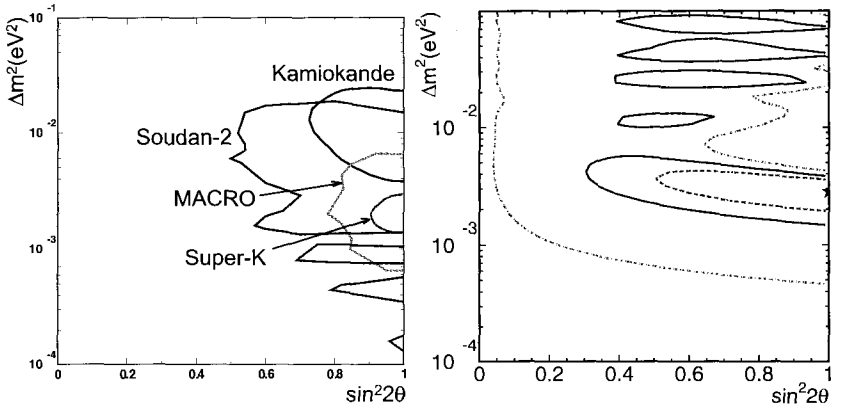

Figure 2. Allowed neutrino oscillation parameter regions for $\nu_\mu \rightarrow \nu_\tau$ from atmospheric neutrino experiments [6] [7] [8] at 90% C.L. (left) and the K2K [10] long baseline neutrino oscillation experiment at 68, 90 and 99% C.L. (right).

are consistent. The best fit point from the Super-Kamiokande allowed regions is $2.0\times10^{-3}\mathrm{eV}^2$ for Δm^2 and 1.00 for $\sin^2 2\theta$ (preliminary). The 90% C.L. allowed region is $1.3\times10^{-3} < \Delta m^2 < 3.0\times10^{-3}\mathrm{eV}^2$ and $\sin^2 2\theta > 0.90$ (preliminary). The present best fit Δm^2 from Super-Kamiokande is lower than the previous estimate by about 20%. Each change in the flux model, interaction model, the detector simulation and the event reconstruction shifted Δm^2 in the same direction. As of this writing, Super-Kamiokande is finalizing the atmospheric neutrino analysis. The final results based on the data taken between 1996 and 2001 will be published soon.

Several alternative hypotheses have been proposed to explain the atmospheric neutrino data. Most of them have been excluded or disfavored for various reasons. Neutrino oscillations between ν_μ and ν_τ give the best fit to the data. For maximal $\nu_\mu \rightarrow \nu_\tau$ oscillations with the Δm^2 preferred by the present data, it is expected that about 1 CC ν_τ interaction should occur per kton per year. Super-Kamiokande has searched for CC ν_τ interactions in the fully-contained atmospheric neutrino sample. Since the τ decays immediately after the production, a typical ν_τ event looks like an energetic NC event in Super-Kamiokande. No single selection criterion can select the ν_τ events efficiently. Therefore, maximum likelihood or neural network methods are used to maximize the detection sensitivity. Finally, the zenith angle distribution is used to statistically estimate the number of τ events, since only upward going events are expected for the τ events. Preliminary results showed that the data are consistent with the τ production [9].

However, the statistical significance is only 2 to 3 standard deviation level. More statistics and improved analysis are required for convincing evidence for τ production.

2.2. *K2K*

It is not trivial for atmospheric neutrino experiments to estimate the Δm^2 value precisely, since it is not possible to precisely estimate the L_ν/E_ν value for each event. On the other hand, a long baseline experiment has only one neutrino flight length. Therefore, it is much easier for a long baseline neutrino oscillation experiment to estimate the Δm^2 value accurately.

K2K is the first long baseline neutrino oscillation experiment. Neutrinos are produced by using a 12 GeV proton beam at KEK. The neutrinos are detected in Super-Kamiokande. The neutrino flight length and the mean neutrino energy are 250 km and about 1.3 GeV, respectively. The estimated Δm^2 value from the atmospheric neutrino experiments suggests that the maximum oscillation effect should occur at the energies of less than 1 GeV for neutrinos whose flight length is 250 km. Therefore, K2K studies energy dependent deficit of muon neutrino events.

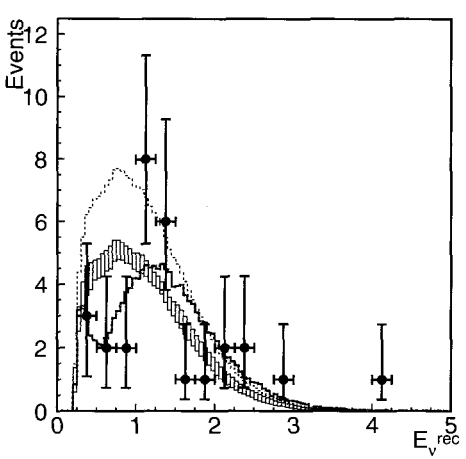

Figure 3. The reconstructed E_ν distribution for single-ring μ-like events. Points with error bars show data. Box histogram shows expected spectrum without oscillations, where the height of the box show the systematic error. Solid line shows the best fit spectrum. These histograms are normalized by the number of observed events (29). Dashed line shows the expectation with no oscillations normalized to the expected number of events (44).

During the first data taking period between 1999 and 2001, 4.8×10^{19} protons were delivered on target. 56 neutrino events have been observed in the far detector (Super-Kamiokande), while the expected number of events is $80.1^{+6.2}_{-5.4}$ for no oscillations [10]. In addition, K2K have studied the neutrino energy distribution using 29 single-ring μ-like events. It is possible to calculate the neutrino energy from the muon energy and the direction assuming a quasi-elastic interaction. Figure 3 shows the observed neutrino energy distribution from these single-ring μ-like events. A deficit of events is observed between 0.5 and 1.0 GeV. (However, the statistics of the present data are not large enough to claim the evidence for energy dependent deficit.)

The allowed oscillation parameter region was estimated using the number of observed events and the reconstructed neutrino energy spectrum. The allowed parameter region is shown in Fig. 2. The beast fit oscillation parameters were $\sin^2 2\theta = 1.00$ and $\Delta m^2 = 2.8\times10^{-3}\mathrm{eV}^2$. The allowed region from K2K is consistent with those from the atmospheric neutrino experiments.. It should be noted that the allowed Δm^2 region from K2K is as small as that from Super-Kamiokande atmospheric neutrino data, while the statistics of the K2K data are less than 1% of the Super-Kamiokande atmospheric neutrino data. It was made possible, because the neutrino flight length is a single number in the K2K neutrino beam, while the flight length varies more than 3 orders of magnitude in the atmospheric neutrino beam.

K2K has resumed the experiment in Jan., 2003. Between Jan. and April, 2003, 16 additional events were observed in Super-Kamiokande, while the expected number of events was $26.4^{+2.3}_{-2.1}$. The event rate in the new data taking period is consistent with the previous rate.

A new front detector with full active scintillator trackers was installed and the data taking with this detector was started in Oct., 2003. This detector will make it possible to better understand the of low energy (of less than 1 GeV) neutrino interactions.

2.3. *Limits on θ_{13}*

It is possible to get information on the other mixing angle (θ_{13}) using the currently available data. Within an approximation that Δm^2_{12} is much smaller than Δm^2_{23} (i.e., $\Delta m^2_{12}/\Delta m^2_{23} = 0$), the neutrino oscillation prob-

ability can be written;

$$P(\nu_e \to \nu_e) = 1 - \sin^2 2\theta_{13} \sin^2 \left(\frac{1.27 \Delta m^2_{13}(\mathrm{eV}^2) L(\mathrm{km})}{E_\nu(\mathrm{GeV})} \right), \quad (2)$$

$$P(\nu_\mu \to \nu_e) = \sin^2 \theta_{23} \sin^2 2\theta_{13} \sin^2 \left(\frac{1.27 \Delta m^2_{13}(\mathrm{eV}^2) L(\mathrm{km})}{E_\nu(\mathrm{GeV})} \right). \quad (3)$$

The best limit is obtained by the CHOOZ [11] reactor experiment. In addition, constraints are obtained from Super-Kamiokande atmospheric neutrino experiment and the K2K experiment [12]. No evidence for finite θ_{13} has been observed. According to a combined analysis [13] of these results, the current upper limit on $\sin^2 \theta_{13}$ is 0.067 (at 3σ). We note that the current limit on θ_{13} is a little weaker than the previous one due to the new Δm^2 value from Super-Kamiokande.

3. Future neutrino oscillation experiments

Although the atmospheric neutrino data together with the K2K results, give convincing evidence for neutrino oscillations, there are several open questions: The measurement of Δm^2_{23} by the atmospheric neutrino experiments is not very accurate. The observed effect has been the zenith angle and energy dependent deficit of CC ν_μ events and the sinusoidal oscillation pattern has not been observed yet. The interactions of ν_τ, which must be generated by oscillations, have not been convincingly observed yet. Finally, θ_{13}, the CP phase δ and the sign of Δm^2 are not known. Future long baseline neutrino oscillation experiments should address these issues and study further details of neutrino oscillations. Many of these experiments use accelerator generated neutrino beams. Since the typical neutrino energy is 1 GeV or higher, and since Δm^2_{23} is about $2.5 \times 10^{-3} \mathrm{eV}^2$, the baseline length must be at least a few hundred km.

3.1. *MINOS and CNGS*

As of this writing, the MINOS experiment [14] is in the preparation stage. This experiment is able to study neutrino oscillations with much higher statistics than those in K2K. To produce neutrinos, the MINOS experiment uses the 120 GeV proton beam from the Main Injector at Fermilab. The MINOS detector is an iron-scintillator sampling calorimeter, which is located 730 km away from the target. The MINOS far detector has the total mass of 5.4 kton. The installation of the MINOS far detector has been completed in the summer of 2003. Since then, it has been taking

atmospheric neutrino data. Because this detector is magnetized, it could give unique data on atmospheric neutrinos as well in the near future. The MINOS long baseline experiment is expected to start in early 2005. MINOS will improve our knowledge on Δm^2 significantly. Some improvement on the mixing angle measurements could also be expected.

In Europe, CNGS (CERN Neutrino to Gran Sasso) project is in progress. 400 GeV proton beam from SPS at CERN produces high energy neutrinos whose mean energy is about 20 - 30 GeV. Neutrinos produced by this beam will be detected by detectors at Gran Sasso, which is 730 km away from the neutrino production point. OPERA [15] is an experiment for the CNGS project. This experiment is aimed to study neutrino oscillations by looking at the appearance of ν_τ in the beam. The OPERA main detector consists of a 1.8 kton lead-emulsion target. Since it is not possible to scan all the images recorded in the emulsion, there are electronic detectors after each emulsion module in order to locate the interaction point in the emulsion. Only a portion of the emulsion that are located by the electronic detectors will be scanned to search for τ decay kinks. After 5 years of operation with 5×10^{19} p.o.t. per year, the expected number of identified CC ν_τ events are 4.3, 10.1 and 26.3 for Δm^2_{23} =0.0016, 0.0025, 0.004 eV^2, while the expected background is 0.65. The experiment will start in 2006.

The other experiment for the CNGS project will be ICARUS [16]. It is a liquid argon TPC detector. The total mass will be 3 ktons. The excellent imaging capability of the detector should make it possible to carry out various neutrino oscillation studies. 600 ton ICARUS detector has been tested on the ground successfully [17]. The same detector will be installed at the Gran Sasso Laboratory soon. The sensitivity for ν_τ appearance is very similar to that of OPERA. It has also a high sensitivity for the θ_{13} measurement.

3.2. *JPARC-Kamioka neutrino project*

There are as-yet-unobserved quantities related to neutrino oscillations: θ_{13}, the sign of Δm^2_{23} and the CP phase in the neutrino sector. These questions can be addressed by the next generation neutrino oscillation experiments. One possible experiment is the JPARC-Kamioka neutrino project [18]. JPARC is a high intensity proton accelerator complex that is under construction at JAERI, Tokai, Japan. 50 GeV PS will be used to produce the high intensity neutrino beam. The construction will be completed in the Japanese FY 2007. At the end of 2003 (about one month after this

meeting) this neutrino project was approved by the Japanese government. The experiment will start in late 2008 or early 2009.

The main goals of the first phase of the project are the observation of non-zero $\sin^2 2\theta_{13}$ and the precise measurement of $\sin^2 2\theta_{23}$ and Δm^2_{23}. The 50 GeV PS is designed to deliver 3.3×10^{14} protons every 3.4 seconds. The beam power is 0.75 MW. A future upgrade of the beam power to 4 MW is considered. The far detector is Super-Kamiokande. The baseline length of the experiment is 295 km. A 1 Mton water Cherenkov detector, Hyper-Kamiokande, is seriously considered as the far detector in the second phase of this neutrino project. The main goal of the second phase of the project is the observation of the CP violation effect.

A feature of this experiment is the use of a low-energy, narrow band, high-intensity neutrino beam. The neutrino energy will be tuned to the maximum oscillation energy. For $\Delta m^2_{23} = 3.0 \times 10^{-3}\mathrm{eV}^2$, it is 715 MeV. To produce high intensity, narrow band beam, the off-axis beam technique will be used [19]. The axis of the beam is displaced by a few degrees from the far detector direction. Due to the two body decay kinematics of pions, the energy of neutrinos that pass through the far detector is low and almost independent of the pion energy spectrum. The neutrino energy can be adjusted by choosing the angle between the pion beam direction and the direction to the detector (off-axis angle).

Detailed Monte Carlo simulations have been carried out to estimate the expected neutrino spectrum and the number of events. If the off-axis angle is determined, the neutrino energy distribution is determined essentially. On the other hand, our present knowledge on Δm^2_{23} is not precise enough to pre-determine the off-axis angle uniquely. Because of these conditions, the decay pipe is designed to accommodate off-axis angles between 2 and 3 degrees. The expected total numbers of events per year, which is equivalent to 10^{21} protons on target, are 3200 and 1100 for 2 and 3 degree off-axis beams, respectively. Throughout the discussion of the JPARC-Kamioka neutrino project, we assume that the true Δm^2_{23} is $3.0 \times 10^{-3}\mathrm{eV}^2$. We also assume the 2 degree off-axis beam.

The neutrino energy can be reconstructed accurately for quasi-elastic interactions assuming that the target nucleon is at rest. Figure 4 shows the reconstructed energy spectrum with and without neutrino oscillations assuming $\sin^2 2\theta_{23} = 1.0$ and $\Delta m^2_{23} = 3.0\times10^{-3}\mathrm{eV}^2$. Events with single μ-like Cherenkov ring are plotted. Since the peak of the neutrino energy distribution is tuned to the maximum oscillation energy, most of the muon neutrinos must be oscillated to tau neutrinos. From this figure it is possible

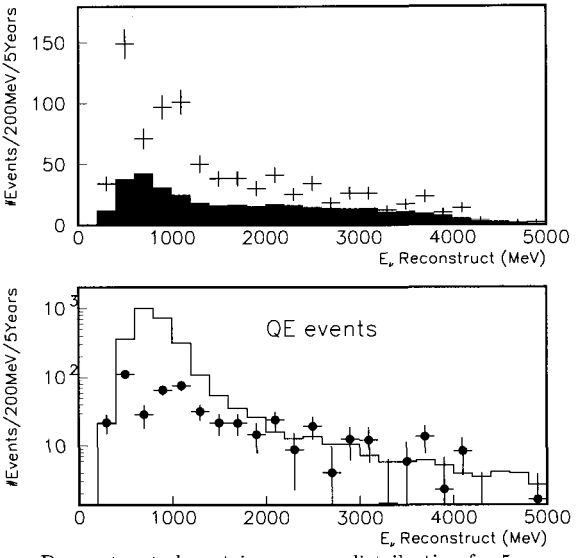

Figure 4. Upper: Reconstructed neutrino energy distribution for 5 year operation of the JPARC-Kamioka experiment with the 2 degree off-axis beam. Events with single μ-like Cherenkov ring are plotted. The shaded histogram shows the contribution of non-quasi-elastic events. $\sin^2 2\theta_{23}$ =1.0 and Δm^2_{23} =3.0×10^{-3}eV^2 are assumed. The maximum oscillation effect is expected to occur at the 0.6 to 0.8 GeV energy bin. Lower: Reconstructed E_ν distributions after subtracting the non-quasi-elastic events. The histogram and the dots show the non-oscillation and oscillation cases, respectively.

to estimate the sensitivities in $\sin^2 2\theta_{23}$ and Δm^2_{23}. The expected accuracy is 1% in $\sin^2 2\theta_{23}$ and 1×10^{-4}eV^2 in Δm^2_{23}. As far as Δm^2_{23} is concerned, the sensitivity is limited by systematic uncertainties, such as uncertainties in absolute energy calibration or in nuclear effects that affect lepton energies.

The JPARC neutrino beam has a small ν_e contamination (0.2% at the energy of the peak flux). Furthermore, the ν_e appearance signal is maximized by tuning the neutrino energy at its oscillation maximum. Thus, this experiment has a high sensitivity to θ_{13}. The signal should be searched for in the single-ring e-like events. The main background processes are contamination of ν_e in the beam, and NC (mostly π^0) events. Special cuts have been developed to reject these NC events (See [18] for details). Figure 5 (left) shows the expected energy distribution for the signal and background. Figure 5 (right) shows the expected sensitivity in $\sin^2 2\theta_{\mu e}$ ($\equiv \sin^2\theta_{23} \cdot \sin^2 2\theta_{13}$ and assumed to be $0.5 \times \sin^2 2\theta_{13}$). The sensitivity of this experiment to $\sin^2 2\theta_{13}$ is about 0.006.

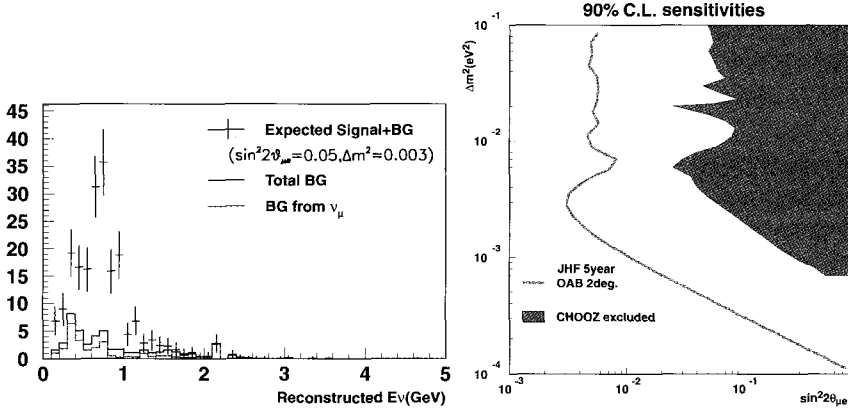

Figure 5. (Left) Expected electron appearance signal in the JPARC-Kamioka neutrino project. It is assumed that $\sin^2 2\theta_{13}$ =0.1 and 5 years of operation. (Right) 90% C.L. sensitivity in $\sin^2\theta_{\mu e}(\equiv 0.5 \cdot \sin^2 2\theta_{13})$ after 5 years of operation. Present limit from reactor experiment [11] is shown by a gray region. In these figures, effects due to the CP violation and the matter are neglected.

3.3. *Competing projects*

The neutrino beam produced by the Main Injector for the MINOS experiment can be used for an off-axis experiment. If a detector is located about 10 or 20 km away from the beam center, the mean beam energy can be about 2 and 1 GeV, respectively. As a far detector, about 50 kton, low-Z detector is considered. This experiment will have a slightly better sensitivity in $\sin^2 2\theta_{13}$ than the JPARC-Kamioka neutrino project [23]. Intensive R&Ds for the detector are in progress.

It is also possible to study θ_{13} using $\overline{\nu}_e$ from nuclear power reactors. Unlike accelerator experiments, the disappearance of $\overline{\nu}_e$ is almost a pure measurement of θ_{13}. Detailed studies have shown that it must be possible to improve the $\sin^2\theta_{13}$ limit by a factor of 5 to 10 (or more) with the present technology, if the systematic error is controlled to an accuracy of about 1%. (See, for example [24].)

3.4. *Toward the measurement of the CP violation*

There are now intense studies of designing experiments that detect CP violation effect. CP violation in the neutrino sector is considered to be the key to understand the baryon asymmetry of the Universe [25]. The CP violating phase is currently unknown and is expected to be observable if

Δm^2_{12} and Δm^2_{23} are close enough so that both come into play in a single measurement and if the Jarlskog factor [26] $J = c_{12}c^2_{13}c_{23}s_{12}s_{13}s_{23}(sin\delta)$ is large enough. Recent solar neutrino [21], [20] and KamLAND [22] data confirm that θ_{12} and Δm^2_{12} are large enough.

One example for such experiments is the second stage of the JPARC-Kamioka neutrino project. The CP violation phase can be measured by observing the difference in the neutrino oscillation probabilities between $\nu_\mu \rightarrow \nu_e$ and $\overline{\nu}_\mu \rightarrow \overline{\nu}_e$. To observe the CP violation effect, a huge detector (1 Mton Hyper-Kamiokande detector), a very high intensity proton accelerator (4 MW beam power) and about 8 years of operation will be required [18].

Even more ambitious projects are under serious discussion and R&D. These discussions assume a very high intensity neutrino beam produced by muon storage rings (neutrino factories), see for example Ref. [27]. The basic idea is to build a muon storage ring with a long straight section where muons decay to produce a collimated neutrino beam. The muon decay is well understood and yields a very well defined beam spectrum. A μ^+ decays to e^+, $\overline{\nu}_\mu$ and ν_e. Therefore, if a μ^- is observed in a neutrino interaction, this event must be an oscillation signal (or a background due to an imperfect detector resolution). Therefore, experiments with muon storage rings are expected to be very sensitive to a very small θ_{13} value. In addition, since the storage of positive and negative muons are possible, it is possible to study the CP violation effect. Detailed studies have shown that the sensitivity of these experiments to the CP violation effect is high. Also, since the baseline is very long (typically longer than 1000 km), the sign of Δm^2_{23} can be determined easily using the matter effect.

4. Summary

Data from various neutrino oscillation experiments to date already give fairly detailed information on the neutrino masses and mixing angles. Two mixing angles, θ_{12} and θ_{23} are large. Δm^2_{23} is significantly larger than Δm^2_{12}. However, our understanding of the neutrino masses and mixing angles is not complete. We do not know how small θ_{13} is. We have no knowledge about the CP phase in the neutrino sector. Future long baseline experiments should address many of these important questions. It is likely that future neutrino oscillation experiments will continue to contribute to our understanding of the particle physics.

This work has been supported by the Japanese Ministry of Education, Culture, Sports, Science and Technology.

References

1. T. Yanagida, in Proc. of the Workshop on the Unified Theory and Baryon Number in the Universe (KEK Report No. 79-18) p.95 (1979).
2. M. Gell-Mann, P. Ramond, R. Slansky, in Supergravity, p.315 (1979).
3. Y. Fukuda, *et al.*, Phys. Rev. Lett. **81**, 1562 (1998).
4. Y. Fukuda, *et al.*, Phys. Lett. B **335**, 237 (1994).
5. M. Honda, *et al.*, Proc. of the 28th International Cosmic Ray Conferences (ICRC2003), Tsukuba, Japan, 31 Jul - 7 Aug 2003, Vol.3, p1415
6. S. Hatakeyama, *et al.*, Phys. Rev. Lett. **81**, 2016 (1998).
7. M. Sanchez, *et al.*, Phys. Rev. D **68**, 113004 (2003).
8. M. Ambrosio, *et al.*, Phys. Lett. B **566**, 35 (2003).
9. C. Saji, for the Super-Kamiokande collaboration, in Proc. of the 28th International Cosmic Ray Conference, Tsukuba, Japan, July-Aug.2003, Vol.3, p.1267.
10. M.H. Ahn, *et al.*, Phys. Rev. Lett. **90**, 041801 (2003).
11. M. Apollonio, *et al.*, Phys. Lett. B **466**, 415 (1999).
12. K. Nishikawa, talk presented at the XXI International Symposium on Lepton and Photon Interactions at High Energies, Fermilab, USA, Aug. 2003.
13. G.L. Fogli, *et al.*, hep-ph/0308055.
14. D. Michael, Nucl. Phys. B (Proc. Suppl.) **118**, 189 (2003).
15. OPERA collaboration, M. Guler, *et al.*, CERN-SPSC-P-318, LNGS-P25-00 (2000).
16. A. Rubbia, Nucl. Phys. B (Proc. Suppl.) **91**, 223 (2001).
17. O. Palamara, for the ICARUS Collaboration, Nucl. Phys. B (Proc. Suppl.) **110**, 329 (2002).
18. Y. Itow, *et al.*, hep-ex/0106019.
19. D. Beavis *et al.*, Proposal, BNL AGS E-889 (1995).
20. M.B. Smy, *et al.*, hep-ex/0309011.
21. S.N. Ahmed, *et al.*, nucl-ex/0309004.
22. K. Eguchi, *et al.*, Phys. Rev. Lett. **90**, 021802 (2003).
23. D. Ayres, *et al.*, hep-ex/0210005.
24. H. Minakata, *et al.*, Phys. Rev. D **68**, 033017 (2003): P. Huber, *et al.*, Nucl. Phys. B **665**, 487 (2003).
25. M. Fukugita, and T. Yanagida, Phys. Lett. B **174**, 45 (1986).
26. C. Jarlskog, Phys. Rev. Lett. **55**, 1039 (1985).
27. S. Geer, J. Phys. G: Nucl. Part. Phys. **29** 1485 (2003).

ASTROPHYSICAL WEAK-INTERACTION PROCESSES AND NUCLEAR EFFECTIVE FIELD THEORY

K. KUBODERA*
Department of Physics and Astronomy,
University of South Carolina,
Columbia, SC 29208, USA
E-mail: kubodera@sc.edu

Low-energy nuclear weak-interaction processes play important roles in many astrophysical contexts, and effective field theory is believed to be a highly useful framework for describing these processes in a model-independent manner. I present a brief account of the basic features of the nuclear effective theory approach, and some examples of actual calculations carried out in this method.

1. Introduction

Low-energy nuclear weak-interaction processes play important roles in many astrophysical phenomena and also in terrestrial experiments designed to detect the astrophysical neutrinos. Obviously, it is important to have reliable estimates of the cross sections for these processes. I wish to describe here some of the recent developments in our endeavor to obtain such estimates.[a] My main emphasis will be placed on comparison between the traditional method, to be designated as the *standard nuclear physics approach* (SNPA), and the newly developed *nuclear effective field theory* (EFT) approach. I shall advocate the viewpoints that (i) nuclear EFT can indeed be a powerful framework for describing low-energy nuclear electroweak processes and (ii) that, in practical applications, EFT and SNPA can play complementary roles.

These points are nicely illustrated by the following three examples: (i) neutrino-deuteron reactions for solar neutrino energies; (ii) solar pp fusion; (iii) solar Hep fusion. Since the process (iii) and related topics will be

*Work partially supported by the US National Science Foundation, Grant No. PHY-0140214

[a]This talk has some overlap with the one I gave at NDM03 [1].

discussed in detail by Dr. Tae-Sun Park at this Symposium, I shall concentrate on the first two reactions. Let me start with a brief explanation of why these processes are of particular current interest.

At SNO (Sudbury Neutrino Observatory), a one-kiloton heavy water Cerenkov counter is used to detect the solar neutrinos. SNO can monitor the neutrino-deuteron reactions:

$$\begin{aligned} &\nu_e + d \to e^- + p + p\,, \quad \nu_x + d \to \nu_x + p + n\,, \\ &\bar{\nu}_e + d \to e^+ + n + n\,, \quad \bar{\nu}_x + d \to \bar{\nu}_x + p + n\,, \end{aligned} \tag{1}$$

as well as the pure leptonic reaction $\nu_x + e^- \to \nu_x + e^-$. Here x stands for a neutrino of any flavor (e, μ or τ). The recent SNO experiments [2] have established that the total solar neutrino flux (counting all neutrino flavors) agrees with the prediction of the standard solar model [3], whereas the electron neutrino flux from the sun is significantly smaller than the total solar neutrino flux. The amount of deficit in the electron neutrino flux was found to be consistent with what had been known as the solar neutrino problem. These results of the SNO experiments have given clear evidence for the transmutation of solar electron neutrinos into neutrinos of other flavors. Obviously, a precise knowledge of the ν-d reaction cross sections is important for the in-depth interpretation of the existing and future SNO data.

Meanwhile, the pp fusion reaction

$$p + p \to d + e^+ + \nu_e \tag{2}$$

is the primary solar thermonuclear reaction that essentially controls the luminosity of the sun, and therefore the exact value of its cross section is a crucial input for any elaborate solar models.

2. Calculational frameworks

2.1. *Standard nuclear physics approach (SNPA)*

The phenomenological potential picture has been highly successful in describing a vast variety of nuclear phenomena. In this picture an A-nucleon system is described by a non-relativistic Hamiltonian of the form

$$H = \sum_{i}^{A} t_i + \sum_{i<j}^{A} V_{ij} + \sum_{i<j<k}^{A} V_{ijk} + \cdots\,, \tag{3}$$

where t_i is the kinetic energy of the i-th nucleon, V_{ij} is a phenomenological two-body potential between the i-th and j-th nucleons, V_{ijk} is a phenomenological three-body potential, and so on. (Since potentials involving

three or more nucleons play much less important roles than the two-body interactions, we shall be concerned here mainly with V_{ij}.) Once the model Hamiltonian H is specified, the nuclear wave function $|\Psi>$ is obtained by solving the Shrödinger equation

$$H|\Psi> = E|\Psi> \ . \tag{4}$$

It is fortunate that the progress of numerical techniques for solving eq.(4) has reached such a level [4] that the wave functions of low-lying levels for light nuclei can now be obtained with essentially no approximation (once the validity of the model Hamiltonian eq.(3) is accepted). This liberates us from the "familar" nuclear physics complications that arise as a result of truncating nuclear Hilbert space down to certain model space (such as shell-model configurations within a limited number of major shells, cluster-model trial functions, etc.)

We note that there is large freedom in selecting possible forms of V_{ij}, apart from the well-established requirement that, for a large enough value of the inter-nucleon distance, V_{ij} should agree with the one-pion exchange Yukawa potential. For the model-dependent short-range part of V_{ij}, the best we could do is to assume certain functional forms and fix the parameters contained in them by demanding that the solutions of eq.(4) for the A=2 case reproduce the nucleon-nucleon scattering data (typically up to the pion-production threshold energy) as well as the deuteron properties. There are by now several so-called *modern high-precision phenomenological* N-N potential that can reproduce all the existing two-nucleon data with normalized χ^2 values close to 1. These potentials differ widely in the ways short-range physics is parametrized, and, as a consequence, they exhibit substantial difference in their off-shell behaviors. To what extent this arbitrariness may affect the observables of our concern is an important question, to which I will come back later.

In normal situataions, nuclear responses to external electroweak probes are given, to good approximation, by one-body terms, which are also called the impulse approximation (IA) terms. To obtain higher accuracy, however, we must include exchange current (EXC) terms, which represent nuclear responses involving two or more nucleons. These exchange currents (usually taken to be two-body operators) are derived from one-boson exchange diagrams, and the vertices featuring in the relevant diagrams are determined to satisfy the low-energy theorems and current algebra [5]. We refer to a formalism based on this picture as the *standard nuclear physics approach* (SNPA). (This is also called a potential model in the literature.)

Schematically, the nuclear matrix element in SNPA is given by

$$\mathcal{M}_{fi}^{\rm SNPA} = < \Psi_f^{\rm SNPA} | \sum_{\ell}^{A} \mathcal{O}_{\ell}^{\rm SNPA} + \sum_{\ell<m}^{A} \mathcal{O}_{\ell m}^{\rm SNPA} | \Psi_i^{\rm SNPA} > , \qquad (5)$$

where the initial (final) nuclear wave function, $\Psi_i^{\rm SNPA}$ ($\Psi_f^{\rm SNPA}$), is a solution of eq.(4); $\mathcal{O}_{\ell}^{\rm SNPA}$ and $\mathcal{O}_{\ell m}^{\rm SNPA}$ are, respectively, the one-body and two-body transition operators for a given electroweak process.

SNPA has been used extensively to describe nuclear electroweak processes in light nuclei, and generally good agreement between theory and experiment [4] gives a strong indication that SNPA essentially captures much of the physics involved.

2.2. *Effective field theory (EFT)*

Even though SNPA has been extremely successful in correlating and explaining a wealth of nuclear phenomana, it is still important from a fundamental point of view to raise the following issues. First, since the hadrons and hadronic systems (such as nuclei) are governed by quantum chromodynamics (QCD), we should ultimately be able to relate nuclear phenomena with QCD, but SNPA is reticent about this relation. In particular, whereas chiral symmetry is known to be a fundamental symmetry of QCD, the SNPA is largely disjoint from this symmetry. Second, even for describing low-energy phenomena, SNPA starts with a "realistic" phenomenological potential which is tailored to encode short-range (high-momentum) and long-range (low-momentum) physics simultaneously. This mixing of the two different scales seems theoretically unsatisfactory. Third, as we write down a phenomenological Lagrangian for describing the nuclear interaction and nuclear responses to the electroweak currents, SNPA does not offer us a clear guiding principle; it is not obvious whether SNPA is equipped with any identifiable expansion parameter that helps us to control the possible forms of terms in the Lagrangian and that provides a general measure of errors in our calculation. To address these and other related issues, a new approach based on EFT was proposed [6] and it has been studied with great intensity; for reviews, see Refs. [7–11].

The intuitive picture of EFT is quite simple. In describing phenomena characterized by a typical energy-momentum scale Q, we may expect that our Lagrangian need not contain explicitly those degrees of freedom that belong to energy-momentum scales much higher than Q. This expectation motivates us to introduce a cut-off scale Λ that is sufficiently large compared

with Q and classify our fields (to be generically represented by ϕ) into two groups: high-frequency fields $\phi_{\rm H}$ whose frequencies are higher than Λ, and low-frequency fields $\phi_{\rm L}$ with frequencies lower than Λ. By eliminating (or *integrating out*) $\phi_{\rm H}$, we arrive at an *effective* Lagrangian that only involves $\phi_{\rm L}$ as explicit dynamical variables. In terms of path integrals, the effective Lagrangian $\mathcal{L}_{\rm eff}$ is related to the original Lagrangian $\mathcal{L}$ as

$$\int [d\phi] \exp\{{\rm i}\int d^4x \mathcal{L}[\phi]\} = \int [d\phi_{\rm H}][d\phi_{\rm L}] \exp\{{\rm i}\int d^4x \mathcal{L}[\phi_{\rm H}, \phi_{\rm L}]\} \tag{6}$$

$$\equiv \int [d\phi_{\rm L}] \exp\{{\rm i}\int d^4x \mathcal{L}_{\rm eff}[\phi_{\rm L}]\} \,. \tag{7}$$

It can be shown that $\mathcal{L}_{\rm eff}$ defined by eq.(7) inherits the symmetries (and the patterns of symmetry breaking, if there are any) of the underlying Lagrangian $\mathcal{L}$. It also follows that $\mathcal{L}_{\rm eff}$ should be the sum of all possible monomials of $\phi_{\rm L}$ and their derivatives that are consistent with the symmetry requirements of $\mathcal{L}$. Because a term involving n derivatives scales like $(Q/\Lambda)^n$, we can organize terms in $\mathcal{L}_{\rm eff}$ into a perturbative series in which Q/Λ serves as an expansion parameter. The coefficients of terms in this expansion scheme are called the low-energy constants (LECs). Provided all the LEC's up to a specified order n can be fixed either from theory or from fitting to the experimental values of relevant observables, $\mathcal{L}_{\rm eff}$ serves as a complete (and hence model-independent) Lagrangian to the given order of expansion.

Having sketched the basic idea of EFT, we now discuss the specific aspects of EFT as applied to nuclear physics. The underlying Lagrangian $\mathcal{L}$ in this case is the QCD Lagrangian $\mathcal{L}_{QCD}$, whereas, for a typical nuclear physics energy-momentum scale $Q \ll \Lambda_\chi \sim 1$ GeV, the effective degrees of freedom that feature in $\mathcal{L}_{\rm eff}$ are the hadrons rather than the quarks and gluons. It is non-trivial to apply the formal definition in eq.(7) to derive $\mathcal{L}_{\rm eff}$ written in terms of hadrons starting from $\mathcal{L}_{QCD}$, because the hadrons cannot be simply identified with the low-frequency field ϕ_L in $\mathcal{L}_{QCD}$. To proceed, we choose to be guided solely by symmetry considerations and the above-mentioned expansion scheme. Chiral symmetry plays an important role here. Chiral symmetry is known to be spontaneously broken, leading to the generation of the pions as Nambu-Goldstone bosons. We can incorporate this feature by assigning suitable chiral transformation properties to the Goldstone bosons and writing down all possible chiral-invariant terms up to a specified chiral order [12]. It is to be noted that the above consideration presupposes exact chiral symmetry in $\mathcal{L}_{QCD}$. In reality, $\mathcal{L}_{QCD}$

contains small but finite quark mass terms, which violate chiral symmetry explicitly and lead to a non-vanishing value of the pion mass m_π. Again, there is a well-defined framework to determine what terms are needed to represent the effect of explicit chiral symmetry breaking [12]. These considerations lead to an EFT called chiral perturbation theory (χPT) [13,14]. The successes of χPT in the meson sector are well known; see, *e.g.,* Ref. [7].

A difficulty we encounter in extending χPT to the nucleon sector is that, because the nucleon mass $m_{\rm N}$ is comparable to the cut-off scale Λ_χ, a simple application of expansion in Q/Λ does not work. We can surmount this obstacle with the use of heavy-baryon chiral perturbation theory (HBχPT), which essentially consists in shifting the reference point of the nucleon energy from 0 to $m_{\rm N}$ and integrating out the small component of the nucleon field as well as the anti-nucleon field. Thus an effective Lagrangian in HBχPT contains as explicit degrees of freedom the pions and the large components of the redefined nucleon field. HBχPT has as expansion parameters Q/Λ_χ, m_π/Λ_χ and $Q/m_{\rm N}$. Since $m_{\rm N} \approx \Lambda_\chi$, it is convenient to combine chiral and heavy-baryon expansions and introduce the chiral index $\bar{\nu}$ defined by $\bar{\nu} = d + (n/2) - 2$. Here n is the number of fermion lines participating in a given vertex, and d is the number of derivatives (with m_π counted as one derivative). A similar power counting scheme can be introduced for Feynman diagrams as well. According to Weinberg [6], a Feynman diagram that contains N_A nucleons, N_E external fields, L loops and N_C disjoint parts scales like $(Q/\Lambda)^\nu$, where the chiral index ν is defined as

$$\nu = 2L + 2(N_C - 1) + 2 - (N_A + N_E) + \sum_i \bar{\nu}_i \,, \tag{8}$$

with the summation running over all the vertices.

Although HBχPT has been very successful in the one-nucleon sector [7], we cannot apply HBχPT in a straightforward manner to nuclei, which contain more than one nucleon. This is because nuclei allow very low-lying excited states, and the existence of this small energy scale invalidates chiral counting [6]. Weinberg avoided this difficulty by classifying Feynman diagrams into two groups, irreducible and reducible diagrams. Irreducible diagrams are those in which every intermediate state has at least one meson in flight; all others are categorized as reducible diagrams. The chiral counting rules should only be applied to irreducible diagrams. The contribution of all the two-body irreducible diagrams (up to a specified chiral order) is treated as an effective potential (to be denoted by $V_{ij}^{\rm EFT}$) that acts on nuclear wave functions. Meanwhile, the contributions of reducible diagrams

can be incorporated [6] by solving the Schrödinger equation

$$H^{\rm EFT}|\Psi^{\rm EFT}> = E|\Psi^{\rm EFT}>, \tag{9}$$

where

$$H^{\rm EFT} = \sum_{i}^{A} t_i + \sum_{i<j}^{A} V_{ij}^{\rm EFT}, \tag{10}$$

We refer to this two-step procedure as *nuclear* χPT, or, to be more specific, *nuclear* χPT in the Weinberg scheme. (This is often called the Λ-counting scheme [9].)

To apply nuclear χPT to a process that involves (an) external current(s), we derive a nuclear transition operator $\mathcal{T}$ by calculating the contributions of all the irreducible diagrams (up to a given chiral order ν) that involve the relevant external current(s). To maintain consistent chiral counting, the nuclear matrix element of $\mathcal{T}$ must be calculated with the use of nuclear wave functions which are governed by nuclear interactions that represent all the irreducible A-nucleon diagrams up to ν-th order. Thus, a transition matrix in nuclear EFT is given by

$$\mathcal{M}_{fi}^{\rm EFT} = <\Psi_f^{\rm EFT}| \sum_{\ell}^{A} \mathcal{O}_{\ell}^{\rm EFT} + \sum_{\ell<m}^{A} \mathcal{O}_{\ell m}^{\rm EFT} |\Psi_i^{\rm EFT}>, \tag{11}$$

where the superscript, "EFT", implies that the relevant quantities are obtained according to EFT as described above. If this program is carried out exactly, it would constitute an *ab initio* calculation. It is worth noting that EFT tells us exactly at what chiral order three-body operators start to contribute to $\mathcal{T}$, and that, to chiral orders of our present concern, we do not need three-body operators. For this reason we have retained in eq.(11) only one- and two-body operators. This type of unambiguous classification of transition operators according to their chiral orders is a great advantage of EFT, which is missing in eq.(5).

I should mention that there exists an alternative form of nuclear EFT based on the power divergence subtraction (PDS) scheme. The PDS scheme proposed by Kaplan, Savage and Wise in their seminal papers [15] uses a counting scheme (often called Q-counting) that differs from the Weinberg scheme. An advantage of the PDS scheme is that it maintains formal chiral invariance, whereas the Weinberg scheme loses manifest chiral invariance. In many practical applications, however, this formal problem is not worrisome up to the chiral order under consideration, *i.e.,* the chiral order up to which our irreducible diagrams are evaluated. Although the PDS scheme

has produced many important results (for a review, see *e.g.* Ref. [10]), I concentrate here on the Weinberg scheme, because this is the framework in which our own work has been done.

2.3. *Hybrid EFT*

In the above I emphasized the formal merits of nuclear EFT. In actual calculations, however, we face the following two problems. First, it is still a great challenge to generate, strictly within the EFT framework, nuclear wave functions whose accuracy is comparable to that of SNPA wave functions. Second, as mentioned earlier, the chiral Lagrangian, $\mathcal{L}_{\rm eff}$, is definite only when the values of all the relevant LECs are fixed, but there may be cases where this requirement cannot be readily met. A pragmatic solution to the first problem is to use in eq.(11) wave functions obtained in SNPA; we refer to this eclectic approach as hybrid EFT. A nuclear transition matrix element in hybrid EFT is given by

$$\mathcal{M}_{fi}^{hyb-\mathrm{EFT}} = < \Psi_f^{\mathrm{SNPA}} | \sum_{\ell}^{A} \mathcal{O}_{\ell}^{\mathrm{EFT}} + \sum_{\ell<m}^{A} \mathcal{O}_{\ell m}^{\mathrm{EFT}} | \Psi_i^{\mathrm{SNPA}} > , \qquad (12)$$

Because, as mentioned, the NN interactions that generate SNPA wave functions reproduce accurately the entirety of the two-nucleon data, the adoption of eq.(12) is almost equivalent to using the empirical data themselves to control the initial and final nuclear wave functions. In the context of theoretically deriving the nuclear interactions based on EFT, hybrid EFT may look like "retrogression". But, if our goal is to obtain a transition matrix element as accurately as possible with the maximum help of available empirical input, hybrid EFT is a justifiable approach insofar as the above-mentioned off-shell problem and the contributions of three-body (and higher-body) interactions are properly addressed. These points will be discussed later on.

The calculations reported in Refs. [19,20] seem to support hybrid EFT. There, the nuclear matrix elements in the A=2 systems for one-body operators (or IA terms) calculated with the use of EFT-generated wave functions were found to be very close to those calculated with the SNPA wave functions. Thus EFT and hybrid EFT should give practically the same IA matrix elements. Meanwhile, we can generally expect that the ratio of the two-body EXC contributions to those of the IA operators should be much less sensitive to the details of the nuclear wave functions than the absolute values are. It therefore seems reasonable to rely on χPT for deriving

transition operators and evaluate their matrix elements using the realistic wave functions obtained in SNPA, and in this sense hybrid EFT is more than a mere expedient.

The issue of possible unknown LECs will be discussed in the next subsection.

2.4. *MEEFT or EFT**

Hybrid EFT can be used for complex nuclei (A = 3, 4, ...) with essentially the same accuracy and ease as for the A=2 system. We should reemphasize in this connection that, in A-nucleon systems (A≥3), the contributions of transition operators involving three or more nucleons are intrinsically suppressed according to chiral counting, and hence, up to a certain chiral order, a transition operator in an A-nucleon system consists of the same EFT-based 1-body and 2-body terms as used for the two-nucleon system. Then, since SNPA provides high-quality wave functions for the A-nucleon system, one can calculate $\mathcal{M}_{fi}^{hyb-\mathrm{EFT}}$ with precision comparable to that for the corresponding two-nucleon case.

Now, in most practical cases, the one-body operator, $\mathcal{O}_{\ell}^{\mathrm{EFT}}$, is free from unknown LECs. So let us concentrate on the two-body operator, $\mathcal{O}_{\ell m}^{\mathrm{EFT}}$, and suppose that $\mathcal{O}_{\ell m}^{\mathrm{EFT}}$ under consideration contains an LEC (call it κ) that cannot be determined with the use of A=2 data alone. It is possible that an observable (call it Ω) in a A-body system (A≥3) is sensitive to κ and that the experimental value of Ω is known with sufficient accuracy. Then we can determine κ by calculating $\mathcal{M}_{fi}^{hyb-\mathrm{EFT}}$ responsible for Ω and adjusting κ to reproduce the empirical value of Ω. Once κ is fixed this way, we can make *predictions* for any other observables for any other nuclear systems that are controlled by the same transition operators. When hybrid EFT is used in this manner, we refer to it as MEEFT (*more effective* EFT) or EFT*.

MEEFT is the most efficient existing formalism for correlating various observables in different nuclei, using the transition operators controlled by EFT. A further notable advantage of MEEFT is that, since correlating the observables in neighboring nuclei is likely to serve as an additional renormalization, the possible effects of higher chiral order terms and/or off-shell ambiguities can be significantly suppressed by the use of MEEFT.[b] I

[b]MEEFT should be distinguished from an earlier naive hybrid EFT model in which the short-range terms were dropped altogether using an intuitive argument based on short-range NN repulsion.

will come back to this point later, when I discuss concrete examples.

We need to recall here the important role of momentum cutoff in EFT. As emphasized before, the effective Lagrangian $\mathcal{L}_{eff}$ is, by construction, valid only below the specified cutoff scale Λ. This basic constraint must be respected in our nuclear EFT calculations; we must ensure that nuclear intermediate states involved in the computation of eq.(11) remain within this constrained regime. It is reasonable to implement this constraint by requiring that the two-nucleon relative momentum should be smaller than Λ. A possible choice of the cutoff function is the Gaussian form $\exp(-\vec{p}^2/\Lambda^2)$. (The detailed form of the cutoff function should not be very important.) As a reasonable range of the value of Λ we may choose: 500 MeV $\lesssim \Lambda \lesssim$ 800 MeV, where the lower bound is dictated by the requirement that Λ should be sufficiently large compared with the pion mass (in order to accommodate pion physics), while the upper bound reflects the fact that our EFT is devoid of the ρ meson.

3. Numerical results

We now discuss the applications of the above-described calculational methods to the two processes of our concern: pp fusion and the ν-d reaction. These reactions share the common feature that a precise knowledge of the Gamow-Teller (GT) transition matrix elements is crucial in estimating their cross sections. We therefore concentrate on the GT transitions. We will show here, following Refs. [23,24], that MEEFT can be used very profitably for these reactions.

We can argue (see, *e.g.,* Ref. [24]) that 1-body IA operators for the GT transition can be fixed unambiguously from the available 1-body data. As for the 2-body operators, to next-to-next-to-next-to-leading order (N^3LO) in chiral counting, there appears one unknown LEC that cannot be at present determined from data for the A=2 systems. This unknown LEC, denoted by $\hat{d}_R$ in Ref. [18], parametrizes the strength of contact-type four-nucleon coupling to the axial current. Park *et al.* [23,24] noted that the same LEC, $\hat{d}_R$, also appears as a single unknown parameter in the calculation of the tritium β-decay rate Γ^t_β, and they used MEEFT to place a constraint on $\hat{d}_R$ from the experimental value of Γ^t_β. Since $\Gamma^t_\beta(\text{exp})$ is known with high precision, and since the accurate wave functions of ^{3}H and ^{3}He are available from a well-developed SNPA calculation [25], we can determine $\hat{d}_R$ with sufficient accuracy for our purposes. Once the value of $\hat{d}_R$ is determined this way, we can carry out parameter-free MEEFT calculations for

pp-fusion [23,24] and the ν-d reactions [27]. I present here a brief summary of the results of these calculations.

For a given value of Λ within the above-mentioned range (500 MeV $\lesssim \Lambda \lesssim$ 800 MeV), $\hat{d}_R$ is adjusted to reproduce $\Gamma^t_\beta(\mathrm{exp})$, and then the cross sections for pp-fusion and the νd reactions are calculated. The results indicate that, although the best-fit value of $\hat{d}_R$ varies significantly as a function of Λ, the observables (in our case the above two reaction cross sections) exhibit a high degree of stability against the variation of Λ. This stability may be taken as an indication that the use of MEEFT for inter-correlating the observables in neighboring nuclei *effectively* renormalizes various effects, such as the contributions of higher-chiral order terms, mismatch between the SNPA and EFT wave functions, etc. This stability is essential in order for MEEFT to maintain its predictive power.

Park *et al.* [23,24] used MEEFT to calculate the rate of pp fusion, $pp \to e^+\nu_e d$. The result expressed in terms of the threshold S-factor is

$$S_{pp}(0) = 3.94 \times (1 \pm 0.005) \times 10^{-25}\,\mathrm{MeV\,b}\,. \tag{13}$$

It has been found that $S_{pp}(0)$ changes only by $\sim$0.1% against changes in Λ, assuring thereby the robustness of the MEEFT prediction. The MEEFT result, eq.(13), is consistent with that obtained in SNPA by Schiavilla *et al.* [26]. Meanwhile, the fact that MEEFT allows us to make an error estimate [as given in eq.(13)] is a notable advantage over SNPA. The details on how we arrive at this error estimate can be found in Refs. [23,24]. Here I just remark that the error indicated in eq.(13) represents an improvement by a factor of $\sim$10 over the previous results based on a naive hybrid EFT [18].

We now move to the ν-d reactions, eq.(1), and give a brief survey of all the recent results obtained in SNPA, EFT and MEEFT. Within SNPA a detailed calculation of the ν-d cross sections, $\sigma(\nu d)$, was carried out by Nakamura, Sato, Gudkov and myself [28,c] and this calculation has recently been updated by Nakamura *et al.* (NETAL) [30]. As demonstrated in Ref.[31], the SNPA exchange currents for the GT transition are dominated by the Δ-particle excitation diagram, and the reliability of estimation of this diagram depends on the precision with which the coupling constant $g_{\pi N\Delta}$ is known. NETAL fixed $g_{\pi N\Delta}$ by fitting $\Gamma^t_\beta(\mathrm{exp})$, and proceeded to calculate $\sigma(\nu d)$. Meanwhile, Butler, Chen and Kong (BCK) [32] carried out an EFT calculation of the ν-d cross sections, using the PDS scheme [15]. The results of BCK agree with those of NETAL in the following sense. BCK's calculation

[c]For a review of the earlier SNPA calculations, see Ref. [29].

involves one unknown LEC (denoted by L_{1A}), which like $\hat{d}_R$ in Ref.[24], represents the strength of a four-nucleon axial-current coupling term. BCK determined L_{1A} by requiring that the νd cross sections of NETAL be reproduced by their EFT calculation. With the value of L_{1A} adjusted this way, $\sigma(\nu d)$'s obtained by BCK show a perfect agreement with those of NETAL for all the four reactions in eq.(1) and for the entire solar neutrino energy range, $E_\nu \lesssim$ 20 MeV. Moreover, the best-fit value, $L_{1A} = 5.6\,\mathrm{fm}^3$, found by BCK [32] is consistent with its magnitude expected from the naturalness argument (based on a dimensional analysis), $|L_{1A}| \leq 6\,\mathrm{fm}^3$. The fact that an EFT calculation (with one parameter fine-tuned) reproduces the results of SNPA very well strongly suggests the robustness of the SNPA calculation of $\sigma(\nu d)$.

Even though it is reassuring that the ν-d cross sections calculated in SNPA and EFT agree with each other (in the above-explained sense), it is desirable to carry out an EFT calculation that is free from any adjustable LEC. Fortunately, MEEFT allows us to carry out an EFT-controlled parameter-free calculation of the ν-d cross sections, and such a calculation was carried out by Ando *et al.* [27]. The $\sigma(\nu d)$'s obtained in Ref. [27] are found to agree within 1% with $\sigma(\nu d)$'s obtained by NETAL using SNPA [30]. These results show that the ν-d cross sections used in interpreting the SNO experiments [2] are reliable at the 1% precision level.

We remark that, as PDS [15] is built on an expansion scheme for transition amplitudes themselves, it does not employ the concept of wave functions. This feature is an advantage in some contexts, but its disadvantage in the present context is that we cannot readily relate the transition matrix elements for an A-nucleon system with those for the neighboring nuclei; in PDS, each nuclear system requires a separate parametrization. This feature underlies the fact that, in the work of BCK [32], L_{1A} remained undetermined, because no experimental data is available to fix L_{1A} within the two-nucleon systems.

4. Discussion

In introducing hybrid EFT, we replace $|\Psi^{\mathrm{EFT}}>$ for the initial and final nuclear states in eq.(11) with the corresponding $|\Psi^{\mathrm{SNPA}}>$'s; see eq.(12). This replacement may bring in a certain degree of model dependence, called the off-shell effect, because the phenomenological NN interactions are

constrained only by the on-shell two-nucleon observables.[d] This off-shell effect, however, is expected to be small for the reactions under consideration, since they involve low momentum transfers and hence are not extremely sensitive to the short-range behavior of the nuclear wave functions. One way to quantify this expectation is to compare a two-nucleon relative wave function generated by the phenomenological potential with that generated by an EFT-motivated potential. Phillips and Cohen [20] made such a comparison in their analysis of the 1-body operators responsible for electron-deuteron Compton scattering, and showed that a hybrid EFT works well up to momentum transfer 700 MeV. A similar conclusion is expected to hold for a two-body operator, so long as its radial dependence has a "smeared-out" structure reflecting the finite momentum cutoff. We can therefore expect that hybrid EFT as applied to low energy should be practically free from the off-shell ambiguities. The off-shell effect should be even less significant in MEEFT, wherein an additional "effective" renormalization is likely to be at work (see subsection 2.4).

Another indication of the stability of the MEEFT results comes from a recently proposed idea of the low-momentum nuclear potential [33]. As mentioned, a "realistic phenomenological" nuclear interaction, V_{ij} in eq.(3), is determined by fitting to the full set of two-nucleon data up to the pion production threshold energy. So, physically, V_{ij} should reside in a momentum regime below a certain cutoff, Λ_c. In the conventional treatment, however, the existence of this cutoff scale is ignored, and eq.(4) is solved in such a manner that the entire momentum range is allowed to participate. Bogner *et al.* proposed to construct an *effective low-momentum* potential V_{low-k} by eliminating (or integrating out) from V_{ij} the momentum components higher than Λ_c, and calculated V_{low-k}'s corresponding to a number of well-established of V_{ij}'s. It was found that all these V_{low-k}'s lead to identical half-off-shell T-matrices, even though the ways short-range physics is encoded in them are highly diverse. This implies that the V_{low-k}'s are free from the off-shell ambiguities, and therefore the use of V_{low-k}'s is essentially equivalent to employing $V_{ij}^{\rm EFT}$ (appearing in eq.(10)), which by construction should be model-independent. Now, as mentioned, our MEEFT calculation has a momentum-cutoff regulator built in, and this essentially ensures that

[d] In a fully consistent theory, physical observables are independent of field transformations that lead to different off-shell behaviors, and therefore the so-called off-shell effect is not really a physical effect. In an approximate theory, observables may exhibit superficial dependence on the off-shell behavior, and it is customary to refer to this dependence as an off-shell "effect".

the matrix element, $\mathcal{M}_{fi}^{hyb-\mathrm{EFT}}$, in eq.(12) is only sensitive to the half-off-shell T-matrices that are controlled by V_{low-k} instead of V_{ij}. Therefore, we can expect that the MEEFT results reported here are essentially free from the off-shell ambiguities.

5. Summary

After giving a very limited survey of nuclear χPT, I must repeat my disclaimer that I have left out many important topics belonging to nuclear χPT. Among others, I did not discuss very important studies by Epelbaum, Glöckle and Meißner [34] to construct a formally consistent framework for applying χPT to complex nuclei. It should be highly informative to apply this type of formalism to electroweak processes and compare the results with those of MEEFT. In this connection I find it noteworthy that the range of the cutoff parameter favored in Ref. [34] is consistent with the range used by Park *et al.* [23,24]

Despite the highly limited scope of topics covered, I hope I have succeeded in demonstrating that MEEFT is a powerful framework for computing the transition amplitudes of low-energy electroweak processes in light nuclei. I also wish to emphasize that, in each of the cases for which both SNPA and MEEFT calculations have been performed, it has been found that the result of MEEFT supports and improves the SNPA result.

Acknowledgments

This talk is based on the work done in collaboration with T.-S. Park, M. Rho, D.-P. Min, F. Myhrer, T. Sato, V. Gudkov and S. Nakamura, and I wish to express my sincere thanks to these colleagues.

References

1. K. Kubodera, Proceedings of the First Yamada Conference on Neutrinos and Dark Matter in Nuclear Physics (NDM03), Nara, Japan, June 2003, On-line publication: http://ndm03.phys.sci.osaka-u.ac.jp/proc/htm; nucl-th/0308055.
2. Q. Ahmad *et al., Phys. Rev. Lett.* **87**, 071301 (2001); *ibid* **89**, 011301 (2002); *ibid* **89**, 011302 (2002).
3. J. Bahcall, M. Pinsonneault and S. Basu, *Astrophys. J.* **555**, 990 (2001).
4. See, *e.g.,* J. Carlson and R. Schiavilla, *Rev. Mod. Phys.* **70**, 743 (1998).
5. M. Chemtob and M. Rho, *Nucl. Phys.* **A163**, 1 (1971); E. Ivanov and E. Truhlik, *Nucl. Phys.* **A316**, 437 (1979); *ibid* **A316**, 451 (1979).

6. S. Weinberg, *Phys. Lett.* **B251**, 288 (1990); *Phys. Lett.* **B295**, 114 (1992).
7. See. *e.g.,* V. Bernard, N. Kaiser and U.-G. Meissner, *Int. J. Mod. Phys.* **E4**, 193 (1995).
8. See, *e.g.,* U. van Kolck, *Prog. Part. Nucl. Phys.* **43**, 337 (1999).
9. G.P. Lepage, in: Proceedings of the Second Workshop on Effective Field Theories in Nuclear Physics, eds. P. Bedaque *et al.,* (World Scientific, 1999), p. 353.
10. S. Beane *et al.,* in *"At the Frontier of Particle Physics – Handbook of QCD"*, ed. M Shifman, vol. 1 (World Scientific, Singapore, 2001).
11. G. Brown and M. Rho, *Phys. Rep.* **363**, 85 (2002).
12. See, *e.g.,* H. Georgi, *Weak Interactions and Modern Particle Physics* (Benjamin, 1984).
13. S. Weinberg, *Physica,* **6A**, 327 (1979).
14. J. Gasser and H. Leutwyler, *Ann. Phys.* **158**, 142 (1984); J. Gasser, M. Sainio and S. Švarc, *Nucl. Phys.* **B307**, 779 (1988).
15. D. Kaplan, M. Savage and M. Wise, *Nucl. Phys.* **B478**, 629 (1996); *ibid* **B535**, 329 (1998).
16. T.-S. Park, D.-P. Min and M. Rho, *Phys. Rev. Lett.* **74**, 4153 (1995).
17. T.-S. Park, K. Kubodera, D.-P. Min and M. Rho, *Phys. Rev.* **C58**, 637 (1998).
18. T.-S. Park, K. Kubodera, D.-P. Min and M. Rho, *Astrophys. J.* **507**, 443 (1998).
19. T.-S. Park, K. Kubodera, D.-P. Min and M. Rho, *Nucl. Phys.* **A646**, 83 (1999).
20. D.R. Phillips and T.D. Cohen, *Nucl. Phys.* **A668**, 45 (2000).
21. T.-S. Park, K. Kubodera, D.-P. Min and M. Rho, nucl-th/9904053; M. Rho, in: Proceedings of the Second Workshop on Effective Field Theories in Nuclear Physics, ed. P. Bedaque, M. Savage, R. Seki, U. van Kolck (World Scientific, Singapore, 1999), p. 225,
22. T.-S. Park, K. Kubodera, D.-P. Min and M. Rho, *Nucl. Phys.* **A684**, 101c (2001).
23. T.-S. Park, L. Marcucci, R. Schiavilla, M. Viviani, A. Kievsky, S. Rosati, K. Kubodera, D.-P. Min and M. Rho, nucl-th/0106026.
24. T.-S. Park, L. Marcucci, R. Schiavilla, M. Viviani, A. Kievsky, S. Rosati, K. Kubodera, D.-P. Min and M. Rho, *Phys. Rev.* **C67**, 055206 (2003).
25. L. Marcucci *et al., Phys. Rev. Lett.* **84**, 5959 (2000); L. Marcucci, R. Sciavilla, M. Viviani, A. Kievsky, S. Rosati and J. Beacom, *Phys. Rev.* **C63**, 015801 (2001).
26. R. Schiavilla *et al., Phys. Rev.*, **C58**, 1263 (1998).
27. S. Ando, Y.H. Song, T.-S. Park, H. Fearing and K. Kubodera, *Phys. Lett.* **B555**, 49 (2003).
28. S. Nakamura, T. Sato, V. Gudkov and K. Kubodera, *Phys. Rev.* **C63**, 034617 (2001).
29. K. Kubodera and S. Nozawa, *Int. J. Mod. Phys.* **E3**, 101 (1994).
30. S. Nakamura, T. Sato, S. Ando, T.-S. Park, V. Gudkov, F. Myhrer and K. Kubodera, *Nucl. Phys.* **A707**, 561 (2002).
31. J. Carlson, D.-O. Riska, R. Schiavilla and R. Wiringa, *Phys. Rev.* **C44**, 619

(1991).
32. M. Butler and J.-W. Chen, *Nucl. Phys.* **A675**, 575 (2000); M. Butler, J.-W. Chen and X. Kong, *Phys. Rev.* **C63**, 035501 (2001).
33. S. Bogner, T.T.S. Kuo and L. Corragio, *Nucl. Phys.* **A684**, 432c (2001); S. Bogner it et al., *Phys. Rev.* **C65**, 051301 (2002); A. Schwenk, G.E. Brown and B. Friman, *Nucl. Phys.* , **A703**, 745 (2002); S.K. Bogner, T.T.S. Kuo and A. Schwenk, *Phys. Rep.* **386**, 1 (2003).
34. E. Epelbaum, W. Glöckle, A. Krüger and U.-G. Meißner, *Nucl. Phys.* **A645**, 413 (1999); E. Epelbaum *et al., Nucl. Phys.* **A671**, 295 (2000); E. Epelbaum et al., *Phys. Rev. Lett.* **86**, 4787 (2001); E. Epelbaum *et al., Phys. Rev.* **C66**, 064001 (2002); E. Epelbaum *et al., Eur. Phys. J.* **A15**, 543 (2002); E. Epelbaum, talk at the LOWq-03: 2nd Workshop on Electromagnetic Nuclear Reactions at Low Momentum Transfer, Halifax, Nova Scotia, Canada; July 2003; http://www.ap.stmarys.ca/LOWq-03.

THE MINIMAL COOLING OF NEUTRON STARS*

DANY PAGE †
Instituto de Astronomía, UNAM
Mexico, D.F. 04340, MEXICO
E-mail: page@astroscu.unam.mx

A general overview of the main physical processes driving the cooling of an isolated neutron star is presented. Among the most important ones are the various possible neutrino emission processes and the occurrence of baryon pairing. Special emphasis is also put on the importance of the chemical composition of the upper layers of the star. A detailed analysis of a Minimal Scenario, which explicitly postulates that no "exotic" form of matter be present, is summarized and compared with presently available observational data. No striking incompatibility of the data with the predictions of the Minimal Scenario is found but two, possibly three, conspicuous stars are identified which may, when better data are available, constitute strong astrophysical evidence for the occurrence of a new state of matter at high density.

1. Introduction

Among the various ways to search for new states of matter at high density the study of neutron stars is a privileged one. Many aspects of the very diverse phenomenology of these stars can provide us with indications of such "exotic" matter (see, e.g., Ref. [1]). In particular, the modeling of the thermal evolution of isolated neutron stars is an avenue along which much effort has been invested. Being born in a supernova at temperatures in excess of 3×10^{11} K, young neutron stars rapidly cool through neutrino emission and the cooling rate is a very sensitive function of the composition of matter at the most extreme densities present in its inner core. Different models predict central densities from around $4 \times \rho_{\rm nucl}$ up to 15 to 20 times $\rho_{\rm nucl}$ ($\rho_{\rm nucl}$ being the nuclear density), which may very probably be within the necessary range to see deconfinement of baryonic matter into quark matter. Less extreme models predict the occurrence of charged meson condensates and/or hyperons populations. Finally, the most extreme model

*Work in collaboration with J.M. Lattimer, M. Prakash, & A. W. Steiner
†Work partially supported by grant #IN-112502 from UNAM-DGAPA

consider that neutron stars may convert into "Strange Stars" made entirely of deconfined quark matter which would have a completely different thermal evolution [2].

Evidence in favor of the presence of a new state of matter in the core of some neutron stars can only be obtained by finding some observed characteristics of these stars which cannot be understood without the assumption of the presence of such matter. Within this point of view I describe a "Minimal Scenario" of neutron star cooling, proposed recently in Ref. [3], which precisely assumes that the neutron star interior is devoid of any form of matter beyond the standard composition consisting of only neutrons and protons, accompanied by the necessary amount of electrons and muon to keep the star charge neutral. This Minimal Scenario is a revised modern version of the "Standard Scenario" incorporating the essential effects of nucleon pairing, i.e., neutron superfluidity and/or proton superconductivity, on the star's specific heat and neutrino emission, particularly the neutrino emission by the very formation, and breaking, of the Cooper pairs. Comparison of the predictions of this Minimal Scenario with data may hence provide us with the long searched for evidence for "exotic" matter.

Section 2 briefly summarizes the presently available data on temperature and luminosity of isolated cooling neutron stars. Section 3 describes the most important input physics for the study of the Minimal Scenario. Section 4 compares the results with data and Section 5 offers conclusions.

An extensive presentation of this work can be found in Ref. [3] to which the present summary could be considered as a, hopefully convenient, *Traveler's Guide.*

2. Observational Data

Numerical calculations of neutron star cooling give as a natural result the evolution of the star's photon thermal luminosity L as a function of time. This luminosity can equally well be described in terms of an effective temperature T_e through the standard relation

$$L \equiv 4\pi R^2 \cdot \sigma_{SB} T_e^4 \qquad \text{or} \qquad L_\infty \equiv 4\pi R_\infty^2 \cdot \sigma_{SB} T_{e\,\infty}^4 \tag{1}$$

(σ_{SB} being the Stefan-Boltzmann constant) where R is the star's radius and the subscripts ∞ indicate quantities as observed "at infinity".

Observations of cooling neutron stars can provide us with data in the form of luminosity L_∞ and/or temperature T_∞ at infinity. The measured T_∞ depends of course on the kind atmosphere assumed in the spectral fits, realistic neutron star atmosphere models giving generally lower values than

blackbodies. The measured L_∞ is obtained from the total observed flux, corrected for interstellar absorption, and the distance D. If D is known with sufficient accuracy Eq. 1 could be used to determine R_∞ [4] *assuming that T_e is also accurately known*, i.e., that the correct atmosphere model has been used in the spectral fit. If the deduced R_∞ is too small or too large compared to the "canonical" 10 km expected for a neutron star it is a strong indication that the atmosphere model is not correct. Nevertheless, some exotic models of compact stars as "Strange Stars" may result in small radii and also some magnetic field configuration may be able to confine the detectable surface thermal emission to an area significantly smaller than the whole surface of the star [5].

The data I will use are shown in Fig. 1 and have been selected according to this self-consistency R_∞-criterium. Two type of spectra have been preferentially used in the spectral fits producing these data: blackbodies and magnetized hydrogen atmospheres. Only the second one has been successful in deducing acceptable values for R_∞ and this lead to the selection of T_∞ and L_∞ of the objects plotted with thick lines in Fig. 1. For the objects plotted with thin lines the magnetized hydrogen atmosphere models require much too large radii while blackbodies seem more reasonable but usually on the low side of the expected range of R_∞. Given this situation, for these objects it is difficult to decide which of T_∞ or L_∞ is the more reliable value to use for comparison with the theoretical models and I hence prefer to use both, leaving the reader draw his/her own conclusions from the analysis.

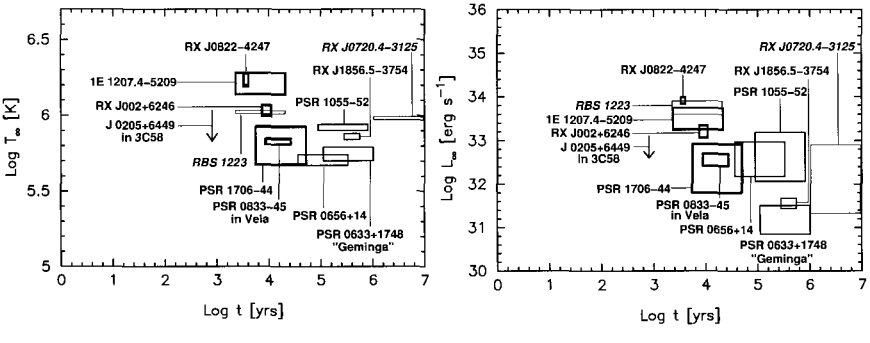

Figure 1. Measured T_∞ and L_∞, for twelve isolated neutron stars, versus age. The age, and their error bars, are either from kinematical information when available or from the pulsar spin-down time scale, in which case an uncertainty of a factor three has been assumed. See [3] for references and more details.

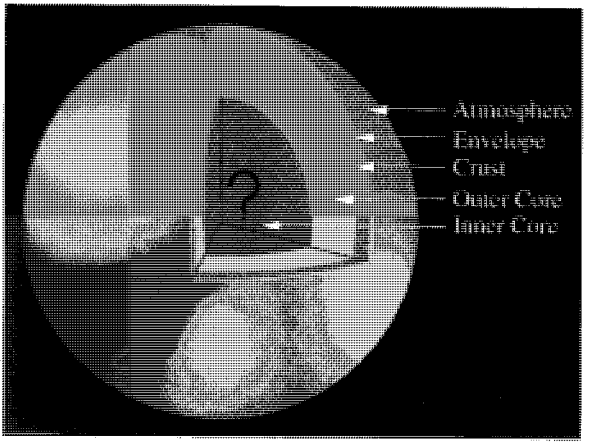

Figure 2. The different layers in a neutron star. [Drawing by the author.]

3. The Physics of Neutron Star Cooling

The picture in Fig. 2 illustrates the most important layers in a neutron star:

- **Atmosphere:** at most a few tens of centimeters thick, this is the visible surface of the star (it may actually be a solid surface instead of an atmosphere) where the thermal photons are emitted. It is of utmost importance for observations since it is where the energy distribution of the thermally emitted photons, i.e., the thermal *spectrum*, is determined. However, since all the heat flowing into it from the interior is reemitted at the surface, the atmosphere does not affect the thermal evolution of the star.
- **Envelope:** this layer is several tens of meters thick and is, by definition, where a large temperature gradient is always present. It is a throttle which controls how much heat can leak out of the star and thus determines the relationship between the interior temperature and the effective temperature or, equivalently, the surface photon luminosity L_γ.
- **Crust:** with a thickness of several hundreds meters, this layer is important only in the cooling of very young stars or in the study of transient phenomena as glitches. For our present purpose its only relevance is its (small) contribution to the specific heat.

In both the envelope and the crust matter is made of nuclei immersed in a gas of electrons and, in the inner part of the crust, at densities higher than $\rho_{\rm drip} \simeq 4.3 \times 10^{11}$ gm cm^{-3}, a quantum liquid of dripped neutrons.

- **Outer Core:** region at densities higher than $\rho_{\rm cc} \simeq 1.6 \times 10^{14}$ gm cm^{-3},

where matter is a quantum liquid predominantly composed of neutrons with a small fraction of protons, plus electrons and muons to maintain charge neutrality.

- **Inner Core:** the mysterious part, which may or may not exist, and where "exotic" forms of matter may appear. In the Minimal Scenario this inner core is explicitly assumed to be non-existent.

All calculations I will present here were performed with a wholly general relativistic Henyey-type stellar evolution code which solves exactly the equations of energy balance and heat transport inside a star whose structure is calculated by solving the Tolman-Oppenheimer-Volkov equation of hydrostatic equilibrium. Nevertheless, the most important features can be understood from the (Newtonian) energy conservation equation

$$\frac{dE_{th}}{dt} = C_v \frac{dT}{dt} = -L_\nu - L_\gamma + H \tag{2}$$

where E_{th} is the thermal energy content of the star, L_ν the neutrino luminosity, L_γ the surface photon luminosity and H would give the contribution from "heating processes" as, e.g., friction within the differentially rotating neutron superfluid or magnetic field decay, and C_v is the total specific heat, T being the interior temperature. Solving the heat transport equation gives us the detailed temperature profile in the interior but within a few tens of years after its birth the star becomes isothermal and its evolution is then entirely controlled by (the GR version of) Eq. 2. At this time a significant temperature gradient is only present in the envelope.

3.1. *The envelope and the photon luminosity*

Once the star is isothermal its interior temperature is equal to the temperature at the bottom of the envelope, T_b, and the relationship between T_b and the "surface", or effective, temperature is called the "$T_b - T_e$ relationship", which then gives us L_γ through Eq. 1. A useful approximation to it is [6]

$$T_e \sim \sqrt{T_b} \qquad \text{with} \qquad T_e \approx 10^6 \text{ K} \longleftrightarrow T_b \approx 10^8 \text{ K}. \tag{3}$$

which gives, very roughly, $L_\gamma \sim T^2$. Nevertheless, significant deviation from Eq. 3 can occur. This equation is based on models which assumed that no magnetic field is present and that the envelope is made of iron, and iron-like, nuclei, but in case light elements, e.g., H, He, C, or O, are present they strongly reduce the blanketing effect of the envelope. A magnetic field also increases the heat permeability of the envelope in the regions where it is pointing radially but strongly suppresses it in regions where it makes

small angles with the surface, thus inducing a highly non-uniform surface temperature distribution (see, e.g., Ref. [9]), and motivating the shaded surface in Fig. 2. Nevertheless the overall effect of the magnetic field is not as strong as the effect of the chemical composition. Figure 3 shows this $T_b - T_e$ relationship for various models of envelope with varying amounts of light elements and an envelope formed entirely of heavy iron-like elements with and without a magnetic field. Notice that an envelope with a significant amount of light elements results, for a given interior temperature T_b, in a luminosity L_γ which is more than one order of magnitude higher than an envelope made of heavy elements.

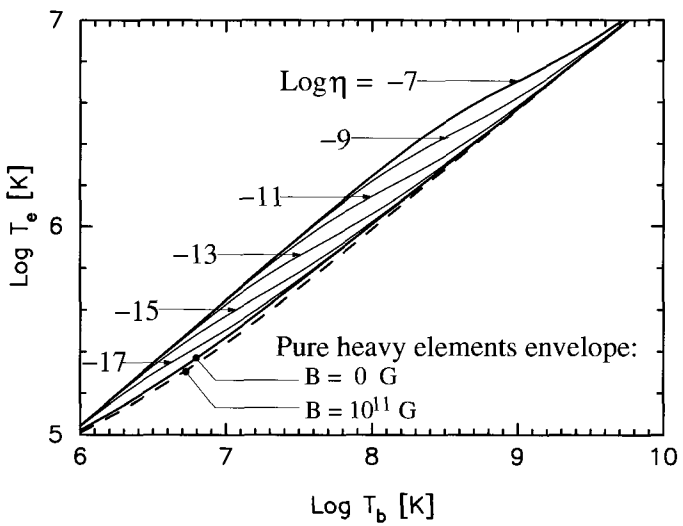

Figure 3. Relationship between the effective temperature T_e and the interior temperature T_b at the bottom of the envelope assuming various amounts of light elements parameterized by $\eta \equiv g_{s\,14}^2 \Delta M_{\rm L}/M$ where $\Delta M_{\rm L}$ is the mass in light elements in the envelope and $g_{s\,14}$ the surface gravity in units of 10^{14} cm s^{-1}, M being the total star's mass, in the absence of a magnetic field [7]. Also shown are the $T_b - T_e$ relationships for an envelope of heavy elements with and without the presence of a dipolar field of strength of 10^{11} G following Ref. [8].

The chemical composition of this envelope is probably determined by poorly understood processes occurring during the first hours of the life of the star, including post-supernova fall-back, and also possible later accretion, bombardment by high energy γ-ray from the magnetosphere, ejection of light nuclei by the pulsar mechanism,... It is hence possibly totally unrelated to the interior structure of the star and may vary from star to star

and/or evolve with time. We have no choice but consider it as a free parameter which has to be varied independently of the internal structure of the star, i.e., within both the Minimal Scenario and any other exotic one. Spectral fits to the thermal spectrum could determine the composition of the atmosphere: an iron atmosphere necessarily implies an heavy element envelope but a light element atmosphere unfortunately does not impose any restriction on the the chemical composition of the layers a few tens of centimeters beneath it.

3.2. *The neutrino luminosity*

The second important term in Eq. 2 is L_ν which is strongly dominated by the neutrino emission from the core. All significant processes are directly related to β- and inverse β-decay of neutrons with protons and several of them are listed in Table 1 with their emissivities q_ν. The simplest such process is the direct Urca ("DUrca") process. However, momentum conservation in this process requires proton fractions x_p above 15% [10] while at nuclear density it is only of the order of 5%. Thus, in the outer core of the neutron star, and this is the definition of the outer core, neutrino emission is due to the modified Urca (MUrca) process in which a second "spectator" nucleon (a neutron for the neutron branch or a proton in the proton branch of MUrca) contributes by giving or absorbing the extra momentum needed. Being a five fermion process instead of a three fermion one, the MUrca process is much less efficient than the DUrca process. It acquires two extra Pauli blocking actors (T/E_F), E_F being the Fermi energy of the extra nucleon: since $E_F \sim 100$ MeV, with $T = 10^9 \cdot T_9$ K, the reduction of MUrca is of the order of $10^{-6}\ T_9^2$ compared to DUrca. Another possibility which allows the DUrca process, but with a reduced efficiency, is the presence of a charged meson (π^- or K^-) condensate which can easily contributes to momentum conservation without introducing any dramatic phase space limitation as a nucleon does in the MUrca process. In case hyperons, or quarks, appear at high density they will also participate in DUrca processes and increase enormously L_ν.

In short, for the chemical composition expected at densities not too much higher than $\rho_{\rm nucl}$ where the proton fraction is small the neutrino emission is due to the MUrca process while any change beyond this will increase the emissivity by many orders of magnitude. This MUrca process is the essence of the Standard Scenario for neutron star cooling but the occurrence of nucleon pairing and its proper treatment makes the subject more complicated and leads to the Minimal Scenario. I refer the reader to

the two excellent reviews by Pethick [11] and Yakovlev et al. [12] for more details on neutrino emission processes.

Table 1. Some core neutrino emission processes and their emissivities.

Process Name	Process	Emissivity q_ν (erg/sec/cm^3)
a) Modified Urca	$\begin{cases} n + n' \to n' + p + e^- + \overline{\nu}_e \\ n' + p + e^- \to n' + n + \nu_e \end{cases}$	$\sim 10^{21} \cdot T_9^8$
b) K-condensate	$\begin{cases} n + K^- \to n + e^- + \overline{\nu}_e \\ n + e^- \to n + K^- + \nu_e \end{cases}$	$\sim 10^{24} \cdot T_9^6$
c) π - condensate	$\begin{cases} n + \pi^- \to n + e^- + \overline{\nu}_e \\ n + e^- \to n + \pi^- + \nu_e \end{cases}$	$\sim 10^{26} \cdot T_9^6$
d) Direct Urca	$\begin{cases} n \to p + e^- + \overline{\nu}_e \\ p + e^- \to n + \nu_e \end{cases}$	$\sim 10^{27} \cdot T_9^6$
e) Quark Urca	$\begin{cases} d \to u + e^- + \overline{\nu}_e \\ u + e^- \to d + \nu_e \end{cases}$	$\sim 10^{26} \alpha_c T_9^6$

3.3. *Baryon paring*

Pairing of baryons, either nucleons or hyperons and also quarks if present, is predicted to occur in most of the interior of a neutron star. At low Fermi momenta neutrons and protons are expected to pair in a $^1S_0$ angular momentum state while at higher momenta a $^3P_2$ state is probably replacing it. The $^1S_0$ neutron gap has been extensively studied and is covering the

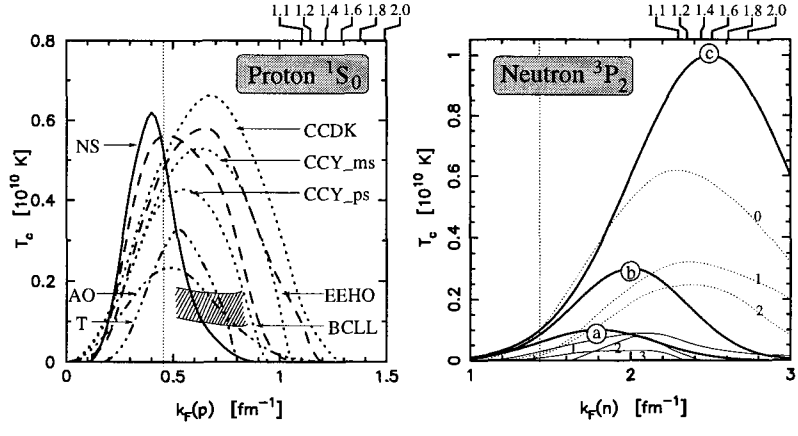

Figure 4. Predictions of critical temperatures T_c for pairing of protons in the $^1S_0$ state and neutrons in the $^3P_2$ state. The dotted vertical lines indicate the crust-core boundary. Values of k_F at center of stars of masses 1.1, 1.2, 1.4, 1.6, 1.8, and 2.0 $M_\odot$ are marked at the upper margin, for stars built with the EOS from [15]. See [3] for references.

inner part of the crust with some extension in the outermost layers of the core. The proton $^1S_0$ gap is also certainly present in the outer core and may or may not reach the center of the star, depending on the specific pairing model considered and on the central density of the star. Figure 4 shows a representative sample of theoretical predictions for the associated critical temperature T_c. Neutron pairing in the $^3P_2$ state is much more delicate and there is a very wide range of predictions as is illustrated by the examples shown in Figure 4. As shown by Baldo et al [13] the poor understanding of the nucleon-nucleon interaction in the $^3P_2$ state *in vacuum* by itself results in a wide range of predictions for T_c, illustrated by the three curves labeled "a", "b", and "c" in Figure 4. Moreover, *in medium* effects were recently shown to have a dramatic effect on this gap [14] which may result to be vanishingly small.

The dramatic effect of pairing on the cooling comes from the gap it introduces in the single particle excitation spectrum which results in a strong suppression of both the specific heat and the neutrino emissivity of the paired component. When $T \ll T_c$ this suppression is similar to a Boltzmann factor $\exp(-\Delta/kT)$ and in general it is taken into account accurately by multiplying the relevant c_v's and q_ν's by appropriate "control functions" (See Fig. 5).

3.4. *The Pair Breaking and Formation ("PBF") neutrino emission process*

The occurrence of pairing has a third effect, beside the suppression of c_v and q_ν, which is the emission of $\nu - \bar{\nu}$ pairs at temperature below, but close to, T_c produced by the formation and breaking of Cooper pairs, the "PBF" process [16, 17]. This process leads to a sudden increase of the neutrino emission in a given layer, when T reaches T_c, which can largely dominates over the emission from the MUrca process. For example, in the case of the neutron $^3P_2$ pairing its emissivity is

$$q_\nu^{\mathrm{n}^3\mathrm{P}_2} = 8.6 \times 10^{21} \left(\frac{\rho}{\rho_0}\right)^{1/3} \left(\frac{m_n^*}{m_n}\right) \times \tilde{F}_{^3\mathrm{P}_2}(T/T_c) \left(\frac{T}{10^9\mathrm{K}}\right)^7 \qquad (4)$$

The control functions $\tilde{F}$ are plotted in Fig. 5 and describe the onset of the process when T reaches T_c and its suppression when $T \ll T_c$. Comparing the emissivities given above with the MUrca process in Table 1 one sees that these PBF processes can dominate the neutrino emission and we will see in the next section that they are an essential ingredient of the Minimal Scenario.

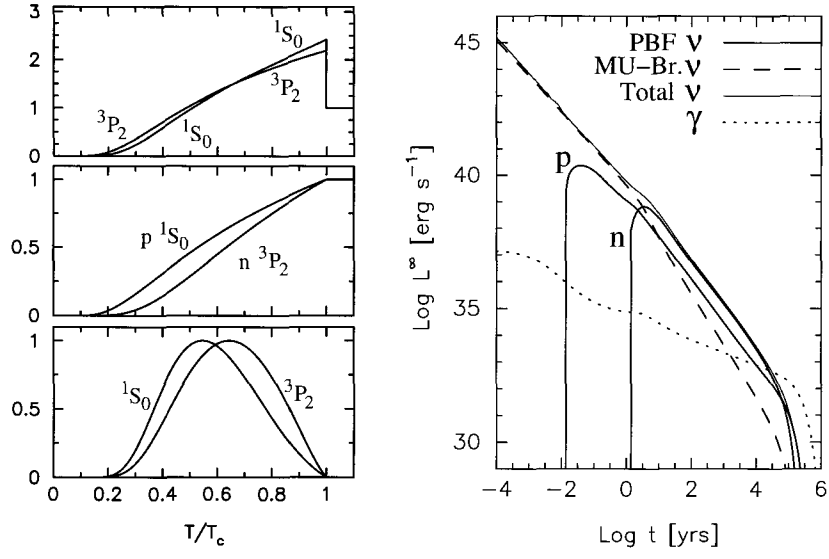

Figure 5. Left panel: control functions, for pairing in the $^1S_0$ and $^3P_2$ phases, of the specific heat (top), MUrca process (middle) and PBF process (bottom). Right panel: comparison of the neutrino luminosities from the two PBF processes due to neutron $^3P_2$ and proton $^1S_0$ gap (the neutron $^1S_0$ gap contribution is small and not shown here), and from the MUrca processes, with the total neutrino luminosity and the photon luminosity. (Neutron $^3P_2$ gap from model "a" and proton $^1S_0$ pairing from model AO, as labeled in Fig 4.

3.5. *The specific heat*

For normal (i.e., unpaired) degenerate spin $\frac{1}{2}$ fermions of type "i", the specific heat (per unit volume) is

$$c_{i,v} = N_i(0)\frac{\pi^2}{3}k_B^2 T = \frac{m_i^* n_i}{p_{i,F}^2}\pi^2 k_B^2 T \tag{5}$$

Most of the specific heat of the star is provided by the core and, in absence of "exotic" matter, nucleons contribute about 90% of it while leptons (e and μ) share the remaining. Once neutrons and/or protons go into a paired state the specific heat is strongly altered: when T reaches T_c there is a discontinuity in c_v which suddenly increases but when $T \ll T_c$ it becomes exponentially suppressed. This effect is also accurately taken into account by introducing a multiplicative "control function" plotted in Fig. 5. It is important to notice that even in case both neutrons and protons are paired in the whole core we still have the contribution of the leptons which remains untouched, i.e., pairing can reduce the total C_v by at most 90% while L_ν

can be suppressed by many orders of magnitude in case baryons involved in all the important processes are paired.

4. The Minimal Scenario

The physical ingredients presented in the previous section constitute all the essential input for the Minimal Scenario. Since, by definition, this scenario does not admit any enhanced neutrino emission the cooling history of a neutron star has only a very weak dependence on its mass. Moreover, the supranuclear EOS is also well constrained within this scenario so that we can generally simply study the evolution of a "canonical" 1.4 $M_\odot$ neutron star. All results presented here are based on the EOS from APR [15]. What is *not* constrained by the requirement of the Minimal Scenario is:

A) the chemical composition of the envelope and

B) the pairing state of the nucleons

and the large uncertainties in these two physical ingredients are, by far, the most important sources of uncertainty in the theoretical predictions of the Minimal Scenario.

The effect of the envelope is illustrated in the left panel of Fig. 6 for the two extreme cases of a star with an envelope consisting only of heavy elements (marked as "H") and with an envelope containing a maximum amount of light elements (marked as "L"). The important features to note are:

A1) first, at age inferior to 10^5 yrs, both stars have the same central temperature but the "L" model has a higher T_e: this correspond to the *neutrino cooling era* where L_ν drives the cooling, hence the same $T_{\rm center}$ for both stars, and the surface temperature simply follows the interior evolutions, hence a higher T_e in presence of a less insulating light element envelope, and

A2) later, during the *photon cooling era* when $L_\gamma \gg L_\nu$, the cooling trajectories get inverted since the light element envelope results in a much larger photon luminosity and hence faster cooling.

With an envelope containing a smaller amount of light elements we obtain an intermediate evolution and in case we allow for a time evolution of the amount of light elements the evolution can switch from one trajectory to the other.

The overall effect of pairing is illustrated in the three cooling curves plotted in the right panel of Fig. 6. The two important features to note are:

B1) comparing the model without pairing with the model with pairing but without the PBF process taken into account, one sees the effect of the suppression of the MUrca neutrino process resulting in a warmer star during the neutrino cooling era while during the photon cooling era the results are inverted because of the suppression of C_v from the pairing, and **B2)** once the neutrino emission from the PBF process is taken into account the cooling is strongly enhanced during the neutrino cooling era, confirming the results of Fig 5 (right panel) that this PBF process can be much more intense than the MUrca one, and finally during the photon cooling era the two paired models, with and without PBF, join once they have forgotten their previous neutrino cooling history.
Of course the PBF process is always acting in presence of pairing and it has been artificially turned-off for this figure, but its efficiency depends on the actual size of the gap, i.e., the actual profile of T_c for either neutrons or protons, and the gaps used in Fig 5 have been chosen to maximalize the effect.

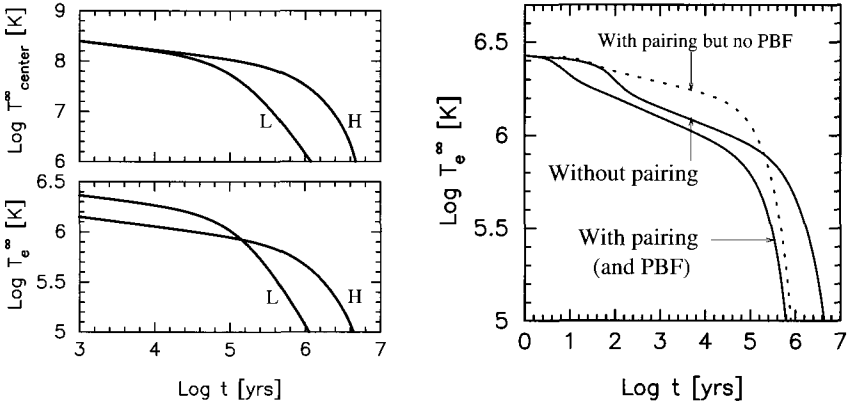

Figure 6. Left panel: effect of the envelope chemical composition in the cooling. Right panel: effect of nucleon pairing on the cooling. (See text for description.)

An extensive comparison of the predictions of the Minimal Scenario with the data presented in Sec. 2 is shown in Fig 7. For the reasons discussed in Sec. 2 results are plotted twice, as T_e vs age (left panels) and L vs age (right panels). The uncertainties due to the exact extent of nucleon pairing are better assessed by classifying the possible models into three families depending on the size of the neutron $^3P_2$ gap since this is the most uncertain one: a vanishing gap and the schematic models "a" and "b" of

Fig. 4. For each of these three families variations of the neutron and proton $^1S_0$ gaps generate a set of closely packed curves and, given the uncertainty about the envelope chemical composition each set is shown twice, assuming an envelope made of heavy elements and an envelope with a maximum amount of light elements. (For clarity only these two extreme cases of envelope are shown, but any trajectory inbetween is possible.)

The overall agreement between theory and data is quite good, which I personally find in itself amazing considering that this is REAL THEORY: these calculations culminate several decades of works from hundreds of physicists and astrophysicists based essentially on only a handful of observational facts (the very existence of "neutron stars", several mass measurements and their extreme compactness known from pulsar timing, ...).

The three sets of models, for the three different neutron $^3P_2$ gaps, are quite similar but do show some essential differences. When considering young stars, particularly J0205+6449 (in 3C58), PSR 0833-45 (in Vela) and PSR 1706-44, one sees that in the models with the $^3P_2$ gap "a" are very close to the upper limits of Vela and 3C58 while the difference is larger with the other two gaps. The interpretation of the data of PSR 1706-44 is more ambiguous due to the presently large uncertainty on both it temperature (or luminosity) and age. Since no thermal emission has been actually detected from 3C58 it is more prudent to consider it on a L-age plotted where the discrepancy with the theoretical predictions is actually the largest.

Several of the older objects may have temperatures higher than some of the theoretical predictions of the Minimal Scenario. This may be attributed to an erroneous age, considering that the only information we have bout their possible age is the spin-down time scale which can be very misleading. Another possibility is that some "heating mechanism' is at work which converts rotational, or magnetic, energy into heat.

5. Conclusions

In the Quest for New States of Dense Matter we have performed an extensive study of the thermal evolution of isolated neutron stars under the hypothesis that no new phase is present and tried to find some incompatibility of the results of this assumption with the best presently available data on cooling neutron stars. The final results, presented in Fig. 7 show now striking incompatibility with, nevertheless two objects, J0205+6449 (in 3C58) and PSR 0833-45, which are conspicuously lower than our predictions.

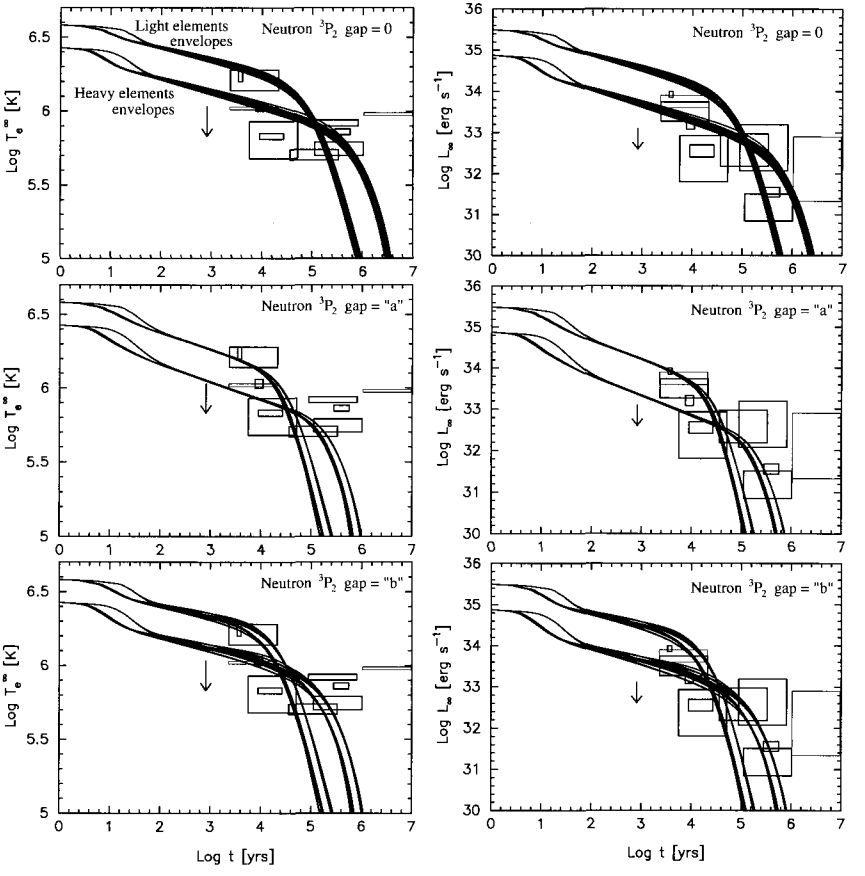

Figure 7. Comparison of predictions of the Minimal Scenario with data. Left panels: effective temperature at infinity T_e^∞ vs. age. Right panels: luminosity at infinity L_∞ vs age. The upper, middle, and lower panels correspond to three different assumption about the size of the neutron $^3P_2$ gap as indicated in the panels. In each panel the two sets of curves correspond to the two extreme models of envelope chemical composition: light elements or heavy elements, as labeled in the upper left panel. For each set of curves, the different 15 curves correspond to different choices of the neutron (3 cases) and proton (5 cases) $^1S_0$ gaps. 1.4 $M_\odot$ star built with the EOS of APR.

Given the capability of both *Chandra* and *XMM-Newton* one can have the hope that in the near future either more such objects will be find or that more data on these two conspicuous stars will permit more detailed studies and confirm them as star which encompass a new state of dense matter.

Acknowledgments

Work partially supported by grants from UNAM-DGAPA (#IN112502) and Conacyt (#36632-E). The author also wants to thank the organizers of this Workshop for the invitation and financial support.

References

1. Van Kerkwijk, M. this volume
2. Page, D., & Usov, V. V. *Phys. Rev. Lett.* **89**, 131101 (2002)
3. Page, D., Lattimer, J. M., Prakash, M., & Steiner, A. W. 2004, submitted to *Astrophys. J.*
4. J. Drake, this volume
5. Geppert, U., Kücker, M., & Page, D. submitted to *Astronom.& Astrophys.* [astro-ph/0403441]
6. Gudmundsson, E.H., Pethick, C.J. & Epstein, R.I. *Astrophys. J.* **272**, 286 (1983)
7. Potekhin, A. Y., Chabrier, G., & Yakovlev, D. G. *Astron. & Astrophys.* **323**, 415 (1997)
8. Potekhin, A. Y., & Yakovlev, D. G. *Astron. & Astrophys.* **374**, 213 (2001)
9. Page, D. *Astrophys. J.* **442**, 273 (1995)
10. Lattimer, J. M., Pethick, C. J., Prakash, M., & Haensel, P. *Phys. Rev. Lett.* **66**, 2701 (1991)
11. Pethick, C. J. 1992, Rev. Mod. Phys., 64, 1133
12. Yakovlev, D. G., Kaminker, A. D., Gnedin, O. Y., & Haensel, P. *Phys. Rep.* **354**, 1 (2001)
13. Baldo, M., Elgarøy, Ø., Engvik, L., Hjorth-Jensen, M., & Schulze, H.-J. *Phys. Rev.* **C58**, 1921 (1998)
14. Schwenk, A., & Friman, B. *Phys. Rev. Lett.* **92**, 082501 (2004)
15. Akmal, A. and Pandharipande, V. R. and Ravenhall, D. G. *Phys. Rev.* **C58**, 1804 (1998)
16. Flowers, E., Ruderman, M., & Sutherland, P. *Astrophys. J.* **205**, 541 (1976)
17. Voskresensky, D. N., & Senatorov, A. V. *Sov. J. Nucl. Phys.* **45**, 411 (1987)

THE SOLAR HEP PROCESS CONFRONTS THE TERRESTRIAL HEN PROCESS

TAE-SUN PARK
Korea Institute for Advanced Study
Seoul 130-722, Korea
E-mail: tspark@kias.re.kr

Recently we succeeded to make a reliable effective field theory (EFT) prediction in a totally parameter-free manner for the S-factor of the solar *hep* process, ${}^3\mathrm{He}+p \to {}^4\mathrm{He}+e^+ + \nu_e$, $S_{hep}(0) = (8.6 \pm 1.3) \times 10^{-20}$ keV-b. The strategy used in there is to embed a highly sophisticated and realistic nuclear potentials into an EFT framework. By applying the same method to the *hen* process, ${}^3\mathrm{He}+n \to {}^4\mathrm{He}+\gamma$, which has many features in common with the *hep*, we have also demonstrated the validity of the theory prediction; Our result, $\sigma_{hen} = (60 \pm 3 \pm 1)\ \mu b$, is in good agreement with the experimental values, $(54 \pm 6)\ \mu b$ and $(55 \pm 3)\ \mu b$.

1. Introduction

In this talk, I wish to report our recent developments on making model-independent theory predictions for the *hep* and *hen* processes,[1,2,3]

$$hep: \ {}^3\mathrm{He} + p \to {}^4\mathrm{He} + e^+ + \nu_e, \tag{1}$$

$$hen: \ {}^3\mathrm{He} + n \to {}^4\mathrm{He} + \gamma\,, \tag{2}$$

where the former figures importantly in solar neutrino physics while the latter demonstrates the validity of the method used in making theory prediction for *hep*.

The basic solar burning mechanism is converting four protons into an alpha particle, $4p \to {}^4\mathrm{He} + 2e^+ + 2\nu_e$, via a series of strong and electroweak nuclear reactions including the *hep* process. The neutrinos generated in these reactions provide us direct information about the interior of the sun. Indeed the deficit of the solar neutrino flux measured in several experiments[4,5,6,7,8,9] compared to the so called standard solar model (SSM) prediction[10] has caused extensive study and finally brought us new physics beyond the Standard Model; the transmutation of neutrino flavor or neutrino oscillation, which has been established by the recent experiment at

Sudbery Neutrino Observatory (SNO)[9].[a] Now that the existence of neutrino oscillations itself has been established, the next important challenge is to determine the accurate values of the mixing parameters and δm^2's. In this context the *hep* process figures importantly.

Compared to other dominant solar neutrinos, the *hep* neutrino flux $\phi_\nu(hep)$ is very small; seven orders of magnitude smaller than the *pp*-fusion neutrinos ($p + p \rightarrow d + e^+ + \nu_e$, $E_\nu \leq 0.4$ MeV) and three orders of magnitude smaller than the ^{8}B neutrinos ($^8\mathrm{B} \rightarrow {}^8\mathrm{Be}^* + e^+ + \nu_e$, $E_\nu \leq 17$ MeV). The *hep* reaction can however produce the highest-energy solar neutrinos with their spectrum extending beyond the maximum energy of the ^{8}B neutrinos, $E_\nu(hep) \leq 18.8$ MeV. Therefore, even though $\phi_\nu(hep)$ is small, there can be, at some level, a significant distortion of the higher end of the ^{8}B neutrino spectrum due to the *hep* neutrinos. This change can influence the interpretation of the results of a recent Super-Kamiokande experiment that have generated many controversies related to neutrino oscillations[13,14]. On the other hand, theoretical estimation of the *hep* astrophysical S-factor,[b] S_{hep}, has suffered huge uncertainty. This may be appreciated by noting that theoretical estimates of S_{hep} have varied by orders of magnitude in the literature. For example, Bahcall and Krastev[15] made a detailed analysis of experimental data considering various neutrino oscillation scenarios and treating S_{hep} as an adjustable parameter; They reported that, by allowing S_{hep} to be larger than 20 times of the "1998 standard value[16]", 2.3×10^{-20} keV-b, one could improve significantly global fits to all the then available solar neutrino data for every case of the neutrino oscillation scenarios studied. The philosophy behind this treatment was that the evaluation of S_{hep} was so challanging that one could not present a reliable and robust upper limit[17].

Why S_{hep} is so difficult to estimate ? The reason is multifold. We first recall that nuclear responses to external electroweak probes consist of 1-body and meson-exchange-current (MEC) contribution, and the latter can be further decomposed into *soft*-one-pion-exchange and the residual parts,

$$\mathcal{M} = \mathcal{M}_{1\mathrm{B}} + \mathcal{M}_{\mathrm{MEC}} = \mathcal{M}_{1\mathrm{B}} + \mathcal{M}_{soft\text{-}1\pi} + \mathcal{M}_{\mathrm{residual}}. \qquad (3)$$

[a]Independent evidence for neutrino oscillations is known from the study of the atmospheric neutrinos at Super-Kamiokande[11], and from the study of the reactor neutrinos at the KamLAND[12].

[b]The S-factor is the cross section modulo overall factor which accounts the Coulomb repulsion between p and ^{3}He, $S(E) = E\sigma(E)\exp(4\pi\alpha/v_{\mathrm{rel}})$, where E is the center-of-mass energy, v_{rel} is the relative velocity, and α is the fine structure constant. $S(E)$ is a smooth function of E that remains finite as $E \rightarrow 0$.

$\mathcal{M}_{1B}$ and $\mathcal{M}_{soft\text{-}1\pi}$ are easy to evaluate with little uncertainty, while we have a poor control on $\mathcal{M}_{\rm residual}$ which includes the contributions from massive degrees of freedom. In EFT, $\mathcal{M}_{1B}$, $\mathcal{M}_{soft\text{-}1\pi}$ and $\mathcal{M}_{\rm residual}$ correspond to leading order (LO), next-to-leading order (NLO) and next-next-next-to-leading order (N^3LO), respectively. In normal circumstances, we thus expect $\mathcal{M}_{1B} \gg \mathcal{M}_{soft\text{-}1\pi} \gg \mathcal{M}_{\rm residual}$, and the poorly known $\mathcal{M}_{\rm residual}$ play only minor role. For the *hep* process, however, $\mathcal{M}_{1B}$ is strongly suppressed due to the symmetries of the initial and final state wave functions. The ^{4}He wavefunction is dominated by a maximum orbital symmetry component characterized by the Young tableau notation [4]. On the other hand, the dominant component of the $p + {}^3$He system has [31]-symmetry, the second most symmetric state. Thus the leading order one-body Gamow-Teller (GT) operator of the form $g_A \sum_i \tau_i^- \boldsymbol{\sigma}_i$ can not mediate the transition between the dominant components. Furthermore, $\mathcal{M}_{soft\text{-}1\pi} = 0$, which is a generic feature of Gamow-Teller (GT) operators (space components of axial-vector current). To make it worse, the two-body corrections to the "leading" one-body GT term generically come with opposite sign causing a large cancellation, $\mathcal{M}_{1B} \simeq -\mathcal{M}_{\rm MEC}$. Therefore, it is necessary to calculate both $\mathcal{M}_{1B}$ and $\mathcal{M}_{\rm MEC}$ with great accuracy, even for a rough estimate.

How can we make a theory prediction for S_{hep} ? The traditional method is based on accurate but phenomenological nuclear potentials, with the Chemtob-Rho type of current operators which are derived from the tree-level resonance-exchange diagrams[18]. We refer this picture to as "standard nuclear physics approach (SNPA)". So far SNPA has scored an enormous success in wide areas of nuclear physics, achieving in some cases an accuracy that defies the existing experimental precision. There are by now a number of so-called high-precision phenomenological potentials that can reproduce all the existing 2-nucleon data with normalized χ^2 values close to unity. Furthermore, recent progress in numerical techniques for obtaining A-body wave functions for a given potential has reached such a level[19] that the wave functions of low-lying levels for light nuclei can now be obtained practically with no approximation.

The first SNPA calculation with realistic wave functions was done by Carlson et al.[20]: Using variational Monte-Carlo with Argonne v_{14} two-nucleon and and Urbana-VII three-nucleon potential, they obtained $S_{hep} = 1.3 \times 10^{-20}$ keV-b. Schiavilla et al.[16] performed a similar calculation but with the explicit Δ degree of freedom and obtained $S = (1.4 - 3.2) \times 10^{-20}$ keV-b, whose central value is the above mentioned "1998 standard value". The latest SNPA calculation of S_{hep} is made by Marcucci et al.[21,22];

they obtained 4-body wave functions using the correlated-hyperspherical-harmonics method with the Argonne v_{18} two-nucleon[23] and Urbana-IX three-nucleon[24] interactions. The resulting S_{hep} at threshold is

$$S_{hep}^{\rm SNPA} = 9.64 \times 10^{-20} \text{ keV-b}, \tag{4}$$

which is 4 times bigger than the "1998 standard value". SNPA suffers however model-dependence and lack of systematic expansion scheme, especially for short-distance physics which plays a crucial role in *hep*.

As mentioned, for accurate and robust estimation of S_{hep}, it is imperative to have good theoretical control of short-distance physics. A first-principle approach based on effective field theory (EFT) should provide a valuable insight in this regard. However, fully consistent EFT wave functions for (bound and $1+3$ scattering) four-body systems are not available, as of now. How can we evaluate an EFT matrix element *without* EFT wave functions ? We have recently addressed this issue by building a formalism where electroweak transition operators are systematically constructed using heavy-baryon chiral perturbation theory (HBχPT), and the corresponding nuclear matrix elements are evaluated with the use of wave functions generated by a state-of-the-art SNPA calculation. Here one may worry the mismatch between the treatments of transition operators and wave functions as well as the model-dependence of SNPA wave functions. We implement in our formalism a feature that allows us to remove the mismatch/model-depndence *order by order*. Thus our formalism is an EFT that inherits the systematic and consistent expansion scheme in a model-independent way but flexible enough to be applied to the the complicated processes including the *hep*. To emphasize this feature, we refer to our present approach as *more-effective* effective-field theory (MEEFT).

The starting point of MEEFT is the observation that, to high accuracy, the leading-order 1B operators in SNPA and EFT (HBχPT) are identical, and that their matrix elements can be reliably estimated with the use of realistic SNPA wave functions for the initial and final nuclear states. Next we note[25] that 2B transition operators in HBχPT are uniquely given by irreducible diagrams in Weinberg's counting scheme[26].[c] The long-range 2B contributions are in fact identical for both SNPA and EFT, as they are strongly constrained by chiral symmetry. It is short-range contributions that introduce model dependence in SNPA. EFT allows us to write down,

[c] Although the same approach can be applied to n-body currents ($n \geq 2$), we concentrate here on the dominant 2B currents.

for a given chiral order, the most general set of operators that govern short-distance physics as

$$\mathcal{O}_{\rm short} = \sum_{i=1}^{N} c_i \mathcal{O}_i, \tag{5}$$

where $\mathcal{O}_i$ is a zero-range operator (which may involve a derivative operator), and c_i is the corresponding low-energy constant (LEC); N is a finite number that depends on the chiral order under consideration. The c_i's, which should in principle be derivable from QCD, are in practice determined by fitting empirical data. Now, a nuclear matrix element in MEEFT is obtained by sandwiching the EFT-controlled transition operator between the relevant SNPA wave functions. This means that, if two (or more) observables belonging to the same nucleus or to neighboring nuclei are sensitive to $\mathcal{O}_{\rm short}$, they can be related via MEEFT. If the experimental value of one of those observables is known, the other(s) can be predicted. Correlating two (or more) observables in this manner is expected to significantly reduce the practical consequences of the afore-mentioned "mismatch problem". The basic soundness of this approach has been proven for the $n + p \to d + \gamma$ process[27,28] and several other processes[29]. We emphasize that MEEFT, which takes into account short-distance physics consistently, should be distinguished from naive hybrid models, which lack this feature.

Our MEEFT prediction for S_{hep}, see eq.(9), turns out to be consistent with the latest SNPA prediction, (4). However it could not be confirmed by experiment, due to the Coulomb repulsion between proton and ^{3}He at a relevant energy for the interior of the sun. This motivates us to study the *hen* process, (2), at threshold; *hen* is a four-body process that has close similarity to *hep* in that the pseudo-orthogonality of the initial and final wave functions strongly suppresses the leading-order one-body contribution. In fact, the degree of suppression for *hen* is such that the exchange current "corrections" become dominant terms. Meanwhile, since the experimental value of the threshold *hen* process is known with reasonable accuracy: $\sigma_{exp} = (54 \pm 6)\ \mu b$[30] and $\sigma_{exp} = (55 \pm 3)\ \mu b$[31], *hen* provides a good testing ground for the validity of MEEFT. It is to be noted that these experimental values have never been explained satisfactorily before. We remark, in particular, that very elaborate SNPA calculations by Carlson *et al.*[32] and by Schiavilla *et al.*[16] give $\sigma = 112\ \mu b$ and $\sigma = 86\ \mu b$, respectively.

2. Theory

The primary amplitudes for the *hep* and *hen* processes are of the Gamow-Teller (GT) and M1 types, respectively. Since the single-particle GT and M1 operators are well known at low energy, a major theoretical task is the accurate estimation of the meson-exchange current (MEC) contributions. In getting the current operators, we rely on the heavy-baryon chiral perturbation theory (HBχPT) with the Weinberg's power counting rule, which is a well-studied EFT that has been proven to be quite powerful and successful in describing low-energy nuclear systems. In HBχPT, we have pions and nucleons as pertinent degrees of freedom, with all other massive degrees of freedom integrated out. The expansion parameter in HBχPT is Q/Λ_χ, where Q stands for the pion mass and/or the typical momentum scale of the system, and $\Lambda_\chi \simeq 1$ GeV. In our studies, we have calculated the MEC up to N^{3}LO, where N$^\nu$LO stands for the order of $(Q/\Lambda_\chi)^\nu$ compared to the leading order (LO) one-body operator. Up to this order, MEC consists of one-pion-ranged, two-pion-ranged and contact-term (CT) two-body currents,

$$\begin{aligned} \boldsymbol{A}_{2\mathrm{B}} &= \boldsymbol{A}^{1\pi}(\mathrm{N^3LO}) + \boldsymbol{A}^{\mathrm{CT}}(\mathrm{N^3LO}), \\ \boldsymbol{V}_{2\mathrm{B}} &= \boldsymbol{V}^{1\pi}(\mathrm{NLO}) + \boldsymbol{V}^{1\pi}(\mathrm{N^3LO}) + \boldsymbol{V}^{2\pi}(\mathrm{N^3LO}) + \boldsymbol{V}^{\mathrm{CT}}(\mathrm{N^3LO}), \end{aligned} \quad (6)$$

where we have indicated the chiral order of each contributions. Three-body and many-body operators appear only in higher orders. As mentioned, the NLO *soft*-1π appears only in GT, while two-pion contributions do only in M1. Here we note that all the operators except but the delta-ranged contributions can be determined unambiguously, thanks to available accurate πN scattering data. The contact-term contributions however contain one ($\hat{d}^R$) and two (g_{4s} and g_{4v}) unknown parameters for $\boldsymbol{A}$ and $\boldsymbol{V}$, respectively,

$$\boldsymbol{A}^{\mathrm{CT}} \propto \hat{d}^R \sum_{i<j} (\tau_i - \tau_j)^{1-i2} (\boldsymbol{\sigma}_j \times \boldsymbol{\sigma}_j) \delta_\Lambda^{(3)}(\boldsymbol{r}_{ij}), \quad (7)$$

$$\boldsymbol{V}^{\mathrm{CT}} \propto \sum_{i<j} i\boldsymbol{q} \times [g_{4S}(\boldsymbol{\sigma}_i + \boldsymbol{\sigma}_j) + g_{4V}(\tau_i \times \tau_j)^3 (\boldsymbol{\sigma}_i \times \boldsymbol{\sigma}_j)] \delta_\Lambda^{(3)}(\boldsymbol{r}), \quad (8)$$

where Λ is the cutoff (which we introduce in the procedure of Fourier transformation from momentum space to coordinate space), and $\delta_\Lambda^{(3)}(\boldsymbol{r})$ is the smeared delta-function with the radius $\simeq 1/\Lambda$. The LECs, $\hat{d}^R$ and $g_{4s,4v}$, represent all the heavy degrees of freedom integrated out, and chiral symmetry (or any other symmetry) does not tell us the value of it. We can however fix them by studying other processes which are sensitive on them.

In other words, we adjust the value of LECs to reproduce the experimental data of those other processes, a procedure which is the *renormalization condition* of $\hat{d}^R$ and $g_{4s,4v}$. This procedure is closely analogous to the EFT approach to effective nuclear potential backed by renormalization group equations as explained in Ref. [33]. The power of the approach is that the constant $\hat{d}^R$ appears in tritium β-decay, μ-capture on a deuteron, and ν–d scattering, as well as in *pp* and *hep* processes and hence is completely fixed. Among them, accurate experimental data is available for the tritium-beta decay rate, Γ^t_β, which we use to fix $\hat{d}^R$. Similarly we fix g_{4s} and g_4v by demanding the experimental values of the magnetic moments of triton and ^{3}He, $\mu(^3\mathrm{H})$ and $\mu(^3\mathrm{He})$, should be reproduced.

3. Results

3.1. *The hep process*

To determine $\hat{d}^R$ from Γ^t_β, we calculate Γ^t_β from the matrix elements of the current operators evaluated for accurate A=3 nuclear wave functions. We employ here the wave functions obtained in Refs. [22, 21] using the correlated-hyperspherical-harmonics (CHH) method[34]. It is obviously important to maintain consistency between the treatments of the A=2, 3 and 4 systems. We shall use here the same Argonne v_{18} (AV18) potential[23] for all these nuclei. For the $A \geq 3$ systems we add the Urbana-IX (AV18/UIX) three-nucleon potential[24]. Furthermore, we apply the same regularization method to all the systems in order to control short-range physics in a consistent manner.

The values of $\hat{d}^R$ that reproduce the experimental value of Γ^t_β for Λ = 500, 600 and 800 MeV are found to be 1.00±0.07, 1.78±0.08 and 3.90±0.10, respectively.

In Table 1, we have listed results for the ratio of the matrix element of 2-body current compared to that of 1-body, $r \equiv \langle 2\mathrm{B}\rangle/\langle 1\mathrm{B}\rangle$, for the *hep* processes. We see from the table that the variation of the two-body

Table 1. The ratio $r \equiv \langle 2\mathrm{B}\rangle/\langle 1\mathrm{B}\rangle$, for the *hep* processes.

Λ (MeV)	500	600	800
r (without $\hat{d}^R$)	−1.67	−2.17	−2.94
r (with $\hat{d}^R$)	−0.60	−0.64	−0.73

GT amplitude (row labelled "r (with $\hat{d}^R$)") is ∼10 % for the range of Λ

under study. It is also noteworthy that the variation of the 2B amplitude as a function of Λ is reduced by a factor of $\sim$7 by introducing the $\hat{d}^R$-term contributions. The resulting S-factor (adding the contributions from non-GT channels) reads

$$S_{hep}(0) = (8.6 \pm 1.3) \times 10^{-20} \text{ keV-b}, \tag{9}$$

where the "error" spans the range of the Λ-dependence for Λ=500–800 MeV. This result should be compared to the SNPA prediction, (4).

The latest analysis of the Super-Kamiokande data[35] gives an upper limit of the solar *hep* neutrino flux, $\phi_\nu(hep)^{\rm SK} < 40 \times 10^3 \text{ cm}^{-2}\text{s}^{-1}$. The standard solar model[36] using the *hep* S-factor of MSVKRB[22] predicts $\phi_\nu(hep)^{\rm SSM} = 9.4 \times 10^3 \text{ cm}^{-2}\text{s}^{-1}$. The use of the central value of our estimate, Eq.(9), of the *hep* S-factor would slightly lower $\phi_\nu(hep)^{\rm SSM}$ but with the upper limit compatible with $\phi_\nu(hep)^{\rm SSM}$ in Ref. [36]. A significantly improved estimate of $S_{hep}(0)$ in Eq.(9) is expected to be useful for further discussion of the solar *hep* problem.

3.2. *The hen process*

We use realistic variational Monte-Carlo wave functions obtained for the Argonne v14 two-nucleon interaction and the Urbana VIII trinucleon interactions; these are the potentials used in the previous SNPA calculation[32]. The asymptotic behavior of the ^{3}He + n system has been taken into account by means of the Woods-Saxon (WS) potential, $V_{WS}(r) = V_0 \left(1 + e^{(r-R_0)/d_0}\right)^{-1}$. We can determine the parameters in the WS potential so as to reproduce the experimental data for the scattering length[37] and the low-energy phase shifts[38]; the results are $V_0 = 8.63637$ MeV, $R_0 = 4.14371$ fm and $d_0 = 0.8$ fm. It should be pointed out[32] that a small difference a_n can affect the *hen* cross section significantly. For this reason the experimental data are directly encoded into theory. The resulting phase shifts are shown in figure 1. The precise measurement of the ^{3}He + n scattering length enables us to limit the uncertainty associated with the scattering length to $\lesssim 1\%$ in the matrix elements. The nuclear matrix elements of the currents are evaluated by taking 1 million samplings in the Metropolis algorithm.

For each value of Λ, we adjust the values of the two independent LECs (denoted by g_{4s} and g_{4v}) so as to reproduce the experimental values of the ^{3}H and ^{3}He magnetic moments. The results are $\{g_{4s}, g_{4v}\} = \{1.079(9), 2.029(6)\}$, $\{1.277(12), 0.981(7)\}$ and $\{1.856(22), -0.235(12)\}$ for

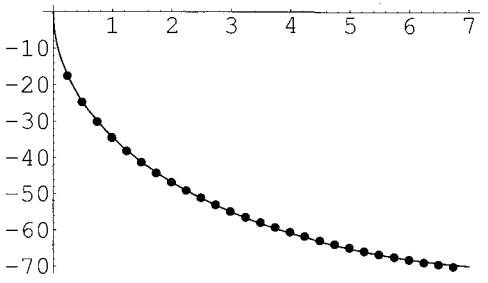

Figure 1. The ^{3}He$+n$ S-wave phase shift in degrees as a function of the center-of-mass energy in MeV. The solid line gives our results obtained with the Woods-Saxon potential, while the full dots represent the experimental data obtained from an R-matrix analysis.

$\Lambda = 500$, 600 and 800 MeV, respectively. Once the values of $g_{4s,4v}$ are fixed, we can predict the $M1$ transition amplitude for *hen* without any unknown parameters.

In Table 2, we list the ratio $r = \langle 2B \rangle / \langle 1B \rangle$ without and with the CT, and the corresponding cross sections, with respect to the cut-off. It is noteworthy that the cutoff dependence seen in the *hen* case is quite similar to that seen in the *hep* case. While the individual contributions of the contact and non-contact terms vary strongly as functions of Λ, their sum shows a greatly reduced Λ-dependence. This can be interpreted as a manifestation (albeit approximate) of the renormalization group invariance of physical observables. The smallness of the cutoff dependence, $\sim 3\%$, seen in Table 2 indirectly indicates that our MEEFT scheme allows us to control short-range dynamics to a satisfactory degree. The remaining small cutoff dependence may be attributed to the contributions of terms ignored in this calculation, *e.g.*, the "fixed" terms, n-body currents for $n > 2$, other higher chiral order terms, etc. Our final value for the threshold *hen* cross section is $\sigma = (60.1 \pm 3.2 \pm 1.0)\ \mu b$, where the first error comes from the cutoff dependence and the second from the statistical errors. Errors arising from

Table 2. The cutoff dependence of the matrix elements (in 10^{-3} fm$^{3/2}$) and the corresponding total cross sections for $\Lambda = 500$, 600 and 800 MeV.

Λ(MeV)	500	600	800
r (w/o CT)	$-2.98(2)$	$-3.86(2)$	$-4.72(3)$
r (with CT)	$-4.00(2)$	$-4.06(2)$	$-4.16(3)$
$\sigma(\mu b)$	56.9(3)	59.2(5)	63.2(10)

the uncertainties in the n-^{3}He scattering length are estimated to be $\sim 1\%$ in the matrix element.

A highly significant feature is that the ratio r for *hen* is about -4, which is much larger in magnitude than the corresponding ratio *hep*, which is about -0.6. This large difference can be understood by recalling the "chiral filter mechanism" argument [39] according to which the N^{1}LO contribution is non-vanishing for *hen*, while the 2B correction in *hep* only starts at N^{3}LO. It is remarkable that, despite this difference, exactly the same MEEFT strategy works for both *hep* and *hen*.

4. Discussion

We have already mentioned that the existing SNPA calculations for *hen* cannot explain σ_{exp}. A comment is in order on this point since, for all the other cases so far studied in both SNPA and MEEFT (*pp* fusion, *hep*, $\nu - d$ scattering, radiative *np*-capture *etc*), the numerical results exhibit a close resemblance (except that the MEEFT results come with systematic error estimates.) As mentioned, one of the most important ingredients of MEEFT is a "renormalization" procedure in which the relevant unknown LECs are fixed using the experimental values of observables in neighboring nuclei. A similar procedure has been done in the SNPA calculations of the above-quoted cases. However, the existing SNPA calculation of $hen^{32,16}$, lacks this "renormalization", and this explains why the "existing" SNPA calculation of σ_{hen} disagrees with σ_{hen}^{exp}.

Acknowledgments

This talk is based on the work done in collaboration with Y.-H. Song, L.E. Marcucci, R. Schiavilla, M. Viviani, A. Kievsky, S. Rosati, K. Kubodera, D.-P. Min and M. Rho, to all of whom I wish to express my sincere thanks.

References

1. T.-S. Park, L.E. Marcucci, R. Schiavilla, M. Viviani, A. Kievsky, S. Rosati, K. Kubodera, D.-P. Min and M. Rho, nucl-th/0107012; *Phys. Rev.* **C67**, 055206 (2003).
2. Y.-H. Song and T.-S. Park, nucl-th/0311055.
3. K. Kubodera and T.-S. Park, nucl-th/0402008.
4. R. Davis, D.S. Harmer, K.C. Hoffman, *Phys. Rev. Lett.* **20**, 1205 (1968); J.K. Rowley, B.T. Cleveland and R. Davis, *Solar Neutrinos and Neutrino Astronomy*, eds. ML Cherry, WA Fowler, K Lande. AIP Conference Proceedings No. 126, p. 1. New York: American Institute of Physics (1985).

5. Y. Fukuda, et al. (Kamiokande Collab.) *Phys. Rev. Lett.* **77**, 1683 (1996).
6. Y. Fukuda, et al. (Super-Kamiokande Collab.) *Phys. Rev. Lett.* **81**, 1158 (1998).
7. J.N. Abdurashitov, et al. (SAGE Collab.) *Phys. Rev. Lett.* **77**, 4708 (1996).
8. P. Anselmann, et al. (GALLEX Collab.) *Phys. Lett.* **B342**, 440 (1995); W. Hampel, et al. (GALLEX Collab.) *Phys. Lett.* **B388**, 364 (1996).
9. Q.R. Ahmad, et al. (SNO Collab.) *Phys. Rev. Lett.* **87**, 071301 (2001).
10. J.N. Bahcall,*Phys. Rev. Lett.* **12**, 300 (1964).
11. Y. Fukuda Y, et al. (Super-Kamiokande Collab.), *Phys. Rev. Lett.* **81**, 1562 (1998).
12. K. Eguchi, et al. (KamLAND Collab.), *Phys. Rev. Lett.* **90**, 021802 (2203).
13. J.N. Bahcall, *Phys. Rep.* **333**, 47 (2000), and references therein.
14. R. Escribano, J.-M. Frere, A. Gevaert, and D. Monderen, *Phys. Lett.* **B444**, 397 (1998).
15. Bahcall JN, Krastev PI. *Phys. Lett. B436*, 243 (1998).
16. R. Schiavilla, R.B. Wiringa, V.R. Pandharipande, and J. Carlson, *Phys. Rev.* **C 45** 2628 (1992).
17. J.N. Bahcall, hep-ex/0002018.
18. M. Chemtob and M. Rho, *Nucl. Phys* **A163**, 1 (1971).
19. For a recent review, see, for example, J. Carlson and R. Schiavilla, *Rev. Mod. Phys.* **70**, 743 (1998)
20. J. Carlson, D.O. Riska, R. Schiavilla and R.B. Wiringa, *Phys. Rev.* **C44**, 619 (1991).
21. L.E. Marcucci, R. Schiavilla, M. Viviani, A. Kievsky and S. Rosati, *Phys. Rev. Lett.* **84**, 5959 (2000).
22. L.E. Marcucci, R. Schiavilla, M. Viviani, A. Kievsky, S. Rosati and J.F. Beacom, *Phys. Rev.* **C63** (2001) 015801.
23. R.B. Wiringa, V.G.J. Stoks, and R. Schiavilla, *Phys. Rev.* **C51** (1995) 38.
24. B.S. Pudliner, V.R. Pandharipande, J. Carlson, and R.B. Wiringa, *Phys. Rev. Lett.* **74** (1995) 4396.
25. T.-S. Park, K. Kubodera, D.-P. Min, and M. Rho, *Nucl. Phys.* **A684**, 101 (2001); see also nucl-th/9904053.
26. S. Weinberg, *Phys. Lett.* **B251**, 288 (1990); *Nucl. Phys.* **B363**,3 (1991); *Phys. Lett.* **B295**, 114 (1992).
27. T.-S. Park, D.-P. Min, and M. Rho, Phys. *Rev. Lett.* **74**, 4153 (1995); *Nucl. Phys.* **A596**, 515 (1996).
28. T.-S. Park, K. Kubodera, D.-P. Min, and M. Rho, *Phys. Lett.* **B472**, 232 (2000).
29. S.R. Beane, V. Bernard, T.-S.H. Lee, and U.-G. Meißner, *Phys. Rev.* **C57**, 424 (1998); S.R. Beane, V. Bernard, T.-S.H. Lee, U.-G. Meißner, and U. van Kolck, *Nucl. Phys.* **A618**, 381 (1997).
30. F.L.H. Wolfs, S.J. Freedman, J.E. Nelson, M.S. Dewey and G.L. Greene, *Phys. Rev. Lett.* **63**, 2721 (1989).
31. R. Wervelman, et al., *Nucl.Phys.* **A526**, 265 (1991)
32. J. Carlson, D.O. Riska, R. Schiavilla and R.B. Wiringa, *Phys. Rev.* **C42**, 830 (1990).

33. G.E. Brown and M. Rho, nucl-th/0305089; S.K. Bogner and T.T.S. Kuo, nucl-th/0308036, and references therein.
34. M. Viviani, S. Rosati and A. Kievsky, *Phys. Rev. Lett.* **81**, 1580 (1998).
35. S. Fukuda *et al.*, *Phys. Rev. Lett.* **86**, 5651 (2001).
36. J.N. Bahcall, M.H. Pinsonneault, and S. Basu, *Astrophys. J.* **555**, 990 (2001); astro-ph/0010346.
37. O. Zimmer *et al.*, *EJPdirect* **A1**, 1 (2002) .
38. H.M. Fofmann and G.M. Hale, *Nucl. Phys.* **A613**, 69 (1997).
39. K. Kubodera, J. Delorme and M. Rho, Phys. Rev. Lett. **40**, 755 (1978); M. Rho, Phys. Rev. Lett. **66**, 1275 (1991).

NEUTRINO PROCESSES IN SUPERNOVAE AND NEUTRON STARS IN THEIR INFANCY AND OLD AGE

M. PRAKASH, S. RATKOVIĆ and S. I. DUTTA

Department of Physics & Astronomy
State University of New York at Stony Brook
Stony Brook, NY 11794-3800, USA

PALS*

Neutrino processes in semi-transparent supernova matter, opaque to semi-transparent protoneutron star matter, and catalyzed neutron stars are discussed.

1. Introduction

In recent years, the study of neutrino emission, scattering, and absorption in matter at high density and/or temperature has gained prominence largely due to its importance in a wide range of astrophysical phenomena. Energy loss in degenerate helium cores of red giant stars,[1,2] cooling in pre-white dwarf interiors,[3] the short- and long-term cooling of neutron stars,[4,5] the deflagration stages of white dwarfs which may lead to type Ia supernovae,[6,7] explosive stages of type II (core-collapse) supernovae,[8] and thermal emission in accretion disks of gamma-ray bursters,[9,10] are examples in which neutral and charged current weak interaction processes that involve neutrinos play a significant role. Since this is a vast subject, we will highlight some recent developments in the context of core-collapse supernovae and neutron stars from their birth to old age.

2. Supernovae

In unravelling the mechanism by which a type-II supernova explodes, the implementation of accurate neutrino transport has been realized to be critical.[11] The basic microphysical inputs of accurate neutrino transport

*Friends who have helped and contributed significantly; see the Acknowledgements.

coupled in hydrodynamical situations are the differential neutrino production and absorption rates and their associated emissivities. The processes and precise forms in which such inputs are required for multienergy treatment of neutrinos for both sub-nuclear and super-nuclear densities (nuclear density $\rho_0 \simeq 2.65 \times 10^{14}$ g cm^{-3}) are detailed in Refs. [12, 13].

At sub-nuclear densities, the relevant processes are:

$$\text{pair production} \; : \; e^+ + e^- \rightarrow \nu + \bar{\nu}\,, \tag{1}$$

$$\text{the photo} - \text{neutrino process} \; : \; e^{\pm} + \gamma^* \rightarrow e^{\pm} + \nu + \bar{\nu}\,, \tag{2}$$

$$\text{the plasma process} \; : \gamma^* \rightarrow \nu + \bar{\nu}\,, \tag{3}$$

$$\text{nucleon} - \text{nucleon bremsstrahlung} \; : \; (n,p) \rightarrow (n,p) + \nu + \bar{\nu}\,, \text{ and} \tag{4}$$

$$\nu - \text{flavor production} \; : \nu_i + \bar{\nu}_i \rightarrow \nu_j + \bar{\nu}_j\,. \tag{5}$$

The relative importance of these processes depends on the temperature and density of ambient matter and is sketched in Figure 1.

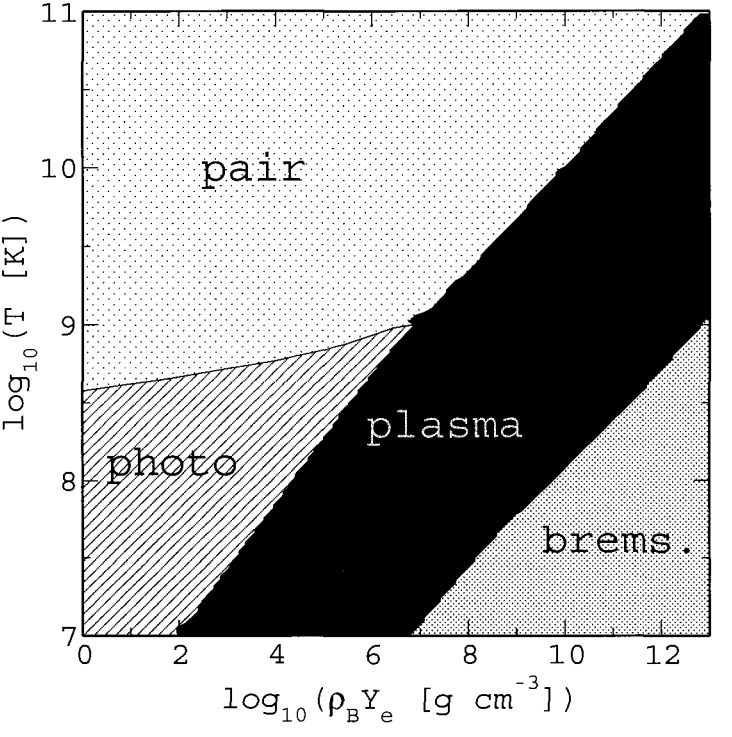

Figure 1. Regions of temperature and density in which the various neutrino emitting processes are operative.

Additional neutrino processes in the supernova environment include

$$p + e^- \rightarrow n + \nu_e, \quad (A,Z) + e^- \rightarrow (A, Z-1) + \nu_e\,, \tag{6}$$

$$\nu + (A,Z) \rightarrow \nu + (A,Z)\,, \tag{7}$$

$$\nu + e^- \rightarrow \nu + e^-, \qquad \nu + (A,Z) \rightarrow \nu + (A,Z)^*\,, \tag{8}$$

$$(A,Z)^* \rightarrow (A,Z) + \nu + \bar{\nu}\,. \tag{9}$$

Reactions (6) begin the process of neutronization and decrease of lepton number per baryon Y_L, whose value after ν-trapping determines the masses of the homologous core and initial PNS, and thus the available energy for the shock and subsequent neutrino emissions. The equation of state also influences these quantities, most importantly through the nuclear symmetry energy. In the subnuclear density regime, the coherent scattering reaction (7) from nuclei in a lattice is the most important opacity source. The reactions (8) are important in changing the neutrino energy and in achieving thermodynamic equilibrium. The reactions (1) and (9) are also important in achieving thermodynamic equilibrium. The bremsstrahlung and modified Urca ($n+p \rightarrow n+n+e^+ + \nu + \bar{\nu}$) processes dominate in many circumstances. For example, the production and thermalization of μ and τ neutrinos, which receives contributions from reactions (1) through (5), and (9), is dominated by nucleon bremsstrahlung (4) for number density $n > 0.005$ fm^{-3} and temperature $T < 15$ MeV. The modified Urca process dominates the cooling of protoneutron stars if direct Urca processes involving nucleons, hyperons or other strange particles do not occur.

3. Kernels for Neutrino Transport Calculations

The evolution of the neutrino distribution function f, generally described by the Boltzmann transport equation in conjunction with hydrodynamical equations of motion together with baryon and lepton number conservation equations, is

$$\frac{\partial f}{\partial t} + v^i \frac{\partial f}{\partial x^i} + \frac{\partial (f F^i)}{\partial p^i} = B_{EA}(f) + B_{NES}(f) + B_{\nu N}(f) + B_{TP}(f)\,. \tag{10}$$

Here, F^i is the force acting on the particle and we have ignored general relativistic effects for simplicity (see, for example, Ref. [12] for full details). The right hand side of the above equation is the neutrino source term in which, $B_{EA}(f)$ incorporates neutrino emission and absorption processes,

$B_{NES}(f)$ accounts for the neutrino-electron scattering process, $B_{\nu N}(f)$ includes scattering of neutrinos off nucleons and nuclei, and $B_{TP}(f)$ considers the thermal production and absorption of neutrino-antineutrino pairs.

Till recently, detailed differential information was not available for the plasma and photoneutrino processes. In prior works in which the total rates and emissivities for these processes were computed, the energy and angular dependences of the emitted neutrinos with 4-momenta q and q' were eliminated by using Lenard's identity:

$$\int \frac{d^3q}{2E_q}\frac{d^3q'}{2E_{q'}}\delta^4(q_t - q - q')q^\mu q'^\nu = \frac{\pi}{24}\Theta(q_t^2)(2q_t^\mu q_t^\nu + q_t^2 g^{\mu\nu})\,. \qquad (11)$$

Although the use of this identity simplifies considerably the calculation of the total emissivity, differential information about the neutrinos is entirely lost. On the other hand, calculations of differential rates and emissivities, such as

$$\frac{d^3\Gamma}{dE_q\, dE_{q'}\, d(\cos\theta_{qq'})} \quad \text{and} \quad \frac{d^3Q}{dE_q\, dE_{q'}\, d(\cos\theta_{qq'})}\,, \qquad (12)$$

where $\theta_{qq'}$ is the angle between the neutrino pairs, entail the calculation of the relevant squared matrix elements hitherto bypassed in obtaining the total rates and emissivities. Realizing this, the squared matrix elements for the plasma and photoneutrino processes were computed in Refs. [16, 17]. Some results from these recent works are highlighted below.

3.1. *The Plasma Process*

As is well known, e^+e^- pairs in a plasma cause the photon to acquire an effective mass, which arises from electromagnetic interactions (cf. Refs. [16, 18] and references therein). Therefore, we can consider the photon to be a massive spin–1 particle that couples to the $\nu\bar{\nu}$ pair through the two one-loop diagrams shown in Figure 2.

Suppressing the dependencies on (r, t) for notational simplicity, the source term for the plasma process can be written as

$$B(f) = [1-f]\frac{1}{(2\pi)^3}\int_0^\infty E_2^2\, dE_2 \int_{-1}^1 d\mu_2 \int_0^{2\pi} d\phi_2\, R^p(E_1, E_2, cos\,\theta)\,[1-\bar{f}]$$
$$- f\frac{1}{(2\pi)^3}\int_0^\infty E_2^2\, dE_2 \int_{-1}^1 d\mu_2 \int_0^{2\pi} d\phi_2\, R^a(E_1, E_2, cos\,\theta)\,\bar{f}\,, \qquad (13)$$

where the first and the second terms correspond to the source (neutrino gain) and sink (neutrino loss) terms, respectively. E_1 and E_2 are the energies of the neutrino and antineutrino, respectively. Angular variables

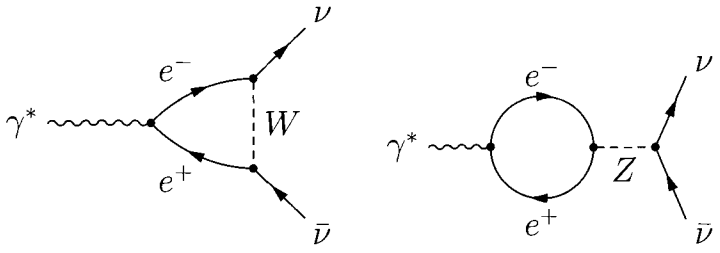

Figure 2. Leading order Feynman diagrams describing the emission of a neutrino pair from the plasma process. The charged current process in which the W-boson is exchanged produces only $\nu_e\bar{\nu}_e$, while that in which the neutral Z-boson is exchanged results in pairs of all three neutrino (e, μ, and τ) flavors.

$\mu_i \equiv \cos\theta_i$ and ϕ_i $(i = 1, 2)$ are defined with respect to the z-axis that is locally set parallel to the outgoing radial vector $\mathbf{r}$. The angle θ between the neutrino and antineutrino pair is related to θ_1 and θ_2 through

$$\cos\theta = \mu_1\mu_2 + \sqrt{(1-\mu_1^2)(1-\mu_2^2)}\,\cos(\phi_1 - \phi_2)\,. \tag{14}$$

Notice that $f \equiv f(E_1, \mu_1)$ and $\bar{f} \equiv \bar{f}(E_2, \mu_2)$. The production and absorption kernels are given by

$$R_a^p(E_1, E_2, \cos\theta) = \int \frac{d^3k}{(2\pi)^3}\, Z_Y(k) \begin{pmatrix} \xi n_B(\omega, T) \\ 1 + n_B(\omega, T) \end{pmatrix} \times \frac{1}{8\omega E_1 E_2}\, \delta^4(K - Q_1 - Q_2)(2\pi)^4 \langle |\mathcal{M}|^2 \rangle\,, \tag{15}$$

where the subscript Y stands for T–"transverse" or L–"longitudinal". The factor ξ accounts for the spin avaraging; $\xi = 2$ for the transverse, axial and mixed cases, while for the longidudinal case $\xi = 1$.

The angular dependences in the kernels $R_a^p(E_1, E_2, \cos\theta)$ are often expressed in terms of Legendre polynomials as

$$R_a^p(E_1, E_2, \cos\theta) = \sum_{l=0}^{\infty} \frac{2l+1}{2} \Phi_l^a(E_1, E_2) P_l(\cos\theta)\,, \tag{16}$$

where the Legendre coefficients $\Phi_l^a(E_1, E_2)$ depend exclusively on energies.

From Eq. (15), it is evident that the kernels are related to the neutrino rates and emissivities. We first consider the production kernel $R^p(E_1, E_2, \cos\theta)$. The corresponding analysis for the absorption kernel $R^a(E_1, E_2, \cos\theta)$ can be made along the same lines, but with the difference

that n_B is replaced by $1 + n_B$. The neutrino production rate is given by

$$\begin{aligned}\Gamma &= \xi \int \frac{d^3k}{(2\pi)^3 2\omega} Z_Y(k) \frac{d^3q_1}{(2\pi)^3 2E_1} \frac{d^3q_2}{(2\pi)^3 2E_2} \\ &\quad \times n_B(\omega, T)\, \delta^4(K - Q_1 - Q_2)(2\pi)^4 \langle |\mathcal{M}|^2 \rangle \\ &= \int \frac{d^3q_1}{(2\pi)^3} \frac{d^3q_2}{(2\pi)^3} R^p(E_1, E_2, \cos\theta)\,, \end{aligned} \tag{17}$$

which defines the kernel $R^p(E_1, E_2, \cos\theta)$ and is to be identified with that in Eq. (15). The emissivity Q can also be cast in terms of R^p using

$$Q = \int \frac{d^3q_1}{(2\pi)^3} \frac{d^3q_2}{(2\pi)^3} (E_1 + E_2) R^p(E_1, E_2, \cos\theta)\,. \tag{18}$$

The Legendre coefficients Φ_l^p for the transverse part of the production kernels are shown in Figure 3 for $l = 0$ through 3. The longitudinal component becomes comparable to the transverse component only in the strongly degenerate regime (see Figure 4), while the axial and mixed components (the latter contributes only to the differential rates and emissivities but not to the total, since it is anti-symmteric in E_1 and E_2) are negligibly small. Notice that the first few Legendre coefficients are all comparable in magnitude. Moreover, the emission process is anisotropic (see also Figure 7 of Ref. 16). "Light" photon ($\omega_p \ll T$) decays result in neutrino pairs with small outgoing angles between them, whereas "massive" photons ($\omega_p \gg T$) yield back-to-back neutrino emission.

Figure 4 shows the individual contributions to the total emissivity from the transverse, longitudinal, and axial channels at $T = 10^{11}$K and $T = 10^9$K, respectively. The curves show results from expressions derived by exploiting the Lenard identity.[16,18] The symbols "$\times$" and "+" show results obtained by integrations of the differential emissivities. At all densities and temperatures, the contribution of the axial channel to the total emissivity is negligible. For each temperature, the emissivity in the transverse channel dominates over that of the longitudinal channel at low densities. However, the peak values in these two channels are attained at nearly the same density; thereafter their individual contributions coincide.

In terms of the density and temperature dependencies of the plasma frequency ω_p and the electron chemical potential μ_e (see Figure 4 of Ref. [16]), a detailed qualitative and quantitative analyses of the basic features of Figure 4 are provided in Ref. [16]. Consider the case of Q_T first. At a fixed temperature, the basic features to note are:

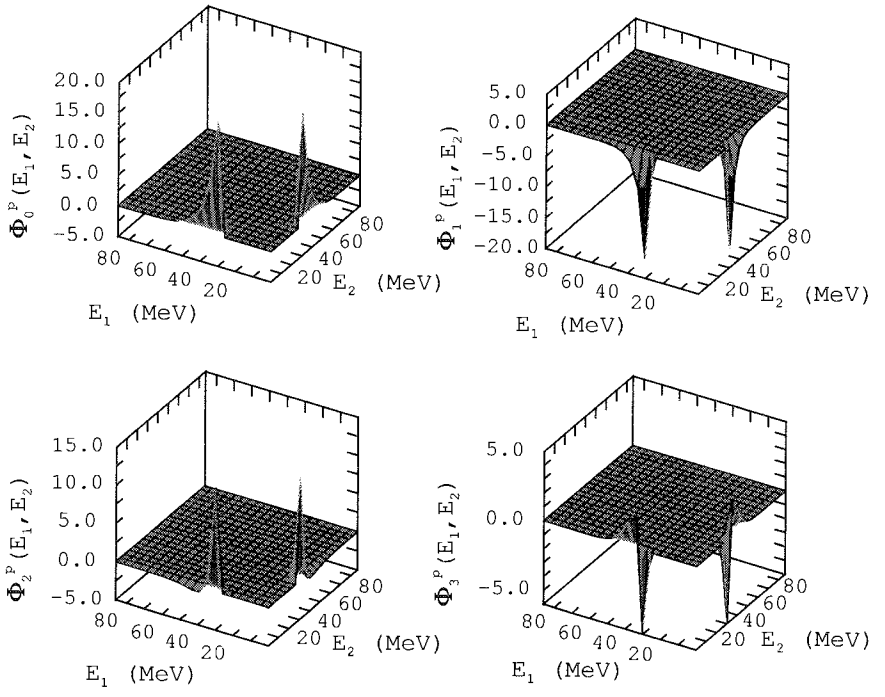

Figure 3. The transverse part of the production kernels for $T = 8.62$ MeV and $\rho_B Y_e < 10^{10}$ g cm^{-3}. The Legendre coefficients Φ_l^p are shown for $l = 0$ through 3. The neutrino energies E_1 and E_2 are in MeV and the Legendre coefficients are in units of 10^{129} $\hbar^6$ erg^{-6} cm^3 s^{-7}.

(1) Q_T is independent of the density $\rho_B Y_e$ until a turn-on density $(\rho_B Y_e)_{\rm to}$ is reached,

(2) For densities larger than this turn-on density, Q_T exhibits a power-law rise until a maximum is reached at $(\rho_B Y_e)_{\rm peak}$, and

(3) For $\rho_B Y_e \gg (\rho_B Y_e)_{\rm peak}$, the fall-off with density is exponential.

In the case of $T \gg \omega_p$ (non-degenerate plasma), the main contribution

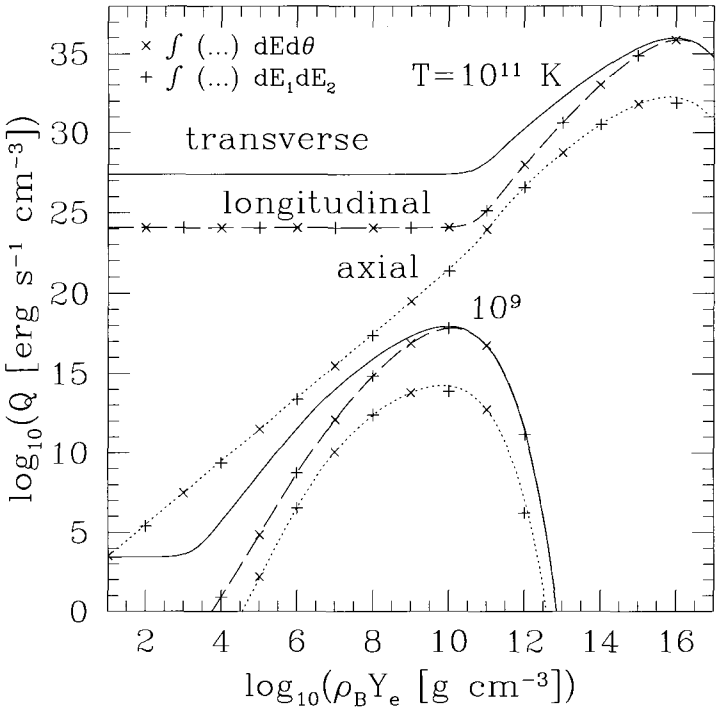

Figure 4. Individual contributions from the transverse, longitudinal, and axial channels to the neutrino emissivity. The mass density of protons in the plasma, $\rho_B Y_e = m_p n_e$, where m_p is the proton mass, $Y_e = n_e/n_B$ is the net electron fraction (n_B is the baryon number density) , and n_e is net electron number density.

to Q_T comes from high photon momenta. To a very good approximation,[18]

$$Q_T \simeq \frac{2\sum_f \left(C_V^f\right)^2 G_F^2}{48\pi^4\alpha}\zeta(3) m_T^6 T^3 , \tag{19}$$

where $\zeta(3) \simeq 1.202$ is Riemann's Zeta function and m_T is the transverse photon mass.

For $T \ll \omega_p$ (degenerate plasma), Q_T takes the form[18]

$$Q_T \simeq \frac{\sum_f \left(C_V^f\right)^2 G_F^2}{48\pi^4\alpha}\sqrt{\frac{\pi}{2}}\omega_p^{15/2} T^{3/2} e^{-\omega_p/T} . \tag{20}$$

The analyses of the longitudinal and axial emissivities can be carried out along the same lines as that for the transverse emissivity.[16]

3.2. *The Photoneutrino Process*

The leading order diagrams for the photoproduction of neutrino pairs, $e^{\pm} + \gamma^* \rightarrow e^{\pm} + \nu_{e,\mu,\tau} + \bar{\nu}_{e,\mu,\tau}$, are shown in Figure 5. The kernels of the collision integral for the photoneutrino process can be calculated along the same lines as for the plasma process and are detailed in Ref. 17.

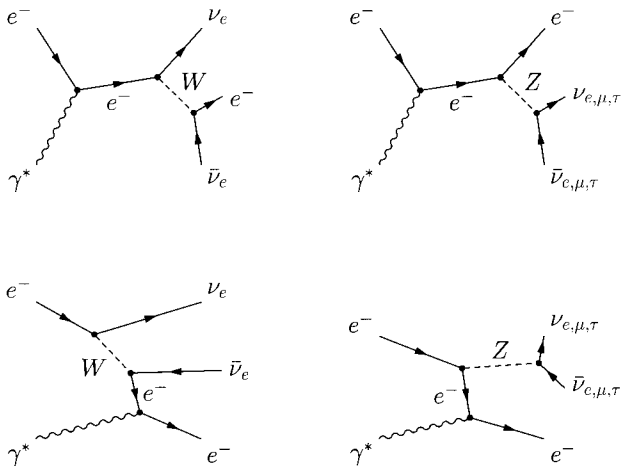

Figure 5. Leading order Feynman diagrams describing the emission of a neutrino pair from the photoneutrino process. The charged current W - exchange channel produces only $\nu_e \bar{\nu}_e$, whereas the neutral Z - exchange results in pairs of all three neutrino (e, μ, and τ) flavors. Contributions from positrons are obtained by the replacement $e^- \rightarrow e^+$.

Numerical results for the symmetric and anti-symmetric components of $\Phi_0^p(E_q, E_{q'})$ and $\Phi_1^p(E_q, E_{q'})$ are shown in Figure 6 for the case $T = 10^{11}$ K= 8.62 MeV and $\rho_B Y_e = 1$ g cm^{-3}. The results explicitly show the expected symmetry properties in neutrino energies E_q and $E_{q'}$. A comparison of the relative magnitudes $\Phi_1^p(E_q, E_{q'})$ (not shown here, but see Figure 6 of Ref. [17]) and $\Phi_0^{p\,(\mathrm{sym})}(E_q, E_{q'})$ shows that the $l = 0$ term is the dominant term. The magnitude of $\Phi_0^{p\,(\mathrm{asym})}$ amounts to only 10% of the leading $\Phi_0^{p\,(\mathrm{sym})}$ contribution. The contributions of $\Phi_1^{p\,(\mathrm{sym})}$ and $\Phi_1^{p\,(\mathrm{asym})}$ are 6% and 3%, respectively. In physical terms, this means that neutrino-pair emission from the photo-neutrino process is dominantly isotropic. Therefore, depending on the required accuracy, $\Phi_0^{p\,(\mathrm{sym})}$ might be adequate in practical applications. Note also that that the production kernels are negligible for energies E_q and $E_{q'} \gtrsim 10T$.

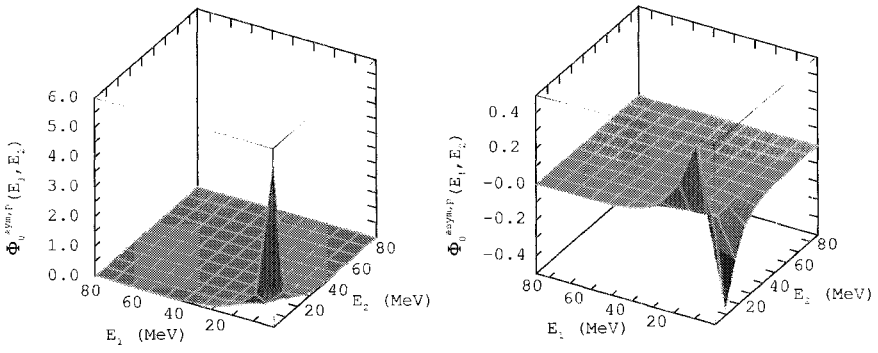

Figure 6. Symmetric and anti-symmetric parts of the Legendre coefficients $\Phi_0^{p\,(\mathrm{sym})}$ and $\Phi_0^{p\,(\mathrm{asym})}$ in the production kernels for the transverse case. The ν-energies E_q and $E_{q'}$ are in MeV and the Legendre coefficients are in units of $10^{129}\ \hbar^6\ \mathrm{erg}^{-6}\ \mathrm{cm}^3\ \mathrm{s}^{-7}$.

Contributions of the transverse and longitudinal components to the total emissivity are shown in Figure 7. For all temperatures at sufficiently high net electron densities n_e (i.e., a degenerate plasma), the inequalities

$$\begin{aligned} \mu_e &\gg T, \quad \mu_e \gg m_e, \\ \omega_P &\gg T, \quad \omega_P \gg m_e \end{aligned} \tag{21}$$

are satisfied. In this case,

$$Q_T \simeq \frac{4}{3}\,\frac{\alpha G_F^2 (C_V^2 + C_A^2)}{(2\pi)^6}\,\omega_p{}^6\, T^3\, e^{-\omega_p/T}\,. \tag{22}$$

The nondegenerate situation occurs at sufficiently low densities for which $\mu_e - m_e \ll T$. In this case, both Q_T and Q_L exhibit a plateau for temperatures $T \geq 10^9$ K. The emissivity and rate can be expressed in terms of the simple expressions

$$\begin{pmatrix} Q_T \\ \Gamma_T \end{pmatrix} = \frac{20\alpha G_F^2 (C_V^2 + C_A^2)}{3(2\pi)^6} \begin{pmatrix} T^9 \times 775.54 \\ T^8 \times 136.50 \end{pmatrix}. \tag{23}$$

The significance of the detailed differential rates and emissivities of neutrino emission and absorption processes in calculations of core-collapse supernovae in which neutrino transport is strongly coupled with hydrodynamics remains to be explored.

4. Protoneutron Stars

A protoneutron star (PNS) is born in the aftermath of the gravitational collapse of the core of a massive star accompanying a successful supernova

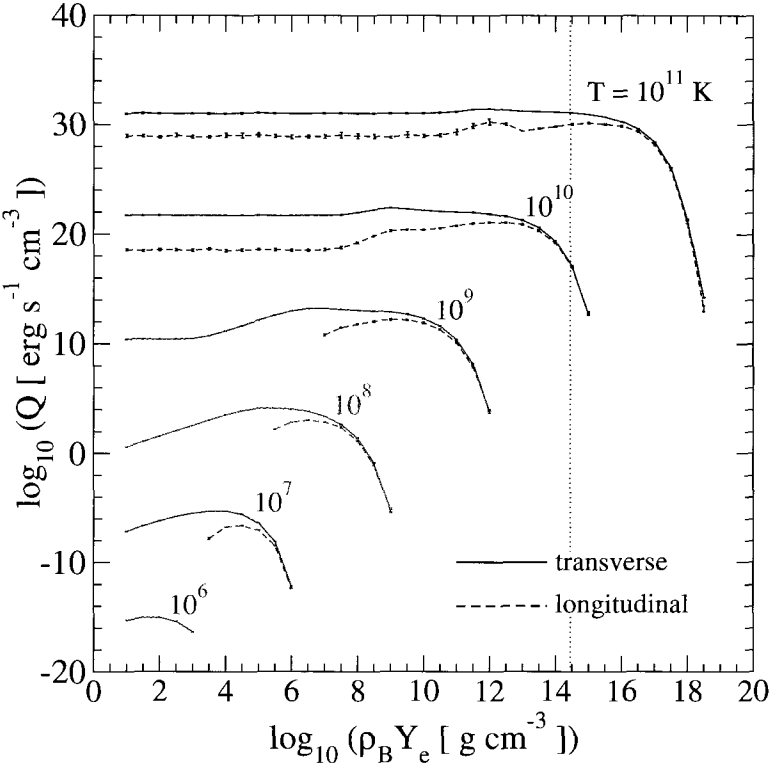

Figure 7. Individual contributions from the transverse and longitudinal channels to the neutrino emissivity as a function of baryon density at the indicated temperatures. The error bars show the variance of the Monte Carlo integration. For densities in excess of nuclear density shown by the dotted vertical line, neutrino production from strongly interacting particles dominate over QED-plasma processes.

explosion. During the first tens of seconds of evolution, nearly all ($\sim$ 99%) of the remnant's binding energy is radiated away in neutrinos of all flavors.[19,22,23,24,25,26] The neutrino luminosities and the emission timescale are controlled by several factors, such as the total mass of the PNS and the opacity at supranuclear density, which depends on the composition and dense matter equation of state (EOS). One of the chief objectives in modeling PNS's is to infer their internal compositions from neutrino signals detected from future supernovae by SuperK, SNO and others under consideration, including UNO.[27]

4.1. *The Evolution of a Protoneutron Star*

The evolution of a PNS proceeds through several distinct stages[19,20] and with various outcomes,[21] as shown schematically in Figure 8. Immediately following core bounce and the passage of a shock through the outer PNS's mantle, the star contains an unshocked, low entropy core of mass $\simeq 0.7$ $M_\odot$ in which neutrinos are trapped (stage 1 in the figure). The core is surrounded by a low density, high entropy ($5 < s < 10$) mantle that is both accreting matter from the outer iron core falling through the shock and also rapidly losing energy due to electron captures and thermal neutrino emission. The mantle extends up to the shock, which is temporarily stalled about 200 km from the center prior to an eventual explosion.

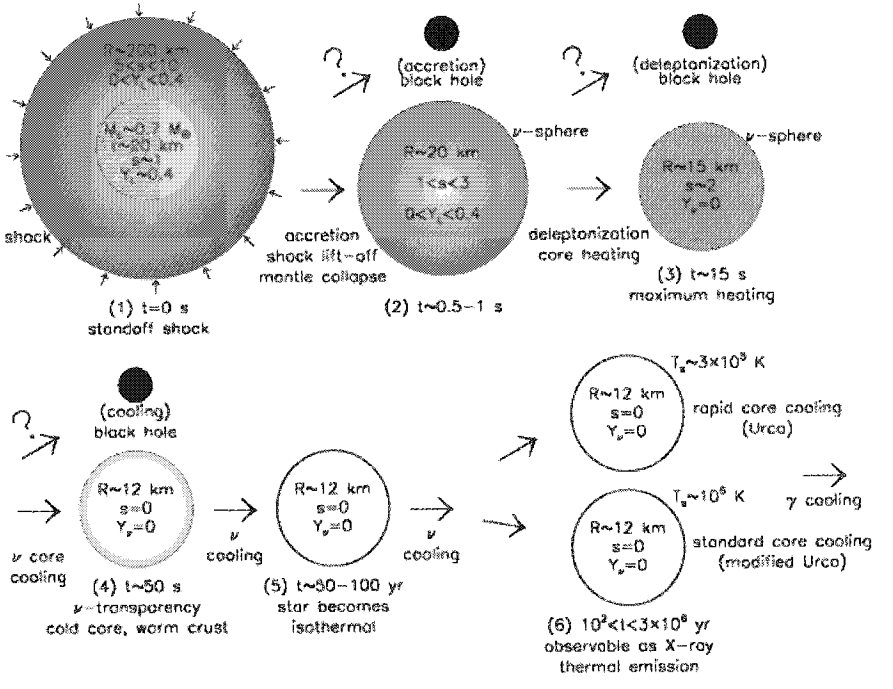

Figure 8. The main stages of evolution of a protoneutron star. Shading approximately indicates relative temperatures.

After a few seconds (stage 2), accretion becomes less important if the supernova is successful and the shock has ejected the stellar envelope.

Extensive neutrino losses and deleptonization will have led to a loss of lepton pressure and the collapse of the mantle. If enough accretion has occurred, however, the star's mass could increase beyond the maximum mass capable of being supported by the hot, lepton-rich matter. If this occurs, the remnant collapses to form a black hole and its neutrino emission is believed to quickly cease.[28]

Neutrino diffusion deleptonizes the core on time scales of 10–15 s (stage 3). Diffusion time scales are proportional to $R^2(c\lambda_\nu)^{-1}$, where R is the star's radius and λ_ν is the effective neutrino mean free path. This generic relation illustrates how both the EOS and the composition influence evolutionary time scales. The diffusion of high-energy (200–300 MeV) ν's from the core to the surface where they escape as low-energy (10–20 MeV) ν's generates heat (a process akin to joule heating). The core's entropy approximately doubles, producing temperatures in the range of 30–60 MeV during this time, even as neutrinos continue to be prodiguously emitted from the star's effective surface, or $\nu-$sphere.

Strange matter, in the form of hyperons, a Bose condensate, or quark matter, suppressed when neutrinos are trapped, could appear at the end of the deleptonization. Its appearance would lead to a decrease in the maximum mass that matter is capable of supporting, implying metastability of the neutron star and another chance for black hole formation.[21] This would occur if the PNS's mass, which must be less than the maximum mass of hot, lepton-rich matter (or else a black hole would already have formed), is greater than the maximum mass of hot, lepton-poor matter. However, if strangeness does not appear, the maximum mass instead increases during deleptonization and the appearance of a black hole would be unlikely unless accretion in this stage remains significant.

The PNS is now lepton-poor, but it is still hot. While the star has zero net neutrino number, thermally produced neutrino pairs of all flavors dominate the emission. The average neutrino energy slowly decreases, and the neutrino mean free path increases. After approximately 50 seconds (stage 4), $\lambda \simeq R$, and the star finally becomes transparent to neutrinos. Since the threshold density for the appearance of strange matter decreases with decreasing temperature, a delayed collapse to a black hole is still possible during this epoch.

Following the onset of neutrino transparency, the core continues to cool by neutrino emission, but the star's crust remains warm and cools less quickly. The crust is an insulating blanket which prevents the star from coming to complete thermal equilibrium and keeps the surface relatively

warm ($T \approx 3 \times 10^6$ K) for up to 100 years (stage 5). The temperature of the surface after the interior of the star becomes isothermal (stage 6) is determined by the rate of neutrino emission in the star's core and the composition of the surface.

4.2. *Neutrino Signals in Terrestrial Detectors*

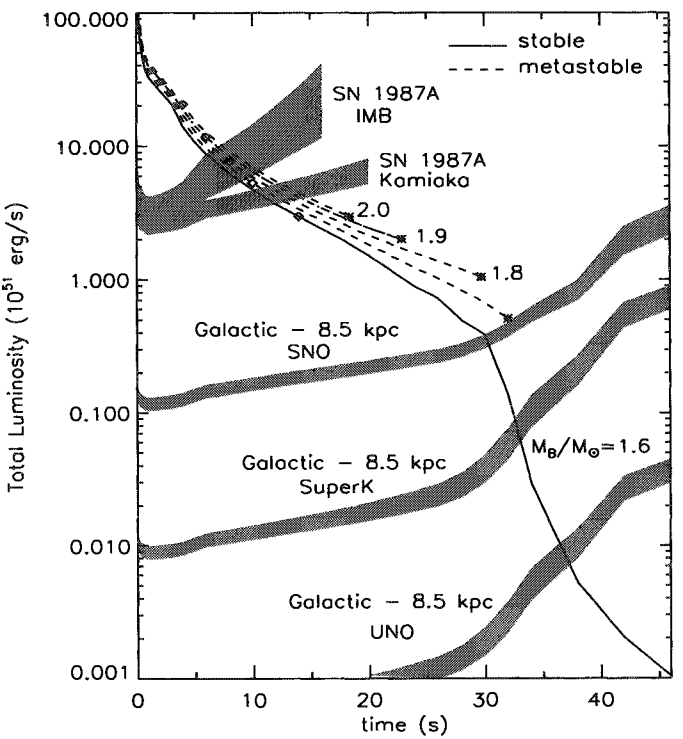

Figure 9. The evolution of the total neutrino luminosity for *npQ* PNS's. Shaded bands illustrate the limiting luminosities corresponding to a count rate of 0.2 Hz, assuming a supernova distance of 50 kpc for IMB and Kamioka, and 8.5 kpc for SNO and SuperK. The widths of the shaded regions represent uncertainties in the average neutrino energy from the use of a diffusion scheme for neutrino transport.

A comparison of the signals observable with different detectors is shown in Figure 9, which displays L_ν as a function of baryon mass M_B for stars containing quarks in their cores. In the absence of accretion, M_B remains

constant during the evolution, while the gravitational mass M_G decreases. The two upper shaded bands correspond to estimated SN 1987A (50 kpc distance) detection limits with KII and IMB, and the lower bands correspond to estimated detection limits in SNO, SuperK, and UNO, for a Galactic supernova (8.5 kpc distance). The detection limits have been set to a count rate $dN/dt = 0.2$ Hz.[25] It is possible that this limit is too conservative and could be lowered with identifiable backgrounds and knowledge of the direction of the signal. The width of the bands represents the uncertainty in $< E_{\bar{\nu}_e} >$ due to the diffusion approximation.[24,25,26] It is possible to distinguish between stable and metastable stars, since the luminosities when metastability is reached are always above conservative detection limits.

4.3. *Metastable Protoneutron Stars*

Protoneutron stars in which strangeness appears following deleptonization can be metastable if their masses are large enough. One interesting diagnostic that could shed light on the internal composition of neutron stars would be the abrupt cessation of the neutrino signal. This would be in contrast to a normal star of similar mass for which the signal continues to fall until it is obscured by the background. In Figure 10 the lifetimes for stars containing hyperons (npH), kaons (npK) and quarks (npQ) are compared.[25] In all cases, the larger the mass, the shorter the lifetime. For the kaon and quark PNSs, however, the collapse is delayed until the final stage of the Kelvin-Helmholtz epoch, while this is not necessarily the case for hyperon-rich stars. In addition, there is a much stronger mass dependence of the lifetimes for the hyperon case.

Clearly, the observation of a single case of metastability, and the determination of the metastability time alone, will not necessarily permit one to distinguish among the various possibilities. Only if the metastability time is less than 10–15 s, could one decide on this basis that the star's composition was that of npH matter. However, as in the case of SN 1987A, independent estimates of M_B might be available.[29] In addition, the observation of two or more metastable neutron stars might permit one to differentiate among these models.

5. Neutron Stars in Their Old Age

See the contribution from Dany Page to this symposium.

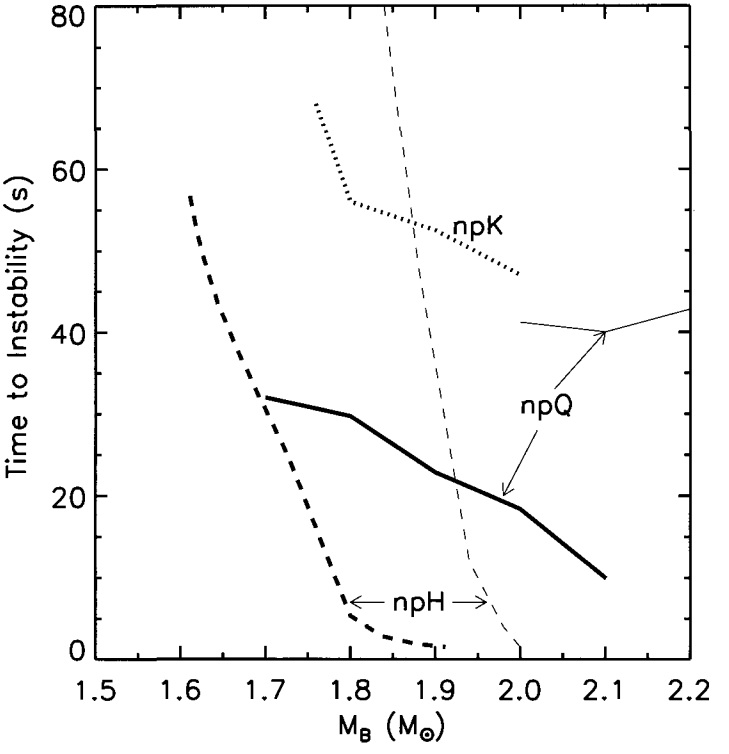

Figure 10. Lifetimes of metastable stars versus the PNS baryon mass M_B. Thick lines denote cases in which the maximum gravitational masses of cold, catalyzed stars are near 1.45 $M_\odot$, which minimizes the metastability lifetimes. The thin lines for the *npQ* and *npH* cases are for EOSs with larger maximum gravitational masses (1.85 and 1.55 $M_\odot$, respectively.)

6. Outlook

The advent of new-generation neutrino detectors such as Super-Kamiokande and the Sudbury Neutrino Observatory promises thousands of neutrino events in the next Galactic supernova. These will provide crucial diagnostics for the supernova mechanism, important limits on the released binding energy and the remnant mass, and critical clues concerning the composition of high density matter. Research in this area will ascertain the extent to which neutrino transport is instrumental in making a supernova explode. Other bonuses include the elucidation of the possible role of supernovae and neutrinos in $r-$process nucleosynthesis.

The main issues that emerge from PNS studies concern the metastability and subsequent collapse to a black hole of a PNS containing quark matter, or other types of matter including hyperons or a Bose condensate, which could be observable in the ν signal. However, discriminating among various compositions may require more than one such observation. This highlights the need for breakthroughs in lattice simulations of QCD at finite baryon density in order to unambiguously determine the EOS of high density matter. In the meantime, intriguing possible extensions of supernova and PNS simulations with npQ and npK matter include the consideration of heterogenoeus structures and quark matter superfluidity.[30] See also the contribution from Sanjay Reddy to this symposium.

7. Conclusions

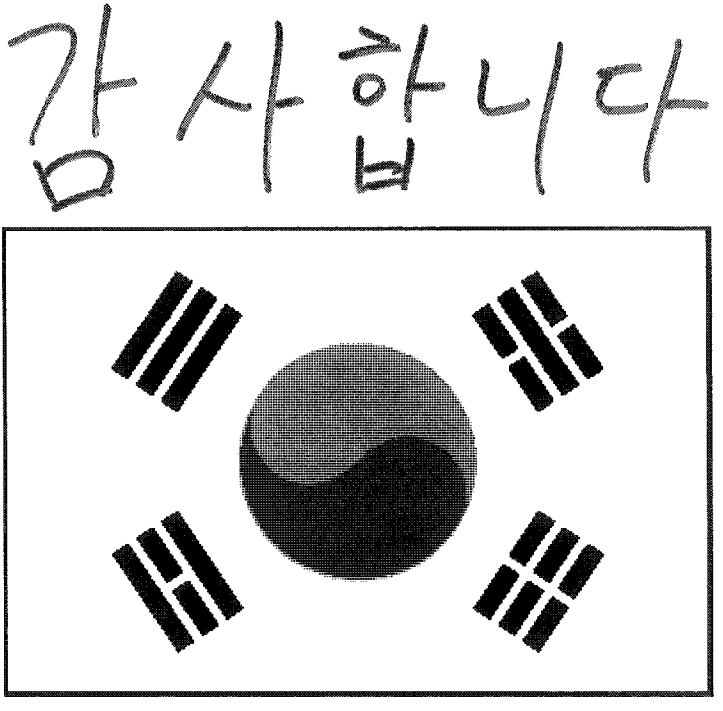

Acknowledgements

MP thanks his "PALS" Paul Ellis, Jim Lattimer, Jose Miralles, Dany Page, Jose Pons, Sanjay Reddy, and Andrew Steiner for benificial collaborations. Research support from DOE grants FG02-88ER-40388 and FG02-87ER-40317 (for MP, SR and SID), and NSF Grant No. 0070998 (for SID), and travel support under the cooperative agreement DE-FC02-01ER41185 for the SciDaC project "Shedding New Light on Exploding Stars: Terascale Simulations of Neutrino-Driven Supernovae and Their Nucleosynthesis" (for MP, SR and SID) are gratefully acknowledged.

References

1. A. V. Sweigart and P. G. Gross, *Astrophys. Jl. Suppl. Ser.* **36**, 405 (1978).
2. G. G. Raffelt, *Phys. Rep.* **333**, 593 (2000).
3. M. S. O'Brien and S. D. Kawaler, *Astrophys. J.* **539**, 372 (2000).
4. M. Prakash, J. M. Lattimer, R. F. Sawyer, and R. R. Volkas, *Ann. Rev. Nucl. Part. Sci.* **51**, 295 (2001).
5. D. G. Yakovlev, A. D. Kaminker, O. Y. Gnedin, and P. Haensel, *Phys. Rep.* **354**, 1 (2001).
6. W. Hillebrandt and J. C. Niemeyer, *Ann. Rev. Astron. and Astrophys.* **38**, 191 (2000).
7. K. Iwamoto, *et al.*, *Astrophys. Jl. Suppl. Ser.* **125**, 439 (1999).
8. A. Burrows, *Nature*, **403**, 727 (2000).
9. T. Di Matteo, R. Perna, and R. Narayan, *Astrophys. J.* **579**, 706 (2002).
10. K. Kohri and S. Mineshige, *Astrophys. J.* **577**, 311 (2002).
11. O. E. B. Messer, A. Mezzacappa, S. W. Bruenn, and M. W. Guidry, *Astrophys. J.* **507**, 353 (1998); S. Yamada, H-Th Janka, H. Suzuki, *Astron. Astrophys.* **344**, 533 (1999); A. Burrows, T. Young, P. Pinto, R. Eastman, T. A. Thompson, *Astrophys. J.* **539**, 865 (2000); M. Rampp, H-Th Janka, *Astrophys. J.* **539**, L33 (2000); M. Liebendoerfer, *et al. Phys. Rev.* **D63**, 104003 (2001).
12. S. W. Bruenn, *Astrophys. Jl. Suppl. Ser.* **58**, 771 (1985).
13. A. Burrows and T. A. Thompson, *astro-ph/0211404*.
14. S. Hannestadt and G. Raffelt, *Astrophys. J.* **507**, 339 (1998).
15. R. Buras, H-T. Janka, M. Th. Keil, G. G. Raffelt, and M. Rampp, *Astrophys. J.* **587**, 320 (2003).
16. S. Ratkovic, S. I. Dutta and M. Prakash *Phys. Rev.* **D67**, 123002 (2003).
17. S. I. Dutta, S. Ratkovic and M. Prakash *Phys. Rev.* **D69**, 023005 (2004).
18. E. Braaten and D. Segel, Phys. Rev. **D48**, 1478-1491 (1993).
19. A. Burrows and J. M. Lattimer, *Astrophys. J.* **307**, 178 (1986).
20. A. Burrows A, *Ann. Rev. Nucl. Sci.* **40**, 181 (1990).
21. M. Prakash, I. Bombaci, Manju Prakash, P. J. Ellis, J. M. Lattimer, and R. Knorren, *Phys. Rep.* **280**, 1 (1997); P. J. Ellis, J. M. Lattimer and M. Prakash, *Comm. Nucl. Part. Phys.* **22**, 63 (1996); M. Prakash, J. R. Cooke,

J. M. Lattimer, *Phys. Rev.* **D52**, 661 (1995); A. W. Steiner, M. Prakash, J. M. Lattimer, *Phys. Lett.* **B486**, 239 (2000).
22. W. Keil and H-T Janka, *Astron. & Astrophys.* **29**, 145 (1995).
23. A. Burrows and R. F. Sawyer, *Phys. Rev.* **C59**, 510 (1999).
24. J. A. Pons, S. Reddy, M. Prakash, J. M. Lattimer, J. A. Miralles, *Astrophys. J.* **513**, 780 (1999).
25. J. A. Pons, J. A. Miralles, M. Prakash, J. M. Lattimer, 2001. *Astrophys. J.*, **553**, 382 (2001).
26. J. A. Pons, A. W. Steiner, M. Prakash, J. M. Lattimer, 2001. *Phys. Rev. Lett.* **86**, 5223 (2001).
27. C. K. Jung, In *Next Generation Nucleon Decay and Neutrino Dectector*, ed. by Diwan N, Jung CK (AIP, New York, 2000), 29.
28. A. Burrows, *Astrophys. J.* **334**, 891 (1988).
29. F. K. Thielemann, M. Hashimoto and K. Nomoto, 1990. *Astrophys. J.* **349**, 222 (1990); H. A. Bethe and G. E. Brown, *Astrophys. J. Lett.* **445**, L129 (1995).
30. G. W. Carter and S. Reddy, *Phys. Rev.* **D62**, 103002 (2000); S. Reddy, M. Sadziokowski, and M. Tachibana, *Nucl. Phys.* **A714**, 337 (2003); *Phys. Rev. D* **68**, 053010 (2003).

THE MICRO-PHYSICS OF NEUTRINO TRANSPORT AT EXTREME DENSITY*

SANJAY REDDY
Los Alamos National Laboratory,
MS B283,
Los Alamos, NM 87545, USA
E-mail: reddy@lanl.gov

Production and propagation of neutrinos in hot and dense matter plays an important role in the thermal evolution of neutron stars. In this article we review the micro-physics that influences weak interaction rates in dense matter containing nucleons, leptons and or quarks. We show that these rates depend sensitively on the strong and electromagnetic correlations between baryons. We present new results, obtained using molecular dynamics, for the response of dense plasma of heavy ions. Neutrino rates are also shown to be sensitive to the phase structure of matter at extreme density. We highlight recent calculations of neutrino rates in dense color superconducting phases of quark matter. We present a brief discussion of how these differences may affect the early evolution of a neutron star.

1. Introduction

Neutrinos play an important role in stellar evolution. By virtue of their weak interactions with matter neutrinos provide a mechanism for energy loss from the dense stellar interiors. In neutron stars, neutrino emission is the dominant cooling mechanism from their birth in a supernova explosion until several thousand years of subsequent evolution. The calculation of these rates are of current interest since several research groups are embarking on large scale numerical simulations of supernova and neutron star evolution [1]. Even moderate changes in the nuclear microphysics associated with the weak interaction rates at high density can impact macroscopic features that are observable. An understanding of the response of strongly interacting nuclear medium to neutrinos and its impact on neutron star evolution promises to provide a means to probe the properties of the dense medium itself.

*This work is supported by dept. of energy contract w7405-eng-36

In §2, we present a brief introduction to the macroscopic aspects of neutrino transport in a newly born neutron star. The discussion relating to neutrino-matter interactions is organized into two sections: (i) neutrino interactions in dense matter containing nuclei , nucleons and leptons (§3) and (ii) neutrino interactions in exotic new phases that are likely to occur in the dense inner core of the neutron star (§4).

2. Early evolution of the proto-neutron star

The illustration in Fig.1, shows the important stages of core-collapse supernova and the birth of a proto-neutron stars. Successive nuclear burning from lighter to heavier elements, which fuels stellar evolution, inevitably results in the formation of a iron core in massive stars ($M \gtrsim 8M_{\odot}$). Since iron is the most stable nucleus, further energy release through nuclear burning is not possible. The Fe-core is supported against gravitational collapse by the electron degeneracy pressure. When the mass of the Fe-core exceeds the Chandrashekar mass ($M_{\rm ch} \simeq 1.4M_{\odot}$), it becomes unstable to gravitational collapse. Detailed numerical simulations indicate that the core collapses, from its initial radius $R_{\rm in} \simeq 1500$ km to a final radius $R_{\rm in} \simeq 100$ km, on a time-scale similar to the free-fall time-scale $\tau_{\rm free-fall} \simeq 100$ ms. Soon after the onset of collapse, the core density exceeds 10^{12} g/cm^3 and the matter temperature $T \simeq 5$ MeV. Under these conditions, thermal neutrinos become trapped on the dynamical time-scale of collapse. Consequently, collapse is nearly adiabatic. The enormous gravitational binding energy $B.E._{\rm Grav.} \simeq GM_{\rm NS}/R_{\rm NS} \simeq 3 \times 10^{53}$ ergs, is stored inside the star as internal thermal energy of the matter components, and thermal and degeneracy energy of neutrinos. The newly born neutron star looses this energy on a time-scale determined by the rate of diffusion of neutrinos [2,3]. Neutrinos emitted from the proto-neutron star can be detected in terrestrial detectors such as Super Kamiokande and SNO. Current estimates indicate that we should see $\sim 10,000$ events in Super Kamiokande and ~ 1000 events in SNO from a supernova at the center of our galaxy[4] (distance=8.5 kpc) . Understanding the micro and macro-physics that affects the spectral and temporal features of the neutrino emission is primarily motivated by this prospect. Supernova neutrinos are the only direct probes of both the dynamics of gravitational collapse and the properties of dense matter inside the newly born neutron star. Since the neutrino emission time scale is set by neutrino diffusion, the duration over which we should expect to see neutrinos in terrestrial detectors is intimately connected with the neutrino

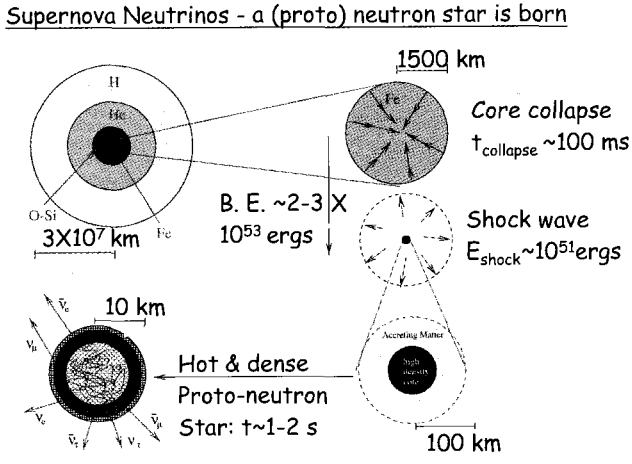

Figure 1. Schematic showing the various stages of a core-collapse supernova explosion.

opacity of matter inside the neutron star. We now turn to address microphysical aspects of neutrino cross sections in dense matter.

3. Neutrino Interactions in Nucleonic Matter

It was realized over a decade ago that the effects due to degeneracy and strong interactions significantly alter the neutrino mean free paths and neutrino emissivities in dense matter [5,6], it is only recently that detailed calculations have become available [7,8,9,10]. The scattering and absorption reactions that contribute to the neutrino opacity are

$$\nu_e + n \rightarrow e^- + p\,, \qquad \bar{\nu}_e + p \rightarrow e^+ + n\,,$$
$$\nu_X + A \rightarrow \nu_X + A\,, \qquad \nu_X + n(p) \rightarrow \nu_X + n(p)\,, \qquad \nu_X + e^- \rightarrow \nu_X + e^-\,,$$

where $n, p, e^{\pm}, A$ represent neutrons, protons, positrons, electrons and heavy Fe-like nuclei, respectively. At low temperature ($T \lesssim 3-5$ MeV) and relatively low density ($\rho \simeq 10^{12} - 10^{13}$ g/cm^3, heavy nuclei are present and dominate the neutrino opacity due to coherent scattering. When the density is higher, $\rho \simeq 10^{13} - 10^{14}$ g/cm^3, novel heterogeneous phases of matter, called the "pasta" phases have been predicted to occur, where nuclei become extended and deformed progressively from spherical to rod-like and slab-like configurations[11]. For densities greater than 10^{14} g/cm^3, matter is

expected to be a homogenous nuclear liquid. In what follows, we discuss the neutrino opacity in these different physical settings.

3.1. $\rho \simeq 10^{12}\ g/cm^3$:

At low temperature ($T \lesssim 5$ MeV), matter at these densities comprises of heavy nuclei (fully ionized), nucleons and degenerate electrons. The typical inter-particle distance, $d \simeq 20 - 40$fm. At these large distances, the nuclear force is small and the correlations between particles is dominated by the coulomb interaction. Since nuclei carry a large charge ($Z \simeq 25$) , the coulomb force between nuclei $F_{\rm Coulomb} \cong Z^2 e^2/d$ dominates the non-ideal behavior of the plasma. Further, for low energy neutrinos which couple coherently to the total weak charge Q_W $25 - 40$ of the nucleus, neutrino scattering off nuclei is far more important than processes involving free nucleons and electrons [12].

The elastic cross-section for low energy coherent scattering off a nucleus (A,Z) with weak charge $Q_W = A - Z + Z \sin^2\theta_W$, where θ_W is the weak mixing angle, is given by[12]

$$\frac{d\sigma}{d\cos\theta} = \frac{1}{16\pi}\, G_{\rm F}^2\, Q_W^2\, E_\nu^2\, (1 + \cos\theta) \tag{1}$$

When neutrinos scattering off nuclei in a plasma we must properly account for the presence of other nuclei since scattering from these different sources can interfere. In the language of many-body theory, this screening is encoded in the density-density correlation function [5,6]. To make concrete, the relation to the density-density correlation function we begin by noting that the effective lagrangian describing the neutral current interaction of low energy neutrinos with nuclei is given by

$$L_{\rm NC} = \frac{G_{\rm F}}{2\sqrt{2}}\, Q_W\, l_\mu\, j^\mu \tag{2}$$

where $l_\mu = \overline{\nu}\gamma_\mu(1 - \gamma_5)\nu$ is the neutrino neutral current. Nuclei are heavy, their thermal velocities are small, $v \ll c$, and it is good approximation to write the neutral current carried by the nuclei as $j^\mu = \psi^\dagger\psi\ \delta_0^\mu$. For simplicity, we will assume that nuclei are bosons characterized only by their charge and baryon number. Using Fermi's golden rule, we can calculate the neutrino cross sections from Eq.2. In matter, it is appropriate to define a cross section per unit volume rather than cross section off a single target particle since more than one target particle contributes to the response. We can write the differential cross section per unit volume in terms of the density operator in momentum space $\rho(\vec{q},t) = \psi^\dagger\psi = \sum_{i=1\cdots N}\ \exp(i\vec{q}\cdot\vec{r}_i(t))$,

where $i = 1 \cdots N$ is the particle index. The cross section for scattering of a neutrino with energy transfer ω and momentum transfer $\vec{q}$ is given by

$$\frac{d\sigma}{V\ d\omega\ d\cos\theta} = \frac{G_F^2}{16\pi}\ Q_W^2\ (1+\cos\theta)\ S(|\vec{q}|,\omega) \tag{3}$$

$$\text{where} \qquad S(|\vec{q}|,\omega) = \frac{1}{2\pi\ N}\int dt\ \exp(i\omega t)\langle\rho(\vec{q},t)\rho(-\vec{q},0)\rangle\,. \tag{4}$$

The function $S(|\vec{q}|,\omega)$ is called the dynamic form factor and embodies all spatial and temporal correlations between target particles arising from strong or electromagnetic interactions. To calculate the dynamic structure function we need to solve for the dynamics ($\vec{r}(t)$) of the ions as they move in the each others presence, interacting via the two body ion-ion interaction potential. The electrons are relativistic and degenerate, the time-scales associated with changes in their density distribution are rapid compared to the slow changes we expect in the density field of the heavy ions. The leading effect of the electrons is therefore to screen the Coulomb potential. Consequently, the ions interact through the potential $V(r) = Z^2e^2\exp(-r/\lambda_e)/(4\pi r)$, where λ_e is the electron Debye screening length. At 10^{12} g/cm^3, where the inter-ion distance $d \lesssim 30$ fm and $\lambda_e \gtrsim 80$ fm, the typical ion-ion interaction energy, $E_{\rm pot} \simeq Z^2e^2/(4\pi d)$ is large. For temperature in the range $1-5$ MeV, the ratio of the potential energy to the kinetic energy, which is characterized by $\Gamma = Z^2e^2/(4\pi d\ kT) \gg 1$. The dynamics

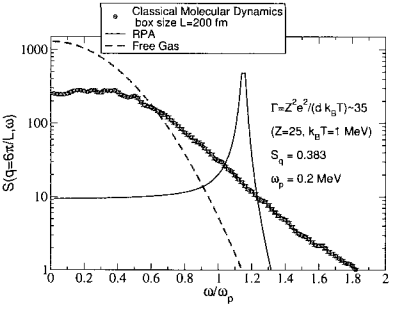

Figure 2. Dynamic structure function of a plasma of ions interacting as a function of energy transfer ω (measured in units of the plasma frequency $\omega_p = 0.2$ MeV) and fixed momentum transfer $|\vec{q}| = 6\pi/L = 18.6$ MeV.

of a strongly coupled plasma is not amenable to analytic methods of perturbation theory, nor are they tractable in approximate non-perturbative methods such as mean field theory or the Random Phase Approximation

(RPA). For a classical system of point particles interacting via a 2-body potential it is possible to simulate the real system. Such numerical simulations confine N particles to a box with periodic boundary conditions and calculate the force on each particle at any time and evolve the particles by using their equations of motion ($Force = Mass \times Acceleration$). This method, which goes by the name molecular dynamics (MD), has been used extensively in condensed matter physics, plasma physics and chemistry [14]. For $T \gtrsim 1$ MeV, the De-Broglie wavelength $\Lambda_D \ll d$ so the ionic gas is classical and we can use MD to calculate $S(|\vec{q}|, \omega)$. Fig.2 , shows the results of such a calculation. We chose to simulate 54 ions (A=50,Z=25) in a box of length $L = 200$ fm. The background electron density was chosen so as to make the system electrically neutral. For the classical simulations, a single, dimensionless, number characterizes $\Gamma = Z^2e^2/(4\pi d\ kT)$ characterizes the system. For $kT = 1$ MeV, $\Gamma \simeq 35$ for our system - corresponding to a strongly coupled plasma. The results in Fig.2 show a comparison between results obtained by MD simulations (dots with error bars) , free (Boltzmann) gas response (dashed-line) and response obtained using Random Phase Approximation (RPA). Details regarding the RPA will be discussed in more detail in the subsequent sections. For now, we simply note that in RPA, Coulomb interactions are accounted for by selective re-summation of bubble graphs involving free excitations which interact via the Coulomb interaction. In particular, RPA is able to correctly predict the presence of well defined collective mode, corresponding to a phonon in the weak coupling regime ($\Gamma \lesssim 1$) and is often expected to provide a fair description of the long-wavelength response of correlated systems. However, as the comparison in Fig.2 indicates, both RPA and the free gas response do poorly compared to MD. MD is exact in the classical limit and corrections to the classical evolution are small and expected to scale as λ_D/d. These results clearly illustrate that correlations can greatly affect the shape of the response and that approximate many-body methods such as RPA can fail when the coupling is strong, even at long-wavelengths.

3.2. $\rho \simeq 10^{13}\ g/cm^3$:

With increasing density, the nuclei get bigger and the inter-nuclear distance become smaller. Under these conditions, the nuclear surface and coulomb contributions to the Free energy of the system become important. It becomes energetically favorable for nuclei to become very deformed and assume novel, non-spherical, shapes such as rods and slabs [11]. Further, the

energy differences between these various shapes are small $\Delta E \simeq 10 - 100$ keV. The dynamics of such an exotic heterogeneous phase is a complex problem involving several scales and forces. For temperatures of interest, $T \lesssim 5$ MeV, the De-Broglie wavelength and the inter-particle distance are comparable and quantum effects cannot be neglected. Recently, there have been attempts to model the behavior of these pasta phases using quantum molecular dynamics[15] and also find rod and slab like configurations.

How does the heterogeneity and existence of several low energy excitations involving shape fluctuations influence the response of this phase to neutrinos ? In the simplest description, the structure size (r) and the inter-structure (R) distance characterize the system. We can expect that neutrinos with wavelength large compared to the structure size but small compared to the inter-structure distance can couple coherently to the total weak charge (excess) of the structure, much like the coherence we discussed in the previous section. The effects of this coherent enhancement in the neutrino cross-sections has recently been investigated [16]. In agreement with our naive expectation, this study finds that the neutrino cross sections are enhanced by as much as an order of magnitude for neutrinos with energy $1/r \gtrsim E_\nu \gtrsim 1/R$. In §4.1, we discuss similar effects in a higher density heterogeneous mixed phase composed of nuclear matter and novel high density phases such as quark matter.

3.3. $\rho \simeq 10^{14}$ g/cm^3:

With increasing density, the novel structures discussed previously merge to form a homogeneous liquid of neutrons, protons and electrons. The response of such a Fermi-liquid has been investigated by several authors[7,9,10]. The general expression for the differential cross section [7,9]

$$\frac{1}{V}\frac{d^3\sigma}{d^2\Omega_3 dE_3} = -\frac{G_F^2}{128\pi^2}\frac{E_3}{E_1}\left[1-\exp\left(\frac{-q_0-(\mu_2-\mu_4)}{T}\right)\right]^{-1} \times (1-f_3(E_3))\ \mathrm{Im}\ (L^{\alpha\beta}\Pi^R_{\alpha\beta}), \tag{5}$$

where the incoming neutrino energy is E_1 and the outgoing electron energy is E_3. The factor $[1-\exp((-q_0-\mu_2+\mu_4)/T)]^{-1}$ maintains detailed balance, for particles labeled '2' and '4' which are in thermal equilibrium at temperature T and in chemical equilibrium with chemical potentials μ_2 and μ_4, respectively. The final state blocking of the outgoing lepton is accounted for by the Pauli blocking factor $(1 - f_3(E_3))$. The lepton tensor

$L_{\alpha\beta}$and the target particle retarded polarization tensor $\Pi_{\alpha\beta}$ is given by[9]

$$\Pi_{\alpha\beta} = -i \int \frac{d^4p}{(2\pi)^4} \mathrm{Tr}\left[T(G_2(p) J_\alpha G_4(p+q) J_\beta)\right]. \tag{6}$$

Above, k_μ is the incoming neutrino four-momentum and q_μ is the four-momentum transfer. The Greens' functions $G_i(p)$ (the index i labels particle species) describe the propagation of free baryons at finite density and temperature. J_μ is γ_μ for the vector current and $\gamma_\mu\gamma_5$ for the axial current.

To account for the effects of strong and electromagnetic correlations between target neutrons, protons and electrons we must find ways to improve $\Pi_{\alpha,\beta}$. This involves improving the Greens functions for the particles and the associated vertex corrections that modify the current operators. In strongly coupled systems, these improvements are notoriously difficult and no exact analytic methods exist. One usually resorts to using mean-field theory to improve the Greens functions. Dressing the single particle Greens functions must be accompanied by corresponding corrections to the neutrino – dressed-particle vertex function. The random-phase approximation (RPA) can be thought of as such a vertex correction. Within RPA, the polarization tensor[7,9]

$$\Pi^{RPA} = \Pi_{\mathrm{MF}} + \Pi^{RPA} D \Pi_{\mathrm{MF}} \ , \tag{7}$$

where D denotes the interaction matrix and Π_{MF} is the polarization tensor in Eq.6 but with the Green's functions computed in the mean-field approximation. Model calculations indicate that neutrino mean free paths computed in RPA tend to roughly a factor 2-3 times larger than in the uncorrelated system[9]. This is primarily because of repulsive forces in the spin-isospin channel, that suppress the axial response at low energies.

4. Neutrino Interactions in Novel Phases at High Density

In this section we explore how phase transitions impact the weak interaction rates. Novel phases of baryonic matter are expected to occur at densities accessible in neutron stars. These new phases include pion condensates, kaon condensates, hyperons and quark matter. An understanding of how these phases might influence neutrino propagation and emission is necessary to enquire if these phase transitions occur inside neutron stars. We consider three specific examples of phase transitions: (i) generic first order transitions; (2) superconducting quark matter and (3) color-flavor locked superconducting quark matter to explore and illustrate the modification of neutrino rates in the novel high density phases of matter.

4.1. *Heterogeneous Phases: Effects of First Order Transitions*

First order phase transitions in neutron stars can result in the formation of heterogeneous phases in which a positively charged nuclear phase coexists with a negatively charged new phase which is favored at higher densities [17]. This is a generic possibility for first order transitions in matter with two conserved charges. In the neutron star context, these correspond to baryon number and electric charge. The pasta phase at sub-nuclear density, which was discussed earlier, where positively charged nuclei coexist with negatively charged neutron rich matter containing electrons is a familiar example of such a transition region. This mixed, heterogeneous, phase exists over a finite interval of pressure, unlike a mixed phase for a system with one conserved charge. Consequently, mixed phases in neutron stars occupy a finite spatial extent and understanding how neutrinos propagate through them becomes a relevant and interesting question.

Reddy, Bertsch and Prakash [18] have studied the effects of heterogeneous phases on ν-matter interactions. Based on simple estimates of the surface tension between nuclear matter and the exotic phase, typical droplet sizes range from $5 - 15$ fm, and inter-droplet spacings range up to several times larger. The propagation of neutrinos whose wavelength is greater than the typical droplet size and less than the inter-droplet spacing, i.e., 2 MeV $\leq E_\nu \leq$ 40 MeV, will be greatly affected by the heterogeneity of the mixed phase, as a consequence of the coherent scattering of neutrinos from the matter in the droplet.

The Lagrangian that describes the neutral current coupling of neutrinos to the droplet is

$$\mathcal{L}_W = \frac{G_F}{2\sqrt{2}}\, Q_W\, \bar{\nu}\gamma_\mu(1-\gamma_5)\nu\; J_D^\mu\,, \tag{8}$$

where J_D^μ is the neutral current carried by the droplet and the total weak charge enclosed in a droplet of radius r_d is Q_W. For non-relativistic droplets, $J_D^\mu = \rho(x)\ \delta^{\mu 0}$ has only a time like component. Here, ρ is the density operator for the droplet and the form factor is $F(q) = (1/Q_W)\int_0^{r_d} d^3x\ \rho(x)\ \sin qx/qx$.
The differential cross section for neutrinos scattering from an isolated droplet is then

$$\frac{d\sigma}{d\cos\theta} = \frac{E_\nu^2}{16\pi} G_F^2 Q_W^2 (1+\cos\theta) F^2(q)\,. \tag{9}$$

In the above equation, E_ν is the neutrino energy and θ is the scattering angle. To properly account for the presence of the other droplets in the medium we must calculate the droplet-droplet correlation function or $S(\vec{q},\omega)$ as was described in §3.1. However, such a calculation is yet to be done for this complex system. In what follows, we adopt a simple mean-field prescription to account for screening due to multiple droplet scattering[18]. This amounts to replacing the form factor as follows

$$F(q) \to \tilde{F}(q) = F(q) - 3\,\frac{\sin qR_W - (qR_W)\cos qR_W}{(qR_W)^3}\,. \tag{10}$$

The neutrino–droplet differential cross section per unit volume then follows:

$$\frac{1}{V}\frac{d\sigma}{d\cos\theta} = N_D\,\frac{E_\nu^2}{16\pi}G_F^2 Q_W^2(1+\cos\theta)\tilde{F}^2(q)\,. \tag{11}$$

Note that even for small droplet density N_D, the factor Q_W^2 acts to enhance the droplet scattering. Models of first order phase transitions in dense mat-

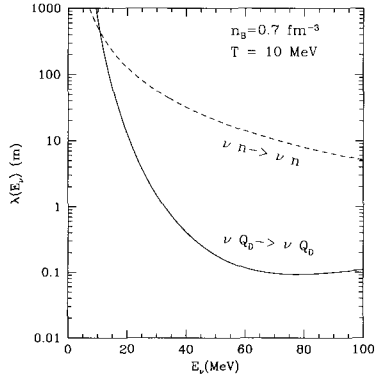

Figure 3. Neutrino mean free path as a function of neutrino energy in a quark - hadron mixed phase. For comparison, the mean free path in uniform neutron matter at the same temperature and density are shown by dashed curve.

ter provide the weak charge and form factors of the droplets and permit the evaluation of ν–droplet scattering contributions to the opacity of the mixed phase. For the results shown in Fig.3, the quark droplets are characterized by $r_d \sim 5$ fm and inter-droplet spacing $2R_W \sim 22$ fm, and an enclosed weak charge $Q_W \sim 850$. For comparison, the neutrino mean free path in uniform neutron matter at the same n_b and T are also shown. It is apparent that there is a large coherent scattering-induced reduction in the mean free path

for the typical energy $E_\nu \sim \pi T$. At much lower energies, the inter-droplet correlations tend to screen the weak charge of the droplet, and at higher energies the coherence is attenuated by the droplet form factor.

4.2. *Effects of Quark Superconductivity*

Although the idea of quark pairing in dense matter is not new [19], but it is only recently that its role in the context of the phase diagram of QCD [20] has been appreciated. Model calculations, mostly based on four-quark effective interactions, predict the restoration of spontaneously broken chiral symmetry through the onset of color superconductivity at low temperatures. They predict an energy gap of $\Delta \sim 100$ MeV for a typical quark chemical potential of $\mu_q \sim 400$ MeV. In this section, we address how neutrinos propagate in superconducting and superfluid quark matter.

As discussed earlier, the main task will be to compute the equivalent of the current-current correlation function defined in Eq.6 for the superconducting quark phase. This was addressed by Carter and Reddy [21]. The free quark propagators are naturally modified in a superconducting medium. As first pointed out by Bardeen, Cooper, and Schrieffer several decades ago, the quasi-particle dispersion relation is modified due to the presence of a gap in the excitation spectrum. In calculating these effects, we will consider the simplified case of QCD with two quark flavors which obey $SU(2)_L \times SU(2)_R$ flavor symmetry, given that the light u and d quarks dominate low-energy phenomena. Furthermore we will assume that, through some unspecified effective interaction which is attractive in the color antisymmetric channel, quarks pair in a manner analogous to the BCS mechanism. In this two flavor, spin zero superconductor (2SC) the anomalous (or Gorkov) propagator[20]

$$F(p)_{abfg} = -i\epsilon_{ab3}\epsilon_{fg}\Delta\left(\frac{\Lambda^+(p)}{p_o^2-\xi_p^2}+\frac{\Lambda^-(p)}{p_o^2-\bar{\xi}_p^2}\right)\gamma_5\, C\,. \tag{12}$$

Here, a, b are color indices, f, g are flavor indices, ϵ_{abc} is the usual antisymmetric tensor and we have conventionally chosen 3 to be the condensate color. This propagator is also antisymmetric in flavor and spin, with $C = -i\gamma_0\gamma_2$ being the charge conjugation operator. The normal quasi-particle propagators are given as

$$S(p)^{bg}_{af} = i\delta^b_a\delta^g_f\left(\frac{\Lambda^+(p)}{p_o^2-\xi_p^2}+\frac{\Lambda^-(p)}{p_o^2-\bar{\xi}_p^2}\right)(p_\mu\gamma^\mu-\mu\gamma_0)\,. \tag{13}$$

This is written in terms of the particle and anti-particle projection operators $\Lambda^+(p)$ and $\Lambda^-(p)$ respectively, where $\Lambda^{\pm}(p) = (1 \pm \gamma_0 \vec{\gamma} \cdot \hat{p})/2$. The quasi-particle energy is $\xi_p = \sqrt{(|\vec{p}| - \mu)^2 + \Delta^2}$, and for the anti-particle $\bar{\xi}_p = \sqrt{(|\vec{p}| + \mu)^2 + \Delta^2}$. The appearance of an anomalous propagator in the

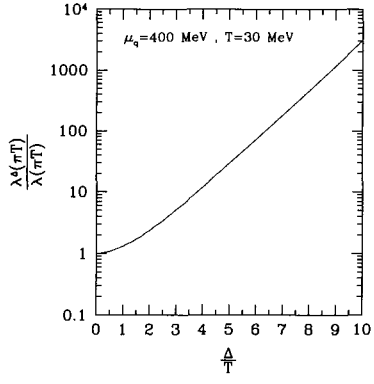

Figure 4. Ratio of the neutrino mean-free path in the superconducting phase to that in the normal phase as function of Δ/T.

superconducting phase indicates that the polarization tensor gets contributions from both normal quasi-particle propagators Eq. 13 and anomalous propagator Eq.12 and is given by

$$\Pi_{\alpha\beta}(q) = -2i \int \frac{d^4p}{(2\pi)^4} \mathrm{Tr}\, [S(p)\Gamma_\alpha S(p+q)\Gamma_\beta + F(p)\Gamma_\alpha \bar{F}(p+q)\Gamma_\beta] \,. \quad (14)$$

Fig.4 shows the results for neutrino mean free paths in the 2 flavor superconducting quark phase. The ratio of mean free path in the superconducting phase to that in the normal phase is shown in the right panel. With increasing Δ, the gap in the quasi-particle excitation spectrum results in an exponential attenuation of the scattering response, resulting in the observed exponential enhancement in the mean free paths.

4.3. *Neutrino Interactions with Goldstone bosons*

The discussion in the preceeding section assumed that there were no low energy collective excitations to which the neutrinos could couple. This is true in the 2 flavor superconducting phase of quark matter. For three flavors and when the strange quark mass is negligible compared to the chemical

potential the ground state is characterized by pairing that involves all nine quarks in a pattern that locks flavor and color [22]. Diquark condensation in the CFL phase breaks both baryon number and chiral symmetries. The Goldstone bosons that arise as consequence introduce a low lying collective excitations to the otherwise rigid state. Thus, unlike in the normal phase where quark excitations near the Fermi surface provide the dominant contribution to the weak interaction rates, in the CFL phase, it is the dynamics of the low energy collective states— the Goldstone bosons that are relevant [23,24,25].

The massless Goldstone boson associated with spontaneous breaking of $U(1)_B$ couples to the weak neutral current. This is because the weak isospin current contains a flavor singlet component. We should expect this mode to dominate the response because the psuedo-Goldstone modes arising from chiral symmetry breaking have non-zero masses. The amplitude for processes involving the $U(1)_B$ Goldstone boson H and the neutrino neutral current is given by

$$A_{H\nu\bar{\nu}} = \frac{4}{\sqrt{3}} G_F \, f_H \, \tilde{p}_\mu \, j_Z^\mu \,, \tag{15}$$

where $\tilde{p}_\mu = (E, v^2\vec{p})$ is the modified four momentum of the Goldstone boson. The decay constant for the $U(1)_B$ Goldstone boson has also been computed in earlier work and is given by $f_H^2 = 3\mu^2/(8\pi^2)$. Neutrinos of

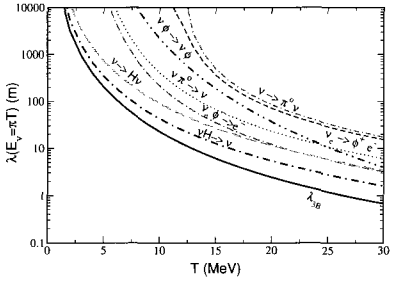

Figure 5. Neutrino mean free path in a CFL meson plasma as a function of temperature. The neutrino energy $E_\nu = \pi T$ and is characteristic of a thermal neutrino.

all energies can absorb a thermal meson and scatter into either a final state neutrino by neutral current processes like $\nu + H \to \nu$ and $\nu + \pi^0 \to \nu$ or via the charged current reaction into a final state electron by the process $\nu_e + \pi^- \to e^-$. They can also emit mesons through processes

like $\nu \rightarrow H + \nu$ and $\nu \rightarrow \pi^0 + \nu$, since the Goldstone modes have space-like dispersion relations. Mean free path due to these processes, which we collectively refer to as Cherenkov processes can be computed[23] and are shown in Fig.5. In contrast to processes involving the emission or absorption of mesons by neutrinos, the usual scattering process involves the coupling of the neutrino current to two mesons is suppressed by the factor p/f_π where p is the meson momentum. The neutrino mean free paths in the CFL phase are very similar to those in the normal quark phase - both numerically and parametrically [23]. It is interesting to note that the existence of one massless mode compensates for the large gap in the particle-hole excitations spectrum. The contrast between the findings of the previous section, where we found a large enhancement in the mean free paths, is striking.

5. Discussion

In the simplest scenario, where rotation, magnetic fields and convection are ignored, the temporal structure of the neutrino emission is directly related to the neutrino mean free path in the inner core of the newly born neutron star. The detection of neutrinos from a galactic supernova in terrestrial detectors such as Super Kamiokande will provide detailed information regarding the temporal structure and motivates theory to address neutrino propagation in hot and dense matter. While there has been some progress in understanding the qualitative aspects of the response of dense matter to neutrinos, reliable quantitative calculations of neutrino mean free paths in dense nuclear and other novel phases of matter are yet to be performed. First principles calculations of the linear response of strongly correlated systems is a difficult problem, with limited success, and a long history in condensed matter, nuclear and particle physics. However, the prospect of probing the phase structure of matter at the most extreme densities through neutrinos from the next galactic supernova is compelling motivation to pursue these efforts. I hope this article has provided a glimpse of the promise and difficulties associated with this enterprise.

6. Acknowledgments

I would like to thank George Bertsch, Greg Carter, Jim Lattimer, Jose Pons, Madappa Prakash, Mariusz Sadzikowski, and Motoi Tachibana for enjoyable collaborations. This work is supported in part by funds provided by the U.S. Department of Energy (D.O.E.) under the D.O.E. contract W-7405-ENG-36.

References

1. R. Buras, et al., Phys. Rev, Lett. **90**, 241101 (2003); A. Mezzacappa et al., Phys. Rev. Lett. **86**, 1935 (2001); Burrows, et al., Astrophys. J. **539**, 865 (2000)
2. A. Burrows, J.M. Lattimer: Astrophys. J. **307**, 178 (1986)
3. M. Prakash, J. M. Lattimer, J. A. Pons, A. W. Steiner and S. Reddy, Lect. Notes Phys. **578**, 364 (2001)
4. A. Burrows, D. Klein and R. Gandhi, Nucl. Phys. Proc. Suppl. **31**, 408 (1993).
5. R. F. Sawyer, Phys. Rev. D **11**, 2740 (1975).
6. N. Iwamoto and C. J. Pethick, Phys. Rev. D **25**, 313 (1982).
7. C.J. Horowitz, K. Wehrberger: Nucl. Phys. A **531**, (1991) 665 ; Phys. Rev. Lett. **66**, 272 (1991); Phys. Lett. B **226**, 236 (1992)
8. G. Raffelt, D. Seckel: Phys. Rev. D **52**, 1780 (1995)
9. S. Reddy, M. Prakash, J.M. Lattimer: Phys. Rev. D **58**, 013009 (1998); S. Reddy, M. Prakash, J.M. Lattimer, J.A. Pons: Phys. Rev. C **59**, 2888 (1999)
10. A. Burrows, R.F. Sawyer: Phys. Rev. C **58**, 554 (1998); A. Burrows, R.F. Sawyer: Phys. Rev. C **59**, 510 (1999)
11. D. G. Ravenhall, C. J. Pethick and J. R. Wilson, Phys. Rev. Lett. **50**, 2066 (1983).
12. D. Z. Freedman, Phys. Rev. D **9**, 1389 (1974).
13. L. B. Leinson, V. N. Oraevsky and V. B. Semikoz, Phys. Lett. B **209**, 80 (1988).
14. J.-P. Hansen, I. R. McDonald and E. L. Pollock, Phys. Rev. D **11**, 1025 (1975)
15. G. Watanabe, K. Sato, K. Yasuoka and T. Ebisuzaki, Phys. Rev. C **68**, 035806 (2003)
16. C. J. Horowitz, M. A. Perez-Garcia and J. Piekarewicz, arXiv:astro-ph/0401079.
17. N. K. Glendenning, Phys. Rev. D **46**, 1274 (1992).
18. S. Reddy, G. Bertsch and M. Prakash, Phys. Lett. B **475**, 1 (2000)
19. B.C. Barrois: Nucl. Phys. B **129**, 390 (1977)
20. M. Alford, K. Rajagopal, F. Wilczek: Phys. Lett. B **422**, 247 (1998) Nucl. Phys. B **357**, 443 (1999) *ibid.* **558**, 219 (1999) R. Rapp, T. Schäffer, E.V. Shuryak, M. Velkovsky: Phys. Rev. Lett. **81**, 53 (1998) Ann. Phys. **280**, 35 (2000)
21. G. W. Carter and S. Reddy, Phys. Rev. D **62**, 103002 (2000)
22. M. G. Alford, K. Rajagopal and F. Wilczek, Nucl. Phys. B **537**, 443 (1999)
23. S. Reddy, M. Sadzikowski and M. Tachibana, Nucl. Phys. A **714**, 337 (2003)
24. P. Jaikumar, M. Prakash and T. Schafer, Phys. Rev. D **66**, 063003 (2002)
25. S. Reddy, M. Sadzikowski and M. Tachibana, Phys. Rev. D **68**, 053010 (2003)

SUPERNOVA EXPLOSIONS AND NEUTRINO BURSTS FROM SUPERNOVAE

KATSUHIKO SATO[1,2], KEITARO TAKAHASHI[1], SHIN'ICHIRO ANDO[1], AND KEI KOTAKE[1]

1) Department of Physics, School of Science, University of Tokyo, Tokyo 113-0033, Japan

2) Research Center for the Early Universe, School of Science, University of Tokyo, Tokyo 113-0033, Japan

E-mail: sato@phys.s.u-tokyo.ac.jp

Supernovae are the most luminous souce of neutrinos in the universe. It was shown that neutrinos have finite masses and convert each other from the solar and atmospheric neutrino observations. The time profile and energy spectrum of neutrino burst from supernovae should be greatly modified by this effect. We review how this conversion happens in a supernova mantle and how the burst will be detected by SK (Super-Kamiokande) and SNO (Sudbury Neutrino Observatory). We show that implications for neutrino parameters (mass hierarchy and the mixing angle between mass eigenstate ν_1, ν_3), are obtained if a supernova appears at Galactic Center. We also discuss effects of neutrino oscillation on the supernova relic neutrino observations. In the end, we discuss the anisotropic neutrino radiation from the rotating stellar cores, which will be important to clarify the explosion mechanism of core collapse supernovae.

1. Introduction

Neutrino mixing and mass spectrum are the keys to probe new physics beyond the standard model of particle physics. Some of the neutrino oscillation parameters have been revealed dramatically by the observation of the atmospheric neutrino [1] and the solar neutrino [2,3]. Recently the first results of the KamLAND experiment have confirmed the Large Mixing Angle (LMA) solution of the solar neutrino problem [4]. An upper bound on θ_{13} has also been obtained from CHOOZ experiment [5] and a lower bound is expected to obtained from single and double beta decay experiments [6]. But there still remain some ambiguities in the properties of neutrinos: the mass hierarchy, i.e., normal or inverted and the magnitude of θ_{13}. Current status is reviewed by many authors [7,8].

In such present situation, much attention have been paid to another

neutrino source, supernova. This is a completely different system from sun, atmosphere, accelerator, and reactor in regard to neutrino energy, flavor of produced neutrinos, propagation length and so forth. Then neutrino emission from a supernova is expected to give valuable information that can not be obtained from neutrinos from other sources. In fact, pioneering observations of neutrinos from SN1987A [9,10] contributed significantly to our knowledge of the fundamental properties of neutrinos [11,12]. Especially there have been many studies about the implication for the mass hierarchy from the observed neutrino events and the inverted hierarchy is disfavored if $\sin^2\theta_{13}$ is rather large ($> 10^{-4}$) [13,14,15]. Here, normal and inverted mass hierarchies are the mass pattern $m_3 \gg m_2 > m_1$ and $m_2 > m_1 \gg m_3$, respectively. In our notation $\Delta m^2_{ij} = m^2_j - m^2_i$, Δm^2_{12} and $\Delta m^2_{13} \sim \Delta m^2_{23}$ are the mass squared differences which are related with the solutions of the solar and atmospheric neutrino problems, respectively. There have also been studies to try to extract the unknown neutrino properties from future supernova [16,17].

In this contribution, we review the neutrino oscillation of supernova neutrino and its implication for neutrino parameters [18,19,20,21] and supernova relic neutrino [22,23].

2. Supernova Neutrino

Here we summarize the properties of supernova neutrino. Almost all of the binding energy of the neutron star,

$$E_{\rm b} \simeq \frac{GM^2_{\rm NS}}{R_{\rm NS}} \simeq 3\times 10^{53}{\rm erg}\left(\frac{M_{\rm NS}}{M_\odot}\right)^2\left(\frac{10{\rm km}}{R_{\rm NS}}\right), \qquad (1)$$

is radiated away as neutrinos. Here G, $M_{\rm NS}$ and $R_{\rm NS}$ are the gravitational constant, the mass and radius of the neutron star, respectively. Due to the difference of interaction strength, average energies are different between flavors. Although quantitative estimate of the difference is difficult, it is qualitatively true that $\langle E_{\nu_e}\rangle < \langle E_{\bar{\nu}_e}\rangle < \langle E_{\nu_x}\rangle$. Here ν_x means ν_μ, ν_τ and their antineutrinos. These differences are essential in this paper.

We use a realistic model of a collapse-driven supernova by the Lawrence Livermore group[24] to calculate the neutrino luminosities and energy spectra. The average energy of each flavor is:

$$\langle E_{\nu_e}\rangle \simeq 13{\rm MeV},\ \ \langle E_{\bar{\nu}_e}\rangle \simeq 16{\rm MeV},\ \ \langle E_{\nu_x}\rangle \simeq 23{\rm MeV}. \qquad (2)$$

Details of this original neutrino spectra are discussed by Totani et al. [25] These neutrinos, which are produced in the high dense region of the iron

core, interact with matter before emerging from the supernova. Due to the nonzero masses and the mixing in vacuum among various neutrino flavors, flavor conversions can occur in supernova. When the mixing angle is small, these conversions occur mainly in the resonance layer, where the density is

$$\rho_{\rm res} \simeq 1.4 \times 10^6 {\rm g/cc} \left(\frac{\Delta m^2}{1{\rm eV}^2}\right) \left(\frac{10{\rm MeV}}{E_\nu}\right) \left(\frac{0.5}{Y_e}\right) \cos 2\theta, \tag{3}$$

where Δm^2 is the mass squared difference, θ is the mixing angle, E_ν is the neutrino energy, and Y_e is the mean number of electrons per baryon. Since the supernova core is dense enough, there are two resonance points in supernova envelope. One that occurs at higher density is called H-resonance and another is called L-resonance. If the mass hierarchy is normal, both resonances occur in neutrino sector. On the other hand, if the mass hierarchy is inverted, H-resonance occurs in antineutrino sector and L-resonance occurs in neutrino sector.

The dynamics of conversions including large mixing case is determined by the adiabaticity parameter γ, which depend on the mixing angle and the mass-squared difference between involved flavors: θ_{13} and Δm^2_{13} at H-resonance, θ_{12} and Δm^2_{12} at L-resonance. When $\gamma \gg 1$, the resonance is called 'adiabatic resonance' and the fluxes of the two involved mass eigenstate are completely exchanged. On the contrary, when $\gamma \ll 1$, the resonance is called 'nonadiabatic resonance' and the conversion does not occur. The dynamics of the resonance in supernova is studied in detail by Dighe and Smirnov [26].

3. Implication for neutrino parameters from supernova neutrino

3.1. *Neutrino oscillation in supernova*

In the framework of three-flavor neutrino oscillation, the time evolution equation of the neutrino wave functions can be written as follows:

$$i\frac{d}{dt}\begin{pmatrix}\nu_e\\ \nu_\mu\\ \nu_\tau\end{pmatrix} = H(t)\begin{pmatrix}\nu_e\\ \nu_\mu\\ \nu_\tau\end{pmatrix}, \tag{4}$$

$$H(t) \equiv U\begin{pmatrix}0 & 0 & 0\\ 0 & \Delta m^2_{12}/2E_\nu & 0\\ 0 & 0 & \Delta m^2_{13}/2E_\nu\end{pmatrix}U^{-1} + \begin{pmatrix}A(t) & 0 & 0\\ 0 & 0 & 0\\ 0 & 0 & 0\end{pmatrix}, \tag{5}$$

where $A(t) = \sqrt{2} G_F n_e(t)$, G_F is Fermi constant, $n_e(t)$ is the electron number density, and Δm^2_{ij} is the mass squared differences. In case of antineutrino, the sign of $A(t)$ changes. Here U is the Cabibbo-Kobayashi-Maskawa (CKM) matrix:

$$U = \begin{pmatrix} c_{12}c_{13} & s_{12}c_{13} & s_{13} \\ -s_{12}c_{23} - c_{12}s_{23}s_{13} & c_{12}c_{23} - s_{12}s_{23}s_{13} & s_{23}c_{13} \\ s_{12}s_{23} - c_{12}c_{23}s_{13} & -c_{12}s_{23} - s_{12}c_{23}s_{13} & c_{23}c_{13} \end{pmatrix}, \qquad (6)$$

where $s_{ij} = \sin\theta_{ij}, c_{ij} = \cos\theta_{ij}$ for $i, j = 1, 2, 3 (i < j)$. We have here put the CP phase equal to zero in the CKM matrix.

By solving numerically these equations along the density profile of progenitor, which is calculated by Woosley and Weaver[27], we obtain conversion probabilities $P(\alpha \to \beta)$, i.e., probability that ν_α at the center of the supernova becomes ν_β at the surface of the progenitor star.

Here we take the following values:

$$\begin{aligned} \sin^2 2\theta_{12} &= 0.84, \quad & \Delta m^2_{12} &= 7 \times 10^{-5}\mathrm{eV}^2, \\ \sin^2 2\theta_{23} &= 1.0, \quad & \Delta m^2_{23} &= 3.2 \times 10^{-3}\mathrm{eV}^2. \end{aligned} \qquad (7)$$

Values of θ_{12} and Δm^2_{12} are taken from the global analysis of the solar neutrino observations and the KamLAND experiment[28] and correspond to the LMA solution of the solar neutrino problem while those of θ_{23} and Δm^2_{23} are taken from the analysis of the atmospheric neutrino observation[1]. As to θ_{13}, we take two fiducial values $\sin^2 2\theta_{13} = 0.043,\ 10^{-6}$. Later we will discuss the case of the other values. Furthermore, we consider both normal and inverted hierarchy. Consequently, there are four models and we call them normal-LMA-L, normal-LMA-S, inverted-LMA-L and inverted-LMA-S. The last character (L or S) represents the magnitude of θ_{13} (large or small).

After obtaining the conversion probabilities, the neutrino fluxes at the Earth are calculated by multiplying the conversion probabilities by the original spectra and the distance factor $1/4\pi d^2$. Here we take 10 kpc for the distance d between the Earth and the supernova. Further, by multiplying these fluxes by the cross sections of the detection interactions, the detector volume and the detector efficiency, we obtain the event rates at the detectors. Here we consider two detectors: SuperKamiokande (SK) and SNO. Properties of these detectors and cross sections used to calculate event rates are described in Ref. [18]. Unfortunate accident at SK lessened the detection efficiency at low energy (< 8 MeV) but this cause negligible effect in the subsequent analysis.

Fig. 1 - 3 show the time-integrated energy spectra (left) and the time evolution of the number of neutrino events (right) at SK and SNO (ν_e charged current (CC) events and $\bar{\nu}_e$ CC events), respectively. In Fig. 1, only $\bar{\nu}_e p$ CC interaction is taken into account.

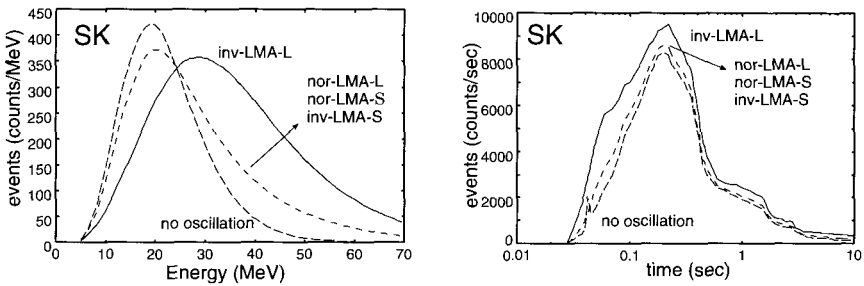

Figure 1. The time-integrated energy spectra (left) and the time evolution of the number of neutrino events (right) at SK. In these figures, only $\bar{\nu}_e p$ CC interaction is taken into account.

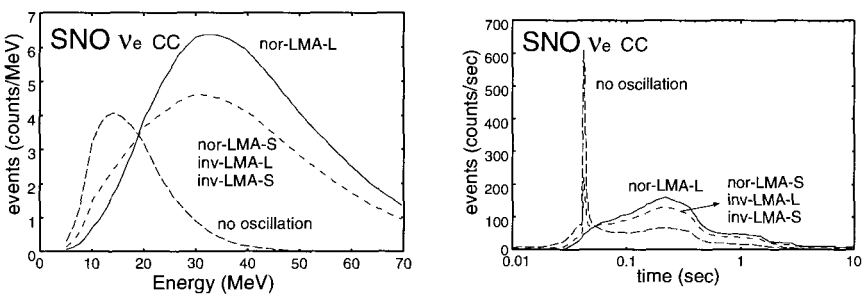

Figure 2. The time-integrated energy spectra (left) and the time evolution of the number of neutrino events (right) at SNO. In these figures, only $\nu_e d$ CC interaction is taken into account.

3.2. *Distinction between models*

In general neutrino oscillation makes the ν_e and $\bar{\nu}_e$ spectra harder, since the original average energies of ν_e and $\bar{\nu}_e$ are smaller than that of ν_x. In other words neutrino oscillation produces high energy ν_e and $\bar{\nu}_e$ from ν_x. As a result, the high-energy events increase and the low-energy events decrease. The boundary between high energy and low energy is around 20 MeV. Note

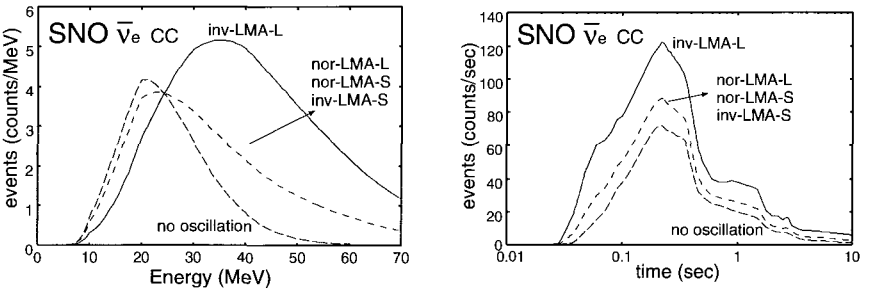

Figure 3. The time-integrated energy spectra (left) and the time evolution of the number of neutrino events (right) at SNO. In these figures, only $\bar{\nu}_e d$ CC interaction is taken into account.

that how much these increase and decrease are depends on the adiabaticity parameters, and then the neutrino oscillation parameters, as can be seen in Fig. 1, 2 and 3. This feature can be used as a criterion of the magnitude of the neutrino oscillation effects. We define the following ratios of high-energy to low-energy events at both detectors:

$$R_{\rm SK} \equiv \frac{\text{number of events at } 20 < E < 70\text{MeV}}{\text{number of events at } 5 < E < 20\text{MeV}}, \tag{8}$$

$$R_{\rm SNO} \equiv \frac{\text{number of events at } 20 < E < 70\text{MeV}}{\text{number of events at } 5 < E < 20\text{MeV}}. \tag{9}$$

The plots of $R_{\rm SK}$ vs $R_{\rm SNO}$ are shown in Fig. 4. In the left figure, we consider only $\nu_e d$ CC events at SNO for $R_{\rm SNO}$ assuming $\nu_e d$ CC event and $\bar{\nu}_e d$ CC event can be distinguished completely. On the other hand, in the right figure we assume that $\nu_e d$ CC event and $\bar{\nu}_e d$ CC event can not be distinguished at all and we sum $\nu_e d$ CC events and $\bar{\nu}_e d$ CC events for $R_{\rm SNO}$. The error bars represent the statistical errors.

Note that ν_e flux and $\bar{\nu}_e$ flux have essentially different information about the neutrino oscillation parameters. For example, inverted-LMA-L and inverted-LMA-S are distinguishable from $\bar{\nu}_e$ events but are not from ν_e events. So it is more effective to distinguish between models if $\nu_e d$ CC events and $\bar{\nu}_e d$ CC events at SNO can be distinguished perfectly. This can be clearly seen in Fig. 4. In the left figure it is easier to distinguish between normal-LMA-L and (normal-LMA-S and inverted-LMA-S) than in the right figure. But even in the left figure, it may be difficult to distinguish between normal-LMA-L and (normal-LMA-S and inverted-LMA-S) considering some ambiguities discussed in the following sections.

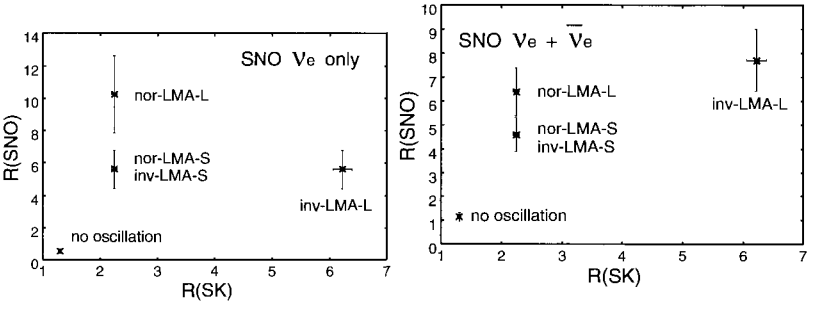

Figure 4. Plots of $R_{\rm SK}$ vs $R_{\rm SNO}$. In the left figure, only $\nu_e d$ CC events at SNO are considered for $R_{\rm SNO}$. In the right figure we sum $\nu_e d$ CC events and $\bar{\nu}_e d$ CC events to calculate $R_{\rm SNO}$. The errorbars show statistical errors only.

3.3. *Uncertainty of the progenitor star*

It affects the mass of the iron core, which affects the neutrino spectra [30,31,32]. Study including the mass uncertainty is now in progress but the preliminary result is that the mass uncertainty is not important in our analysis [33]. Fig. 5 shows the progenitor mass dependence of the event ratio at SNO and SK. Here events only 0.2 sec after bounce are considered.

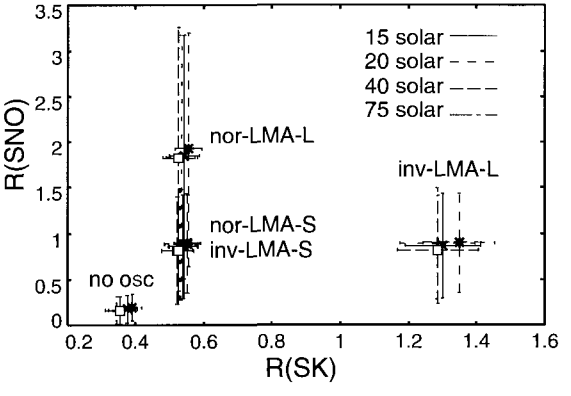

Figure 5. Progenitor mass dependence of the event ratio at SNO and SK. Events only 0.2 sec after bounce are considered.

4. Supernova Relic Neutrinos and Neutrino Oscillation

4.1. *The detectability*

It is generally believed that the core-collapse supernova explosions have traced the star formation history in the universe and have emitted a great number of neutrinos, which should make a diffuse background. This supernova relic neutrino (SRN) background is one of the targets of the currently working large neutrino detectors, SK and SNO. Comparing the predicted SRN spectrum with the observations by these detectors provides us potentially valuable information on the nature of neutrinos as well as the star formation history in the universe. This SRN background has been discussed in a number of previous papers.[34,35,36,37,38,39,40,41,42,43,22,23]

Ando et al.[22] calculated SRN flux and the event rate at SK, and discussed the detectability of SRN, with the following new aspects compared with previous studies: (1) Realistic neutrino oscillation parameters are incorporated based on the recent solar and atmospheric neutrino experiments, (2) a realistic neutrino spectrum from one supernova explosion is used, which is obtained from a numerical simulation by the Lawrence Livermore group, [25] and (3) we have examined other contaminating background events against the detection of SRN, in more detail than previous studies.

The SRN flux can be calculated by the formula

$$\frac{\mathrm{d}F_\nu}{\mathrm{d}E_\nu} = c\int_0^{z_{\max}} R_{\mathrm{SN}}(z)\frac{\mathrm{d}N_\nu(E'_\nu)}{\mathrm{d}E'_\nu}(1+z)\frac{\mathrm{d}t}{\mathrm{d}z}\mathrm{d}z, \tag{10}$$

where $E'_\nu = (1+z)E_\nu$, $R_{\mathrm{SN}}(z)$ is supernova rate per comoving volume at redshift z, $\mathrm{d}N_\nu/\mathrm{d}E_\nu$ energy spectrum of emitted neutrinos, $z_{\max}$ the redshift when the gravitational collapses began, which we assumed to be 5. As supernova rate, we use the most reasonable model to date, which is based on the rest-frame UV observation of star formation history in the universe by Hubble Space Telescope (model "SF1" in Ref. [44]).

In Fig. 6, we show the calculated SRN flux for no oscillation model, and in Fig. 7 the expected event rate at SK detector for both no oscillation and LMA model. Above $\sim$ 10 MeV, we expect more event rate for the LMA model, because $\bar{\nu}_{\mu,\tau}$'s which have higher average energy at production have more changed into $\bar{\nu}_e$'s. We show in Table 1, the integrated flux over the entire neutrino energy range and event rate at SK integrated for detection energy range $17 < (T_e/\mathrm{MeV}) < 25$ (the reason why this range is selected for detection is given below).

There are several background events which hinder the detection of SRN. These includes atmospheric and solar neutrinos, anti-neutrinos from nuclear

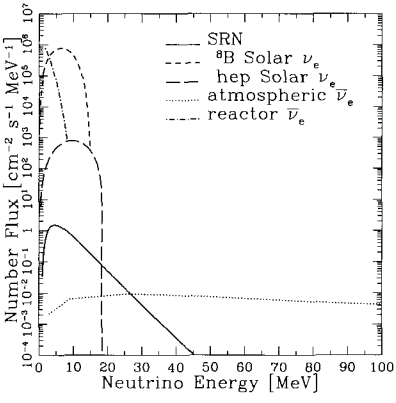

Figure 6. Number flux of SRN compared to other background neutrinos. No oscillation model is assumed for SRN flux.

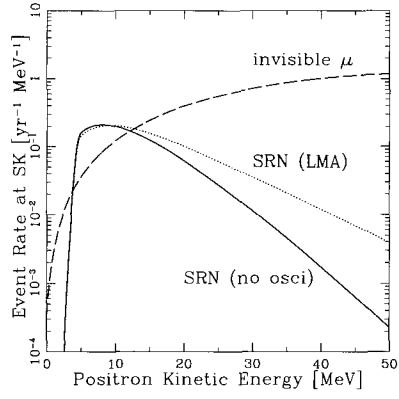

Figure 7. Event rate at SK detector of SRN and invisible μ decay products. Two oscillation models are shown (no oscillation and LMA)

Model	Flux	Event rate for $17 < (T_e/\mathrm{MeV}) < 25$
No oscillation	11.9 cm^{-2} s^{-1}	0.44 yr^{-1}
LMA	11.2 cm^{-2} s^{-1}	0.73 yr^{-1}

reactors, spallation products, and decay electrons from invisible muons. We should find the energy region which is not contaminated by these background events and then calculate the detectable event rate of SRN. By careful examination of these events, we found that there is a narrow energy window from 19 MeV to 27 MeV, which is free from solar, atmospheric, and reactor neutrinos (see Fig. 6). (Although the solar neutrino events can be avoided owing to the directional analysis are,there are also another serious background due to spallation products below 16 MeV. See Ref. [22] for details.)

However, it is known that, for water Čherenkov detector, electrons or positrons from invisible muons are the largest background in the energy window. This invisible muon event is illustrated as follows. The atmospheric neutrinos produce muons by interaction with the nucleons (both free and bound) in the fiducial volume. If these muons are produced with energies below Čherenkov radiation threshold (kinetic energy less than 53 MeV), then they will not be detected ("invisible muons"), but their decay-produced electrons and positrons will be. Since the muon decay signal will

mimic the $\bar{\nu}_e p \to n e^+$ process in SK, it is difficult to distinguish SRN from these events. In Fig. 7, SRN event rate is compared with the invisible muon events.

Thus, it appears there is no energy window of SRN, but still we can detect the SRN events by statistical analysis with the other background events. Consider the energy range $17 < (T_e/\mathrm{MeV}) < 25$. This range corresponds to $19 < (E_{\bar{\nu}_e}/\mathrm{MeV}) < 27$ by a simple relation, $E_{\bar{\nu}_e} = T_e + 1.8\mathrm{MeV}$. There are two advantages in using this energy region. First, SRN event rate is rather large, and second, the background (invisible muon) event rate is fairly well known by SK observation. The SRN event rate at SK in this energy range is $0.4 - 0.7\ \mathrm{yr}^{-1}$ (Table 1), in contrast, the event rate of the invisible muon over the same energy range is $3.4\ \mathrm{yr}^{-1}$. When SRN event rate is larger than the statistical error of background event rate, we can conclude that the SRN is detectable as a distortion of the expected invisible muon background event. Unfortunately, only one year observation does not provide any useful information about SRN, however, we can expect that ten-year observation provides several statistically meaningful results. The statistical error of invisible muon events in ten years is $\sqrt{34} = 5.8$, which is smaller than the event rate of the LMA model. In consequence, although there is no energy window, in which the SRN signal is the largest, the statistically meaningful SRN signals might be detected using the data for ten years or so.

4.2. *Implications of recent observational results*

Recently (September 2002), SK collaboration set very severe constraint on the SRN flux,[45] which is only factor three larger than typical theoretical predictions. For example, while Ando et al.[22] predicted that the total SRN flux integrated over entire energy was $11\ \mathrm{cm}^{-2}\ \mathrm{s}^{-1}$, the corresponding SK limit is $31\ \mathrm{cm}^{-2}\ \mathrm{s}^{-1}$. Since the theoretical calculations contain many ambiguities such as the supernova rate in the universe and neutrino spectrum from each supernova, this severe observational SRN limit can provide a number of valuable information on the various fields in astrophysics and cosmology. Further, in the near future, it is expected that the upper limit will be much lower (about factor 3) when the current SK data of 1496 days are reanalyzed using some technique to reduce invisible muon background.[46]

Thus, it is obviously important and very urgent to give a prediction for the SRN flux with the oscillation parameters, which has not been

considered; while in the previous subsection we gave the prediction with LMA parameters in the case of normal mass hierarchy, here we also include the case of inverted mass hierarchy, which is not ruled out at all. Note that in that case, the resonance also occurs in antineutrino sector, and it is expected that the SRN spectrum would be quite different from that in the case of normal mass hierarchy. From this point on, we use four parameter sets, named as NOR-S, NOR-L, INV-S, and INV-L, where NOR and INV represent the normal and inverted mass hierarchy respectively, and the suffixes -L and -S attached to NOR and INV stand for large (0.04) and small (10^{-6}) values for $\sin^2 2\theta_{13}$, respectively. Further, when we calculate the neutrino conversion probability in supernova, we adopt the realistic *time-dependent* density and Y_e profiles, which are calculated by the Lawrence Livermore group. [47] This is because during the neutrino burst ($\sim$ 10 sec), the shock wave propagating the supernova matter changes density profile dramatically, and it is expected to affect the adiabaticity of resonance points. In addition, we also include the Earth matter effect, which was neglected in almost all the past publications including Ref. [22].

Figure 8 shows SRN flux for the various oscillation models; the case of no oscillation is also shown for comparison. We also repeated discussions given in the SK paper[45] and obtained the 90% C.L. upper limit for the various SRN fluxes; the results of the calculation is summarized in Table 2. The upper limit is more severe for the INV-L model. However, since theoretical predictions contain many uncertainties, we cannot trust the values given in Table 2 without any doubt. More detailed discussions are given in Ref. [23].

Model	Predicted flux	SK limit (90% C.L.)	Prediction/Limit
NOR-S	12 cm^{-2} s^{-1}	< 35 cm^{-2} s^{-1}	0.34
NOR-L	11 cm^{-2} s^{-1}	< 34 cm^{-2} s^{-1}	0.33
INV-S	11 cm^{-2} s^{-1}	< 34 cm^{-2} s^{-1}	0.33
INV-L	9.0 cm^{-2} s^{-1}	< 12 cm^{-2} s^{-1}	0.74
No oscillation	12 cm^{-2} s^{-1}	< 73 cm^{-2} s^{-1}	0.17

5. Anisotropic neutrino radiation in rotational core collapse

The study of core collapse supernovae is important not only for itself but also for the understanding of astrophysical relevance, such as radiations of neutrinos, as we have stated in the preceding sections, and gravitational

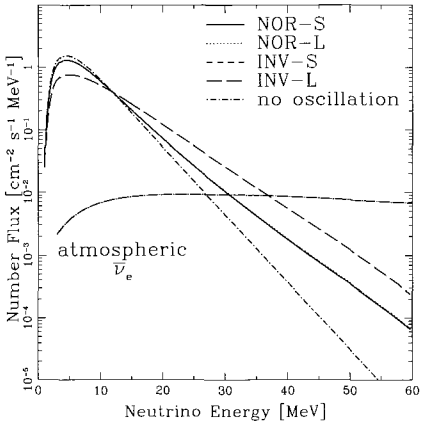

Figure 8. Number flux of SRN for various neutrino oscillation models. The spectra for NOR-S, NOR-L, and INV-S are degenerated, while that for INV-L is the hardest one. The flux of atmospheric $\bar{\nu}_e$ is also shown.

waves [48,49], nucleosynthesis of heavy elements and chemical evolutions in the universe, and possibly gamma-ray bursts as well as hypernovae [50]. In spite of its importance and extensive investigations done so far, the explosion mechanism has not been clarified yet.

Except for special cases, the shock wave generated by core bounce stalls and becomes an accreting shock in the core. Although neutrino heatings are expected to revive the shock wave and lead to successful explosions, recent theoretical studies with elaborate neutrino transport methods and detailed microphysics and/or general relativity failed to produce explosions [51,52,53,54]. However, it should be noted that most of them assume spherical symmetry (see, however, [54]).

On the other hand, there are convincing observations, which require the revision of the spherically symmetric stellar collapse. Rather common correlation between the asymmetry and the collapse-driven supernovae has been reported by the observation of polarization [55]. It is also well known that SN 1987A is globally asymmetric [56,57], which is directly confirmed by images of *Hubble Space Telescope (HST)* [58]. Provided the facts that the progenitors of collapse-driven supernovae are a rapid rotator on the main sequence [59] and that the recent theoretical studies suggest a fast rotating core prior to the collapse [60], it is important to incorporate rotations in simulations of core collapse. So far there have been some works devoted to

the understanding of the effect of rotation upon the supernova explosion mechanism [63]. It seems clear that the rotation does not good to the prompt shock propagation. This is simply because the centrifugal force tends to halt the core collapse, which then reduces the conversion of the gravitational energy to the kinetic energy. Here we pay attention to the effect of rotation on the neutrino heating mechanism. Shimizu et al. [62] demonstrated that anisotropic neutrino radiations induced by rotation may be able to enhance local heating rates near the rotational axis and trigger globally asymmetric explosions. The required anisotropy of neutrino luminosity appears to be not very large ($\sim$ 3%). It is important to note that this mechanism is effective only when the explosion does not occur in spherical symmetry. Fryer & Heger [61] found in their two-dimensional SPH simulations little effect of neutrino anisotropy on the explosions. This is probably because their models explode even without rotation.

In the work of Shimizu et al. [62], the anisotropy of neutrino heatings was given just by hand and the rotation was not taken into account either. Recently Kotake et al [66] investigated how large the anisotropy of neutrino radiation could be, based on the rotational core collapse simulations from the onset of gravitational collapse of the core through the core bounce to the shock-stall.

In the left panel of Figure 9, the neutrino spheres for the spherical and rotating model are shown. It is clearly seen from the comparison with the spherical model that the the neutrino spheres are indeed deformed. For the rotating model, it is found that the neutrino sphere forms deeper inside at the pole than in the spherical model. This is a result of the fact that the density is lower on the rotational axis in the rotation models than in the spherical model because the matter tends to move away from the axis due to the centrifugal force. The above features are also true for the slow and rapid rotation models. Furthermore, the configurations are more deformed from slow to rapid rotation models due to stronger centrifugal forces.

The neutrino temperature profile on the neutrino sphere for the moderate rotation models are presented in the right panel Figure 9. Here it is assumed that the neutrino temperature is identical to that of the matter. It is seen from the figure that the temperature varies with the polar angle. The neutrino temperature is higher at the pole for the rotating model than for the spherical model. This can be understood from the fact that the neutrino sphere is formed deeper inside for rotational models than for the spherical case, as already mentioned.

From the above facts, it is a natural consequence that the neutrino radiation becomes anisotropic.

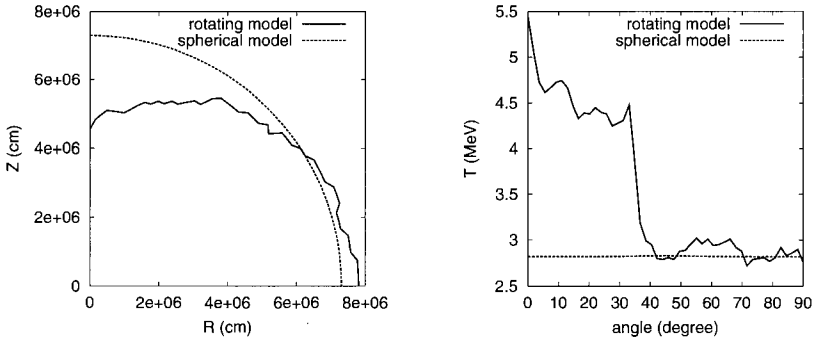

Figure 9. Shapes of neutrino sphere (left panel), neutrino temperature vs. polar angle on the neutrino sphere (right panel) in the rotating model and the spherical model.

In Figure 10, we show the contour plots of the heating rate for the spherical (left panel) and the rotating model (right panel). It is clearly seen from the right panel of the figure (the rotating model) that the neutrino heating occurs anisotropically and is strong along the rotational axis. This is mainly because the neutrino temperatures at the rotational axis are higher than on the equatorial plane. It should be mentioned that in the vicinity of the neutrino sphere, the heating rate around the rotational axis are enhanced up to about one order of magnitude in the rotating model from that in the spherical model (see Figure 10), which will help launch the jet in that direction further. The outcome will be a jet-like explosion considered in [62]. It should be mentioned that the jet like explosion plays important roles in the nucleosynthesis of heavy elements [64,65]. Note, however, too fast a rotation might lead to a very quick stagnation of the shock wave near the rotational axis and the net heating region may not emerge in the first place. Then the outcome will be a rotating black hole and yield gamma-ray bursts later. In order to confirm the above scenarios, it is necessary to include more elaborate transport for all neutrino species in our calculations, which is currently undertaken [67].

Acknowledgments

We would like to thank Y.Totsuka, Y.Suzuki, T.Kajita, M. Nakahata and Y.Fukuda for valuable discussion on the neutrino oscillation analysis and the observation on supernova relic neutrinos at SuperKamiokande. We also

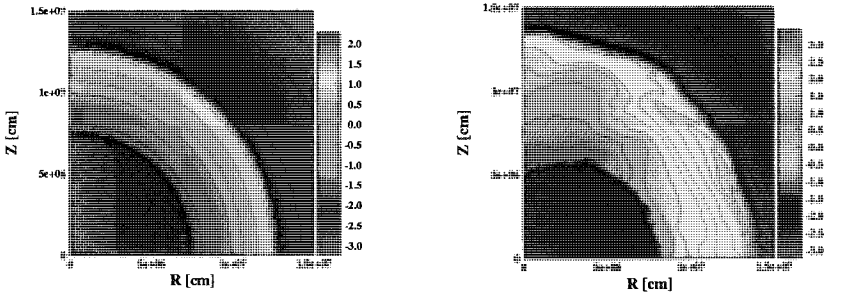

Figure 10. The heating rates outside the neutrino sphere for the spherical model (left panel) and the rotating model (right panel). The figures show color-coded contour plots for the logarithm of the heating rate Q_ν^+ (MeV/ nucleon · s). The neutrino sphere and the stalled shock are seen as thick lines separating bright color from dark color region. Note that the value within the neutrino sphere is artificially modified to dark colors and has no physical meanings.

want to acknowledge T. A. Thompson, A. Burrows, J. R. Wilson and H. E. Dalhed for the neutrino emission data from the supernova explosion. Some parts of this proceedings are based on the collaboration with them. This contribution is also indebted to S. Yamada for valuable discussions and his indispensable assistant to the numerical methods in section 5. This research was supported in part by Grant-in-Aid for Scientific Research provided by the Ministry of Education, Science and Culture of Japan through Research Grant (s) No.S14102004,Grant-in-Aid for Scientific Research on priority Areas No.14079202. K.T and S.A.'s works are supported by Grant-in-Aid for JSPS Fellows.

References

1. Y. Fukuda et al., Phys. Rev. Lett. 82 (1999) 2644.
2. S. Fukuda et al., Phys. Rev. Lett. **86** (2001) 5656.
3. SNO Collaboration, Phys. Rev. Lett. **87** (2001) 071301, Phys. Rev. Lett. **89** (2002) 011302.
4. KamLAND Collaboration, K. Eguchi et al., Phys. Rev. Lett. **90** (2003) 021802.
5. M. Apollonio et al., Phys. Lett. B **466** (1999) 415.
6. H. Minakata and H. Sugiyama, Phys. Lett. B **526** (2002) 335.
7. G. G. Raffelt, astro-ph/0302589.
8. S. M. Bilenky, C. Giunti, J. A. Grifols and E. Massó, Phys. Rept. **379** (2003) 69.
9. K. Hirata et al., Phys. Rev. Lett. **58**, 1490 (1987).
10. R. M. Bionta et al., Phys. Rev. Lett. **58**, 1494 (1987).
11. J. Arafune and M. Fukugita, Phys. Rev. Lett. **59**, 367 (1987).

12. K. Sato and H. Suzuki, Phys. Rev. Lett. **58**, 2722 (1987).
13. B. Jegerlehner, F. Neubig and G. Raffelt, Phys. Rev. D **54** (1996) 1194.
14. C. Lunardini and A. Yu. Smirnov, Phys. Rev. D **63** (2001) 073009.
15. H. Minakata and H. Nunokawa, Phys. Lett. B **504** 301 (2001).
16. C. Lunardini and A. Yu. Smirnov, JCAP **06** (2003) 009.
17. A. S. Dighe, M. Th. Keil and G. G. Raffelt, hep-ph/0303210.
18. K. Takahashi, M. Watanabe, K. Sato and T. Totani, Phys. Rev. D **64** (2001) 093004.
19. K. Takahashi and K. Sato, Prog.Theor. Phys. **109** (2003) 919.
20. K. Takahashi and K. Sato, Phys. Rev. D **66** (2002) 033006.
21. K. Takahashi, M. Watanabe and K. Sato, Phys. Lett. B **510** (2001) 189.
22. S. Ando, K. Sato, and T. Totani, Astropart. Phys. **18** (2003) 307.
23. S. Ando and K. Sato, Phys. Lett. **B559** (2003) 113.
24. J. R. Wilson, R. Mayle, S. Woosley, T. Weaver, Ann. NY Acad. Sci. **470**, 267 (1986).
25. T. Totani, K. Sato, H. E. Dalhed and J. R. Wilson, Astrophys. J. **496** (1998) 216.
26. A. S. Dighe and A. Yu. Smirnov, Phys. Rev. D **62** (2000) 033007.
27. S. E. Woosley and T. A. Weaver, ApJ. Suppl. **101** (1995) 181.
28. J. N. Bahcall, M. C. Gonzalez-Garcia and C. Pena-Garay, JHEP **02** (2003) 009.
29. H. -T. Janka, R. Buras, K. Kifonidis, T. Plewa and M. Rampp, in *Core Collapse of Massive Stars*, edited by C. L. Fryer (Kluwer Academic Publ., Dordrecht, 2003), astro-ph/0212314; G. G. Raffelt, M. Th. Keil, R. Buras, H. -T. Janka and M. Rampp, Proc. NOON 03 (10-14 February 2003, Kanazawa, Japan), astro-ph/0303226; R. Buras, M. Rampp, H. -T. Janka and K. Kifonidis, astro-ph/0303171.
30. T. A. Thompson, A. Burrows, P. A. Pinto, astro-ph/0211194.
31. R. Mayle, Ph. D. Thesis, University of California (1987).
32. R. Mayle, J. R. Wilson, and D. N. Schramm, Astrophys. J. **318** (1987) 288.
33. K. Takahashi, K. Sato, T. A. Thompson and A. Burrows, Phys. Rev **D68** (2003) 113009.
34. G.S. Bisnovatyi-Kogan, S.F. Seidov, Ann. N.Y. Acad. Sci. **422** (1984) 319.
35. L.M. Krauss, S.L. Glashow, D.N. Schramm, Nature **310** (1984) 191.
36. S.E. Woosley, J.R. Wilson, and R. Mayle, Astrophys. J. **302** (1986) 19.
37. K.S. Hirata (1991) PhD theses, University of Tokyo.
38. Y. Totsuka, Rep. Prog. Phys. **55** (1992) 377.
39. T. Totani and K. Sato, Astropart. Phys. **3** (1995) 367.
40. T. Totani, K. Sato, and Y. Yoshii, Astrophys. J. **460** (1996) 303.
41. R.A. Malaney, Astropart. Phys. **7** (1997) 125.
42. D.H. Hartmann and S.E. Woosley, Astropart. Phys. **7** (1997) 137.
43. M. Kaplinghat, G. Steigman and T.P. Walker, Phys. Rev. **D62** (2000) 043001.
44. C. Porciani and P. Madau, Astrophys. J. **548** (2001) 522.
45. M. Malek et al. (The Super-Kamiokande Collaboration), Phys. Rev. Lett. **90** (2003) 061101.

46. Y. Suzuki, private communication.
47. K. Takahashi, K. Sato, H.E. Dalhed and J.R. Wilson, astro-ph/0212195.
48. N. Andersson, Class. Quant. Grav. **20** (2003) R105.
49. K. Kotake, S. Yamada, and K. Sato, Phys. Rev. D. **68** (2003) 44023.
50. A.I. MacFadyen and S.E. Woosley, Astrophys. J. **524** (1999) 262.
51. M. Rampp and H.-T. Janka, Astrophys. J. Lett. **539** (2000) L33.
52. M. Liebendörfer, A. Mezzacappa, F.-K. Thilemann, O.E.B. Messer, W.R. Hix, and S.W. Bruenn, Phys. Rev. Lett. **63** (2001) 103004.
53. T.A. Thompson, A. Burrows, and P.A. Pinto, Astrophys. J. **592** (2003) 434.
54. R. Buras, M. Rampp, H.-T. Janka, and K. Kifonidis, Phys. Rev. Lett. **90** (2003) 241101.
55. L. Wang et al. Astrophys. J. **579** (2002) 671.
56. M. Cropper et al. Mon. Not. R. Astron. Soc. **231** (1988) 695.
57. C. Papaliolis et al. Nature **338** (1989) 13.
58. P.C. Plait et al. Astrophys. J. **439** (1995) 730.
59. J.L. Tassoul 1978, Theory of Rotating Stars (Princeton: Princeton Univ. Press).
60. A. Heger, N. Langer, and S.E. Woosley Astrophy. J. **528** (2000) 368.
61. C.L. Fryer and A. Heger, Astrophys. J. **541** (2000) 1033.
62. T.M. Shimizu, T. Ebisuzaki, K. Sato, and S. Yamada, Astrophys. J. **552** (2001) 756.
63. E. Müller and W. Hillebrandt, Astron. Astrophys. **103** (1981) 358, R. Mönchmeyer, G. Schäfer, E. Müller, and R.E. Kates, Astron. Astrophys. **246** (1991) 417, S. Yamada and K. Sato, Astrophy. J. **434** (1994) 268, C.L. Fryer and A. Heger, Astrophys. J. **541** (2000) 1033, E. Symbalisty, Astrophys. J. **360** (1984) 242.
64. S. Nagataki, M. Hashimoto, K. Sato, and S. Yamada, Astrophy. J. **486** (1997) 1026.
65. S. Nagataki, Astrophys. J. Suppl. **127** (2000) 141.
66. K. Kotake, S. Yamada, and K. Sato, Astrophys. J. 595 (2003) 304.
67. K. Kotake, N. Ohnishi, S. Yamada and K. Sato, Astrophys. J. to be published.